Topographic Organization of the Human Insular Cortex and Subcortex in Health and Neuropsychiatric Illness

Ye Tian

orcid.org/0000-0003-3107-5550

DOCTOR OF PHILOSOPHY

May 2020

Melbourne Neuropsychiatry Centre, Department of Psychiatry

Faulty of Medicine, Dentistry and Health Science

The University of Melbourne

Thesis submitted in total fulfilment of the requirement of the degree of Doctor of Philosophy

Abstract

The structure, function and connectivity of the human brain are topographically organized. This topographic organization provides profound insight into cortical information processing, representation of mental states, and accounts for individual variation in behavioral traits and cognition. Whereas classical models of brain topography focus on distinct cortical patches defined by discrete boundaries, contemporary evidence from neuroimaging suggests that topographic variation may be better conceptualized in terms of a set of continuous gradients of gradual change that overlap in space. My work aims to reconcile these two conceptualizations of brain topography, particularly with respect to the insular cortex, a topographically complex and functionally heterogeneous cortical lobe whose organization has remained disputed for centuries.

Using modern functional neuroimaging techniques, I showed that the insula's topography is best conceptualized as a continuum of gradual change oriented along an anterior-posterior axis. I found that individual variation in the insula's functional topography associates with human cognitive and emotional traits as well as somatosensory functions.

Having characterized the functional architecture of the insular cortex in healthy adults, my next aim was to investigate whether neuropsychiatric illness is associated with alterations in the insula's functional organization. To this end, I compared the insula's functional connectivity gradients between individuals with schizophrenia and healthy controls. I found evidence suggesting subtle reorganization of the insula's functional topography in schizophrenia. In particular, the connectivity profile along the anterior-posterior topographic axis of the insular cortex was altered and less differentiated in individuals with schizophrenia. I showed that the extent of reorganization of the insula's functional topography significantly associates with the severity of clinical symptoms, particularly negative symptoms of psychosis and intellectual impairment.

Finally, I applied the new methodology that I developed to map the insula's topography to study other brain regions, including the entire human subcortex. This unveiled four hierarchical scales of subcortical organization, recapitulating well-known anatomical nuclei at

the coarsest scale and delineating 27 new bilateral regions at the finest. Based on this work, I developed a new MRI subcortical atlas to enable holistic connectome mapping and characterization of cortico-subcortical circuits. The new subcortex atlas was personalized to account for connectivity differences across individuals and utilized to uncover a reproducible association between subcortical functional connectivity and tobacco use.

Overall, this thesis provides fundamental insight into the functional organization of the human insular cortex and subcortex in health and neuropsychiatric illness, particularly focusing on the distinction between classical models of topographic variation based on discrete regions and contemporary representations involving continuous gradients. The new methodology that I developed is not limited to the insular cortex and the subcortex and can be applied to other cortical and subcortical regions in humans as well as other species.

Declaration

This to clarify that:

i) the thesis comprises only my original work towards the Doctor of Philosophy except where indicated;

ii) due acknowledgement has been made in the text to all other material used;

iii) the thesis is fewer than the maximum limit of 100,000 words in length, exclusive of tables, figure captions, bibliographies and appendices.

Preface

I am the sole first author of all three studies presented in this thesis in Chapter 3, 4 and 5. I am the most significant contributor to all study components, including conceptualization of the research questions, experimental design, imaging processing, coding, statistical analysis and manuscript preparation and dissemination. The data used in Chapter 3 and 5 was provided by the Human Connectome Project, funded by the 16 NIH Institutes and Centers that support NIH Blueprint for Neuroscience Research; and by the McDonnel Center for Systems Neuroscience at Washington University. This dataset is publicly available and comprises more than 1000 participants. Participants were recruited from the general community in the United States of America. The data used in Chapter 4 is part of the Cooperative Research Centre (CRC) Psychosis Study led by Professor Ian Everall and Professor Christos Pantelis. Participants for this study were sourced, in part, through the Australian Schizophrenia Research Bank (ASRB), which is supported by the National Health and Medical Research Council of Australia.

Publications

First author articles comprising this thesis:

1. **Tian Y**, Zalesky A. Characterizing the functional connectivity diversity of the insula cortex: Subregions, diversity curves and behavior. *Neuroimage* 183, 716-733 (2018).

2. **Tian Y**, Zalesky A, Bousman C, Everall I, Pantelis C. Insula functional connectivity in schizophrenia: Subregions, gradients, and symptoms. *Biological Psychiatry: Cognitive neuroscience and neuroimaging* 4, 399-408 (2019).

3. **Tian Y**, Margulies DS, Breakspear M, Zalesky A. Topographic organization of the human subcortex unveiled with functional connectivity gradients. *Nature Neuroscience* 23, 1421-1432 (2020).

Co-authored articles applying methods and knowledge obtained from this thesis:

1. Kottaram A, Johnston LA, **Tian Y**, Ganella EP, Laskaris L, Cocchi L, McGorry P, Pantelis C, Kotagiri R, Cropley V, Zalesky A. Predicting individual improvement in schizophrenia symptom severity at one-year follow-up: Comparison of connectomic, structural and clinical predictors. *Human Brain Mapping* 1-16 (2020).

2. Lv J, Di Biase M, Cash RFH, Cocchi L, Cropley V, Klauser P, **Tian Y**, Bayer J, Schmaal L, Cetin-Karayumak S, Rathi Y, Pasternak O, Bousman C, Pantelis C, Calamante F, Zalesky A. Individual deviations from normative models of brain structure in a large cross-sectional schizophrenia cohort. *Molecular Psychiatry* (2020).

3. Cropley V, **Tian Y**, Fernada K, Mansour SL, Pantelis C, Cocchi L, Zalesky A. Brain-predicted age associates with psychopathology dimensions in youth. *Biological Psychiatry: Cognitive neuroscience and neuroimaging* (2020).

4. Seguin C, **Tian Y**, Zalesky A. Network communication models improve the behavioral and functional predictive utility of the human structural connectome. *Network Neuroscience* (2020).

5. Bolton T, Urunuela E, **Tian Y**, Zalesky A, Caballero-Gaudes C, Van De Ville D. Sparse coupled logistic regression to estimate co-activation and modularity influence of brain regions. *Journal of Neural Engineering* (2020).

6. Cash RFH, Zalesky A, Thomson RH, **Tian Y**, Cocchi L, Fitzgerald PB. Subgenual Functional Connectivity Predicts Antidepressant Treatment Response to Transcranial Magnetic Stimulation: Independent Validation and Evaluation of Personalization. *Biological Psychiatry* 86: e5-e7 (2019).

7. Liu C, Kanazawa T, **Tian Y**, Mohamed Saini S, Mancuso S, Mostaid MS, Takahashi A, Zhang D, Zhang F, Yu H, Doo Shin H, Sub Cheong H, Ikeda M, Kubo M, Iwata N, Woo SI, Yue W, Kamatani Y, Shi Y, Li Z, Everall I, Pantelis C, Bousman C. The schizophrenia

genetics knowledgebase: a comprehensive update of findings from candidate gene studies. *Translational Psychiatry* 9:205 (2019).

8. Mansour SL, **Tian Y**, Cropley V, Zalesky A (in revision). High-resolution connectomics unravels correlates of neural identity and behavior.

9. Sarwar T, **Tian Y**, Yeo BT, Ramamohanarao K, Zalesky A (in revision). Investigating structure-function coupling in the human connectome using deep learning.

10. Ye H, Zalesky A, Cetin-Karayumak S, Rathi Y, Lv J, **Tian Y**, Pantelis C, Di Biase M (in revision). Network analysis of symptom comorbidity in schizophrenia: relationship to illness course and brain white matter microstructure.

Acknowledgements

I would like to express my huge thanks to everyone who has been part of my PhD journey. I would not be able to complete this thesis without their generous support, time and ideas.

I would like to first express my generalized thanks to all participants involved in all three studies and all researchers, clinicians, radiologists, research coordinators and research assistants who I cannot name but have worked on the recruitment of study participants and data acquisition. I shamelessly utilized the data but contributed little to its acquisition. I would not be able to conduct my research project without their efforts in the data collection in the last a few years, for which I am truly grateful.

I would particularly like to thank my PhD supervisors: Associate Professor Andrew Zalesky, Assistant Professor Chad Bousman and Professor Christos Pantelis. The PhD expedition has been challenging but also pleasurable and inspiring under their supervision and guidance. Andrew has always been supportive, patient and encouraging. Despite his remarkable achievement in academia, he has always been humble and sincere, and his passion and curiosity for knowledge have never stopped. I am deeply appreciative for his teaching, insight and feedback (though sometimes painful) throughout this entire journey, taking me from a medical student with no background in neuroimaging and programming, toward the career path of becoming a neuroscientist. Doubtlessly, Andrew has been a constant source of encouragement and his support has always been invaluable. Most importantly, I realize that he has helped me, perhaps unintentionally, rebuild my faith in doing science, which was once lost. I would also like to thank Chad, who is the first English-speaking person I knew in the lab and is also the person who introduced me to every other new face in the lab. I would like to thank Chad for his welcoming and patience, particularly during the first few months when I had not yet psychologically prepared for living and studying in a foreign country. Chad has always been responsive and efficient in sending back his comments despite the significant time difference, for which I feel really thankful. Finally, I would like to thank Christos, who is an outstanding psychiatrist and scientist. I am truly inspired by his vision, his commitment and his persistence in schizophrenia research as well as the intensive care he has devoted to

patients with schizophrenia. I would also like to thank Christos for his feedback in every meeting we had when discussing research ideas, which was very helpful in evolving this thesis.

I am also grateful to collaborators and contributors, including Daniel Margulies, Michael Breakspear, Luca Cocchi and Ian Everall for their indispensable feedback and generous provision of data for the studies presented in this thesis. Moreover, I would like to express a special thanks to Dr Vanessa Cropley, who has been my supervisor for a casual position as a research assistant. It has been a really pleasurable working experience and thanks for the freedom and flexibility that you provided, which made it much easier for me to manage time in between different tasks.

I would like to express my gratitude to all past and current MNC students, who have been sweet companions and a source of laugher and creativity all the time. It has been a great joy to come to work and to hang out together after work. Thanks to our lab manager Barbara Stachlewki for her cheerfulness and warm-hearted support and Chester Kang for his important technical tips. I would also like to thank Dr Tracey Varker for chairing my PhD committee and ensuring that I was on track throughout the journey. I want to thank many of my old and new friends for those beautiful memories that we share. In particular, a big thanks to my enduring companion, Dr Jing Cai, who commenced her PhD on the same day as mine and has been the best housemate and hiking/camping partner in the last three years. Thanks for her company and the magnificent birthday cake she baked for me. No one else would be able to reproduce such a masterpiece.

I feel that I owe particular thanks to my family, especially my parents, who have been always supportive with their unconditional love. They have been always supportive of every decision I made, given me freedom as much as they can and tried their best to comfort me and ease my mind. My dear mum and dad, thank you for always considering my happiness in the first place. I know that you are all very proud of me and always hold great confidence in me, for which I am deeply appreciative. I am so lucky to grow up in this lovely family. I would also like to thank my cousin, who has been my lovely big brother all the time. He is the very first Doctor (PhD in physics) in my family and I will become the second, of which I am very proud. I grew up with him and have been constantly inspired and amazed by his enthusiasm for science and

knowledge. Without this real model, I may have never commenced my PhD, not even mentioning the ability to appreciate and enjoy the beauty of science that I developed later on.

Finally, I would like to thank those who have provided direct and indirect help in completing this thesis.

Table of Contents

ABSTRACT I

DECLARATION III

PREFACE IV

PUBLICATIONS V

ACKNOWLEDGEMENTS VII

LIST OF TABLES XII

LIST OF FIGURES XII

CHAPTER 1

GENERAL INTRODUCTION 1

BRAIN TOPOGRAPHY 2
AIM 1 5
TOPOGRAPHIC ORGANIZATION OF THE INSULAR CORTEX 5
AIM 2 12
SCHIZOPHRENIA 12
DYSFUNCTION OF THE INSULAR CORTEX IN SCHIZOPHRENIA 13
AIM 3 16
SUBCORTEX NEUROANATOMY 16
TOPOGRAPHIC ORGANIZATION OF THE HUMAN SUBCORTEX 18
SUMMARY AND THESIS OVERVIEW 25
Summary of key outcomes 26

REFERENCES 28

CHAPTER 2

BACKGROUND AND METHODS 42

MODELS OF BRAIN TOPOGRAPHY 43
MICROSCALE ARCHITECTURE 43
MACROSCALE CONNECTIVITY ARCHITECTURE 46
FUNCTIONAL MAGNETIC RESONANCE IMAGING AND FUNCTIONAL CONNECTIVITY 47
CONNECTIVITY-BASED PARCELLATION 50
Challenges in determining the optimal number of clusters 52
CONNECTIVITY GRADIENTS 55
Methods for mapping connectivity gradients 55
Biological interpretation of connectivity gradients 57
MODEL SELECTION: DISCRETE OR CONTINUOUS REPRESENTATIONS? 59
PARTICIPANTS, DATASETS AND DATA PREPROCESSING 63
Data preprocessing 64
Statistical analysis and methods 65

REFERENCES 68

CHAPETER 3

CHARACTERIZING THE FUNCTIONAL CONNECTIVITY DIVERSITY OF THE INSULA CORTEX 80

CHAPETER 4

INSULA FUNCTIONAL CONNECTIVITY IN SCHIZOPHRENIA 119

CHAPETER 5

TOPOGRAPHIC ORGANIZATION OF THE HUMAN SUBCORTEX 141

CHAPTER 6

GENERAL DISCUSSION 210

SUMMARY 211
INSULAR CONNECTIONAL TOPOGRAPHY IS BEST MODELED AS A CONTINUUM OF GRADUAL CHANGES RATHER THAN DISTINCT SUBREGIONS 213
THE TOPOGRAPHIC ORGANIZATION OF THE INSULAR CORTEX IS REORGANIZED IN SCHIZOPHRENIA AND RELATES TO CLINICAL SYMPTOMS 215
INVESTIGATING THE TOPOGRAPHIC ORGANIZATION OF THE HUMAN SUBCORTEX 217
MULTISCALE SUBCORTEX ATLAS 218
INTRINSIC AND DYNAMIC FUNCTIONAL TOPOGRAPHY 219
RELATIONSHIP BETWEEN TOBACCO USE AND SUBCORTICAL FUNCTIONAL CONNECTIVITY 221
LIMITATIONS AND FUTURE WORK 222
CONCLUSIONS 228

REFERENCES 229

List of Tables

Table 3.1. Parcellating the human insula cortex with functional and diffusion MRI

Table S3.1. List of 59 selected behavioral measures

Table S3.2. Distribution across individuals in the optimal number of clusters (right insula) found with classic evaluation criteria (%)

Table S3.3. Correlation between measures of intra-scan head motion and the optimal number of clusters (right insula) indicated by W, W^{norm} and W^{diff}

Table 4.1. Demographic and clinical characteristics

Table S4.1. Information of group-level insula sub-regions, in MNI152 standard anatomical space

Table S4.2. Anatomical locations of clusters associated with significantly reduced functional connectivity with insula subregions in the schizophrenia group, relative to the group of healthy comparison individuals (p<0.05, corrected).

Table S5.1. Basic demographic characteristics and acquisition details

Table S5.2. Nomenclature for 3T parcellation hierarchy

Table S5.3. Comparison parcellation atlases of the human subcortex and specific subcortical nuclei

Table S5.4. List of 109 selected behavioral items

Table S5.5. NIFTI and CIFTI file names for 3T and 7T atlas

List of Figures

Figure 1.1. Topographic maps of the human cerebral cortex

Figure 1.2. Human insular cortex

Figure 1.3. Cytoarchitecture of the human insular cortex

Figure 1.4. Parcellating the human insular cortex with MRI

Figure 1.5. Altered functional connectivity of the insular cortex in psychosis inferred from function MRI

Figure 1.6. Representative structural, diffusion and functional MRI atlases of subcortical structures

Figure 1.7. Connectivity gradients of hippocampus and striatum inferred from resting-state functional MRI

Figure 1.8. Connectivity-based atlases comprising more than one subcortical region

Figure 2.1. Physiological and physical events associated with intensity fluctuation of fMRI BOLD signals

Figure 2.2. Functional connectivity profile of the pre supplementary motor area (pre-SMA) and SMA

Figure 2.3. Connectivity gradients overlap in space

Figure 3.1. Schematic of clustering methodology and null model

Figure 3.2. Diversity curve, linear piecewise model and model selection
Figure 3.3. Bipartite parcellation of the human insula cortex based on resting-state functional connectivity
Figure 3.4. Optimal number of insula subregions
Figure 3.5. Homogeneity of the insula and its subregions
Figure 3.6. Diversity curves for the insula cortex and insula-putamen combined
Figure 3.7. Model selection: diversity curves for the insula cortex compared to benchmark diversity curves
Figure 3.8. Relation between behavior and insula functional connectivity diversity
Figure S3.1. Example of identification of spurious clusters showing high concordance across individuals
Figure S3.2. Validation of classic cluster evaluation criteria on insula-like synthetic data
Figure S3.3. Cluster evaluation measures and their validation on insula-like synthetic data
Figure S3.4. Tripartite parcellation of the human insula cortex based on resting-state functional connectivity
Figure S3.5. Group-consensus Laplacian eigenmaps for the insula cortex and the insula-putamen benchmark
Figure S3.6. Within-subject replication of diversity curves and the effect of spatial smoothing
Figure S3.7. Validation of CCA mode in second fMRI session
Figure S3.8. Diversity curves for the left insula
Figure 4.1. Bipartite parcellation of the right insular cortex based on functional connectivity in individuals with schizophrenia and healthy comparison individuals
Figure 4.2. Altered resting-state functional connectivity of the anterior and posterior insular cortex in schizophrenia
Figure 4.3. Diversity curves for the insular cortex in schizophrenia
Figure 4.4. Association between insula functional connectivity and interindividual variation in clinical characteristics.
Figure S4.1. Individual bipartite parcellation of the insula based on resting-state functional connectivity in individuals with schizophrenia and healthy comparison individuals
Figure S4.2. Comparison of cluster shape between schizophrenia and healthy comparison groups
Figure S4.3. Bipartite parcellation of the left insula cortex based on resting-state functional connectivity in individuals with schizophrenia and healthy comparison individuals
Figure S4.4. Altered resting-state functional connectivity of left anterior and posterior insula in schizophrenia

Figure S4.5. The main effect of hemisphere in resting-state functional connectivity of anterior and posterior insula cortex
Figure 5.1. Gradientography in the human subcortex
Figure 5.2. Model selection: Which gradient magnitude peaks are sufficiently large to warrant boundary delineation?
Figure 5.3. Multiscale group-consensus parcellation atlas derived from 3 Tesla resting-state functional MRI acquired in 1080 healthy adults
Figure 5.4. Organization of the human subcortex
Figure 5.5. Parcellation homogeneity
Figure 5.6. Replication of 3 Tesla parcellation using 7 Tesla resting-state functional MRI
Figure 5.7. Personalization of the Scale IV atlas
Figure 5.8. Association between individual variation in behavioral dimensions and subcortical functional connectivity
Figure S5.1. Mapping of Gradient II and III
Figure S5.2. Variance explained by successive gradients
Figure S5.3. Impact of left-right symmetrization on gradient magnitude images
Figure S5.4. Spatial variation in primary MRI signal properties in the subcortex
Figure S5.5. Testing whether gradient magnitude peaks are large enough to warrant boundary delineation
Figure S5.6. Criteria used to justify boundary delineation
Figure S5.7. Organization of connectivity gradients in the human subcortex
Figure S5.8. Schematic of fMRI data preprocessing and boundary delineation
Figure S5.9. Spatial correspondence between the new atlas and histological parcellations of thalamus and hippocampus
Figure S5.10. Projection of gradients within specific subcortical nuclei onto the cortical surface
Figure S5.11. Schematic of parcellation homogeneity estimation
Figure S5.12. Parcellation homogeneity of the new and existing subcortical parcellation atlases
Figure S5.13. Parcellation homogeneity estimated in an independent validation dataset
Figure S5.14. Quantifying the extent to which task-evoked activity is circumscribed to regions comprising the atlas for Scale I-IV
Figure S5.15. 3 Tesla and 7 Tesla subcortex parcellation at Scale IV
Figure S5.16. Quantitative comparison between 3 Tesla and 7 Tesla atlas across parcellation scales
Figure S5.17. Schematic of methodology for parcellation personalization
Figure S5.18. Within-subject variation in Dice coefficient across subcortical regions

Figure S5.19. Variation in subcortical connectivity gradients between rest and task-evoked conditions
Figure S5.20. Linking canonical cortical networks based on their functional connectivity with subcortical regions.
Figure S5.21. Behavioral dimensions
Figure S5.22. Association between subcortical functional connectivity and the behavioral dimension characterizing tobacco use reproduced using functional MRI from a second session
Figure S5.23. Model selection with Kolmogorov-Smirnov (KS) test
Figure S5.24. Determining the optimal number of independent components.
Figure 6.1. Effects of Gaussian smoothing kernel and Wishart filter on connectivity gradient mapping
Figure 6.2. BOLD signal decays as a function of time for different T2* relaxation value at 7T

CHAPTER 1

GENERAL INTRODUCTION

Brain topography

The brain constitutes a major part of the central nervous system, hosting the mind and controlling most activities of the rest of the body. While the concept of brain topography is relatively broad, it most commonly refers to spatial variation in brain structure, function and/or connectivity, which is evident from cyto- and myeloarchitecture at the microscale, and the organization of neuronal connections at the macroscale (Eickhoff et al. 2018a). This spatial organization of brain structure, function and connectivity is crucial in maintaining mental states and information processing (Fox and Friston 2012), and accounts for cross-species (Van Essen and Glasser 2018) and cross-individual distinctiveness and individual variation in behavioral traits (Finn et al. 2015; Wang et al. 2015; Gordon et al. 2017; Kong et al. 2019). Over the last century, researchers have devoted a great amount of effort to understand the structural and functional topography of the human brain. Brain topography is classically represented in terms of a map or parcellation atlas and the process of constructing such maps is referred to as brain cartography. Each delineated area in a topographic map of the brain is deemed to be different in structure and/or function, compared to its neighboring areas. This is exemplified by early endeavors focusing on mapping local cytoarchitectonic and myeloarchitectonic differences across the cerebral cortex from postmortem specimens decades ago (Brodmann 1909; Vogt 1910; Von Economo and Koskinas 1925), to contemporary non-invasive brain mapping using advanced *in vivo* neuroimaging modalities, such as magnetic resonance imaging (MRI) (Eickhoff et al. 2018b). Indeed, since the early nineteenth century, brain cartography and parcellation have remained an ongoing topic and a major goal in neuroscience.

The topographic organization of the human brain is complex, and the complexity of brain topography is marked by varied spatial scales and modalities, from molecules and cells, to large-scale brain networks (Eickhoff et al. 2018a); in multiple overlapping organizational axes (Huntenburg et al. 2018); and in the particular brain area studied, which can be as broad as the whole brain (Craddock et al. 2012), the entire cerebral cortex (Glasser et al. 2016), or as specific as one cortical lobe, such as the insular cortex (Nieuwenhuys 2012) or subcortical nuclei, such as the thalamus (Morel et al. 1997; Behrens et al. 2003) and striatum (Haber and

Knutson 2010; Choi et al. 2012). Indeed, comprehending brain organization appears to be an insurmountable ambition that has engrossed scientists for centuries.

Brain topography is usually conceptualized using one of two paradigms: i) spatially distinct partitions with discrete areal boundaries (Brodmann 1909; Van Essen et al. 1981; Yeo et al. 2011; Craddock et al. 2012; Glasser et al. 2016; Gordon et al. 2016; Schaefer et al. 2018; King et al. 2019); and more recently, ii) continuous gradients of gradual change (Mesulam and Mufson 1985; Cerliani et al. 2012; Strange et al. 2014; Margulies et al. 2016; Guell et al. 2018; Haak et al. 2018; Huntenburg et al. 2018; Paquola et al. 2019; Paquola et al. 2020). The first concept posits that the brain is structurally and functionally specialized into a mosaic of discrete patches, each of which shows a distinct pattern of structure, function and/or connectivity. As one moves from one patch to another, abrupt changes in one or more biological features would be expected, corresponding to locations of cortical boundaries. In contrast, the latter representation assumes that brain structure and function vary gradually across the brain's topography, in the absence of sharp boundaries. Instead of a sharp and clearly defined boundary separating two cortical areas, this representation proposes that cortical structure, function and connectivity vary gradually across the spatial extent of the brain. The two topographic representations complement each other and both feature in many recent brain maps (atlases), ranging from microstructure to large-scale structural and functional connectivity (Strange et al. 2014; Eickhoff et al. 2018a; Eickhoff et al. 2018b; Huntenburg et al. 2018). Indeed, the two conceptualizations of brain topography have largely simplified and facilitated the characterization of brain organization in recent years. Figure 1.1 exemplifies several well-known topographic maps of the human brain, particularly for the cerebral cortex, which are characterized by the two representations.

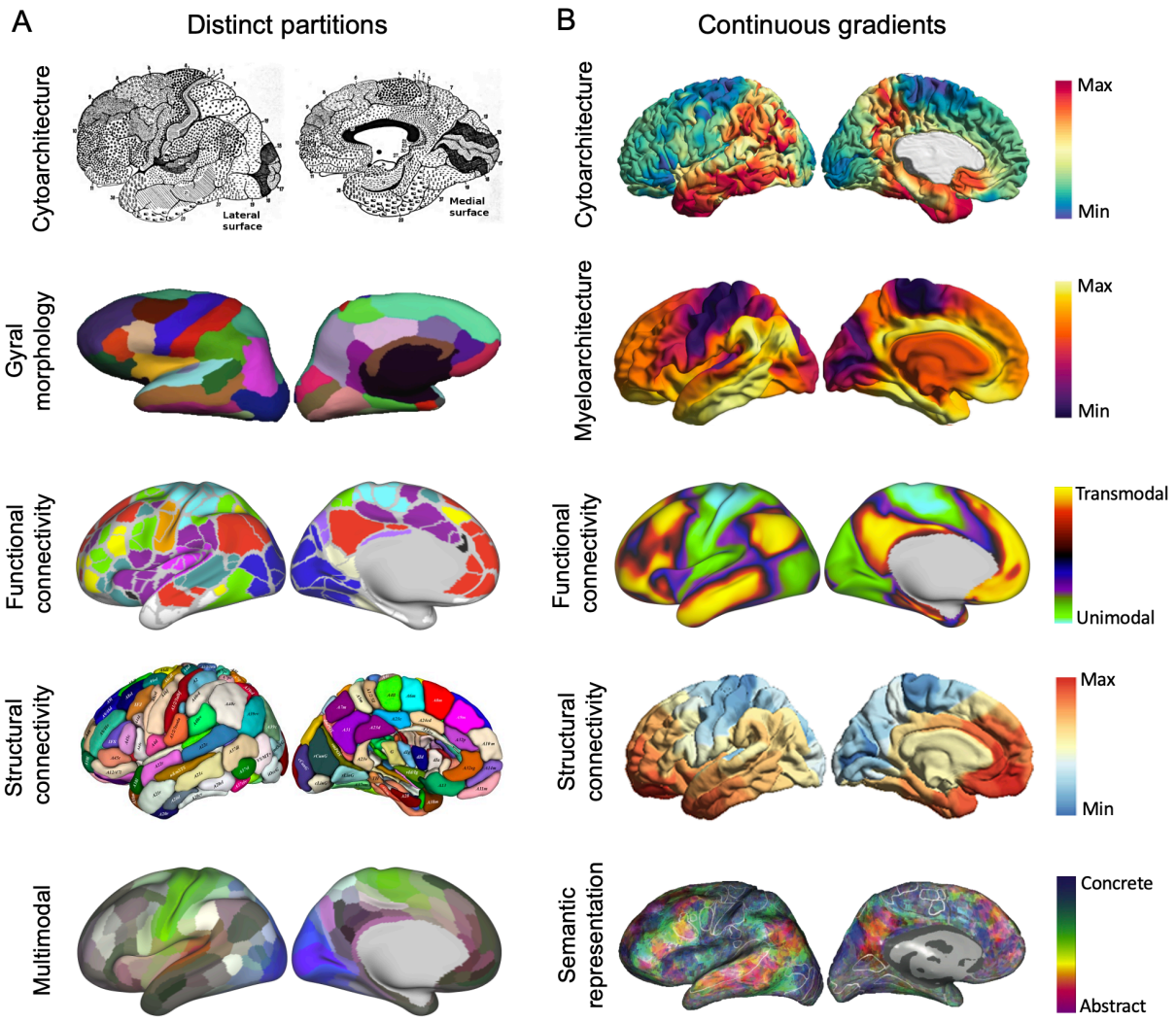


Figure 1.1. Topographic maps of the human cerebral cortex. A, Classic models of brain topography parse spatial variation in brain structure, function and connectivity into distinct partitions with discrete boundaries. Examples of brain atlases delineated based on cytoarchitecture (Brodmann 1909), gyral morphology (Desikan et al. 2006), functional connectivity (Gordon et al. 2016), structural connectivity (Fan et al. 2016) and multiple structural and functional imaging modalities (Glasser et al. 2016). **B,** Contemporary evidence from neuroimaging suggests that brain structure and function may potentially vary in a gradual manner across the brain's spatial extent, in the absence of sharp boundaries. Principal gradient of variation in brain's cytoarchitecture (Paquola et al. 2019), myeloarchitecture (Paquola et al. 2019), functional connectivity (Margulies et al. 2016), structural connectivity (Paquola et al. 2020) and activity in response to semantic stimuli (Huth et al. 2016).

Nevertheless, questions and challenges associated with topographic representations and models of the brain are yet to be solved (Chapter 2). It remains disputed whether topographic change in brain structure, function and connectivity is better conceptualized in terms of continuous gradients that potentially overlap in space (Huntenburg et al. 2018) or a mosaic of discrete cortical patches (Eickhoff et al. 2018a). The insular cortex is one such topographically complex and functionally heterogeneous cortical lobe. Neuroanatomists have encountered *great difficulties* in subdividing the insula into individual subregions in early

studies (Brodmann 1909; Von Economo and Koskinas 1925; Rose 1928). While the insula's topography has been studied for over a century, controversy remains about whether the insula comprises distinct subregions and the precise location of putative boundaries between subregions (Nieuwenhuys 2012; Cauda and Vercelli 2013). In the first part of this thesis, I therefore aimed to investigate and characterize the topographic organization of the insular cortex using modern *in vivo* neuroimaging techniques applied to healthy adult humans.

Aim 1

To investigate the topographic organization of the insular cortex in healthy humans using functional MRI. Specifically, I aimed to determine whether the functional architecture of the insula is best represented as a continuum of gradual change or by parcellating into discrete subregions. I also aimed to evaluate whether inter-individual variation in the insula's topographic organization would associate with behavioral traits and cognitive performance (Chapter 3).

Topographic organization of the insular cortex

The insular cortex, together with the other four cortical lobes, including the frontal, parietal, temporal and occipital cortices, form the entire cerebral cortex. The insula comprises 2% of the total cortical area (Nieuwenhuys 2012) and is completely obscured by the frontal, temporal and parietal opercula in the lateral view of the exposed cerebral cortex. The five to six gyri comprising the insula are arranged in a vertical fan-like appearance, being separated from other cortical lobes by the superior circular, inferior circular sulcus and orbitoinsular sulcus (Figure 1.2). Based on the location of the central insula sulcus, the insular cortex is conventionally divided into an anterior portion comprising 3-4 short gyri and a posterior insula with two long gyri (Clark 1896; Afif and Mertens 2010). This anterior-posterior distinction provides one of the coarsest representations of insula's topography (Afif and Mertens 2010), where the location of central insula sulcus is considered a fundamental landmark between the two portions.

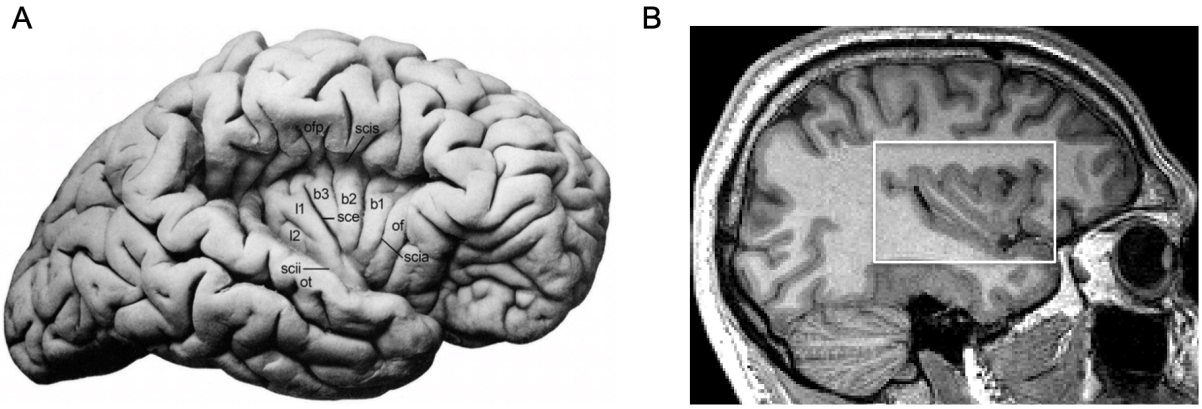


Figure 1.2. Human insular cortex. A, Lateral view of the right hemisphere with the overlying opercula removed. b1, b2 and b3, short gyrus; l1 and l2, long gyrus; sce, sulcus centralis insulae; of, operculum orbitofrontal; ofp, operculum frontoparietale; ot, operculum of temporale; scia, scii and scis: sulcus circulars insula. Reproduced from (Retzius 1896). **B,** Sagittal view of a standard T1-weighted *in vivo* MR image. Anatomical location of the insular cortex is outlined by a white rectangular box.

However, this coarse division does not capture the extensive functional and structural heterogeneity of the insula. The insular cortex is connected to many cortical and subcortical regions, receiving both interoceptive and exteroceptive sensory information (Mufson et al. 1981; Mufson and Mesulam 1982; Mesulam and Mufson 1985; Augustine 1996; Mufson et al. 1997). It is broadly involved in many functions, ranging from lower-order sensorimotor function (e.g. viscerosensory, somatosensory and somatomotor) to higher-order cognitive-affective processes (Augustine 1996; Craig 2009; Mutschler et al. 2009; Singer et al. 2009; Kurth et al. 2010a; Kurth et al. 2010b; Xue et al. 2010; Stephani et al. 2011; Uddin et al. 2014; Segerdahl et al. 2015). Studies have sought to map these diverse functions onto distinct gyri and insular subregions, yielding a putative anterior-to-posterior differentiation in the insula's function. Specifically, the anterior insula is primarily associated with viscerosensory functions such as gustatory and abdominal sensation (Small et al. 2003; Stephani et al. 2011), subjective emotion (Uddin et al. 2014) and cognitive abilities (Uddin 2015). In contrast, the posterior insula responds to a variety of somesthetic stimuli (Craig et al. 2000; Ostrowsky et al. 2000; Stephani et al. 2011) that are associated with general somatosensory process as well as thermal and pain perception.

This anterior-posterior division of the insula's function is consistent with and partly supported by the cytoarchitecture and connectional architecture of the insular cortex. Studies of histology and axonal tracing suggest that the cytoarchitecture and axonal fiber connections

of the insular cortex are topographically organized along an anterior-posterior axis (Mesulam and Mufson 1982; Mufson and Mesulam 1982; Mesulam and Mufson 1985; Friedman et al. 1986; Gallay et al. 2012). While studies suggest that the cytoarchitecture of the insular cortex varies from agranular to granular with a transitional dysgranular zone in between them, the exact cytoarchitectonic boundaries of the insular cortex have yet to be characterized (Kurth et al. 2010a; Nieuwenhuys 2012). This is reflected by the enormous discordance among previous studies in the number of putative subregions comprising the insular cortex, ranging from 2 to 31 (Brodmann 1909; Von Economo and Koskinas 1925; Rose 1928) as illustrated in Figure 1.3. Rather than imposing hard boundaries between putative insular subregions, some neuroanatomists claimed that the insula's cytoarchitecture and axonal connectivity varies gradually and continuously across its spatial extent, consistent with studies in macaque (Mesulam and Mufson 1982; Mufson and Mesulam 1982; Mesulam and Mufson 1985; Friedman et al. 1986). This may explain the "*great difficulties*" early neuroanatomists had in consistently subdividing the human insular cortex (Brodmann 1909; Von Economo and Koskinas 1925; Rose 1928) and the discrepancy among studies in the number of putative subregions. Perhaps alternative models and topographic representations are required to represent the insula?

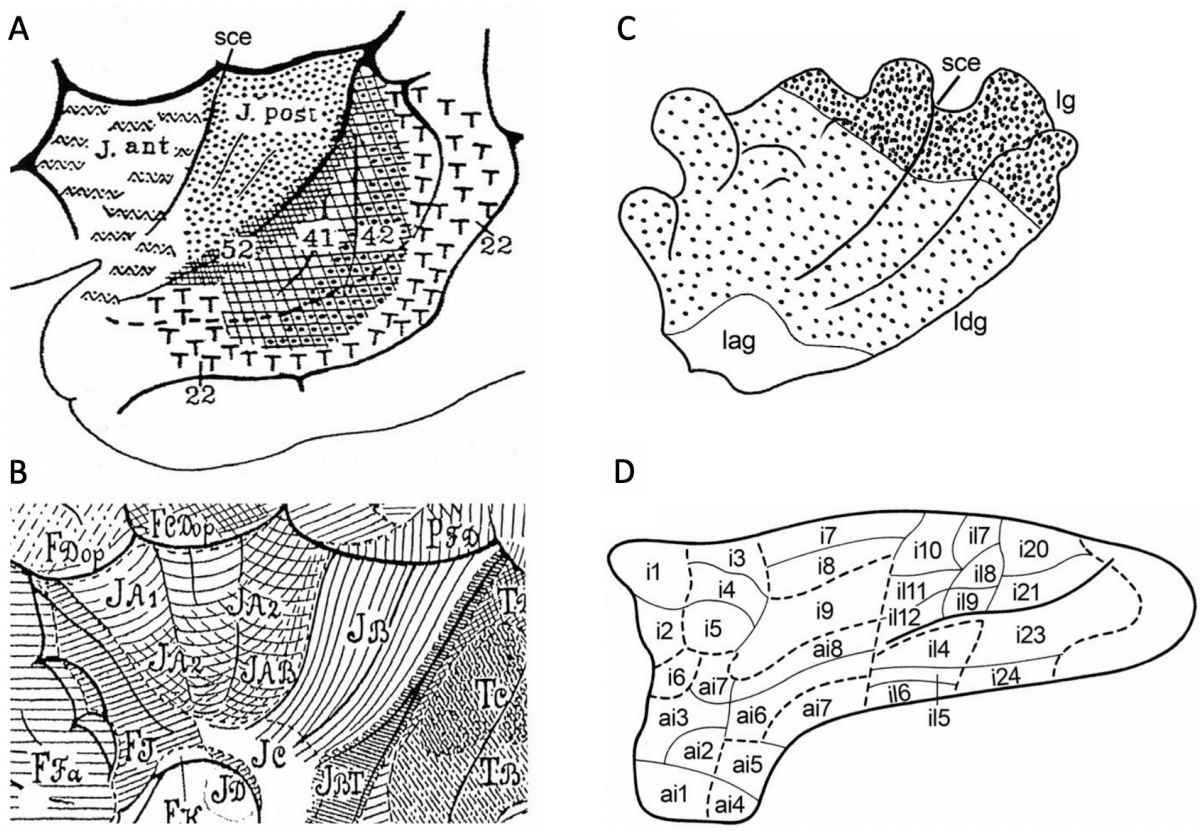


Figure 1.3. Cytoarchitecture of the human insular cortex. A, Broadmann (1909) delineated anterior and posterior insular subregions. J.ant, agranular anterior insula; J.post, granular posterior insula; sce, sulcus centralis insulae. **B,** von Economo and Koskins (1925) divided the insular cortex into three cytoarchitectonic zones, including the frontoinsularis (FJ), pracentralis insulae (JA) and postcntralis insule (JB). **C,** Three insular subdivisions: including an agranular (Iag), a dysgranular (Idg) and a granular (Ig) zone delineated by Bonthius et al. (2005). **D,** 31 subregions of the insula delineated by Rose (1928). Images are adapted from Nieuwenhuys (2012).

Early studies of the insula's topography mainly relied on histological investigations of postmortem human brain or axonal tracing techniques in experimental animals, usually non-human primates. Due to their invasiveness and requirement of postmortem tissue, while directly observable, these studies are limited and cannot be directly compared with living subjects. Using magnetic resonance imaging (MRI), studies are now able to characterize the topography of the human insular cortex *in vivo.* Specifically, the insular cortex was segmented into six subregions based on gyral morphology using standard T1-weighted MR images (Faillenot et al. 2017). The six subregions are (Figure 1.4A) largely consistent with patterns of the insula's gyrification observed in postmortem specimens (Figure 1.2A). However, significant technical challenges remain with respect to imaging cytoarchitecture *in vivo*. Recent technical advances have facilitated the mapping of the microstructural organization of the insular cortex using myelin-sensitive MR contrasts, such as the T1 relaxation time (Bock

et al. 2009; Stüber et al. 2014), the ratio of T1- and T2-weighted image intensities (Glasser and Van Essen 2011) and the magnetization transfer technique (Schmierer et al. 2007). Although these MR techniques cannot directly measure microstructure, they are sensitive to variation in gray matter myelin content. Consistent with the anterior-posterior organizational axis in macaque (Mesulam and Mufson 1982; Mufson and Mesulam 1982; Mesulam and Mufson 1985; Friedman et al. 1986), a recent study found that this *in vivo* proxy of myeloarchitecture varies gradually and continuously across the topography of the insula (Royer et al. 2020).

Likewise, the structural and functional connectivity of the insular cortex can be mapped using diffusion (Le Bihan and Breton 1985) and functional MRI (Thulborn et al. 1982; Ogawa et al. 1990) techniques, respectively. In brief, diffusion MRI measures the diffusion process of water molecules, which presumably reflects the organization of white matter tracts interconnecting regions, referred to as structural connectivity. In contrast, functional MRI measures brain activity over time and the temporal co-activation between brain regions is referred to as functional connectivity (see Chapter 2). Many studies have investigated the structural and functional connectivity architecture of the human insular cortex using one of the two neuroimaging approaches. Although cytoarchitectural boundaries within the insula are not clearly demarcated (Kurth et al. 2010a; Nieuwenhuys 2012), it is possible that the macroscale insular connectivity maps inferred from functional or diffusion MRI would yield undisputable and reproducible insular subregions. However, findings from recent neuroimaging studies do not seem to support this notion. Some studies reported bipartite subdivisions of the insular cortex comprising an anterior and a posterior subregion (Nanetti et al. 2009; Cauda et al. 2011; Cauda et al. 2012; Jakab et al. 2012; Kelly et al. 2012; Alcauter et al. 2015), whereas the anterior insula was further divided into dorsal and ventral components in other studies (Deen et al. 2011; Chang et al. 2013; Moran et al. 2013; Ryali et al. 2015). The bipartite and tripartite subdivisions appear to be in line with most histological findings (Brodmann 1909; Von Economo and Koskinas 1925; Bonthius et al. 2005), however, maps comprising more than three subregions have also been proposed, resulting in insula maps with a mosaic of distinct subdivisions (Mutschler et al. 2009; Nelson et al. 2010; Power et al. 2011; Yeo et al. 2011; Kelly et al. 2012; Ryali et al. 2013; Glasser et al. 2016; Nomi et al. 2016; Vercelli et al. 2016; Yamada et al. 2016). Figure 1.4 exemplifies the substantial variation in contemporary

parcellations of the insula mapped with modern neuroimaging techniques. See Table 1 in Chapter 3 for a detailed summary of these previous studies.

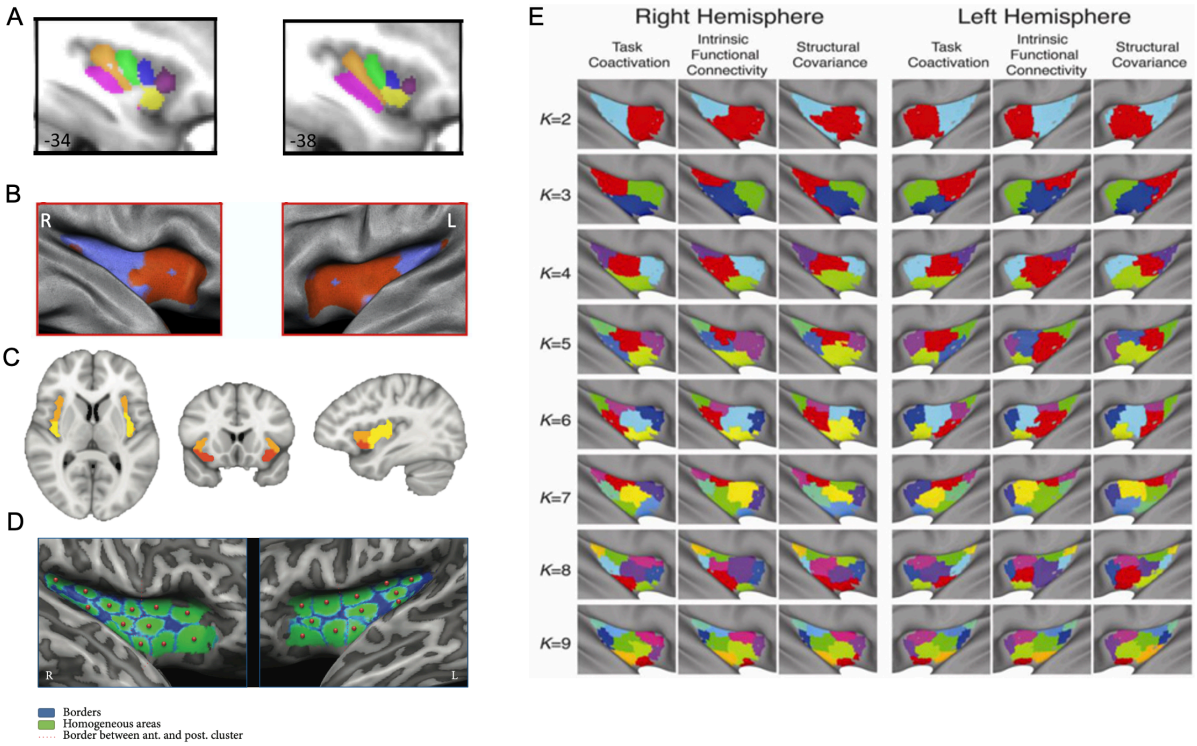


Figure 1.4. Parcellating the human insular cortex with MRI. A, Insula segmentation based on gyral and sulcus inferred from T1-weighted MR images (adapted from Faillenot et al.2017). **B,** Bipartite insular subdivisions based on functional connectivity inferred from resting-state fMRI (adapted from Cauda et al. 2012). **C,** Tripartite insular subdivisions based on functional connectivity inferred from resting-state fMRI (adapted from Deen et al. 2011). **D,** Twelve insular subdivisions based on functional connectivity inferred from resting-state fMRI (adapted from Vercelli et al. 2016). **E,** Varied parcellation solutions for the insula cortex using different structural or functional MRI modalities (adapted Kelly et al. 2012).

Given the ambiguities in delineating sharp areal borders and disagreement about the number of subregions comprising the insula among both early neuroanatomists and contemporary researchers, I hypothesized that representations based on discrete subregions differentiated by hard boundaries might not provide the most parsimonious model of the insula's topography. Therefore, I sought to consider alternative topographic representations, particularly focusing on models based on continuous gradients of gradual change (Huntenburg et al. 2018).

As alluded to above, the function of the insula is diverse, and insular activation is associated with a wide range of psychological events (Chang et al. 2013; Uddin et al. 2014; Uddin 2015).

In particular, studies suggest that functional heterogeneity of the insular cortex is topographically organized, in which the anterior insula, especially the ventral component is primarily co-activated with limbic areas in the brain that correspond to affective processing, whereas the dorsal component is more activated in relation to higher-order cognitive tasks and executive control and co-activated with fronto-parietal association cortices. In contrast, the activation of the posterior extreme of the insula is preferentially co-activated with sensorimotor cortices, in response to somatosensory, pain, auditory and language-related events (Chang et al. 2013; Uddin et al. 2014; Uddin 2015). Given this topographic segregation of the insula's functional roles, I hypothesized that inter-individual variation in the insula's topography, particularly the anterior aspect, would associate with human behaviors relating to cognitive and affective processes, whereas individual variation in the topography among the posterior aspect of the insula would more likely explain behavioral variance relating to sensorimotor functions.

Aim 2

Having characterized the functional organization of the insular cortex in healthy adults (Chapter 3), I next aimed to test whether neuropsychiatric illness, particularly schizophrenia, associates with alterations in the functional organization of the insular cortex. I also aimed to test whether alterations in the insula's functional topography are associated with the severity of clinical symptoms and cognitive deficits in the disorder (Chapter 4).

Schizophrenia

Schizophrenia is a severe, devastating and chronic neuropsychiatric illness affecting more than 20 million people worldwide (Theo Vos et al. 2017). Despite a relatively low prevalence (0.24-0.31%) globally compared to other mental conditions (James et al. 2018), schizophrenia contributes to substantial global burden (Charlson et al. 2018) and was ranked the 12th most disabling illness among more than 300 diseases and injuries globally in 2016 (Theo Vos et al. 2017). Schizophrenia is often characterized by a collection of symptoms, including distortions in perception, thinking and abnormal emotional, motor and social behaviors. Common clinical manifestations of schizophrenia are typically grouped into three categories, which include i) positive symptoms: delusions, hallucinations, disorganized thinking and speech and abnormal motor behaviors; ii) negative symptoms: diminished emotional expression and avolition as well as alogia, anhedonia and asociality; and, iii) cognitive and intellectual impairment. While cognitive impairment, such as deficits in memory and attention, is not included in the current Diagnostic and Statistical Manual of Mental Disorder (DSM-V; American Psychiatric Association, 2013), it has been increasingly recognized as one of the core features of this disorder (Keefe and Fenton 2007; Kahn and Keefe 2013). Nevertheless, the disorder's etiology remains unknown (Insel 2010).

Schizophrenia has long been considered as a disorder of brain connectivity (Wernicke 1906). Modern functional and structural neuroimaging techniques have greatly expanded and supported the notion of brain connectivity abnormalities in individuals with schizophrenia (reviewed by (Fornito et al. 2012; van den Heuvel and Fornito 2014). It has been suggested that aberrant patterns of connectivity between spatially distributed brain regions and functional systems result in disturbances in information integration between cognitive

processes and sensory perception (Allen et al. 2008; Javitt 2009; Kaufmann et al. 2015), potentially giving rise to the complex symptomatology associated with schizophrenia (Friston 1998). While the precise brain regions and neural circuits implicated in the pathophysiology of schizophrenia remain debated, mounting evidence suggests that the insular cortex is a key region that requires further investigation not only in schizophrenia, but in neuropsychiatric disorders more generally (Nagai et al. 2007; Wylie and Tregellas 2010; Menon 2011; Goodkind et al. 2015; Uddin 2015).

Dysfunction of the insular cortex in schizophrenia

Given the rich repertoire of functional roles performed by the insular cortex in sensory perception and cognitive-emotional processing, it is not surprising that the insula is commonly affected in a spectrum of psychiatric conditions. Gray matter atrophy of the insula has been consistently observed in individuals with schizophrenia across different illness stages (Kasai et al. 2003; Honea et al. 2005; Ellison-Wright et al. 2008; Glahn et al. 2008; Goodkind et al. 2015). One recent ROI-based meta-analysis further confirmed significant gray matter reduction in bilateral insula in both first episode and chronic schizophrenia patients, with the greatest magnitude of reduction in anterior insula (Shepherd 2012). Abnormal gray matter loss in the insula may affect information processing within the insula and other brain regions to which the insula is tightly connected. Indeed, dysconnectivity of the insular cortex has been repeatedly reported in individuals with first-episode (Kasparek et al. 2013; Mallikarjun et al. 2018); chronic schizophrenia (Fornito et al. 2009; Palaniyappan et al. 2011; Palaniyappan and Liddle 2012; Moran et al. 2013; Palaniyappan et al. 2013), as well as individuals at high risk for the disorder (Seiferth et al. 2008; Dandash et al. 2014; Wotruba et al. 2014; Heinze et al. 2015). Most commonly, the insular cortex shows reduced functional connectivity with the cingulate cortex as well as regions comprising the central executive network and the default mode network in individuals with schizophrenia, compared to healthy controls (Moran et al. 2013; Palaniyappan et al. 2013; Dandash et al. 2014; Wotruba et al. 2014). However, the extent of functional dysconnectivity shows significant heterogeneity between individuals and depends on illness stage and other clinical factors, such as severity of illness. In particular, recent studies suggest that aberrant connectivity patterns of the insular cortex relate to the severity of psychotic symptoms (Palaniyappan et

al. 2013; Manoliu et al. 2014; Wotruba et al. 2014) and cognitive deficits (Moran et al. 2013; Wotruba et al. 2014) in the spectrum of psychosis disorders. However, most studies have mainly focused on the anterior aspect of the insular cortex (Figure 1.5) or the broader salience network (Seeley et al. 2007) of which the anterior portion of the insula comprises (Moran et al. 2013; Palaniyappan et al. 2013; Dandash et al. 2014; Manoliu et al. 2014; Wotruba et al. 2014; Wang et al. 2016). Therefore, variations in patterns of connectivity across the spatial extent of the insular cortex require investigation.

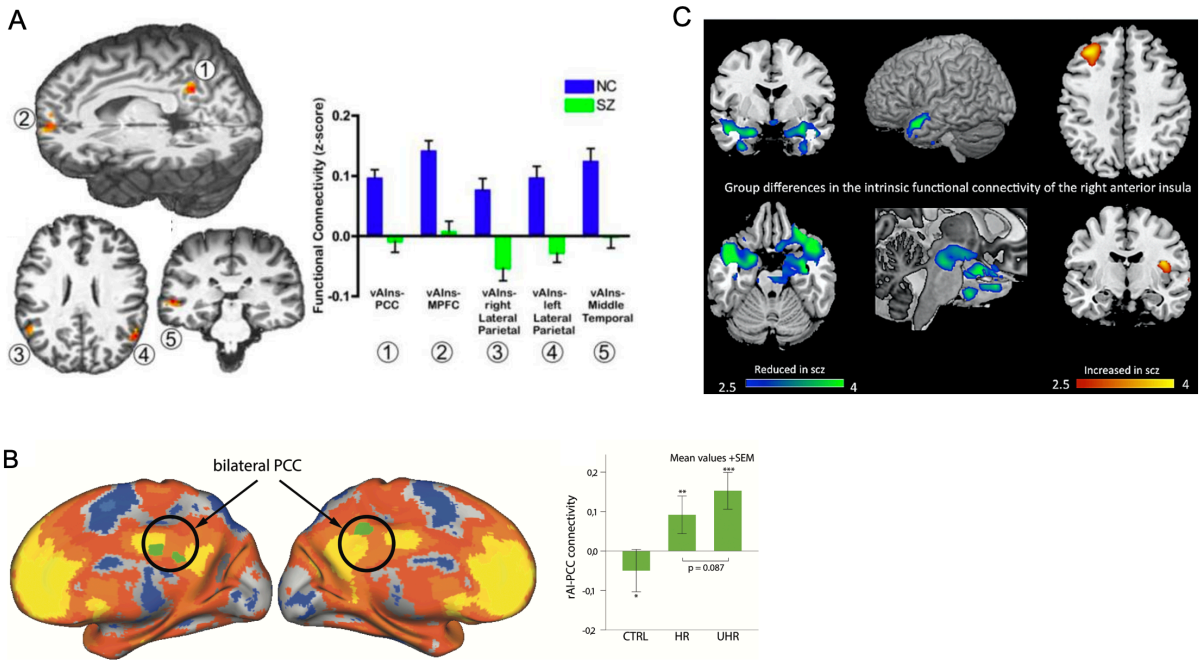


Figure 1.5. Altered functional connectivity of the insular cortex in psychosis inferred from functional MRI. A, Reduced functional connectivity between right ventral anterior insula (vAIns) and regions of the default mode network. Reproduced from Moran et al. 2013. PCC, posterior cingulate cortex; MPFC, medial prefrontal cortex; NC, normal control; SZ, schizophrenia. **B,** Altered functional coupling between right anterior insula and the posterior cingulate cortex in individuals at high risk (HR) and ultra-high risk (UHR) for psychosis compared to healthy comparison individuals (CTRL). Reproduced from Motruba et al. 2014. **C,** Altered functional connectivity pattern of the right anterior insula in individuals with schizophrenia compared to healthy controls (reproduced from Palaniyappan et al. 2013).

In Chapter 3, I show that the insula's connectional topography is best represented as a continuum of gradual change oriented along an anterior-posterior axis. The anterior-posterior topographic organization facilitates, at least in part, the functional specialization of the insular cortex, ranging from sensorimotor processing to higher-order cognitive function. I hypothesized that connectivity profiles of the insula along the anterior-posterior topographic axis would differ in individuals with schizophrenia compared to healthy controls, potentially resulting in altered topographic orientation and/or altered magnitude of spatial

variation in functional connectivity across the topography of the insula. This could produce connectivity profiles that are less differentiated along the insula's main topographic axis in schizophrenia, given the overall reduced segregation between functional brain networks that is typically found in the disorder (Fornito et al. 2012). Moreover, schizophrenia often shows widespread reductions in functional connectivity across many brain regions (van den Heuvel and Fornito 2014; Ganella et al. 2017), I therefore hypothesized that the altered topographic organization of the insula would be coupled with overall reduced functional connectivity between the insula and other brain regions to which it typically connects. Finally, I hypothesized that the extent of reorganization of insula's connectional topography would associate with the severity of clinical symptoms and cognitive impairment. In particular, given the patterns of functional differentiation between the anterior and posterior aspect of the insula, I hypothesized that alterations in functional connectivity of the anterior portion of the insula would more likely associate with symptoms relating to distortions in thinking, emotion and cognitive deficits, whereas the posterior part of the insula would link to abnormalities in sensory perception.

Aim 3

Having successfully characterized the topographic organization of the insular cortex in health (Chapter 3) and neuropsychiatric illness (Chapter 4), I next applied the new methodology and concepts that I developed to study the insula to the entire subcortex. Compared to cortical structures, the human subcortex remains one the brain's remaining *terra incognita* (Alkemade et al. 2013; Forstmann et al. 2016) and the functional topography of some subcortical areas is not well characterized. The main aim in Chapter 5 was to utilize the methods developed and refined on the insula, to establish a new MRI atlas of the human subcortex, and to use the atlas to investigate the organization of the subcortex. Most MRI atlases focus on the cerebral cortex (see Figure 1.1), and thus there is a pressing need to develop a comprehensive atlas of the subcortex. I aimed to use the new subcortex atlas to enable holistic connectome mapping and characterization of cortico-subcortical circuits, and to investigate the relationship between subcortical organization and human behavioral traits and cognition.

Subcortex neuroanatomy

The subcortex lies deep below the cerebral cortex. The subcortex comprises approximately 25% of the entire brain volume (Dunbar 1992) in humans but consists of more than 400 small, unique and functional heterogeneous nuclei (FCAT 1998). These nuclei form three gross anatomical and functional divisions including i) basal ganglia; ii) diencephalon; and, iii) limbic structures. Nuclei located in the brainstem such as the red nucleus and ventral tegmental area are not discussed in this thesis.

The basal ganglia is a group of interconnected gray matter nuclei, including the caudate nucleus, nucleus accumbens, putamen, globus pallidus, substantia nigra and subthalamic nucleus. While the substantia nigra and the subthalamic nucleus are not anatomical constituents of the rest of the basal ganglia, their functions are closely related. The basal ganglia has long been considered crucial in voluntary and involuntary movement control, evident from their unequivocal role in Parkinson's disease (Obeso et al. 2000), in which the extrapyramidal motor system is primarily affected. In addition to the prominent motor control function, the basal ganglia is also involved in a variety of reward and goal-directed

behaviors through their dense reciprocal connections with the thalamus and the cerebral cortex, known as the cortico-basal ganglia-thalamo-cortical circuit (Maia and Frank 2011).

The thalamus is part of the diencephalon and serves as a relay centre in the brain for sensory information and motor control signals. The thalamus also participates in higher-order cognitive function via reciprocal and nonreciprocal connections with a wide range of cortical regions (Sherman 2016). Other subcortical structures belonging to diencephalon include hypothalamus, epithalamus, subthalamus as well as metathalamus. Each of them comprises even smaller nuclei, functionally specialized through associated neuronal pathways. For example, the hypothalamus, which is located below the thalamus, links the central nervous system to the body's endocrine system via synthesizing and secreting neurohormones. It regulates many aspects of metabolic processes and autonomic nervous system function such as body temperature, hunger, thirst, anger, feeding and sexual behaviors (Hennig 2001).

The remaining part of the subcortex consists of the limbic system, including the hippocampus and the amygdala (amygdaloid complex). The hippocampus or a more-broad definition of hippocampal formation is a bulb-like structure buried deep within the medial temporal lobe. Broadly, it consists of dentate gyrus, hippocampus, subiculum, presubiculum, parasuiculum and entorhinal cortex (Andersen et al. 2007). While the hippocampus is a layered structure and is traditionally considered part of the medial temporal lobe, the hippocampus is often studied separately from the cerebral cortex in modern neuroimaging studies due to its deep location, unique cytoarchitectonic composition, complex anatomical organization, as shown in Figure 1.6. In terms of the function, the hippocampus, especially the dorsoposterior portion, plays a critical role in episodic memory and spatial navigation, whereas the ventroanterior hippocampus mediates anxiety-related emotional response (Strange et al. 2014) via its connections with the amygdala. Indeed, the amygdala, which is an almond-like structure comprising a collection of interconnected nuclei, located directly rostral to the hippocampal formation, plays an essential role in detecting and learning of objects with emotional significance, including both fearful (negative) and rewarding (positive) environmental stimuli (Janak and Tye 2015). Studies also suggest the existence of a sublenticular extended amygdaloid continuum within the stria terminalis to the bed nucleus of the stria terminalis.

This group of structures is referred to as extended amygdala and is considered an important output channel for the limbic system (Heimer et al. 2008).

Topographic organization of the human subcortex

Current anatomical and functional knowledge of the more than 400 subcortical structures have been obtained mainly through laboratory work in postmortem brain tissues using histological techniques or invasive tract-tracing and lesion studies in experimental animals. However, fewer than 7-10% of these structures are delineated in non-invasive, *in vivo* MRI-based atlases (Evans et al. 2012; Forstmann et al. 2016). For example, the thalamus is conventionally divided into approximately 30 cytoarchitectonic nuclei (Morel et al. 1997), whereas boundaries between thalamic nuclei are hardly distinguishable in standard MRI images. Even less is known about the functional organization and connectivity architecture of the subcortex in living humans. Subcortical structures are widely implicated in the pathophysiology of many neurological and neuropsychiatric disorders and are greatly involved in cortical information processing that gives rise to cognition (Shepherd 2013). Nevertheless, many leading brain atlases delineate only cortical regions (Yeo et al. 2011; Glasser et al. 2016; Gordon et al. 2016; Langs et al. 2016; Schaefer et al. 2018); examples are shown in Figure 1.1. The subcortex features in fewer than five of the more than twenty parcellation atlases surveyed in a recent review (Eickhoff et al. 2018b). The field's preponderance for the cerebral cortex, coupled with technical challenges inherent to imaging the subcortex, such as its deep location and iron-rich properties (Forstmann et al. 2016; Puckett et al. 2018), has led to the subcortex remaining a *terra incognita* (Alkemade et al. 2013; Forstmann et al. 2016).

Modern neuroimaging techniques such as the high-resolution MRI have enabled the delineation of broad anatomical structures in the subcortex *in vivo.* In particular, segmentations based on T1-weighted structural images provide delineations of caudate nucleus, nucleus accumbens, putamen, globus pallidus, thalamus, hippocampus and amygdala (Fischl et al. 2002; Jenkinson et al. 2012), whereas combining T1- and T2-weighted images facilitates the delineation of much smaller nuclei, such as the substantia nigra and subthalamic nucleus (Pauli et al. 2018) as well as hippocampal subfields (Iglesias et al. 2015)

and sub-nuclei comprising the amygdala (Saygin et al. 2017) when integrating information from *ex vivo* MRI (Figure 1.6A).

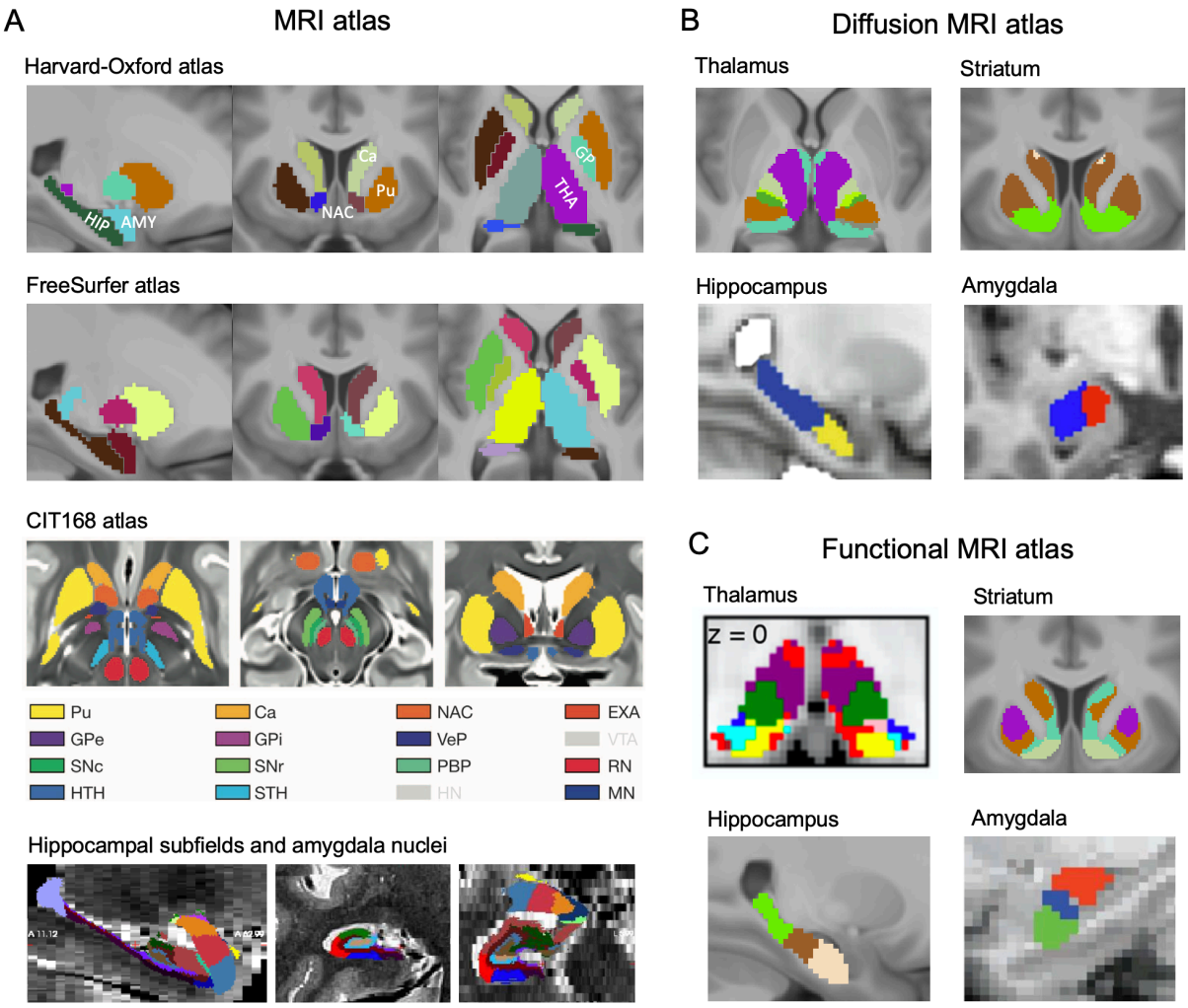


Figure 1.6. Representative structural, diffusion and functional MRI atlases of subcortical structures. A, Anatomical structures in the subcortex delineated based on standard T1-weighted MRI images available in FSL (Harvard-Oxford atlas, Jenkinson et al. 2012) and FreeSurfer (Fischl et al. 2002). Combining T1- and T2-weighted images facilitates the delineation of additional small nuclei (CIT168 atlas, adapted from Pauli et al. 2018), as well as hippocampal subfields (Iglesias et al. 2015) and sub-nuclei comprising the amygdala with ancillary labeling inferred from *ex vivo* MRI (Saygin et al. 2017). HIP, hippocampus; AMY, amygdala; NAC, nucleus accumbens; Ca, caudate nucleus; Pu, putamen; THA, thalamus; GP, globus pallidus. Gpe, globus pallidus external; Gpi, globus pallidus internal; SNc, substantia nigra compacta; SNr, substantia nigra reticulata; HTH, hypothalamus; STH, subthalamic nucleus; VeP, ventral pallidum; PBP, parabrachial pigmented nucleus; HN, habenular nuclei; EXA, extended amygdala; VTA, ventral tegmental area; RN, red nucleus; MN, mammillary nucleus; **B,** Subdivisions of thalamus (Behrens et al. 2003), striatum (Tziortzi et al. 2013), hippocampus (adapted from Adnan et al. 2016) and amygdala (adapted from Solano-Castiella et al. 2010) based on structural connectivity inferred from diffusion MRI. **C,** Functional subdivisions of thalamus (adapted from Hwang et al. 2017), striatum (Choi et al. 2012), hippocampus (Plachti et al. 2019) and amygdala (adapted from Mishra et al. 2014) based on functional connectivity inferred from resting-state functional MRI.

Moreover, the development of diffusion MRI techniques first enabled non-invasive mapping of subcortical connectivity architecture in living humans, resulting in *in vivo* maps of white matter connectivity. Earlier work focused on applying tractography to characterize the structural connectivity architecture of the thalamus (Behrens et al. 2003), striatum (Lehericy et al. 2004; Leh et al. 2007; Tziortzi et al. 2013), hippocampus and amygdala (Smith et al. 2009; Colnat-Coulbois et al. 2010; Solano-Castiella et al. 2010; Adnan et al. 2016) as exemplified in Figure 1.6B. Many of these pioneering studies sought to recapitulate neural circuits predominantly reported in rodents and non-human primates, thereby yielding correspondence between humans and these species. For the first time, the thalamus was parcellated non-invasively into seven subregions, and each subregion is thought to be most strongly connected to one of the seven broadly defined anatomical areas in the cortex (Behrens et al. 2003). The delineated thalamic subregions were found to be spatially consistent with thalamic nuclei identified from histology (Morel et al. 1997). Similarly, based on cortical regions to which subcortical nuclei are connected, the connectivity architecture of the striatum was topographically characterized in terms of posterior-sensorimotor, anterior-associative and ventral-limbic pathways (Lehericy et al. 2004), paralleling axonal tracing studies in experimental animals (Alexander et al. 1986). In contrast to the abundant long distance thalamo-cortical and striato-cortical connections, the hippocampus and amygdala appear to be more densely connected to surrounding cortical and subcortical structures. For example, tract-tracing studies in rodents and monkeys have repeatedly shown that the hippocampus and other limbic structures are topographically interconnected, forming a complex system of hippocampal-diencephalic-cingulate network for memory and emotion processes (Bubb et al. 2017). While it remains technically challenging to map all efferent and afferent fibers of the hippocampus in living humans using diffusion MRI, fiber tracts connecting the hippocampus to mammillary bodies (postcommissural fornix), anterior thalamic nuclei (fornix), and the cingulate cortex (cingulum) have been successfully reconstructed (Granziera et al. 2011; Christiansen et al. 2016; Wei et al. 2017; Maller et al. 2019).

The emergence of functional MRI facilitated further investigation of the connectivity architecture of the human subcortex from the perspective of a complementary MRI modality. As aforementioned, diffusion MRI captures the diffusion process of water molecules (Le Bihan

and Breton 1985), which can be used to generate tractograms that represent white matter tracts (i.e. structural connectivity) in the brain, whereas functional MRI provides an index of brain activity and the statistical patterns of co-activation are referred to as functional connectivity (Biswal et al. 1995). See Chapter 2 for a detailed description of the two techniques. Di Martino and colleagues (Di Martino et al. 2008) mapped functional connectivity from six striatal activation hotspots (Postuma and Dagher 2005) to the rest of the brain. They found that patterns of connectivity across the six striatal seeds are different and the cortico-striatal connectivity maps produced were consistent with findings of cortico-striatal circuits in macaque (Alexander et al. 1986; Di Martino et al. 2008). Rather than selecting striatal seeds beforehand, Barnes and colleagues (Barnes et al. 2010) grouped striatal voxels into three clusters on the basis of similarity in patterns of whole-brain functional coupling. Each cluster thus represents one putative striatal subregion. Choi and colleagues (Choi et al. 2012) instead assigned striatal voxels to cortical networks (Yeo et al. 2011) according to the network with which they are most strongly connected, yielding a 7- and 17-network equivalent striatal parcellations. Building on this previous work, many different clustering methods, community detection algorithms or network assignment approaches have been proposed to investigate the functional organization of subcortical structures, yielding an assemblage of parcellation atlases for the striatum (Jung et al. 2014; Janssen et al. 2015; Pauli et al. 2016; Ogawa et al. 2018), thalamus (Hwang et al. 2017; Zhang and Li 2017), hippocampus (Chase et al. 2015; Robinson et al. 2015; Barnett et al. 2019; Plachti et al. 2019; Zhong et al. 2019), and amygdala (Bickart et al. 2012; Mishra et al. 2014; Zhang et al. 2018) . Representative functional atlases of these subcortical structures are shown in Figure 1.6C.

More recently, an alternative model of topographic organization based on the concept of cortical gradients has garnered increasing attention in the field (Margulies et al. 2016; Haak et al. 2018; Tian and Zalesky 2018) and has recently been applied to investigate the connectivity architecture of specific subcortical structures (Marquand et al. 2017; Vos de Wael et al. 2018; Przeździk et al. 2019). These studies show that the principal axis of variation in connectivity within the hippocampus is topographically organized along an anterior-posterior axis (Vos de Wael et al. 2018; Przeździk et al. 2019), which is consistent with the longitudinal functional organization of the hippocampus (Poppenk et al. 2013; Strange et al.

2014). Interestingly, the secondary connectivity gradient recapitulates the media-lateral axis that is typically presented in hippocampal histology (Vos de Wael et al. 2018), see Figure 1.7A. Another subcortical structure that has been examined using gradient representations is the striatum (Marquand et al. 2017). According to the authors' observations, the dominant striatal connectivity gradient separates the three major neuroanatomical divisions in the striatum, including caudate nucleus, nucleus accumbens and putamen (Figure 1.7B, upper), whereas the second gradient organizes along a ventral-to-dorsal axis that traverses both putamen and caudate. This spatial layout is in line with the theoretical reward circuit of the striatum inferred from invasive tract-tracing studies (Haber et al. 2000; Haber 2003; Haber and Knutson 2010)(Figure 1.7B, bottom). More interestingly, Marquand and colleagues (2017) found that individual variation in striatal connectivity gradients associates with goal-directed human behaviors, particularly delayed discounting, confirming the role of the striatum in the brain's reward system.

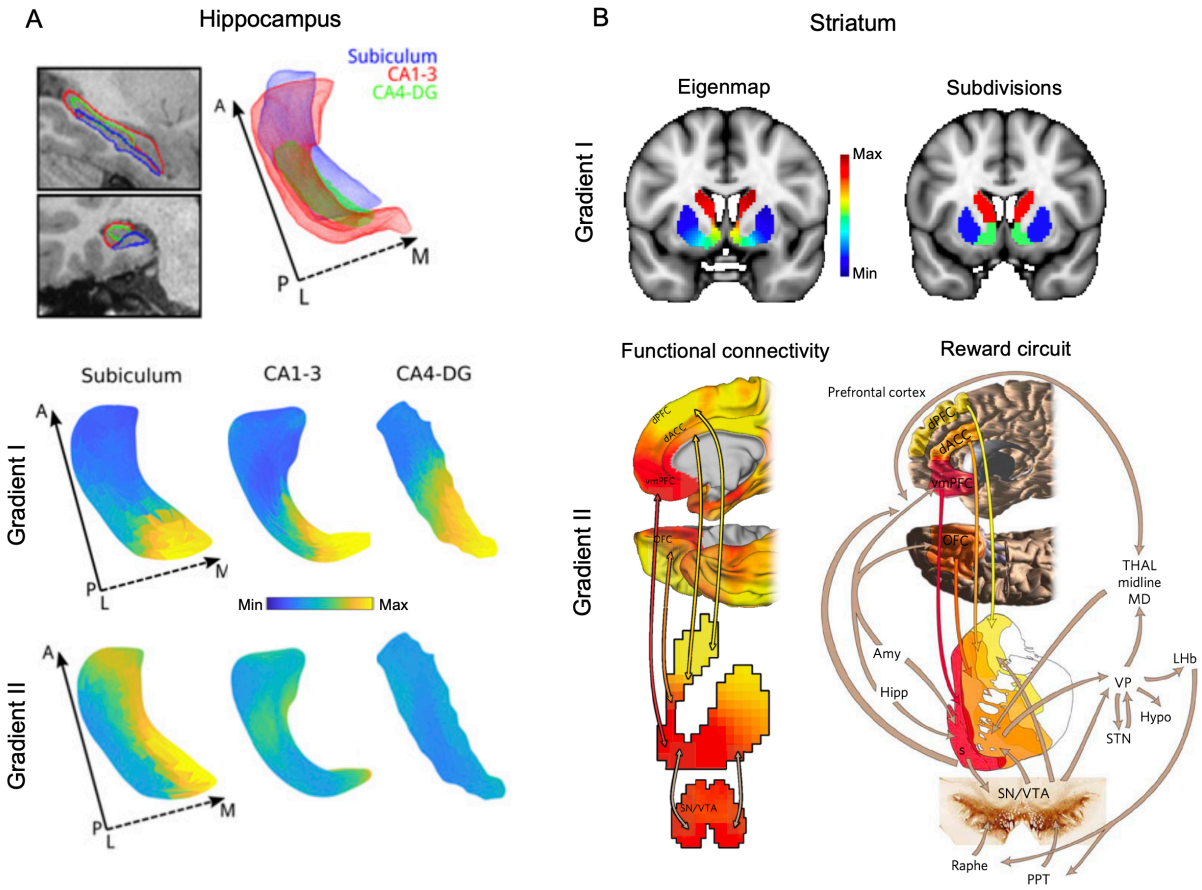


Figure 1.7. Connectivity gradients of hippocampus and striatum inferred from resting-state functional MRI. A, Connectivity gradients within hippocampal subfields (subiculum, CA1-3 and CA4-DG). The first principal gradient (Gradient I) in hippocampal functional connectivity varies along an anterior-posterior, whereas the second gradient (Gradient II) runs along the medial-lateral axis that is consistent with the hippocampal infolding

(adapted from Vos de Wael et al. 2018). CA, cornu ammonis; DG, dentate gyrus. **B,** Connectivity gradients within the striatum. The first gradient (Gradient I) distinguishes connectivity variation between three major neuroanatomical divisions in the striatum, including caudate nucleus (red), nucleus accumbens (green) and putamen (blue), whereas the second gradient (Gradient II, left, adapted from Marquand et al. 2017) recapitulates the topographic organization of striatum, the theoretical reward circuit, predicted from tract-tracing studies (right, adapted from Marquand et al. 2017; Haber and Kuntson 2010). dPFC, dorsal prefronal cortex; dACC; dorsal anterior cingulate cortex; vmPFC, ventral medial prefrontal cortex; OFC, orbital fronal cortex; Amy, amygdala; Hipp, hippocampus; SN, substantia nigra; VTA, ventral tegmental area; PPT, pedunculopontine nucleus; STN, subthalamic nucleus; VP, ventral pallidum; Hypo, hypothalamus; LHb, laterla habenula; THAL, thalamus.

Nevertheless, most previous studies examined specific subcortical regions, such as the striatum, thalamus, hippocampus and amygdala in isolation (Figure 1.6 B&C and Figure 1.7), without first establishing whether functional boundaries or gradual transitions exist between these regions. In other words, a piecemeal approach has been taken to investigate the topography of the subcortex, whereby individual subcortical nuclei are studied in isolation, potentially overlooking global topographic effects encompassing the entire subcortical volume. It may seem reasonable to study individual subcortical regions in isolation because anatomical boundaries between broad subcortical nuclei are generally well established and represented in numerous MRI atlases, such as Lead-DBS (Horn and Kuhn 2015), FSL (Jenkinson et al. 2012) and FreeSurfer (Fischl et al. 2002), as exemplified in Figure 1.6A. Surprisingly however, the very few existing connectivity-based atlases (Figure 1.8) encompassing more than one subcortical region (Bellec et al. 2010; Craddock et al. 2012; Fan et al. 2016; Ji et al. 2019) usually do not preserve established anatomical boundaries (Figure 1.6A). This may suggest structure-function divergence or methodological variation across previous studies.

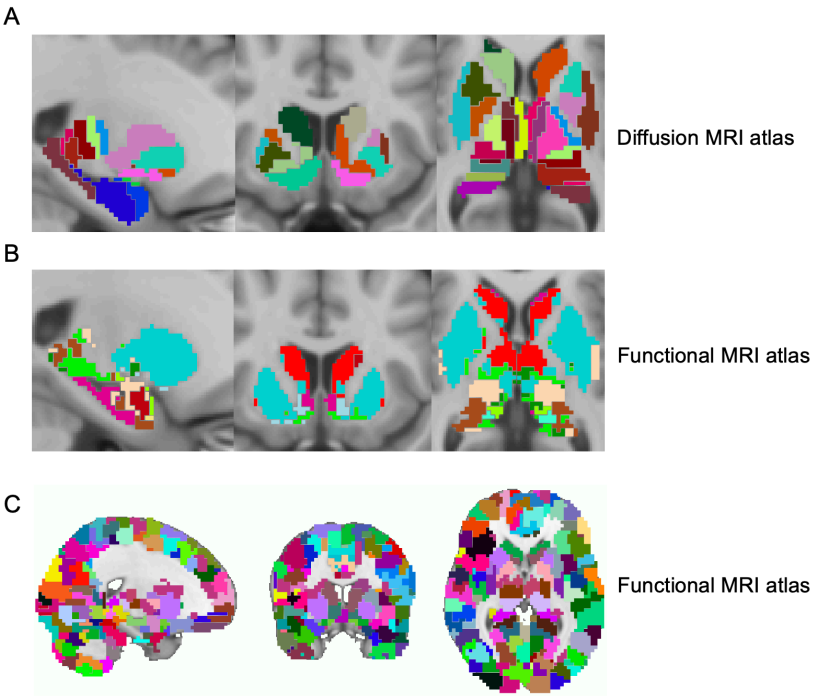


Figure 1.8. Connectivity-based atlases comprising more than one subcortical region. A, Subcortex atlas delineated based on structural connectivity using diffusion MRI data (Fan et al. 2016), with cortex, brainstem and cerebellum removed. **B,** Subcortex atlas delineated based on functional connectivity using data from resting-state functional MRI (Ji et al. 2019), with brainstem and cerebellum removed. **C,** Whole brain atlas including the subcortex delineated based on functional connectivity inferred from resting-state functional MRI (Bellec et al. 2010).

Given these considerations, I aimed to map the functional connectivity architecture across the entire topography of the subcortex, with the goal of delineating a new functional MRI atlas for the subcortex. In particular, I aimed to apply the new methodology I developed to map the insula's topography (Chapter 3) to investigate the functional organization of the subcortex. I hypothesized i) a rudimentary alignment between the anatomical and functional architecture of the subcortex; and, ii) some functional subsystems that potentially diverge from the anatomy. For example, the anterior-posterior functional specification of hippocampus is divergent from the topography of anatomical subfields, which is medial-laterally organized (Poppenk et al. 2013; Strange et al. 2014), and therefore the connectivity topography of the hippocampus may be different to the topographic organization of hippocampal subfields. I also aimed to use this new subcortex atlas to characterize the organization of cortico-subcortical circuits and investigate the relationship between subcortical functional organization and human behaviors. In particular, subcortical nuclei are widely implicated in numerous cognitive processes and neuropsychiatric disorders, acting through the brain's dopaminergic and mesolimbic reward systems (Maia and Frank 2011; Shepherd 2013). Information processing and exchange within these systems are crucial in learning and guiding behaviors so as to avoid punishments while acquiring rewards (Maia 2009; Pennartz et al. 2009). Hence, I hypothesized that subcortical functional connectivity

would associate with human cognition, especially the cognitive processes that relate to rewards, decision making and goal-directed behaviors.

Summary and thesis overview

The overarching aim of this thesis is to comprehensively characterize the topographic organization of the human insular cortex and subcortex using modern functional neuroimaging techniques. These brain areas are widely implicated in the pathophysiology of numerous neuropsychiatric and neurological disorders, yet their topographic architectures are some of the most disputed of all brain areas. Variation in the number of putative subregions comprising the insular cortex is highly discrepant between studies, ranging between 2 and 31 subdivisions, while the large-scale topography of the subcortex is not well understood. Before the role of these key brain areas in the pathophysiology of neuropsychiatric disorders can be elucidated, these challenges must first be resolved, and a deeper understanding of topographic organization established. Indeed, in this thesis, I demonstrated how a novel gradient-based characterization of insula's topography (Chapter 3) can be utilized to uncover new insights into insula's dysfunction associated with schizophrenia (Chapter 4).

To develop a more principled understanding of brain topography, I aimed to reconcile the distinction between classical models of topographic variation based on discrete regions and contemporary representations involving continuous gradients. The next chapter (Chapter 2) introduces these two complementary conceptualizations of brain topography and provides the necessary background information for the remaining chapters, including a brief overview of functional neuroimaging techniques and the key methodologies used throughout the thesis. Chapter 3 investigated the topography of the insular cortex using functional neuroimaging in 100 healthy adults, aiming to establish whether topographic variation is most parsimoniously represented in terms of continuous gradients or discrete regions. Next, Chapter 4 applied these new insights to investigate whether a serious neuropsychiatric disorder (schizophrenia) is associated with reorganization of the insula's topography and alterations in its functional connectivity architecture. Having developed and tested a successful model of the insula's topography in health and illness, I next aimed to extend the

novel model to the entire human subcortex using functional neuroimaging in more than 1000 health adults, with the goal of developing a new subcortical MRI atlas and investigating the functional connectivity architecture of the subcortex in rest and in response to task demands, as well as associations with inter-individual variation in cognitive performance and behavioral traits. Work pertaining to the subcortex is presented in Chapter 5. Finally, Chapter 6 provides an extended discussion, consideration of key limitations of the studies and brief prospective of potential future work.

Summary of key outcomes

- I provided a principled approach to reconcile classical (i.e. distinct regions) and contemporary (i.e. continuous gradients) representations of brain topography. In particular, I developed a formal model selection procedure based on null hypothesis testing to reconcile these two complementary models of brain topography, enabling topographic representations that parsimoniously combine distinct regions and continuous gradients.

- I showed that the functional connectivity architecture of the insular cortex is most parsimoniously represented using continuous gradients of gradual change oriented along an anterior-posterior axis. In contrast to previous studies, I argued that evidence for the insula comprising distinct functional regions differentiated by hard boundaries is relatively weak, although further investigation is warranted.

- I demonstrated that inter-individual variation in the insula's topographic organization significantly associates with measures of behavior and cognitive performance. In particular, individuals with greater differentiation within the anterior insula are associated with higher scores in measures of positive affect, self-efficacy, emotion recognition, motor dexterity and gustatory sensation. Contrastingly, individuals who score high on sleep disturbances, underpinned by somatosensory sensation, are associated with greater differentiation within the posterior insula.

- I presented new evidence for subtle reorganization of insula's topography in individuals with schizophrenia. In particular, I showed that the insula is less differentiated along its anterior-posterior axis among patients with schizophrenia, compared to healthy controls, with patterns of functional connectivity between the insula and key cortical areas also showing disruptions. Crucially, I presented evidence suggesting that inter-individual variation in the extent of insula differentiation significantly associates with the severity of clinical symptoms in the group of patients studied.

- I developed a new multiscale MRI atlas of the human subcortex, called the *Melbourne Subcortex Atlas*. The atlas unveils four hierarchical scales of subcortical organization, recapitulating well-known anatomical nuclei at the coarsest scale and delineating 27 new bilateral regions at the finest. The atlas is made publicly available to the neuroscience community and has already been used in numerous connectomic studies and to help guide targeting of brain stimulation therapies in ongoing clinical trials.

- I unveiled the astoundingly complex topographic organization of the human subcortex using both 3 Tesla and ultra-high field strength (7 Tesla) functional neuroimaging. The improved contrast to noise ratio and spatial resolution of 7T enabled the delineation of finer functional architecture in the subcortex, particularly within the hippocampus and the amygdala, where more functional subdivisions were delineated. Moreover, the new subcortical atlas is personalized to account for individual connectivity differences and utilized to uncover reproducible relationships between subcortical connectivity and individual variation in human behaviors. I also established new links between cortical networks and subcortical regions and presented evidence for a significant and reproducible association between tobacco use and subcortical connectivity.

References

Adnan A, Barnett A, Moayedi M, McCormick C, Cohn M, McAndrews MP. 2016. Distinct hippocampal functional networks revealed by tractography-based parcellation. Brain Structure and Function 221:2999-3012.

Afif A, Mertens P. 2010. Description of sulcal organization of the insular cortex. Surgical and radiologic anatomy 32:491-498.

Alcauter S, Lin W, Keith Smith J, Gilmore JH, Gao W. 2015. Consistent anterior-posterior segregation of the insula during the first 2 years of life. Cereb Cortex 25:1176-1187.

Alexander GE, DeLong MR, Strick PL. 1986. Parallel organization of functionally segregated circuits linking basal ganglia and cortex. Annu Rev Neurosci 9:357-381.

Alkemade A, Keuken M, Forstmann B. 2013. A perspective on terra incognita: uncovering the neuroanatomy of the human subcortex. Frontiers in Neuroanatomy 7.

Allen P, Larøi F, McGuire PK, Aleman A. 2008. The hallucinating brain: a review of structural and functional neuroimaging studies of hallucinations. Neurosci Biobehav Rev 32:175-191.

Andersen P, Morris R, Amaral DE, Bliss T, O'Keefe JE. 2007. The hippocampus book. New York, NY, US: Oxford University Press.

Augustine JR. 1996. Circuitry and functional aspects of the insular lobe in primates including humans. Brain Res Brain Res Rev 22:229-244.

Barnes KA, Cohen AL, Power JD, Nelson SM, Dosenbach YB, Miezin FM, Petersen SE, Schlaggar BL. 2010. Identifying Basal Ganglia divisions in individuals using resting-state functional connectivity MRI. Front Syst Neurosci 4:18.

Barnett AJ, Man V, McAndrews MP. 2019. Parcellation of the Hippocampus Using Resting Functional Connectivity in Temporal Lobe Epilepsy. Frontiers in Neurology 10.

Behrens TE, Johansen-Berg H, Woolrich MW, Smith SM, Wheeler-Kingshott CA, Boulby PA, Barker GJ, Sillery EL, Sheehan K, Ciccarelli O et al. 2003. Non-invasive mapping of connections between human thalamus and cortex using diffusion imaging. Nat Neurosci 6:750-757.

Bellec P, Rosa-Neto P, Lyttelton OC, Benali H, Evans AC. 2010. Multi-level bootstrap analysis of stable clusters in resting-state fMRI. Neuroimage 51:1126-1139.

Bickart KC, Hollenbeck MC, Barrett LF, Dickerson BC. 2012. Intrinsic amygdala-cortical functional connectivity predicts social network size in humans. J Neurosci 32:14729-14741.

Biswal B, Yetkin FZ, Haughton VM, Hyde JS. 1995. Functional connectivity in the motor cortex of resting human brain using echo-planar MRI. Magn Reson Med 34:537-541.

Bock NA, Kocharyan A, Liu JV, Silva AC. 2009. Visualizing the entire cortical myelination pattern in marmosets with magnetic resonance imaging. J Neurosci Methods 185:15-22.

Bonthius DJ, Solodkin A, Van Hoesen GW. 2005. Pathology of the insular cortex in Alzheimer disease depends on cortical architecture. J Neuropathol Exp Neurol 64:910-922.

Brodmann K. 1909. Brodmann's localisation in the cerebral cortex. New York, USA: Springer.

Bubb EJ, Kinnavane L, Aggleton JP. 2017. Hippocampal - diencephalic - cingulate networks for memory and emotion: An anatomical guide. Brain Neurosci Adv 1.

Cauda F, Costa T, Torta DM, Sacco K, D'Agata F, Duca S, Geminiani G, Fox PT, Vercelli A. 2012. Meta-analytic clustering of the insular cortex: characterizing the meta-analytic connectivity of the insula when involved in active tasks. Neuroimage 62:343-355.

Cauda F, D'Agata F, Sacco K, Duca S, Geminiani G, Vercelli A. 2011. Functional connectivity of the insula in the resting brain. Neuroimage 55:8-23.

Cauda F, Vercelli A. 2013. How many clusters in the insular cortex? Cereb Cortex 23:2779-2780.

Cerliani L, Thomas RM, Jbabdi S, Siero JC, Nanetti L, Crippa A, Gazzola V, D'Arceuil H, Keysers C. 2012. Probabilistic tractography recovers a rostrocaudal trajectory of connectivity variability in the human insular cortex. Hum Brain Mapp 33:2005-2034.

Chang LJ, Yarkoni T, Khaw MW, Sanfey AG. 2013. Decoding the role of the insula in human cognition: functional parcellation and large-scale reverse inference. Cereb Cortex 23:739-749.

Charlson FJ, Ferrari AJ, Santomauro DF, Diminic S, Stockings E, Scott JG, McGrath JJ, Whiteford HA. 2018. Global Epidemiology and Burden of Schizophrenia: Findings From the Global Burden of Disease Study 2016. Schizophrenia Bulletin 44:1195-1203.

Chase HW, Clos M, Dibble S, Fox P, Grace AA, Phillips ML, Eickhoff SB. 2015. Evidence for an anterior-posterior differentiation in the human hippocampal formation revealed by meta-analytic parcellation of fMRI coordinate maps: focus on the subiculum. Neuroimage 113:44-60.

Choi EY, Yeo BT, Buckner RL. 2012. The organization of the human striatum estimated by intrinsic functional connectivity. J Neurophysiol 108:2242-2263.

Christiansen K, Aggleton JP, Parker GD, O'Sullivan MJ, Vann SD, Metzler-Baddeley C. 2016. The status of the precommissural and postcommissural fornix in normal ageing and mild cognitive impairment: An MRI tractography study. Neuroimage 130:35-47.

Clark TE. 1896. The comprative anatomy of the insula. Journal of Comparative Neurology 6:59-100.

Colnat-Coulbois S, Mok K, Klein D, Penicaud S, Tanriverdi T, Olivier A. 2010. Tractography of the amygdala and hippocampus: anatomical study and application to selective amygdalohippocampectomy. J Neurosurg 113:1135-1143.

Craddock RC, James GA, Holtzheimer PE, 3rd, Hu XP, Mayberg HS. 2012. A whole brain fMRI atlas generated via spatially constrained spectral clustering. Hum Brain Mapp 33:1914-1928.

Craig AD. 2009. How do you feel--now? The anterior insula and human awareness. Nat Rev Neurosci 10:59-70.

Craig AD, Chen K, Bandy D, Reiman EM. 2000. Thermosensory activation of insular cortex. Nat Neurosci 3:184-190.

Dandash O, Fornito A, Lee J, Keefe RS, Chee MW, Adcock RA, Pantelis C, Wood SJ, Harrison BJ. 2014. Altered striatal functional connectivity in subjects with an at-risk mental state for psychosis. Schizophr Bull 40:904-913.

Deen B, Pitskel NB, Pelphrey KA. 2011. Three systems of insular functional connectivity identified with cluster analysis. Cereb Cortex 21:1498-1506.

Desikan RS, Segonne F, Fischl B, Quinn BT, Dickerson BC, Blacker D, Buckner RL, Dale AM, Maguire RP, Hyman BT et al. 2006. An automated labeling system for subdividing the human cerebral cortex on MRI scans into gyral based regions of interest. Neuroimage 31:968-980.

Di Martino A, Scheres A, Margulies DS, Kelly AMC, Uddin LQ, Shehzad Z, Biswal B, Walters JR, Castellanos FX, Milham MP. 2008. Functional Connectivity of Human Striatum: A Resting State fMRI Study. Cerebral Cortex 18:2735-2747.

Dunbar RIM. 1992. Neocortex size as a constraint on group size in primates. Journal of Human Evolution 22:469-493.

Eickhoff SB, Constable RT, Yeo BTT. 2018a. Topographic organization of the cerebral cortex and brain cartography. Neuroimage 170:332-347.

Eickhoff SB, Yeo BTT, Genon S. 2018b. Imaging-based parcellations of the human brain. Nature Reviews Neuroscience 19:672-686.

Ellison-Wright I, Glahn DC, Laird AR, Thelen SM, Bullmore E. 2008. The anatomy of first-episode and chronic schizophrenia: an anatomical likelihood estimation meta-analysis. Am J Psychiatry 165:1015-1023.

Evans AC, Janke AL, Collins DL, Baillet S. 2012. Brain templates and atlases. Neuroimage 62:911-922.

Faillenot I, Heckemann RA, Frot M, Hammers A. 2017. Macroanatomy and 3D probabilistic atlas of the human insula. Neuroimage 150:88-98.

Fan L, Li H, Zhuo J, Zhang Y, Wang J, Chen L, Yang Z, Chu C, Xie S, Laird AR et al. 2016. The Human Brainnetome Atlas: A New Brain Atlas Based on Connectional Architecture. Cereb Cortex 26:3508-3526.

FCAT. 1998. Terminologia Anatomica: International Anatomical Terminology 1st edn Thieme Stuttgart.

Finn ES, Shen X, Scheinost D, Rosenberg MD, Huang J, Chun MM, Papademetris X, Constable RT. 2015. Functional connectome fingerprinting: identifying individuals using patterns of brain connectivity. Nature Neuroscience 18:1664.

Fischl B, Salat DH, Busa E, Albert M, Dieterich M, Haselgrove C, van der Kouwe A, Killiany R, Kennedy D, Klaveness S et al. 2002. Whole brain segmentation: automated labeling of neuroanatomical structures in the human brain. Neuron 33:341-355.

Fornito A, Yucel M, Patti J, Wood SJ, Pantelis C. 2009. Mapping grey matter reductions in schizophrenia: an anatomical likelihood estimation analysis of voxel-based morphometry studies. Schizophr Res 108:104-113.

Fornito A, Zalesky A, Pantelis C, Bullmore ET. 2012. Schizophrenia, neuroimaging and connectomics. Neuroimage 62:2296-2314.

Forstmann BU, de Hollander G, van Maanen L, Alkemade A, Keuken MC. 2016. Towards a mechanistic understanding of the human subcortex. Nature Reviews Neuroscience 18:57.

Fox PT, Friston KJ. 2012. Distributed processing; distributed functions? Neuroimage 61:407-426.

Friedman DP, Murray EA, O'Neill JB, Mishkin M. 1986. Cortical connections of the somatosensory fields of the lateral sulcus of macaques: evidence for a corticolimbic pathway for touch. J Comp Neurol 252:323-347.

Friston KJ. 1998. The disconnection hypothesis. Schizophr Res 30:115-125.

Gallay DS, Gallay MN, Jeanmonod D, Rouiller EM, Morel A. 2012. The insula of Reil revisited: multiarchitectonic organization in macaque monkeys. Cereb Cortex 22:175-190.

Ganella EP, Bartholomeusz CF, Seguin C, Whittle S, Bousman C, Phassouliotis C, Everall I, Pantelis C, Zalesky A. 2017. Functional brain networks in treatment-resistant schizophrenia. Schizophr Res 184:73-81.

Glahn DC, Laird AR, Ellison-Wright I, Thelen SM, Robinson JL, Lancaster JL, Bullmore E, Fox PT. 2008. Meta-analysis of gray matter anomalies in schizophrenia: application of anatomic likelihood estimation and network analysis. Biol Psychiatry 64:774-781.

Glasser MF, Coalson TS, Robinson EC, Hacker CD, Harwell J, Yacoub E, Ugurbil K, Andersson J, Beckmann CF, Jenkinson M et al. 2016. A multi-modal parcellation of human cerebral cortex. Nature 536:171-178.

Glasser MF, Van Essen DC. 2011. Mapping human cortical areas in vivo based on myelin content as revealed by T1- and T2-weighted MRI. J Neurosci 31:11597-11616.

Goodkind M, Eickhoff SB, Oathes DJ, Jiang Y, Chang A, Jones-Hagata LB, Ortega BN, Zaiko YV, Roach EL, Korgaonkar MS et al. 2015. Identification of a common neurobiological substrate for mental illness. JAMA Psychiatry 72:305-315.

Gordon EM, Laumann TO, Adeyemo B, Huckins JF, Kelley WM, Petersen SE. 2016. Generation and Evaluation of a Cortical Area Parcellation from Resting-State Correlations. Cereb Cortex 26:288-303.

Gordon EM, Laumann TO, Gilmore AW, Newbold DJ, Greene DJ, Berg JJ, Ortega M, Hoyt-Drazen C, Gratton C, Sun H et al. 2017. Precision Functional Mapping of Individual Human Brains. Neuron 95:791-807.e797.

Granziera C, Hadjikhani N, Arzy S, Seeck M, Meuli R, Krueger G. 2011. In-vivo magnetic resonance imaging of the structural core of the Papez circuit in humans. Neuroreport 22:227-231.

Guell X, Schmahmann JD, Gabrieli J, Ghosh SS. 2018. Functional gradients of the cerebellum. Elife 7.

Haak KV, Marquand AF, Beckmann CF. 2018. Connectopic mapping with resting-state fMRI. Neuroimage 170:83-94.

Haber SN. 2003. The primate basal ganglia: parallel and integrative networks. J Chem Neuroanat 26:317-330.

Haber SN, Fudge JL, McFarland NR. 2000. Striatonigrostriatal pathways in primates form an ascending spiral from the shell to the dorsolateral striatum. J Neurosci 20:2369-2382.

Haber SN, Knutson B. 2010. The reward circuit: linking primate anatomy and human imaging. Neuropsychopharmacology 35:4-26.

Heimer L, Van Hoesen GW, Trimble M, Zahm DS. 2008. 3 - THE ANATOMY OF THE BASAL FOREBRAIN. In: Heimer L, Van Hoesen GW, Trimble M, Zahm DS, editors. Anatomy of Neuropsychiatry San Diego: Academic Press p 27-67.

Heinze K, Reniers RL, Nelson B, Yung AR, Lin A, Harrison BJ, Pantelis C, Velakoulis D, McGorry PD, Wood SJ. 2015. Discrete alterations of brain network structural covariance in individuals at ultra-high risk for psychosis. Biol Psychiatry 77:989-996.

Hennig J. 2001. Hypothalamus. In: Smelser NJ, Baltes PB, editors. International Encyclopedia of the Social & Behavioral Sciences Oxford: Pergamon p 7113-7118.

Honea R, Crow TJ, Passingham D, Mackay CE. 2005. Regional deficits in brain volume in schizophrenia: a meta-analysis of voxel-based morphometry studies. Am J Psychiatry 162:2233-2245.

Horn A, Kuhn AA. 2015. Lead-DBS: a toolbox for deep brain stimulation electrode localizations and visualizations. Neuroimage 107:127-135.

Huntenburg JM, Bazin PL, Margulies DS. 2018. Large-Scale Gradients in Human Cortical Organization. Trends Cogn Sci 22:21-31.

Huth AG, de Heer WA, Griffiths TL, Theunissen FE, Gallant JL. 2016. Natural speech reveals the semantic maps that tile human cerebral cortex. Nature 532:453-458.

Hwang K, Bertolero MA, Liu WB, D'Esposito M. 2017. The Human Thalamus Is an Integrative Hub for Functional Brain Networks. J Neurosci 37:5594-5607.

Iglesias JE, Augustinack JC, Nguyen K, Player CM, Player A, Wright M, Roy N, Frosch MP, McKee AC, Wald LL et al. 2015. A computational atlas of the hippocampal formation using ex vivo, ultra-high resolution MRI: Application to adaptive segmentation of in vivo MRI. Neuroimage 115:117-137.

Insel TR. 2010. Rethinking schizophrenia. Nature 468:187-193.

Jakab A, Molnar PP, Bogner P, Beres M, Berenyi EL. 2012. Connectivity-based parcellation reveals interhemispheric differences in the insula. Brain Topogr 25:264-271.

James SL, Abate D, Abate KH, Abay SM, Abbafati C, Abbasi N, Abbastabar H, Abd-Allah F, Abdela J, Abdelalim A et al. 2018. Global, regional, and national incidence, prevalence, and years lived with disability for 354 diseases and injuries for 195 countries and territories, 1990–2017: a systematic analysis for the Global Burden of Disease Study 2017. The Lancet 392:1789-1858.

Janak PH, Tye KM. 2015. From circuits to behaviour in the amygdala. Nature 517:284-292.

Janssen RJ, Jylänki P, Kessels RPC, van Gerven MAJ. 2015. Probabilistic model-based functional parcellation reveals a robust, fine-grained subdivision of the striatum. NeuroImage 119:398-405.

Javitt DC. 2009. Sensory processing in schizophrenia: neither simple nor intact. Schizophr Bull 35:1059-1064.

Jenkinson M, Beckmann CF, Behrens TE, Woolrich MW, Smith SM. 2012. FSL. Neuroimage 62:782-790.

Ji JL, Spronk M, Kulkarni K, Repovs G, Anticevic A, Cole MW. 2019. Mapping the human brain's cortical-subcortical functional network organization. Neuroimage 185:35-57.

Jung WH, Jang JH, Park JW, Kim E, Goo E-H, Im O-S, Kwon JS. 2014. Unravelling the Intrinsic Functional Organization of the Human Striatum: A Parcellation and Connectivity Study Based on Resting-State fMRI. PLOS ONE 9:e106768.

Kahn RS, Keefe RS. 2013. Schizophrenia is a cognitive illness: time for a change in focus. JAMA Psychiatry 70:1107-1112.

Kasai K, Shenton ME, Salisbury DF, Onitsuka T, Toner SK, Yurgelun-Todd D, Kikinis R, Jolesz FA, McCarley RW. 2003. Differences and similarities in insular and temporal pole MRI gray matter volume abnormalities in first-episode schizophrenia and affective psychosis. Arch Gen Psychiatry 60:1069-1077.

Kasparek T, Prikryl R, Rehulova J, Marecek R, Mikl M, Prikrylova H, Vanicek J, Ceskova E. 2013. Brain functional connectivity of male patients in remission after the first episode of schizophrenia. Hum Brain Mapp 34:726-737.

Kaufmann T, Skåtun KC, Alnæs D, Doan NT, Duff EP, Tønnesen S, Roussos E, Ueland T, Aminoff SR, Lagerberg TV et al. 2015. Disintegration of Sensorimotor Brain Networks in Schizophrenia. Schizophrenia Bulletin 41:1326-1335.

Keefe RS, Fenton WS. 2007. How should DSM-V criteria for schizophrenia include cognitive impairment? Schizophr Bull 33:912-920.

Kelly C, Toro R, Di Martino A, Cox CL, Bellec P, Castellanos FX, Milham MP. 2012. A convergent functional architecture of the insula emerges across imaging modalities. Neuroimage 61:1129-1142.

King M, Hernandez-Castillo CR, Poldrack RA, Ivry RB, Diedrichsen J. 2019. Functional boundaries in the human cerebellum revealed by a multi-domain task battery. Nature Neuroscience 22:1371-1378.

Kong R, Li J, Orban C, Sabuncu MR, Liu H, Schaefer A, Sun N, Zuo XN, Holmes AJ, Eickhoff SB et al. 2019. Spatial Topography of Individual-Specific Cortical Networks Predicts Human Cognition, Personality, and Emotion. Cereb Cortex 29:2533-2551.

Kurth F, Eickhoff SB, Schleicher A, Hoemke L, Zilles K, Amunts K. 2010a. Cytoarchitecture and probabilistic maps of the human posterior insular cortex. Cereb Cortex 20:1448-1461.

Kurth F, Zilles K, Fox PT, Laird AR, Eickhoff SB. 2010b. A link between the systems: functional differentiation and integration within the human insula revealed by meta-analysis. Brain Struct Funct 214:519-534.

Langs G, Wang D, Golland P, Mueller S, Pan R, Sabuncu MR, Sun W, Li K, Liu H. 2016. Identifying Shared Brain Networks in Individuals by Decoupling Functional and Anatomical Variability. Cerebral Cortex 26:4004-4014.

Le Bihan D, Breton E. 1985. Imagerie de diffusion in vivo par résonance magnétique nucléaire. C R Académie Sci.

Leh SE, Ptito A, Chakravarty MM, Strafella AP. 2007. Fronto-striatal connections in the human brain: a probabilistic diffusion tractography study. Neurosci Lett 419:113-118.

Lehericy S, Ducros M, Van de Moortele PF, Francois C, Thivard L, Poupon C, Swindale N, Ugurbil K, Kim DS. 2004. Diffusion tensor fiber tracking shows distinct corticostriatal circuits in humans. Ann Neurol 55:522-529.

Maia TV. 2009. Reinforcement learning, conditioning, and the brain: Successes and challenges. Cognitive, Affective, & Behavioral Neuroscience 9:343-364.

Maia TV, Frank MJ. 2011. From reinforcement learning models to psychiatric and neurological disorders. Nature Neuroscience 14:154.

Maller JJ, Welton T, Middione M, Callaghan FM, Rosenfeld JV, Grieve SM. 2019. Revealing the Hippocampal Connectome through Super-Resolution 1150-Direction Diffusion MRI. Scientific Reports 9:2418.

Mallikarjun PK, Lalousis PA, Dunne TF, Heinze K, Reniers RL, Broome MR, Farmah B, Oyebode F, Wood SJ, Upthegrove R. 2018. Aberrant salience network functional connectivity in auditory verbal hallucinations: a first episode psychosis sample. Transl Psychiatry 8:69.

Manoliu A, Riedl V, Zherdin A, Muhlau M, Schwerthoffer D, Scherr M, Peters H, Zimmer C, Forstl H, Bauml J et al. 2014. Aberrant dependence of default mode/central executive network interactions on anterior insular salience network activity in schizophrenia. Schizophr Bull 40:428-437.

Margulies DS, Ghosh SS, Goulas A, Falkiewicz M, Huntenburg JM, Langs G, Bezgin G, Eickhoff SB, Castellanos FX, Petrides M et al. 2016. Situating the default-mode network along a principal gradient of macroscale cortical organization. Proc Natl Acad Sci U S A 113:12574-12579.

Marquand AF, Haak KV, Beckmann CF. 2017. Functional corticostriatal connection topographies predict goal directed behaviour in humans. Nat Hum Behav 1:0146.

Menon V. 2011. Large-scale brain networks and psychopathology: a unifying triple network model. Trends Cogn Sci 15:483-506.

Mesulam MM, Mufson EJ. 1982. Insula of the old world monkey. I. Architectonics in the insulo-orbito-temporal component of the paralimbic brain. J Comp Neurol 212:1-22.

Mesulam MM, Mufson EJ. 1985. The Insula of Reil in Man and Monkey. In: Peters A, Jones EG, editors. Association and Auditory Cortices Boston, MA: Springer US p 179-226.

Mishra A, Rogers BP, Chen LM, Gore JC. 2014. Functional connectivity-based parcellation of amygdala using self-organized mapping: a data driven approach. Hum Brain Mapp 35:1247-1260.

Moran LV, Tagamets MA, Sampath H, O'Donnell A, Stein EA, Kochunov P, Hong LE. 2013. Disruption of anterior insula modulation of large-scale brain networks in schizophrenia. Biological Psychiatry 74:467-474.

Morel A, Magnin M, Jeanmonod D. 1997. Multiarchitectonic and stereotactic atlas of the human thalamus. J Comp Neurol 387:588-630.

Mufson EJ, Mesulam MM. 1982. Insula of the old world monkey. II: Afferent cortical input and comments on the claustrum. J Comp Neurol 212:23-37.

Mufson EJ, Mesulam MM, Pandya DN. 1981. Insular interconnections with the amygdala in the rhesus monkey. Neuroscience 6:1231-1248.

Mufson EJ, Sobreviela T, Kordower J. 1997. Chapter VII Chemical neuroanatomy of the primate insula cortex: Relationship to cytoarchitectonics, connectivity, function and neurodegeneration. Handbook of chemical neuroanatomy 13:377-454.

Mutschler I, Wieckhorst B, Kowalevski S, Derix J, Wentlandt J, Schulze-Bonhage A, Ball T. 2009. Functional organization of the human anterior insular cortex. Neurosci Lett 457:66-70.

Nagai M, Kishi K, Kato S. 2007. Insular cortex and neuropsychiatric disorders: a review of recent literature. Eur Psychiatry 22:387-394.

Nanetti L, Cerliani L, Gazzola V, Renken R, Keysers C. 2009. Group analyses of connectivity-based cortical parcellation using repeated k-means clustering. Neuroimage 47:1666-1677.

Nelson SM, Dosenbach NU, Cohen AL, Wheeler ME, Schlaggar BL, Petersen SE. 2010. Role of the anterior insula in task-level control and focal attention. Brain structure and function 214:669-680.

Nieuwenhuys R. 2012. The insular cortex: a review. Prog Brain Res 195:123-163.

Nomi JS, Farrant K, Damaraju E, Rachakonda S, Calhoun VD, Uddin LQ. 2016. Dynamic Functional Network Connectivity Reveals Unique and Overlapping Profiles of Insula Subdivisions. Hum Brain Mapp 37:1770-1787.

Obeso JA, Rodriguez-Oroz MC, Rodriguez M, Lanciego JL, Artieda J, Gonzalo N, Olanow CW. 2000. Pathophysiology of the basal ganglia in Parkinson's disease. Trends in Neurosciences 23:S8-S19.

Ogawa A, Osada T, Tanaka M, Hori M, Aoki S, Nikolaidis A, Milham MP, Konishi S. 2018. Striatal subdivisions that coherently interact with multiple cerebrocortical networks. Hum Brain Mapp 39:4349-4359.

Ogawa S, Lee TM, Kay AR, Tank DW. 1990. Brain magnetic resonance imaging with contrast dependent on blood oxygenation. Proc Natl Acad Sci U S A 87:9868-9872.

Ostrowsky K, Isnard J, Ryvlin P, Guenot M, Fischer C, Mauguiere F. 2000. Functional mapping of the insular cortex: clinical implication in temporal lobe epilepsy. Epilepsia 41:681-686.

Palaniyappan L, Liddle PF. 2012. Differential effects of surface area, gyrification and cortical thickness on voxel based morphometric deficits in schizophrenia. Neuroimage 60:693-699.

Palaniyappan L, Mallikarjun P, Joseph V, White TP, Liddle PF. 2011. Regional contraction of brain surface area involves three large-scale networks in schizophrenia. Schizophr Res 129:163-168.

Palaniyappan L, Simmonite M, White TP, Liddle EB, Liddle PF. 2013. Neural primacy of the salience processing system in schizophrenia. Neuron 79:814-828.

Paquola C, Seidlitz J, Benkarim O, Royer J, Klimes P, Bethlehem RAI, Larivière S, Vos de Wael R, Hall JA, Frauscher B et al. 2020. A cortical wiring space links cellular architecture, functional dynamics and hierarchies in humans. bioRxiv:2020.2001.2008.899583.

Paquola C, Vos De Wael R, Wagstyl K, Bethlehem RAI, Hong S-J, Seidlitz J, Bullmore ET, Evans AC, Misic B, Margulies DS et al. 2019. Microstructural and functional gradients are increasingly dissociated in transmodal cortices. PLOS Biology 17:e3000284.

Pauli WM, Nili AN, Tyszka JM. 2018. A high-resolution probabilistic in vivo atlas of human subcortical brain nuclei. Sci Data 5:180063.

Pauli WM, O'Reilly RC, Yarkoni T, Wager TD. 2016. Regional specialization within the human striatum for diverse psychological functions. Proceedings of the National Academy of Sciences 113:1907-1912.

Pennartz CM, Berke JD, Graybiel AM, Ito R, Lansink CS, van der Meer M, Redish AD, Smith KS, Voorn P. 2009. Corticostriatal Interactions during Learning, Memory Processing, and Decision Making. J Neurosci 29:12831-12838.

Plachti A, Eickhoff SB, Hoffstaedter F, Patil KR, Laird AR, Fox PT, Amunts K, Genon S. 2019. Multimodal Parcellations and Extensive Behavioral Profiling Tackling the Hippocampus Gradient. Cereb Cortex.

Poppenk J, Evensmoen HR, Moscovitch M, Nadel L. 2013. Long-axis specialization of the human hippocampus. Trends Cogn Sci 17:230-240.

Postuma RB, Dagher A. 2005. Basal Ganglia Functional Connectivity Based on a Meta-Analysis of 126 Positron Emission Tomography and Functional Magnetic Resonance Imaging Publications. Cerebral Cortex 16:1508-1521.

Power JD, Cohen AL, Nelson B, Wig GS, Barnes KA, Church JA, Vogel AC, Laumann T, Miezin FM, Schlaggar BL et al. 2011. Functional network organization of the human brain. 72:665-678.

Przeździk I, Faber M, Fernández G, Beckmann CF, Haak KV. 2019. The functional organisation of the hippocampus along its long axis is gradual and predicts recollection. Cortex 119:324-335.

Puckett AM, Bollmann S, Poser BA, Palmer J, Barth M, Cunnington R. 2018. Using multi-echo simultaneous multi-slice (SMS) EPI to improve functional MRI of the subcortical nuclei of the basal ganglia at ultra-high field (7T). Neuroimage 172:886-895.

Retzius. 1896. Das Menschenhirn. Stockholm: Königliche Buchdruckerei P.A.: Norstedt und Söner.

Robinson JL, Barron DS, Kirby LA, Bottenhorn KL, Hill AC, Murphy JE, Katz JS, Salibi N, Eickhoff SB, Fox PT. 2015. Neurofunctional topography of the human hippocampus. Hum Brain Mapp 36:5018-5037.

Rose M. 1928. Die inselrinde des menschen und der tiere. Journal fur Psychologie und Neurologie 37:470-624.

Royer J, Paquola C, Larivière S, Vos de Wael R, Tavakol S, Lowe AJ, Benkarim O, Evans AC, Bzdok D, Smallwood J et al. 2020. Myeloarchitecture gradients in the human insula: Histological underpinnings and association to intrinsic functional connectivity. NeuroImage 216:116859.

Ryali S, Chen T, Padmanabhan A, Cai W, Menon V. 2015. Development and validation of consensus clustering-based framework for brain segmentation using resting fMRI. J Neurosci Methods 240:128-140.

Ryali S, Chen T, Supekar K, Menon V. 2013. A parcellation scheme based on von Mises-Fisher distributions and Markov random fields for segmenting brain regions using resting-state fMRI. Neuroimage 65:83-96.

Saygin ZM, Kliemann D, Iglesias JE, van der Kouwe AJW, Boyd E, Reuter M, Stevens A, Van Leemput K, McKee A, Frosch MP et al. 2017. High-resolution magnetic resonance imaging reveals nuclei of the human amygdala: manual segmentation to automatic atlas. Neuroimage 155:370-382.

Schaefer A, Kong R, Gordon EM, Laumann TO, Zuo XN, Holmes AJ, Eickhoff SB, Yeo BTT. 2018. Local-Global Parcellation of the Human Cerebral Cortex from Intrinsic Functional Connectivity MRI. Cereb Cortex 28:3095-3114.

Schmierer K, Tozer DJ, Scaravilli F, Altmann DR, Barker GJ, Tofts PS, Miller DH. 2007. Quantitative magnetization transfer imaging in postmortem multiple sclerosis brain. Journal of Magnetic Resonance Imaging 26:41-51.

Seeley WW, Menon V, Schatzberg AF, Keller J, Glover GH, Kenna H, Reiss AL, Greicius MD. 2007. Dissociable intrinsic connectivity networks for salience processing and executive control. Journal of Neuroscience 27:2349-2356.

Segerdahl AR, Mezue M, Okell TW, Farrar JT, Tracey I. 2015. The dorsal posterior insula subserves a fundamental role in human pain. Nature Neuroscience 18:499.

Seiferth NY, Pauly K, Habel U, Kellermann T, Shah NJ, Ruhrmann S, Klosterkotter J, Schneider F, Kircher T. 2008. Increased neural response related to neutral faces in individuals at risk for psychosis. Neuroimage 40:289-297.

Shepherd GM. 2013. Corticostriatal connectivity and its role in disease. Nat Rev Neurosci 14:278-291.

Sherman SM. 2016. Thalamus plays a central role in ongoing cortical functioning. Nat Neurosci 19:533-541.

Singer T, Critchley HD, Preuschoff K. 2009. A common role of insula in feelings, empathy and uncertainty. Trends Cogn Sci 13:334-340.

Small DM, Gregory MD, Mak YE, Gitelman D, Mesulam MM, Parrish T. 2003. Dissociation of neural representation of intensity and affective valuation in human gustation. Neuron 39:701-711.

Smith CD, Lori NF, Akbudak E, Sorar E, Gultepe E, Shimony JS, McKinstry RC, Conturo TE. 2009. MRI diffusion tensor tracking of a new amygdalo-fusiform and hippocampo-fusiform pathway system in humans. J Magn Reson Imaging 29:1248-1261.

Solano-Castiella E, Anwander A, Lohmann G, Weiss M, Docherty C, Geyer S, Reimer E, Friederici AD, Turner R. 2010. Diffusion tensor imaging segments the human amygdala in vivo. Neuroimage 49:2958-2965.

Stephani C, Fernandez-Baca Vaca G, Maciunas R, Koubeissi M, Luders HO. 2011. Functional neuroanatomy of the insular lobe. Brain Struct Funct 216:137-149.

Strange BA, Witter MP, Lein ES, Moser EI. 2014. Functional organization of the hippocampal longitudinal axis. Nature Reviews Neuroscience 15:655-669.

Stüber C, Morawski M, Schäfer A, Labadie C, Wähnert M, Leuze C, Streicher M, Barapatre N, Reimann K, Geyer S et al. 2014. Myelin and iron concentration in the human brain: A quantitative study of MRI contrast. NeuroImage 93:95-106.

Theo Vos AAA, Cristiana Abbafati, Abbas KM. 2017. Global, regional, and national incidence, prevalence, and years lived with disability for 328 diseases and injuries for 195 countries, 1990-2016: a systematic analysis for the Global Burden of Disease Study 2016. Lancet 390:1211-1259.

Thulborn KR, Waterton JC, Matthews PM, Radda GK. 1982. Oxygenation dependence of the transverse relaxation time of water protons in whole blood at high field. Biochim Biophys Acta 714:265-270.

Tian Y, Zalesky A. 2018. Characterizing the functional connectivity diversity of the insula cortex: Subregions, diversity curves and behavior. Neuroimage 183:716-733.

Tziortzi AC, Haber SN, Searle GE, Tsoumpas C, Long CJ, Shotbolt P, Douaud G, Jbabdi S, Behrens TEJ, Rabiner EA et al. 2013. Connectivity-Based Functional Analysis of Dopamine Release in the Striatum Using Diffusion-Weighted MRI and Positron Emission Tomography. Cerebral Cortex 24:1165-1177.

Uddin LQ. 2015. Salience processing and insular cortical function and dysfunction. Nat Rev Neurosci 16:55-61.

Uddin LQ, Kinnison J, Pessoa L, Anderson ML. 2014. Beyond the tripartite cognition-emotion-interoception model of the human insular cortex. J Cogn Neurosci 26:16-27.

van den Heuvel MP, Fornito A. 2014. Brain networks in schizophrenia. Neuropsychol Rev 24:32-48.

Van Essen DC, Glasser MF. 2018. Parcellating Cerebral Cortex: How Invasive Animal Studies Inform Noninvasive Mapmaking in Humans. Neuron 99:640-663.

Van Essen DC, Maunsell JH, Bixby JL. 1981. The middle temporal visual area in the macaque: myeloarchitecture, connections, functional properties and topographic organization. J Comp Neurol 199:293-326.

Vercelli U, Diano M, Costa T, Nani A, Duca S, Geminiani G, Vercelli A, Cauda F. 2016. Node Detection Using High-Dimensional Fuzzy Parcellation Applied to the Insular Cortex. Neural Plast 2016:1938292.

Vogt O. 1910. Die myeloarchitektonische Felderung des menschlichen Stirnhirns. J Psychol Neurol XV:221-232.

Von Economo CF, Koskinas GN. 1925. Die Cytoarchitektonik der Hirnrinde des erwachsenen Menschen. Wien-Berlin: Julius Springer.

Vos de Wael R, Lariviere S, Caldairou B, Hong SJ, Margulies DS, Jefferies E, Bernasconi A, Smallwood J, Bernasconi N, Bernhardt BC. 2018. Anatomical and microstructural determinants of hippocampal subfield functional connectome embedding. Proc Natl Acad Sci U S A 115:10154-10159.

Wang C, Ji F, Hong Z, Poh JS, Krishnan R, Lee J, Rekhi G, Keefe RSE, Adcock RA, Wood SJ et al. 2016. Disrupted salience network functional connectivity and white-matter microstructure in persons at risk for psychosis: findings from the LYRIKS study. Psychological Medicine 46:2771-2783.

Wang D, Buckner RL, Fox MD, Holt DJ, Holmes AJ, Stoecklein S, Langs G, Pan R, Qian T, Li K et al. 2015. Parcellating cortical functional networks in individuals. Nat Neurosci 18:1853-1860.

Wei PH, Mao ZQ, Cong F, Yeh FC, Wang B, Ling ZP, Liang SL, Chen L, Yu XG. 2017. In vivo visualization of connections among revised Papez circuit hubs using full q-space diffusion spectrum imaging tractography. Neuroscience 357:400-410.

Wernicke C. 1906. Grundrisse der Psychiatrie. Leipzig, Germany: Thieme.

Wotruba D, Michels L, Buechler R, Metzler S, Theodoridou A, Gerstenberg M, Walitza S, Kollias S, Rossler W, Heekeren K. 2014. Aberrant coupling within and across the default mode, task-positive, and salience network in subjects at risk for psychosis. Schizophr Bull 40:1095-1104.

Wylie KP, Tregellas JR. 2010. The role of the insula in schizophrenia. Schizophr Res 123:93-104.

Xue G, Lu Z, Levin IP, Bechara A. 2010. The Impact of Prior Risk Experiences on Subsequent Risky Decision-Making: The Role of the Insula. Neuroimage 50:709-716.

Yamada T, Itahashi T, Nakamura M, Watanabe H, Kuroda M, Ohta H, Kanai C, Kato N, Hashimoto RI. 2016. Altered functional organization within the insular cortex in adult males with high-functioning autism spectrum disorder: evidence from connectivity-based parcellation. Mol Autism 7:41.

Yeo BT, Krienen FM, Sepulcre J, Sabuncu MR, Lashkari D, Hollinshead M, Roffman JL, Smoller JW, Zollei L, Polimeni JR et al. 2011. The organization of the human cerebral cortex estimated by intrinsic functional connectivity. J Neurophysiol 106:1125-1165.

Zhang S, Li CR. 2017. Functional Connectivity Parcellation of the Human Thalamus by Independent Component Analysis. Brain Connect 7:602-616.

Zhang X, Cheng H, Zuo Z, Zhou K, Cong F, Wang B, Zhuo Y, Chen L, Xue R, Fan Y. 2018. Individualized Functional Parcellation of the Human Amygdala Using a Semi-supervised Clustering Method: A 7T Resting State fMRI Study. Frontiers in Neuroscience 12.

Zhong Q, Xu H, Qin J, Zeng L-L, Hu D, Shen H. 2019. Functional parcellation of the hippocampus from resting-state dynamic functional connectivity. Brain Research 1715:165-175.

CHAPTER 2

BACKGROUND AND METHODS

Models of brain topography

In this chapter, I survey the literature that has considered different representations of the topographic organization of the human brain. I consider micro- to macro-scale organizational properties, as well as brain structure and function. I discuss advantages, disadvantages as well as challenges that are associated with these topographic models, which are increasingly used to investigate brain organization. Finally, I provide a brief overview of the methodologies used in this thesis as well as details about the neuroimaging datasets and study participants.

Microscale architecture

Early brain atlases of microarchitecture were largely based on histological investigations (Brodmann 1909; Vogt 1910; Von Economo and Koskinas 1925), with the use of Nissl-stained brain tissue sections for neuronal cell bodies (cytoarchitecture) or myelinated nerve fibers (myeloarchitecture). Most regions of the human cerebral cortex comprise six layers, namely, the isocortex, except the motor cortex which does not have a clear recognizable layer IV (Brodmann 1909). The cytoarchitectonic feature of the isocortex is often characterized by the distribution of the type, size of neuronal cell bodies and the density across the six conventional cortical layers as well as the degree of columnar arrangement of the neurons. By contrast, myeloarchitecture is often characterized by the length, thickness and spacing of radial (vertically oriented) fiber bundles as well as the existence and spatial distribution of tangential (horizontally oriented) fiber bands across layers, such as the inner and outer Baillarger stripes, Kaes-Bechterew, and Cajal-Retzius strip (Zilles and Palomero-Gallagher 2001).

Despite the existence of consensus classification criteria among neuroanatomists, practical observations are usually subjective and observer-dependent, yielding varied definitions of cortical maps, ranging from 43 (Brodmann 1909) to 150 (Von Economo and Koskinas 1925) cytoarchitectonic areas as well as a myeloarchitecture map that comprises 185 areas (Vogt and Vogt 1919). For example, Brodmann divided the postcentral region into four cytoarchitectonic zones including BA 3, 1, 2, and 43, whereas von Economo and Koskinas delineated six areas named PA_1, PA_2, PB_1, PB_2, PC and PD. The parietal region comprises four cytoarchitectonic distinct areas in Brodmann's map, whereas eight parietal areas were

delineated according to von Economo and Koskinas. Brodmann and some other contemporary neuroanatomists including Vogt were certainly in favor of delineating distinct cortical areas separated by sharp borders. The notion was emphasized in Vogt's observation of myeloarchitecture, in which he posited that the areal border is as sharp as a hair. In contrast, von Economo and Koskinas were inclined to also describe transitional zones, which were characterized by a continuum of gradual change in the cytoarchitecture, in the absence of abrupt local differentiation. For example, the caudal part of Brodmann area 2 (BA 2) in the intraparietal sulcus was characterized by von Economo and Koskinas as a transitional zone, in which the variation in the cytoarchitecture continued for a considerable distance on the upper and lower bank of the intraparietal sulcus. Likewise, von Economo and Koskinas marked the great difficulties in delineating clear-cut borders between the angular gyrus (Brodmann area 39) and surrounding areas. Interestingly, while Brodmann also found the lack of sharp borders between BA 39 and its neighbors, the hard boundaries with surrounding BA 7, BA 19 and BA 37 were still imposed regardless. The disagreement among neuroanatomists may be due to the lack of objective and observer-independent measures and the limited number of postmortem samples. The lack of a common reference space also made it difficult to combine and compare results across different studies, which may have yielded discrepant conclusions.

The development of automated image analysis approaches, combined with three-dimensional reconstruction and spatial registration of multiple postmortem brain tissues onto a standard common space (Eickhoff et al. 2005; Amunts and Zilles 2015) enabled significant advances in the field. This enabled cortical cytoarchitecture to be mapped quantitatively with the consideration of a set of different laminar features. One of the earliest measures is called the gray level index (Wree et al. 1982), which estimates the volume fraction of neuronal bodies along the cortical ribbons. This index was then developed further to estimate the relationship between supra- and infragranular layers with respect to the volume fraction of neuronal bodies (Schleicher et al. 2000; Schleicher et al. 2005). These measurements are observer-independent, and the degree of spatial variation in the cortical cytoarchitecture can be informed from statistically testable criterion such as the Mahalanobis distance (Amunts et al. 2000; Schleicher et al. 2005). Instead of relying on traditional visual inspection, researchers sought to quantify how *sharp* or *gradual* the change is between two

cortical areas. Indeed, the abrupt and significant increase of the Mahalanobis distance has been used to indicate significant changes in the cytoarchitecture, such as the sharp transition between the two subregions of the posterior fusiform gyrus (FG1 and FG2) (Caspers et al. 2013). In contrast, the cytoarchitecture of the dorsal extrastriate cortex was found to be more complicated and showing transitional phenomena (Amunts et al. 2000; Kujovic et al. 2013). These researchers concluded that the cytoarchitecture or laminar organization across the cerebral cortex is indeed heterogeneous and perhaps more heterogeneous than Brodmann's initial observations. Researchers therefore proposed that the spatial layout of cytoarchitecture may vary from abrupt changes to more gradual and grade-like transitions across the topography of the cerebral cortex (Amunts and Zilles 2015).

More recently, studies have sought to simplify the characterization of the complex cortical microstructure into a single neuronal index, such as the neuron number or density per unit space of cortical surface (Collins et al. 2010; Cahalane et al. 2012; Charvet et al. 2013; Charvet et al. 2017). Although not optimal, since neuronal architecture reflected by the single neuronal index cannot comprehensively represent neuronal function, the authors demonstrated that neuron density varies substantially across the spatial extent of the cerebral cortex along a rostrocaudal axis. Across different mammal species, neuron density is generally found to be highest in the caudal part of the brain, where primary sensory information is processed (e.g. visual cortex and somatosensory cortex), and gradually decreases toward more rostral brain regions. This rostrocaudal gradient may associate with the temporal trajectory of neurogenesis, during which neurogenesis ends earlier in rostral regions compared to the caudal part (Cahalane et al. 2014; Charvet and Finlay 2014). Neurons residing in the caudal part of the brain undergo a higher number of cell cycles, resulting in a larger number of neurons but smaller in size. Contrastingly, the neurogenesis of rostral regions terminates earlier, allocating more time for neurons to grow and form abundant axonal and synaptic connections (Elston 2000).

Other microstructural properties, such as the density of neurotransmitter receptors (Zilles et al. 2002; Amunts and Zilles 2015) or more comprehensively, genome-wide maps of brain transcriptome (Hawrylycz et al. 2012) have also been proposed to facilitate the understanding of brain organization. Local differentiations of microstructural properties are direct and

observable and have largely enriched our understanding of the topographic organization of the human brain. Nevertheless, the brain is also densely connected, forming networks at multiple scales, to facilitate information processing and communication. It has been suggested that regions sharing similar microstructure are more likely to be strongly connected (van den Heuvel et al. 2015; Goulas et al. 2016; Huntenburg et al. 2017). The macroscale connectivity architecture thus complements local differentiations, providing an integrative and comprehensive characterization of brain organization (Toga et al. 2006).

Macroscale connectivity architecture

Brain connectivity traditionally refers to the physical connections between neurons and brain regions (i.e. axons and axonal fiber bundles), which can be measured using invasive fiber tracing techniques in experimental animals or *ex vivo* fiber-dissection in the postmortem human brain. Due to their invasiveness and the requirement of postmortem tissues, while directly observable, these approaches cannot yield comparable functional references for living subjects. Moreover, these approaches require extensive laboratory examinations, limiting the sample size to a few subjects. Fortunately, the development of magnetic resonance imaging (MRI) and other neuroimaging techniques in recent decades, have enabled the estimation of regional connectivity noninvasively in a large number of human populations.

In particular, one of the techniques, referred to as diffusion-weighted imaging, generates contrast in MR images based on the diffusion of water molecules (Le Bihan and Breton 1985). The diffusion process of water molecules and associated computational approaches such as tractography can then be used to generate tractograms that represent white matter tracts in the brain. White matter tracts connecting two regions give rise to the concept of structural connectivity. However, one major challenge of tract reconstruction using diffusion-weighted tractography is the mapping of considerable numbers of false-positive fiber bundles (Zalesky et al. 2016; Maier-Hein et al. 2017). Therefore, caution is required when interpreting results inferred from structural connectivity.

Another commonly used connectivity measure is functional connectivity, which measures statistical co-activation patterns in brain activity between spatially distributed brain regions, under certain external task stimuli or in the absence of any behavioral task, that is, at rest (Biswal et al. 1995). Although both structural and functional connectivity reflect important organizational properties of the human brain, I focus on the topographic organization of the human brain in the context of functional connectivity in this thesis. Specifically, I use the technique of functional MRI to provide an indirect index of brain activity and investigate patterns of synchronized fluctuations in this activity. The technique of functional MRI was used in all three studies (Chapter 3-5) presented in this thesis.

Functional magnetic resonance imaging and functional connectivity

Functional magnetic resonance imaging (fMRI), in particular, the blood oxygenation level dependent (BOLD) fMRI is a non-invasive, *in vivo* imaging technique for measuring neuronal activity associated with regional cerebral blood flow (CBF) that arises from physiological events (Ogawa et al. 1990). This technique indirectly reflects the neuronal activity given the localized coupling between the cerebral metabolic rate of oxygen consumption, cerebral metabolic rate of glucose consumption and the CBF (Raichle 1987). Specifically, CBF increases as a consequence of increased metabolic and oxygen demands due to increased neuronal activity. The agent that carries and transports oxygen is called hemoglobin, which is an iron-containing metalloprotein in red blood cells. It exists in two forms: i) saturated with oxygen molecules, named oxyhemoglobin; and, ii) desaturated with oxygen molecules, known as deoxyhemoglobin.

As a response to increased neuronal activity, the blood flow increases, however, to a greater extent that exceeds the local cerebral metabolic rate of oxygen consumption in the neurons, yielding a locally increased oxygen saturation in veins and capillaries, and therefore, an increased ratio of oxygenated to deoxygenated hemoglobin in the region of neuronal activation (Buxton et al. 2004; Buchbinder 2016). Compared to brain tissues, the deoxyhemoglobin is paramagnetic whereas the oxyhemoglobin is diamagnetic (Pauling and Coryell 1936). As a result, dynamic changes in the local deoxyhemoglobin concentration in the brain lead to signal intensity fluctuations in the functional magnetic images, i.e. the BOLD

contrast (Thulborn et al. 1982; Ogawa et al. 1990). Figure 2.1 illustrates psychological and physical processes associated with the intensity fluctuation of BOLD signals.

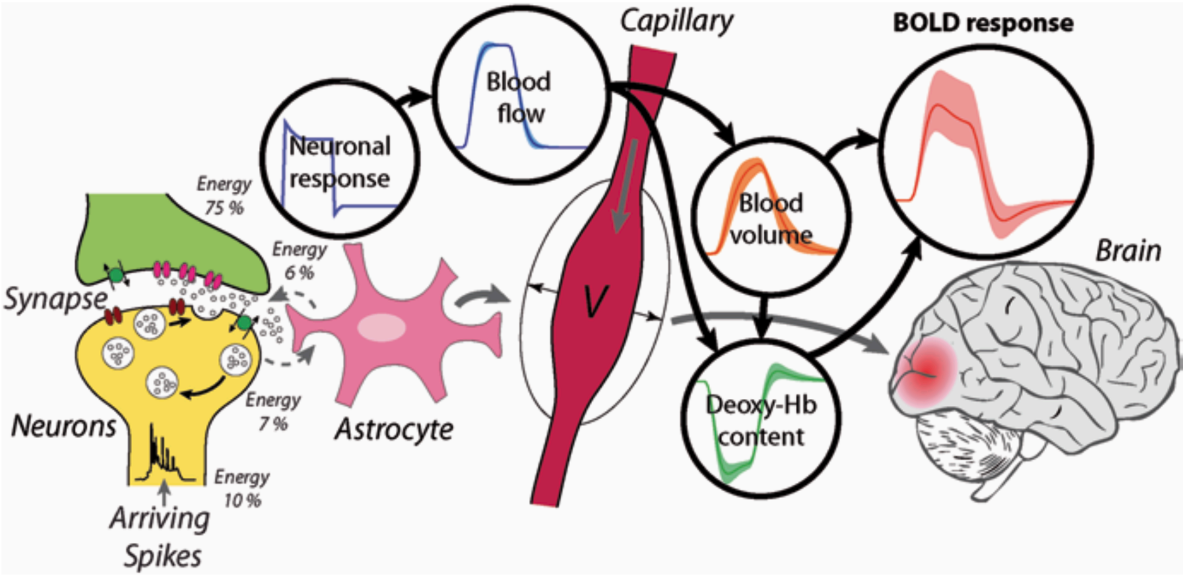


Figure 2.1. Physiological and physical events associated with intensity fluctuation of fMRI BOLD signals. Blood flow and volume increases as a consequence of increased neuronal activity such as action potentials and synaptic activity, metabolic and oxygen consumption, which leads to a change in blood oxygenation. In turn, the dynamic changes in the local deoxyhemoglobin concentration in the brain lead to signal intensity fluctuations in the BOLD contrast of functional magnetic image (reproduced from (Uludağ and Uğurbil 2015).

Two modalities of fMRI are commonly implemented, depending on research questions. The first modality is task-evoked fMRI, which measures BOLD signal changes associated with explicit task stimuli. Specifically, during the fMRI scan, participants are requested to perform one or more cognitive tasks designed to target different aspects of neurophysiological and neuropsychological process, such as working memory, emotional processing, motor execution, visual, auditory and somatosensory processing, decision making and many others (Cole et al. 2010; Barch et al. 2013). The detected BOLD signal changes are deemed to reflect regional neuronal activation in response to certain task paradigms. However, this approach typically requires constrained hypotheses and may induce idiosyncrasies and paradigm bias that might present in certain cognitive tasks.

In contrast, another fMRI modality, known as resting-sate fMRI aims to measure functional interaction between different brain regions that occurs when an individual is not performing any explicit task, i.e. at rest. Specifically, in a standard procedure, participants are instructed to keep eyes closed or fixed to a crosshair without thinking about anything in particular for a

period of time, usually around 10 minutes in a clinical setting. BOLD signals are recorded at each time point, yielding a set of time series for each voxel in the acquired MRI images. The spacing between time points in this series is dependent on the pulse sequence of fMRI acquisitions, i.e. the repetition time (TR), whereby the shorter the TR, the more the time points are acquired under a certain period of time. It was first discovered that the spontaneous low frequency (<0.1HZ) fluctuations of BOLD signal are temporally correlated between brain regions related to motor function in the absence of external stimuli (Biswal et al. 1995). Since this initial discovery, these correlations, referred to as functional connectivity, have yielded great insights into the large-scale intrinsic functional architecture of the brain (Fox and Raichle 2007). Mathematically, functional connectivity can be expressed as the statistical dependence of BOLD signal time series between two regions (voxels), and is most commonly estimated with the Pearson's correlation coefficient, which assumes a linear relationship between the time series (Marrelec et al. 2008). Functional connectivity measured by resting-state fMRI is sensitive to coupling between spatially distributed brain regions as well as adjacent areas (Sepulcre et al. 2010). Although not a direct measure of anatomical connectivity, functional couplings between brain regions are largely constrained by brain anatomy (i.e. white matter connectivity), as demonstrated in a number of previous studies in humans (Skudlarski et al. 2008; Honey et al. 2009; Hermundstad et al. 2013) as well as studies using tract-tracing data in non-human primates (Vincent et al. 2007; Miranda-Dominguez et al. 2014). The correspondence between structural and functional connectivity has enabled resting-state fMRI to be used to investigate properties of circuitry organization in the brain (Fox and Raichle 2007; Van Dijk et al. 2010). It is also noteworthy that while constrained by anatomy, functional connectivity is not fully dictated by physical connections and can also present in the absence of direct axonal fiber tracts (Honey et al. 2009; Adachi et al. 2012).

While functional connectivity has been predominantly examined in the context of resting-state fMRI, recent studies have also moved toward characterizing functional connectivity during various task-evoked states (Greicius et al. 2003; Fox et al. 2005; Fair et al. 2007; Fox et al. 2007). These studies suggest that regions routinely showing increased and deceased activation during a variety of cognitive attention-demanding tasks are intrinsically represented in the brain, forming anticorrelated networks in the absence of explicit stimuli (Fox et al. 2005; Uddin et al. 2009). In particular, brain networks comprising regions that

commonly show task-related activation are referred to as task-positive networks, whereas regions typically showing task-related deactivation are collectively referred to as task-negative networks. This task-related activation dichotomy thus potentially reflects the underlying intrinsic functional organization of the brain (Fox et al. 2005). Studies have also found a shared intrinsic functional connectivity architecture across different brain states (Greicius et al. 2003; Fox et al. 2005; Fair et al. 2007; Fox et al. 2007), although variation in the pattern of functional coupling (Buckner et al. 2013; Hermundstad et al. 2013; Mennes et al. 2013) and the reconfiguration in topography are nevertheless evident in response to changing cognitive demands (Cole et al. 2014; Greene et al. 2018; Salehi et al. 2019).

Characterization of functional connectivity topography is necessary for a more systematic understanding of the functional organization of the brain. To begin with, I review studies that characterize the variation in functional connectivity across the brain's topography as either an assembly of distinct partitions with discrete boundaries (i.e. parcellation) or continuous gradients of gradual variation.

Connectivity-based parcellation

Connectivity-based parcellation attempts to parcellate the brain into spatially discrete regions based on connectivity fingerprints (Passingham et al. 2002) in a data-driven manner. The connectivity fingerprints can be estimated using i) structural connectivity inferred from diffusion MRI, measuring putative white matter fiber bundles connecting two regions; and, ii) functional connectivity computed from resting-state or task-evoked fMRI data, measuring co-activation between distributed regions when the brain is at rest or engaging a task (see above). Each delineated region is thus characterized in terms of its specific interactions with other regions (usually the whole brain). For example (Figure 2.2), the supplementary motor area (SMA) is primarily connected to somatosensory and motor regions, whereas a neighboring region (i.e. pre-SMA) is more strongly connected to cortical regions associated with complex cognitive and motor control, such as regions in the angular gyrus, prefrontal and anterior cingulate cortices, and is therefore considered as a distinct area (Kim et al. 2010).

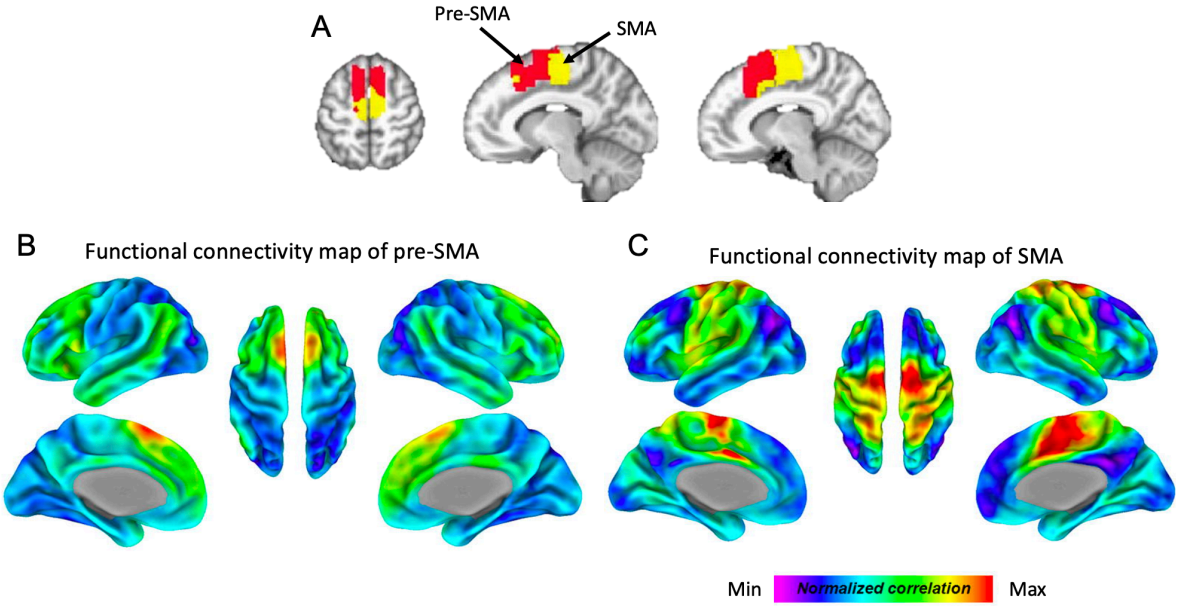


Figure 2.2. Functional connectivity profile of the pre supplementary motor area (pre-SMA) and SMA. A, Anatomical locations of pre-SMA and SMA. **B,** pre-SMA is primarily connected to brain regions in the prefrontal cortex, the inferior frontal gyrus, the anterior cingulate cortex and the angular gyrus. **C,** SMA is primarily connected to brain regions in the primary motor, premotor, somatosensory and middle cingulate cortices. The cortical surface is colored according to the strength of functional connectivity (adapted from Kim et al. 2010).

Brain parcellation can be achieved using two broad approaches: i) grouping voxels that share similar connectivity profile into clusters (i.e. clustering methodology), where each resulting cluster is assumed to delineate a putative brain region; and, ii) boundary mapping or gradient-based parcellation, which is a method that detects locations of abrupt spatial change in connectivity profiles across the topography of the brain, yielding areal boundaries. In addition to the two main methodological streams, many other alternative techniques are also available, including but not limited to, independent component analysis, Bayesian modelling, and Markov random fields. Indeed, all the above mentioned approaches can be applied to most connectivity measures and have been widely used in the whole-brain (Bellec et al. 2010; Craddock et al. 2012; Shen et al. 2013) and cortical parcellation (Power et al. 2011; Yeo et al. 2011; Glasser et al. 2016a; Gordon et al. 2016; Schaefer et al. 2018), as well as parcellating specific regions of interest, such as the thalamus (Behrens et al. 2003), cingulate cortex (Cha et al. 2017), orbitofrontal cortex (Kahnt et al. 2012), supplementary motor area (Nanetti et al. 2009) and the insular cortex (Deen et al. 2011). Examples of brain parcellation are shown in Chapter 1 (Figure 1.1, 1.4 & 1.6). Of note, each technique has its own assumptions, strengths and shortcomings and might result in different parcellation schemes when applied to the same dataset (Cha et al. 2017; Arslan et al. 2018; Schaefer et al. 2018).

Challenges in determining the optimal number of clusters

In this section, I review challenges associated with parcellating the brain into clusters that represent putative regions using data clustering techniques. I contextualize these challenges in terms of the insular cortex, given that this is one of the key regions investigated in the thesis. However, it is important to remark that clustering techniques can be applied to other brain regions and the entire cortex, which results in similar challenges and ambiguities in determining the optimal number of clusters.

Many of the above-mentioned approaches have been applied to parse the macroscale connectivity architecture of the insular cortex. However, the number of insular subregions delineated varies markedly between studies and approaches. Table 1 in Chapter 3 catalogues approximately twenty of these previous studies and exemplifies the inconsistent number of insular subregions reported. The number of putative subregions comprising the insular cortex thus remains controversial and widely debated (Cauda and Vercelli 2013).

Among the variety of clustering techniques, K-means has been one of the most extensively used methods in the studies of connectivity-based parcellation. This is perhaps because of its simplicity and ease of implementation. One of the difficulties of this method is the requirement to predefine the number of clusters a priori, which is typically unknown (see below). However, other methods such as hierarchical clustering (Ward's linkage and centroid linkage), fuzzy c-means, spectral clustering, independent component analysis as well as Markov random fields have also been employed. While clustering algorithms generally find *hard* clusters, where each voxel/vertex can only be assigned to either one cluster or another, fuzzy c-means provides a *soft* clustering solution, whereby each element is characterized with a probability of belonging to each of multiple clusters.

Despite methodological variations, most algorithms require a pre-selected number of clusters and the search for the optimal number of clusters is particularly challenging because many clustering algorithms can always partition any set of data points into any number of clusters (Jain 2010), regardless of whether the number of clusters is optimally supported by the data or the delineated brain regions are biologically meaningful. The optimal number of insular clusters (subregions) is typically determined based on: i) prior expectations informed by

macaque studies of insular cytoarchitecture or axonal tract-tracing (Nanetti et al. 2009; Cauda et al. 2011; Deen et al. 2011; Jakab et al. 2012; Moran et al. 2013); ii) concordance across different modalities or cohorts (Kelly et al. 2012; Chang et al. 2013; Alcauter et al. 2015; Yamada et al. 2016); or, iii) cluster evaluation criteria (Cauda et al. 2012; Ryali et al. 2013; Ryali et al. 2015; Vercelli et al. 2016). The first approach may be biologically valid but also subjective, especially given the lack of clear distinction in the change of cytoarchitecture along the insula's topography (Nieuwenhuys 2012).

While the microscale insular cytoarchitecture appears to be not well differentiated, it is possible that macroscale insular connectivity maps inferred from functional or diffusion MRI provide a different window into the insular topographic organization, by which distinct insular subregions can be sufficiently and reproducibly identified. It has been assumed that consistently identified partitions are more likely driven by the underlying neurobiology rather than methodological artifacts. Many studies have thus sought to evaluate the stability and reproducibility of insular clusters across different modalities, or different cohorts (Kelly et al. 2012; Chang et al. 2013; Alcauter et al. 2015; Yamada et al. 2016). However, replicating clusters does not ensure that a given cluster solution is necessarily valid, optimal and supported by the data. Many of the clustering algorithms are able to identify reproducible clusters in data that is inherently continuous (i.e. no clusters). One such phenomenon is shown in Supplementary Figure S1 in Chapter 3. I showed that while a linear relation is evident and the data comprises no true clusters, the K-means clustering algorithm reproducibly generates clusters with high concordance across individuals. Therefore, reproducibility and stability *per se* are not sufficient criteria to establish whether a cluster-based brain parcellation is valid and/or meaningful.

The third common procedure for selecting the optimal number of clusters is using cluster evaluation criteria (Cauda et al. 2012; Ryali et al. 2013; Ryali et al. 2015; Vercelli et al. 2016). These criteria are generic and have been widely used to assess cluster structure across a diverse range of applications. The idea behind these criteria is to quantitively estimate the quality of cluster separation, whereby a good clustering is supported by maximized variance between clusters and minimized variance within clusters. Some of the most widely used measures include the silhouette criterion (Rousseeuw 1987), the Calinski-Harabasz criterion

(Calinski and Harabasz 1974) and the gap statistic (Tibshirani et al. 2001). Among them, the silhouette criterion has been used in previous insular parcellation studies (Cauda et al. 2012; Vercelli et al. 2016). Detailed methodological implementation varies across these criteria (Milligan and Cooper 1985). Typically, the cluster evaluation criterion is used to estimate the cluster separation quality (value) under a given criterion for a range of candidate cluster solutions K (K>1), and the solution with the highest value is then considered optimal. However, global cluster evaluation criteria such as the silhouette criterion and Calinski-Harabasz criterion cannot assess the scenario where the absence of any clusters is the most parsimonious solution (Gordon 1999), such as the single-cluster case shown in Supplementary Figure S1 in Chapter 3. Moreover, these criteria are not benchmarked to a null reference distribution, and thus statistical support for the optimal number of clusters is not provided. While the gap statistic considers the single-cluster solution by benchmarking the within-cluster variation with that expected in a null reference distribution (Tibshirani et al. 2001), the null data used by the gap statistic is uniformly sampled (Tibshirani et al. 2001) and thus does not necessarily preserve the spatial properties of fMRI data. Therefore, it is a crucial step to generate null data that is explicitly matched to the characteristics of fMRI data, to enable more accurate delineation of functionally distinct brain regions. Further details and proposed solutions to address these challenges are discussed in Chapter 3.

In addition to clustering approaches, boundary mapping methods that identify areal borders with abrupt spatial changes in structure, function and connectivity have also been widely used in studies of brain mapping (Van Essen et al. 1981; Glasser et al. 2016a; Gordon et al. 2016; Schaefer et al. 2018). Note that principles associated with connectivity-based boundary mapping and connectivity gradients are conceptually similar, given that both approaches seek to characterize local differences in functional connectivity across the spatial extent of a region. The main difference is that boundary mapping and parcellation aim to identify definite and well defined cortical or subcortical parcels, whereas the concept of continuous gradients (Huntenburg et al. 2018) offers a complementary representation of the cortical topography, whereby topographic variation is represented as a continuum, in the absence of abrupt transitions. I will discuss them together in the next section.

Connectivity gradients

Rather than delineating sharp boundaries, topographic variation in brain structure, function and connectivity is represented continuously along overlapping organizational axes (Figure 1.1B & 2.3), referred to as cortical gradients (Cerliani et al. 2012; Sepulcre et al. 2012; Langs et al. 2014; Schröder et al. 2015; Atasoy et al. 2016; Langs et al. 2016; Margulies et al. 2016; Haak et al. 2018; Paquola et al. 2019; Paquola et al. 2020). In this section, I focus on cortical gradients with respect to brain connectivity especially functional connectivity, given that this is the key topographic feature studied in this thesis.

Methods for mapping connectivity gradients

One intuitive method to map continuous spatial patterns in functional connectivity is to quantify the change in connectivity across a set of spatially confined seed regions (Sepulcre et al. 2012; Taylor et al. 2015). For example, in one study, eight seeds in the primary visual cortex were selected, and the functional connectivity was mapped between each seed to the rest of the cortex (Sepulcre et al. 2012). Several visual pathways were defined based on prior knowledge of the cytoarchitecture and this study showed the presence of gradual decreasing visual-to-cortical connectivity strength along different spatial trajectories. Although it should be acknowledged that studies like this explored alternative representations of the connectivity topography beyond conventional brain parcellation, seed-based approaches have their limitations. In particular, the size and location of selected seeds can be subjective, and the connectivity maps yielded largely depend on these prior selected seeds. Inaccuracies in the delineation of seeds can therefore bias the results. In this previous work (Sepulcre et al. 2012), functional connectivity patterns were only characterized for the eight cubic-shaped seeds, whereas any other areas within the primary visual cortex were ignored, potentially yielding only a partial characterization of topographic variation. Also, using predefined seeds assumes that each seed is a discrete entity and thus any gradual patterns of change between seeds is potentially overlooked.

Rather than delineating seeds beforehand, recent studies have instead used data-driven approaches to characterize continuous spatial patterns of variation in brain connectivity (Cerliani et al. 2012; Langs et al. 2014; Schröder et al. 2015; Atasoy et al. 2016; Langs et al.

2016; Margulies et al. 2016; Haak et al. 2018; Paquola et al. 2019; Paquola et al. 2020). Specifically, the high-dimensional connectivity matrix representing the whole-brain connectivity fingerprint of each cortical/subcortical vertex/voxel is decomposed into an ensemble of orthogonal low dimensions that capture most of the variance in the data. One of the most well-known classic eigendecomposition methods is perhaps the singular value decomposition (i.e. principal component analysis, PCA), which is a linear dimensionality reduction technique that is most efficient and suitable for linearly distributed data (Mardia et al. 1980) and generally does not consider the data's intrinsic geometry. However, neural interactions are thought to be highly nonlinear (McClurkin et al. 1991) and thus a linear approach is perhaps not appropriate and may yield disorganized, biologically implausible representations (Haak et al. 2018). In contrast, nonlinear manifold learning techniques such as Laplacian eigenmaps (Belkin and Niyogi 2003), diffusion embedding (Coifman et al. 2005), isometric feature mapping (Tenenbaum et al. 2000), locally linear embedding (Roweis and Saul 2000) and Hessian eigenmaps (Donoho and Grimes 2003) have been recently proposed and applied to parse high-dimensional structural (Cerliani et al. 2012; Ye et al. 2015; Atasoy et al. 2016; Paquola et al. 2020) and functional (Langs et al. 2014; Schröder et al. 2015; Langs et al. 2016; Margulies et al. 2016; Marquand et al. 2017; Haak et al. 2018) connectivity data into a small set of eigenvectors (gradients). The constructed gradient maps are relatively robust with respect to different nonlinear manifold learning techniques (Vos de Wael et al. 2020). Each eigenvector characterizes a continuous mode of spatial variation in structural or functional connectivity across the spatial extent of the brain (Figure 2.3). The eigenvectors are inherently ordered such that each eigenvector captures part of the variance in the original high-dimensional data. Of note, the eigenvector associated with the smallest eigenvalue (zero) is a constant and thus discarded, whereas the eigenvector associated with the second smallest eigenvalue explains the most variance and is usually referred to as Gradient I. Likewise, eigenvectors with the third and fourth smallest eigenvalue are referred to as Gradient II and III respectively in this thesis. The variance explained by successive eigenvectors decreases as a function of increasing eigenvalues. Each successive gradient therefore provides a different aspect of connectional topography, potentially associated with underlying neurobiology.

Biological interpretation of connectivity gradients

Each gradient provides a mapping of continuous variation in connectivity across the brain's topography. Specifically, the value in the dominant gradient (Gradient I), which explains the most variance, characterizes the principal difference in patterns of whole-brain connectivity across the topography of the cerebral cortex (Figure 2.3A), extending from primary unimodal to integrative transmodal areas. In contrast, the second principal gradient (Gradient II) characterizes the topography of connectivity differences within the unimodal areas, spanning from the visual cortex to auditory, somatosensory and motor cortices. Importantly, researchers have shown that the two organizational axes of cortical gradients are in line with the theory of cortical hierarchy in information processing proposed by Mesulam (Mesulam 1998), as reproduced in Figure 2.3A, suggesting a recapitulation of cortical hierarchy.

In addition to the large-scale cortical hierarchy, gradient mapping within specific brain regions enables characterizations of finer organizational structures. For example, Haak and colleagues (2018) showed that the dominant functional connectivity gradient of the primary motor cortex recapitulates its well-established somatotopic organization (Penfield and Boldrey 1937; van den Heuvel and Hulshoff Pol 2010). The functional connectivity organization of the primary visual cortex instead, can be well characterized by two principal gradients that correspond to known orthogonally organized retinotopy, namely the eccentricity and polar angle (Tootell et al. 1998; Amunts et al. 2000), as shown in Figure 2.3B. Likewise, the dominant organizational axes of cerebellar connectivity are associated with the extent of neuronal engagement when performing cognitive tasks (Guell et al. 2018b). In particular, the first principal gradient of cerebellar connectivity spans from motor to non-motor areas, whereas the second gradient extends along an axis from regions participating in low (task-unfocused) to high (task-focused) cognitive demands processes (Figure 2.3C).

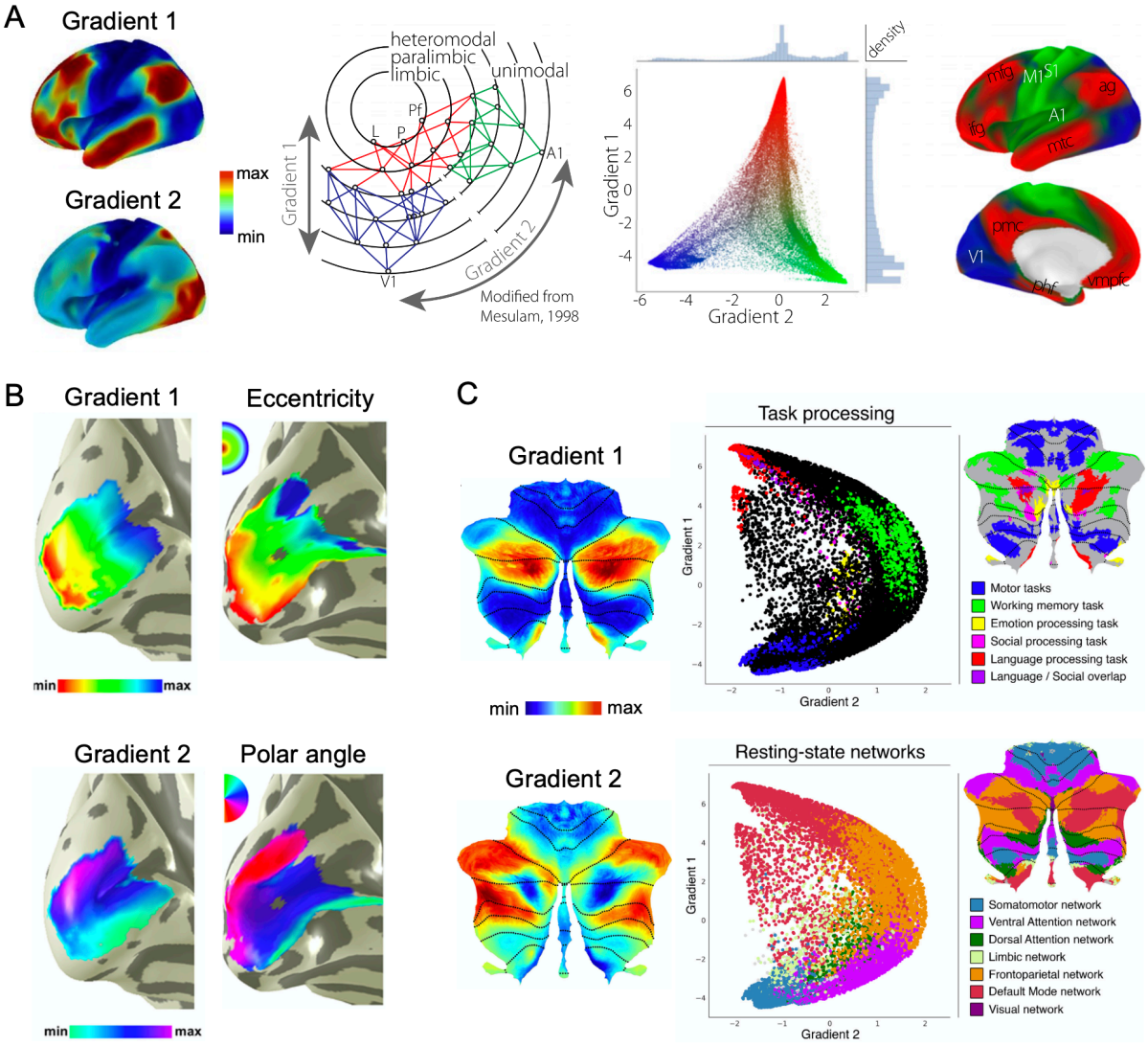


Figure 2.3. Connectivity gradients overlap in space. A, Principal gradients of functional connectivity across the topography of the cerebral cortex (adapted from Margulies et al. 2016). The first gradient (Gradient 1) characterizes variation in functional connectivity from primary sensorimotor (unimodal) to transmodal association cortices, whereas the second gradient separates the visual cortex (V1) from auditory (A1), somatosensory (S1) and motor (M1) areas. The organization of the two functional connectivity gradients is consistent with the cortical hierarchy proposed by Mesulam (1998). L, limbic; P, parietal; Pf, prefrontal; ifg, intermediate frontal sulcus; mfg, middle frontal gyrus; ag, angular gyrus; mtc, middle temporal cortex; pmc, posteromedial cortex; phf, parahippocampal formation; vmpfc, ventromedial prefrontal cortex. **B,** Principal gradients of functional connectivity within the visual cortex (adapted from Haak et al. 2018). The first gradient of functional connectivity in the visual cortex recapitulates the eccentricity of retinotopy, whereas the second gradient corresponds to the polar angle. **C,** Principal gradients of functional connectivity within the cerebellum (adapted from Guell et al. 2018), in relation to task activity (Guell et al. 2018a) and cortical networks (Buckner et al. 2011). The first cerebellar connectivity gradient extends from language/ default mode network (non-motor) to motor regions, whereas the second gradient separates regions participating in high cognitive demands processes (working memory/frontoparietal network) from regions involving in relatively low cognitive demands tasks and networks (motor and language/somatomotor and default mode network).

However, the overlapping spatial patterns in connectivity gradients are not always biologically interpretable (Huntenburg et al. 2017), especially in higher-order association cortices, where detailed organization of the information processing hubs is less clear (Haak et al. 2018).

Specifically, while the principal spatial layout of cortical gradients in functional connectivity (Margulies et al. 2016) is associated with the spatial distribution of intracortical myelin content, especially in the unimodal areas, the correspondence in transmodal cortices is relatively low (Huntenburg et al. 2017). Although the deviation in transmodal areas is reduced by adding information from two additional gradients, the exact biological interpretation of the additional variance explained by these gradients remains to be unpacked.

Pioneering work using the gradient approach to study the fine-grained topographic structure of transmodal association cortex was conducted by Cerliani and colleagues (2012). In this study, probabilistic tractography and Laplacian eigenmaps were used to map the spatial pattern of variation in structural connectivity across the topography of the human insular cortex. In contrast to a relatively sharp transition that was found in the medial premotor cortex separating supplementary motor area (SMA) and pre-SMA, the structural connectivity of the insular cortex varied more gradually along an anteroposterior axis. This continuous pattern of spatial variation in the insular cortex recapitulates the anterior-to-posterior topography in insula's cytoarchitecture (Mesulam and Mufson 1982; Mesulam and Mufson 1985; Friedman et al. 1986), myeloarchitecture (Mesulam and Mufson 1982; Friedman et al. 1986) as well as direct axonal connectivity measured from tract-tracing data in macaques (Mufson et al. 1981; Mufson and Mesulam 1982). Moreover, the anterior-to-posterior insular gradient is consistent with the putative anterior-to-posterior differentiation of insula's function, ranging from basic somatosensory, somatomotor control and homeostasis that primarily involves the posterior part of the insula, to the processing of emotional and higher-level cognitive function that is mainly subserved by the more anterior insula portion (Augustine 1996; Craig 2009; Mutschler et al. 2009; Singer et al. 2009; Kurth et al. 2010a; Kurth et al. 2010b; Xue et al. 2010; Stephani et al. 2011; Uddin et al. 2014; Segerdahl et al. 2015).

Model selection: Discrete or continuous representations?

Whereas classic models of brain topography tend to focus on parcellating the brain into distinct regions with discrete boundaries, recent evidence suggests that topographic variation may be better conceptualized in terms of continuous gradients of gradual change. Are these

two topographic representations contradictory? The answer is, perhaps not. Spatial variation across expanses of the brain might be evident, but if the variation is too gradual to warrant boundary delineation, a continuum might be deemed to provide the most parsimonious representation. Several recent studies have attempted to delineate discrete boundaries based on the connectivity gradients (Glasser et al. 2016a; Gordon et al. 2016; Langs et al. 2016; Marquand et al. 2017; Guell et al. 2018b; Schaefer et al. 2018), but without performing statistical testing to evaluate if a change in the gradient magnitude is sufficiently sharp and/or abrupt to warrant delineation of a hard boundary. I refer to this step as model selection. Without model selection, boundaries are inevitably delineated at all locations where a change in the gradient magnitude is detected, potentially leading to over-parcellation and delineation of boundaries at subtle gradient changes that are attributable to noise and other confounds.

It is worth noting that most studies of gradient-based parcellation conceptually followed one of the two popular approaches aforementioned, i.e. clustering or boundary mapping. Specifically, the spatial pattern of variation in cortical connectivity is typically first mapped into a set of low-dimensional embedding space using one of the non-linear eigendecomposition methods. A clustering algorithm is then used to group vertices/voxels with similar connectivity fingerprints represented in the embedding maps into distinct clusters, yielding discrete cortical networks (Langs et al. 2016) and subdivisions in the cerebellum (Guell et al. 2018b) and striatum (Marquand et al. 2017). Traditional studies of connectivity-based parcellation typically apply clustering methodology on a PCA-transformed connectivity space. In contrast, clustering approaches are applied to the data that is transformed to a nonlinear embedding space in studies of gradient-based parcellation. This approach is conceptually similar to the idea of conventional parcellations but may better account for individual variability in neuroanatomy (Langs et al. 2016). However, challenges in selecting the optimal number of clusters are inevitable as discussed above, regardless of the analytic space, i.e. PCA or embedding. Using the same diffusion embedding method (Coifman et al. 2005), Margulies and colleagues (2016) highlighted the continuous and smooth gradient of variation in functional connectivity across the cerebral cortex from unimodal to transmodal areas, whereas Langs and colleagues (2016) imposed hard cut-off clustering solutions and parcellated the cerebral cortex into 7 and 17 networks, to be consistent with existing cortical network partitions (Yeo et al. 2011). Likewise, Marquand and colleagues (2017) delineated

three striatal clusters, recapitulating the three anatomical nuclei in the striatum (i.e. putamen, caudate and nucleus accumbens), whereas Guell et al (2018) reported 5, 14 as well as 18-clusters solutions for the cerebellum in a *post hoc* analysis.

Alternatively, discrete partitions can be delineated based on the magnitude of connectivity gradient, which means that areal borders are delineated at locations of abrupt change in functional connectivity. This approach is often broadly referred to as boundary mapping or boundary detection and has been widely used in detecting areal boundaries in the cerebral cortex (Cohen et al. 2008; Wig et al. 2014a; Wig et al. 2014b; Glasser et al. 2016a; Gordon et al. 2016). In contrast to the technical challenges in selecting an optimal number of clusters in clustering approaches, boundary mapping techniques encounter the difficult tasks of initializing seed locations as well as the selection of a cutting threshold for the gradient magnitude. Ideally, each seed corresponds to the centre of a parcel, possessing the local minimal magnitude compared to surrounding vertices/voxels. The delineation of parcels starts from these seeds and gradually expands outward until the location where the magnitude reaches a certain threshold. This can be achieved by initializing all possible local minima, however, may result in over-parcellation, with one-vertex wide borders. Post hoc adjustment is often performed to group very small parcels that share similar magnitude profiles, while a subjective threshold is required to determine the extent of similarity/dissimilarity (Gordon et al. 2016). In a more neurobiologically principled approach, all candidate borders are examined and interpreted by neuroanatomists based on extensive cytoarchitectural and myeloarchitectural knowledge, to minimize potential imaging artifacts (e.g. signal drop) and biases arising from computational models (Glasser et al. 2016a). However, histological investigations inferred from limited samples of postmortem specimens may not necessarily reflect functional brain organization in living humans.

In a brief summary, existing gradient-based parcellation approaches typically do not consider the extent to which the gradient magnitude could be explained by brain geometry, chance variation and/or other confounds such as spatial smoothing of fMRI data. In contrast, studies characterizing the spatial pattern of variation in connectivity as a set of continuous gradients do not consider the magnitude of change in the gradient, whereby any abrupt transitions may have been potentially overlooked. Given these shortcomings, I aimed to develop a formalized

model selection framework based on null hypothesis testing to determine whether an abrupt change in a brain gradient is sufficiently large to warrant delineation of a hard boundary. A boundary should only be delineated when justified by the formal model selection process, otherwise a continuum is deemed to provide a more parsimonious representation of the underlying topography.

First, I aimed to apply this model selection process to investigate the functional organization of the topographically complex insular cortex (Chapter 3). Functional organization of the insula has been most extensively studied using classical models of brain topography, by parcellating the insula into distinct subregions using clustering methodology, as summarized in Chapter 1. However, the number of insular subregions varies substantially across studies, suggesting that the topographic variation in the insula may be better conceptualized as a continuum, in the absence of abrupt change in the spatial gradient. Likewise, studies investigating the pathophysiology of the insula in neuropsychiatric illness typically adopted predefined insular subregions, particular the anterior aspect, without first assessing whether the anterior-posterior topographic organization of the insula is altered in the disorder (Moran et al. 2013; Palaniyappan et al. 2013; Dandash et al. 2014; Manoliu et al. 2014; Wotruba et al. 2014; Uddin 2015; Wang et al. 2016). I therefore first aimed to investigate the functional organization of the insula with respect to these two representations of brain topography. I aimed to apply the model selection process to determine whether the functional architecture of the insula is best represented by parcellating into distinct subregions or as continuous gradients of gradual change (Chapter 3). After establishing the best model to represent the insula's topography, I next aimed to investigate whether a serious neuropsychiatric illness (schizophrenia) associates with alterations in the topographic organization of the insula (Chapter 4). Finally, I aimed to apply these new insights in model selection that I developed to investigate the insular cortex to the entire subcortex (Chapter 5), wherein functional topography of some subcortical areas has not been well characterized (Alkemade et al. 2013; Forstmann et al. 2016). In particular, I aimed to investigate the topographic organization of the subcortex with the goal of developing a new subcortex atlas, in which boundary demarcation is justified by the model selection framework.

Participants, datasets and data preprocessing

The main aims of this thesis are addressed using neuroimaging and behavioral data acquired in healthy adults (Chapter 3 and 5) and adults diagnosed with schizophrenia (Chapter 4). The data used in Chapter 3 and 5 was sourced with permission from the Human Connectome Project (HCP; Van Essen et al. 2013), a publicly available dataset comprising high-quality structural, functional and diffusion-weighted MRI of the brain in more than 1000 participants. In this thesis, only the functional MRI data, including resting-state data acquired at 3T and 7T and task-evoked data acquired at 3T, was analyzed. Participants in the HCP are between 18 and 37 years of age and were recruited from the general community in the United States of America. Measures of cognitive performance, personality traits, mental health and other medical conditions were assessed in most participants and are used in this thesis to establish associations between brain topography and inter-individual variation in behavior. The HCP made efforts to recruit participants broadly reflecting the ethnic and racial composition of the population as represented in the 2000 decennial census. Exclusion criteria included severe neurodevelopmental disorders, documented neuropsychiatric disorders or neurologic disorders. Individuals with illnesses such as diabetes or high blood pressure were also excluded during recruitment. Further details about the demographics of the HCP cohort and technical details about the MRI acquisition can be found in the next chapters as well as other literatures (Barch et al. 2013; Smith et al. 2013; Van Essen et al. 2013).

In Chapter 4, resting-state functional MRI acquired in patients with schizophrenia was used to investigate whether the disorder is associated with reorganization of the insula's topography and functional connectivity. Patients with an established diagnosis of schizophrenia were recruited in Melbourne, Australia, and MRI was acquired using a 3T MR scanner. The quality of this data is lower than the HCP data, particularly in terms of duration of acquisition, temporal sampling and fidelity. Measures of clinical severity, cognitive performance and general functioning were assessed in all patients using established instruments, as described in Chapter 4. These data are not publicly available.

Data preprocessing

In Chapter 3 and 5, minimally preprocessed volumetric functional MRI data was sourced from the HCP online repository. Details of the minimal preprocessing pipeline can be found elsewhere (Glasser et al. 2013). In brief, this pipeline includes removal of spatial artefacts and distortions and alignment to MNI (Montreal Neurological Institute) standard space. Head motion artefacts, non-neuronal physiological related noise were corrected with an independent component analysis (ICA)-based regression strategy (FMRIB's ICA-based X-noiseifier; (Griffanti et al. 2014), which removes more than 99% of the artefactual ICA components (Salimi-Khorshidi et al. 2014) and outperforms most alternative approaches (Parkes et al. 2018). Further temporal and spatial filtering as well as nuisance regression were not included in this pipeline.

In addition to the minimal preprocessing pipeline, 3T resting-state fMRI data used in Chapter 3 was spatially smoothed with a Gaussian smoothing kernel of 4 mm FWHM (full width at half maximum). A smoothing kernel of 1.5 mm FWHM was investigated in ancillary analyses. In Chapter 5, the minimally preprocessed resting-state and task-evoked fMRI data was used, with additional spatial smoothing (3T: 6 mm FWHM; 7T: 4 mm FWHM) and adjustment with Wishart filter (Glasser et al. 2016b; Glasser et al. 2018), to dampen the noise and enhance subcortical signal-to-noise ratio.

Resting-state fMRI data of patients with schizophrenia and healthy comparison individuals (Chapter 4) was preprocessed using FSL (Jenkinson et al. 2012). The preprocessing pipeline includes slice-timing correction, brain extraction, linear registration for intrascan head motion correction and non-linear alignment to MNI standard space. Head motion artefacts were further corrected with ICA-AROMA (ICA-based automatic removal of motion artefacts; (Pruim et al. 2015a; Pruim et al. 2015b) after spatial smoothing with a Gaussian kernel of 4 mm FWHM. Mean white matter and cerebrospinal fluid signals were regressed and the residuals were band-pass filtered (0.01-0.1HZ).

Statistical analysis and methods

In all three studies, functional connectivity was quantified using the Pearson correlation coefficient computed between fMRI time series of spatially distributed brain regions (see Chapter 2).

In Chapter 3, functional connectivity was computed between each insula voxel and all gray matter voxels, yielding a whole-brain functional connectivity fingerprint for each insular voxel and individual. Clustering (Ward's linkage) was used to group insular voxels into clusters based on shared connectivity profile. The quality of cluster separation was estimated by established cluster evaluation criteria, including silhouette criterion (Rousseeuw 1987), Calinski-Harabasz criterion (Calinski and Harabasz 1974) and gap statistic (Tibshirani et al. 2001). A novel null model with null hypothesis testing was developed to determine the optimal number of clusters and whether insula subregions are more clustered than expected due to chance. On the other hand, Laplacian eigenmaps (Belkin and Niyogi 2003) and associated eigendecomposition methods were used to continuously characterize the spatial variation in function connectivity across the topography of the insula. The novel concept of diversity curves was developed to parametrize the connectional variation across the topography, which in turn facilitated model selection. The diversity curve computed for the actual insula was compared to three benchmarks for which the underlying connectional topography was known (i.e. distinct subregions, continuum and homogeneous benchmark). A piecewise linear function was fitted to the diversity curve for each individual, and canonical correlation analysis (CCA) (Hotelling 1936) was used to test for a multivariate association between model parameters describing the piecewise linear functions and individual variation in human behaviors. Familywise error was corrected across all CCA models with permutation testing.

In Chapter 4, insular connectional topography was represented by continuous gradients of gradual change (diversity curves) and traditional subregions in each individual with schizophrenia and each healthy comparison individual as described in Chapter 3. A two-sample *t* test was used to test for between-group difference at each point along the diversity curves. The false discovery rate was controlled at an alpha of 0.05 for multiple comparisons across the set of all points. To test the difference between schizophrenia and healthy controls

in insular functional connectivity with respect to cortical and subcortical regions to which it connects, the insula was further parcellated into subregions using conventional clustering techniques as described in Chapter 3. Modularity analysis (Newman and Mark 2006) was used to estimate the degree of differentiation in functional connectivity profile between insular subregions, whereby the null hypothesis of equality in the degree of differentiation between schizophrenia and healthy comparison group was assessed with permutation testing. Main effects of diagnosis, subregions and laterality on insular functional connectivity as well as the interaction between diagnosis and the latter two main effects was tested using within-subjects analysis of variance. Non-parametric cluster-based inference as implemented in Randomise (Winkler et al. 2014) available in FSL (Jenkinson et al. 2012) was used to control for familywise error across the set of all gray matter voxels. Functional connectivity between insular subregions and clusters for which the main or interaction effects were significant was computed for each individual with schizophrenia. Canonical correlation analysis (Hotelling 1936) was performed to test for a multivariate association between the functional connectivity estimates and the severity of clinical symptoms and cognitive impairment in the disorder. Familywise error was corrected across all CCA models with permutation testing.

In Chapter 5, a whole-brain functional connectivity profile was mapped for each subcortical voxel. Continuous gradients of connectivity variation across the topography of the subcortex was computed using Laplacian eigenmaps (Belkin and Niyogi 2003) as described in Chapter 3. A new technique called *gradientography*, an fMRI analogue of diffusion MRI tractography, was developed to map curvilinear trajectories of connectivity variation in the gradient field. Gradient magnitudes were computed and projected onto the curvilinear trajectories, yielding a two-dimensional representation of connectivity gradients, i.e. diversity curves as introduced in Chapter 3. Local peaks in the diversity curves indicate local maxima in the gradient magnitude image, indicating locations of putative functional boundaries. A null model was developed to enable null hypothesis testing of whether values of local maxima are sufficiently large to warrant hard boundaries. Diversity curves generated from the null data were referred to as null diversity curves. For each candidate boundary, a p-value was given by the proportion of null diversity curves with local maxima that exceeded or equaled the observed maximum. The false discovery rate was controlled at an alpha of 0.05 across the set of all observed maxima. If the null can be rejected, the watershed transform algorithm (Meyer

1994) was then used to segment subcortical voxels into contiguous parcels, whereby parcels represented water catchment basins and boundaries were equivalent to watershed ridge lines. Gradients mapping and null hypothesis testing were performed iteratively until the null hypothesis could not be further rejected, yielding a new subcortex atlas comprising four scales (Scale I-IV). The validity and reproducibility of the new atlas were further estimated by computing the parcellation homogeneity based on within-parcel synchrony of fMRI time series (estimated by the principal component analysis) acquired in a second session of fMRI data, whereas the first session was used for parcellation. This subcortical atlas was replicated using ultra-high field strength (7T) data and the spatial correspondence between 3T and 7T atlas was quantified by the normalized mutual information (Lancichinetti et al. 2009), whereas a machine learning approach (support vector machine, SVM) was used to generate personalized subcortical atlases to account for individual variability in functional connectivity. To investigate whether the connectional topography of the subcortex at rest reconfigures in response to changing cognitive demands, diversity curves were mapped for connectivity gradients under seven task conditions, including emotion, gambling, language, relational matching, social inference, working memory and motor execution (Barch et al. 2013). Similarity in the diversity curves between each pair of rest and task conditions was quantified using the Pearson correlation coefficient. Permutation testing was used to determine a p-value for each correlation coefficient and the Bonferroni correction was used to control for multiple comparisons across the set of pairs of conditions. Likewise, patterns of similarity between cortical networks with respect to their functional connectivity with subcortical regions were tested and the significance level was established by permutation testing. Finally, the subcortex atlas was used to test for an association between subcortical functional connectivity and individual variation in behaviors. A large set of behavioral items was first decomposed into five orthogonal behavioral dimensions using independent component analysis, thereafter the network-based statistic (Zalesky et al. 2010) was implemented to test whether subcortical functional connectivity is associated with individual variation in each of the five behavioral dimensions. Further details are provided in Chapter 5.

References

Adachi Y, Osada T, Sporns O, Watanabe T, Matsui T, Miyamoto K, Miyashita Y. 2012. Functional connectivity between anatomically unconnected areas is shaped by collective network-level effects in the macaque cortex. Cereb Cortex 22:1586-1592.

Alcauter S, Lin W, Keith Smith J, Gilmore JH, Gao W. 2015. Consistent anterior-posterior segregation of the insula during the first 2 years of life. Cereb Cortex 25:1176-1187.

Alkemade A, Keuken M, Forstmann B. 2013. A perspective on terra incognita: uncovering the neuroanatomy of the human subcortex. Frontiers in Neuroanatomy 7.

Amunts K, Malikovic A, Mohlberg H, Schormann T, Zilles K. 2000. Brodmann's areas 17 and 18 brought into stereotaxic space-where and how variable? Neuroimage 11:66-84.

Amunts K, Zilles K. 2015. Architectonic Mapping of the Human Brain beyond Brodmann. Neuron 88:1086-1107.

Arslan S, Ktena SI, Makropoulos A, Robinson EC, Rueckert D, Parisot S. 2018. Human brain mapping: A systematic comparison of parcellation methods for the human cerebral cortex. Neuroimage 170:5-30.

Atasoy S, Donnelly I, Pearson J. 2016. Human brain networks function in connectome-specific harmonic waves. Nature Communications 7:10340.

Augustine JR. 1996. Circuitry and functional aspects of the insular lobe in primates including humans. Brain Res Brain Res Rev 22:229-244.

Barch DM, Burgess GC, Harms MP, Petersen SE, Schlaggar BL, Corbetta M, Glasser MF, Curtiss S, Dixit S, Feldt C et al. 2013. Function in the human connectome: task-fMRI and individual differences in behavior. Neuroimage 80:169-189.

Behrens TE, Johansen-Berg H, Woolrich MW, Smith SM, Wheeler-Kingshott CA, Boulby PA, Barker GJ, Sillery EL, Sheehan K, Ciccarelli O et al. 2003. Non-invasive mapping of connections between human thalamus and cortex using diffusion imaging. Nat Neurosci 6:750-757.

Belkin M, Niyogi P. 2003. Laplacian Eigenmaps for Dimensionality Reduction and Data Representation. Neural Computation 15:1373-1396.

Bellec P, Rosa-Neto P, Lyttelton OC, Benali H, Evans AC. 2010. Multi-level bootstrap analysis of stable clusters in resting-state fMRI. Neuroimage 51:1126-1139.

Biswal B, Yetkin FZ, Haughton VM, Hyde JS. 1995. Functional connectivity in the motor cortex of resting human brain using echo-planar MRI. Magn Reson Med 34:537-541.

Brodmann K. 1909. Brodmann’s localisation in the cerebral cortex. New York, USA: Springer.

Buchbinder BR. 2016. Chapter 4 - Functional magnetic resonance imaging. In: Masdeu JC, González RG, editors. Handbook of Clinical Neurology Elsevier p 61-92.

Buckner RL, Krienen FM, Castellanos A, Diaz JC, Yeo BT. 2011. The organization of the human cerebellum estimated by intrinsic functional connectivity. J Neurophysiol 106:2322-2345.

Buckner RL, Krienen FM, Yeo BT. 2013. Opportunities and limitations of intrinsic functional connectivity MRI. Nat Neurosci 16:832-837.

Buxton RB, Uludag K, Dubowitz DJ, Liu TT. 2004. Modeling the hemodynamic response to brain activation. Neuroimage 23 Suppl 1:S220-233.

Cahalane DJ, Charvet CJ, Finlay BL. 2012. Systematic, balancing gradients in neuron density and number across the primate isocortex. Front Neuroanat 6:28.

Cahalane DJ, Charvet CJ, Finlay BL. 2014. Modeling local and cross-species neuron number variations in the cerebral cortex as arising from a common mechanism. Proceedings of the National Academy of Sciences 111:17642-17647.

Calinski T, Harabasz J. 1974. A dendrite method for cluster analysis. Communications in Statistics 3:1-27.

Caspers J, Zilles K, Eickhoff SB, Schleicher A, Mohlberg H, Amunts K. 2013. Cytoarchitectonical analysis and probabilistic mapping of two extrastriate areas of the human posterior fusiform gyrus. Brain Structure and Function 218:511-526.

Cauda F, Costa T, Torta DM, Sacco K, D'Agata F, Duca S, Geminiani G, Fox PT, Vercelli A. 2012. Meta-analytic clustering of the insular cortex: characterizing the meta-analytic connectivity of the insula when involved in active tasks. Neuroimage 62:343-355.

Cauda F, D'Agata F, Sacco K, Duca S, Geminiani G, Vercelli A. 2011. Functional connectivity of the insula in the resting brain. Neuroimage 55:8-23.

Cauda F, Vercelli A. 2013. How many clusters in the insular cortex? Cereb Cortex 23:2779-2780.

Cerliani L, Thomas RM, Jbabdi S, Siero JC, Nanetti L, Crippa A, Gazzola V, D'Arceuil H, Keysers C. 2012. Probabilistic tractography recovers a rostrocaudal trajectory of connectivity variability in the human insular cortex. Hum Brain Mapp 33:2005-2034.

Cha J, Jo HJ, Gibson WS, Lee JM. 2017. Functional organization of the human posterior cingulate cortex, revealed by multiple connectivity-based parcellation methods. Hum Brain Mapp 38:2808-2818.

Chang LJ, Yarkoni T, Khaw MW, Sanfey AG. 2013. Decoding the role of the insula in human cognition: functional parcellation and large-scale reverse inference. Cereb Cortex 23:739-749.

Charvet CJ, Cahalane DJ, Finlay BL. 2013. Systematic, Cross-Cortex Variation in Neuron Numbers in Rodents and Primates. Cerebral Cortex 25:147-160.

Charvet CJ, Finlay BL. 2014. Evo-Devo and the Primate Isocortex: The Central Organizing Role of Intrinsic Gradients of Neurogenesis. Brain, Behavior and Evolution 84:81-92.

Charvet CJ, Stimpson CD, Kim YD, Raghanti MA, Lewandowski AH, Hof PR, Gómez-Robles A, Krienen FM, Sherwood CC. 2017. Gradients in cytoarchitectural landscapes of the isocortex: Diprotodont marsupials in comparison to eutherian mammals. Journal of Comparative Neurology 525:1811-1826.

Cohen AL, Fair DA, Dosenbach NU, Miezin FM, Dierker D, Van Essen DC, Schlaggar BL, Petersen SE. 2008. Defining functional areas in individual human brains using resting functional connectivity MRI. Neuroimage 41:45-57.

Coifman RR, Lafon S, Lee AB, Maggioni M, Nadler B, Warner F, Zucker SW. 2005. Geometric diffusions as a tool for harmonic analysis and structure definition of data: Diffusion maps. Proceedings of the National Academy of Sciences of the United States of America 102:7426-7431.

Cole MW, Bagic A, Kass R, Schneider W. 2010. Prefrontal dynamics underlying rapid instructed task learning reverse with practice. J Neurosci 30:14245-14254.

Cole MW, Bassett DS, Power JD, Braver TS, Petersen SE. 2014. Intrinsic and task-evoked network architectures of the human brain. Neuron 83:238-251.

Collins CE, Airey DC, Young NA, Leitch DB, Kaas JH. 2010. Neuron densities vary across and within cortical areas in primates. Proceedings of the National Academy of Sciences 107:15927-15932.

Craddock RC, James GA, Holtzheimer PE, 3rd, Hu XP, Mayberg HS. 2012. A whole brain fMRI atlas generated via spatially constrained spectral clustering. Hum Brain Mapp 33:1914-1928.

Craig AD. 2009. How do you feel--now? The anterior insula and human awareness. Nat Rev Neurosci 10:59-70.

Dandash O, Fornito A, Lee J, Keefe RS, Chee MW, Adcock RA, Pantelis C, Wood SJ, Harrison BJ. 2014. Altered striatal functional connectivity in subjects with an at-risk mental state for psychosis. Schizophr Bull 40:904-913.

Deen B, Pitskel NB, Pelphrey KA. 2011. Three systems of insular functional connectivity identified with cluster analysis. Cereb Cortex 21:1498-1506.

Donoho DL, Grimes C. 2003. Hessian eigenmaps: Locally linear embedding techniques for high-dimensional data. Proceedings of the National Academy of Sciences 100:5591-5596.

Eickhoff SB, Stephan KE, Mohlberg H, Grefkes C, Fink GR, Amunts K, Zilles K. 2005. A new SPM toolbox for combining probabilistic cytoarchitectonic maps and functional imaging data. Neuroimage 25:1325-1335.

Elston GN. 2000. Pyramidal Cells of the Frontal Lobe: All the More Spinous to Think With. The Journal of Neuroscience 20:RC95-RC95.

Fair DA, Schlaggar BL, Cohen AL, Miezin FM, Dosenbach NU, Wenger KK, Fox MD, Snyder AZ, Raichle ME, Petersen SE. 2007. A method for using blocked and event-related fMRI data to study "resting state" functional connectivity. Neuroimage 35:396-405.

Forstmann BU, de Hollander G, van Maanen L, Alkemade A, Keuken MC. 2016. Towards a mechanistic understanding of the human subcortex. Nature Reviews Neuroscience 18:57.

Fox MD, Raichle ME. 2007. Spontaneous fluctuations in brain activity observed with functional magnetic resonance imaging. Nat Rev Neurosci 8:700-711.

Fox MD, Snyder AZ, Vincent JL, Corbetta M, Van Essen DC, Raichle ME. 2005. The human brain is intrinsically organized into dynamic, anticorrelated functional networks. Proc Natl Acad Sci U S A 102:9673-9678.

Fox MD, Snyder AZ, Vincent JL, Raichle ME. 2007. Intrinsic fluctuations within cortical systems account for intertrial variability in human behavior. Neuron 56:171-184.

Friedman DP, Murray EA, O'Neill JB, Mishkin M. 1986. Cortical connections of the somatosensory fields of the lateral sulcus of macaques: evidence for a corticolimbic pathway for touch. J Comp Neurol 252:323-347.

Glasser MF, Coalson TS, Bijsterbosch JD, Harrison SJ, Harms MP, Anticevic A, Van Essen DC, Smith SM. 2018. Using temporal ICA to selectively remove global noise while preserving global signal in functional MRI data. NeuroImage 181:692-717.

Glasser MF, Coalson TS, Robinson EC, Hacker CD, Harwell J, Yacoub E, Ugurbil K, Andersson J, Beckmann CF, Jenkinson M et al. 2016a. A multi-modal parcellation of human cerebral cortex. Nature 536:171-178.

Glasser MF, Smith SM, Marcus DS, Andersson JL, Auerbach EJ, Behrens TE, Coalson TS, Harms MP, Jenkinson M, Moeller S et al. 2016b. The Human Connectome Project's neuroimaging approach. Nat Neurosci 19:1175-1187.

Glasser MF, Sotiropoulos SN, Wilson JA, Coalson TS, Fischl B, Andersson JL, Xu J, Jbabdi S, Webster M, Polimeni JR et al. 2013. The minimal preprocessing pipelines for the Human Connectome Project. Neuroimage 80:105-124.

Gordon AD. 1999. Classification, 2nd Edition (Chapman & Hall/CRC Monographs on Statistics & Applied Probability): Chapman and Hall/CRC.

Gordon EM, Laumann TO, Adeyemo B, Huckins JF, Kelley WM, Petersen SE. 2016. Generation and Evaluation of a Cortical Area Parcellation from Resting-State Correlations. Cereb Cortex 26:288-303.

Goulas A, Werner R, Beul S, Säring D, Heuvel Mvd, Triarhou L, Hilgetag C. 2016. Cytoarchitectonic similarity is a wiring principle of the human connectome. In: bioRxiv.

Greene AS, Gao S, Scheinost D, Constable RT. 2018. Task-induced brain state manipulation improves prediction of individual traits. Nature Communications 9:2807.

Greicius MD, Krasnow B, Reiss AL, Menon V. 2003. Functional connectivity in the resting brain: A network analysis of the default mode hypothesis. Proceedings of the National Academy of Sciences 100:253-258.

Griffanti L, Salimi-Khorshidi G, Beckmann CF, Auerbach EJ, Douaud G, Sexton CE, Zsoldos E, Ebmeier KP, Filippini N, Mackay CE et al. 2014. ICA-based artefact removal and accelerated fMRI acquisition for improved resting state network imaging. Neuroimage 95:232-247.

Guell X, Gabrieli JDE, Schmahmann JD. 2018a. Triple representation of language, working memory, social and emotion processing in the cerebellum: convergent evidence from task and seed-based resting-state fMRI analyses in a single large cohort. NeuroImage 172:437-449.

Guell X, Schmahmann JD, Gabrieli J, Ghosh SS. 2018b. Functional gradients of the cerebellum. Elife 7.

Haak KV, Marquand AF, Beckmann CF. 2018. Connectopic mapping with resting-state fMRI. Neuroimage 170:83-94.

Hawrylycz MJ, Lein ES, Guillozet-Bongaarts AL, Shen EH, Ng L, Miller JA, van de Lagemaat LN, Smith KA, Ebbert A, Riley ZL et al. 2012. An anatomically comprehensive atlas of the adult human brain transcriptome. Nature 489:391-399.

Hermundstad AM, Bassett DS, Brown KS, Aminoff EM, Clewett D, Freeman S, Frithsen A, Johnson A, Tipper CM, Miller MB et al. 2013. Structural foundations of resting-state and task-based functional connectivity in the human brain. Proc Natl Acad Sci U S A 110:6169-6174.

Honey CJ, Sporns O, Cammoun L, Gigandet X, Thiran JP, Meuli R, Hagmann P. 2009. Predicting human resting-state functional connectivity from structural connectivity. Proceedings of the National Academy of Sciences 106:2035-2040.

Hotelling H. 1936. Relations between two sets of variates. Biometrika 28:321-377.

Huntenburg JM, Bazin PL, Goulas A, Tardif CL, Villringer A, Margulies DS. 2017. A Systematic Relationship Between Functional Connectivity and Intracortical Myelin in the Human Cerebral Cortex. Cereb Cortex 27:981-997.

Huntenburg JM, Bazin PL, Margulies DS. 2018. Large-Scale Gradients in Human Cortical Organization. Trends Cogn Sci 22:21-31.

Jain AK. 2010. Data clustering: 50 years beyond K-means. Pattern Recognition Letters 31:651-666.

Jakab A, Molnar PP, Bogner P, Beres M, Berenyi EL. 2012. Connectivity-based parcellation reveals interhemispheric differences in the insula. Brain Topogr 25:264-271.

Jenkinson M, Beckmann CF, Behrens TE, Woolrich MW, Smith SM. 2012. FSL. Neuroimage 62:782-790.

Kahnt T, Chang LJ, Park SQ, Heinzle J, Haynes JD. 2012. Connectivity-based parcellation of the human orbitofrontal cortex. J Neurosci 32:6240-6250.

Kelly C, Toro R, Di Martino A, Cox CL, Bellec P, Castellanos FX, Milham MP. 2012. A convergent functional architecture of the insula emerges across imaging modalities. Neuroimage 61:1129-1142.

Kim JH, Lee JM, Jo HJ, Kim SH, Lee JH, Kim ST, Seo SW, Cox RW, Na DL, Kim SI et al. 2010. Defining functional SMA and pre-SMA subregions in human MFC using resting state fMRI: functional connectivity-based parcellation method. Neuroimage 49:2375-2386.

Kujovic M, Zilles K, Malikovic A, Schleicher A, Mohlberg H, Rottschy C, Eickhoff SB, Amunts K. 2013. Cytoarchitectonic mapping of the human dorsal extrastriate cortex. Brain Structure and Function 218:157-172.

Kurth F, Eickhoff SB, Schleicher A, Hoemke L, Zilles K, Amunts K. 2010a. Cytoarchitecture and probabilistic maps of the human posterior insular cortex. Cereb Cortex 20:1448-1461.

Kurth F, Zilles K, Fox PT, Laird AR, Eickhoff SB. 2010b. A link between the systems: functional differentiation and integration within the human insula revealed by meta-analysis. Brain Struct Funct 214:519-534.

Lancichinetti A, Fortunato S, Kertész J. 2009. Detecting the overlapping and hierarchical community structure in complex networks. New Journal of Physics 11:033015.

Langs G, Sweet A, Lashkari D, Tie Y, Rigolo L, Golby AJ, Golland P. 2014. Decoupling function and anatomy in atlases of functional connectivity patterns: Language mapping in tumor patients. NeuroImage 103:462-475.

Langs G, Wang D, Golland P, Mueller S, Pan R, Sabuncu MR, Sun W, Li K, Liu H. 2016. Identifying Shared Brain Networks in Individuals by Decoupling Functional and Anatomical Variability. Cerebral Cortex 26:4004-4014.

Le Bihan D, Breton E. 1985. Imagerie de diffusion in vivo par résonance magnétique nucléaire. C R Académie Sci.

Maier-Hein KH, Neher PF, Houde JC, Côté MA, Garyfallidis E, Zhong J, Chamberland M, Yeh FC, Lin YC, Ji Q et al. 2017. The challenge of mapping the human connectome based on diffusion tractography. Nat Commun 8:1349.

Manoliu A, Riedl V, Zherdin A, Muhlau M, Schwerthoffer D, Scherr M, Peters H, Zimmer C, Forstl H, Bauml J et al. 2014. Aberrant dependence of default mode/central executive network interactions on anterior insular salience network activity in schizophrenia. Schizophr Bull 40:428-437.

Mardia K, Kent J, Bibby J. 1980. Multivariate analysis. London: Academic Press.

Margulies DS, Ghosh SS, Goulas A, Falkiewicz M, Huntenburg JM, Langs G, Bezgin G, Eickhoff SB, Castellanos FX, Petrides M et al. 2016. Situating the default-mode network along a

principal gradient of macroscale cortical organization. Proc Natl Acad Sci U S A 113:12574-12579.

Marquand AF, Haak KV, Beckmann CF. 2017. Functional corticostriatal connection topographies predict goal directed behaviour in humans. Nat Hum Behav 1:0146.

Marrelec G, Bellec P, Krainik A, Duffau H, Pelegrini-Issac M, Lehericy S, Benali H, Doyon J. 2008. Regions, systems, and the brain: hierarchical measures of functional integration in fMRI. Med Image Anal 12:484-496.

McClurkin JW, Optican LM, Richmond BJ, Gawne TJ. 1991. Concurrent Processing and Complexity of Temporally Encoded Neuronal Messages in Visual Perception. Science 253:675-677.

Mennes M, Kelly C, Colcombe S, Castellanos FX, Milham MP. 2013. The extrinsic and intrinsic functional architectures of the human brain are not equivalent. Cereb Cortex 23:223-229.

Mesulam MM. 1998. From sensation to cognition. Brain 121 (Pt 6):1013-1052.

Mesulam MM, Mufson EJ. 1982. Insula of the old world monkey. I. Architectonics in the insulo-orbito-temporal component of the paralimbic brain. J Comp Neurol 212:1-22.

Mesulam MM, Mufson EJ. 1985. The Insula of Reil in Man and Monkey. In: Peters A, Jones EG, editors. Association and Auditory Cortices Boston, MA: Springer US p 179-226.

Meyer F. 1994. Topographic distance and watershed lines. Signal Processing 38:113-125.

Milligan GW, Cooper MC. 1985. An examination of procedures for determining the number of clusters in a data set. Psychometrika 50:159-179.

Miranda-Dominguez O, Mills BD, Grayson D, Woodall A, Grant KA, Kroenke CD, Fair DA. 2014. Bridging the gap between the human and macaque connectome: a quantitative comparison of global interspecies structure-function relationships and network topology. J Neurosci 34:5552-5563.

Moran LV, Tagamets MA, Sampath H, O'Donnell A, Stein EA, Kochunov P, Hong LE. 2013. Disruption of anterior insula modulation of large-scale brain networks in schizophrenia. Biological Psychiatry 74:467-474.

Mufson EJ, Mesulam MM. 1982. Insula of the old world monkey. II: Afferent cortical input and comments on the claustrum. J Comp Neurol 212:23-37.

Mufson EJ, Mesulam MM, Pandya DN. 1981. Insular interconnections with the amygdala in the rhesus monkey. Neuroscience 6:1231-1248.

Mutschler I, Wieckhorst B, Kowalevski S, Derix J, Wentlandt J, Schulze-Bonhage A, Ball T. 2009. Functional organization of the human anterior insular cortex. Neurosci Lett 457:66-70.

Nanetti L, Cerliani L, Gazzola V, Renken R, Keysers C. 2009. Group analyses of connectivity-based cortical parcellation using repeated k-means clustering. Neuroimage 47:1666-1677.

Newman ME, Mark E. 2006. Modularity and community structure in networks. Proc Natl Acad Sci U S A 103:8577-8582.

Nieuwenhuys R. 2012. The insular cortex: a review. Prog Brain Res 195:123-163.

Ogawa S, Lee TM, Kay AR, Tank DW. 1990. Brain magnetic resonance imaging with contrast dependent on blood oxygenation. Proc Natl Acad Sci U S A 87:9868-9872.

Palaniyappan L, Simmonite M, White TP, Liddle EB, Liddle PF. 2013. Neural primacy of the salience processing system in schizophrenia. Neuron 79:814-828.

Paquola C, Seidlitz J, Benkarim O, Royer J, Klimes P, Bethlehem RAI, Larivière S, Vos de Wael R, Hall JA, Frauscher B et al. 2020. A cortical wiring space links cellular architecture, functional dynamics and hierarchies in humans. bioRxiv:2020.2001.2008.899583.

Paquola C, Vos De Wael R, Wagstyl K, Bethlehem RAI, Hong S-J, Seidlitz J, Bullmore ET, Evans AC, Misic B, Margulies DS et al. 2019. Microstructural and functional gradients are increasingly dissociated in transmodal cortices. PLOS Biology 17:e3000284.

Parkes L, Fulcher B, Yucel M, Fornito A. 2018. An evaluation of the efficacy, reliability, and sensitivity of motion correction strategies for resting-state functional MRI. Neuroimage 171:415-436.

Passingham RE, Stephan KE, Kotter R. 2002. The anatomical basis of functional localization in the cortex. Nat Rev Neurosci 3:606-616.

Pauling L, Coryell CD. 1936. The Magnetic Properties and Structure of Hemoglobin, Oxyhemoglobin and Carbonmonoxyhemoglobin. Proceedings of the National Academy of Sciences 22:210-216.

Penfield W, Boldrey E. 1937. SOMATIC MOTOR AND SENSORY REPRESENTATION IN THE CEREBRAL CORTEX OF MAN AS STUDIED BY ELECTRICAL STIMULATION1. Brain 60:389-443.

Power JD, Cohen AL, Nelson B, Wig GS, Barnes KA, Church JA, Vogel AC, Laumann T, Miezin FM, Schlaggar BL et al. 2011. Functional network organization of the human brain. 72:665-678.

Pruim RHR, Mennes M, Buitelaar JK, Beckmann CF. 2015a. Evaluation of ICA-AROMA and alternative strategies for motion artifact removal in resting state fMRI. NeuroImage 112:278-287.

Pruim RHR, Mennes M, van Rooij D, Llera A, Buitelaar JK, Beckmann CF. 2015b. ICA-AROMA: A robust ICA-based strategy for removing motion artifacts from fMRI data. NeuroImage 112:267-277.

Raichle ME. 1987. Circulatory and Metabolic Correlates of Brain Function in Normal Humans.: American Physiology Society

Rousseeuw PJ. 1987. Silhouettes: a graphical aid to the interpretation and validation of cluster analysis. Journal of computational and applied mathematics 20:53-65.

Roweis ST, Saul LK. 2000. Nonlinear Dimensionality Reduction by Locally Linear Embedding. Science 290:2323-2326.

Ryali S, Chen T, Padmanabhan A, Cai W, Menon V. 2015. Development and validation of consensus clustering-based framework for brain segmentation using resting fMRI. J Neurosci Methods 240:128-140.

Ryali S, Chen T, Supekar K, Menon V. 2013. A parcellation scheme based on von Mises-Fisher distributions and Markov random fields for segmenting brain regions using resting-state fMRI. Neuroimage 65:83-96.

Salehi M, Greene AS, Karbasi A, Shen X, Scheinost D, Constable RT. 2019. There is no single functional atlas even for a single individual: Functional parcel definitions change with task. NeuroImage:116366.

Salimi-Khorshidi G, Douaud G, Beckmann CF, Glasser MF, Griffanti L, Smith SM. 2014. Automatic denoising of functional MRI data: combining independent component analysis and hierarchical fusion of classifiers. Neuroimage 90:449-468.

Schaefer A, Kong R, Gordon EM, Laumann TO, Zuo XN, Holmes AJ, Eickhoff SB, Yeo BTT. 2018. Local-Global Parcellation of the Human Cerebral Cortex from Intrinsic Functional Connectivity MRI. Cereb Cortex 28:3095-3114.

Schleicher A, Amunts K, Geyer S, Kowalski T, Schormann T, Palomero-Gallagher N, Zilles K. 2000. A stereological approach to human cortical architecture: identification and delineation of cortical areas. J Chem Neuroanat 20:31-47.

Schleicher A, Palomero-Gallagher N, Morosan P, Eickhoff SB, Kowalski T, de Vos K, Amunts K, Zilles K. 2005. Quantitative architectural analysis: a new approach to cortical mapping. Anat Embryol (Berl) 210:373-386.

Schröder TN, Haak KV, Zaragoza Jimenez NI, Beckmann CF, Doeller CF. 2015. Functional topography of the human entorhinal cortex. eLife 4.

Segerdahl AR, Mezue M, Okell TW, Farrar JT, Tracey I. 2015. The dorsal posterior insula subserves a fundamental role in human pain. Nature Neuroscience 18:499.

Sepulcre J, Liu H, Talukdar T, Martincorena I, Yeo BTT, Buckner RL. 2010. The Organization of Local and Distant Functional Connectivity in the Human Brain. PLoS Comput Biol 6.

Sepulcre J, Sabuncu MR, Yeo TB, Liu H, Johnson KA. 2012. Stepwise Connectivity of the Modal Cortex Reveals the Multimodal Organization of the Human Brain. The Journal of Neuroscience 32:10649-10661.

Shen X, Tokoglu F, Papademetris X, Constable RT. 2013. Groupwise whole-brain parcellation from resting-state fMRI data for network node identification. Neuroimage 82:403-415.

Singer T, Critchley HD, Preuschoff K. 2009. A common role of insula in feelings, empathy and uncertainty. Trends Cogn Sci 13:334-340.

Skudlarski P, Jagannathan K, Calhoun VD, Hampson M, Skudlarska BA, Pearlson G. 2008. Measuring brain connectivity: diffusion tensor imaging validates resting state temporal correlations. Neuroimage 43:554-561.

Smith SM, Beckmann CF, Andersson J, Auerbach EJ, Bijsterbosch J, Douaud G, Duff E, Feinberg DA, Griffanti L, Harms MP et al. 2013. Resting-state fMRI in the Human Connectome Project. Neuroimage 80:144-168.

Stephani C, Fernandez-Baca Vaca G, Maciunas R, Koubeissi M, Luders HO. 2011. Functional neuroanatomy of the insular lobe. Brain Struct Funct 216:137-149.

Taylor P, Hobbs JN, Burroni J, Siegelmann HT. 2015. The global landscape of cognition: hierarchical aggregation as an organizational principle of human cortical networks and functions. Scientific Reports 5:18112.

Tenenbaum JB, de Silva V, Langford JC. 2000. A Global Geometric Framework for Nonlinear Dimensionality Reduction. Science 290:2319-2323.

Thulborn KR, Waterton JC, Matthews PM, Radda GK. 1982. Oxygenation dependence of the transverse relaxation time of water protons in whole blood at high field. Biochim Biophys Acta 714:265-270.

Tibshirani R, Walther G, Hastie T. 2001. Estimating the number of clusters in a data set via the gap statistic. Journal of the Royal Statistical Society: Series B (Statistical Methodology) 63:411-423.

Toga AW, Thompson PM, Mori S, Amunts K, Zilles K. 2006. Towards multimodal atlases of the human brain. Nat Rev Neurosci 7:952-966.

Tootell RB, Hadjikhani NK, Vanduffel W, Liu AK, Mendola JD, Sereno MI, Dale AM. 1998. Functional analysis of primary visual cortex (V1) in humans. Proc Natl Acad Sci U S A 95:811-817.

Uddin LQ. 2015. Salience processing and insular cortical function and dysfunction. Nat Rev Neurosci 16:55-61.

Uddin LQ, Kelly AM, Biswal BB, Castellanos FX, Milham MP. 2009. Functional connectivity of default mode network components: correlation, anticorrelation, and causality. Hum Brain Mapp 30:625-637.

Uddin LQ, Kinnison J, Pessoa L, Anderson ML. 2014. Beyond the tripartite cognition-emotion-interoception model of the human insular cortex. J Cogn Neurosci 26:16-27.

Uludağ K, Uğurbil K. 2015. Physiology and Physics of the fMRI Signal. In: Uludag K, Ugurbil K, Berliner L, editors. fMRI: From Nuclear Spins to Brain Functions Boston, MA: Springer US p 163-213.

van den Heuvel MP, Hulshoff Pol HE. 2010. Specific somatotopic organization of functional connections of the primary motor network during resting state. Hum Brain Mapp 31:631-644.

van den Heuvel MP, Scholtens LH, Feldman Barrett L, Hilgetag CC, de Reus MA. 2015. Bridging Cytoarchitectonics and Connectomics in Human Cerebral Cortex. The Journal of Neuroscience 35:13943-13948.

Van Dijk KR, Hedden T, Venkataraman A, Evans KC, Lazar SW, Buckner RL. 2010. Intrinsic functional connectivity as a tool for human connectomics: theory, properties, and optimization. J Neurophysiol 103:297-321.

Van Essen DC, Maunsell JH, Bixby JL. 1981. The middle temporal visual area in the macaque: myeloarchitecture, connections, functional properties and topographic organization. J Comp Neurol 199:293-326.

Van Essen DC, Smith SM, Barch DM, Behrens TEJ, Yacoub E, Ugurbil K. 2013. The WU-Minn Human Connectome Project: An overview. NeuroImage 80:62-79.

Vercelli U, Diano M, Costa T, Nani A, Duca S, Geminiani G, Vercelli A, Cauda F. 2016. Node Detection Using High-Dimensional Fuzzy Parcellation Applied to the Insular Cortex. Neural Plast 2016:1938292.

Vincent JL, Patel GH, Fox MD, Snyder AZ, Baker JT, Van Essen DC, Zempel JM, Snyder LH, Corbetta M, Raichle ME. 2007. Intrinsic functional architecture in the anaesthetized monkey brain. Nature 447:83-86.

Vogt C, Vogt O. 1919. Allgemeinere Ergebnisse unserer Hirnforschung (English Translation: Results of our brain research in a broader context). J Psychol Neurol 25:292-398.

Vogt O. 1910. Die myeloarchitektonische Felderung des menschlichen Stirnhirns. J Psychol Neurol XV:221-232.

Von Economo CF, Koskinas GN. 1925. Die Cytoarchitektonik der Hirnrinde des erwachsenen Menschen. Wien-Berlin: Julius Springer.

Vos de Wael R, Benkarim O, Paquola C, Lariviere S, Royer J, Tavakol S, Xu T, Hong S-J, Langs G, Valk S et al. 2020. BrainSpace: a toolbox for the analysis of macroscale gradients in neuroimaging and connectomics datasets. Communications Biology 3:103.

Wang C, Ji F, Hong Z, Poh JS, Krishnan R, Lee J, Rekhi G, Keefe RSE, Adcock RA, Wood SJ et al. 2016. Disrupted salience network functional connectivity and white-matter microstructure in persons at risk for psychosis: findings from the LYRIKS study. Psychological Medicine 46:2771-2783.

Wig GS, Laumann TO, Cohen AL, Power JD, Nelson SM, Glasser MF, Miezin FM, Snyder AZ, Schlaggar BL, Petersen SE. 2014a. Parcellating an individual subject's cortical and subcortical brain structures using snowball sampling of resting-state correlations. Cereb Cortex 24:2036-2054.

Wig GS, Laumann TO, Petersen SE. 2014b. An approach for parcellating human cortical areas using resting-state correlations. Neuroimage 93 Pt 2:276-291.

Winkler AM, Ridgway GR, Webster MA, Smith SM, Nichols TE. 2014. Permutation inference for the general linear model. NeuroImage 92:381-397.

Wotruba D, Michels L, Buechler R, Metzler S, Theodoridou A, Gerstenberg M, Walitza S, Kollias S, Rossler W, Heekeren K. 2014. Aberrant coupling within and across the default mode, task-positive, and salience network in subjects at risk for psychosis. Schizophr Bull 40:1095-1104.

Wree A, Schleicher A, Zilles K. 1982. Estimation of volume fractions in nervous tissue with an image analyzer. J Neurosci Methods 6:29-43.

Xue G, Lu Z, Levin IP, Bechara A. 2010. The Impact of Prior Risk Experiences on Subsequent Risky Decision-Making: The Role of the Insula. Neuroimage 50:709-716.

Yamada T, Itahashi T, Nakamura M, Watanabe H, Kuroda M, Ohta H, Kanai C, Kato N, Hashimoto RI. 2016. Altered functional organization within the insular cortex in adult males with high-functioning autism spectrum disorder: evidence from connectivity-based parcellation. Mol Autism 7:41.

Ye AQ, Ajilore OA, Conte G, GadElkarim J, Thomas-Ramos G, Zhan L, Yang S, Kumar A, Magin RL, G. Forbes A et al. 2015. The intrinsic geometry of the human brain connectome. Brain Informatics 2:197-210.

Yeo BT, Krienen FM, Sepulcre J, Sabuncu MR, Lashkari D, Hollinshead M, Roffman JL, Smoller JW, Zollei L, Polimeni JR et al. 2011. The organization of the human cerebral cortex estimated by intrinsic functional connectivity. J Neurophysiol 106:1125-1165.

Zalesky A, Fornito A, Bullmore ET. 2010. Network-based statistic: identifying differences in brain networks. Neuroimage 53:1197-1207.

Zalesky A, Fornito A, Cocchi L, Gollo LL, van den Heuvel MP, Breakspear M. 2016. Connectome sensitivity or specificity: which is more important? Neuroimage 142:407-420.

Zilles K, Palomero-Gallagher N. 2001. Cyto-, Myelo-, and Receptor Architectonics of the Human Parietal Cortex. NeuroImage 14:S8-S20.

Zilles K, Palomero-Gallagher N, Grefkes C, Scheperjans F, Boy C, Amunts K, Schleicher A. 2002. Architectonics of the human cerebral cortex and transmitter receptor fingerprints: reconciling functional neuroanatomy and neurochemistry. Eur Neuropsychopharmacol 12:587-599.

CHAPTER 3

CHARACTERIZING THE FUNCTIONAL CONNECTIVITY DIVERSITY OF THE INSULA CORTEX

NeuroImage 183 (2018) 716–733

Contents lists available at ScienceDirect

NeuroImage

journal homepage: www.elsevier.com/locate/neuroimage

Characterizing the functional connectivity diversity of the insula cortex: Subregions, diversity curves and behavior

Ye Tian [a,*], Andrew Zalesky [a,b]

[a] Melbourne Neuropsychiatry Centre, Department of Psychiatry, The University of Melbourne and Melbourne Health, Carlton South, VIC, Australia
[b] Department of Biomedical Engineering, The University of Melbourne, Parkville, VIC, Australia

ARTICLE INFO

Keywords:
Behavior
Clustering
Diversity
Insula
Parcellation
Resting-state fMRI

ABSTRACT

The connectivity of the insula cortex is diverse. We present new models to characterize the resting-state connectional diversity of the human insula cortex and perform model selection using high-quality fMRI data from the Human Connectome Project. We first attempt to parcellate the insula into distinct subregions using traditional clustering methods, but find that the resulting subregions are not homogeneous and that the optimal number of subregions is substantially influenced by data smoothness. We then introduce the concept of a diversity curve, which we use to continuously parameterize the insula's Laplacian eigenmap with respect to streamlines propagated through the eigenmap's gradient field. To perform model selection, we compare the insula's diversity curve to benchmark diversity curves for: i) two distinct regions; ii) a continuum of gradual change; and, iii) an absence of any connectional diversity (i.e. homogenous region). Of the three benchmarks tested, we find that the insula's connectional diversity is most parsimoniously modeled as continuum of gradual change, from dorsal-posterior to ventral-anterior. We find that individuals who score high on measures of positive affect, self-efficacy, emotion recognition, motor dexterity and gustation show greater diversity within the anterior insula. Our findings are replicated using data from a second fMRI session. We conclude that the functional connectivity diversity of the insula can be characterized parsimoniously as a continuum, avoiding the vexed task of determining an optimal number of insula subregions, and that inter-individual variation in this continuum can explain significant variation in behavior.

1. Introduction

The insula cortex is a heterogeneously connected cerebral lobe, having abundant cortical and subcortical reciprocal connections that receive interoceptive and exteroceptive sensory information (Mufson et al. 1981, 1997; Mufson and Mesulam, 1982; Mesulam and Mufson, 1985; Augustine, 1996). The rich diversity of the insula's connectional architecture is consistent with the diverse range of functional roles that it is known to subserve, ranging from basic motor control and homeostasis, to the processing of interoception, self-awareness, perception, emotion and high-level cognitive function (Augustine, 1996; Craig, 2009; Mutschler et al., 2009; Singer et al., 2009; Kurth et al. 2010a, 2010b; Xue et al., 2010; Stephani et al., 2011; Uddin et al., 2014; Segerdahl et al., 2015).

These functions are thought to map onto distinct gyri and subregions of the insula. For example, functional neuroimaging studies associate activation of the anterior portion of the insula with viscerosensory functions such as gustation, nausea and abdominal sensation (Ostrowsky et al., 2000; Small et al., 2003; Stephani et al., 2011), as well as subjective emotions such as anger (Damasio et al., 2000), sexual arousal (Ortigue et al., 2007), disgust (Phillips et al., 1997), and empathy (Singer et al., 2004). Contrastingly, the posterior insula responds to somesthetic modalities such as temperature sensation, tingling and innocuous or painful cutaneous stimuli (Schneider et al., 1993; Davis et al., 1998; Ostrowsky et al., 2000; Singer et al., 2004; Stephani et al., 2011). This putative anterior-posterior differentiation of insula function is supported by histological and axonal tract-tracing studies of the macaque insula cortex undertaken decades ago, which report that cytoarchitectural organization and axonal connectivity differ topographically along an anterior-posterior insula gradient (Mufson et al., 1981; Mesulam and Mufson 1982, 1985; Mufson and Mesulam, 1982).

More recently, magnetic resonance imaging (MRI) has been used to investigate the macroscale connectional topography of the human insula *in vivo*. Early studies mapped functional (Taylor et al., 2009; Cauda et al.,

* Corresponding author. Melbourne Neuropsychiatry Centre, Level 3, Alan Gilbert Building 161 Barry Street, Carlton South, VIC, 3053, Australia.
E-mail address: yetianmed@gmail.com (Y. Tian).

https://doi.org/10.1016/j.neuroimage.2018.08.055
Received 6 August 2018; Accepted 23 August 2018
Available online 29 August 2018
1053-8119/© 2018 Elsevier Inc. All rights reserved.

2011; Ebisch et al., 2011; Touroutoglou et al., 2012; Baur et al., 2013; Wiech et al., 2014; Zhao et al., 2017) and structural connectivity (Cloutman et al., 2012; Wiech et al., 2014; Ghaziri et al., 2017) of putative insula subregions defined *a priori*. These studies found that the anterior insula forms part of an emotional salience and cognitive control network (Cole and Schneider, 2007; Seeley et al., 2007; Uddin, 2015), while the posterior insula predominantly connects to the parietal and posterior temporal cortices. Rather than delineating subregions *a priori*, recent studies have instead used data-driven segmentation and clustering algorithms to segment, or *parcellate*, the insula into subregions. Specifically, functional or structural connectivity is first mapped between each insula voxel and all other gray matter voxels, yielding a voxel-to-whole-brain connectivity map for each insula voxel. Cluster analysis is then used to cluster insula voxels that share similar connectivity maps and connect with similar cortical and subcortical areas. Each cluster is assumed to delineate a putative insula subregion. Many studies parcellating the insula in this way have found that bipartite subdivisions comprising anterior and posterior subregions provide the most parsimonious model of insula connectional diversity (Nanetti et al., 2009; Cauda et al. 2011, 2012; Jakab et al., 2012; Kelly et al., 2012; Alcauter et al., 2015). However, other studies report tripartite subdivisions in which the anterior insula is further subdivided into dorsal and ventral components (Deen et al., 2011; Chang et al., 2013; Moran et al., 2013; Ryali et al., 2015), as well as a mosaic of subdivisions comprising more than three subregions (Mutschler et al., 2009; Kurth et al., 2010b; Nelson et al., 2010; Power, 2011; Yeo et al., 2011; Kelly et al., 2012; Ryali et al., 2013; Glasser et al., 2016; Nomi et al., 2016; Vercelli et al., 2016; Yamada et al., 2016). Table 1 catalogues these previous studies and exemplifies the discordance in the number of subregions reported. The number of putative clusters comprising the insula cortex thus remains disputed (Cauda and Vercelli, 2013).

Using cluster analysis to segregate the insula into distinct subregions based on connectivity inferred from MRI is predicated on three key assumptions: (i) the connectional architecture of the insula is topographically diverse; (ii) this diversity is inherently segregated into distinct clusters (subregions); (iii) connectivity maps inferred from functional or diffusion MRI (tractography) provide sufficient fidelity to differentiate these clusters. The first assumption is perhaps beyond doubt, given that the cytoarchitecture, and connectivity patterns of afferent and efferent nerves of the macaque insula are known to be heterogeneous and topographically diverse (Mufson et al., 1981; Mesulam and Mufson, 1982; Mufson and Mesulam, 1982). However, the remaining two assumptions warrant scrutiny. As remarked by Cerliani et al. (2012), macaque studies suggest that insula cytoarchitecture and connectivity vary *gradually* and *continuously*, arranged topographically along a rostrocaudal axis, with the agranular and granular insula portions separated by a transitional dysgranular zone (Mesulam and Mufson, 1982; Mufson and Mesulam, 1982; Friedman et al., 1986). Quoting from Brodmann (1909), Cerliani and colleagues reiterate that, "*there are great difficulties in dividing [the insula] into individual fields.*"

Given Brodmann's observations and the discordance in the number of insula subregions evident between previous studies, we hypothesized that topographic heterogeneity in macroscale insula connectivity may be parsimoniously modeled as a continuum or gradient of gradual change (Huntenburg et al., 2018), rather than with discrete subregions. In this study, we aim to characterize the functional connectivity diversity of the insula using high-quality resting-state functional MRI acquired as part of the Human Connectome Project (HCP; Smith et al., 2013). We begin by clustering the insula into distinct subregions using well-known clustering methods and established criteria to choose the optimal number of clusters. However, we find that these criteria often perform poorly in identifying the correct number of clusters in insula-like synthetic data for which the precise number of clusters is known in advance. We therefore develop: i) novel measures to ascertain the optimal number of insula subregions; and, ii) a novel null model to test whether insula subregions are more clustered than expected due to chance. We find that insula subregions vary markedly in shape and number between individuals, often showing less homogeneity in functional connectivity than identically-sized patches of gray matter sampled randomly throughout the cortex.

Table 1
Parcellating the human insula cortex with functional and diffusion MRI.

Study[a]	Sample size	Modality	Smoothing (FWHM)	Clustering methodology	Criterion to determine optimal cluster number	Null model	Clusters (K)
Functional MRI							
Cauda et al., 2011	16	Resting-state FC	8 mm	Fuzzy c-means	Similarity index (Esposito et al., 2005)	No	2
				K-means	No	No	3
				Centroid linkage	No	No	2
Deen et al., 2011	30	Resting-state FC	No	K-means	No	No	3
Cauda et al., 2012	Meta-analysis	Task co-activation	NA	K-means	Silhouette criterion	No	2
				Ward's linkage	Cophenetic correlation distance (Sokal and Rohlf, 1962); Visual inspection	No	2
Kelly et al., 2012	355	Resting-state FC Task co-activation	6 mm	K-means	Variation of information (Meilă, 2007); Cross-models consistency	No	2, 9
Chang et al., 2013	18	Resting-state FC	5 mm	K-means	Validity indicator (Ray and Turi, 1999)	No	3
Moran et al., 2013	88	Resting-state FC	No[b]	K-means	No	No	3
Ryali et al., 2013	21	Resting-state voxel-wise time series	4 mm	VMF-MRF	Stability analysis (Monti et al., 2003) and evidence accumulation approach (Fred and Jain, 2005)	No	4
Alcauter et al., 2015	143	Resting-state FC	No	K-means	Validity indicator (Ray and Turi, 1999); Cross-subjects consistency	No	2
Ryali et al., 2015	21	Resting-state voxel-wise time series	6 mm	K-means &Hierarchical clustering	Probabilistic rand index (Carpineto and Romano, 2012)	No	3
Nomi et al., 2016	31	Resting-state FC	6 mm	ICA	No	No	4
Vercelli et al., 2016	38	Resting-state FC	8 mm	Fuzzy c-means	Silhouette criterion	No	12
Yamada et al., 2016	74	Resting-state FC	6 mm	Spectral-clustering	Variation of information; Mutual information (Meilă, 2007)	No	8
Diffusion MRI							
Nanetti et al., 2009	10	Tractography	NA	K-means	No	No	2
Jakab et al., 2012	40	Tractography	NA	K-means	No	No	2
Cerliani et al., 2012	10	Tractography	NA	Laplacian eigenmap	NA	NA	Gradual[c]

FC: functional connectivity; VMF-MRF: von Mises-Fisher distribution and Markov random fields.
[a] Whole-brain parcellation studies not listed (Power, 2011; Yeo et al., 2011; Glasser et al., 2016; Gordon et al., 2016).
[b] Images were resampled from 1 mm^3 to 3 mm^3 voxel resolution, resulting in implicit smoothing due to resampling.
[c] Variation in structural connectivity across the insula was deemed gradual, without distinct transitions between putative subregions.

Given the shortcomings of parcellating the insula into distinct subregions identified in the first part of this study, we propose the concept of a diversity curve to represent the insula's functional connectivity diversity as a continuum. Diversity curves provide a simple and intuitive method to parameterize Laplacian eigenmaps (Cerliani et al., 2012; Schröder et al., 2015; Haak et al., 2018) and their spatial gradients (Cohen et al., 2008; Gordon et al., 2016), and thereby enabled explicit comparison of competing models of the insula's connectional diversity. We aim to compare the insula's diversity curve with benchmark diversity curves inferred from: i) data that is known to comprise distinct subregions (i.e. insula and putamen combined); ii) data that is consistent with a continuum of gradual change in connectivity; and, iii) data that is known to be absent of any connectional diversity (i.e. homogeneous region). Finally, we aim to test whether our continuum model of the insula's connectional diversity can explain variation between individuals in behavioral measures relating to cognition, emotion, and sensorimotor processing. While we present several lines of evidence suggesting that the insula's functional connectivity diversity can be parsimoniously characterized as a continuum, it is important to remark that our study is limited to a single neuroimaging modality (resting-state functional MRI) and as such does not necessarily generalize to task-based functional connectivity (Vogt et al., 2016), anatomical connectivity (Cerliani et al., 2012), anatomical structure (Faillenot et al., 2017) and other modalities (Glasser et al., 2016).

2. Materials and methods

2.1. Participants, image acquisition and image preprocessing

2.1.1. Participants

Behavioral measures and resting-state functional MRI (fMRI) data were sourced from the Human Connectome Project (HCP) for 100 healthy, young adults (50 females; age range: 22–35 years). Individuals were selected at random from the HCP database before study commencement to yield a sample with a 1:1 sex ratio.

2.1.2. Behavioral measures

Before study commencement, measures that tapped functional domains known to be subserved by the insula were selected from a broad catalogue of behavioral measures. Measures were selected to assess cognition, emotion, somatosensory and viscerosensory processing. For psychological tests with multiple correlated outcomes, only the total or subtotal scores were selected. For measures with both raw and age-adjusted scores, only the age-adjusted scores were selected. Finally, measures with missing data were excluded, resulting in 59 measures for each participant (Supplementary Table S1).

2.1.3. Image acquisition

Acquisition of resting-state fMRI is described in detail elsewhere (Smith et al., 2013). In brief, participants completed four resting-state fMRI sessions, where 14min and 33s of resting-state fMRI was acquired in each session using a multiband acquisition (TR: 720 ms, voxel dimension: 2 mm isotropic). Data acquired in the first two sessions were used in this study: the first session (left-to-right phase encoding) was the primary dataset, while the second session (right-to-left) was used to assess replicability (within-subject).

2.1.4. Resting-state fMRI data preprocessing

Minimally processed resting-state fMRI data was sourced from the HCP. The minimal processing pipeline is described in detail elsewhere (Glasser et al., 2013) and includes head motion correction with ICA + FIX (Griffanti et al., 2014), which removes more than 99% of the artefactual ICA components (Salimi-Khorshidi et al., 2014). The pipeline also includes spatial artefact/distortion removal and alignment to MNI (Montreal Neurological Institute) standard space. Additional temporal filtering and nuisance regression were not performed. The artefactual ICA components removed with ICA + FIX account for the noise components corrected with traditional nuisance regression (e.g. motion artefacts, non-neuronal physiological noise and scanner artefacts). In addition to the minimal preprocessing pipeline, unless specified otherwise, images were spatially smoothed with a Gaussian smoothing kernel of 4 mm FWHM (full width at half maximum). In ancillary analyses, a smoothing kernel of 1.5 mm FWHM was investigated.

2.2. PART I: cluster analysis and discrete subregions

Clustering methodology

Binary insula masks were delineated based on the Harvard-Oxford Cortical Structural Atlas (https://fsl.fmrib.ox.ac.uk/fsl/fslwiki/Atlases) using a probability threshold of 40%, resulting in 798 voxels (6.38 cm^3) for right insula and 795 voxels (6.36 cm^3) for left insula. These masks were slightly smaller than previous studies (Cauda et al., 2011; Deen et al., 2011; Chang et al., 2013), with the aim of minimizing contamination from white matter and cerebrospinal fluid signals due to partial volume effects. The MNI152 standard gray matter atlas was thresholded at 42% to yield a gray matter mask comprising $M = 164{,}615$ voxels (1316 cm^3), which included the cerebellum, midbrain and pons. The preprocessed fMRI signal at each insula voxel was correlated (Pearson correlation) with all gray matter voxels, resulting in a connectivity matrix of dimension $N \times M$, where N denotes the number of insula voxels and M denotes the number of gray matter voxels. Each row of this connectivity matrix provided a connectional fingerprint (Finn et al., 2015) of a small portion (voxel) of the insula. Correlation coefficients were r-to-z transformed (Fisher transformation). Principal component analysis (PCA) was then applied to the z-transformed connectivity matrix to reduce its dimensionality and increase the signal-to-noise ratio. For all individuals, 5 principal components were sufficient to explain more than 80% of the connectivity variance across insula voxels. The $N \times M$ connectivity matrix was thus reduced to a matrix of dimension $N \times 5$ with PCA. Including additional principal components had negligible impact. The Euclidean distance between all pairs of insula voxels was computed in this five-dimensional space, yielding a symmetric distance matrix of dimension $N \times N$. Ward's linkage was applied to this distance matrix to partition insula voxels into groups (subregions) that share similar connectivity patterns. We use K to denote the desired number of clusters. Constraints were not imposed to ensure spatial contiguity. Fig. 1A shows a schematic of the clustering methodology.

2.2.1. Optimal number of clusters

Parcellations ranging from 1 (no subregions) to 10 clusters were delineated. We used cluster evaluation criteria to determine the optimal number of clusters. Three established criteria were used: i) gap statistic (Tibshirani et al., 2001); ii) silhouette criterion (Rousseeuw, 1987); and, iii) Calinski-Harabasz criterion (Calinski and Harabasz, 1974). Further details about the three cluster evaluation criteria are provided in Supplementary Material S1.

Given that the optimal number of clusters was discordant between the three cluster evaluation criteria and varied markedly between individuals (Supplementary Table S2), we sought to evaluate the performance of these criteria using insula-like synthetic data for which the ground truth number of clusters was known in advance. Simulation of the insula-like synthetic data is described in Supplementary Material S2, while the performance evaluation results are presented in Supplementary Material S3 and Figure S2.

2.2.2. Group-level consensus parcellation

Having partitioned the insula into subregions for each individual, we next sought to combine these individual partitions to yield a representative group-level insula parcellation. To this end, a consensus matrix of dimension $N \times N$ was computed, where cell (i, j) stored the proportion of individuals for which insula voxels i and j comprised the same cluster. Newman's spectral community detection algorithm (Newman and Mark,

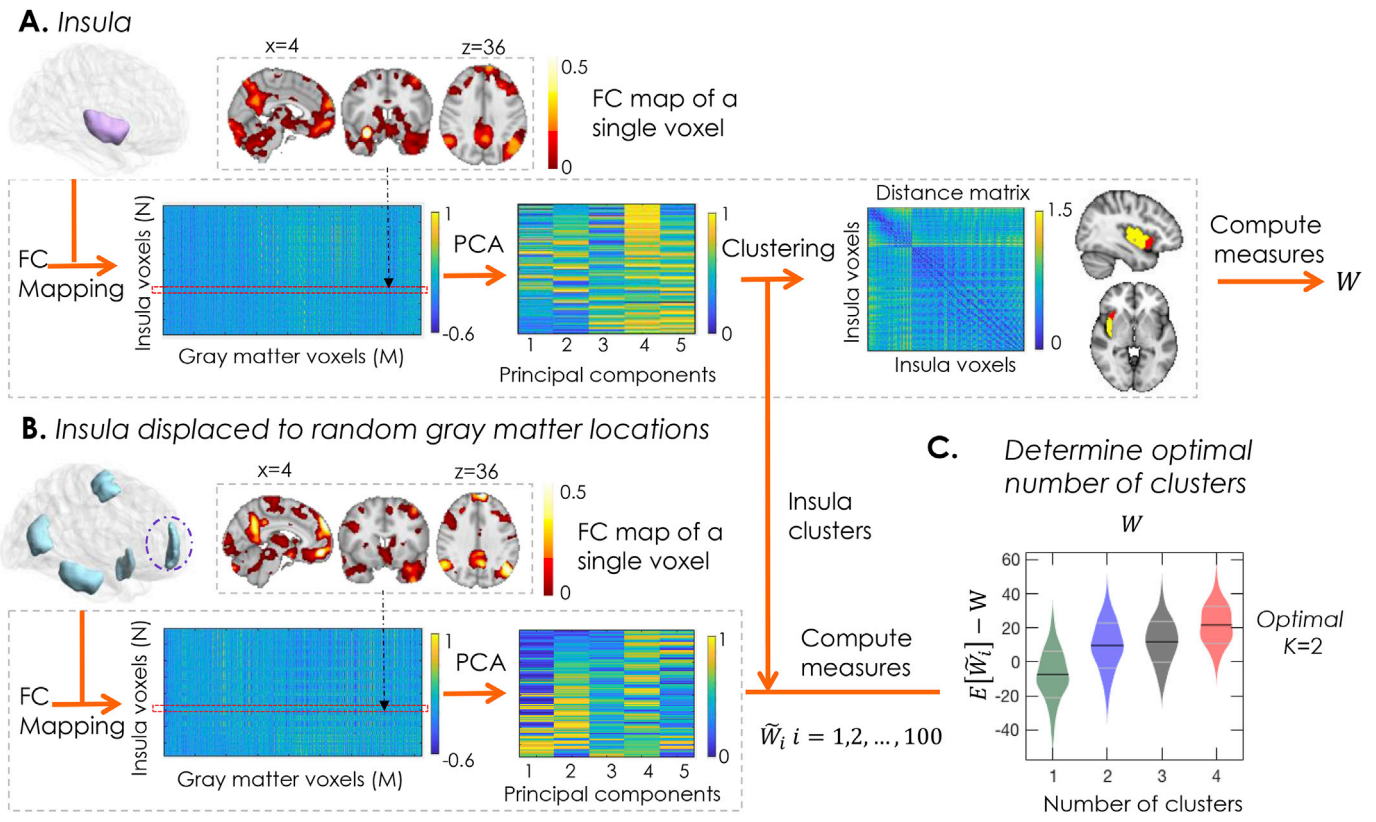


Fig. 1. Schematic of clustering methodology and null model. Panel A: The binary insula mask (purple) was delineated using the Harvard-Oxford Cortical Structural Atlas. The correlation in fMRI signals between each insula voxel and all gray matter voxels was computed, resulting in a connectivity matrix (insula voxels × gray matter voxels). The dashed red box indicates the connectional fingerprint for the illustrated voxel-to-whole-brain functional connectivity map. Principal component analysis (PCA) was applied to reduce the number of columns in the connectivity matrix to five and the Euclidean distance between all pairs of insula voxels was computed in this five-dimensional space, resulting in a distance matrix (insula voxels × insula voxels). Ward's linkage was applied to the distance matrix to cluster insula voxels with similar connectional fingerprints, and thus parcellate the insula into putative subregions. The bipartite cluster solution shown in Panel **A** is for a representative individual and can be seen to subdivide the right insula into anterior (red) and posterior (yellow) subregions. Cluster evaluation measures (W) were computed to assess the quality of cluster separation and determine the optimal number of clusters. **Panel B:** Null data consistent with the null hypothesis of an absence of any insula subregions (clusters) were generated by randomly displacing and/or rotating the insula mask to $T = 100$ new gray matter locations. Five such randomly displaced insula masks are shown (blue). For each displaced insula, a connectivity matrix was mapped using the fMRI data sampled from the new gray matter location. The same steps shown in Panel **A** were then performed on the connectivity matrix for each randomly displaced insula. However, rather than computing a new cluster solution for each displaced insula, the cluster solution for the true insula (Panel **A**) was imposed on each displaced insula, as emphasized by the vertical arrow (orange) from Panels **A** to **B**. Computing the cluster evaluation measures for each displaced insula yielded 100 samples from the null distribution of these measures, denoted $\tilde{W}(t),\ t = 1, 2, \ldots, T$. **Panel C:** Violin plot showing the distribution of gap values $\tilde{W}_K(t) - W_{K_{t=1,\ldots,T}}$ for cluster solutions comprising $K = 1$, 2, 3 and 4 clusters, where the mean gap value, $gap_K = \sum_{t=1}^{T} \tilde{W}_K(t)/T - W_K$, is indicated with a solid black line and the gray lines indicate confidence intervals (±1 standard error). The bipartite parcellation was deemed optimal because the gap value for $K = 3$ is within the confidence interval of the gap value for $K = 2$ (Tibshirani et al., 2001).

2006; Newman, 2013) was used to delineate modules in this consensus matrix, where modules delineated insula subregions that were representative of the group. The modularity Q score was used to quantify the extent to which the consensus matrix was modular (Clauset et al., 2004; Newman and Mark, 2006). The modularity resolution parameter (γ) was kept at its default value of 1, which is the most commonly used value and leads to a natural partition (Reichardt and Bornholdt, 2006). This resolution parameter value always resulted in the same number of modules as the number of insula clusters in the data that was provided as input to the modularity detection algorithm. Values of Q range between −0.5 and 1. Higher Q scores provide stronger evidence of modular structure. Under the null hypothesis of absence of any modular structure, it can be shown that $Q = 0$ when $\gamma = 1$ (Supplementary Material S4). Therefore, Q scores substantially exceeding 0 were taken as evidence of modular structure. The presence of modular structure indicated that the shape and location of insula clusters were consistent across individuals, thus warranting the construction of a representative group-level parcellation. In contrast, if the consensus matrix was not modular ($Q \approx 0$), variation in the shape and location of insula clusters across individuals was considered too extensive to warrant construction of a meaningful group-level parcellation.

2.3. Cluster evaluation and null model

We found that several of the classic criteria for evaluating the optimal number of clusters in cluster analyses may be prone to shortcomings when applied to parcellate the insula based on functional connectivity inferred from fMRI data. In particular, the silhouette and Calinski-Harabasz criteria performed poorly when applied to insula-like synthetic data for which the ground truth number of clusters was known (Supplementary Material S3 & Figure S2). In contrast, while the gap statistic performed well on the synthetic data, it suggested that the insula comprised 8 or more subregions in the majority of individuals (Supplementary Table S2), which is unexpectedly high compared to previous studies (Table 1). Furthermore, given that the null model inherent to the gap statistic did not necessarily preserve the spatial smoothness of the empirical fMRI data, we were cautious about drawing inferences based exclusively on the gap statistic. Using null data that did not preserve the

smoothness of the fMRI data could have resulted in overestimation of the true number of insula clusters because smoothed data is inherently more clustered than unsmoothed data. These shortcomings motivated us to develop novel cluster evaluation criteria and an fMRI-specific null model. More specifically, we developed three cluster evaluation measures: i) the intra-cluster distance, W; ii) the normalized intra-to-inter cluster distance, W^{norm}; and iii) the difference between the inter- and intra-cluster distances, W^{diff} (Supplementary Material S5). Our measures take into account both the inter- and intra-cluster distances and are benchmarked against fMRI-specific null data that preserves the smoothness of the fMRI data.

2.3.1. Null model

A null model was needed to generate null data to set expectations for the cluster evaluation measures under the null hypothesis of no insula clusters. We generated null data that was explicitly sampled from the fMRI data, thereby preserving spatial and temporal characteristics of the data, but annihilating any potential subregional structure that was specific to the insula. Conceptually, we followed the approach proposed by Gordon et al. (2016)) in which cortical regions were randomly repositioned across the cortical surface to generate null data. More specifically, the mask delineating the insula and its candidate subregions was displaced and/or rotated to a random location in gray matter, subject to the constraints that: i) the displaced/rotated mask remained entirely confined to gray matter; and, ii) the relative positions of clusters were preserved. This was achieved by uniformly sampling random displacement vectors and rotation matrices until the displaced and rotated insula mask resided entirely within gray matter. Crucially, displacing and rotating the parcellated insula to a random gray matter location ensured that the candidate subregions delineated for the true insula were unlikely to map onto any potential subregions at the random location. Therefore, the cluster evaluation measures (W, W^{norm} and W^{diff}) were evaluated with respect to the clusters identified in the true insula, but using the fMRI data from the voxels comprising the displaced insula. Functional connectivity mapping and PCA were performed using the fMRI data from the voxels comprising the displaced insula, but further clustering was not undertaken; rather, clusters defined for the true insula were imposed and used to compute the cluster evaluation measures. This process was repeated for $T = 100$ trials to generate an empirical null distribution for each cluster evaluation measure. For each trial, the true insula was randomly displaced to a new gray matter location. We use $\tilde{W}_K(t)$, $\tilde{W}_K^{norm}(t)$ and $\tilde{W}_K^{diff}(t)$ to denote the tth null sample for the cluster solution with K clusters. A schematic of our null model is shown in Fig. 1B, including an illustration of five randomly displaced insulae. The vertical arrow in Fig. 1 from Panel A to Panel B of this figure emphasizes that the cluster solution for the true insula (Panel A) was imposed on the displaced insula (Panel B) to compute null data.

2.3.2. Optimal number of clusters

The optimal number of clusters was determined based on a methodology that was conceptually the same as the gap statistic (Tibshirani et al., 2001). The gap value was computed as, $gap_K = \sum_{t=1}^{T} \tilde{W}_K(t)/T - W_K$, $K \geq 1$, which quantified the mean difference (gap) in the intra-cluster distance between the null data and true insula for the cluster solution with K clusters. The larger the gap, the more likely the cluster solution was not due to chance. The gap value was computed analogously for W^{norm} and W^{diff}, except that the range of K was limited to cluster solutions comprising more than one cluster for these measures. Based on previous recommendations (Yan and Ye, 2007; Mohajer et al., 2010), the logarithm of the W measures was not taken prior to computing gap values. Following the gap statistic, the optimal number of clusters was determined as the first value of K that satisfied, $gap_K \geq gap_{K+1} - se_{K+1}$, $K = 1, \ldots, K^{max} - 1$, where $se_K = \sigma_K\sqrt{1 + 1/T}$ and σ_K denotes the standard deviation across the T samples from the null distribution $\tilde{W}_K(t)$, $t = 1,\ldots,T$. If this inequality was not satisfied for any value of K, it was assumed that the insula either comprised K^{max} or more subregions, or that the insula could not be unequivocally parcellated into discrete subregions. In this study, we set K^{max} to 4. Given that most previous studies suggest that the insula comprises at most 3 subregions (Table 1), we assumed that the insula could not be unequivocally parcellated if the above inequality was not satisfied for $K = 2$ or 3. Therefore, if the above inequality was not satisfied for $K = 2$ or 3, we considered this case to be conceptually equivalent to the $K = 1$ case. Individuals were therefore assigned to one of three categories: i) no evidence of unequivocal insula subregions ($K = 1$ or $K \geq 4$); ii) two subregions ($K = 2$); or, iii) three subregions ($K = 3$). Our procedure to determine the optimal number of clusters was validated on insula-like synthetic data for W, W^{norm} and W^{diff} (Supplementary Material S6 & Figure S3).

2.3.3. Subregion homogeneity

Ideally, parcellation of the insula should yield subregions that are homogenous; namely, all voxels comprising a given insula cluster should share a common connectional fingerprint, otherwise the cluster may be considered too diverse to constitute a subregion. After parcellating the insula into discrete subregions (clusters), we sought to test whether each subregion was more homogeneous than expected under an appropriate null model. The homogeneity of each cluster $k = 1, \ldots, K$ was measured using the intra-cluster distance w_k (Supplementary Material S5). To set expectations for w_k under the null hypothesis of absence of cluster homogeneity, the intra-cluster distance was measured for clusters comprising each randomly displaced insula (see Null Model). When displacing and rotating the true insula to T random positions in gray matter, each insula cluster was also repositioned accordingly, and thus an empirical null distribution $\{\tilde{w}_k(t)\}_{t=1,\ldots,T}$ could be generated for each cluster $k = 1, \ldots, K$. The p-value for the null hypothesis of absence of homogeneity was given by the proportion of samples in the null distribution for which the intra-cluster distance was less than or equal to the intra-cluster distance for the actual insula clusters. Specifically, $p_k = 1/T\sum_{t=1}^{T} 1_{\tilde{w}_k(t) \leq w_k}$, where p_k denotes the p-value for insula cluster $k = 1, \ldots, K$. This was repeated independently for each individual. If $p_k < 0.05$, the kth insula subregion was considered homogenous.

2.4. PART II: diversity curves and continuum model

In the second part of this study, the diversity of functional connectivity across the topography of the insula was modeled as a continuum. This involved three steps: i) mapping the Laplacian eigenmap for each individual's insula; ii) inferring a curvilinear trajectory through the insula representing the trajectory of maximal change in the eigenmap; and, iii) projecting the Laplacian eigenmap for each individual onto the inferred trajectory of maximal change to yield a diversity curve. Diversity curves thus provided a one-dimensional parameterization of an individual's Laplacian eigenmap for the trajectory along which the insula's connectivity varied the most. The last two steps are novel to this study, while the first step follows well-established methods.

Step I - Mapping Laplacian Eigenmaps: Laplacian eigenmaps (Belkin and Niyogi, 2003) and associated eigendecomposition techniques have found utility in mapping continuous spatial patterns of variation in the cerebral cortex (Cerliani et al., 2012; Schröder et al., 2015; Margulies et al., 2016; Haak et al., 2018; Huntenburg et al., 2018). We followed the procedure described by Haak et al. (2018) to map Laplacian eigenmaps for each individual. In brief, the preprocessed fMRI signals were stacked together for all gray matter voxels to yield a matrix of dimension $T \times M$, where T denotes the number of time points and M denotes the number of gray matter voxels. PCA was used to reduce this to a full rank matrix of dimension $T \times (T - 1)$. The fMRI signal at each insula voxel was then correlated (Pearson correlation) with the PCA-transformed matrix, resulting in a connectivity

matrix of dimension $N \times (T-1)$, where N denotes the number of insula voxels. Correlation coefficients were r-to-z transformed (Fisher transformation). Each row of this matrix quantified the connectional fingerprint of a particular insula voxel in the PCA-transformed space. The η^2 coefficient of similarity was then used to measure the similarity in connectional fingerprints between each pair of insula voxels, yielding a symmetric similarity matrix of dimension $N \times N$. The similarity matrix was transformed into the adjacency matrix for a weighted graph in which each node represented an insula voxel. To describe this transformation, we denote the ith row of the similarity matrix with S_i and use S_{ij} to denote the similarity between insula voxels i and $j = 1, \ldots, N$. To define a sparse graph, the adjacency matrix, denoted W, was thresholded such that $W_{ij} = S_{ij}$ if $||S_i - S_j|| < d$, otherwise $W_{ij} = 0$, where the distance threshold, d, was chosen as small as possible, subject to the graph characterized by W comprising only one connected component (Haak et al., 2018). In practice, this resulted in graphs with connection densities of 1–3% across individuals. Finally, eigendecomposition was performed on the Laplacian matrix $L = D - W$, where D denotes the diagonal matrix of node strengths. The eigenvector with the second smallest eigenvalue, known as the Fiedler eigenvector, defined the Laplacian eigenmaps considered in this study. The eignmap was mapped to insula voxels in MNI space to enable three-dimensional visualization of the eigenmap and further image processing.

Step II - Inferring Trajectories of Maximal Change: A group-consensus eigenmap representing consensus across all individuals was computed by averaging the similarity matrices for all individuals and performing the above described eigendecomposition on the resulting group-averaged similarity matrix. The group-consensus eigenmap was then mapped to insula voxels in MNI space, resulting in a three-dimensional image. The Sobel gradient operator was then used to determine the directional gradients for each insula voxel in this image. Before gradient estimation, the image was dilated by one voxel to avoid estimation of spurious boundary gradients due to edge effects. The estimated gradient field is shown in Fig. 2A (lower panel), where each arrow indicates the gradient direction of a particular insula voxel. Streamlines were initiated from each insula voxel and propagated step-by-step in the direction of the local gradient by a step length of one tenth of a voxel. Propagation was terminated as soon as a streamline exceeded the insula mask. Each streamline provided a curvilinear trajectory through the insula, representing the trajectory of maximal change in the group-consensus eigenmap. Most

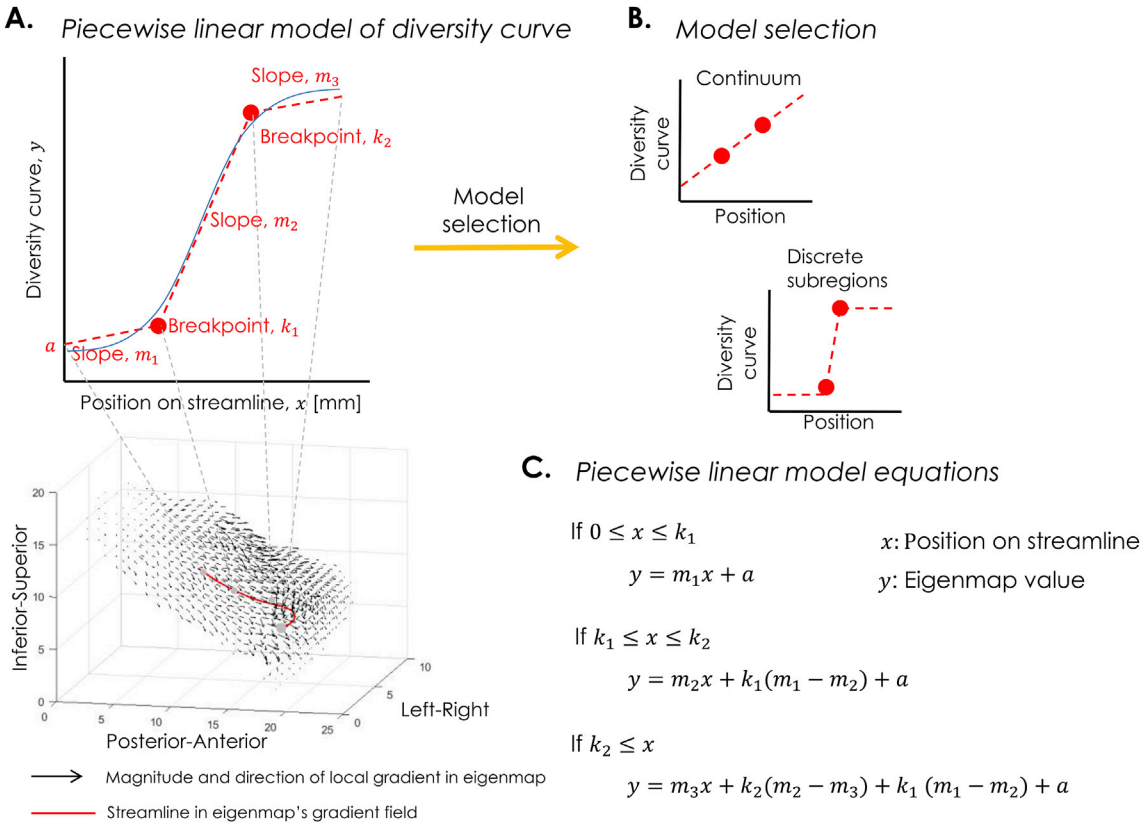


Fig. 2. Diversity curve, linear piecewise model and model selection. Panel A: Hypothetical diversity curve (blue curve) and piecewise linear fit (dashed red lines). Diversity curves were mapped by projecting the insula's Laplacian eigenmap (Fiedler eigenvector) from the three-dimensional space of the insula to the one-dimensional line parameterizing the curvilinear trajectory of maximal change in the eigenmap (red streamline, lower panel). This curvilinear trajectory was determined by propagating a streamline through the gradient field estimated from the eigenmap. Arrows indicate the gradient direction of each insula voxel and arrow lengths convey gradient magnitude. The gradient field shown (lower panel) was derived from the group-consensus eigenmap. The diversity curves shown are hypothetical and were not derived from empirical data. **Panel B:** Model selection was performed based on diversity curve shape and slope. Diversity curves with a relatively constant but non-zero slope (upper panel) indicated that connectional diversity was characterized by a continuum of gradual change. Diversity curves resembling a step function (lower panel) indicated a discrete transition between two putative subregions with distinct connectional profiles. Diversity curves with a near-zero gradient indicated an absence of connectional diversity (i.e. homogeneous region). **Panel C:** To formalize model selection, a piecewise linear function comprising two breakpoints (solid red circles) was fitted to each individual's diversity curve. Nonlinear least squares analysis was used to fit the six model parameters: two breakpoints (k_1 and k_2), three gradients (m_1, m_2 and m_3) and an intercept (a). Dashed lines indicate hypothetical model fits. Connectional diversity characterized by a continuum of change was indicated by approximate equality in the gradients of the three line segments ($m_1 \approx m_2 \approx m_3$), whereas a relatively steep gradient of the middle line segment (m_3) compared to the other two segments suggested a discrete transition between two putative subregions.

streamlines traversed only a small portion of the insula's spatial extent. These streamlines were discarded. The longest streamline (Fig. 2A, lower panel, red trajectory) provided the most comprehensive coverage of the insula's spatial extent and was chosen as the curvilinear trajectory onto which each individual's eigenmap was projected.

Step III - Diversity Curves: Diversity curves were computed by projecting the eigenmap for each individual (Step I) onto the curvilinear trajectory of maximal change (Step II). To this end, the point on the trajectory that was closest in Euclidean distance to the center of each insula voxel was determined. This defined a projection from the three-dimensional space of the insula to the one-dimensional line parameterizing the trajectory of maximal change. Diversity curves were mapped by applying this projection to each individual's eigenmap as well as the eigenmap's gradient magnitude. Diversity curves thus provided a parameterization of an individual's eigenmap (or its gradient magnitude) for the trajectory along which the insula's connectivity varied the most. Finally, diversity curves were spatially smoothed with a moving average filter. The span of the filter was commensurate to the voxel dimension (2 mm). A hypothetical diversity curve is shown in Fig. 2A (upper panel, blue curve). The dashed lines linking points on the diversity curve (upper panel) with points on the trajectory of maximum change (lower panel, red trajectory) emphasize the projection from the space of the insula to the curvilinear parameterization.

The gradient of the diversity curve provided insight into the topographic organization of the insula's connectional diversity and facilitated model selection. Diversity curves with a constant but non-zero gradient suggested that connectional diversity was characterized by a continuum of gradual change (Fig. 2B, upper panel). Abrupt changes in the diversity curve gradient suggested the location of putative boundaries between distinct subregions (Fig. 2B, lower panel). Stretches where the gradient was near-zero indicated a lack of connectional diversity (i.e. homogenous area).

Piecewise linear model

To formalize model selection, a piecewise linear function with two breakpoints was fitted to each individual's diversity curve. Two breakpoints were fitted, denoted k_1 and k_2, where $0 < k_1 < k_2 < L$ and L denotes the length of the curvilinear trajectory. The piecewise linear function thus comprised three line segments, with gradients denoted m_1, m_2 and m_3. Fig. 2A shows the piecewise linear function (red dashed lines) fitted to a hypothetical diversity curve (blue). Using two breakpoints provided sufficient flexibility to compare and select between the two hypothesized models of insula connectional diversity: i) continuum of gradual change, which was suggested by approximate equality in gradients of the three line segment (Fig. 2B, upper panel, $m_1 \approx m_2 \approx m_3$); and, ii) two discrete subregions, which was indicated by a steeper gradient of the middle line segment, relative to the first and last segments (lower panel, $|m_1| < |m_2|$ and $|m_3| < |m_2|$). In the case of two subregions, the first and last segments were assumed to characterize homogenous areas corresponding to the two putative subregions, whereas the middle segment characterized the transition between these two homogeneous areas. The gradient of the middle segment (m_2) was thus assumed to be larger than the other two segments (m_1 and m_3) because the middle segment spanned greater connectional variation per unit length. Using more than two breakpoints was not supported by the data. The equations defining the piecewise linear function used in this study are shown in Fig. 2C and comprise 6 parameters (3 gradients, 2 breakpoints and 1 intercept). The six model parameters were fitted to each individual's diversity curve using the Levenberg-Marquardt algorithm. The intraclass correlation coefficient (ICC; Bartko, 1966) was used to evaluate the replicability (within-subject) of the model parameters across the two fMRI sessions.

2.5. Diversity curve benchmarks

Diversity curves computed for the actual insula were compared to three benchmark diversity curves for which the topography of connectional diversity was known.

- ***Insula-Putamen Benchmark:*** Diversity curves were mapped for the insula and putamen combined, yielding prototype diversity curves for a known transition between two well-known regions. The trajectory of maximal change through the eigenmap for the insula-putamen was linear and oriented in a medial-lateral orientation. This trajectory was approximately equal in length to the insula's curvilinear trajectory (28 mm), and thus the dynamic range of eigenmap values per unit length was comparable between the insula and insula-putamen. The diversity curve for the insula-putamen provided a benchmark diversity curve for the case of two regions and was compared to the insula's diversity curve to test for evidence of insula subregions. The thin strip of gray matter (claustrum) and white matter (external capsule) separating the insula and putamen was excluded before computing diversity curves.
- ***Continuum Benchmark:*** Diversity curves were mapped for insula-shaped patches randomly distributed throughout gray matter, yielding prototype diversity curves for the case where connectional diversity varied as a continuum. Insula-shaped patches were generated by randomly displacing and/or rotating the insula mask and its curvilinear trajectory to new gray matter locations (see Null Model). Diversity curves were computed with respect to the fMRI data at these new locations. This was repeated for 100 randomizations and the resulting diversity curves were averaged and compared to the diversity curve for the actual insula. Because potential boundaries between subregions were not necessarily positioned consistently across the 100 insula-shaped patches, the *average* diversity curve was characterized by a constant gradient that represented the whole-brain average change in connectional diversity per unit length.
- ***Homogeneous Benchmark:*** Diversity curves were mapped after randomly permuting the spatial position of insula voxels, thereby annihilating any spatial structure in functional connectivity. This yielded prototype diversity curves for the absence of any connectional diversity. Diversity curves were computed by projecting the voxel-randomized fMRI data onto the curvilinear trajectory for the actual insula. This yielded diversity curves with zero gradient (horizontal lines), which were consistent with a homogeneous area with no diversity in functional connectivity across its topography. This process was repeated for 100 randomizations and the resulting diversity curves were averaged.

The three benchmarks were computed separately for each individual. Group-averaged diversity curves and confidence intervals were then determined for each benchmark.

2.6. Relating insula diversity and behavior

Canonical correlation analysis (CCA; Hotelling, 1936) was used to test whether individual variation in behavioral and personality traits was associated with the insula's functional connectivity diversity. CCA aims to identify multivariate associations between two groups of variables, such as between neuroimaging metrics and behavioral measures (Smith et al., 2015; Moser et al., 2017). In this study, one group of variables comprised 59 behavioral measures that tap functional domains known to be subserved by the insula (see Behavioral Measures), while the other group comprised the parameters characterizing the linear piecewise function fitted to each individual's diversity curve (see Piecewise Linear Model, Fig. 2C). The CCA was performed using: i) all six model parameters; and, ii) only the model parameters that were deemed most replicable across the two fMRI sessions (i.e. ICC >0.5). The slope of the first line segment (m_3) and the intercept term (a) were most replicable, and thus selected

for the latter (Supplementary Figure S6). Individuals with diversity curves for which the linear piecewise function was a poor fit (sum of squared errors > 0.005) were excluded from the CCA (8 individuals excluded; 4 females).

We use X to denote the $N \times P$ matrix of parameter estimates for the linear piecewise model (individuals × model parameters) and Y to denote the $N \times 59$ matrix of behavioral measures (individuals × behaviors). Each column of these two matrices was demeaned and normalized by its standard deviation. PCA was used to reduce the dimension of matrix Y to $N \times 40$, with the top 40 principal components explaining more than 90% of the variance across individuals. Matrices X and Y were then provided to the CCA function (*canoncorr*) available in *MATLAB*. The CCA function computed canonical coefficients to weight each behavioral measure and each model parameter. The weighted behavioral measures (PCA components) were then summed to yield a single canonical score for each individual with respect to matrix Y, and canonical scores were similarly computed for matrix X. The canonical coefficients (weights) were computed to maximize the correlation across individuals in the canonical scores. Further details about the CCA are provided in Supplementary Material S7.

Images were visualized using BrainNetViewer1.6 (Xia et al., 2013) and FslView software (https://fsl.fmrib.ox.ac.uk/fsl/fslwiki/FslView). Numerical computation was performed in MATLAB R2017b.

3. Results

In the first part of this study, we delineated discrete insula subregions (clusters) to parse the diversity of resting-state functional connectivity across this heterogeneous cerebral lobe in 100 young adults. We found that the minimum number of insula subregions required to parsimoniously characterize the insula's connectional diversity varied markedly between individuals and no consensus could be reached based on established cluster evaluation criteria for determining the optimal number of clusters (Supplementary Table S2). We therefore investigated the accuracy of these criteria for fMRI parcellation tasks and evaluated their performance on insula-like synthetic data for which the ground truth number of clusters was known. We found that some of the criteria performed poorly in this validation (Supplementary Figure S2), while others (gap statistic) were based on null data that did not preserve the spatial properties of fMRI data. To address these shortcomings in the present study, we developed novel criteria and fMRI-specific null data to determine the most parsimonious number of insula subregions, and proposed the concept of a diversity curve to model continuous topographic variation in functional connectivity across the insula. Diversity curves enabled principled model selection. In this section, results pertain to the right insula, unless laterality is explicitly indicated. For brevity, results pertaining to the left insula are only described in this section if a significant laterality effect was evident.

3.1. Insula subregions

Bipartite and tripartite insula parcellations were constructed by clustering insula voxels that shared similar connectional fingerprints. Group-level parcellations representing a consensus across all individuals were then determined with modularity analysis. Bipartite parcellation resulted in subdivision of the insula into ventral-anterior and dorsal-posterior subregions of approximately equal size (Fig. 3). While the consensus matrices (Fig. 3A) show evidence of moderate modular structure, as assessed with the modularity Q-score (right insula: 0.23; left: 0.22), the probabilistic maps in Fig. 3B suggest a rather gradual transition between the anterior and posterior subdivisions, without evidence of a distinct boundary.

Tripartite parcellation resulted in subdivision of the insula into ventral-anterior, dorsal-posterior and ventral-medial subregions (Supplementary Figure S4). Evidence of modular structure was weaker for the tripartite parcellations (Q-score right insula: 0.17; left: 0.18), suggesting that the boundaries separating these three subregions are either less well defined and/or vary more between individuals than the bipartite parcellation.

3.2. Optimal number of insula subregions

We sought to determine which of the two candidate parcellations—bipartite or tripartite—provided the most parsimonious model. For each individual, three cluster evaluation measures (W, W^{norm}, W^{diff}) were computed to determine the optimal number of insula subregions: bipartite ($K = 2$), tripartite ($K = 3$), or an absence of any clusters. An absence of clusters was declared when neither the bipartite nor the tripartite solution was optimal (i.e. $K = 1$ or $K \geq 4$; see Materials and Methods). While three cluster evaluation measures were considered, the optimal number of clusters suggested by the W^{norm} measure was given precedence, given that this measure outperformed the others when evaluated on insula-like synthetic data (Supplementary Figure S3).

The spatial smoothness of the fMRI data was found to influence the optimal number of insula subregions. The optimal number of clusters was therefore determined separately for moderate (FWHM: 4 mm; Fig. 4A, left panel) and minimal (FWHM: 1.5 mm; right) levels of spatial smoothing. With moderate smoothing (FWHM: 4 mm), the W^{norm} and W^{diff} measures suggested that a bipartite parcellation was optimal for the majority of individuals, although a tripartite solution was indicated for approximately 30% of individuals and neither of these parcellations was supported for 2–3% of individuals. In contrast, the W measure indicated no clusters for the majority of individuals (97%). With minimal smoothing (FWHM: 1.5 mm), the absence of any clusters was the optimal solution suggested by all three measures for the majority of individuals. Nevertheless, some individuals were optimally represented with bipartite (12%) and tripartite parcellations (3–11%; Fig. 4A, right panel). Fig. 4B shows gap values as a function of the number of candidate clusters (K) for representative individuals for which the optimal number of insula clusters was deemed to be $K = 2$ (leftmost plot), $K = 3$ (middle) and ambiguous ($K = 1$ or $K \geq 4$, rightmost). Of note, variation in the optimal number of clusters across individuals was not correlated with measures of intrascan head motion (absolute and relative RMS) ($p > 0.05$, Supplementary Table S3).

3.3. Homogeneity of insula subregions

A complementary measure of parcellation quality is the extent to which the voxels within each cluster are homogenous and share a common connectional fingerprint. Each subregion should not only be distinct from other subregions, but also show a homogenous functional connectivity pattern across its spatial extent. To investigate subregion homogeneity, we tested whether the connectional fingerprints of voxels comprising each subregion were more similar than null data.

Fig. 5A shows the proportion of individuals for which subregions comprising the bipartite and tripartite parcellations were homogeneous ($p < 0.05$). The homogeneity of the insula as a whole is also shown (leftmost bar). The insula as a whole was found to be homogeneous in only 5% of individuals, warranting efforts to characterize the insula's connectional diversity with simpler and more homogenous elements. However, characterizing this diversity with discrete subregions resulted in a relatively modest improvement in the homogeneity of the resulting subregions. The two subregions comprising the bipartite parcellation were homogeneous in less than 10–16% of individuals, while the tripartite parcellation resulted in subregions that were marginally more homogeneous (Fig. 5A).

In summary, while anatomically plausible bipartite and tripartite insula parcellations were mapped in the first part of this study, several potential challenges and shortcomings of representing the insula with discrete subregions became apparent: First, the optimal number of subregions was substantially influenced by the extent to which the fMRI data

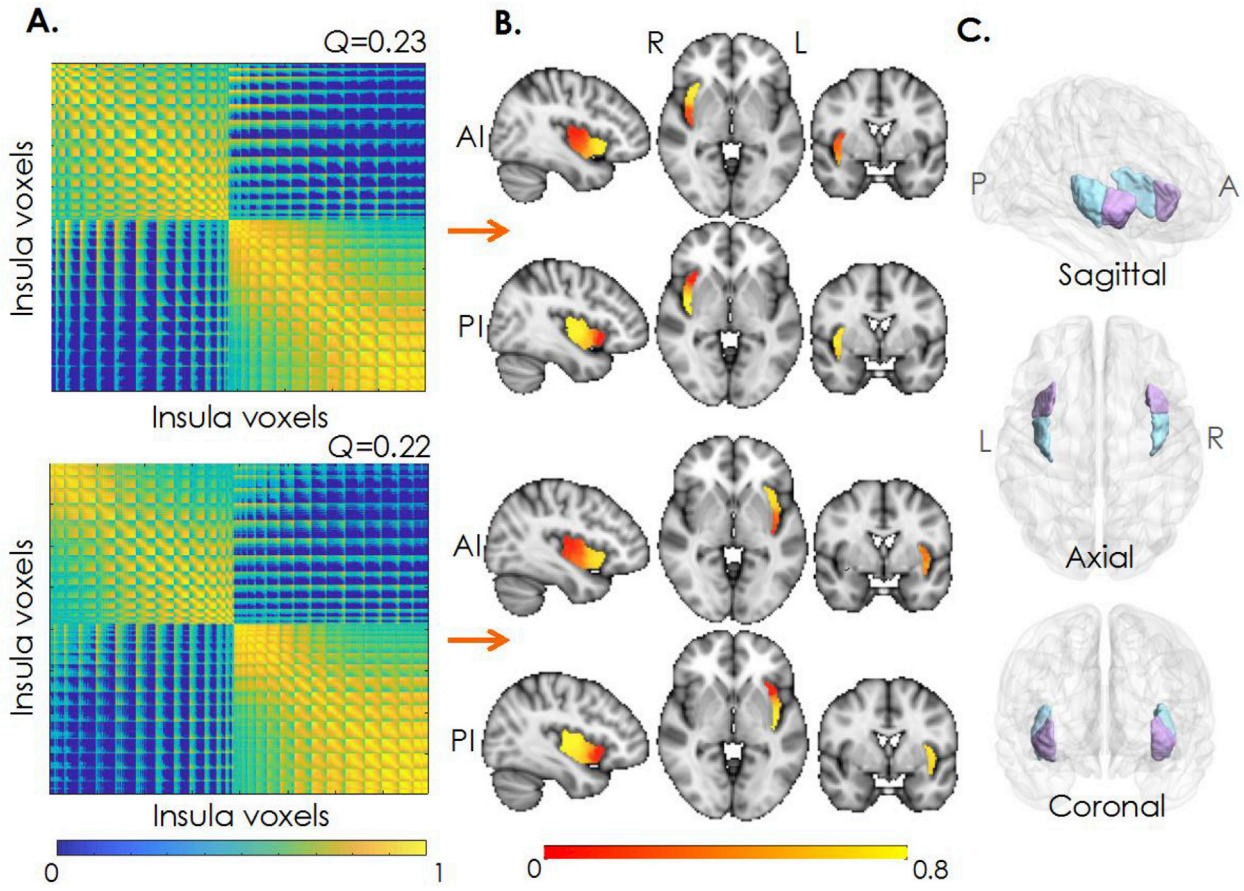


Fig. 3. Bipartite parcellation of the human insula cortex based on resting-state functional connectivity. **Panel A:** Group consensus matrices (insula voxels × insula voxels) for the right (upper matrix) and left insula (lower). Element (i, j) of the consensus matrix shows the proportion of 100 individuals for which insula voxels i and j comprise the same insula subregion. Warm tones (yellow) indicate pairs of voxels consistently comprising the same subregion, whereas cool tones (blue) indicate pairs of voxels consistently comprising distinct subregions. Both consensus matrices are modular ($Q = 0.23$, right insula; $Q = 0.22$, left) and comprise two distinct modules, which delineate insula subregions that represent a group consensus. The rows/columns of the consensus matrices are ordered such that all insula voxels comprising the anterior insula (AI) module are listed first, followed by all voxels in the posterior insula (PI). This ordering endows the consensus matrices with a distinct block structure that accentuates the modular structure. **Panel B:** The consensus matrices are mapped to the right (upper) and left (lower) insula to yield probabilistic maps of the AI and PI subregions. The color of each insula voxel is modulated by the proportion of individuals for which the voxel comprised the AI or PI subregion (module). Yellow tones indicate voxels that consistently comprise the AI or PI subregion across individuals, whereas red tones indicate voxels that rarely comprise the subregion. Slice coordinates (MNI152, mm): $x = 40$, $y = 6$, $z = -2$. **Panel C:** Probability maps converted to binary (hard) segmentations to delineate discrete AI (purple) and PI subregions (blue). Parcellations visualized sagittally, axially and coronally.

was smoothed and varied between individuals (Fig. 4A). Inter-individual variation in the number of optimal subregions might be explained by differences in brain anatomy, but the absence of entire anatomical subregions in otherwise healthy individuals is unlikely. Second, one of the goals of parcellation was to delineate subregions that were more homogeneous than the insula as whole with respect to diversity in functional connectivity. However, insula subregions were found not to be homogeneous in the majority of individuals when benchmarked against null data from random gray matter locations (Fig. 5A). These shortcomings warrant consideration of alternative models to characterize the insula's functional connectivity diversity. In the second part of this study, we consider one such alternative model and propose the concept of a diversity curve to model continuous topographic variation in functional connectivity across the insula.

3.4. Diversity curves and continuum model

Diversity curves were used to measure the extent of connectional diversity per unit length across the topography of the insula. Fig. 6A shows group-averaged diversity curves for the insula and insula-putamen benchmark. Diversity curves were mapped for the Fiedler eigenvector (blue curves) and the magnitude of its gradient (red curves). The insula's diversity curve is approximately linear, suggesting that the insula's connectional diversity is distributed uniformly across its spatial extent. In contrast, the diversity curve for the insula-putamen is step shaped. The insula-putamen serves as a benchmark diversity curve for the case of two distinct regions. The abrupt step corresponds to the boundary between the insula and putamen.

To formalize comparison with the insula-putamen benchmark, piecewise linear functions comprising three line segments were fitted to each of the diversity curves (dashed red lines). For the insula-putamen, the three line segments delineate the insula ($m_1 = 1.9 \times 10^{-4}$), insula-putamen boundary ($m_2 = 6.7 \times 10^{-3}$) and putamen ($m_3 = 8.2 \times 10^{-6}$) (m_2) of the middle line segment is orders of magnitude greater than the slope of the other two segments (i.e. $m_2/m_1 = 35$ and $m_2/m_3 = 808$), providing evidence of a clear distinction in the connectional profiles of the insula and putamen. Relative to this benchmark, the insula's diversity curve shows little evidence of an abrupt step that is comparable in slope to the insula-putamen boundary. For the insula, the three line segments share slopes that are of the same order of magnitude ($m_1 = 0.004$, $m_2 = 0.006$, $m_3 = 0.002$) and the slope of middle line segment is at most 3 times greater than the other line segments (i.e. $m_2/m_1 = 1.5$ and $m_2/m_3 = 3$). The insula's diversity curve is therefore not consistent with the benchmark diversity curve for two distinct regions. Nevertheless, it is

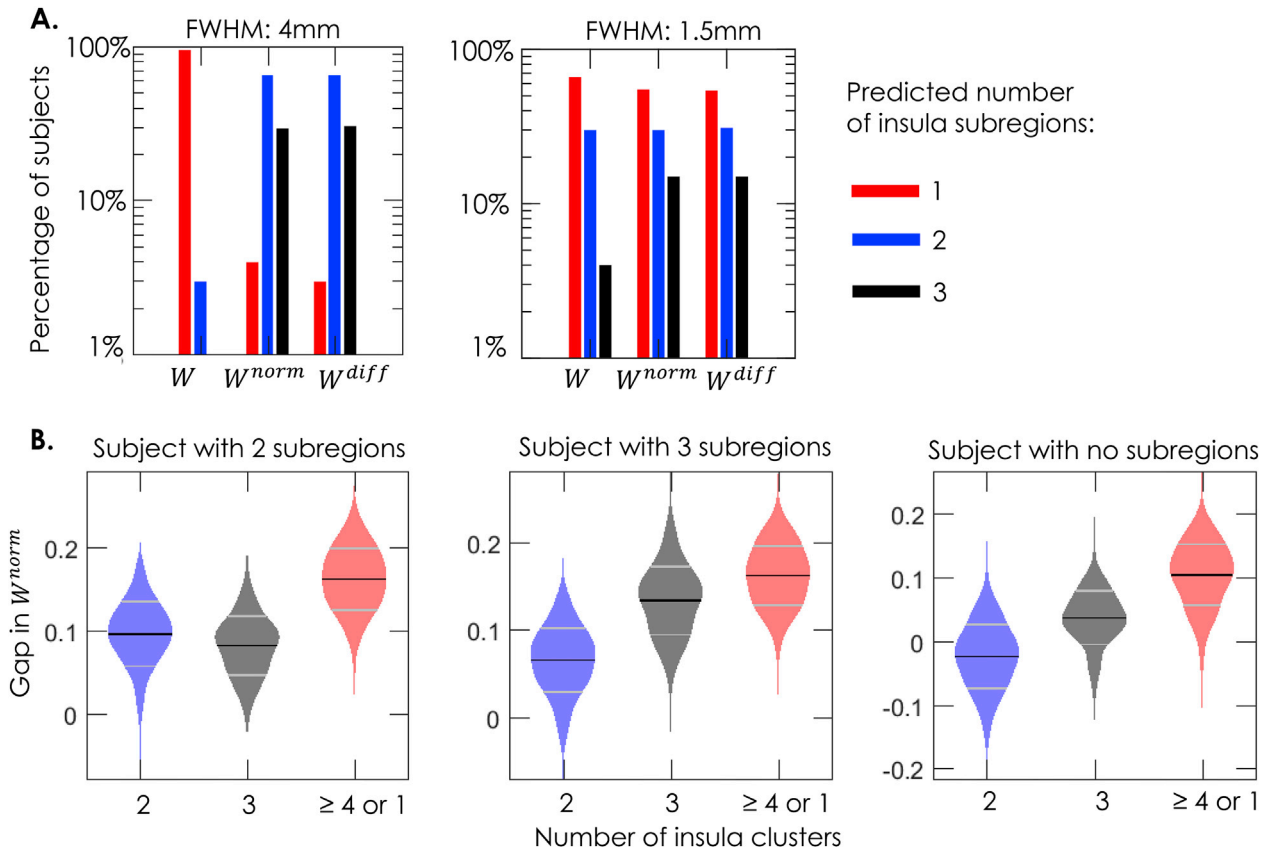


Fig. 4. Optimal number of insula subregions. Panel A: Bar plots show the percentage of individuals for which the right insula comprises 1 (red bar), 2 (blue) or 3 (black) subregions, as determined by three cluster evaluation measures (W, W^{norm}, W^{diff}). Separate bar plots are shown for moderate (FWHM: 4 mm, left) and minimal (1.5 mm, right) spatial smoothing of the fMRI data. The optimal number of insula subregions is influenced by smoothing and can be seen to vary markedly between individuals. **Panel B:** Violin plots showing the distribution of gap values for representative individuals with $K = 2$ (leftmost plot), 3 (middle) and ambiguous (rightmost) subregions. The mean gap value is indicated with a solid black line and the gray lines indicate confidence intervals (± 1 standard error). For the first individual (leftmost), the gap value for $K = 2$ is within the confidence interval of the gap value for $K = 3$, and thus moving from a bipartite to a tripartite solution is not supported. However, for the second individual (middle), the gap for $K = 2$ is below the confidence interval of the gap for $K = 3$, but the gap for $K = 3$ is within the confidence interval of the gap for $K = 3$, and thus a tripartite solution is deemed optimal. Finally, the gap values as a function of K for the third individual (rightmost) do not show an obvious elbow and the gap value for K is always below the confidence interval of the gap value for $K + 1$, and thus the optimal number of clusters is ambiguous ($K = 1$ or $K \geq 4$).

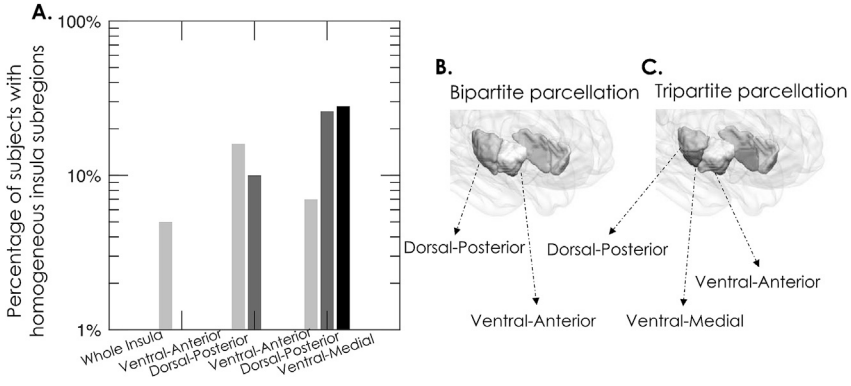


Fig. 5. Homogeneity of the insula and its subregions. Panel A: Proportion of individuals for which subregions comprising bipartite and tripartite insula parcellations were homogeneous ($p < 0.05$). The subregion of each individual was relabeled to either ventral-anterior, dorsal-posterior or ventral-medial according to the number of voxels in the individual subregion that overlapped with group-level bipartite (Panel **B**) or tripartite (Panel **C**) subdivisions. The homogeneity of the insula as a whole is also shown (leftmost bar). A subregion is considered homogeneous if its intra-cluster distance (w_k) does not exceed or equal the intra-cluster distance measured in more than 5% of null data samples drawn from random patches of gray matter. One of the goals of parcellation is to yield homogeneous subregions, however, it can be seen that both the bipartite and tripartite insula subregions are not homogeneous for the majority of individuals.

important to remark that while the insula's diversity curve is not step shaped to the same extent as the insula-putamen benchmark (i.e. insula: 3; insula-putamen: 808), the steepness of the insula's diversity curve increases slightly within a putative 'transition zone' between the anterior and posterior portions of the insula (Fig. 6A). The middle line segment comprising the piecewise linear function spans this transition zone, while the first and last segments span the anterior and posterior insula. Therefore, while the insula's diversity curve does not show evidence of a discrete transition between subregions, connectional variation per unit length increases marginally within an area straddling the anterior and posterior insula, possibly suggesting a putative transition zone.

Diversity curves for the gradient magnitude of the eigenmap were also mapped (Fig. 6A, red curves). The insula's gradient magnitude varies gradually compared to the insula-putamen benchmark, which shows a peak at the boundary between these regions. Fig. 6B shows projections of the group-consensus eigenmap to the voxels of the insula and insula-

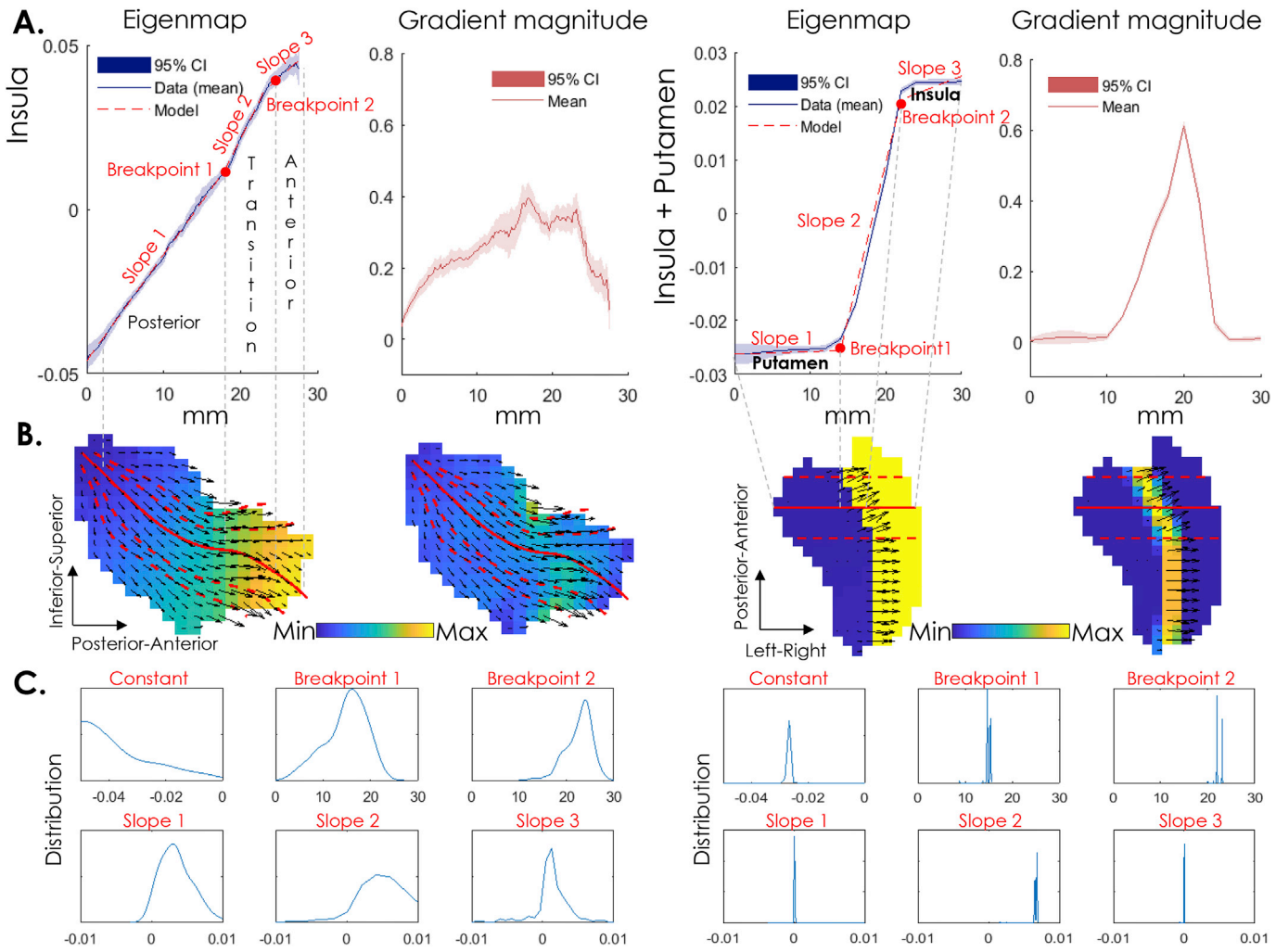


Fig. 6. Diversity curves for the insula cortex and insula-putamen combined. Panel A: Group-averaged diversity curves for the insula were compared to benchmark diversity curves for the case of two regions (insula-putamen combined). Diversity curves were mapped for the Fiedler eigenvector (blue curves) and the magnitude of its gradient (red curves). Diversity curves were modeled with piecewise linear functions (dashed red lines) comprising two breakpoints (solid red circles). The slope of the middle line segment of the insula's diversity curve is marginally (× 3) steeper than the other two segments, suggesting a gradual 'transition zone' between the anterior and posterior portions of the insula. However, the insula's diversity curve is not consistent with the step-shaped diversity curve of the insula-putamen benchmark, where the middle line segment is 35–808 times steeper than the other two segments. Shading denotes 95% confidence intervals (CI). **Panel B:** Eigenmap values were mapped to the voxels of the insula and insula-putamen to enable anatomical visualization of the eigenmaps. The dynamic range of eigenmap values is uniformly distributed across the spatial extent of the insula along a curvilinear gradient indicated by the streamlines (red lines). In contrast, the insula-putamen is characterized by a bimodal distribution of eigenmap values. The streamlines superposed onto the anatomical images represent trajectories of maximal change in the eignemaps. Streamlines were propagated in the gradient field estimated from the eigenmaps. Arrows indicate the gradient direction estimated for each voxel and arrow lengths convey gradient magnitude. Diversity curves were mapped with respect to the longest streamline (solid red line). **Panel C:** Distributions characterizing inter-individual variation in the model parameters describing the piecewise linear functions fitted to the diversity curves.

putamen in MNI space. These anatomical images show a gradual continuum of variation across the topography of the insula, from dorsal-posterior to ventral-anterior. In contrast, projecting the eigenmap of the insula-putamen into anatomical space yields an image with a sharp contrast between these two regions. Further anatomical images are shown in Supplementary Figure S5.

Fig. 6C shows distributions characterizing inter-individual variation in the model parameters describing the piecewise linear functions fitted to the diversity curves for each individual. Unlike the insula-putamen benchmark, substantial inter-individual variation is evident in the parameter estimates for the insula, which provides motivation for investigating whether this variation relates to inter-individual variation in behavior. The intercept term (a) and slope of the first line segment (m_1) show good within-subject replicability across fMRI sessions (ICC > 0.5), whereas the breakpoint locations (k_1 and k_2) show poor replicability (Supplementary Figure S6). This suggests that the spatial extent of the insula's putative transition zone cannot be reliably identified. For the insula-putamen, all model parameters show good within-subject replicability.

Given that the insula's diversity curve was not consistent with the benchmark diversity curve for two distinct regions (Fig. 6), to aid model selection, we investigated two alternative diversity curve benchmarks; namely, i) continuum of gradual change in connectional diversity; and ii) absence of connectional diversity (i.e. homogenous region). Diversity curves for the continuum benchmark were mapped for insula-shaped patches that were randomly distributed throughout the gray matter volume (Fig. 7A, left image), yielding prototype diversity curves for the case where connectional diversity varied as a gradual continuum. The average diversity curve for the continuum benchmark has a constant gradient (Fig. 7B, cyan line), and represents the average change in

connectional diversity per unit length across the cortex. Diversity curves for the homogeneous benchmark were mapped after randomly permuting the spatial position of insula voxels, thereby annihilating any spatial structure in functional connectivity. This yielded prototype diversity curves for the absence of any connectional diversity (Fig. 7B, black line). To enable comparison, Fig. 7B also shows diversity curves for the actual insula (blue line) as well as the insula-putamen benchmark (green line). Bar plots show the Euclidean distance between the insula diversity curves and each of the three benchmarks. The benchmark diversity curves mapped for the Fiedler eigenvectors (Fig. 7B, left axis) suggest that:

i) The insula is *not* a homogeneous region with respect to its functional connectivity, since the insula's diversity curve is markedly steeper than the homogeneous benchmark.
ii) The insula's connectional diversity does *not* appear to be characterized by discrete transitions between putative subregions, since the insula's diversity curve is not consistent with the step shape of the insula-putamen benchmark.
iii) Based on the three benchmarks investigated (insula-putamen, continuum and homogeneous), the insula's connectional diversity is most parsimoniously modeled as a continuum, since the insula's diversity curve shows the same characteristics as the continuum

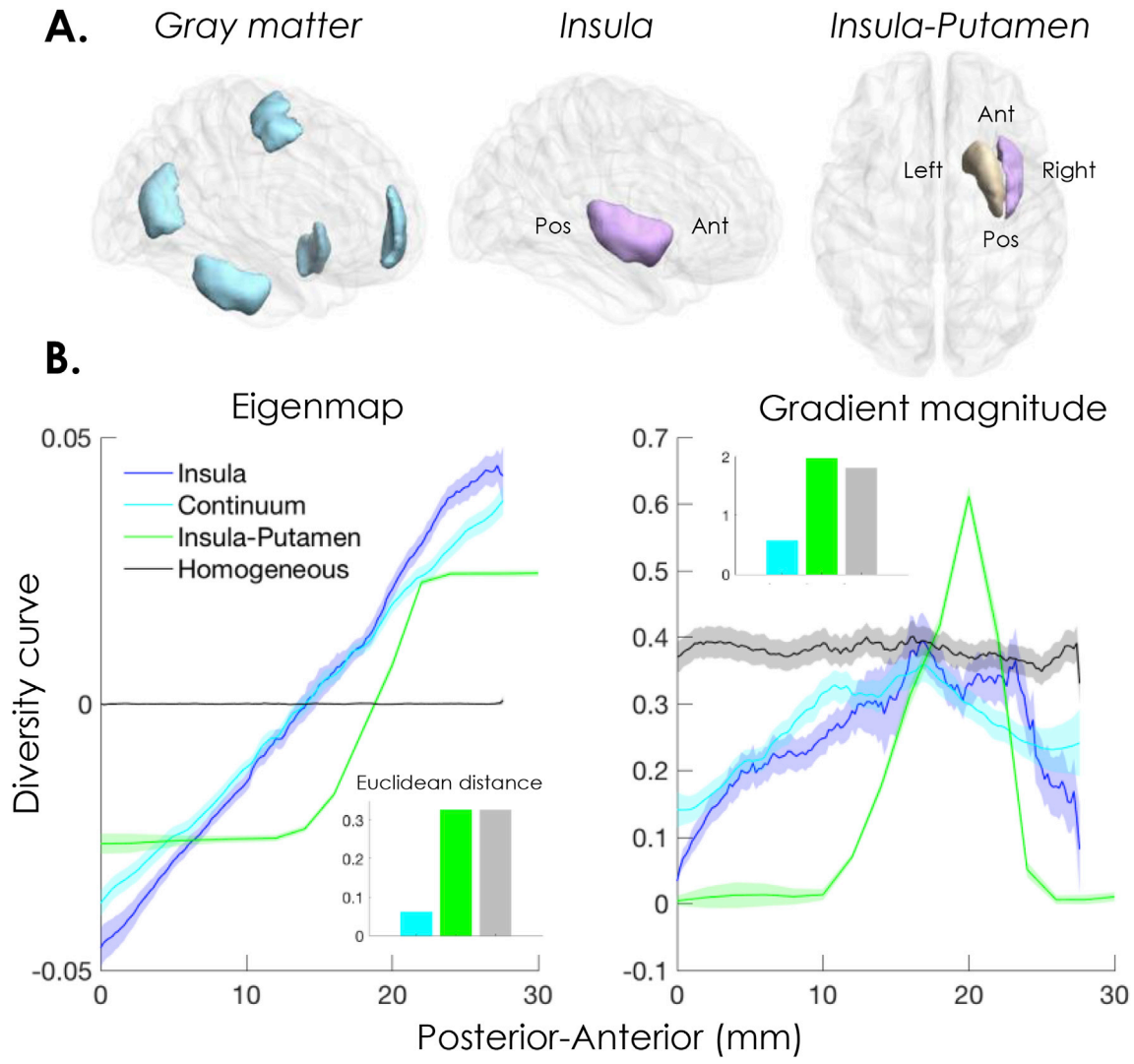


Fig. 7. Model selection: diversity curves for the insula cortex compared to benchmark diversity curves. Benchmark diversity curves were mapped for the cases of: i) connectional diversity segregated into two distinct regions (insula-putamen benchmark); ii) connectional diversity characterized by a continuum of gradual change (continuum benchmark); and, iii) an absence of any connectional diversity (homogenous benchmark). **Panel A:** Diversity curves for the continuum benchmark were mapped for insula-shaped patches that were randomly distributed throughout the gray matter volume (leftmost image). While regional boundaries may potentially straddle the randomly placed insula-shaped patches, the location of any boundaries was not consistent across patches, and thus averaging diversity curves across many patches yielded a continuum of change. Diversity curves for the homogenous benchmark were generated by randomizing the spatial location of voxels comprising the insula (center image). Diversity curves for the combined insula-putamen (right image) were mapped to yield a benchmark for the case of two distinct regions. **Panel B:** Diversity curves for the actual insula (blue line), compared to benchmark diversity curves for the insula-putamen (green), continuum (cyan) and homogeneous (black) benchmarks. Diversity curves are shown for the Fiedler eigenvector (left axis) and the magnitude of its gradient (right axis). Diversity curves for the actual insula and the insula-putamen benchmark are averaged over 100 individuals. Diversity curves for the continuum and homogeneous benchmarks are averaged over 100 randomizations. Shading denotes 95% confidence intervals. The insula's diversity curve shares characteristics of the continuum benchmark. Unlike the insula-putamen benchmark, the insula's diversity curve is not step shaped; and unlike the homogenous benchmark, its slope is not zero. Bar plots show the Euclidean distance between insula diversity curves and each of the three benchmarks (Eigenmap, continuum: 0.06, insula-putamen: 0.33, homogeneous: 0.33; Gradient magnitude, continuum: 0.57, insula-putamen: 1.98, homogeneous: 1.81). This suggests that the insula's connectional diversity is most parsimoniously modeled as a continuum of gradual change.

benchmark (i.e. approximately linear with a non-zero gradient). Moreover, the continuum benchmark provides a substantially better fit for the insula's diversity curve (Euclidean distance: 0.06) than the other two benchmarks (0.33; Fig. 6B).

The benchmark diversity curves mapped with respect to the gradient magnitude of the eigenmaps (Fig. 7B, right axis) provide further support for these conclusions. In particular, the insula's diversity curve is most closely matched to the continuum benchmark and does not show a peak with magnitude that is comparable to the insula-putamen benchmark. Note that the diversity curve based on gradient magnitude is non-zero for the homogeneous benchmark (right axis); even though the eigenmap-based diversity curve (left axis) has a gradient of zero. While gradients in the eigenmap for the homogeneous benchmark are oriented randomly, their magnitudes are non-zero and these non-zero gradient magnitudes are conveyed in the diversity curve.

3.5. Relating insula diversity to behavior

Insula diversity curves show substantial variation between individuals (Fig. 6C). Canonical correlation analysis (CCA) was used to test whether this inter-individual variation in insula diversity was associated with variation in behavioral measures associated with the insula. CCA was performed on the parameters describing the linear piecewise

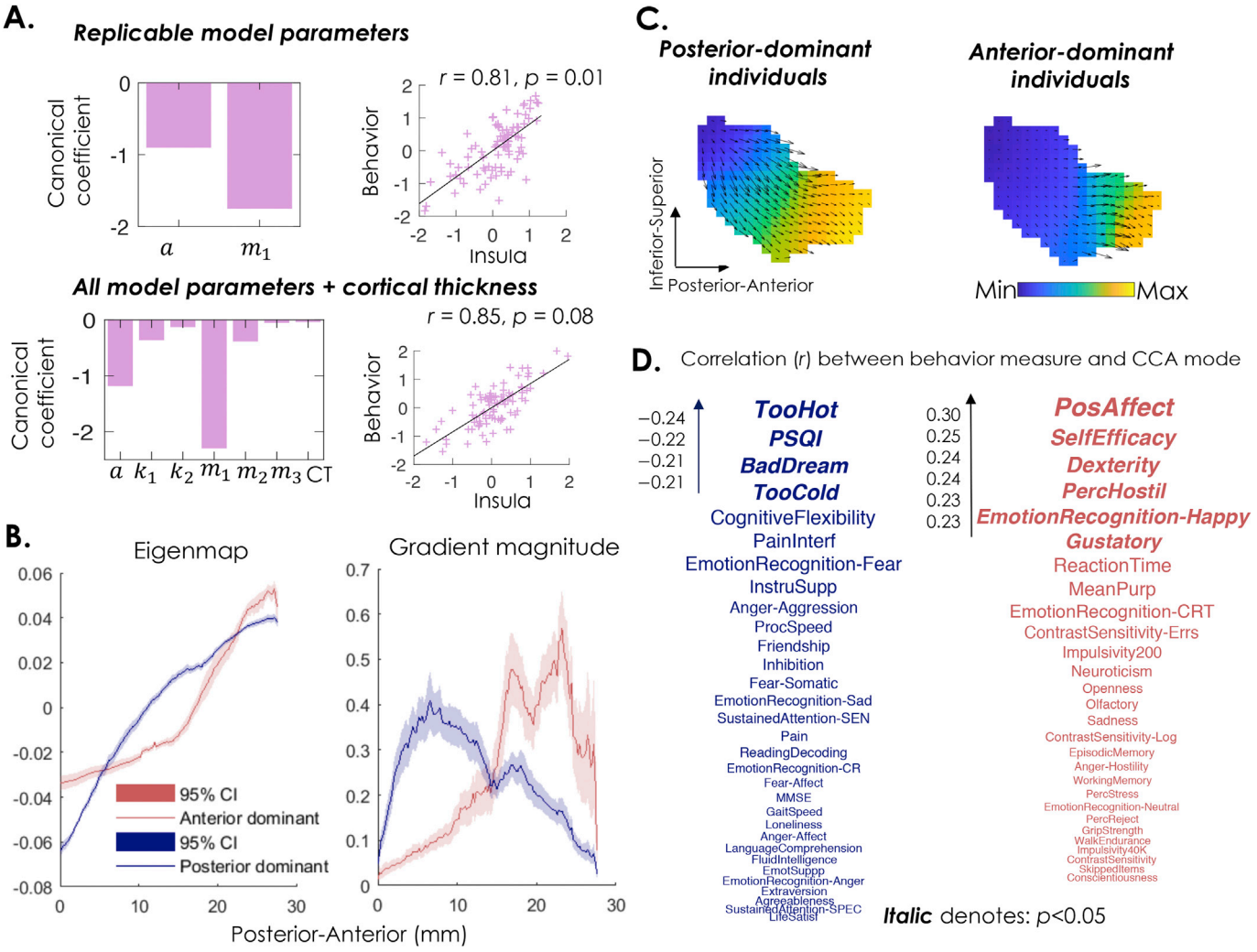


Fig. 8. Relation between behavior and insula functional connectivity diversity. Canonical correlation analysis (CCA) was used to test whether inter-individual variation in the insula's connectional diversity is associated with 59 selected behavioral measures. CCA was performed on the parameters describing the linear piecewise function fitted to each individual's diversity curve. **Panel A:** CCA was performed on: i) the two most reliable model parameters (upper panel); and, ii) all six model parameters as well as an estimate of the insula's cortical thickness (CT) for each individual (lower panel). A significant CCA mode was found in the case of two parameters: $r = 0.81$, $p = 0.01$; and trend-level significance in the case of six parameters + CT: $r = 0.85$, $p = 0.08$; familywise error corrected across all CCA modes with permutation testing. Bar plots show canonical coefficients for each model parameter. Scatter plots show the correlation between canonical scores. The slope of the first line segment (m_1) provides the most explanatory power. Canonical coefficients are as follows: two parameters: a: −0.90, m_1: −1.75; six parameters + CT: a : −1.18, k_1 : −0.36, k_2: −0.13, m_1: −2.30, m_2: −0.38, m_3: −0.05, CT: −0.04. **Panel B:** Group-averaged diversity curves for anterior-dominant (red curve) and posterior-dominant (blue) individuals. Anterior or posterior dominance is determined based on whether an individual's diversity curve is positively (anterior) or negatively (posterior) correlated with the canonical score. Anterior-dominant individuals are characterized by greater connectional diversity per unit length within the anterior insula, indicated by increased steepness of the diversity curve in the anterior insula. **Panel C:** Group-averaged eigenmaps (Fiedler eigenvector) mapped to insula voxels in anatomical space for the group of posterior-dominant (left) and anterior-dominant (right) individuals. **Panel D:** Ranked behavioral measures that are positively (right list) and negatively (left) correlated with the CCA mode (Supplementary Materials S7). Individuals who scored high on the positively correlated behaviors and low on the negatively correlated behaviors are associated with the positively-correlated insula diversity curve (Panel **B**, red curve) and considered anterior-dominant individuals. The positively and negatively correlated behaviors were displayed separately in order of descending effects size, where font size is modulated by effect size. Behaviors with significant correlations are shown in *Italic* font.

function fitted to each individual's diversity curve. More specifically, the CCA was performed on the model parameters showing good within-subject replicability (ICC > 0.5, Supplementary Figure S6); namely, the intercept term (a) and the slope of the first line segment (m_1). In ancillary analyses, a second CCA was performed on all six model parameters as well as an estimate of the insula's cortical thickness (CT) for each individual. The second CCA was undertaken to evaluate the contribution of all model parameters and to determine whether the insula's connectional diversity or cortical thickness explained the most variation in behavior.

CCA identified a significant relation between the insula's connectional diversity and behavior (two parameters: $r = 0.81$, $p = 0.01$; familywise error corrected across all CCA modes with permutation testing). When all six model parameters were included (as opposed to only the two most reliable parameters), the relation was trend-level significant (six parameters + CT: $r = 0.85$, $p = 0.08$). Fig. 8A shows the canonical coefficients for each model parameter (left) and scatter plots of the correlation between canonical scores (right). The slope of the first line segment (m_1) is the model parameter with the largest canonical score by absolute value and provides substantially greater explanatory power than all other parameters, including cortical thickness.

Each individual's diversity curve was categorized as either having a positive or negative canonical score with respect to the significant CCA mode. Fig. 8B shows diversity curves averaged over the top 25% individuals with the most negative (blue curve) and positive (red curve) canonical scores. The positively-correlated diversity curves are characterized by greater connectional diversity per unit length within the anterior insula, indicated by increased steepness of the diversity curve in the anterior insula. We refer to individuals with positively-correlated diversity curves as *anterior-dominant individuals*. Conversely, the negatively-correlated diversity curves are characterized by greater connectional diversity within the posterior insula and represent *posterior-dominant individuals*.

Group-averaged eigenmaps for these two groups of individuals are shown in Fig. 8C, where the eigenmaps have been mapped to voxels comprising the insula to yield anatomical images. It can be seen that the dynamic range of eigenmap values is mostly exhausted on the anterior insula for the group of anterior-dominant individuals. Note that we have shown two groups of representative diversity curves only to assist in explaining the variation between individuals underpinning the CCA mode. It is important to remark that CCA is an inherently continuous method, and no such dichotomy between individuals is formalized by the method.

Fig. 8D shows ranked lists of the behavioral measures that are positively (right list) and negatively (left) correlated with the significant CCA mode. Anterior-dominant individuals scored high on the positively correlated behaviors and low on the negatively correlated behaviors (Fig. 8B, red curve). In contrast, posterior-dominant individuals scored low (high) on the positively (negatively) correlated behaviors (blue curve). In Fig. 8C, the positively and negatively correlated behaviors are displayed separately in order of descending effects size, where font size is modulated by effect size. The positively correlated behaviors are associated with cognitive-emotional (positive affect, emotion recognition, self-efficacy, perceived hostility), fine motor skills (dexterity) and viscerosensory (gustatory) functions. On the contrary, the negatively correlated behaviors are attributed to sleep disturbances, underpinned by somatosensory processing (temperature sensations).

Therefore, higher sensitivity to temperature sensation is associated with greater differentiation (i.e. more diversity) of the posterior insula, whereas individuals with greater differentiation of the anterior insula are associated with better motor dexterity, high sensitivity in gustatory sensation and a range of cognitive-affective behaviors such as pleasurable engagement with environment (positive affect), self-efficacy, emotional sensibility in both positive (happy) and negative (perceived hostility) ways.

Finally, the canonical coefficients fitted using data from the first fMRI session (model fitting) were applied to data from the second fMRI session to determine the within-subject replicability of the CCA model. Diversity curves (Supplementary Figure S6) and the fitted CCA model (Supplementary Figure S7) were highly replicable between fMRI sessions. In addition, the diversity curves for the left insula were also modeled (Supplementary Figure S8), yielding a significant relation between insula diversity curves and behavior ($r = 0.22$, $p = 0.03$).

4. Discussion

We comprehensively characterized the diversity of resting-state functional connectivity across the topography of the human insula cortex. Resting-state fMRI was used to map a connectional fingerprint for each insula voxel in each of 100 healthy individuals. Following the methodology of several previous studies (Cauda et al. 2011, 2012; Deen et al., 2011; Cauda and Vercelli, 2013; Chang et al., 2013; Moran et al., 2013), we used a clustering algorithm to cluster these connectional fingerprints into groups and thereby parcellate the insula into discrete subregions. Clustering techniques have also been used to dissociate the roles of the insula and adjacent regions such as the inferior frontal cortex (Cai et al., 2014). To begin with, we used classic cluster evaluation criteria to determine the optimal number of insula clusters (subregions). However, we found that some of these criteria performed poorly in determining the ground truth number of clusters for insula-like synthetic data, while other criteria (i.e. gap statistic) relied on null data that did not preserve the spatial smoothness of the empirical fMRI data, and thus could have overestimated the true number of insula subregions. Indeed, we found that the optimal number of insula subregions suggested by classic cluster evaluation criteria varied markedly between individuals and was generally higher than reported in most previous studies (Kelly et al., 2012; Vercelli et al., 2016; Yamada et al., 2016). As an alternative to cluster evaluation criteria, we considered determining the optimal number of clusters based on maximum concordance in cluster solutions between individuals, but found that this criterion can identify spurious clusters in data that is inherently un-clustered (Supplementary Figure S1).

Bipartite parcellation of the insula resulted in an anterior-posterior subdivision, which is consistent with several previous studies (Nanetti et al., 2009; Cauda et al. 2011, 2012; Jakab et al., 2012; Kelly et al., 2012; Alcauter et al., 2015). Tripartite parcellation yielded ventral-anterior, dorsal-posterior and ventral-medial subregions, which is consistent with the insula division reported by Chang et al. (2013) but not two other studies (Deen et al., 2011; Moran et al., 2013). The inconsistency between studies in the boundaries of tripartite insula parcellations may be due to the clustering of group-averaged functional connectivity maps in the latter two studies, thereby potentially mischaracterizing inter-individual heterogeneity.

Despite the use of fMRI-specific null data, novel cluster evaluation measures and fMRI data of the highest temporal and spatial resolution used to date, we were unable to unequivocally ascertain which of the bipartite or tripartite parcellations provided the most parsimonious (optimal) model of insula functional connectivity diversity. More specifically, we found that the most parsimonious number of insula subregions was strongly influenced by the extent to which the fMRI data was spatially smoothed and varied substantially between individuals. While inter-individual variation in insula neuroanatomy is inevitable, it would seem improbable that entire insula subregions are absent in certain individuals. It might be argued that clusters should be delineated using unsmoothed fMRI data, although it is important to remark that MRI data is intrinsically smooth due to the point spread function (PSF) and thus some degree of smoothing is unavoidable. Given that the spatial extent of the PSF can marginally vary between MRI scanners, this may explain some of the inconsistencies in the number of insula subregions reported in previous studies (Table 1). With minimal smoothing (1.5 mm), we found that neither bipartite nor tripartite parcellations were most parsimonious for the majority of individuals. In contrast, with moderate smoothing (4 mm), the bipartite solution was optimal for most

individuals, although the tripartite solution was determined most parsimonious for many individuals. Given the substantial influence of smoothing and the variation between individuals in the most parsimonious number of subregions, we contend that the question of how many subregions comprise the insula is ambiguous. As previously suggested by Cerliani et al. (2012), perhaps models of insula heterogeneity that do not mandate the delineation of discrete subregional boundaries can provide a more fruitful characterization.

Moreover, irrespective of whether the bipartite or tripartite parcellation was deemed optimal, the resulting insula subregions were found not to be homogenous for most subregions. One of the key goals of parcellation is to yield subregions comprising a set of voxels that share a common connectional fingerprint; namely, when traversing the topography of a subregion, drastic variation should not be seen across voxels with respect to the cortical and subcortical regions to which they connect. We referred to this property as subregion homogeneity. However, we found that for the majority of individuals, insula subregions were not significantly more homogeneous than null data in which the insula was repeatedly repositioned to random gray matter locations.

We thus encountered three key shortcomings associated with parcellating the insula into discrete subregions: i) ambiguity in the most parsimonious number of subregions, due to effects such as smoothing; ii) substantial inter-individual variation in the optimal number of clusters; and, iii) lack of homogeneity of subregions. Given these challenges, in the second part of this study, we considered alternative models to characterize the diversity of functional connectivity across the topography of the insula, aiming to part with the prevalent paradigm of parcellating the insula's functional connectivity diversity into discrete subregions. Nevertheless, it is important to make clear that these challenges do not invalidate parcellation of the insula into subregions.

We proposed the concept of a diversity curve, which enabled us to continuously characterize the insula's connectional diversity. Diversity curves provide an intuitive approach to topographically parameterize Laplacian eigenmaps and perform model selection. Laplacian eigenmaps can also be parameterized using the coefficients of spatial basis functions (Haak et al., 2018). In this study, we only considered eigenmaps corresponding to the Fiedler eigenvector. The eigenmap corresponding to the next largest eigenvalue showed less consistency across individuals and was not given further consideration. Considering multiple eigenmaps has proven useful in characterizing connectional diversity along multiple gradients in regions larger than the insula (Haak et al., 2018) and across the whole cortex (Margulies et al., 2016). Cerliani et al. (2012) used eigenmaps to study the insula's *anatomical* connectivity and found a gradual rostro-caudal gradient of connectivity derived from white matter fiber tractography. Our work extends this previous study by investigating resting-state functional connectivity, undertaking explicit model selection, relating connectional diversity to behavior and developing the concept of a diversity curve.

To perform model selection, we compared the insula's diversity curve to benchmark diversity curves for i) two distinct regions (i.e. insula-putamen combined); ii) a continuum of gradual change; and, iii) an absence of any connectional diversity (i.e. homogenous region). Of the three benchmarks considered, the insula's diversity curve was most accurately characterized by the benchmark diversity curve for a continuum. This was confirmed with quantitative model selection, where the continuum benchmark was found to provide a model fit that was five times better than the other two benchmarks. The homogenous benchmark was rejected because the slope of the insula's diversity curve was non-zero, indicating that the insula is not topographically homogeneous with respect to its functional connectivity. The benchmark for distinct regions was also rejected because the insula's diversity curve showed no evidence of an abrupt step. Boundaries between regions were characterized by sharp gradients in the diversity curve. We found no evidence of gradients in the insula's diversity curve that were comparable in magnitude to the insula-putamen benchmark. However, it is important to remark that gradients differentiating putative subregions *within* the insula may be subtler than gradients *between* larger regions such as those associated with the insula-putamen benchmark. On the other hand, the diversity curve for the insula spanned approximately the same length (28 mm) as the insula-putamen benchmark, and thus the connectional diversity per unit length of cortex was matched between the insula and its benchmarks. Interestingly, Glasser et al. (2016) applied a gradient-based approach to parcellate the entire cortex using multi-modal neuroimaging data (architecture, connectivity, function and topography) and found that the insula could be parcellated into six subregions. This suggests that functional connectivity alone may not be sufficient to delineate subregions, although it is important to note that this multi-modal study did not use an explicit null model to establish expectations about how large a gradient should be to warrant subdivision.

To formalize model selection, a piecewise linear function comprising three line segments was fitted to the insula's diversity curve and the three benchmark diversity curves. While the insula's diversity curve was approximately linear, the slope of the middle line segment was marginally steeper than the other two line-segments, providing evidence for a gradual transition zone between the anterior and posterior insula. However, it is important to remark that the ratio of slopes between the three line segments was orders of magnitude smaller than the step-shaped diversity curve for the insula-putamen benchmark, and the breakpoints marking the boundaries of the putative transition zone showed poor replicability across fMRI sessions (Supplementary Figure S6).

We found that inter-individual variation in diversity curves was significantly associated with variation in behavioral traits. For individuals who scored high on measures of somatosensory function, the posterior insula was more diverse than poor-scoring individuals (i.e. steeper gradient in diversity curve), but the most anterior aspect of the insula was more homogeneous (i.e. more gradual gradient). We referred to these individuals as posterior-dominant because their posterior insula showed greater diversity per unit length than their anterior insula. In contrast, for individuals who scored high on measures of cognitive-emotional, motor dexterity and viscerosensory functions, the anterior insula showed greater connectional diversity, whereas the diversity curve's gradient in the posterior insula was more gradual. These individuals were called anterior-dominant individuals. However, as we remarked above, CCA is an inherently continuous method, and no such dichotomy between individuals is formalized by the method. What we observed here is a mode of population covariation that links the insula's diversity curve to behaviors. We therefore reason that the connectional diversity of the posterior insula is associated with somatosensory function, whereas cognitive-emotional (positive affect, emotion recognition and self-efficacy), motor dexterity and viscerosensory processing is associated with the intricate functional organization of the anterior insula.

This anterior-posterior division of insula function is consistent with previous studies. In particular, previous studies report that the anterior insula is associated with emotion (Uddin et al., 2014), viscerosensory sensation (Small et al., 2003), high-level cognition (Uddin, 2015), including the attentional control for motor dexterity (Craig, 2002; Rinne et al., 2017). Previous studies also suggest that the posterior insula is associated with somatosensory responses, such as temperature sensation (Craig et al., 2000; Ostrowsky et al., 2000; Stephani et al., 2011). We found that this anterior-posterior division of insula function is facilitated, at least in part, by the insula's connectional diversity. Moreover, individuals with a more anterior- or posterior-dominant insula responded behaviorally in a way that is consistent with this dominance. For comparison, a supplementary CCA analysis was performed on the optimal number of clusters computed from the first part of our study, and the results suggested that inter-individual variation in behavior was not associated with the optimal number of insula clusters. Modeling the insula's connectional diversity as a continuum, as opposed to discrete subregions, thus may afford a more accurate characterization of function and inter-individual variation in behavior.

Nevertheless, complex human social cognitive-emotional behavior, such as self-efficacy and positive affect, are likely to engage multiple segregated brain networks that are bridged by hub regions. The insula serves as one of the central hubs of functional and structural brain networks (Sridharan et al., 2008; van den Heuvel and Sporns, 2013; Uddin, 2015; Ryali et al., 2016) and emerges as a hub in early stages of brain development (Fransson et al., 2011; Gao et al., 2011; Shi et al., 2012). As a key hub region, the connectivity patterns of the insula may facilitate integration between neural networks that subserve social cognitive-emotional functioning. Accurately characterizing the diversity in functional connectivity across the insula is therefore crucial to gain insight into the neural correlates of these behavioral traits.

Some limitations require consideration. First, fMRI data is inherently discrete (voxelized) and thus the extent to which spatial variation in fMRI data can be modeled as a continuum is limited by the resolution of individual voxels. This intrinsic discretization is a general limitation of MRI. Second, the inability to unequivocally parcellate the insula into subregions with resting-state fMRI should not be interpreted to mean that the insula does not comprise subregions. Insula subregions may be evident at different spatial scales (e.g. cellular) and may be evident with alternative imaging modalities (e.g. electrophysiology). The optimal number of insula subregions may be influenced by data quality and the fMRI protocol. The data used in this study is characterized by a higher resolution and a shorter TR than most previous studies that have sought to parcellate the insula into distinct subregions (Table 1). Ambiguity in the optimal number of subregions may have been due to fMRI limitations, such as spatial resolution. For example, some degree of spatial smoothing is unavoidable with fMRI, which may have led to the blurring of boundaries between putative subregions. An interesting avenue for future investigation is to characterize insula diversity by combining data from multiple imaging modalities, including connectivity, cyto- and myelo-architecture, cortical architecture, electrophysiology, gene expression and function.

5. Conclusions

Resting-state fMRI indicates that the anterior insula is functionally connected with frontal-limbic and paralimbic areas, whereas the posterior insula connects with the precentral-postcentral gyrus and occipital lobe. Many studies have sought to parse this connectional diversity by parcellating the insula into a fixed number of discrete subregions with clustering algorithms applied to functional connectivity maps. In this study, we found several shortcomings of representing the insula's connectional diversity with discrete subregions; namely, i) the most parsimonious number of insula subregions varied markedly between individuals and was substantially influenced by the extent to which the fMRI data was spatially smoothed; and, ii) insula subregions were not homogenous for the majority of individuals studied (i.e. insula subregions were not significantly more homogenous than randomly chosen patches of gray matter of the same size and shape as the subregions). Given these shortcomings, we advocate for development of alternative models to characterize the insula's connectional diversity that do not necessitate delineation of discrete subregions. In this study, we developed one such model based on the concept of a diversity curve, which provides an intuitive way to parameterize and perform model selection on eigenmaps produced by established eigendecomposition techniques for mapping continuous patterns of variation in the cerebral cortex (Huntenburg et al., 2018). We performed model selection with respect to three benchmark diversity curves and found that the insula's diversity curve was most accurately modeled by the benchmark characterizing a continuum of gradual change. Unlike the benchmark for distinct regions, the insula's diversity curve was not step shaped; and unlike the homogenous benchmark, its slope was not zero. We also found that inter-individual variation in these diversity curves correlated with variation in measures of human behavior across multiple cognitive, affective and sensorimotor domains. While some fMRI applications necessitate delineation of discrete subregions (e.g. delineation of network nodes for connectomic studies), when possible, we suggest characterizing the insula's connectional diversity as a continuum in fMRI investigations. The diversity curve concept developed in this study provides an intuitive method to analyze Laplacian eigenmaps for the purpose of performing model selection and can be applied to other cortical and subcortical regions.

Funding

Y.T. was supported by the China Scholarship Council - University of Melbourne Research Scholarship. A.Z. was supported by the Australian National Health and Medical Research Council (NHMRC) Senior Research Fellowship B (ID: 1136649).

Declarations of interest

None.

Acknowledgements

Data were provided by the Human Connectome Project, WU-Minn Consortium (Principal Investigators: David Van Essen and Kamil Ugurbil; 1U54MH091657) funded by the 16 NIH Institutes and Centers that support the NIH Blueprint for Neuroscience Research; and by the McDonnell Center for Systems Neuroscience at Washington University.

Appendix A. Supplementary data

Supplementary data related to this article can be found at https://doi.org/10.1016/j.neuroimage.2018.08.055.

References

Alcauter, S., Lin, W., Keith Smith, J., Gilmore, J.H., Gao, W., 2015. Consistent anterior-posterior segregation of the insula during the first 2 years of life. Cerebr. Cortex 25, 1176–1187.

Augustine, J.R., 1996. Circuitry and functional aspects of the insular lobe in primates including humans. Brain Res Brain Res Rev 22, 229–244.

Bartko, J.J., 1966. The intraclass correlation coefficient as a measure of reliability. Psychol. Rep. 19, 3–11.

Baur, V., Hänggi, J., Langer, N., Jäncke, L., 2013. Resting-state functional and structural connectivity within an insula-amygdala route specifically index state and trait anxiety. Biol. Psychiatr. 73, 85–92.

Belkin, M., Niyogi, P., 2003. Laplacian eigenmaps for dimensionality reduction and data representation. Neural Comput. 15, 1373–1396.

Brodmann, K., 1909. Brodmann's Localisation in the Cerebral Cortex. Springer, New York, USA.

Cai, W., Ryali, S., Chen, T., Li, C.-S.R., Menon, V., 2014. Dissociable roles of right inferior frontal cortex and anterior insula in inhibitory control: evidence from intrinsic and task-related functional parcellation, connectivity, and response profile analyses across multiple datasets. J. Neurosci. 34, 14652–14667.

Calinski, T., Harabasz, J., 1974. A dendrite method for cluster analysis. Commun. Stat. 3, 1–27.

Carpineto, C., Romano, G., 2012. Consensus clustering based on a new probabilistic rand index with application to subtopic retrieval. IEEE Trans. Pattern Anal. Mach. Intell. 34, 2315–2326.

Cauda, F., Costa, T., Torta, D.M., Sacco, K., D'Agata, F., Duca, S., Geminiani, G., Fox, P.T., Vercelli, A., 2012. Meta-analytic clustering of the insular cortex: characterizing the meta-analytic connectivity of the insula when involved in active tasks. Neuroimage 62, 343–355.

Cauda, F., D'Agata, F., Sacco, K., Duca, S., Geminiani, G., Vercelli, A., 2011. Functional connectivity of the insula in the resting brain. Neuroimage 55, 8–23.

Cauda, F., Vercelli, A., 2013. How many clusters in the insular cortex? Cerebr. Cortex 23, 2779–2780.

Cerliani, L., Thomas, R.M., Jbabdi, S., Siero, J.C., Nanetti, L., Crippa, A., Gazzola, V., D'Arceuil, H., Keysers, C., 2012. Probabilistic tractography recovers a rostrocaudal trajectory of connectivity variability in the human insular cortex. Hum. Brain Mapp. 33, 2005–2034.

Chang, L.J., Yarkoni, T., Khaw, M.W., Sanfey, A.G., 2013. Decoding the role of the insula in human cognition: functional parcellation and large-scale reverse inference. Cerebr. Cortex 23, 739–749.

Clauset, A., Newman, M.E.J., Moore, C., 2004. Finding community structure in very large networks. Phys. Rev. 70, 066111.

Cloutman, L.L., Binney, R.J., Drakesmith, M., Parker, G.J., Lambon Ralph, M.A., 2012. The variation of function across the human insula mirrors its patterns of structural

connectivity: evidence from in vivo probabilistic tractography. Neuroimage 59, 3514–3521.
Cohen, A.L., Fair, D.A., Dosenbach, N.U.F., Miezin, F.M., Dierker, D., Van Essen, D.C., Schlaggar, B.L., Petersen, S.E., 2008. Defining functional areas in individual human brains using resting functional connectivity MRI. Neuroimage 41, 45–57.
Cole, M.W., Schneider, W., 2007. The cognitive control network: integrated cortical regions with dissociable functions. Neuroimage 37, 343–360.
Craig, A.D., 2002. How do you feel? Interoception: the sense of the physiological condition of the body. Nat. Rev. Neurosci. 3, 655–666.
Craig, A.D., 2009. How do you feel–now? The anterior insula and human awareness. Nat. Rev. Neurosci. 10, 59–70.
Craig, A.D., Chen, K., Bandy, D., Reiman, E.M., 2000. Thermosensory activation of insular cortex. Nat. Neurosci. 3, 184–190.
Damasio, A.R., Grabowski, T.J., Bechara, A., Damasio, H., Ponto, L.L., Parvizi, J., Hichwa, R.D., 2000. Subcortical and cortical brain activity during the feeling of self-generated emotions. Nat. Neurosci. 3, 1049–1056.
Davis, K.D., Kwan, C.L., Crawley, A.P., Mikulis, D.J., 1998. Functional MRI study of thalamic and cortical activations evoked by cutaneous heat, cold, and tactile stimuli. J. Neurophysiol. 80, 1533–1546.
Deen, B., Pitskel, N.B., Pelphrey, K.A., 2011. Three systems of insular functional connectivity identified with cluster analysis. Cerebr. Cortex 21, 1498–1506.
Ebisch, S.J., Gallese, V., Willems, R.M., Mantini, D., Groen, W.B., Romani, G.L., Buitelaar, J.K., Bekkering, H., 2011. Altered intrinsic functional connectivity of anterior and posterior insula regions in high-functioning participants with autism spectrum disorder. Hum. Brain Mapp. 32, 1013–1028.
Esposito, F., Scarabino, T., Hyvarinen, A., Himberg, J., Formisano, E., Comani, S., Tedeschi, G., Goebel, R., Seifritz, E., Di Salle, F., 2005. Independent component analysis of fMRI group studies by self-organizing clustering. Neuroimage 25, 193–205.
Faillenot, I., Heckemann, R.A., Frot, M., Hammers, A., 2017. Macroanatomy and 3D probabilistic atlas of the human insula. Neuroimage 150, 88–98.
Finn, E.S., Shen, X., Scheinost, D., Rosenberg, M.D., Huang, J., Chun, M.M., Papademetris, X., Constable, R.T., 2015. Functional connectome fingerprinting: identifying individuals using patterns of brain connectivity. Nat. Neurosci. 18, 1664.
Fransson, P., Aden, U., Blennow, M., Lagercrantz, H., 2011. The functional architecture of the infant brain as revealed by resting-state fMRI. Cerebr. Cortex 21, 145–154.
Fred, A.L.N., Jain, A.K., 2005. Combining multiple clusterings using evidence accumulation. IEEE Trans. Pattern Anal. Mach. Intell. 27, 835–850.
Friedman, D.P., Murray, E.A., O'Neill, J.B., Mishkin, M., 1986. Cortical connections of the somatosensory fields of the lateral sulcus of macaques: evidence for a corticolimbic pathway for touch. J. Comp. Neurol. 252, 323–347.
Gao, W., Gilmore, J.H., Giovanello, K.S., Smith, J.K., Shen, D., Zhu, H., Lin, W., 2011. Temporal and spatial evolution of brain network topology during the first two years of life. PLoS One 6 e25278.
Ghaziri, J., Tucholka, A., Girard, G., Houde, J.-C., Boucher, O., Gilbert, G., Descoteaux, M., Lippé, S., Rainville, P., Nguyen, D.K., 2017. The corticocortical structural connectivity of the human insula. Cerebr. Cortex 27, 1216–1228.
Glasser, M.F., Coalson, T.S., Robinson, E.C., Hacker, C.D., Harwell, J., Yacoub, E., Ugurbil, K., Andersson, J., Beckmann, C.F., Jenkinson, M., et al., 2016. A multi-modal parcellation of human cerebral cortex. Nature 536, 171–178.
Glasser, M.F., Sotiropoulos, S.N., Wilson, J.A., Coalson, T.S., Fischl, B., Andersson, J.L., Xu, J., Jbabdi, S., Webster, M., Polimeni, J.R., et al., 2013. The minimal preprocessing pipelines for the Human Connectome Project. Neuroimage 80, 105–124.
Gordon, E.M., Laumann, T.O., Adeyemo, B., Huckins, J.F., Kelley, W.M., Petersen, S.E., 2016. Generation and evaluation of a cortical area parcellation from resting-state correlations. Cerebr. Cortex 26, 288–303.
Griffanti, L., Salimi-Khorshidi, G., Beckmann, C.F., Auerbach, E.J., Douaud, G., Sexton, C.E., Zsoldos, E., Ebmeier, K.P., Filippini, N., Mackay, C.E., et al., 2014. ICA-based artefact removal and accelerated fMRI acquisition for improved resting state network imaging. Neuroimage 95, 232–247.
Haak, K.V., Marquand, A.F., Beckmann, C.F., 2018. Connectopic mapping with resting-state fMRI. Neuroimage 170, 83–94.
Hotelling, H., 1936. Relations between two sets of variates. Biometrika 28, 321–377.
Huntenburg, J.M., Bazin, P.-L., Margulies, D.S., 2018. Large-Scale gradients in human cortical organization. Trends Cognit. Sci. 22, 21–31.
Jakab, A., Molnar, P.P., Bogner, P., Beres, M., Berenyi, E.L., 2012. Connectivity-based parcellation reveals interhemispheric differences in the insula. Brain Topogr. 25, 264–271.
Kelly, C., Toro, R., Di Martino, A., Cox, C.L., Bellec, P., Castellanos, F.X., Milham, M.P., 2012. A convergent functional architecture of the insula emerges across imaging modalities. Neuroimage 61, 1129–1142.
Kurth, F., Eickhoff, S.B., Schleicher, A., Hoemke, L., Zilles, K., Amunts, K., 2010a. Cytoarchitecture and probabilistic maps of the human posterior insular cortex. Cerebr. Cortex 20, 1448–1461.
Kurth, F., Zilles, K., Fox, P.T., Laird, A.R., Eickhoff, S.B., 2010b. A link between the systems: functional differentiation and integration within the human insula revealed by meta-analysis. Brain Struct. Funct. 214, 519–534.
Margulies, D.S., Ghosh, S.S., Goulas, A., Falkiewicz, M., Huntenburg, J.M., Langs, G., Bezgin, G., Eickhoff, S.B., Castellanos, F.X., Petrides, M., et al., 2016. Situating the default-mode network along a principal gradient of macroscale cortical organization. Proc. Natl. Acad. Sci. U. S. A. 113, 12574–12579.
Meilă, M., 2007. Comparing clusterings—an information based distance. J. Multivariate Anal. 98, 873–895.
Mesulam, M.M., Mufson, E.J., 1982. Insula of the old world monkey. I. Architectonics in the insulo-orbito-temporal component of the paralimbic brain. J. Comp. Neurol. 212, 1–22.
Mesulam, M.M., Mufson, E.J., 1985. The insula of reil in man and monkey. In: Peters, A., Jones, E.G. (Eds.), Association and Auditory Cortices. Springer US, Boston, MA, pp. 179–226.
Mohajer, M., Englmeier, K., Schmid, V., 2010. A Comparision of Gap Statistic Definitions with and without Logarithm Function. Technical Reports No. 96. Department of Statistics.
Monti, S., Tamayo, P., Mesirov, J., Golub, T., 2003. Consensus clustering: a resampling-based method for class discovery and visualization of gene expression microarray data. Mach. Learn. 52, 91–118.
Moran, L.V., Tagamets, M.A., Sampath, H., O'Donnell, A., Stein, E.A., Kochunov, P., Hong, L.E., 2013. Disruption of anterior insula modulation of large-scale brain networks in schizophrenia. Biol. Psychiatr. 74, 467–474.
Moser, D.A., Doucet, G.E., Ing, A., Dima, D., Schumann, G., Bilder, R.M., Frangou, S., 2017. An integrated brain–behavior model for working memory. Mol. Psychiatr.
Mufson, E.J., Mesulam, M.M., 1982. Insula of the old world monkey. II: afferent cortical input and comments on the claustrum. J. Comp. Neurol. 212, 23–37.
Mufson, E.J., Mesulam, M.M., Pandya, D.N., 1981. Insular interconnections with the amygdala in the rhesus monkey. Neuroscience 6, 1231–1248.
Mufson, E.J., Sobreviela, T., Kordower, J., 1997. Chapter VII Chemical neuroanatomy of the primate insula cortex: relationship to cytoarchitectonics, connectivity, function and neurodegeneration. Handbook of chemical neuroanatomy 13, 377–454.
Mutschler, I., Wieckhorst, B., Kowalevski, S., Derix, J., Wentlandt, J., Schulze-Bonhage, A., Ball, T., 2009. Functional organization of the human anterior insular cortex. Neurosci. Lett. 457, 66–70.
Nanetti, L., Cerliani, L., Gazzola, V., Renken, R., Keysers, C., 2009. Group analyses of connectivity-based cortical parcellation using repeated k-means clustering. Neuroimage 47, 1666–1677.
Nelson, S.M., Dosenbach, N.U., Cohen, A.L., Wheeler, M.E., Schlaggar, B.L., Petersen, S.E., 2010. Role of the anterior insula in task-level control and focal attention. Brain Struct. Funct. 214, 669–680.
Newman, M.E., 2013. Spectral methods for community detection and graph partitioning. Phys. Rev. 88, 042822.
Newman, M.E., Mark, E., 2006. Modularity and community structure in networks. Proc. Natl. Acad. Sci. U. S. A. 103, 8577–8582.
Nomi, J.S., Farrant, K., Damaraju, E., Rachakonda, S., Calhoun, V.D., Uddin, L.Q., 2016. Dynamic functional network connectivity reveals unique and overlapping profiles of insula subdivisions. Hum. Brain Mapp. 37, 1770–1787.
Ortigue, S., Grafton, S.T., Bianchi-Demicheli, F., 2007. Correlation between insula activation and self-reported quality of orgasm in women. Neuroimage 37, 551–560.
Ostrowsky, K., Isnard, J., Ryvlin, P., Guenot, M., Fischer, C., Mauguiere, F., 2000. Functional mapping of the insular cortex: clinical implication in temporal lobe epilepsy. Epilepsia 41, 681–686.
Phillips, M.L., Young, A.W., Senior, C., Brammer, M., Andrew, C., Calder, A.J., Bullmore, E.T., Perrett, D.I., Rowland, D., Williams, S.C., et al., 1997. A specific neural substrate for perceiving facial expressions of disgust. Nature 389, 495–498.
Power, J.D., 2011. Functional network organization of the human brain. Neuron 72, 665–678.
Ray, S., Turi, R., 1999. Determination of number of clusters in K-means clustering and application in colour image segmentation. In: Proceeding of the 4th International Conference on Advances in Pattern Recognition and Digital Techniques, pp. 137–143.
Reichardt, J., Bornholdt, S., 2006. Statistical mechanics of community detection. Phys. Rev. 74, 016110.
Rinne, P., Hassan, M., Fernandes, C., Han, E., Hennessy, E., Waldman, A., Sharma, P., Soto, D., Leech, R., Malhotra, P.A., et al., 2017. Motor dexterity and strength depend upon integrity of the attention-control system. Proc. Natl. Acad. Sci. U. S. A.
Rousseeuw, P.J., 1987. Silhouettes: a graphical aid to the interpretation and validation of cluster analysis. J. Comput. Appl. Math. 20, 53–65.
Ryali, S., Chen, T., Padmanabhan, A., Cai, W., Menon, V., 2015. Development and validation of consensus clustering-based framework for brain segmentation using resting fMRI. J. Neurosci. Meth. 240, 128–140.
Ryali, S., Chen, T., Supekar, K., Menon, V., 2013. A parcellation scheme based on von Mises-Fisher distributions and Markov random fields for segmenting brain regions using resting-state fMRI. Neuroimage 65, 83–96.
Ryali, S., Chen, T., Supekar, K., Tu, T., Kochalka, J., Cai, W., Menon, V., 2016. Multivariate dynamical systems-based estimation of causal brain interactions in fMRI: group-level validation using benchmark data, neurophysiological models and human connectome project data. J. Neurosci. Meth. 268, 142–153.
Salimi-Khorshidi, G., Douaud, G., Beckmann, C.F., Glasser, M.F., Griffanti, L., Smith, S.M., 2014. Automatic denoising of functional MRI data: combining independent component analysis and hierarchical fusion of classifiers. Neuroimage 90, 449–468.
Schneider, R.J., Friedman, D.P., Mishkin, M., 1993. A modality-specific somatosensory area within the insula of the rhesus monkey. Brain Res. 621, 116–120.
Schröder, T.N., Haak, K.V., Zaragoza Jimenez, N.I., Beckmann, C.F., Doeller, C.F., 2015. Functional topography of the human entorhinal cortex. eLife 4.
Seeley, W.W., Menon, V., Schatzberg, A.F., Keller, J., Glover, G.H., Kenna, H., Reiss, A.L., Greicius, M.D., 2007. Dissociable intrinsic connectivity networks for salience processing and executive control. J. Neurosci. 27, 2349–2356.
Segerdahl, A.R., Mezue, M., Okell, T.W., Farrar, J.T., Tracey, I., 2015. The dorsal posterior insula subserves a fundamental role in human pain. Nat. Neurosci. 18, 499.
Shi, F., Yap, P.T., Gao, W., Lin, W., Gilmore, J.H., Shen, D., 2012. Altered structural connectivity in neonates at genetic risk for schizophrenia: a combined study using morphological and white matter networks. Neuroimage 62, 1622–1633.

Singer, T., Critchley, H.D., Preuschoff, K., 2009. A common role of insula in feelings, empathy and uncertainty. Trends Cognit. Sci. 13, 334–340.
Singer, T., Seymour, B., O'Doherty, J., Kaube, H., Dolan, R.J., Frith, C.D., 2004. Empathy for pain involves the affective but not sensory components of pain. Science 303, 1157–1162.
Small, D.M., Gregory, M.D., Mak, Y.E., Gitelman, D., Mesulam, M.M., Parrish, T., 2003. Dissociation of neural representation of intensity and affective valuation in human gustation. Neuron 39, 701–711.
Smith, S.M., Beckmann, C.F., Andersson, J., Auerbach, E.J., Bijsterbosch, J., Douaud, G., Duff, E., Feinberg, D.A., Griffanti, L., Harms, M.P., et al., 2013. Resting-state fMRI in the human connectome project. Neuroimage 80, 144–168.
Smith, S.M., Nichols, T.E., Vidaurre, D., Winkler, A.M., Behrens, T., Glasser, M., Ugurbil, K., Barch, D., Van Essen, D., Miller, K.L., 2015. A positive-negative mode of population covariation links brain connectivity, demographics and behavior. Nat. Neurosci. 18, 1565–1567.
Sokal, R.R., Rohlf, F.J., 1962. The comparison of dendrograms by objective methods. Taxon 11, 33–40.
Sridharan, D., Levitin, D.J., Menon, V., 2008. A critical role for the right fronto-insular cortex in switching between central-executive and default-mode networks. Proc. Natl. Acad. Sci. Unit. States Am. 105, 12569–12574.
Stephani, C., Fernandez-Baca Vaca, G., Maciunas, R., Koubeissi, M., Luders, H.O., 2011. Functional neuroanatomy of the insular lobe. Brain Struct. Funct. 216, 137–149.
Taylor, K.S., Seminowicz, D.A., Davis, K.D., 2009. Two systems of resting state connectivity between the insula and cingulate cortex. Hum. Brain Mapp. 30, 2731–2745.
Tibshirani, R., Walther, G., Hastie, T., 2001. Estimating the number of clusters in a data set via the gap statistic. J. Roy. Stat. Soc. B 63, 411–423.
Touroutoglou, A., Hollenbeck, M., Dickerson, B.C., Barrett, L.F., 2012. Dissociable large-scale networks anchored in the right anterior insula subserve affective experience and attention. Neuroimage 60, 1947–1958.
Uddin, L.Q., 2015. Salience processing and insular cortical function and dysfunction. Nat. Rev. Neurosci. 16, 55–61.
Uddin, L.Q., Kinnison, J., Pessoa, L., Anderson, M.L., 2014. Beyond the tripartite cognition-emotion-interoception model of the human insular cortex. J. Cognit. Neurosci. 26, 16–27.
van den Heuvel, M.P., Sporns, O., 2013. Network hubs in the human brain. Trends Cognit. Sci. 17, 683–696.
Vercelli, U., Diano, M., Costa, T., Nani, A., Duca, S., Geminiani, G., Vercelli, A., Cauda, F., 2016. Node detection using high-dimensional fuzzy parcellation applied to the insular cortex. Neural Plast. 2016, 1938292.
Vogt, K.M., Becker, C.J., Wasan, A.D., Ibinson, J.W., 2016. Human posterior insula functional connectivity differs between electrical pain and the resting state. Brain Connect. 6, 786–794.
Wiech, K., Jbabdi, S., Lin, C., Andersson, J., Tracey, I., 2014. Differential structural and resting state connectivity between insular subdivisions and other pain-related brain regions. Pain 155, 2047–2055.
Xia, M., Wang, J., He, Y., 2013. BrainNet viewer: a network visualization tool for human brain connectomics. PLoS One 8.
Xue, G., Lu, Z., Levin, I.P., Bechara, A., 2010. The impact of prior risk experiences on subsequent risky decision-making: the role of the insula. Neuroimage 50, 709–716.
Yamada, T., Itahashi, T., Nakamura, M., Watanabe, H., Kuroda, M., Ohta, H., Kanai, C., Kato, N., Hashimoto, R.I., 2016. Altered functional organization within the insular cortex in adult males with high-functioning autism spectrum disorder: evidence from connectivity-based parcellation. Mol. Autism. 7, 41.
Yan, M., Ye, K., 2007. Determining the number of clusters using the weighted gap statistic. Biometrics 63, 1031–1037.
Yeo, B.T., Krienen, F.M., Sepulcre, J., Sabuncu, M.R., Lashkari, D., Hollinshead, M., Roffman, J.L., Smoller, J.W., Zollei, L., Polimeni, J.R., et al., 2011. The organization of the human cerebral cortex estimated by intrinsic functional connectivity. J. Neurophysiol. 106, 1125–1165.
Zhao, Q., Li, H., Yu, X., Huang, F., Wang, Y., Liu, L., Cao, Q., Qian, Q., Zang, Y., Sun, L., et al., 2017. Abnormal resting-state functional connectivity of insular subregions and disrupted correlation with working memory in adults with attention deficit/hyperactivity disorder. Front. Psychiatr. 8, 200.

Supplementary Materials

Characterizing the functional connectivity diversity of the insula cortex: subregions, diversity curves and behavior

Ye Tian [a], Andrew Zalesky [a,b]

[a] Melbourne Neuropsychiatry Centre, Department of Psychiatry, The University of Melbourne and Melbourne Health, Carlton South, VIC Australia

[b] Department of Biomedical Engineering, The University of Melbourne, Parkville, VIC Australia

Table of Contents

S1. Classic Cluster Evaluation Criteria 2
S2. Simulation of Insula-like Synthetic Data 3
S3. Validation of Silhouette, Calinski-Harabasz and Gap Statistic 3
S4. Assessing Modular Structure with the Modularity *Q* score 4
S5. Cluster Evaluation Measures 5
S6. Validation of W, W^{norm} and W^{diff} 6
S7. Canonical Correlation Analysis 6
Figure S1. Example of the identification of spurious clusters showing high concordance across individuals 8
Figure S2. Validation of classic cluster evaluation criteria on insula-like synthetic data. 9
Figure S3. Cluster evaluation measures and their validation on insula-like synthetic data. 10
Figure S4. Tripartite parcellation of the human insula cortex based on resting-state functional connectivity 11
Figure S5. Group-consensus Laplacian eigenmaps for the insula cortex and the insula-putamen benchmark 12
Figure S6. Within-subject replication of diversity curves and the effect of spatial smoothing 13
Figure S7. Validation of CCA mode in second fMRI session. 14
Figure S8. Diversity curves for the left insula 15
Table S1. 16
Table S2. 18
Table S3. 18
Supplementary References 19

S1. Classic Cluster Evaluation Criteria

The optimal number of insula clusters is typically determined based on: (i) prior expectations informed by macaque studies of insula cytoarchitecture or axonal tract-tracing (Nanetti et al. 2009; Cauda et al. 2011; Deen et al. 2011; Jakab et al. 2012; Moran et al. 2013); (ii) concordance across different modalities or cohorts (Kelly et al. 2012; Chang et al. 2013; Alcauter et al. 2015; Yamada et al. 2016); or, (iii) with the use of cluster evaluation criteria (Cauda et al. 2012; Ryali et al. 2013; Ryali et al. 2015; Vercelli et al. 2016). The first approach might be considered subjective. While the second approach is less subjective, replicating clusters across different modalities or different cohorts does not ensure that a given cluster solution is necessarily valid, optimal or supported by the data. For example, many clustering algorithms will identify reproducible clusters in data that is inherently un-clustered. An example of this phenomenon is shown in Supplementary Figure S1. Many cluster evaluation criteria have been developed to assess the quality of cluster solutions and determine the optimal number of clusters. These criteria are generic and have been used to assess cluster organization across a diverse range of applications. Some of the most widely used measures include the silhouette criterion (Rousseeuw 1987), the Calinski-Harabasz criterion (Calinski and Harabasz 1974) and the gap statistic (Tibshirani et al. 2001). The silhouette criterion has been used in previous insula parcellation studies (Cauda et al. 2012; Vercelli et al. 2016). The Calinski-Harabasz criterion is another global cluster evaluation method that has been suggested as the best performing index among a group of global cluster evaluation methods including the silhouette criterion (Milligan and Cooper 1985). However, disadvantages of these global procedures include: (i) the absence of any clusters (e.g. one-cluster solution) cannot be explicitly assessed (Gordon 1999); and, (ii) the criteria are not benchmarked to a null reference distribution, and thus statistical support for the optimal number of clusters is not provided. In contrast, the gap statistic is a method that compares the within-cluster dispersion with that expected in a null reference distribution. The null distribution is built by uniformly sampling the data points in a bounding box encapsulating the principal components (Tibshirani et al. 2001). The null model of an absence of any clusters is rejected in favour of a multi-cluster solution if this is warranted by the null data. The null data used by the gap statistic does not necessarily preserve the spatial smoothness of fMRI data, particularly when the null data is generated by uniformly sampling over the range of observed values. This may lead to an overestimation of clusters. In this study, we therefore generated fMRI-specific null data that explicitly preserved spatial smoothness. The optimal number of clusters under the gap statistic was chosen as the smallest value of K such that $gap_K \geq gap_{K+1} - se_{K+1}$, where gap_K and se_K denote the mean and standard error of the gap value, respectively, for the clustering solution with K clusters (Tibshirani et al. 2001).

S2. Simulation of Insula-like Synthetic Data

Insula-like synthetic data comprising $K = 1$, 2 or 3 clusters were generated to quantify the performance of the cluster evaluation criteria. The synthetic data were generated at the level of the $N \times 5$ PCA matrix (Figure 1), where N denotes the number of insula voxels and the 5 columns of this matrix denote PCA components. Each insula voxel was randomly assigned to one of K clusters defined in five-dimensional space (5 PCA components). Clusters were equally sized, and thus comprised approximately N/K voxels. Two cases were considered: i) *nil cluster separation* (null case) in which the centre of each cluster was separated by a negligible distance in the five-dimensional space, and thus clusters substantially overlapped and were virtually indistinguishable; ii) *typical cluster separation* in which the center of each cluster was randomly chosen such that clusters were separated on average by the same distance as the clusters identified in the fMRI data for the relevant value of K. In this way, the synthetic data comprised clusters that were distinguishable to the same extent as putative clusters found in the insula. If the ith voxel belonged to cluster $k \in \{1, \dots, K\}$, then element (i, j) of the $N \times 5$ PCA matrix was populated with a random sample from a Gaussian distribution with mean $\mu_k(j)$ and unity variance, where $\boldsymbol{\mu}_k = [\mu_k(1), \dots, \mu_k(5)]$ denotes the center of cluster k. The nil cluster separation case enabled evaluation of whether no clusters would be found when no clusters were present (specificity), while the typical cluster separation case enabled evaluation of whether the correct number of clusters would be found when clusters were present (sensitivity). For each value of $K = 1$, 2 and 3, a total of 100 PCA matrices were simulated by randomly sampling from the Gaussian distribution described above and cluster analysis was performed on each matrix independently.

S3. Validation of Silhouette, Calinski-Harabasz and Gap Statistic

The gap statistic correctly predicted the number of clusters in the insula-like synthetic data, whereas the silhouette and Calinski-Harabasz criteria yielded poor specificity, meaning that more than one cluster was suggested for cases where the ground truth comprised no clusters (Supplementary Figure S2). These performance evaluation results therefore afforded some confidence in the accuracy of the gap statistic, but not the other two cluster evaluation criteria. However, given that most previous studies report that the insula comprises 2 or 3 clusters (Table 1), we considered the suggestion of 8 or more subregions unexpectedly high. Furthermore, we hypothesized that if the functional connectivity diversity of the insula can indeed be validly parsed into 8 or more subregions, then modeling this diversity as a continuum of variation may provide a more parsimonious representation.

It is important to remark that while we found that the gap statistic performed well on the synthetic data, this cannot be assumed to guarantee accurate performance of the gap statistic on the empirical fMRI data, since the synthetic data provided only an approximate match to the fMRI data. For example, the synthetic data was sampled from a Gaussian distributed (Supplementary Material S2),

whereas in practice, we observed that data points defined by the top-five PCA components form clusters that are nonlinear and distributed as ellipses, spirals and other highly non-convex shapes. This nonlinearity may challenge the performance of the gap statistic. Moreover, the null data that is used by the gap statistic does not preserve the spatial smoothing intrinsic to fMRI data, which is due to the unavoidable spatial blur caused by the point spread function, or explicit smoothing performed as part of data preprocessing. Spatial smoothing can result in the formation of spurious cluster structure, and thus any null data should ideally comprise the same extent of smoothing as the actual data.

Given these considerations, we aimed to develop a null model to generate null data that was explicitly matched to the characteristics of fMRI data. This enabled us to determine whether the unexpectedly large number of insula subregions predicted by the gap statistic was spurious and due to the reliance of this statistic on null data that does not preserve properties of fMRI data.

S4. Assessing Modular Structure with the Modularity Q score

Group consensus matrices (insula voxels × insula voxels) were mapped for the right and left insula, where element (i, j) of the consensus matrices stored the proportion of individuals for which insula voxels i and j comprised the same insula subregion. Newman's spectral community detection algorithm (Newman and Mark 2006; Newman 2013) was employed to delineate modules in the consensus matrices, and thus delineate insula subregions that represent a group consensus. The extent to which the consensus matrices showed modular structure was quantified with the modularity Q score (Clauset et al. 2004; Newman and Mark 2006),

$$Q = \frac{1}{2m}\sum_{ij=1}^{N}(\omega_{ij} - \gamma\frac{k_i k_j}{2m})\delta\,(c_i, c_j)$$

where N denotes the total number of insula voxels, c_i denotes the module (community) to which voxel i belongs, ω_{ij} denotes the consensus matrix, $m = \sum_{i,j=1}^{N}\omega_{ij}\,/2$, $k_i = \sum_{j=1}^{N}\omega_{ij}$ and $\delta\,(c_i, c_j) = 1$ if insula voxels i and j comprise the same module, otherwise $\delta\,(c_i, c_j) = 0$. The resolution parameter γ was kept at its default value of 1, which is the most commonly used value and leads to a natural partition (Reichardt and Bornholdt 2006).

Under the null hypothesis of absence of any modular structure (i.e. no group-level clusters): i) putative insula subregions show no concordance between individuals, and thus ω_{ij}=0.5, $k_i = k_j = (N-1)/2$; and, ii) the consensus matrix comprises one module incorporating all voxels, and thus $\delta\,(c_i, c_j) = 1$. Under these two conditions, it can be shown that,

$$Q = \frac{2}{N(N-1)}\sum_{i,j=1}^{N}\left(\frac{1}{2} - \gamma\frac{(N-1)^2}{4} \times \frac{2}{N(N-1)}\right)$$

$$= \frac{2}{N(N-1)}\left(\frac{1}{2} - \gamma\frac{(N-1)^2}{4} \times \frac{2}{N(N-1)}\right) \times N(N-1)$$

When N is very large, $N \cong N - 1$, and thus the above expression simplifies to

$$Q = 1 - \gamma$$

Thus, $Q = 0$ when γ=1, which was a resolution parameter used in our study. Therefore, Q scores substantially exceeding 0 were taken as evidence of non-random modular structure.

S5. Cluster Evaluation Measures

To quantify the quality of differentiation between clusters, we first considered the *intra-cluster distance*, denoted with W and defined as the sum of the Euclidean distances between all voxels that comprise the same cluster. For a cluster solution comprising K clusters,

$$W_K = \sum_{k=1}^{K} w_k \,, \qquad w_k = \sum_{u \neq v} \frac{2 d_{uv} \delta_{m_u = m_v = k}}{n_k (n_k - 1)},$$

where K denotes the total number of clusters, d_{uv} is the Euclidean distance between voxels u and v in the five-dimensional space of the $N \times 5$ PCA-reduced connectivity matrix; m_u and m_v are the cluster indices of voxels u and v, respectively; n_k is the number of voxels comprising cluster k; and, $\delta_{m_u = m_v = k} = 1$ if voxels u and v comprise cluster k, otherwise $\delta_{m_u = m_v = k} = 0$. The intra-cluster distance bears much similarity to the within-cluster dispersion measure associated with the gap statistic (Tibshirani et al. 2001). Indeed, W is precisely the distance measure that defines the *weighted* gap statistic (Yan and Ye 2007). A limitation of quantifying cluster separation solely in terms of intra-cluster distances is that the extent of differentiation *between* clusters is overlooked. Clusters that are well differentiated are typically characterized by low intra-cluster distances and high inter-cluster distances. We therefore considered two additional measures based on both the intra- and inter-cluster distance. The inter-cluster distance is defined as,

$$U_K = \frac{1}{L_K} \sum_{u \neq v} d_{uv} \, \delta_{m_u \neq m_v} \,,$$

where $L_K = \sum_{k_1 \neq k_2 \mid k = 1, \ldots, K} n_{k_1} n_{k_2}$ is total number of inter-cluster pairs of voxels; and, $\delta_{m_u \neq m_v} = 1$ if voxels u and v are not in the same cluster, otherwise $\delta_{m_u \neq m_v} = 0$. The inter-cluster distance is not defined for clusters solutions comprising only one cluster ($K = 1$). The ratio of W_K to U_K yields the *normalized intra-to-inter-cluster distance*,

$$W_K^{norm} = W_K / U_K, \qquad K > 1,$$

and the *difference between the inter- and intra-cluster distances* gives,

$$W_K^{diff} = W_K - U_K, \qquad K > 1.$$

We thus defined three measures to evaluate cluster separation. While W is applicable to all cluster solutions, W^{norm} and W^{diff} are only defined for cluster solutions comprising more than one cluster. A schematic of these three measures is shown in Supplementary Figure S3.

S6. Validation of W, W^{norm} and W^{diff}

Following the validation of the classic cluster evaluation criteria (Supplementary Material S3), insula-like synthetic data were once again simulated and the ground truth number of clusters was compared to the number of clusters suggested by W, W^{norm} and W^{diff}. The null data used for this evaluation included clusters to mimic the fact that repositioning the insula to random gray matter locations may have resulted in the repositioned insula straddling multiple cortical regions. The repositioned insula was therefore likely to comprise clusters corresponding to the regions straddled, although it was unlikely for these clusters to match putative subregions of the true insula. Consistent with the *in vivo* experiments, $T = 100$ null samples were generated to estimate an empirical null distribution. Supplementary Figure S3 shows the performance of W, W^{norm} and W^{diff} in delineating the ground truth number of clusters in the insula-like synthetic data. It can be seen that W and W^{norm} provided adequate specificity, correctly indicating the absence of clusters in more than 90% of trials for the nil separation case. However, the specificity of W^{diff} was poor, often estimating two of three clusters in the absence of any. The highest sensitivity was provided by W^{norm}, as evident from the typical cluster separation case in Supplementary Figure S3, panel C. The W^{norm} measure correctly identified the ground truth number of clusters in 90% of trials when the true number of clusters was $K = 1$, 100% of trials when $K = 2$ and 99% of trials when $K = 3$. The W measure yielded comparable performance, but had difficulty in differentiating whether two or three clusters were optimal when the ground truth comprised $K = 3$ clusters. Therefore, while we considered all three measures, we placed the most confidence in W^{norm} based on the findings of our evaluation using synthetic data.

It is important to remark that the gap statistic (Supplementary Figure S2) marginally outperformed W^{norm} (Supplementary Figure S3) in determining the correct number of clusters in the synthetic data. It might therefore be argued that the gap statistic should be preferred over W^{norm} or any of the other W measures to determine the optimal number of insula's subregions in the *in vivo* data. However, it is crucial to remember that the gap statistic is benchmarked against generic null data that is not matched to the spatial and temporal properties of fMRI. Therefore, while the gap statistic performed well on the Gaussian-distributed synthetic data, its performance may deteriorate for smoothed data with more complex distributions, since the null model used by the gap statistic may not be able to preserve data smoothness and complex distributional properties.

S7. Canonical Correlation Analysis

Canonical correlation analysis (CCA) was used to investigate whether inter-individual variation in diversity curves explained variance across a range of behavioral measures. CCA was performed on the parameters describing the piecewise linear function fitted to each individual's diversity curve. We selected the two model parameters with good within-subject replicability (Intraclass correlation coefficient ICC > 0.5; Bartko 1966); namely, the slope of the first line segment (m_1) and the intercept

term (a). The ICC for each model parameter is shown in Supplementary Figure S6. We performed a second CCA on all six model parameters as well as an estimate of the insula's cortical thickness for each individual. Cortical thickness estimates were sourced from the Human Connectome Project based on FreeSurfer version 5.2, recon-all pipeline, described in detail elsewhere (Glasser et al. 2013). The CCA estimated the canonical coefficients (weights) $A \in \mathbb{R}^{P\times P}$ and $B \in \mathbb{R}^{40\times P}$ to maximize the correlation between the latent canonical scores $U \in \mathbb{R}^{N\times P}$ (diversity curve parameters) and $V \in \mathbb{R}^{N\times P}$ (behavioral measures), where $U = X \times A$, $V = Y \times B$, and N denotes the number of individuals included in the CCA and P denotes the number of model parameters. The nth column of U was correlated with the n th column of V (Pearson correlation) to yield P correlation coefficients corresponding to the P CCA modes. Permutation testing was then used to estimate familywise-error corrected p-values for these P correlations. The rows of Y were randomly permuted and CCA was performed on the permuted matrices. This was repeated independently for 10,000 permutations and the maximum of the P correlation coefficients for each permutation was recorded to generate an empirical null distribution. The p-value for each CCA mode was given by the proportion of permutations with a maximum correlation that exceeded or equaled the mode's correlation in the unpermuted data. The threshold of statistical significance was $p < 0.05$. Finally, *post hoc* analysis was performed to map the PCA components back to single behavioral measure and thereby rank the measures according to their importance to any significant CCA mode. Each of the behavioral measures was separately correlated with the canonical scores (V) of any significant CCA mode, resulting in groups of behaviors that were either positively or negatively correlated with the CCA mode.

Supplementary Figures

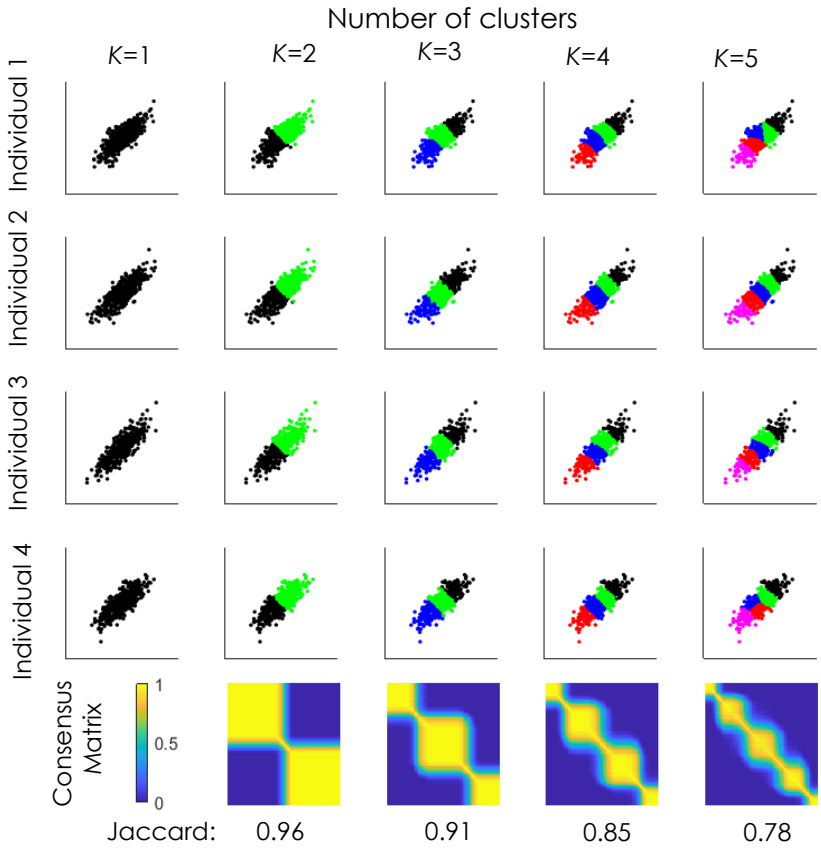


Figure S1. Example of the identification of spurious clusters showing high concordance across individuals. Data were generated by independently drawing 500 samples from a bivariate Gaussian distribution with unit standard deviation and covariance of 0.6. This was repeated to generate an independent dataset for each of 100 hypothetical individuals. The first four rows show the datasets generated for four example individuals. While a liner relation is evident, it can be seen that the data for each individual are inherently un-clustered. The data for each individual were clustered into $K = 1$, 2, 3, 4 and 5 clusters with the k-means clustering algorithm. Data points comprising the same cluster are shown with the same color. To quantify the extent to which the identified clusters were concordant (consistent) between the 100 individuals, consensus matrices were generated (bottom row) and the Jaccard index computed for the $K = 2$, 3, 4 and 5 cluster solutions. Element (i, j) of the consensus matrices shows the proportion of the 100 individuals for which data points i and j comprise the same cluster. The consensus matrices show clear modular (block) structure, providing evidence for concordant clusters between the 100 individuals. The rows/columns of the consensus matrices are ordered to accentuate this block structure. Furthermore, while the data was inherently un-clustered and comprised no true clusters, the k-means clustering algorithm reproducibly generated clusters with high Jaccard values across individuals: 0.96: ($K = 2$), 0.91($K = 3$), 0.85 ($K = 4$), 0.78 ($K = 5$).

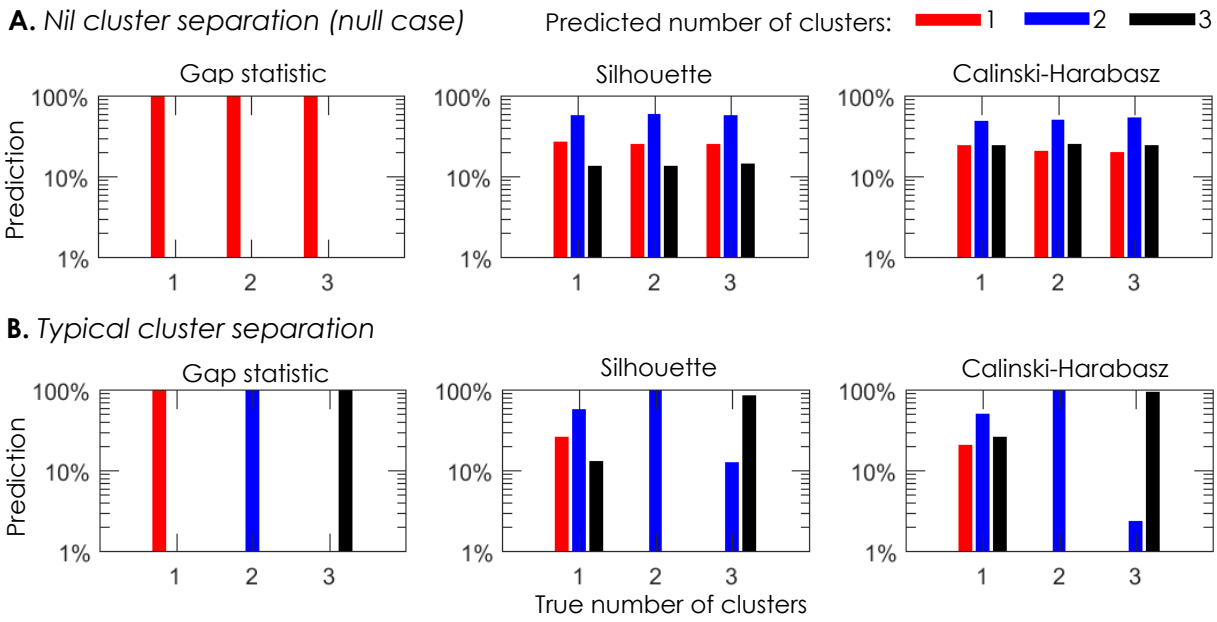


Figure S2. Validation of classic cluster evaluation criteria on insula-like synthetic data.
Insula-like synthetic data was generated to evaluate the performance of three classic cluster evaluation measures in determining the ground truth number of clusters ($K = 1$, 2 or 3, horizontal axis). Two types of synthetic data were simulated: i) nil cluster separation (null case) in which clusters were not separated and thus indistinguishable (Panel **A**); and, ii) typical cluster separation in which clusters were separated on average by the same distance as the insula clusters identified in the empirical fMRI data (Panel **B**). The nil cluster separation case enabled evaluation of whether no clusters would be found when no clusters were present (specificity), while the typical cluster separation case enabled evaluation of whether the correct number of clusters would be found when clusters were present (sensitivity). A total of 100 synthetic datasets were generated for each ground truth number of clusters. The bar plots show the percentage of synthetic datasets that were predicted to comprise 1 (red bar), 2 (blue) or 3 (black) clusters for each of the three cluster evaluation measures. Note that the one cluster case (red bar) denotes $K = 1$ or $K \geq 4$ since one-cluster solution is not defined for silhouette and Calinski-Harabasz criteria. The gap statistic accurately predicted the ground truth number of clusters with flawless specificity (Panel **A**, leftmost) and sensitivity (Panel **B**, leftmost), whereas the silhouette (Panel **A**, middle) and Calinski-Harabasz (Panel **A**, rightmost) criteria yield poor specificity and suggested two or more clusters when the ground truth comprised no clusters. In the typical cluster separation case (Panel **B**), the silhouette (middle) and Calinski-Harabasz (rightmost) criteria showed slightly improved sensitivity when $K = 2$ and $K = 3$. Note that the vertical axis of the bar plots is logarithmic.

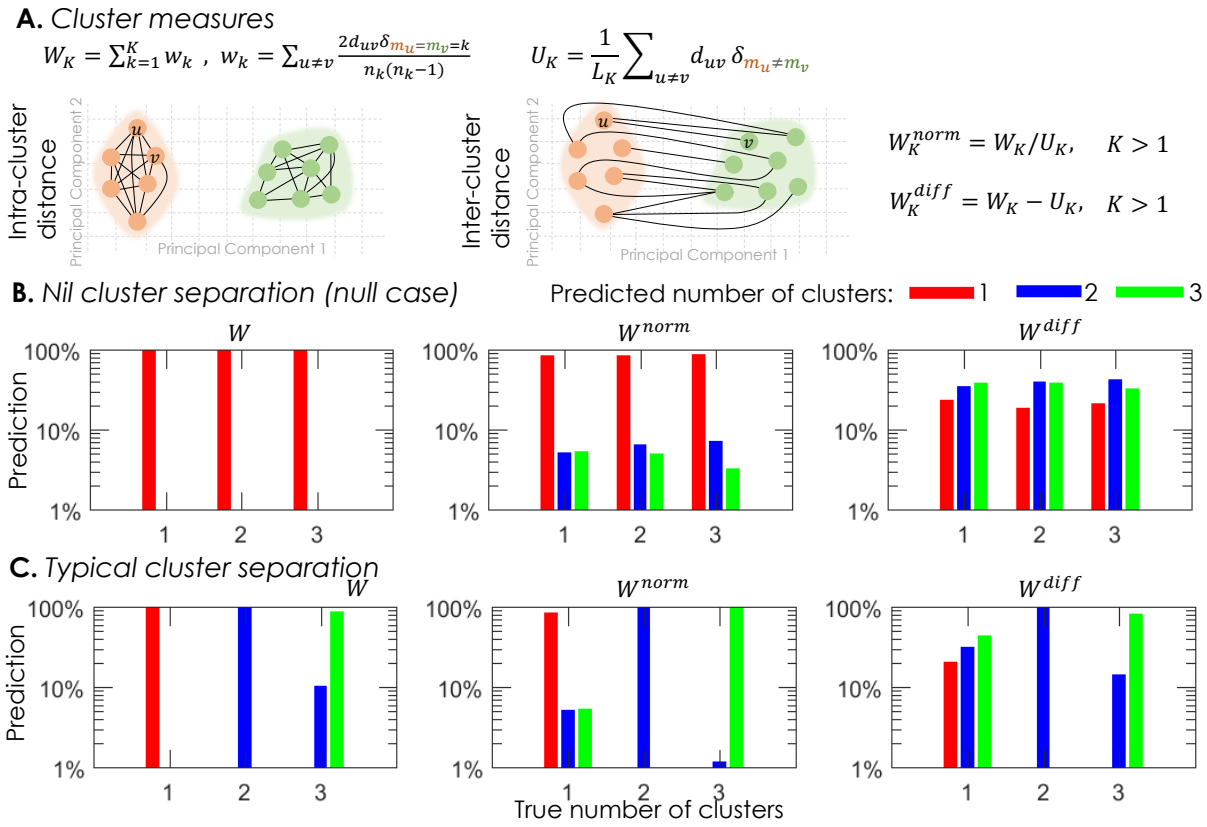


Figure S3. Cluster evaluation measures and their validation on insula-like synthetic data.

Panel A: Three cluster evaluation measures were devised to assess the quality of cluster separation and determine the optimal number of clusters: i) intra-cluster distance (W_K); ii) the ratio of intra-to-inter cluster distances (W_K^{norm}); and, iii) the difference between the intra- and inter-cluster distances (W_K^{diff}). Illustration of intra- (left image) and inter-cluster (right) distances for two hypothetical clusters defined in two dimensions. Solid circles represent data points (insula voxels) and shading denotes distinct clusters. The intra-cluster distance (W_K) is the sum of the average distances between data points in each cluster, while the inter-cluster distance (U_K) is the average distance between pairs of data points in distinct clusters. The total number of clusters is denoted with K and $k = 1,\ldots,K$ indexes specific clusters. In this example, $K = 2$. Note that d_{uv} denotes the distance between nodes u and v, L_K is total number of inter-cluster pairs, δ is the binary indicator function and n_k is the number of data points in cluster k. **Panels B & C:** Insula-like synthetic data was generated to evaluate the performance of the cluster evaluation measures in determining the ground truth number of clusters ($K = 1$, 2 or 3, horizontal axis). Two types of synthetic data were simulated: i) nil cluster separation (null case) in which clusters were not separated and thus indistinguishable (Panel **B**); and, ii) typical cluster separation in which clusters were separated on average by the same distance as the insula clusters identified in the empirical fMRI data (Panel **C**). The nil cluster separation case enabled evaluation of whether no clusters would be found when no clusters were present (specificity), while the typical cluster separation case enabled evaluation of whether the correct number of clusters would

be found when clusters were present (sensitivity). A total of 100 synthetic datasets were generated for each ground truth number of clusters. The bar plots show the percentage of synthetic datasets that were predicted to comprise 1 (red bar), 2 (blue) or 3 (green) clusters for each of the three cluster evaluation measures. Note that the one cluster case (red bar) denotes $K = 1$ or $K \geq 4$. It can be seen that W and W^{norm} provided adequate specificity, correctly indicating the absence of clusters in more than 90% of trials for the nil separation case. However, the specificity of W^{diff} was poor, often estimating two of three clusters in the absence of any clusters (Panel **B**). The highest sensitivity was provided by W^{norm}. The W^{norm} measure correctly identified the ground truth number of clusters in 90% of trials when the true number of clusters was $K = 1$, 100% of trials when $K = 2$ and 99% of trials when $K = 3$. The W measure yielded comparable performance, but had difficulty in differentiating whether two or three clusters were optimal when the ground truth comprised $K = 3$ clusters (Panel **C**). Note that vertical axis of the bar plots is logarithmic.

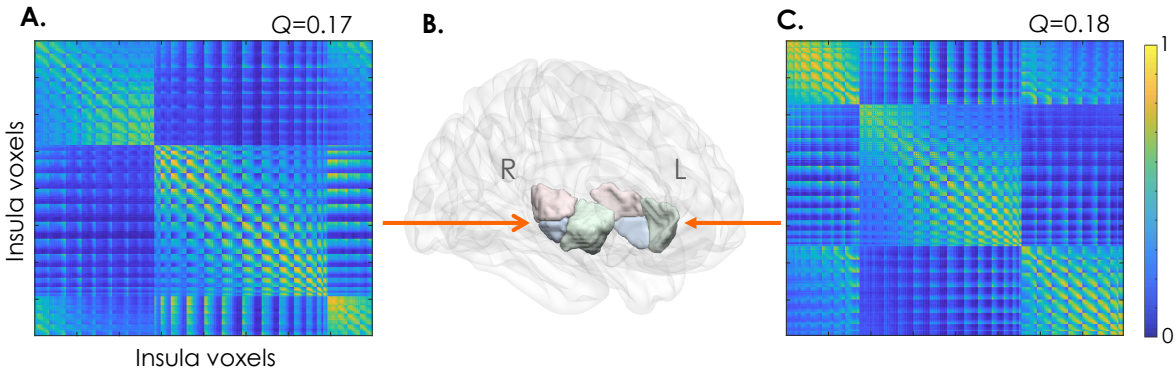


Figure S4. Tripartite parcellation of the human insula cortex based on resting-state functional connectivity. Consensus matrices for the right (Panel **A**) and left (Panel **C**) insula as well as anatomical visualization of the parcellations (Panel **B**). Functional connectivity was mapped between each insula voxel and all gray matter voxels, resulting in a whole-brain connectivity fingerprint for each insula voxel. Cluster analysis (Ward's linkage) was used to partition insula voxels that shared similar connectivity fingerprints into 3 clusters. Clusters were delineated independently for each individual. Group-level parcellations were then derived by forming a consensus matrix for the right insula (Panel **A**) and left insula (Panel **C**). Both consensus matrices comprise 3 modules (clusters). Voxels with high probabilities (yellow tones) consistently belong to the same module for all individuals. Both consensus matrices were modular, with Q = 0.17 for right insula and Q = 0.18 for left insula. Probability maps were converted to binary (hard) segmentations to delineate discrete subregions: a dorsal-posterior (pink), ventral-medial (blue) and ventral-anterior (green) subdivisions (Panel **B**).

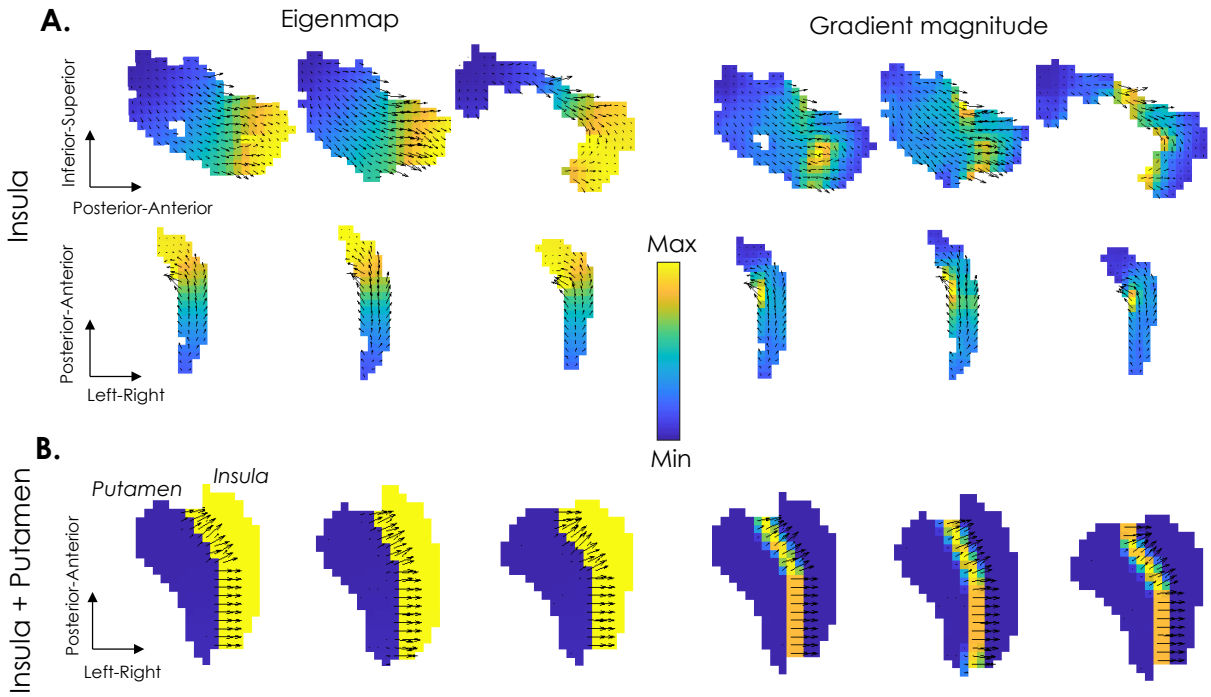
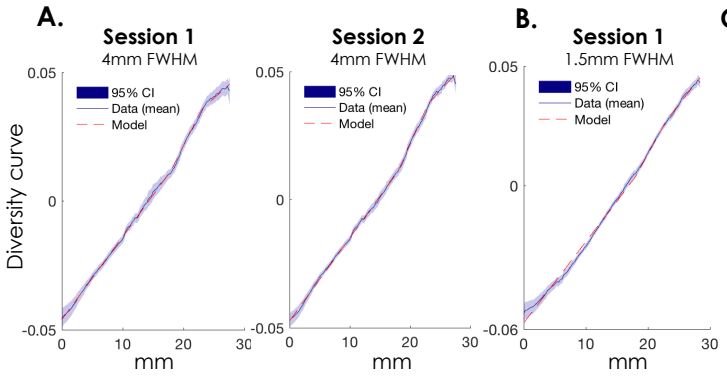


Figure S5. Group-consensus Laplacian eigenmaps for the insula cortex and the insula-putamen benchmark. Group-consensus eigenmaps for the insula (Panel **A**) were compared to benchmark eigenmaps for the case of two regions (insula-putamen combined, Panel **B**). Eigenmap values were mapped to the voxels of the insula and insula-putamen to enable anatomical visualization. Eigenmaps correspond to the Fiedler eigenvector (left images) and the magnitude of eigenmap's gradient (right images). Arrows indicate the gradient direction for each voxel and arrow lengths indicate gradient magnitude. Eigenmap gradients were computed using the Sobel operator. The insula's connectional diversity is arranged as a continuum along a dorsal-posterior to ventral-anterior orientation. It can be seen that the gradient magnitude in the most posterior part of insula is relatively small but gradually increases, until reaching a maximum in the middle-to-anterior insula. In contrast, the combined insula-putamen shows an abrupt transition corresponding to the anatomical boundary between these two regions.



C. Replicability of model parameters across fMRI sessions

Model parameters	Session 1 4mmFWHM	Session 2 4mmFWHM	ICC
Constant a	-0.05	-0.05	**0.54**
Breakpoint $k1$	15.11	15.02	0.10
Breakpoint $k2$	22.34	22.28	0.12
Slope $m1$	0.004	0.003	**0.55**
Slope $m2$	0.006	0.006	0.19
Slope $m3$	0.002	0.006	0.01

ICC: intraclass correlation coefficient

Figure S6. Within-subject replication of diversity curves and the effect of spatial smoothing. **Panel A:** Group-averaged diversity curves for the first (left axis) and second (right axis) fMRI sessions. Solid blue lines indicate the group-averaged diversity curves for 100 individuals. Dashed red lines indicate the piecewise linear function fitted to the group-averaged diversity curves. The piecewise linear function comprised two breakpoints (k_1 and k_2) and three line segments, with slopes denoted as m_1, m_2 and m_3. **Panel B:** Group-averaged diversity curve (blue line) and piecewise linear fit (dashed red line) for diversity curves that were mapped with minimally smoothed fMRI data (FWHM: 1.5 mm). The insula's diversity curve is consistent between fMRI data smoothed with 1.5 and 4 mm FWHM. In contrast, the extent of smoothing substantially influenced the number of insula subregions identified with clustering algorithms (Figure 4). **Panel C:** For each of 100 individuals, diversity curves were mapped for each of two separate fMRI sessions. The intra-class correlation coefficient (ICC; Bartko 1966) was used to evaluate the within-subject replicability of the six parameters describing the piecewise linear functions fitted to the two separate diversity curves mapped for each individual. The intercept term (a) and the slope of first line segment (m_1) show good within-subject replicability (ICC > 0.5), whereas the replicability of the other parameters is low.

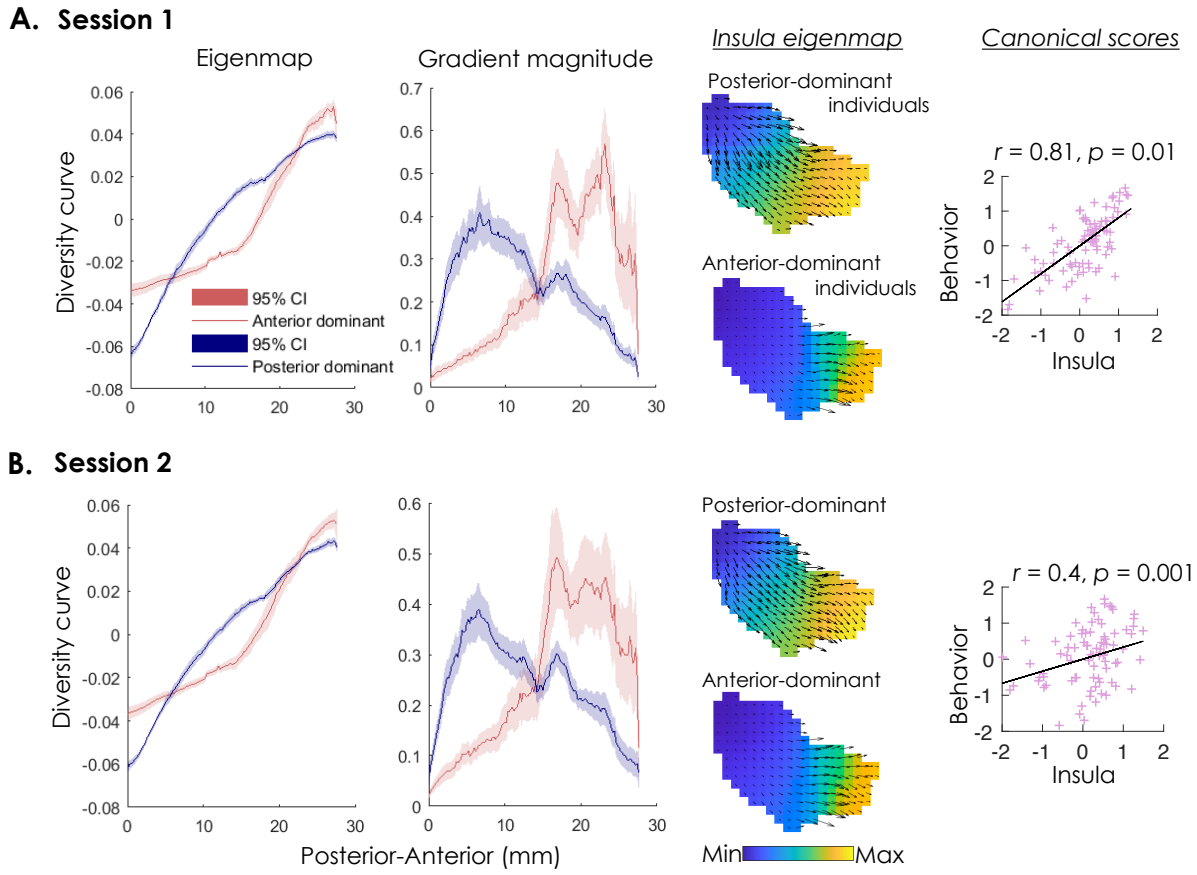


Figure S7. Validation of CCA mode in second fMRI session. Canonical correlation analysis (CCA) was performed to test whether inter-individual variation in insula diversity was associated with variation in behavioral measures. The CCA was performed using data from the first fMRI session (Panel **A**). The canonical coefficients fitted using data from the first session were then applied to data from the second fMRI session (Panel **B**) to assess the within-subject replicability of the CCA model. Note that canonical coefficients were not re-fitted to the data from the second session. The second session was rather used to validate the canonical coefficients fitted using data from the first session. In other words, canonical coefficients fitted using the first session were imposed on the CCA in the second session. Consistent with the first session (Panel **A**), the Pearson correlation between the canonical scores for the second fMRI session is significant (Panel **B**, r=0.4, p=0.001) and shows a similar pattern of co-variation among individuals. Diversity curves for the group of anterior- (red curves) and posterior-dominant (blue) individuals are consistent between the two fMRI sessions. Anterior-dominant individuals are defined by diversity curves that are positively correlated with the canonical coefficients. These individuals show greater connectional diversity within the anterior insula. Posterior-dominant individuals are defined conversely. Eigenmaps mapped to the anatomical space of the insula also show good consistency across fMRI sessions.

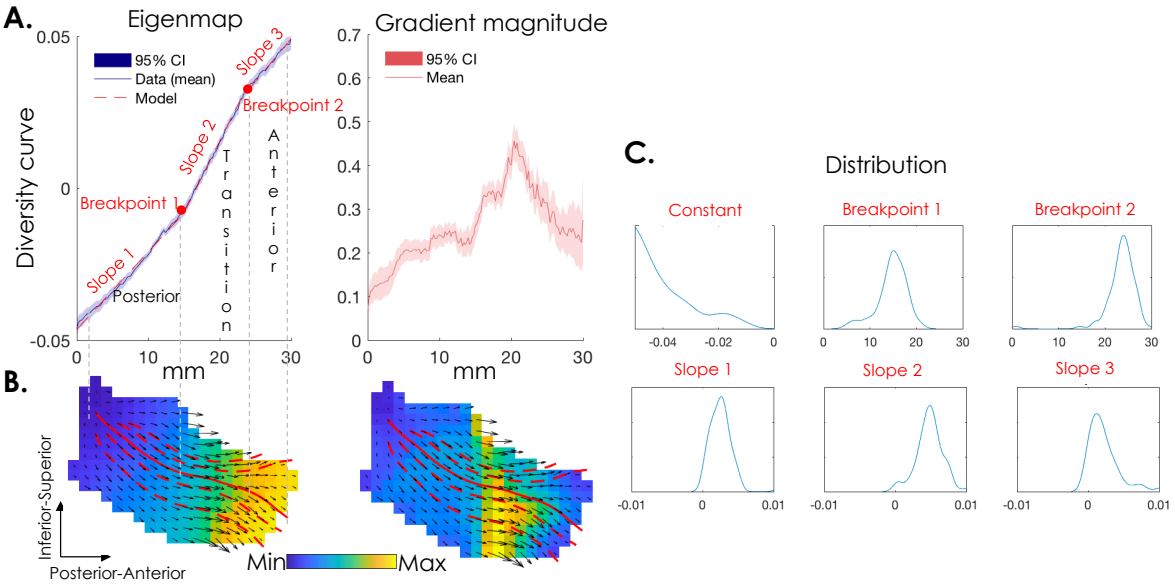


Figure S8. Diversity curves for the left insula. **Panel A:** Diversity curves for the left insula based on the Fiedler eigenvector (blue curve, left image) and the magnitude of its gradient (red curve, right image). Consistent with the right insula, diversity curves for the left insula were modeled with piecewise linear functions (dashed red lines) comprising two breakpoints (solid red circles). The slope of the middle line segment of the insula's diversity curve ($m_2 = 0.005$) is marginally (×2) steeper than the other two segments ($m_1 = 0.0025$, $m_3 = 0.0031$), suggesting a gradual 'transition zone' between the anterior and posterior portions of the insula. Shading denotes 95% confidence intervals (CI). **Panel B:** Eigenmap values were mapped to the voxels of the insula to enable anatomical visualization of the eigenmaps. The dynamic range of eigenmap values is uniformly distributed across the spatial extent of the insula along a curvilinear gradient indicated by the streamlines (red lines). The streamlines superposed onto the anatomical images represent trajectories of maximal change in the eignemaps. Streamlines were propagated in the gradient field estimated from the eigenmaps. Arrows indicate the gradient direction estimated for each voxel and arrow lengths convey gradient magnitude. Diversity curves were mapped with respect to the longest streamline (solid red line). **Panel C:** Distributions characterizing inter-individual variation in the model parameters describing the piecewise linear functions fitted to the diversity curves.

Supplementary Tables

Table S1.

List of 59 selected behavioral measures.

Category	Intuitive Name	Formal Name	Psychological Test
Alertness	MMSE	MMSE_Score	Mini Mental Status Exam
	PSQI	PSQI_Score	Pittsburgh Sleep Questionnaire
	TooCold	PSQI_TooCold	Pittsburgh Sleep Questionnaire
	TooHot	PSQI_TooHot	Pittsburgh Sleep Questionnaire
	BadDream	PSQI_BadDream	Pittsburgh Sleep Questionnaire
	Pain	PSQI_Pain	Pittsburgh Sleep Questionnaire
Cognition	EpisodicMemory	PicSeq_AgeAdj	NIH Toolbox Picture Sequence Memory Test
	CognitiveFlexibility	CardSort_AgeAdj	NIH Toolbox Dimensional Change Card Sort
	Inhibition	Flanker_AgeAdj	NIH Toolbox Flanker Inhibitory Control and Attention
	FluidIntelligence	PMAT24_A_CR	Penn Progressive Matrices
	SkippedItems	PMAT24_A_SI	Penn Progressive Matrices
	ReactionTime	PMAT24_A_RTCR	Penn Progressive Matrices
	ReadingDecoding	ReadEng_AgeAdj	NIH Toolbox Oral Recognition Test
	LanguageComprehension	PicVocab_AgeAdj	NIH Toolbox Picture Vocabulary Test
	ProcSpeed	ProcSpeed_AgeAdj	NIH Toolbox Pattern Comparison Processing Speed Test
	Impulsivity200	DDisc_AUC_200	Delay Discounting
	Impulsivity40K	DDisc_AUC_40K	Delay Discounting
	SustainedAttention-SEN	SCPT_SEN	Short Penn Continuous Performance Test
	SustainedAttention-SPEC	SCPT_SPEC	Short Penn Continuous Performance Test
	WorkingMemory	ListSort_AgeAdj	NIH Toolbox List Sorting Working Memory Test
Emotion	EmotionRecognition-CR	ER40_CR	Penn Emotion Recognition Test
	EmotionRecognition-CRT	ER40_CRT	Penn Emotion Recognition Test
	EmotionRecognition-Anger	ER40ANG	Penn Emotion Recognition Test
	EmotionRecognition-Fear	ER40FEAR	Penn Emotion Recognition Test
	EmotionRecognition-Happy	ER40HAP	Penn Emotion Recognition Test
	EmotionRecognition-Neutral	ER40NOE	Penn Emotion Recognition Test
	EmotionRecognition-Sad	ER40SAD	Penn Emotion Recognition Test
	Anger-Affect	AngAffect_Unadj	NIH Toolbox Anger-Affect Survey
	Anger-Hostility	AngHostil_Unadj	NIH Toolbox Anger-Hostility Survey
	Anger-Aggression	AngAggr_Unadj	NIH Toolbox Anger-Physical Aggression Survey
	Fear-Affect	FearAffect_Unadj	NIH Toolbox Fear-Affect Survey
	Fear-Somatic	FearSomat_Unadj	NIH Toolbox Fear-Somatic Arousal Survey
	Sadness	Sadness_Unadj	NIH Toolbox Sadness Survey
	LifeSatisf	LifeSatisf_Unadj	NIH Toolbox General Life Satisfaction Survey
	MeanPurp	MeanPurp_Unadj	NIH Toolbox Meaning and Purpose Survey
	PosAffect	PosAffect_Unadj	NIH Toolbox Positive Affect Survey
	Friendship	Friendship_Unadj	NIH Toolbox Friendship Survey
	Loneliness	Loneliness_Unadj	NIH Toolbox Loneliness Survey

	PercHostil	PercHostil_Unadj	NIH Toolbox Perceived Hostility Survey
	PercReject	PercReject_Unadj	NIH Toolbox Perceived Rejection Survey
	EmotSuppp	EmotSupp_Unadj	NIH Toolbox Emotional Support Survey
	InstruSupp	InstruSupp_Unadj	NIH Toolbox Instrumental Support Survey
	PercStress	PercStress_Unadj	NIH Toolbox Perceived Stress Survey
	SelfEfficacy	SelfEff_Unadj	NIH Toolbox Self-Efficacy Survey
Motor	WalkEndurance	Endurance_AgeAdj	NIH Toolbox 2-minute Walk Endurance Test
	GaitSpeed	GaitSpeed_Comp	NIH Toolbox 4-Meter Walk Gait Speed Test
	Dexterity	Dexterity_AgeAdj[1]	NIH Toolbox 9-hole Pegboard Dexterity Test
	GripStrength	Strength_AgeAdj	NIH Toolbox Grip Strength Test
Personality	Agreeableness	NEOFAC_A	Five Factor Model (NEO-FFI)
	Openness	NEOFAC_O	Five Factor Model (NEO-FFI)
	Conscientiousness	NEOFAC_C	Five Factor Model (NEO-FFI)
	Neuroticism	NEOFAC_N	Five Factor Model (NEO-FFI)
	Extraversion	NEOFAC_E	Five Factor Model (NEO-FFI)
Sensory	Olfactory	Odor_AgeAdj	NIH Toolbox Odor Identification
	PainInterf	PainInterf_Tscore	NIH Toolbox Pain Interference Survey
	Gustatory	Taste_AgeAdj	NIH Toolbox Regional Taste Intensity
	ContrastSensitivity-Log	Mars_Log_Score	Mars Contrast Sensitivity
	ContrastSensitivity-Errs	Mars_Errs	Mars Contrast Sensitivity
	ContrastSensitivity	Mars_Final	Mars Contrast Sensitivity

[1] Dexterity scores were multiplied by -1 so that higher scores denoted better motor dexterity.

Table S2.

Distribution across individuals in the optimal number of clusters (right insula) found with classic evaluation criteria (%).

	Cluster solution (*K*)									
	1	**2**	**3**	**4**	**5**	**6**	**7**	**8**	**9**	**10**
Gap statistic	0	0	0	0	1	7	13	20	19	40
Silhouette	0	3	1	2	8	35	25	12	3	11
C-H	0	5	0	1	12	25	22	18	14	3

C-H: Calinski-Harabasz

Table S3.

Correlation between measures of intra-scan head motion and the optimal number of clusters (right insula) indicated by W, W^{norm} and W^{diff}.

		$\boldsymbol{W}$	$\boldsymbol{W^{norm}}$	$\boldsymbol{W^{diff}}$
Absolute RMS	r-value	0.01	-0.05	-0.02
	p-value	0.94	0.65	0.79
Relative RMS	r-value	0.09	-0.02	-0.01
	p-value	0.36	0.83	0.93

RMS: Root-mean-square of the head motion translation parameters. P-value < 0.05 was deemed significant. FWHM: full width at half maximal of the Gaussian smoothing kernel.

Supplementary References

Alcauter S, Lin W, Keith Smith J, Gilmore JH, Gao W. 2015. Consistent anterior-posterior segregation of the insula during the first 2 years of life. Cereb Cortex 25:1176-1187.

Bartko JJ. 1966. The Intraclass Correlation Coefficient as a Measure of Reliability. Psychological Reports 19:3-11.

Calinski T, Harabasz J. 1974. A dendrite method for cluster analysis. Communications in Statistics 3:1-27.

Cauda F, Costa T, Torta DM, Sacco K, D'Agata F, Duca S, Geminiani G, Fox PT, Vercelli A. 2012. Meta-analytic clustering of the insular cortex: characterizing the meta-analytic connectivity of the insula when involved in active tasks. NeuroImage 62:343-355.

Cauda F, D'Agata F, Sacco K, Duca S, Geminiani G, Vercelli A. 2011. Functional connectivity of the insula in the resting brain. NeuroImage 55:8-23.

Chang LJ, Yarkoni T, Khaw MW, Sanfey AG. 2013. Decoding the role of the insula in human cognition: functional parcellation and large-scale reverse inference. Cereb Cortex 23:739-749.

Clauset A, Newman MEJ, Moore C. 2004. Finding community structure in very large networks. Physical Review E 70:066111.

Deen B, Pitskel NB, Pelphrey KA. 2011. Three systems of insular functional connectivity identified with cluster analysis. Cereb Cortex 21:1498-1506.

Glasser MF, Sotiropoulos SN, Wilson JA, Coalson TS, Fischl B, Andersson JL, Xu J, Jbabdi S, Webster M, Polimeni JR et al. 2013. The minimal preprocessing pipelines for the Human Connectome Project. NeuroImage 80:105-124.

Gordon AD. 1999. Classification, 2nd Edition (Chapman & Hall/CRC Monographs on Statistics & Applied Probability): Chapman and Hall/CRC.

Jakab A, Molnar PP, Bogner P, Beres M, Berenyi EL. 2012. Connectivity-based parcellation reveals interhemispheric differences in the insula. Brain Topogr 25:264-271.

Kelly C, Toro R, Di Martino A, Cox CL, Bellec P, Castellanos FX, Milham MP. 2012. A convergent functional architecture of the insula emerges across imaging modalities. NeuroImage 61:1129-1142.

Milligan GW, Cooper MC. 1985. An examination of procedures for determining the number of clusters in a data set. Psychometrika 50:159-179.

Moran LV, Tagamets MA, Sampath H, O'Donnell A, Stein EA, Kochunov P, Hong LE. 2013. Disruption of anterior insula modulation of large-scale brain networks in schizophrenia. Biol Psychiatry 74:467-474.

Nanetti L, Cerliani L, Gazzola V, Renken R, Keysers C. 2009. Group analyses of connectivity-based cortical parcellation using repeated k-means clustering. NeuroImage 47:1666-1677.

Newman ME. 2013. Spectral methods for community detection and graph partitioning. Physical Review E 88:042822.
Newman ME, Mark E. 2006. Modularity and community structure in networks. Proc Natl Acad Sci U S A 103:8577-8582.
Reichardt J, Bornholdt S. 2006. Statistical mechanics of community detection. Physical Review E 74:016110.
Rousseeuw PJ. 1987. Silhouettes: a graphical aid to the interpretation and validation of cluster analysis. Journal of computational and applied mathematics 20:53-65.
Ryali S, Chen T, Padmanabhan A, Cai W, Menon V. 2015. Development and validation of consensus clustering-based framework for brain segmentation using resting fMRI. J Neurosci Methods 240:128-140.
Ryali S, Chen T, Supekar K, Menon V. 2013. A parcellation scheme based on von Mises-Fisher distributions and Markov random fields for segmenting brain regions using resting-state fMRI. NeuroImage 65:83-96.
Tibshirani R, Walther G, Hastie T. 2001. Estimating the number of clusters in a data set via the gap statistic. Journal of the Royal Statistical Society: Series B (Statistical Methodology) 63:411-423.
Vercelli U, Diano M, Costa T, Nani A, Duca S, Geminiani G, Vercelli A, Cauda F. 2016. Node Detection Using High-Dimensional Fuzzy Parcellation Applied to the Insular Cortex. Neural Plast 2016:1938292.
Yamada T, Itahashi T, Nakamura M, Watanabe H, Kuroda M, Ohta H, Kanai C, Kato N, Hashimoto RI. 2016. Altered functional organization within the insular cortex in adult males with high-functioning autism spectrum disorder: evidence from connectivity-based parcellation. Mol Autism 7:41.
Yan M, Ye K. 2007. Determining the Number of Clusters Using the Weighted Gap Statistic. Biometrics 63:1031-1037.

CHAPTER 4

INSULA FUNCTIONAL CONNECTIVITY IN SCHIZOPHRENIA

Archival Report

Insula Functional Connectivity in Schizophrenia: Subregions, Gradients, and Symptoms

Ye Tian, Andrew Zalesky, Chad Bousman, Ian Everall, and Christos Pantelis

ABSTRACT

BACKGROUND: The insular cortex is connected to a diverse network of cortical and subcortical areas. This study aimed to investigate whether the diversity in functional connectivity across the insula's topography is altered in individuals with schizophrenia and relates to the clinical symptoms of the disorder.

METHODS: Insula-to-whole-brain functional connectivity was mapped using resting-state functional magnetic resonance imaging at the resolution of voxels in individuals with schizophrenia (n = 49) and healthy comparison individuals (n = 52). Diversity in functional connectivity across the insula's topography was represented as discrete subregions and gradients of continuous variation. Canonical correlation analysis was used to relate interindividual variation in insula connectivity to clinical symptoms.

RESULTS: Insula connectional diversity was parcellated into two subregions: dorsoanterior and ventroposterior. Compared with the healthy comparison group, subjects with schizophrenia were associated with an overall reduction in insula functional connectivity as well as reduced differentiation in connectivity profiles between these subregions. A significant interaction effect between diagnosis and insula subregion indicated that the anterior subregion in schizophrenia was connected with increased strength to the somatosensory, motor, occipital, and parietal cortices, whereas the posterior subregion showed increased connectivity with the thalamus and prefrontal cortex. Insula connectivity with the anterior cingulate and auditory cortices was significantly associated with cognitive impairment, negative symptoms, poor psychosocial functioning, and longer duration of illness (r = .64, p = .03).

CONCLUSIONS: Diversity in functional connectivity across the insula's rostrocaudal axis is reduced in schizophrenia, resulting in reduced differentiation between anterior and posterior insula. Interindividual variation in insula connectivity explains variability in some of the clinical symptoms of schizophrenia.

Keywords: Clustering, Diversity curve, Insular cortex, Parcellation, Resting-state fMRI, Schizophrenia

https://doi.org/10.1016/j.bpsc.2018.12.003

Functional dysconnectivity of the insular cortex is consistently observed in psychosis spectrum disorders, including individuals with first-episode psychosis (1–3), individuals with chronic schizophrenia (4,5), and individuals at high risk for the disorder (6–8). Specifically, the insula shows aberrant patterns of connectivity with the cingulate cortex as well as regions comprising the default mode network and central executive network (4–7). Most previous neuroimaging studies investigating the connectivity of the insula in schizophrenia have treated the insula as a single, homogeneous region (3) or have considered only its anterior aspect (4,5,7–9). In particular, neuroimaging data are typically averaged over all voxels comprising the insula to provide a summary characterization, and thus any potential variation in connectivity across the topography (spatial extent) of the insula may be overlooked. We refer to this topographic variation as connectional diversity. A region with greater connectional diversity shows greater variation across its topography with respect to the cortical and subcortical regions to which it connects.

Recently, functional and structural magnetic resonance imaging (MRI) studies have sought to characterize the insula's connectional diversity using one of two models: 1) discrete subregions (clusters) (10) or 2) continua of variation (diversity curves) (11). These studies have generally been limited to healthy individuals. According to the subregions model, the insula can be parcellated into clusters, where each cluster is associated with a distinct connectivity pattern. Many studies employing the subregions model suggest that the insula is best represented with a bipartite subdivision comprising anterior and posterior subregions (10,12–16), whereas other studies provide evidence of a tripartite clustering in which the anterior insula is further subdivided into dorsal and ventral components (4,17,18) as well as parcellations comprising more than three subdivisions (14,19–27). Particular subregions have been linked to specific aspects of cognition, emotion, and somatosensory sensations (18,28,29). More recently, it has been suggested that the insula's connectional diversity can be represented more parsimoniously as a continuum of gradual variation along a rostrocaudal axis, rather than with discrete subregions (30). Interindividual variation in the rate of variation along this axis of the insula has been found to explain significant variation in behavioral traits assessed in healthy adults (11).

© 2018 Society of Biological Psychiatry. Published by Elsevier Inc. All rights reserved.

ISSN: 2451-9022

The aim of the present study was to characterize the diversity in functional connectivity across the topography of the insular cortex in adults with schizophrenia. To this end, we acquired resting-state functional MRI (fMRI) data in individuals with schizophrenia and healthy comparison individuals and used these data to map the functional connectivity profile of each insula voxel with respect to all other cortical and subcortical voxels. We clustered insula voxels into distinct subregions based on similarity in their connectivity profiles as well as modeled variation in connectivity among insula voxels continuously using the recently proposed concept of a diversity curve. An individual's diversity curve quantifies how rapidly the insula's connectivity with the rest of the cortex changes per unit length along the insula's rostrocaudal axis (11). We then performed statistical analyses to compare the functional connectivity profiles of distinct insula subregions between the schizophrenia and healthy comparison groups. Finally, we assessed whether patterns of insula functional connectivity in the schizophrenia group were associated with interindividual variation in the severity of psychosis symptoms, cognition, and psychosocial functioning. Given the widespread reductions in functional connectivity previously reported in this cohort (31) and the known association between insula connectional diversity and cognitive-affective function (11), we hypothesized that schizophrenia would be associated with reduced insula connectional diversity and reduced segregation (differentiation) between the connectivity profiles of putative insula subregions. Our hypothesis is supported by evidence of reduced segregation on the global scale of whole-brain functional networks in the disorder (32) as well as loss of functional specialization within specific areas such as the prefrontal cortex (33). This is the first study to comprehensively characterize connectional pathology across the topography of the insula in individuals with schizophrenia.

METHODS AND MATERIALS

Participants, Image Acquisition, and Image Preprocessing

Participants. This study was approved by the Melbourne Health Human Research Ethics Committee (ID No. 2012.069). All participants gave written consent before participation. Individuals with established schizophrenia (n = 49, mean age 41.02 ± 9.93 years, 15 female subjects) and healthy comparison individuals matched for average age, sex, and handedness (n = 52, mean age 39.85 ± 10.46 years, 17 female subjects) were included in this study. The majority of individuals with schizophrenia (n = 44) were considered resistant to treatment (34) and currently prescribed and taking clozapine. The diagnosis of schizophrenia was further confirmed by the Mini International Neuropsychiatric Interview (35). Healthy comparison individuals were recruited from the local community. Individuals satisfying at least one of the following exclusion criteria were not considered: current or history of psychiatric diagnoses, substance dependence, mental retardation (IQ <70), first-degree relatives with psychiatric illness, neurological disorders, impaired thyroid function, diabetes, and other major medical conditions.

The severity of clinical symptoms was assessed using the Positive and Negative Syndrome Scale (PANSS) (36), Scale for the Assessment of Positive Symptoms (37), and Scale for Assessment of Negative Symptoms (SANS) (38) on the day of screening. For all individuals, social, occupational, and psychological functioning were measured with the Global Assessment of Functioning (GAF) (39), Social and Occupational Functioning Assessment Scale (SOFAS) (40), and Wechsler Adult Intelligence Scale for cognition (41) (Table 1). Antipsychotic dosage was converted to chlorpromazine equivalent dose using an established conversion methodology (42).

Table 1. Demographic and Clinical Characteristics

	Schizophrenia Group (n = 49)	Comparison Group (n = 52)	Statistic	p Value
Age, Years	41.02 (±9.93)	39.85 (±10.46)	t = 0.58	.56
Sex, Male/Female	34/15	35/17	χ^2 = 0.05	.82
Handedness, Right/Left	45/4	50/2	χ^2 = 0.84	.36
Current IQ	91.34 (±18.70)	111.51 (±14.04)	t = 5.91	< .001
GAF Score	47.85 (±13.50)	79.27 (±11.34)	t = 12.52	< .001
SOFAS Score	48.38 (±14.81)	79.44 (±11.63)	t = 11.66	< .001
Age at Illness Onset, Years	22.71 (±6.44)	—	—	—
Duration of Illness, Years	17.95 (±9.16)	—	—	—
PANSS-POS	16.08 (±5.72)	—	—	—
PANSS-NEG	18.5 (±7.90)	—	—	—
PANSS-GEN	22.25 (±9.72)	—	—	—
PANSS-T	51.32 (±24)	—	—	—
SAPS Total Score	20.37 (±16.31)	—	—	—
SANS Total Score	40.60 (±19.28)	—	—	—
Clozapine Dosage, mg/day	383.70 (±134.20)	—	—	—
CPZ Equivalent, mg/day	498.80 (±281.10)	—	—	—

Values are presented as n or mean (±SD).

CPZ, chlorpromazine; GAF, Global Assessment of Functioning; PANSS-GEN, Positive and Negative Syndrome Scale–General Psychopathology subtotal score; PANSS-NEG, Positive and Negative Syndrome Scale–Negative subtotal score; PANSS-POS, Positive and Negative Syndrome Scale–Positive subtotal score; PANSS-T, Positive and Negative Syndrome Scale total score; SANS, Scale for the Assessment of Negative Symptoms; SAPS, Scale for the Assessment of Positive Symptoms; SOFAS, Social and Occupational Functioning Assessment Scale.

Image Acquisition and Image Preprocessing. Image acquisition and resting-state fMRI data preprocessing are described in the Supplement.

Insula Discrete Subregions Model

Cluster Analysis. For each individual, the left and right insula were separately parcellated into distinct subregions using cluster analysis. In brief, functional connectivity was mapped between each insula voxel and all other gray matter voxels, and Ward's linkage was then used to cluster insula voxels according to similarity in connectional profiles. The morphology of the resulting clusters (i.e., volume and length measurements) was then tested for differences between the schizophrenia and healthy comparison group using the Wilcoxon rank sum test. Functional connectivity mapping and cluster analysis is described in detail in the Supplement. Modularity analysis (Newman's spectral community detection algorithm) was used to combine each individual's insula parcellation to generate a group-level consensus parcellation of the insula for each of the two groups. The modularity Q value was then used to test whether the degree of differentiation in functional connectivity profiles between the anterior and posterior insula subregions differed between the two groups (Supplement).

Whole-Brain Functional Connectivity Profile of Insula Subregions. Using the cluster analysis described above, we found that the insula was most parsimoniously partitioned into two clusters for the majority of individuals with schizophrenia (88%) and healthy comparison (87%) individuals. While substantial variation in the shape and location of clusters across individuals was evident (Supplemental Figure S1), the group-level consensus parcellation comprised two modules that mapped to anterior and posterior insula subregions. We sought to test whether whole-brain functional connectivity patterns differed between anterior and posterior insula or between the schizophrenia and healthy comparison groups. To this end, the intersection between the separate anterior and posterior insula masks for each group was computed to yield a single anterior and posterior insula mask that was common to both groups (Figure 1C and Supplemental Table S1). For each individual, the fMRI signal was averaged across all voxels comprising the anterior and posterior mask, and this averaged signal was then correlated (Pearson's correlation) with all other gray matter voxels, yielding a whole-brain anterior and posterior insula functional connectivity map for each person. For each gray matter voxel comprising this map, within-subjects analysis of variance was used to test the main effects of diagnosis (schizophrenia/control), subregion (anterior/posterior), and laterality (left/right) on insula connectivity as well as the interaction between diagnosis and the latter two main effects. Nonparametric cluster-based inference, as implemented in Randomise (43), was used to control the familywise error across the set of all voxels and to identify voxel clusters for which the main or interaction effects were significant (permutations: n = 10,000; cluster forming threshold: t = 2.5, $p < .05$).

Insula Continuum Model and Diversity Curves

It has recently been suggested that connectional diversity across the insula's topography is more parsimoniously represented as continua of gradual variation, rather than with discrete subregions (11). Given this consideration, we employed the recently proposed concept of a diversity curve (11) to represent the insula's connectional diversity for each individual as a continuum of variation. In brief, Laplacian eigenmaps (44) were mapped for each individual's insula using established methods (45), and the eigenmaps were projected onto a rostrocaudal curvilinear trajectory through the insula representing the trajectory of maximal change in the eigenmap (11). This yielded a separate diversity curve for each individual. Further details are provided in the Supplement. We compared the diversity curves between the schizophrenia and healthy comparison groups to test the hypothesis that schizophrenia would be associated with a reduction in insula connectional diversity. To this end, a two-sample t test was performed to test for a difference in diversity between the schizophrenia and healthy comparison individuals at each point along the diversity curves. The false discovery rate was used to control for multiple comparisons across the set of all points.

Clinical Associations

We hypothesized that interindividual variation in the extent of insula connectivity reductions with the anterior cingulate cortex (ACC) and superior temporal gyrus (STG) would be associated with clinical severity in the schizophrenia group. This hypothesis is supported by suggestions that 1) the ACC and anterior insula are key regions of the salience network (28), which is known to show aberrant network switching in schizophrenia (5,46), and 2) the STG is crucial for language (Wernicke's area) and auditory (Heschl's gyrus and planum temporale) processing, and dysconnectivity of this region has been associated with auditory hallucinations in schizophrenia (47–49). To test this hypothesis, for each individual with schizophrenia, fMRI data were averaged across all voxels comprising the ACC and STG clusters identified with Randomise as well as the masks delineating the posterior and anterior insula subregions. Note that the ACC cluster identified with Randomise included a portion of the supplementary motor area (SMA), and thus we refer to this cluster as ACC/SMA. The resulting regionally averaged time series were then correlated (Pearson's correlation) to yield functional connectivity estimates between 1) anterior insula and ACC and 2) posterior insula and STG. Finally, canonical correlation analysis (50) was used to test for a multivariate association between these two functional connectivity estimates and several measures of symptom severity: PANSS, Scale for the Assessment of Positive Symptoms, SANS, GAF, SOFAS, Wechsler Adult Intelligence Scale, and duration of illness (Supplement).

Numeric computation was performed in MATLAB R2017b (The MathWorks, Inc., Natick, MA). Images were visualized using BrainNetViewer1.6 (51) and FSLView software.

RESULTS

Demographic and clinical characteristics are shown in Table 1. The schizophrenia and healthy comparison groups were matched in terms of mean age, sex, and handedness, and thus these factors were not controlled when performing group comparisons. However, IQ and measures of social and general

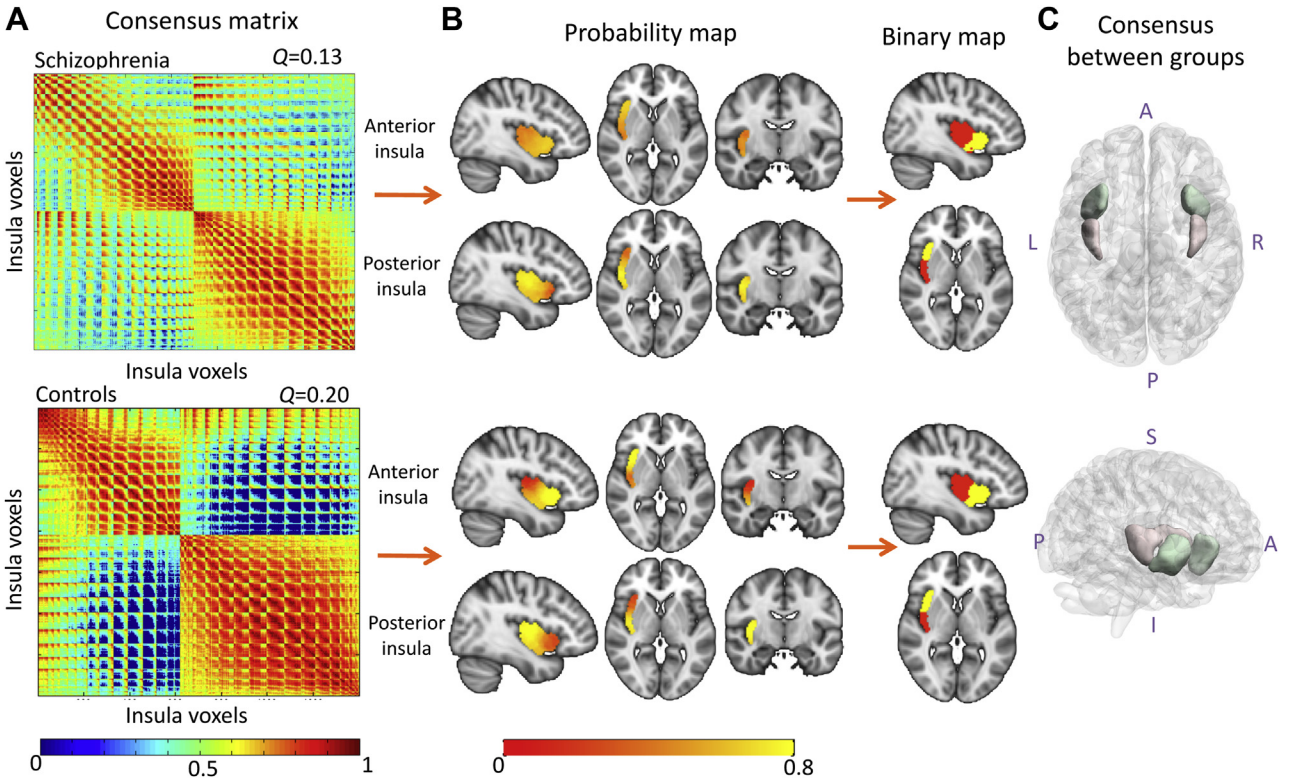


Figure 1. Bipartite parcellation of the right insular cortex based on resting-state functional connectivity in individuals with schizophrenia and healthy comparison individuals. **(A)** Group consensus matrices (insula voxels × insula voxels) for the schizophrenia (upper matrix) and healthy comparison groups (lower). Each cell stores the proportion of individuals for which a given pair of insula voxels comprised the same cluster. Warm tones (red) indicate pairs of voxels consistently comprising the same subregions, whereas cool tones (blue) indicate pairs of voxels consistently comprising distinct subregions. While two modules were identified in both groups, modular separation was significantly reduced in the schizophrenia group ($Q = 0.13$, $p = .0038$) compared with the healthy comparison group ($Q = 0.20$). The rows and columns of the consensus matrices are ordered such that all insula voxels comprising the anterior insula module are listed first, followed by all voxels in the posterior insula. **(B)** The consensus matrices are mapped to the insula to yield probabilistic maps of the anterior and posterior insula subregions. The color of each insula voxel is modulated by the proportion of individuals for which the voxel comprised the relevant subregion (module). Yellow tones indicate voxels that consistently comprise the relevant subregion across individuals, whereas red tones indicate voxels that rarely comprise the subregion. Probability maps were converted to binary (hard) segmentations to delineate discrete anterior (yellow) and posterior (red) insula subregions for both groups. **(C)** The intersection of the anterior insula subregion delineated for each of the two groups was determined to define a consensus anterior insula subregion for both groups (green) and similarly for the posterior insula subregion (pink). Slice coordinates (Montreal Neurological Institute, mm): x = 40, y = −10, z = 2. A, anterior; I, inferior; L, left; P, posterior; R, right; S, superior.

functioning were significantly reduced in the schizophrenia group.

Reduced Differentiation Between Anterior and Posterior Insula Subregions

Bipartite parcellation of the insula into anterior and posterior subregions yielded the most parsimonious representation in the majority of individuals with schizophrenia (88%) and healthy comparison individuals (87%). For the remaining individuals, insula voxels were partitioned into two clusters according to the individual's best-fitting bipartite solution. To facilitate between-group comparison, only bipartite insula parcellations were analyzed here. The volume (cluster size) of each insula subregion was estimated by enumerating the number of voxels assigned to the cluster of voxels delineating each subregion and multiplying this number by the volume of each individual voxel (8×10^{-3} cm^3). The anterior insula subregion was significantly reduced in the schizophrenia group (right: $z = 3.81$, schizophrenia: 4.59 ± 2.2 cm^3, comparison group: 6.41 ± 2.2 cm^3, $p < .001$; left: $z = 4.47$, $p < .001$), whereas the posterior insula was significantly increased (right: $z = 3.44$, schizophrenia: 5.60 ± 2.3 cm^3, comparison group: 4.40 ± 2.2 cm^3, $p < .001$; left: $z = 3.92$, $p < .001$) and extended further anteriorly (right: $z = 3.89$, $p < .001$; left: $z = 3.13$, $p = .0017$) and laterally (right: $z = 3.89$, $p < .001$; left: $z = 3.87$, $p < .001$) relative to the healthy comparison group (Supplemental Figure S2). We found that the differentiation between these two putative insula subregions was significantly reduced in the schizophrenia group (Q value right insula, schizophrenia: 0.13, comparison group: 0.20, $p = .0038$; Q value left insula, schizophrenia: 0.12, comparison group: 0.21, $p = .002$) (Figure 1A, B and Supplemental Figure S3).

Altered Insula Functional Connectivity

Having parcellated the insula into two distinct subregions (anterior and posterior), we next sought to investigate whether

the functional connectivity between these two subregions and the rest of the cortex was altered in schizophrenia. We investigated three main effects (subregion, diagnosis, laterality) and two interaction effects (diagnosis × subregion, diagnosis × laterality). We identified regional clusters associated with each of these effects.

Main Effect of Subregion (Anterior vs. Posterior). Across all individuals (individuals with schizophrenia and healthy comparison individuals combined), we found that the anterior insula was preferentially connected to the frontolimbic and paralimbic areas (peak $t = 24.2$, $p < .001$) and the posterior cerebellar lobes (crus I and crus II) (peak $t = 8.17$, $p = .006$), whereas the posterior insula was characterized by extensive parietotemporo-occipital and anterior cerebellar connectivity (peak $t = 22.4$, $p < .001$) (Figure 2A).

Main Effect of Diagnosis (Schizophrenia vs. Healthy Comparison Group). Functional connectivity was significantly reduced in the schizophrenia group between the insula and multiple cortical and subcortical areas. Specifically, schizophrenia was associated with significant reductions in connectivity between the anterior insula and regions located at the bilateral ACC, SMA, paracingulate cortex, and superior frontal gyrus (peak $t = 5.51$, $p = .0118$) as well as regions in the frontal and central operculum; orbitofrontal cortex; inferior frontal gyrus; temporal pole; ventral medial prefrontal cortex; and subcortical areas such as the amygdala, putamen, parahippocampal gyrus, and pallidum (peak $t = 5.7$, $p = .0035$) (Figure 2B, upper panel). In contrast, the posterior insula showed significantly reduced connectivity with the bilateral STG, planum temporale, Heschl's gyrus, middle temporal gyrus, and parietal and central operculum (right cluster: peak $t = 5.31$, $p = .0018$; left cluster: peak $t = 4.59$, $p = .0091$). Furthermore, functional connectivity between the posterior insula and the bilateral precentral and postcentral gyrus, posterior and anterior cingulate cortex, precuneus, and SMA was significantly reduced in the schizophrenia group (peak $t = 5.4$, $p = .0018$) (Figure 2B, lower panel). Significant increases in connectivity were not found in the schizophrenia group ($p > .05$).

Main Effect of Laterality (Left vs. Right). Whereas the insula's cerebral connections showed an ipsilateral preference (anterior: peak $t = 16.8$, $p < .001$; posterior: peak $t = 17.9$, $p < .001$), the insula was more extensively connected to the cerebellum in the contralateral hemisphere (peak $t = 4.68$, $p = .025$) (Supplemental Figure S5).

Interaction Effect (Diagnosis × Subregion). A significant interaction was found between diagnosis and subregion. More specifically, the anterior insula in the schizophrenia group

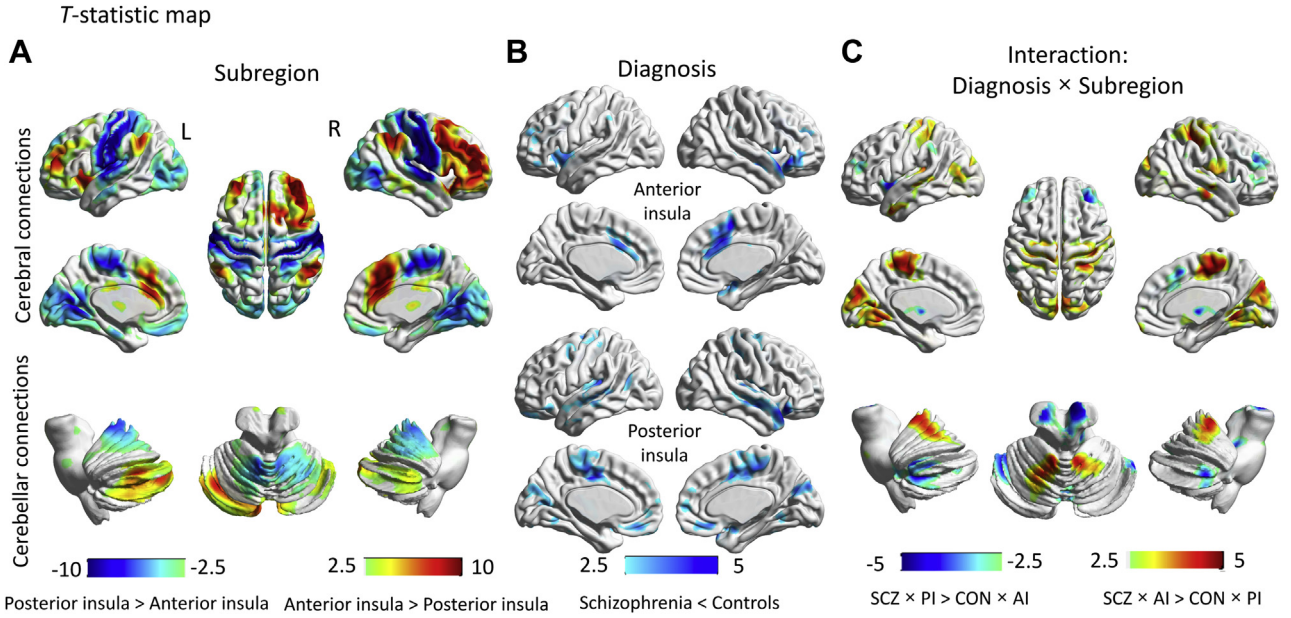


Figure 2. Altered resting-state functional connectivity of the anterior and posterior insular cortex in schizophrenia. Functional connectivity was mapped between the anterior and posterior insula subregions and all other gray matter voxels. Analysis of variance was then used to test the main effect of subregion (anterior vs. posterior) and diagnosis (schizophrenia vs. healthy comparison group) on insula connectivity at each gray matter voxel as well as the interaction between these two main effects. **(A)** Main effect of subregion. The anterior and posterior insula subregions showed unique connectivity patterns: the anterior insula was preferentially connected to frontolimbic areas and the posterior cerebellar lobe, whereas the posterior insula was characterized by increased connectivity with the parietotemporo-occipital cortices and the anterior cerebellar lobe. **(B)** Main effect of diagnosis. Schizophrenia was associated with significant reductions in connectivity between the insula and multiple cortical and subcortical areas, relative to the healthy comparison group. Connectivity increases were not evident in the schizophrenia group. **(C)** Interaction effect. A significant interaction between subregion and diagnosis was found: the anterior insula subregion showed increased connectivity with the somatosensory/motor and occipital cortex in the schizophrenia group, whereas connectivity between the posterior insula and prefrontal cortex and thalamus was increased in schizophrenia. AI, anterior insula; PI, posterior insula; SCZ, schizophrenia group; CON, healthy comparison (control) group. Clusters are colored according to *t* statistic. All images pertain to right insula.

showed increased connectivity with the precentral and postcentral gyrus (i.e., primary motor and somatosensory cortex; peak $t = 5.3$, $p = .001$), the occipital cortex and anterior lobe of the cerebellum (peak $t = 5.34$, $p < .001$), and a cluster located in the primary and secondary auditory cortices (peak $t = 4.99$, $p = .023$). In contrast, the posterior insula in the schizophrenia group showed increased connectivity to the prefrontal cortex (peak $t = 4.37$, $p = .04$), bilateral thalamus (peak $t = 5.27$, $p = .036$), and pons and posterior cerebellar lobes (peak $t = 5.75$, $p = .017$). Comparable findings were evident for the left insula (Supplemental Figure S4).

Interaction Effect (Diagnosis × Laterality). No significant interaction was found between diagnosis and laterality, suggesting that the disorder does not preferentially affect the left or right insula.

Diversity Curves

Diversity curves based on Fielder eigenvectors were mapped for each individual to continuously characterize the rate at which the insula's connectional profile to the rest of the cortex changed along the insula's rostrocaudal axis. Figure 3A shows group-averaged diversity curves for the schizophrenia (green curve) and healthy comparison groups (blue curve). Consistent with previous work (11), the diversity curves show a relatively constant slope, suggesting that the insula's connectivity profile varies gradually and continuously across its topography, from dorsoposterior to ventroanterior. The connectional diversity for the schizophrenia group was reduced in the anterior portion of the insula, indicated by a reduction in the diversity curve's slope (dashed box in Figure 3A); however, this between-group difference did not survive correction for multiple comparisons ($p < .05$) (Figure 3A). Group-consensus eigenmaps were projected to insula voxels in Montreal Neurological Institute space to enable anatomical visualization (Figure 3B).

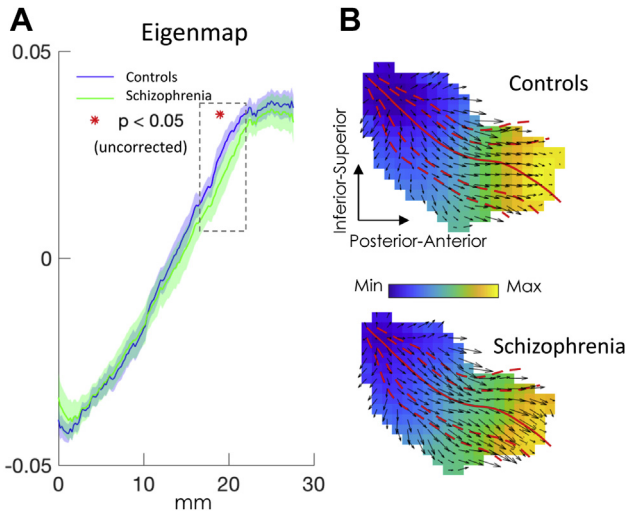


Figure 3. Diversity curves for the insular cortex in schizophrenia. **(A)** Group-averaged insula diversity curves for the schizophrenia (green curve) and healthy comparison (blue) groups. Dashed box indicates the portion of the diversity curve showing a significant reduction in the schizophrenia group ($p < .05$, uncorrected). Shading denotes 95% confidence intervals. **(B)** Group-consensus eigenmap values were mapped to the voxels of the insula to enable anatomical visualization of variation in connectional diversity for the schizophrenia (lower panel) and healthy comparison (upper) groups. The streamlines superposed onto the anatomical images were previously computed as part of a previous study (40). Diversity curves were mapped by projecting each individual's eigenmap onto the longest streamline (solid red line). Arrows indicate the gradient direction estimated for each voxel, and the lengths convey gradient magnitude. Max, maximum; Min, minimal.

Clinical Associations

Canonical correlation analysis identified a significant mode of covariance between interindividual variation in nine measures of disorder severity and two measures of insula functional connectivity ($r = .64$, $p = .03$, familywise error corrected) (Figure 4A). The canonical coefficients for each of the two functional connectivity estimates (Figure 4B) quantify the extent to which each of two connectivity estimates contributed to the significant mode of covariance. Figure 4C shows that IQ, GAF, and SOFAS are positively correlated with the significant mode of covariance, whereas SANS, PANSS-Negative, and duration of illness are negative. Therefore, higher insula functional connectivity with the ACC/SMA and STG was associated with higher IQ and psychosocial functioning (i.e., GAF and SOFAS) as well as less severity of psychotic symptoms (SANS and PANSS-Negative) and shorter duration of illness. Conversely, individuals with lower insula functional connectivity with the ACC/SMA and STG are more likely to show poorer cognitive performance and psychosocial functioning as well as more severe psychotic symptoms and longer illness duration.

In supplementary analyses, an exploratory canonical correlation analysis was conducted on the other six regions found to show significant functional connectivity reductions with the insula in the schizophrenia group (Supplemental Table S2). The exploratory canonical correlation analysis did not identify any significant associations between interindividual variation in symptoms and insula functional connectivity among this broader set of regions.

Interindividual variation in age, sex, and antipsychotic dose (chlorpromazine equivalent dose) did not associate with functional connectivity between the insula and eight clusters (Supplemental Table S2) found to show significantly reduced connectivity with the insula in the schizophrenia group. Supplemental Table S3 shows test statistics and p values for each of these 3 (age, sex, CPZ) × 8 (clusters) = 24 tests.

DISCUSSION

This study comprehensively characterized the functional connectivity architecture of the insular cortex in individuals with schizophrenia. In contrast to previous functional connectivity studies of the insula in schizophrenia, rather than treating the insula as a single, homogeneous region or considering only its anterior aspect, we specifically focused on investigating how the insula's connectivity with the rest of the cortex varied across its topography (i.e., across its spatial extent). The insular cortex is a connectionally diverse region, in that its most dorsoposterior extremity connects with markedly different cortical and subcortical areas compared with its ventroanterior aspect (11). In this study, we aimed to determine whether this connectional diversity was aberrant in

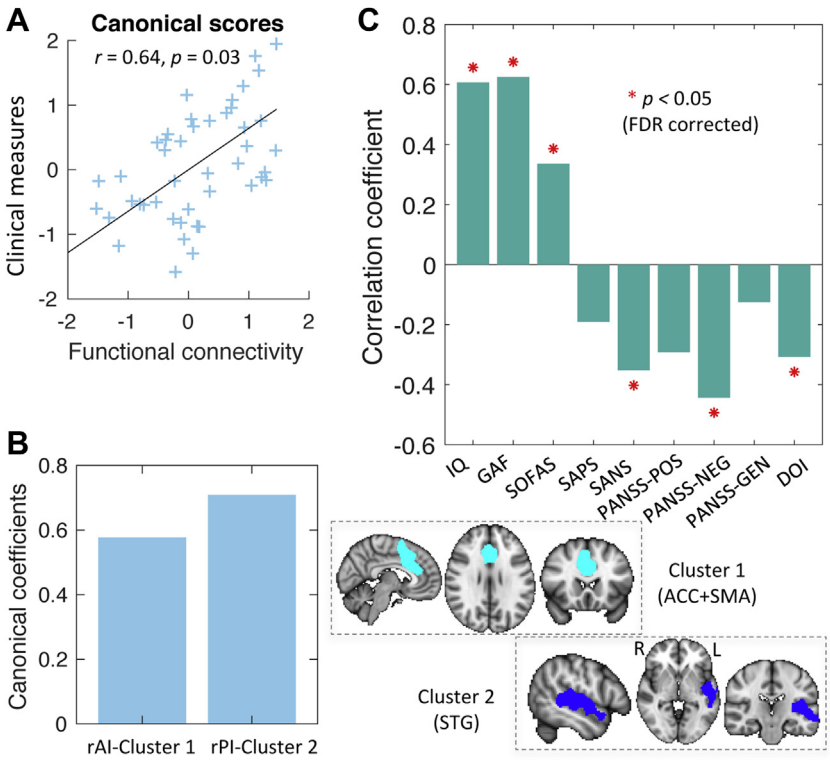


Figure 4. Association between insula functional connectivity and interindividual variation in clinical characteristics. Canonical correlation analysis identified a significant mode of covariance between interindividual variation in two measures of insula functional connectivity and nine measures of disorder severity, including measures of cognition, psychosocial functioning, psychotic symptoms, and duration of illness (DOI). **(A)** Scatter plot of canonical scores for the functional connectivity measures (horizontal axis) and measures of disorder severity (vertical axis). The mode of covariance remained significant after correction for multiple comparisons (r = .64, p = .03; familywise error corrected across all canonical correlation analysis modes with permutation testing, n = 10,000). **(B)** Bar plot showing canonical coefficients for the functional connectivity strengths corresponding to right anterior insula (rAI) and anterior cingulate cortex/supplementary motor area (ACC/SMA) (cyan cluster, .57) and right posterior insula (rPI) and superior temporal gyrus (STG) (blue cluster, .71). **(C)** Bar plot showing correlation coefficients between the nine measures of disorder severity and the significant canonical correlation analysis mode. Measures with positive canonical coefficients are positively correlated with the canonical correlation analysis mode of variance. Therefore, increased insula functional connectivity is associated with increased IQ, Global Assessment of Functioning (GAF), and Social and Occupational Functioning Assessment Scale (SOFAS) but decreased Scale for Assessment of Negative Symptoms (SANS), Positive and Negative Syndrome Scale–Negative (PANSS-NEG), and DOI. Red asterisks indicate measures that are significantly correlated with the canonical score (false discovery rate [FDR] corrected). PANSS-GEN, Positive and Negative Syndrome Scale–General Psychopathology; PANSS-POS, Positive and Negative Syndrome Scale–Positive; SAPS, Scale for Assesment of Positive Symptoms.

schizophrenia. We found that the connectivity profiles of the anterior and posterior insula were less well differentiated in schizophrenia and that the extent of reduction in connectivity between insula subregions and key regions of the salience network and auditory cortex were associated with interindividual variation in symptom severity.

Our initial clustering analysis suggested that the insula was most parsimoniously parcellated into two subregions in the majority of individuals with schizophrenia and healthy comparison individuals. Volumetrically, we found that the posterior insula subregion was significantly larger in the schizophrenia group, whereas the anterior insula was significantly reduced, relative to the healthy comparison group. It is important not to confuse these volumetric differences with previous studies reporting that schizophrenia is associated with reduced insula gray matter volume, particularly the anterior aspect of the insula (52–56). We used a common mask to delineate the insula in all individuals, and thus we did not model any potential interindividual variation in the entire insula volume. The volumetric differences found in the present study relate to segregation of functional connectivity (57–59) and are not necessarily related to gray matter morphology. In particular, the increased volume of the posterior insula subregion suggests that the characteristic connectivity profile of the posterior insula encompasses a larger share of the insula's entire volume in individuals with schizophrenia. This is at the expense of the anterior insula occupying a smaller volume.

We found that the differentiation between the anterior and posterior insula subregions was significantly reduced in the schizophrenia group relative to the healthy comparison group as quantified by the modularity Q value. This suggests that the connectional diversity of the insula is reduced in schizophrenia; namely, the network of areas with which the anterior insula connects is less well differentiated from the network of areas with which the posterior insula connects. In fact, differentiation between the anterior and posterior insula was only marginally higher than chance level in the schizophrenia group ($Q \approx 0.1$). Specifically, the anterior insula subregion preferentially connects to the frontolimbic and paralimbic areas and cerebellar nonmotor regions, whereas the posterior subregion shows extensive connectivity with the parietotemporo-occipital lobe and motor regions of cerebellum. This anterior-posterior subdivision is consistent with previous functional/diffusional parcellation studies in humans (10,12,13,15,60,61) and axonal tracing studies in macaques (62,63).

We found that functional connectivity between the insula and multiple cortical and subcortical areas as well as the cerebellum was significantly reduced in the schizophrenia group. Many of the areas affected comprise cognitive networks (20,21) and are associated with a wide range of cognitive, affective, and sensorimotor functions that are disturbed in schizophrenia (64–66). We found a significant interaction in the connectivity profiles between diagnosis (schizophrenia vs. healthy comparison group) and insula subregion (anterior vs. posterior). In the schizophrenia group, the anterior insula

connected with increased strength to regions that are normally connected with the posterior insula (i.e., the precentral/postcentral gyrus, occipital/parietal cortex, and anterior cerebellar lobe). Conversely, the posterior insula showed increased connectivity in schizophrenia with regions that are preferentially connected with the anterior insula in healthy individuals (i.e., prefrontal cortex, thalamus, and posterior cerebellar lobe). This interaction effect suggests that the connectivity profiles of the anterior and posterior insula are less well differentiated in schizophrenia, consistent with lack of insula connectional diversity in the disorder.

Using the recently developed concept of a diversity curve (11), we found that the insula's connectional diversity varied gradually along a rostrocaudal axis in both the schizophrenia and the healthy comparison groups. Furthermore, we found no evidence of a discrete boundary between putative insula subregions, which would have been evidenced by an abrupt change in the diversity curve slope. It is important to note that while we did not find any evidence of discrete insula subregions, modeling the insula's connectional diversity with subregions can nevertheless provide meaningful insight. Discrete approximations can simplify continuous systems, which, in turn, facilitates inference and more intuitive interpretations. For example, mapping of neural connectomes mandates the delineation of discrete subregions to serve as network nodes (67). Anterior and posterior insula subregions can thus represent distinct nodes in connectomic studies. Insula diversity curves for the schizophrenia group were reduced within an anterior portion of the insula; however, this between-group difference did not survive correction for multiple comparisons. Within the anterior portion of the insula implicated (dashed box in Figure 3A), the slope of the diversity curve showed a trend toward reduction in the schizophrenia group, which may suggest that this portion of the insula is abnormally homogeneous in the disorder.

Importantly, we found that the reduced functional connectivity between anterior insula and ACC including SMA, known as the salience network, and the functional connectivity between posterior insula and the language and auditory cortex (STG, Heschl's gyrus, planum temporale, and Wernicke's area) were associated with poor clinical outcomes, including cognitive impairment and general social and occupational functioning as well as the severity of symptoms, particularly negative symptoms. Our findings support the emerging hypothesis that the salience network is significantly involved in the pathophysiology of psychosis (7,46,68,69), particularly with respect to disturbances in the integration of sensory perception facilitated by the posterior insula (68). Of note, reduced insula functional connectivity was also associated with longer illness duration, suggesting progressive deterioration of connectivity over the course of illness, although longitudinal neuroimaging would be required to confirm this suggestion. We therefore conclude that impaired functional connectivity between the insula and these key regions may be a determinant of disorder severity.

Limitations

First, our sample is moderate in size, and our fMRI data are of poorer spatial and temporal resolution compared with the data used in our previous analysis of the insula in healthy individuals (11). Second, although antipsychotic dose was not correlated with any of the functional connectivity effects reported in this study, medication cannot be excluded as a potential confound (70–72). Interestingly, analysis of functional connectivity during a salience attribution task indicated that schizophrenia-related reductions in connectivity between the insula and ACC were evident only in the subgroup of untreated individuals with first-episode psychosis and not in the medicated subgroup (72). However, these findings require replication, given the small size of the medicated subgroup. Finally, IQ was significantly reduced in the schizophrenia group, representing a potential confounding effect on the neuroimaging findings reported in our study. However, it is generally difficult to disentangle low IQ from the illness because of the widespread neurocognitive deficits evident in the majority of individuals with schizophrenia (65), and controlling for IQ as part of statistical inference may be considered inappropriate for this reason (73).

Conclusions

Using resting-state fMRI, we comprehensively characterized functional connectivity across the topography of the insular cortex in individuals with schizophrenia. We represented the insula's connectional diversity using discrete subregions (anterior and posterior) as well as a continuum of gradual variation. We found that the anterior and posterior insula subregions were connected to distinct cortical and subcortical regions in the healthy comparison individuals. However, in the schizophrenia group, this distinction in the connectivity profiles of the anterior and posterior insula was significantly reduced, suggesting a lack of segregation between these two subregions in the disorder. This was evidenced by a significant interaction between diagnosis and subregion, whereby the anterior insula showed increased connectivity with somatosensory/motor cortices, occipital/parietal cortices, and motor regions of cerebellum in schizophrenia, whereas the connectivity between the posterior insula and prefrontal cortex, thalamus, and cerebellar nonmotor region was stronger. Insula diversity curves suggested that the anterior insula may be abnormally homogeneous in the schizophrenia group. Finally, we found that impaired insula functional connectivity was associated with interindividual variation in cognitive deficits, psychotic symptoms, and psychosocial functioning. We conclude that the anterior and posterior insula show differential connectivity profiles, but this differentiation is reduced in schizophrenia, resulting in reduced connectional diversity across the insula and possibly contributing to the psychotic symptoms of schizophrenia. Future research may focus on mapping the subregional architecture of the insular cortex as a function of age using longitudinal neuroimaging data. This would establish the age range during which the connectivity profiles of the anterior and posterior insula significantly differentiate and whether this differentiation is evident before the onset of psychosis.

ACKNOWLEDGMENTS AND DISCLOSURES

This work was supported by the China Scholarship Council–University of Melbourne Research Scholarship (to YT), Australian National Health and Medical Research Council Senior Research Fellowship B (Grant No.

1136649 [to AZ]), and Australian National Health and Medical Research Council Senior Principal Research Fellowship (Grant Nos. 628386 and 1105825 [to CP]).

We thank the Cooperative Research Centre Scientific Advisory Committee as well as the study participants; clinicians at recruitment services; staff at the Murdoch Children's Research Institute; staff at the Australian Imaging, Biomarkers and Lifestyle Flagship Study of Aging; and research staff at the Melbourne Neuropsychiatry Centre, including coordinators C. Phassouliotis and A. Merritt and research assistants A. Burnside, H. Cross, S. Gale, and S. Tahtalian.

CP has participated on advisory boards for Janssen-Cilag, AstraZeneca, Lundbeck, and Servier and has received honoraria for talks presented at educational meetings organized by AstraZeneca, Janssen-Cilag, Eli Lilly and Company, Pfizer, Lundbeck, and Shire. All are unrelated to the current study. All other authors report no biomedical financial interests or potential conflicts of interest.

ARTICLE INFORMATION

From the Melbourne Neuropsychiatry Centre (YT, AZ, CB, CP), Department of Psychiatry, The University of Melbourne and Melbourne Health, Carlton South; Department of Biomedical Engineering (AZ) and Centre for Neural Engineering (CP), The University of Melbourne; Florey Institute for Neuroscience and Mental Health (CP), Parkville; Cooperative Research Centre for Mental Health (CB, IE, CP), Carlton, Victoria, Australia; Departments of Medical Genetics (CB), Psychiatry (CB), and Physiology and Pharmacology (CB), University of Calgary, Calgary, Alberta, Canada; and Institute of Psychiatry, Psychology and Neuroscience (IE), King's College London, London, United Kingdom.

Address correspondence to Ye Tian, M.D., Melbourne Neuropsychiatry Centre, Level 3, Alan Gilbert Building, 161 Barry Street, The University of Melbourne, Carlton South, Victoria 3053, Australia; E-mail: yetianmed@gmail.com.

Received Oct 12, 2018; revised Nov 26, 2018; accepted Dec 5, 2018.

Supplementary material cited in this article is available online at https://doi.org/10.1016/j.bpsc.2018.12.003.

REFERENCES

1. Kasparek T, Prikryl R, Rehulova J, Marecek R, Mikl M, Prikrylova H, *et al.* (2013): Brain functional connectivity of male patients in remission after the first episode of schizophrenia. Hum Brain Mapp 34:726–737.
2. Mallikarjun PK, Lalousis PA, Dunne TF, Heinze K, Reniers RL, Broome MR, *et al.* (2018): Aberrant salience network functional connectivity in auditory verbal hallucinations: A first episode psychosis sample. Transl Psychiatry 8:69.
3. Pang L, Kennedy D, Wei Q, Lv L, Gao J, Li H, *et al.* (2017): Decreased functional connectivity of insular cortex in drug naïve first episode schizophrenia: In relation to symptom severity. PloS One 12:e0167242.
4. Moran LV, Tagamets MA, Sampath H, O'Donnell A, Stein EA, Kochunov P, *et al.* (2013): Disruption of anterior insula modulation of large-scale brain networks in schizophrenia. Biol Psychiatry 74:467–474.
5. Palaniyappan L, Simmonite M, White TP, Liddle EB, Liddle PF (2013): Neural primacy of the salience processing system in schizophrenia. Neuron 79:814–828.
6. Dandash O, Fornito A, Lee J, Keefe RS, Chee MW, Adcock RA, *et al.* (2014): Altered striatal functional connectivity in subjects with an at-risk mental state for psychosis. Schizophr Bull 40:904–913.
7. Wotruba D, Michels L, Buechler R, Metzler S, Theodoridou A, Gerstenberg M, *et al.* (2014): Aberrant coupling within and across the default mode, task-positive, and salience network in subjects at risk for psychosis. Schizophr Bull 40:1095–1104.
8. Wang C, Ji F, Hong Z, Poh JS, Krishnan R, Lee J, *et al.* (2016): Disrupted salience network functional connectivity and white-matter microstructure in persons at risk for psychosis: findings from the LYRIKS study. Psychol Med 46:2771–2783.
9. Manoliu A, Riedl V, Zherdin A, Muhlau M, Schwerthoffer D, Scherr M, *et al.* (2014): Aberrant dependence of default mode/central executive network interactions on anterior insular salience network activity in schizophrenia. Schizophr Bull 40:428–437.
10. Cauda F, D'Agata F, Sacco K, Duca S, Geminiani G, Vercelli A (2011): Functional connectivity of the insula in the resting brain. Neuroimage 55:8–23.
11. Tian Y, Zalesky A (2018): Characterizing the functional connectivity diversity of the insula cortex: Subregions, diversity curves and behavior. Neuroimage 183:716–733.
12. Cauda F, Costa T, Torta DM, Sacco K, D'Agata F, Duca S, *et al.* (2012): Meta-analytic clustering of the insular cortex: Characterizing the meta-analytic connectivity of the insula when involved in active tasks. Neuroimage 62:343–355.
13. Nanetti L, Cerliani L, Gazzola V, Renken R, Keysers C (2009): Group analyses of connectivity-based cortical parcellation using repeated k-means clustering. Neuroimage 47:1666–1677.
14. Kelly C, Toro R, Di Martino A, Cox CL, Bellec P, Castellanos FX, *et al.* (2012): A convergent functional architecture of the insula emerges across imaging modalities. Neuroimage 61:1129–1142.
15. Jakab A, Molnar PP, Bogner P, Beres M, Berenyi EL (2012): Connectivity-based parcellation reveals interhemispheric differences in the insula. Brain Topogr 25:264–271.
16. Alcauter S, Lin W, Keith Smith J, Gilmore JH, Gao W (2015): Consistent anterior-posterior segregation of the insula during the first 2 years of life. Cereb Cortex 25:1176–1187.
17. Deen B, Pitskel NB, Pelphrey KA (2011): Three systems of insular functional connectivity identified with cluster analysis. Cereb Cortex 21:1498–1506.
18. Chang LJ, Yarkoni T, Khaw MW, Sanfey AG (2013): Decoding the role of the insula in human cognition: Functional parcellation and large-scale reverse inference. Cereb Cortex 23:739–749.
19. Mutschler I, Wieckhorst B, Kowalevski S, Derix J, Wentlandt J, Schulze-Bonhage A, *et al.* (2009): Functional organization of the human anterior insular cortex. Neurosci Lett 457:66–70.
20. Power JD (2011): Functional network organization of the human brain. Neuron 72:665–678.
21. Yeo BT, Krienen FM, Sepulcre J, Sabuncu MR, Lashkari D, Hollinshead M, *et al.* (2011): The organization of the human cerebral cortex estimated by intrinsic functional connectivity. J Neurophysiol 106:1125–1165.
22. Nelson SM, Dosenbach NU, Cohen AL, Wheeler ME, Schlaggar BL, Petersen SE (2010): Role of the anterior insula in task-level control and focal attention. Brain Struct Funct 214:669–680.
23. Glasser MF, Coalson TS, Robinson EC, Hacker CD, Harwell J, Yacoub E, *et al.* (2016): A multi-modal parcellation of human cerebral cortex. Nature 536:171–178.
24. Yamada T, Itahashi T, Nakamura M, Watanabe H, Kuroda M, Ohta H, *et al.* (2016): Altered functional organization within the insular cortex in adult males with high-functioning autism spectrum disorder: Evidence from connectivity-based parcellation. Mol Autism 7:41.
25. Kurth F, Zilles K, Fox PT, Laird AR, Eickhoff SB (2010): A link between the systems: Functional differentiation and integration within the human insula revealed by meta-analysis. Brain Struct Funct 214:519–534.
26. Nomi JS, Farrant K, Damaraju E, Rachakonda S, Calhoun VD, Uddin LQ (2016): Dynamic functional network connectivity reveals unique and overlapping profiles of insula subdivisions. Hum Brain Mapp 37:1770–1787.
27. Vercelli U, Diano M, Costa T, Nani A, Duca S, Geminiani G, *et al.* (2016): Node detection using high-dimensional fuzzy parcellation applied to the insular cortex. Neural Plast 2016:1938292.
28. Seeley WW, Menon V, Schatzberg AF, Keller J, Glover GH, Kenna H, *et al.* (2007): Dissociable intrinsic connectivity networks for salience processing and executive control. J Neurosci 27:2349–2356.
29. Cole MW, Schneider W (2007): The cognitive control network: Integrated cortical regions with dissociable functions. Neuroimage 37: 343–360.
30. Cerliani L, Thomas RM, Jbabdi S, Siero JC, Nanetti L, Crippa A, *et al.* (2012): Probabilistic tractography recovers a rostrocaudal trajectory of connectivity variability in the human insular cortex. Hum Brain Mapp 33:2005–2034.
31. Ganella EP, Bartholomeusz CF, Seguin C, Whittle S, Bousman C, Phassouliotis C, *et al.* (2017): Functional brain networks in treatment-resistant schizophrenia. Schizophr Res 184:73–81.

32. Fornito A, Zalesky A, Pantelis C, Bullmore ET (2012): Schizophrenia, neuroimaging and connectomics. Neuroimage 62:2296–2314.
33. Tan HY, Sust S, Buckholtz JW, Mattay VS, Meyer-Lindenberg A, Egan MF, *et al.* (2006): Dysfunctional prefrontal regional specialization and compensation in schizophrenia. Am J Psychiatry 163:1969–1977.
34. Howes OD, McCutcheon R, Agid O, de Bartolomeis A, van Beveren NJ, Birnbaum ML, *et al.* (2017): Treatment-resistant schizophrenia: Treatment Response and Resistance in Psychosis (TRRIP) working group consensus guidelines on diagnosis and terminology. Am J Psychiatry 174:216–229.
35. Sheehan DV, Lecrubier Y, Sheehan KH, Amorim P, Janavs J, Weiller E, *et al.* (1998): The Mini-International Neuropsychiatric Interview (M.I.N.I.): The development and validation of a structured diagnostic psychiatric interview for DSM-IV and ICD-10. J Clin Psychiatry 59(suppl 20):22–33 [quiz: 34–57].
36. Kay SR, Fiszbein A, Opfer LA (1987): The Positive and Negative Syndrome Scale (PANSS) for schizophrenia. Schizophr Bull 13:261.
37. Andreasen N (1985): The Scale for the Assessment of Positive Symptoms. Iowa City, IA: University of Iowa Press.
38. Andreasen NC (1989): Scale for the Assessment of Negative Symptoms (SANS). Br J Psychiatry 155:53–58.
39. Hall RC, Parks J (1995): The modified global assessment of functioning scale: Addendum. Psychosomatics 36:416–417.
40. Goldman HH, Skodol AE, Lave TR (1992): Revising axis V for DSM-IV: A review of measures of social functioning. Am J Psychiatry 149: 1148–1156.
41. Wechsler D (2008): Wechsler Adult Intelligence Scale–Fourth Edition (WAIS–IV). San Antonio, TX: NCS Pearson.
42. Leucht S, Samara M, Heres S, Davis JM (2016): Dose equivalents for antipsychotic drugs: The DDD method. Schizophr Bull 42(suppl 1): S90–S94.
43. Winkler AM, Ridgway GR, Webster MA, Smith SM, Nichols TE (2014): Permutation inference for the general linear model. Neuroimage 92:381–397.
44. Belkin M, Niyogi P (2003): Laplacian eigenmaps for dimensionality reduction and data representation. Neural Comput 15:1373–1396.
45. Haak KV, Marquand AF, Beckmann CF (2018): Connectopic mapping with resting-state fMRI. Neuroimage 170:83–94.
46. Uddin LQ (2015): Salience processing and insular cortical function and dysfunction. Nat Rev Neurosci 16:55–61.
47. Kasai K, Shenton ME, Salisbury DF, Hirayasu Y, Onitsuka T, Spencer MH, *et al.* (2003): Progressive decrease of left Heschl gyrus and planum temporale gray matter volume in first-episode schizophrenia: A longitudinal magnetic resonance imaging study. Arch Gen Psychiatry 60:766–775.
48. Shinn AK, Baker JT, Cohen BM, Ongur D (2013): Functional connectivity of left Heschl's gyrus in vulnerability to auditory hallucinations in schizophrenia. Schizophr Res 143:260–268.
49. Morch-Johnsen L, Nesvag R, Jorgensen KN, Lange EH, Hartberg CB, Haukvik UK, *et al.* (2017): Auditory cortex characteristics in schizophrenia: Associations with auditory hallucinations. Schizophr Bull 43:75–83.
50. Hotelling H (1936): Relations between two sets of variates. Biometrika 28:321–377.
51. Xia M, Wang J, He Y (2013): BrainNet Viewer: A network visualization tool for human brain connectomics. PloS One 8:e68910.
52. Ellison-Wright I, Glahn DC, Laird AR, Thelen SM, Bullmore E (2008): The anatomy of first-episode and chronic schizophrenia: An anatomical likelihood estimation meta-analysis. Am J Psychiatry 165: 1015–1023.
53. Glahn DC, Laird AR, Ellison-Wright I, Thelen SM, Robinson JL, Lancaster JL, *et al.* (2008): Meta-analysis of gray matter anomalies in schizophrenia: Application of anatomic likelihood estimation and network analysis. Biol Psychiatry 64:774–781.
54. Takahashi T, Wood SJ, Soulsby B, Tanino R, Wong MT, McGorry PD, *et al.* (2009): Diagnostic specificity of the insular cortex abnormalities in first-episode psychotic disorders. Prog Neuropsychopharmacol Biol Psychiatry 33:651–657.
55. Takahashi T, Wood SJ, Yung AR, Phillips LJ, Soulsby B, McGorry PD, *et al.* (2009): Insular cortex gray matter changes in individuals at ultra-high-risk of developing psychosis. Schizophr Res 111:94–102.
56. Takahashi T, Wood SJ, Soulsby B, McGorry PD, Tanino R, Suzuki M, *et al.* (2009): Follow-up MRI study of the insular cortex in first-episode psychosis and chronic schizophrenia. Schizophr Res 108:49–56.
57. Tononi G, Sporns O, Edelman GM (1994): A measure for brain complexity: Relating functional segregation and integration in the nervous system. Proc Natl Acad Sci U S A 91:5033–5037.
58. Cohen JR, D'Esposito M (2016): The segregation and integration of distinct brain networks and their relationship to cognition. J Neurosci 36:12083–12094.
59. Fornito A, Zalesky A, Bullmore ET (2016): Fundamental of Brain Network Analysis. London: Academic Press.
60. Taylor KS, Seminowicz DA, Davis KD (2009): Two systems of resting state connectivity between the insula and cingulate cortex. Hum Brain Mapp 30:2731–2745.
61. Cloutman LL, Binney RJ, Drakesmith M, Parker GJ, Lambon Ralph MA (2012): The variation of function across the human insula mirrors its patterns of structural connectivity: Evidence from in vivo probabilistic tractography. Neuroimage 59:3514–3521.
62. Mesulam MM, Mufson EJ (1982): Insula of the Old World monkey. I. Architectonics in the insulo-orbito-temporal component of the paralimbic brain. J Comp Neurol 212:1–22.
63. Mufson EJ, Mesulam MM (1982): Insula of the Old World monkey. II. Afferent cortical input and comments on the claustrum. J Comp Neurol 212:23–37.
64. Kaufmann T, Skåtun KC, Alnæs D, Doan NT, Duff EP, Tønnesen S, *et al.* (2015): Disintegration of sensorimotor brain networks in schizophrenia. Schizophr Bull 41:1326–1335.
65. Keefe RS, Fenton WS (2007): How should DSM-V criteria for schizophrenia include cognitive impairment? Schizophr Bull 33:912–920.
66. Kohler CG, Walker JB, Martin EA, Healey KM, Moberg PJ (2010): Facial emotion perception in schizophrenia: A meta-analytic review. Schizophr Bull 36:1009–1019.
67. Sotiropoulos SN, Zalesky A (2019): Building connectomes using diffusion MRI: Why, how and but. NMR Biomed 32:e3752.
68. Menon V, Uddin LQ (2010): Saliency, switching, attention and control: A network model of insula function. Brain Struct Funct 214:655–667.
69. Palaniyappan L, Liddle PF (2012): Does the salience network play a cardinal role in psychosis? An emerging hypothesis of insular dysfunction. J Psychiatry Neurosci 37:17–27.
70. Radua J, Borgwardt S, Crescini A, Mataix-Cols D, Meyer-Lindenberg A, McGuire PK, *et al.* (2012): Multimodal meta-analysis of structural and functional brain changes in first episode psychosis and the effects of antipsychotic medication. Neurosci Biobehav Rev 36:2325–2333.
71. Abbott CC, Jaramillo A, Wilcox CE, Hamilton DA (2013): Antipsychotic drug effects in schizophrenia: A review of longitudinal FMRI investigations and neural interpretations. Curr Med Chem 20:428–437.
72. Schmidt A, Palaniyappan L, Smieskova R, Simon A, Riecher-Rossler A, Lang UE, *et al.* (2016): Dysfunctional insular connectivity during reward prediction in patients with first-episode psychosis. J Psychiatry Neurosci 41:367–376.
73. Miller GA, Chapman JP (2001): Misunderstanding analysis of covariance. J Abnorm Psychol 110:40–48.

Insula Functional Connectivity in Schizophrenia: Subregions, Gradients and Symptoms

Supplementary Information

Table of Contents

S1. Image Acquisition and Resting-state fMRI data preprocessing 2

S2. Cluster Analysis 2

S3. Group-level Consensus Parcellation 3

S4. Diversity Curves and Continuum Model 3

S5. Clinical Measures and Canonical Correlation Analysis 4

Figure S1. Individual bipartite parcellation of the insula based on resting-state functional connectivity in individuals with schizophrenia and healthy comparison individuals. 5

Figure S2. Comparison of cluster shape between schizophrenia and healthy comparison groups. 6

Figure S3. Bipartite parcellation of the left insula cortex based on resting-state functional connectivity in individuals with schizophrenia and healthy comparison individuals. 7

Figure S4. Altered resting-state functional connectivity of left anterior and posterior insula in schizophrenia. 8

Figure S5. The main effect of hemisphere in resting-state functional connectivity of anterior and posterior insula cortex 9

Table S1. 10

Table S2. 10

Table S3. 11

Supplementary References 11

S1. Image Acquisition and Resting-state fMRI data preprocessing

Image Acquisition: Imaging was performed in all participants using a Siemens Avanto 3T Magetom TIM Trio scanner. Structural images of brain anatomy were acquired using an optimized Magnetization-Prepared Rapid Acquisition Gradient Echo (MPRAGE) T1-weighted sequence with 176 sagittal slices of 1.2mm thickness; field of view (FOV) = 256×256 mm^2; flip angle = 9°; repetition time (TR) = 2300ms; echo time (TE) = 2.98ms; voxel size =1.0×1.0×1.2 mm^3. Resting-state fMRI was acquired using a T2*-weighted echo-planar imaging sequence. A total of 8 min of resting-state data was acquired, resulting in 234 volumes (TR = 2000ms; TE = 32.0ms; voxel size = 3.3×3.3×3.5 mm^3).

Resting-state fMRI Data Preprocessing: Resting-state fMRI data were preprocessed using FSL 5.0.8 (http://fsl.fmrib.ox.au.uk/fsl/fslwiki/). In brief, preprocessing steps included: slice-timing correction; brain extraction; linear registration of all volumes to the middle volume to correct for intrascan head motion; warping of all volumes to MNI space and resampling to 2mm isotropic voxels. These steps were performed independently for each individual. Motion artefacts were further corrected with ICA-AROMA (v0.3-beta, ICA-based automatic removal of motion artefacts) after spatial smoothing with a Gaussian kernel of 4mm FWHM (full width at half maximum). ICA-AROMA is a data-driven method to identify and automatically remove motion-related variance (1, 2). For each voxel, the preprocessed fMRI data was then regressed against the motion-related components identified with ICA-AROMA, together with mean white matter and cerebrospinal fluid signals (CSF). The residuals of this regression were temporally band-pass filtered (0.01-0.1 Hz) and used in all further analyses.

S2. Cluster Analysis

Binary insula masks were delineated based on the Harvard-Oxford Cortical Structural Atlas (https://fsl.fmrib.ox.ac.uk/fsl/fslwiki/Atlases) using a probability threshold of 20%, resulting in 1399 voxels (11.19cm^3) for right insula and 1397 voxels (11.17cm^3) for left insula. The fMRI signal at each insula voxel was correlated (Pearson correlation) with all other gray matter voxels, yielding a voxel-wise functional connectivity matrix (*r*-to-*z* transformed) of dimension $N \times M$, where N denotes the number of insula voxels and M denotes the number of all other gray matter voxels. Principal component analysis (PCA) was then applied to the z-transformed connectivity matrix. These steps were performed independently for each individual and the top three principal components were found to explain more than 80% of the variance across gray matter voxels for each individual. The Euclidean distance between all pairs of insula voxels was computed in this three-dimensional space ($N \times 3$), yielding a symmetric distance matrix of dimension $N \times N$. Ward's linkage (3) was then applied to this distance matrix to partition insula voxels into groups that shared similar connectivity patterns and connected to the same cortical and subcortical areas. To determine the most parsimonious number of clusters (subregions) comprising the insula, we used the W^{norm} cluster

evaluation measure (4), which quantifies the normalized intra-to-inter-cluster distance. Specifically, we generated fMRI-specific null data to compare W^{norm} with its expected value under the null hypothesis of no insula clusters. This approach has been shown to outperform classic cluster evaluation criteria when applied to fMRI data (4). Clusters were delineated independently for the right and left insula and for each individual.

S3. Group-level Consensus Parcellation

For each of the two groups, an $N \times N$ consensus matrix was formed in which cell (i, j) was populated with the proportion of individuals for which voxels i and j resided in the same cluster. Newman's spectral community detection algorithm (5, 6) was then applied to each consensus matrix in an iterative manner (7) to yield a consensus parcellation. Each module in the consensus parcellation delineated an insula subregion. The modularity Q score was used to quantify the extent to which the consensus parcellation was modular (5, 8). Higher values of Q indicated stronger separation between putative insula subregions and/or increased consistency in the morphology of subregions across individuals. We used permutation testing to assess the null hypothesis of equality in Q scores between the schizophrenia and healthy comparison groups. Individuals were randomly permuted between the two groups and a consensus parcellation was computed for each group, as well as corresponding Q scores. This was repeated for 5000 permutations and the absolute difference between Q scores ($\Delta Q = |Q_1 - Q_2|$) was stored for each permutation to generate an empirical null distribution that denoted the difference. The p-value was given by the proportion of permutations for which ΔQ exceeded or equalled the value of ΔQ in the true (unpermuted) groups.

S4. Diversity Curves and Continuum Model

Laplacian eigenmaps for the insula were mapped using the procedure described by Haak et al. (9). Diversity curves were mapped as described by Tian and Zalesky (4). Given that the temporal and spatial resolution of the fMRI data used in this study was lower than the data analyzed in these two previous studies, we implemented the following additional procedures to assist in alleviating the effects of noise:

I. Rather than globally thresholding the similarity graph to yield the minimum connection density required to ensure a single connected component in the graph, we instead used the disparity filter (10) to perform thresholding. The disparity filter is a local thresholding method that may provide greater robustness to the effects of noisy edges. The significance level for the disparity filter was set independently for each individual according to the minimum connection density required to yield a single connected component. This resulted in graphs with connection densities of 5-28% across individuals.

II. The eigendecomposition described in Haak et al. (9) was performed on the symmetric normalized Laplacian matrix rather than the unnormalized Laplacian matrix. When visualized in the anatomical space of the insula, this yielded eigenmaps that were visibly less noisy.

S5. Clinical Measures and Canonical Correlation Analysis

The following measures were included in the canonical correlation analysis (CCA): PANSS, SAPS, SANS, GAF, SOFAS, WASI and duration of illness (DOI). For each measure, scores were not available for between 0% and 6% of the individuals (missing data). For PANSS, an average item score across each of the subscales (ignoring the missing values) was calculated, yielding mean score for positive (PANSS-POS), negative (PANSS-NEG) and general psychopathology (PANSS-GEN) symptoms for each individual. Similarly, mean scores for SAPS and SANS, ignoring the missing values were computed. This mean score approach avoided potential underestimation of the severity of psychotic symptoms when item scores were summed in the presence of missing data. For GAF, SOFAS and WASI, missing values were replaced with nearest neighbor values based on Euclidean distance. DOI was recorded for all individuals. The sum of item scores for each measure is provided in Table 1 (ignoring individuals with missing values).

CCA was then used to test whether inter-individual variation in clinical features was associated with insula functional connectivity. In this study, one group of variables comprised 9 clinical measures, while the other group comprised the functional connectivity strength between insula subregion and regions (clusters) that were found to show significant between-group differences. The two groups of variables were submitted to the CCA function (*canoncorr*) available in *MATLAB*. The familywise error (FWE) was controlled with permutation testing. For each of the permutations (n=10,000), clinical measures were randomly permuted among individuals and CCA was repeated for the permuted data. The FWE corrected p-value for each CCA mode was given by the proportion of permutations with a maximum correlation coefficient that exceeded or equaled the mode's correlation in the unpermuted data. $p < 0.05$ was considered statistically significant.

Supplementary Figures

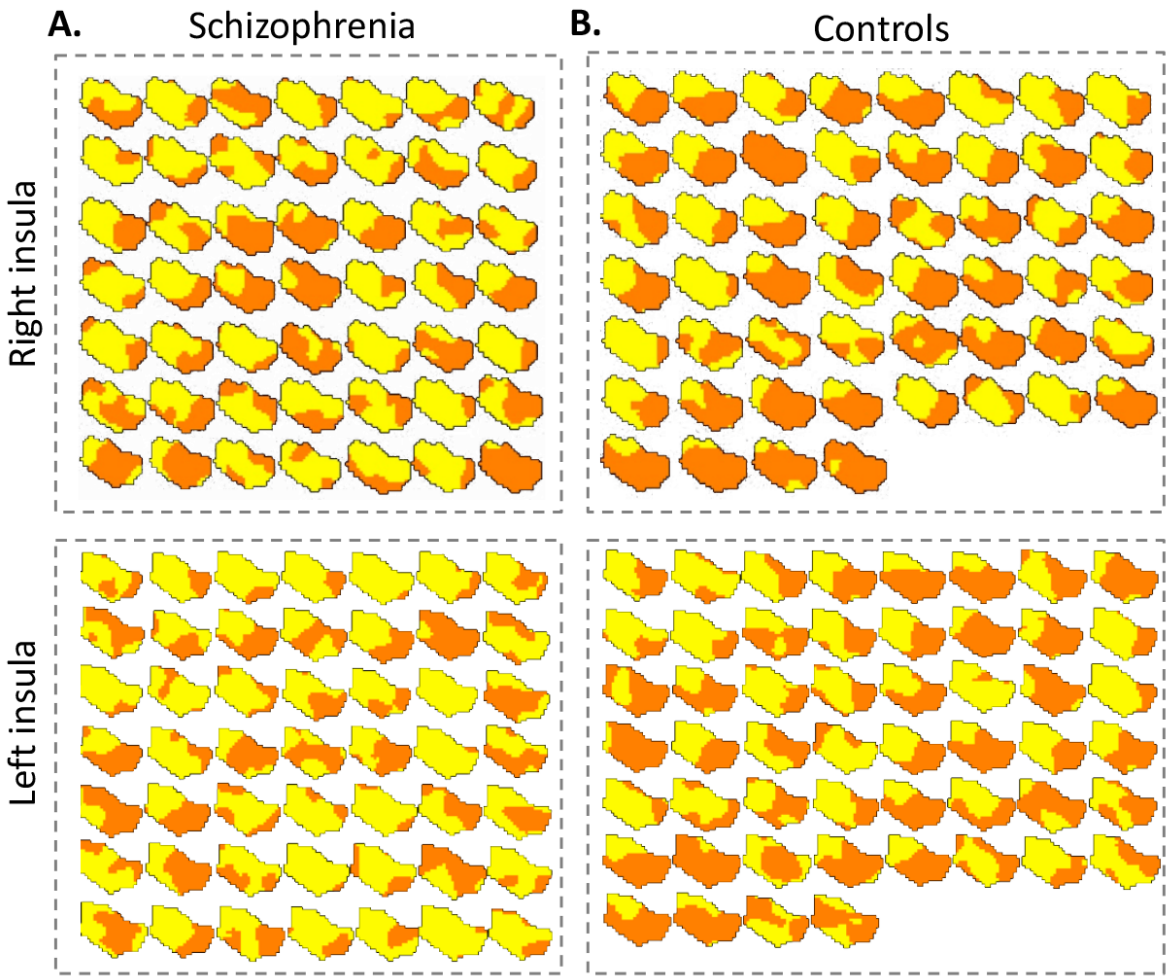


Figure S1. Individual bipartite parcellation of the insula based on resting-state functional connectivity in individuals with schizophrenia and healthy comparison individuals. Functional connectivity was mapped between each insula voxel and all other gray matter voxels, resulting in a whole-brain connectivity fingerprint for each insula voxel. Cluster analysis (*Ward's* linkage) was used to partition insula voxels that shared similar connectivity fingerprints into two clusters. Clusters were delineated independently in right (upper) and left insula (bottom) for each subject. The discrete subregions were mapped for each healthy comparison individual (Panel **A**) and each individual with schizophrenia (Panel **B**). For each individual, the cluster that overlapped to the greatest extent with the group-level segmented anterior insula (see Figure 1) was colored with orange. The other cluster was colored yellow. Note the significant variation across individuals in the shape and location of the two-putative insula subregions. Slice coordinates (MNI152, mm): right insula: x=38, y=0, z=8; left insula: x=−38, y=0, z=8.

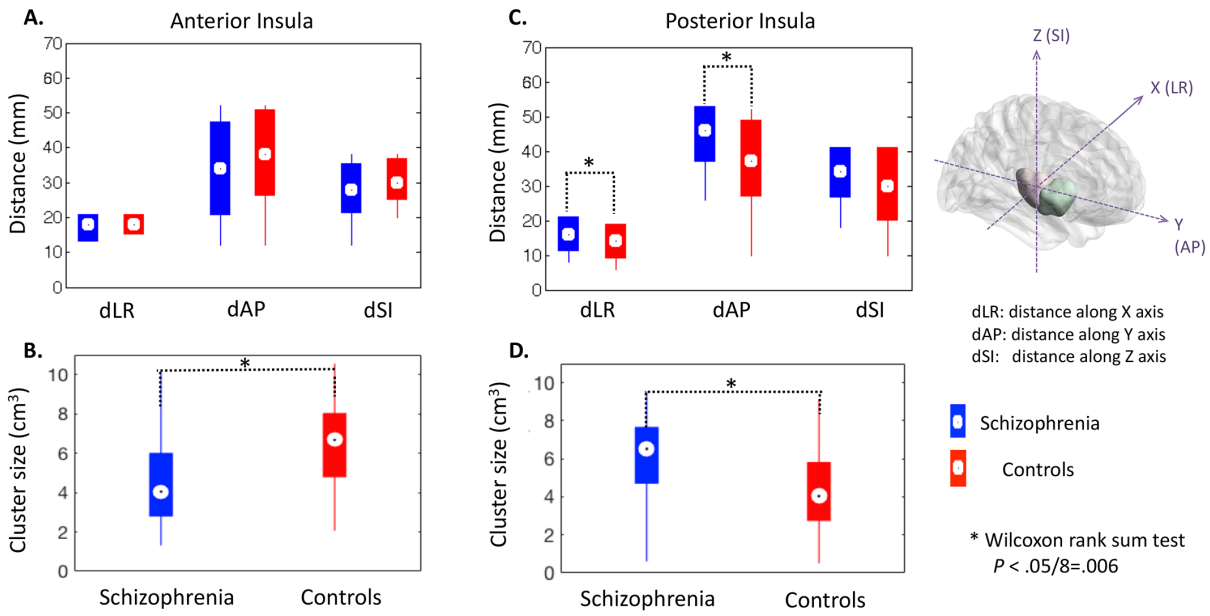


Figure S2. Comparison of cluster shape between schizophrenia and healthy comparison groups. Cluster analysis indicated that the left and right insula each comprise two subregions in both groups. For the schizophrenia group, the size of right anterior insula was smaller (z=3.81, p <0.0001, Panel **B**), while right posterior insula was larger (z=3.58, p <0.001, Panel **D**) and extended further anteriorly (z=3.44, p <0.001) and laterally (z=3.89, p <0.001, Panel **C**). Similar abnormalities were observed on the left side. Bonferroni correction was used for controlling for multiple comparison for the eight variables.

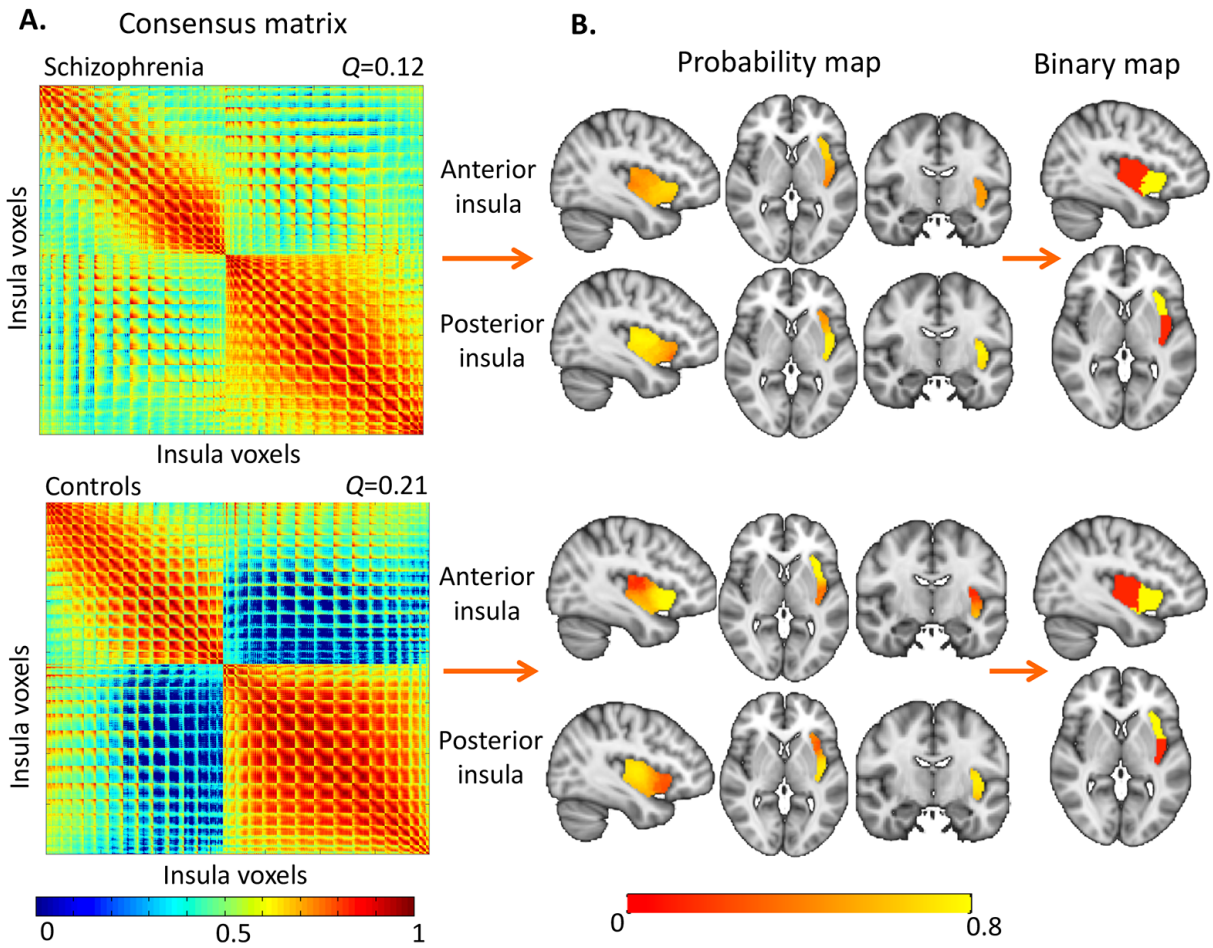


Figure S3. Bipartite parcellation of the left insula cortex based on resting-state functional connectivity in individuals with schizophrenia and healthy comparison individuals.

Panel A: Group consensus matrices (insula voxels × insula voxels) for the schizophrenia (upper matrix) and healthy comparison groups (lower). Each cell stores the proportion of individuals for which a given pair of insula voxels comprised the same cluster. Warm tones (red) indicate pairs of voxels consistently comprising the same subregions, whereas cool tones (blue) indicate pairs of voxels consistently comprising distinct subregions. While two modules were identified in both groups, modular separation was significantly reduced in the schizophrenia group (Q = 0.12, P = 0.002), compared to the healthy comparison group (Q = 0.21). The rows/columns of the consensus matrices are ordered such that all insula voxels comprising the anterior insula module are listed first, followed by all voxels in the posterior insula. **Panel B:** The consensus matrices are mapped to the insula to yield probabilistic maps of the anterior and posterior insula subregions. The color of each insula voxel is modulated by the proportion of individuals for which the voxel comprised the relevant subregion (module). Yellow tones indicate voxels that consistently comprise the relevant subregion across individuals, whereas red tones indicate voxels that rarely comprise the subregion. Probability maps were converted to binary (hard) segmentations to delineate discrete anterior (yellow) and posterior (red) insula subregions for both groups. The intersection of the anterior insula subregions delineated

for each of the two groups was determined to define a consensus anterior insula subregion for both groups (green), and similarly for the posterior insula subregion (pink) (see Figure 1, Panel C). Slice coordinates (MNI152, mm): x=−38, y=−10, z=2.

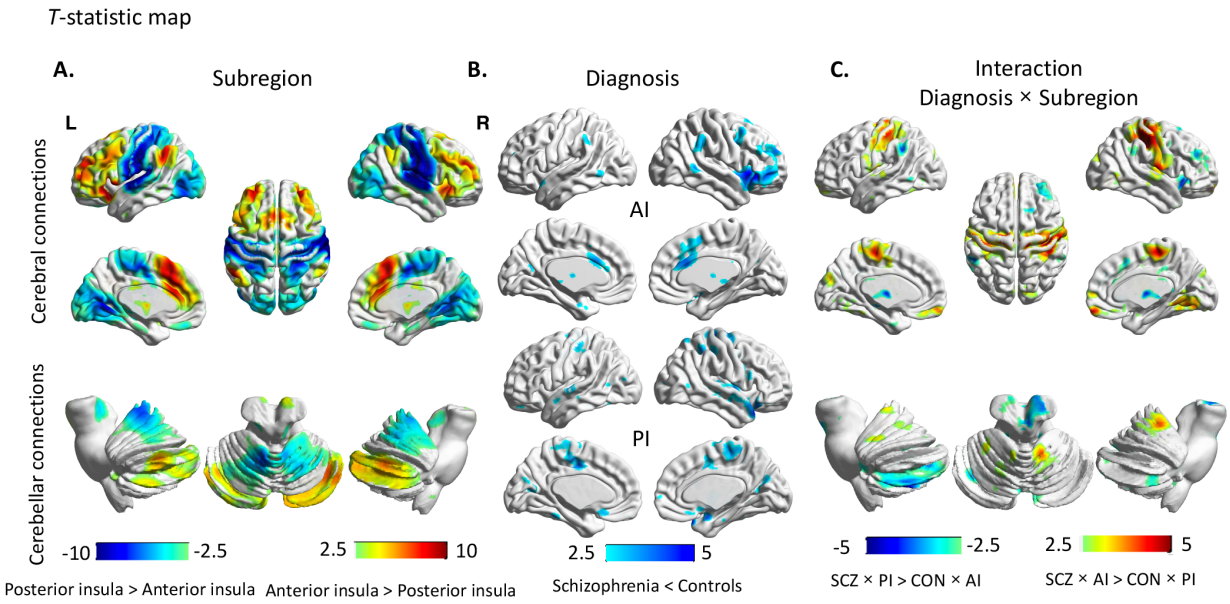


Figure S4. Altered resting-state functional connectivity of left anterior and posterior insula in schizophrenia. Functional connectivity was mapped between the anterior and posterior insula subregion and all other gray matter voxels. Analysis of variance was formulated to test the main effect of subregion (anterior vs posterior) and diagnosis (schizophrenia vs healthy comparison group) on insula connectivity at each gray matter voxel, as well as the interaction between these two main effects. **Panel A:** Main effect of subregion. The anterior and posterior insula subregions showed unique connectivity patterns: The anterior insula was preferentially connected to frontal-limbic areas and the posterior cerebellar lobe, whereas the posterior insula was characterized by increased connectivity with the parietal-temporal-occipital cortices and anterior cerebellar. **Panel B:** Main effect of diagnosis. Schizophrenia was associated with significant reductions in connectivity between the insula and multiple cortical/subcortical areas, relative to the healthy comparison group. Connectivity increases were not evident in the schizophrenia group. **Panel C:** Interaction effect. A significant interaction between subregion and diagnosis was found: The anterior insula subregion showed increased connectivity with the somatosensory/motor and occipital cortex in the schizophrenia group, whereas connectivity between the posterior insula and prefrontal cortex was increased in schizophrenia. AI: anterior insula; PI: posterior insula; SCZ: schizophrenia group; CON: healthy comparison group. Clusters are coloured according to t-statistic. All images pertain to left insula.

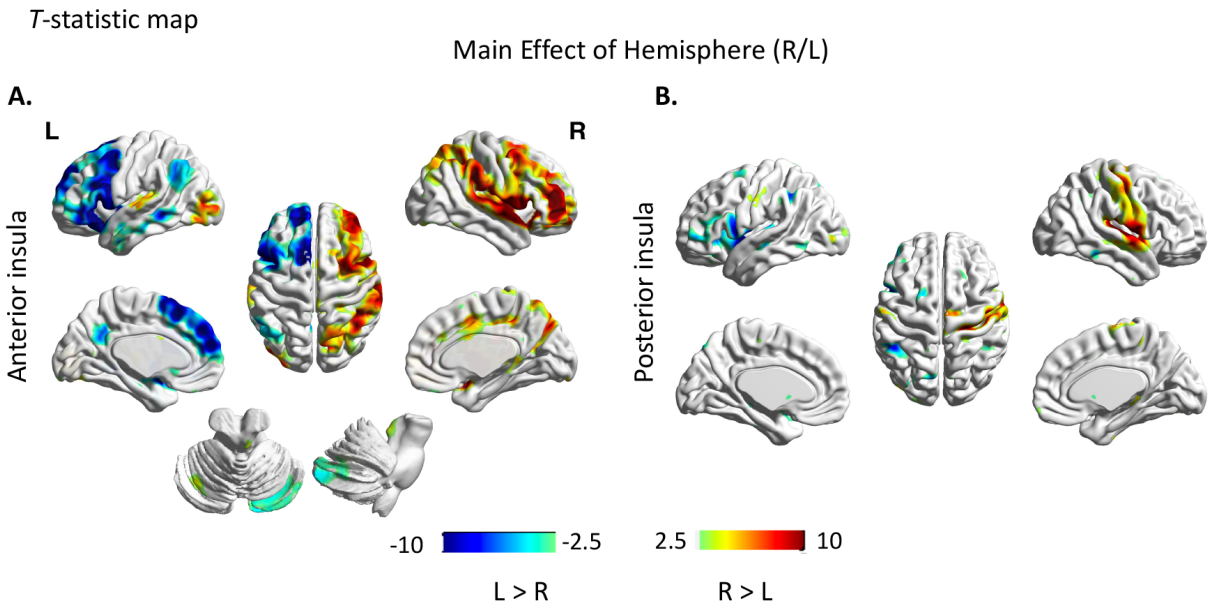


Figure S5. The main effect of hemisphere in resting-state functional connectivity of anterior and posterior insula cortex. An analysis of variance (ANOVA) was formulated to test the main effect of hemisphere (right and left) and diagnosis (controls and patients) on connectivity at each gray matter voxel. The interaction between hemisphere and diagnosis was also tested. The cerebral and cerebellar connections of insula cortex were bilateral and hemisphere preference was noted. While the cerebral connections showed an ipsilateral preference for both anterior insula (Panel **A**) and posterior insula (Panel **B**), cerebellar connections to anterior insula was more extensively connected to the cerebellum at the contralateral hemisphere (Panel **A**). No significant interaction was detected in contrast to diagnosis. Clusters are colored according to t-statistic.

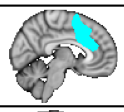
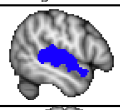
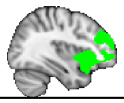
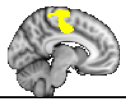
Supplementary Tables

Table S1.
Information of group-level insula sub-regions, in MNI152 standard anatomical space.

Insula subregions	Healthy comparison group				Schizophrenia				Intersection			
	Cluster size (cm^3)	Mean coordinates (mm)			Cluster size (cm^3)	Mean coordinates (mm)			Cluster size (cm^3)	Mean coordinates (mm)		
		X	y	z		x	y	z		x	y	z
Right AI	6.24	35	14	-2	5.58	34	16	-2	5.48	34	16	-4
Right PI	4.94	35	-8	6	5.62	36	-6	6	4.85	36	-8	8
Left AI	6.00	-38	14	-2	5.42	-38	14	-2	5.28	-36	16	-2
Left PI	5.17	-40	-8	6	5.76	-40	-6	6	5.03	-40	-8	6

AI: anterior insula
PI: posterior insula

Table S2.
Anatomical locations of clusters associated with significantly reduced functional connectivity with insula subregions in the schizophrenia group, relative to the group of healthy comparison individuals (p<0.05, corrected). Clusters are shown in MNI152 standard anatomical space.

Clusters	**Mean coordinates** (COG, mm)			**Anatomical visualization**	**Hemisphere**	**Peak t-stats**	**P-value**	**Seed region**
	x	**y**	**z**					
Cluster 1	3.22	18	37.6		_	5.51	0.0118	Right AI
Cluster 2	-49	-17.5	0.78		Left	4.59	0.0091	Right PI
Cluster 3	38.7	11.2	-10.1		Right	5.7	0.0035	Right AI
Cluster 4	36.5	7.06	-9.83		Right	5.31	0.0018	Right PI
Cluster 5	-4.62	-15.9	56.1		_	5.4	0.0018	Right PI
Cluster 6	38.3	28.2	0.1		Right	5.66	0.0049	Left AI
Cluster 7	45.8	0.38	-8.48		Right	5.35	0.0087	Left PI
Cluster 8	6.12	-17.3	59.8		_	4.69	0.0081	Left PI

COG, centre of gravity; AI, anterior insula; PI, posterior insula

Table S3.
Association between insula functional connectivity and age, sex and CPZ equivalent.

Clusters	FC-AGE		FC-SEX		FC-CPZ	
	r	p	t-stats	p	r	p
Cluster 1	-0.1598	0.2779	0.9843	0.3302	-0.1418	0.3364
Cluster 2	-0.0942	0.5242	1.4357	0.158	0.0269	0.8559
Cluster 3	-0.0971	0.5115	1.2292	0.2254	-0.0474	0.7491
Cluster 4	0.0714	0.6294	1.8223	0.0751	0.0108	0.9422
Cluster 5	0.102	0.4901	-0.0074	0.9942	-0.0775	0.6005
Cluster 6	-0.1451	0.3251	1.1861	0.2418	-0.1584	0.2823
Cluster 7	-0.0004	0.9977	-0.6698	0.5064	0.0366	0.805
Cluster 8	0.1171	0.4282	0.9187	0.3632	0.1559	0.29

FC, functional connectivity; CPZ, chlorpromazine.

References

1. Pruim RHR, Mennes M, Buitelaar JK, Beckmann CF (2015): Evaluation of ICA-AROMA and alternative strategies for motion artifact removal in resting state fMRI. *NeuroImage*. 112:278-287.
2. Pruim RHR, Mennes M, van Rooij D, Llera A, Buitelaar JK, Beckmann CF (2015): ICA-AROMA: A robust ICA-based strategy for removing motion artifacts from fMRI data. *NeuroImage*. 112:267-277.
3. Ward J, Joe H (1963): Hierarchical grouping to optimize an objective function. *Journal of the American statistical association*. 58:236-244.
4. Tian Y, Zalesky A (2018): Characterizing the functional connectivity diversity of the insula cortex: Subregions, diversity curves and behavior. *Neuroimage*. 183:716-733.
5. Newman ME, Mark E (2006): Modularity and community structure in networks. *Proceedings of the National Academy of Sciences of the United States of America*. 103:8577-8582.
6. Newman ME (2013): Spectral methods for community detection and graph partitioning. *Physical Review E*. 88:042822.
7. Lancichinetti A, Fortunato S (2012): Consensus clustering in complex networks. *Scientific Reports*. 2:336.
8. Clauset A, Newman MEJ, Moore C (2004): Finding community structure in very large networks. *Physical Review E*. 70:066111.
9. Haak KV, Marquand AF, Beckmann CF (2018): Connectopic mapping with resting-state fMRI. *Neuroimage*. 170:83-94.
10. Serrano MÁ, Boguñá M, Vespignani A (2009): Extracting the multiscale backbone of complex weighted networks. *Proceedings of the National Academy of Sciences*. 106:6483-6488.

CHAPTER 5

TOPOGRAPHIC ORGANIZATION OF THE HUMAN SUBCORTEX

nature neuroscience

ARTICLES

https://doi.org/10.1038/s41593-020-00711-6

Check for updates

Topographic organization of the human subcortex unveiled with functional connectivity gradients

Ye Tian[1]✉, Daniel S. Margulies[2], Michael Breakspear[3,4] and Andrew Zalesky[1,5]✉

Brain atlases are fundamental to understanding the topographic organization of the human brain, yet many contemporary human atlases cover only the cerebral cortex, leaving the subcortex a terra incognita. We use functional MRI (fMRI) to map the complex topographic organization of the human subcortex, revealing large-scale connectivity gradients and new areal boundaries. We unveil four scales of subcortical organization that recapitulate well-known anatomical nuclei at the coarsest scale and delineate 27 new bilateral regions at the finest. Ultrahigh field strength fMRI corroborates and extends this organizational structure, enabling the delineation of finer subdivisions of the hippocampus and the amygdala, while task-evoked fMRI reveals a subtle subcortical reorganization in response to changing cognitive demands. A new subcortical atlas is delineated, personalized to represent individual differences and used to uncover reproducible brain–behavior relationships. Linking cortical networks to subcortical regions recapitulates a task-positive to task-negative axis. This new atlas enables holistic connectome mapping and characterization of cortico–subcortical connectivity.

The ubiquity of MRI has enabled high-throughput mapping of standardized brain parcellation atlases that represent consensus cortical boundaries across hundreds of scanned people[1]. Compared with the cerebral cortex, efforts to parcellate the human subcortex are scarcer. Indeed, many leading brain atlases delineate only cortical regions[2,3].

The subcortex is widely implicated in the pathophysiology of many neuropsychiatric disorders, and its role in cognition is unequivocal[4]. To better elucidate the role of the subcortex in health and disease, further work is needed to advance recent efforts to map the functional architecture of the subcortex[5,6]. This study aims to unravel the incredibly complex functional organization of the human subcortex by developing and validating a comprehensive subcortical atlas using 3 Tesla (3T) and 7T fMRI.

Cortical boundaries[7] within a brain atlas are often delineated at locations of abrupt spatial change in cortical microstructure, function and/or connectivity[2,8,9]. Cortical gradients[10] and the related connectopy concept[11] offer a complementary representation of cortical topography. Rather than delineating discrete spatial boundaries, topographic change is represented continuously along overlapping organizational axes[12].

Brain cartography studies tend to espouse one or the other of these two representations[1]. This is exemplified by current contention about whether the functional topography of the cerebellum is best represented by continuous gradients[13] or discrete boundaries[14]. However, the two paradigms are not necessarily contradictory. Spatial variation across expanses of the cerebrum may be evident but too gradual to warrant boundary delineation; thus, a continuum might be deemed to provide the most parsimonious representation. This leads to the following question of model selection: how sharp and conspicuous must a change be to warrant boundary delineation[15]? Here, we map functional connectivity gradients of the human subcortex and delineate subcortical boundaries only when justified by a formal model selection process.

Subcortical geometry is fundamentally different to the convoluted sheet-like structure of the cerebral cortex[16]. New paradigms are therefore required to facilitate subcortical cartography. To this end, we developed gradientography, a fMRI analog of diffusion MRI tractography that enables the quantification of subcortical connectivity gradients and a statistically principled formalism to guide boundary delineation. This allows us to comprehensively parcellate the subcortex on the basis of resting-state functional connectivity profiles and to produce a standardized atlas representing consensus boundaries among more than 1,000 healthy adults. The new atlas comprises four scales that recapitulate well-known anatomical nuclei at the coarsest scale and reveal 27 bilateral regions at the finest. The new atlas is replicated using ultrahigh field strength fMRI (7T) and is personalized to account for individual connectivity differences. An analysis of task-evoked fMRI (tfMRI) reveals a subtle reorganization of subcortical topography in response to changing cognitive demands. We use the new atlas to uncover correlational relationships between subcortical functional connectivity and individual variation in five behavioral domains and to reveal a new task-positive to task-negative organizational axis in cortico–subcortical connectivity[17]. This study provides an important step toward understanding the functional organization of the human subcortex.

Results

We investigated the functional connectivity architecture of the human subcortex using resting-state fMRI (rfMRI) data acquired at 3T ($n=1,080$) and 7T ($n=183$) and tfMRI data acquired at 3T ($n=725$) from healthy adults participating in the Human Connectome Project (HCP)[18]. Demographics are shown in Supplementary Table 1. Two 3T rfMRI sessions were acquired for

[1]Melbourne Neuropsychiatry Centre, Department of Psychiatry, The University of Melbourne, Parkville, Victoria, Australia. [2]Centre National de la Recherche Scientifique (CNRS) UMR 8002, Integrative Neuroscience and Cognition Center, Université de Paris, Paris, France. [3]Discipline of Psychiatry, Faculty of Health and Medicine, University of Newcastle, Newcastle, New South Wales, Australia. [4]School of Psychology, Faculty of Science, University of Newcastle, Newcastle, New South Wales, Australia. [5]Department of Biomedical Engineering, Melbourne School of Engineering, The University of Melbourne, Parkville, Victoria, Australia. ✉e-mail: ye.tian2@unimelb.edu.au; azalesky@unimelb.edu.au

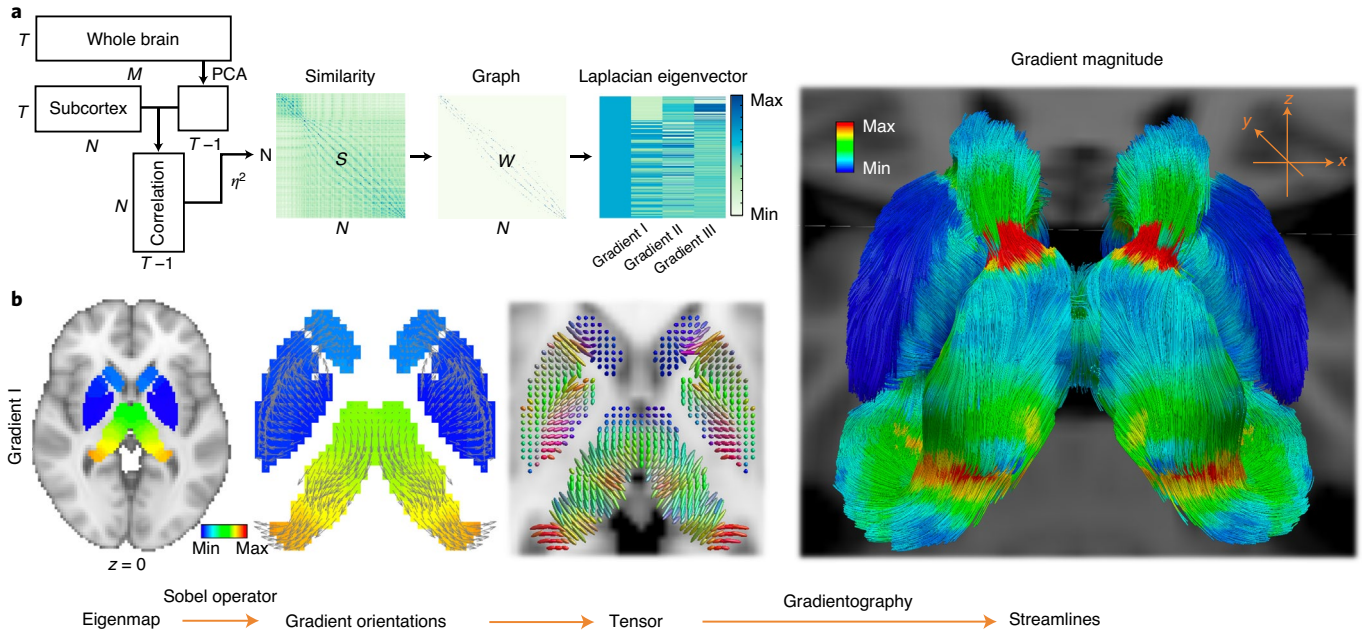


Fig. 1 | Gradientography in the human subcortex. a, A schematic of functional connectivity gradient mapping. The similarity in connectional fingerprints between pairs of subcortical voxels was measured using the η^2 coefficient. Pairs of voxels with similar fingerprints connected to similar brain areas. The similarity matrix (*S*) shown represents a group consensus for 1,080 healthy adults. The similarity matrix was transformed into a sparse graph with adjacency matrix *W*. The graph nodes correspond to subcortical voxels. Eigenvalues and eigenvectors were computed for the graph Laplacian. The eigenvectors with the second, third and fourth smallest eigenvalue are called gradients I, II and III, respectively. Each gradient provides a mapping of continuous variation in functional connectivity across the topography of the subcortex. *N*, number of subcortical voxels; *M*, number of whole-brain gray matter voxels; *T*, number of time frames. **b**, A schematic of the gradientography pipeline. Gradients were projected onto subcortical voxels to enable anatomical visualization. The axial slice shown is for gradient I. The Sobel operator was used to estimate the local gradient direction and magnitude for each subcortical voxel. The arrows shown point in the direction of the estimated gradients. Arrow lengths are normalized to unit length. Tensors were fitted to the gradient field. Tensors are colored according to the gradient direction (red, left–right; green, posterior–anterior; blue, superior–inferior). Streamlines were propagated through the tensor field using methods for diffusion MRI tractography. Streamlines are shown from a posterior viewpoint and colored according to the gradient magnitude. The red bands indicate peaks in the gradient magnitude that demarcate hippocampus–thalamus and caudate–thalamus boundaries.

each individual, with the first session used as the primary dataset (REST1) and the second used for replication (REST2). Gradients in functional connectivity were mapped using Laplacian eigenmaps and a newly developed procedure called gradientography. Formal model selection was used to determine whether gradient magnitude peaks were sufficiently large to warrant boundary delineation. The competing model posited a gradual spatial change in connectivity without discrete boundaries. This resulted in a new fMRI-based multiscale parcellation atlas of the subcortex, which we used to reveal new insights into subcortical function and architecture.

Connectivity gradients and gradientography. Whole-brain functional connectivity fingerprints[19] were mapped for each subcortical voxel and individual. Spatial gradients characterizing continuous modes of functional connectivity variation across the topography of the subcortex were computed using Laplacian eigenmaps and the connectopy method[11] (Fig. 1a). The eigenmap, or connectopy, explaining the most variance in functional connectivity was called gradient I (Fig. 1b), and the next two successive eigenmaps were called gradient II and gradient III, respectively (Supplementary Fig. 1). Further gradients explained substantially less variance and were therefore not considered (Supplementary Fig. 2). A new technique called gradientography was developed to visualize the connectivity gradients. Gradientography involves estimation of the principal gradient direction for each subcortical voxel, representing gradient directions and magnitudes with tensors, and then propagation of streamlines through the tensor field using established tools for diffusion MRI tractography. In this way, approximately 15,000 streamlines were initialized and propagated throughout the entire subcortical volume to map the principal organizational axes of the subcortex for gradient I (Fig. 1b) and for gradients II and III (Supplementary Fig. 1).

Gradient magnitude peaks indicated the locations of putative functional boundaries between regions. To visualize peak locations, streamlines were colored according to the gradient magnitude. Peak locations are shown as circumscribed red bands (Fig. 1b) and recapitulated boundaries between well-known anatomical nuclei. Local maxima in the gradient magnitude images showed moderate consistency among the three gradients (Supplementary Figs. 1 and 3); thus, only gradient I was used for boundary delineation. Gradient I streamlines were partitioned into dorsal and ventral groups at the location of the anatomical discontinuity between the caudate tail and the anterior extent of the thalamus. The dorsal group covered the globus pallidus (GP) and the striatum (Fig. 2a), whereas the amygdala, hippocampus and thalamus constituted the ventral group (Fig. 2b).

We next sought to quantify the size of each gradient magnitude peak to determine whether gradients were sufficiently abrupt to warrant boundary delineation. To this end, gradient magnitude images were projected onto two-dimensional trajectories called diversity curves[15]. A separate diversity curve was mapped for the dorsal and ventral streamline group. The dorsal diversity curve comprised three distinct local maxima indicating the locations of putative boundaries between the GP–putamen, the putamen–nucleus

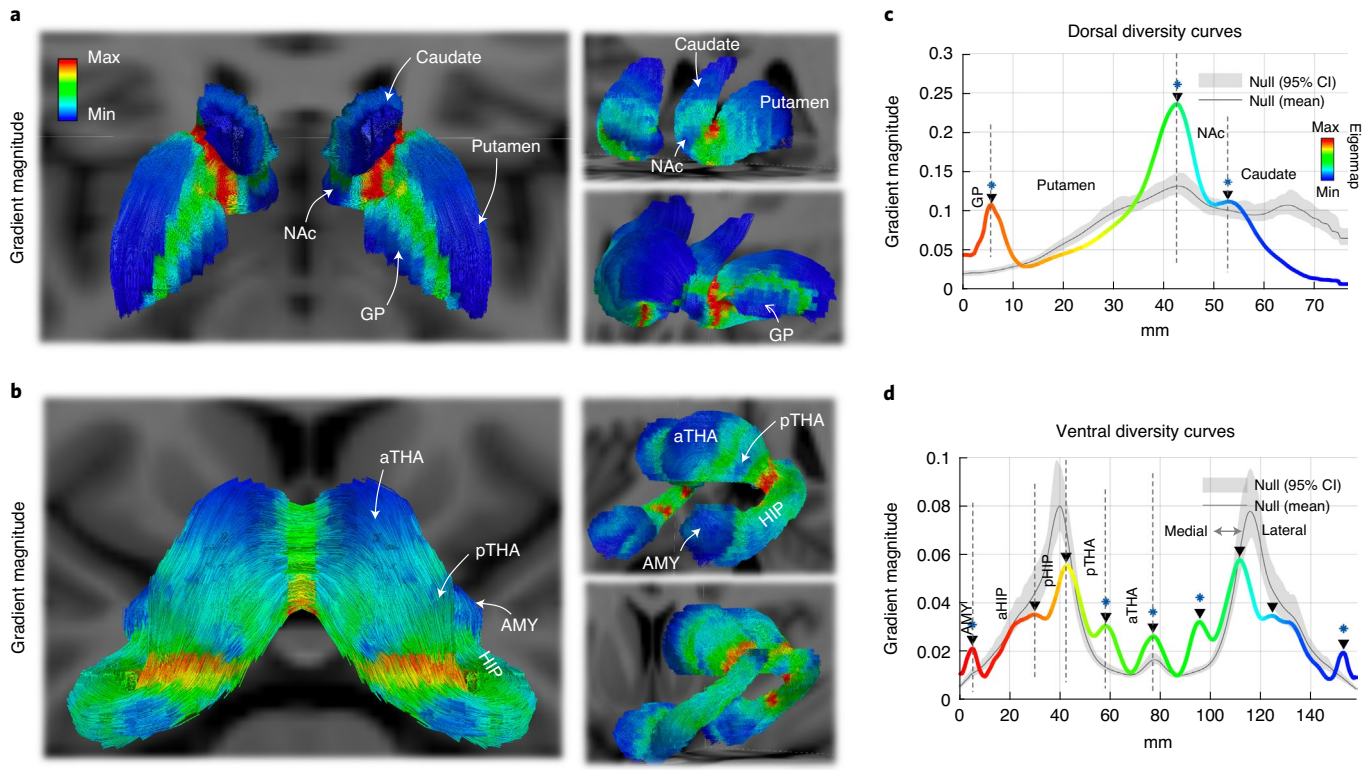


Fig. 2 | Model selection: which gradient magnitude peaks are sufficiently large to warrant boundary delineation? a,**b**, Streamlines were partitioned into bilaterally symmetric dorsal (**a**) and ventral (**b**) groups. The streamlines shown are colored according to the gradient magnitude. Dorsal streamlines traverse the GP, the putamen, the NAc and the caudate. Ventral streamlines traverse the left and right thalamus (THA; where a is anterior and p is posterior), the hippocampus (HIP) and the amygdala (AMY). **c**,**d**, Dorsal (**c**) and ventral (**d**) diversity curves were mapped to parameterize the gradient magnitude as a function of spatial position along the length of dorsal and ventral streamline trajectories. Black triangles indicate diversity curve peaks (local maxima) demarcating locations of putative functional boundaries. Diversity curves are colored according to eigenmap values for gradient I. Null diversity curves ($n = 100$) for the null hypothesis of an absence of discrete boundaries are shown in gray, with shading used to show 95% confidence intervals (CI) and solid lines indicating the mean. Peaks in the null diversity curves are due to the effects of geometry. Peaks for which the null hypothesis could be rejected are demarcated with blue asterisks ($P < 0.05$ one-sided, FDR-corrected for all 12 peaks).

accumbens (NAc) and the NAc–caudate (Fig. 2c). Nine local maxima were evident in the ventral diversity curve, which suggested boundary locations that distinguished the amygdala, the anterior and posterior hippocampus, the anterior and posterior thalamus, as well as the left and right thalamus (Fig. 2d). Locations of gradient magnitude peaks could not be explained by structural MRI signal properties and potential confounds, including the fMRI signal-to-noise ratio (SNR), the fMRI signal magnitude and the T1-weighted and T1/T2-weighted contrast (Supplementary Fig. 4).

A new subcortical atlas. The magnitude of local maxima in the diversity curves varied by a factor of more than ten, which suggests that putative boundaries between some regions were markedly more abrupt than others. How large should a peak be to warrant boundary delineation? Small peaks can emerge due to the convoluted geometry of the subcortex and other confounds (Supplementary Fig. 5). False-positive boundaries should not be delineated at such peaks. Therefore, for each peak, a formal model selection procedure was used to test the null hypothesis that the peak magnitude could be explained by geometry and/or other confounds. Rejection of the null hypothesis indicated that boundary delineation was warranted. Otherwise, if the peak magnitude was not sufficiently large to enable rejection of the null hypothesis, a continuous representation of spatial variation in connectivity was deemed to be the most parsimonious model[15]. The null hypothesis was tested using a geometry-preserving null model (Methods). Diversity curves generated using the null model are colored gray in Fig. 2c,d. The actual peaks significantly exceeded all null data ($P < 0.05$, false discovery rate (FDR)-corrected for all 12 peaks), except for peaks separating the bilateral hippocampus/thalamus and the anterior–posterior hippocampus. However, given that the hippocampus and the thalamus are anatomically and functionally distinct and that the peak separating these two regions was unequivocal, we made an exception and delineated a boundary here, whereas the putative anterior–posterior hippocampus boundary was not delineated, which is consistent with the null data. While peaks in the null diversity curves often corresponded with locations to peaks in the actual diversity curves, including the functional boundaries between the putamen–NAc, the posterior hippocampus–posterior thalamus and the left–right thalamus, distinct peaks were also evident where the effect of geometry is minimal (Supplementary Fig. 5a), such as the amygdala–anterior hippocampus, the anterior–posterior thalamus and the GP–putamen. This indicates that subcortical geometry can predict and account for the location of some functional boundaries, but geometry per se cannot explain the magnitude of all boundaries, except for the hippocampus–thalamus (see "Further methodological considerations" in the Methods). Finally, the watershed transform algorithm was used to segment subcortical voxels into contiguous regions such that boundaries demarcated watershed lines.

This resulted in eight bilateral regions that constituted a relatively coarse atlas, referred to as the scale I atlas (Fig. 3a). The scale I atlas recapitulated well-known anatomical nuclei, namely, the amygdala,

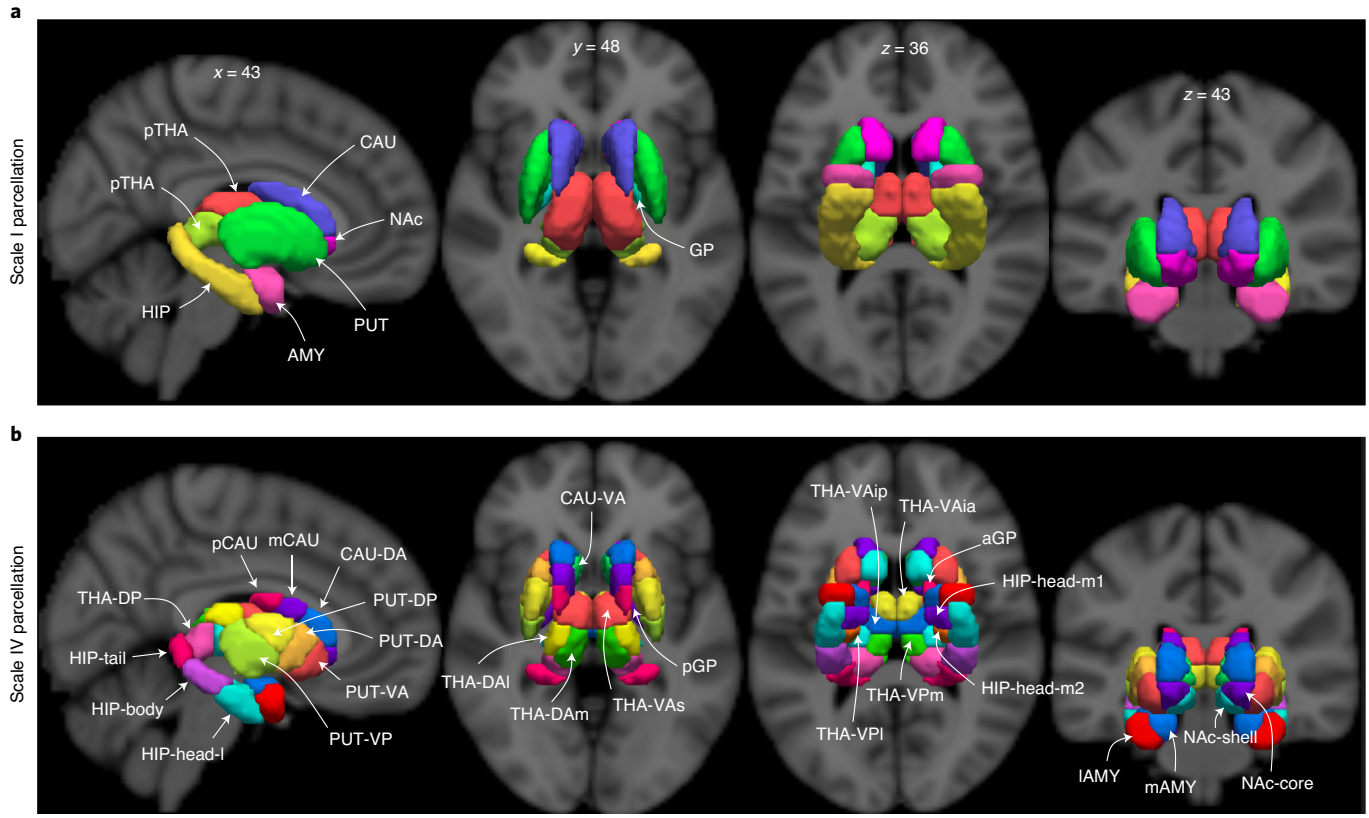


Fig. 3 | A multiscale group-consensus parcellation atlas derived from 3T-rfMRI acquired in 1,080 healthy adults. a, Scale I is the coarsest atlas and comprises eight bilateral regions that recapitulate anatomical nuclei, including the caudate nucleus (CAU), the NAc, the putamen (PUT), the amygdala, the hippocampus and the thalamus. An anteroposterior division within the thalamus is also present. **b**, Scale IV is the finest scale of the parcellation hierarchy and comprises 27 bilateral regions. Homologous regions are identically colored. d, dorsal; i, inferior; l, lateral; m, medial; s, superior; v, ventral (detailed nomenclature for all regions is provided in Supplementary Table 2).

the hippocampus, the thalamus, the GP, the NAc, the caudate and the putamen, as well as an anteroposterior thalamic partition, which corresponded to the spatial distribution of the two subpopulations of thalamic projection cells (matrix and core)[20]. Gradient mapping, boundary delineation and model selection were then iteratively performed separately for each region constituting the scale I atlas. This resulted in a finer atlas, called the scale II atlas, comprising 16 bilateral regions. In turn, the null hypothesis was independently tested for each region in the scale II atlas. Recursively continuing this process until the null hypothesis could not be rejected for any regions yielded four progressively more detailed atlases of the subcortex (scale I: 16 regions (Fig. 3a); scale II: 32 regions; scale III: 50 regions; scale IV: 54 regions (Fig. 3b); Supplementary Fig. 6). The new atlas is hierarchically organized, with the entire subcortex residing at the base of a hierarchical tree and the smallest regions constituting the scale IV atlas defining the leaves (Fig. 4a,b). Subcortical gradients were also hierarchically organized (Fig. 4b,c and Supplementary Fig. 7). A schematic of the recursive procedure is provided in Supplementary Fig. 8.

Parcellation of the amygdala terminated at scale II, and striatal parcellation continued until scale III, while only the thalamus and the hippocampus progressed to scale IV. A nomenclature scheme for all delineated regions was developed (Supplementary Table 2). In particular, regions that could be unequivocally matched to homologous anatomical structures were labeled as such, while the remaining regions were labeled with reference to standard anatomical planes (for example, anterior–posterior, medial–lateral, dorsal–ventral and superior–inferior).

Scales I and II generally recapitulated anatomical boundaries, whereas some divergence emerged at finer scales between anatomy and the boundaries delineated here based on functional connectivity. The eight thalamic subregions constituting scale IV showed moderate spatial correspondence with histologically delineated thalamic nuclei (Supplementary Fig. 9a). The hippocampus was segmented along its long axis into anterior (head) and posterior (body and tail) components (Supplementary Fig. 9b), which is consistent with previous functional-based hippocampal parcellations[21]. Although the head of the hippocampus was further divided into medial and lateral components, the overall long-axis organization diverged from the characteristic mediolateral organization that is histologically found[22].

Connectivity gradients (gradients I–III) for the hippocampus, the striatum and the thalamus were projected onto the cortical surface on the basis of the cortical vertices with which they were most strongly connected[11,23] (Supplementary Fig. 10a–c).

Parcellation homogeneity. Having delineated a new subcortical atlas, we next sought to investigate the validity and reproducibility of the atlas. A key marker of parcellation validity is within-parcel homogeneity of functional signals[1]. Homogeneity was measured on the basis of within-parcel synchrony of fMRI time series acquired in the second fMRI session (REST2), whereas the first session (REST1) was used for parcellation. Homogeneity was separately computed for each region and then averaged across all regions to yield parcellation homogeneity estimates for scales I–IV (Supplementary Fig. 11a).

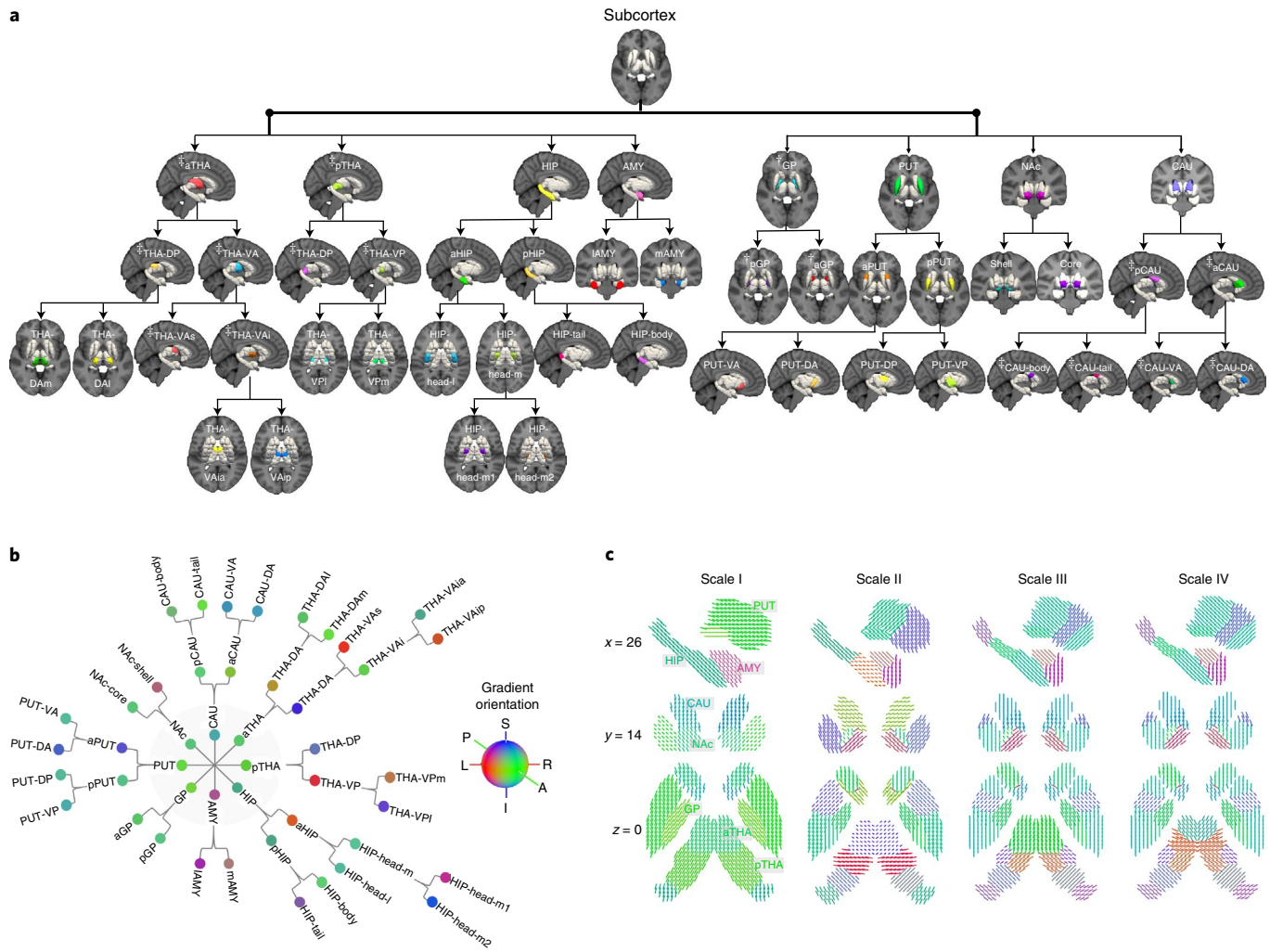


Fig. 4 | Organization of the human subcortex. Model selection and null hypothesis testing was used to determine whether gradient magnitude peaks were sufficiently large to warrant boundary delineation. This process was recursively repeated for each new region delineated, unveiling a multiscale parcellation architecture. The null hypothesis of an absence of boundaries could not be rejected for any of the regions constituting scale IV; thus, further (finer) parcellation was not warranted. **a**, A top-down representation of the parcellation hierarchy. Regions are shown atop a reference structural MRI image. Homologous regions are identically colored. †The caudate was removed for visualization purposes; ‡the putamen and the GP were removed for visualization purposes. **b**, A parcellation hierarchy visualized in the form of a circular tree. The central node represents the entire subcortex and the other nodes represent distinct regions. Regions are arranged within four concentric circles, where the innermost circle (gray) is the first level (scale I). Nodes are colored according to principal gradient orientations within each region (red, left–right; green, posterior–anterior; blue, superior–inferior). The principal gradient orientation was estimated by averaging the local gradient directions across all voxels within each region. **c**, Region-averaged gradient directions represented with quiver lines for scales I–IV. The same images without region averaging are shown in Supplementary Fig. 7. Detailed nomenclature for all regions is provided in Supplementary Table 2.

As expected[8], homogeneity monotonically increased from scale I to scale IV (Fig. 5a). To test whether parcellation homogeneity was significantly greater than expected due to chance, homogeneity was also estimated for ensembles of random subcortical parcellations (Supplementary Fig. 11b). Random parcellations were generated by delineating boundaries at arbitrary locations, subject to preservation of key geometric properties (Methods). Scales II–IV were significantly more homogeneous than expected due to chance ($P<0.01$), whereas this was not the case for scale I ($P=0.23$; Fig. 5a). Scale I regions (Fig. 3a) encompassed multiple functionally distinct substructures, which potentially explains the relatively low within-parcel homogeneity of this scale. Parcellation homogeneity was compared between the new atlas and existing imaging- and histology-based subcortical parcellations (Supplementary Table 3). Striatal, hippocampal and thalamic parcellations were isolated from the new atlas to enable comparisons with existing parcellations of these regions. The new atlas was significantly more homogeneous than existing imaging-based parcellations of the entire subcortex (subcortex-I: $P<0.001$; subcortex-II: $P<0.001$), the hippocampus ($P<0.001$), the thalamus ($P<0.001$) or the striatum ($P<0.001$), as well as a histological atlas of the hippocampus (Hippocampus-His: $P<0.001$; Fig. 5b and Supplementary Fig. 12). These results were replicated in an independent dataset comprising ten healthy adults (six males, mean age of 26 ± 2.1 years; Supplementary Fig. 13).

In auxiliary analyses, we tested whether task-evoked activity mapped onto the new atlas and respective atlas boundaries. To this end, the standard deviation in task-evoked activity was computed across voxels constituting each region and then averaged over all regions. This was repeated for scales I–IV. The lower the standard deviation, the more circumscribed task-evoked activity was to

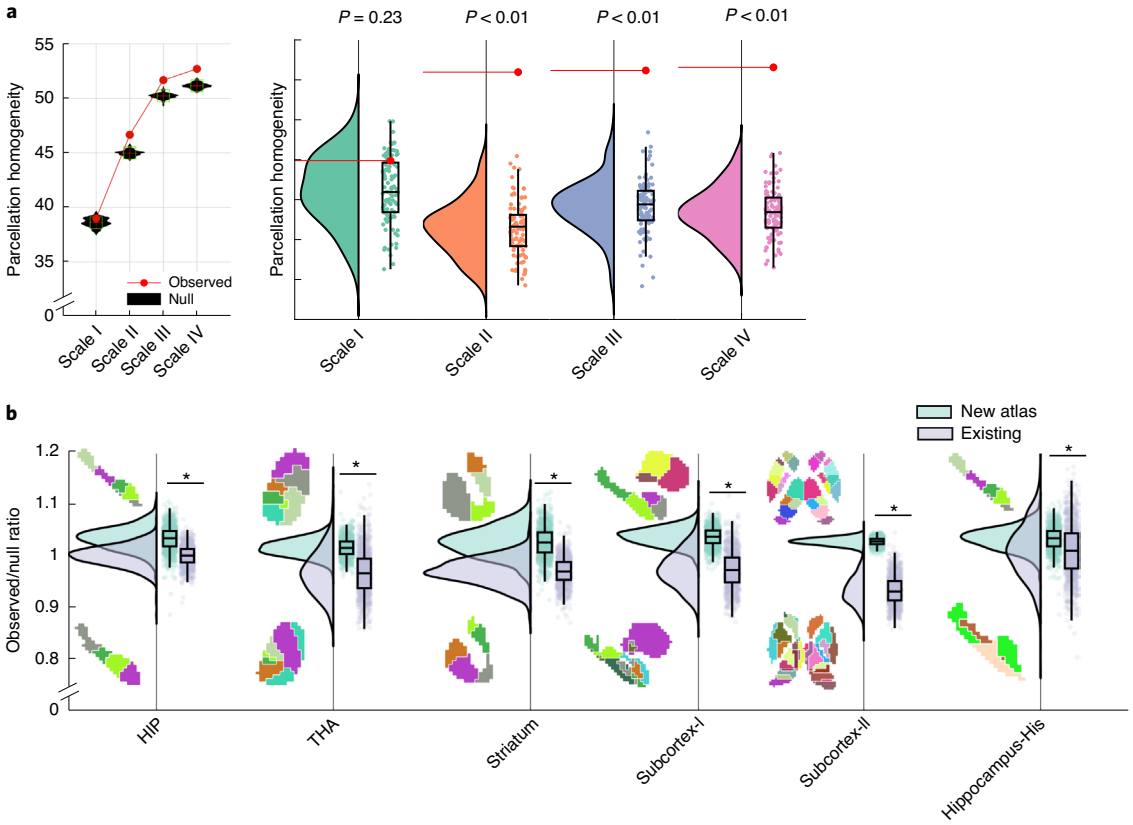


Fig. 5 | Parcellation homogeneity. a, Parcellation homogeneity of the new atlas was benchmarked to random parcellations of the subcortex comprising an identical number of regions and a comparable distribution of region sizes. Violin plots show the distribution of parcellation homogeneity measured within ensembles of 100 random parcellations. The *P* value (one-sided) shown for each scale is the proportion of random parcellations comprising the ensemble that were more homogeneous than the observed parcellation. The horizontal red lines indicate the observed parcellation homogeneity values. The bottom and top edges of the boxes indicate the 25th and 75th percentiles of the distribution, respectively. The central mark indicates the median. The whiskers extend to the most extreme data points that are not considered outliers (1.5-times the interquartile range). The vertical axis is omitted to aid visualization. The null hypothesis of parcellation homogeneity that is no better than chance could be rejected for all scales except scale I. **b**, Parcellation homogeneity comparisons between the new atlas and existing parcellation atlases of the entire subcortex and specific subcortical nuclei (Supplementary Table 3). Parcellation homogeneity was separately computed for each individual (REST2, $n = 1{,}021$) and normalized by the random parcellation homogeneity, yielding an observed-to-null ratio. The box plots show the distribution of this ratio across individuals for the new (turquoise) and existing (violet) parcellation atlases. The bottom and top edges of the boxes indicate the 25th and 75th percentiles of the distribution, respectively. The central mark indicates the median. The whiskers extend to the most extreme data points that are not considered outliers (1.5-times the interquartile range). Homogenous parcellations have a ratio that exceeds one. Asterisks indicate that the observed-to-null ratio is significantly higher for the new atlas relative to the existing atlas used for comparison ($P < 0.001$, two-sided two-sample *t*-test). Anatomical visualizations of the new and comparison atlases are shown above and below the box plots, respectively.

particular atlas regions. For all task conditions, we found that standard deviations were significantly lower for the new atlas than comparable random parcellations of the subcortex ($P < 0.01$; Supplementary Fig. 14). This cross-modality validation suggests that task-evoked activity is circumscribed to specific subcortical atlas regions more than expected by chance.

Parcellation replication. Ultrahigh field strength MRI can alleviate several technical challenges associated with subcortical imaging[24]. Hence, we sought to investigate whether the new atlas could be replicated using 7T fMRI. Qualitatively, gradient magnitude peaks were sharper and more circumscribed at 7T than at 3T (Fig. 6). Gradientography, model selection and boundary delineation applied to 7T data yielded a comparable but more detailed atlas of the subcortex that also comprised four scales (scale I: 16 regions; scale II: 34 regions; scale III: 54 regions; scale IV: 62 regions). The number of regions delineated at scale I was identical between 3T and 7T data (Fig. 6). However, additional boundaries could be identified with 7T data at scales II–IV (Supplementary Figs. 15 and 16). In particular, the amygdala was partitioned into medial and lateral subregions at 3T, whereas its medial extent was further divided into centromedial and superomedial components at 7T, and the body of the hippocampus was further divided mediolaterally. Based on normalized mutual information (NMI), the spatial correspondence between the 3T and 7T atlases was excellent (NMI = 0.93, 0.88, 0.84 and 0.83 for scale I, scale II, scale III and scale IV, respectively; Supplementary Fig. 16). Correspondence between 3T and 7T atlases was significantly higher than expected due to chance at all parcellation scales ($P < 0.01$; Supplementary Fig. 16).

Personalized parcellation. Having delineated a group-consensus atlas of the subcortex, we next sought to personalize the new atlas to account for individual variation in connectivity architecture[25,26]. Following previous work on cortical atlas individualization[2],

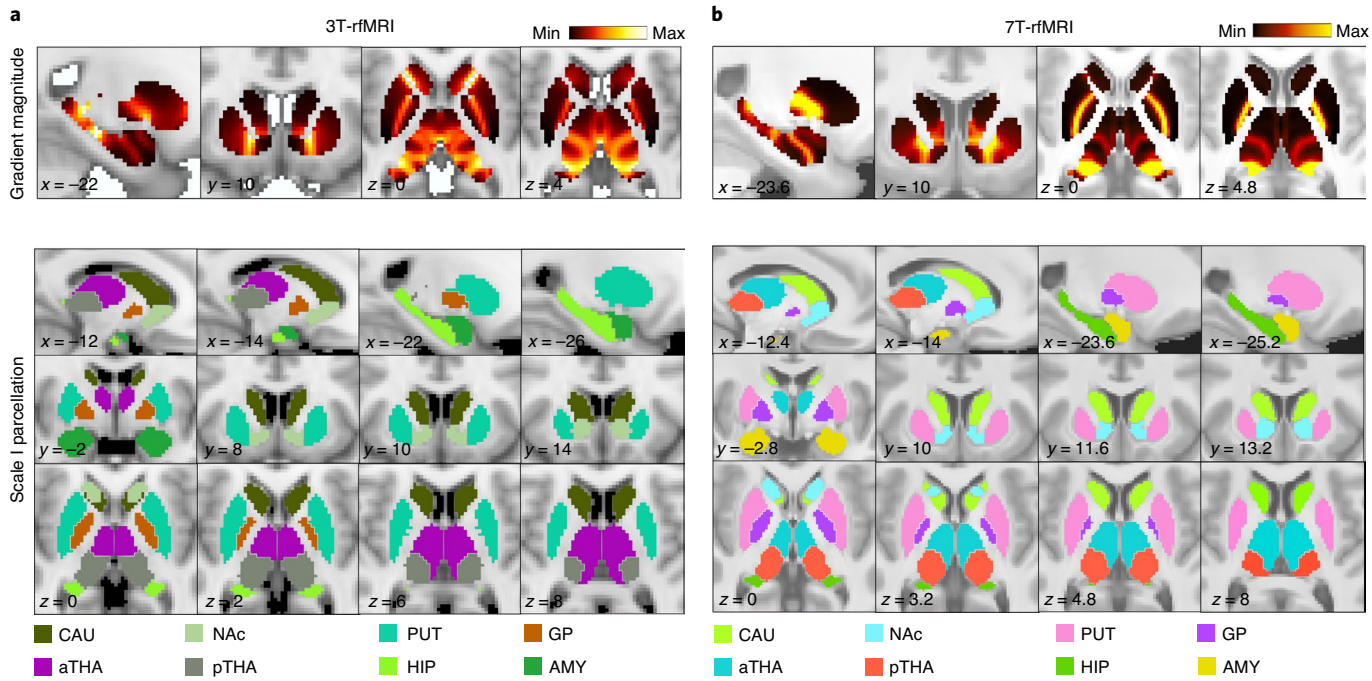


Fig. 6 | Replication of 3T parcellation using 7T-rfMRI. a, Group-consensus gradient magnitude image (top row) and scale I atlas (bottom three rows) delineated using 3T-rfMRI ($n=1,080$). Bands colored in yellow–orange indicate local maxima in the gradient magnitude image. Homologous regions are identically colored. **b**, Same as **a**, but delineated using 7T-rfMRI ($n=183$). The eight regions comprising scale I were replicated with 7T imaging. All slice coordinates are indicated in MNI space (mm). A reference structural MRI image is used as the background.

a machine-learning classifier was trained ($n=100$, REST2) to recognize putative connectivity fingerprints characteristic of each scale IV region. The trained classifier was then used to delineate personalized boundaries for each region in an independent group ($n=921$, REST2). In particular, for each individual, voxels were assigned a classification probability of belonging to each region and a winner-takes-all rule was used to delineate personalized parcellations (Supplementary Fig. 17).

Quantification using the Dice coefficient showed that the extent to which the personalized atlases recapitulated the group-consensus atlas is markedly varied among individuals and regions. This was most evident within the striatum (Fig. 7a) and the medial subdivisions of the hippocampal head. Group-averaged Dice coefficients (Fig. 7b) varied from 0.22 (subdivision of the medial hippocampal head (HIP-head-m2-lh)) to 0.85 (dorsoposterior putamen (PUT-DP-rh)) for a classification probability threshold of 50%. Hotspots in the group-averaged classification probability maps were encircled by the group-consensus boundaries (Fig. 7c), which indicates self-consistency in classification performance. Individual variation in Dice coefficients was highly skewed, as evidenced for the dorsoposterior putamen and the hippocampal body (Fig. 7d). Specifically, a majority of individuals recapitulated the group-consensus (Dice>0.8), but 2–7% showed marked divergence (Dice<0.5). Boundary contraction was the most common source of divergence among individuals and the group-consensus atlas (Fig. 7c). The same individuals consistently deviated from the group-consensus atlas for all regions, which suggests that this deviation was specific to individuals rather than regions (Supplementary Fig. 18).

It was possible for the classifier to fail to detect particular regions in some individuals. For each region, the proportion of individuals for whom at least one voxel was assigned to that region, called the regional detection rate, was analyzed as a function of the classification probability threshold (Fig. 7e). The regional detection rate for a classification probability threshold of 50% was rendered on the group-consensus atlas (Fig. 7e, inset). The averaged regional detection rate was 97.8%, with detection rates falling below 95% for only two bilateral regions (that is, the HIP-head-m1 and the HIP-head-m2). This suggests that the group-consensus atlas is representative of most individuals, although a minority of individuals may benefit from delineation of individual-specific atlases to account for inter-individual variation in regional boundaries.

Rest compared to task-evoked conditions. We have thus far focused on rfMRI data. Using tfMRI, we next investigated the extent to which the functional topography of the subcortex reconfigures in response to changing cognitive demands[27]. For each of the seven tasks and the two rest sessions, gradient magnitudes (gradient I) were projected onto the previously mapped ventral and dorsal streamlines, which yielded task-evoked diversity curves.

Qualitatively, diversity curve peaks were consistent among the seven task conditions, but some peak locations and magnitudes differed relative to the rest condition (Supplementary Fig. 19a). The most prominent task–rest variation was bifurcation of the boundary separating the putamen–NAc and the NAc–caudate during the task conditions. Functional separation between the amygdala and the anterior extreme of the hippocampus, the posterior hippocampus and the thalamus, as well as anterior–posterior partition within the thalamus were also weaker during task compared to rest conditions, whereas separation between the anterior and posterior hippocampus was stronger and anteriorly extended (Supplementary Fig. 19a). To investigate this further, the Pearson correlation coefficient was used to quantify the similarity in diversity curves between all pairs of conditions, which yielded correlation matrices (Supplementary Fig. 19b) that were visualized as correlation graphs (Supplementary Fig. 19c). Diversity curves were highly consistent between the two rest sessions (dorsal: $r=0.91$, $P<0.0001$; ventral: $r=0.98$, $P<0.0001$), but were distinct from the seven task conditions, thereby resulting in distinct task and rest modules (Supplementary

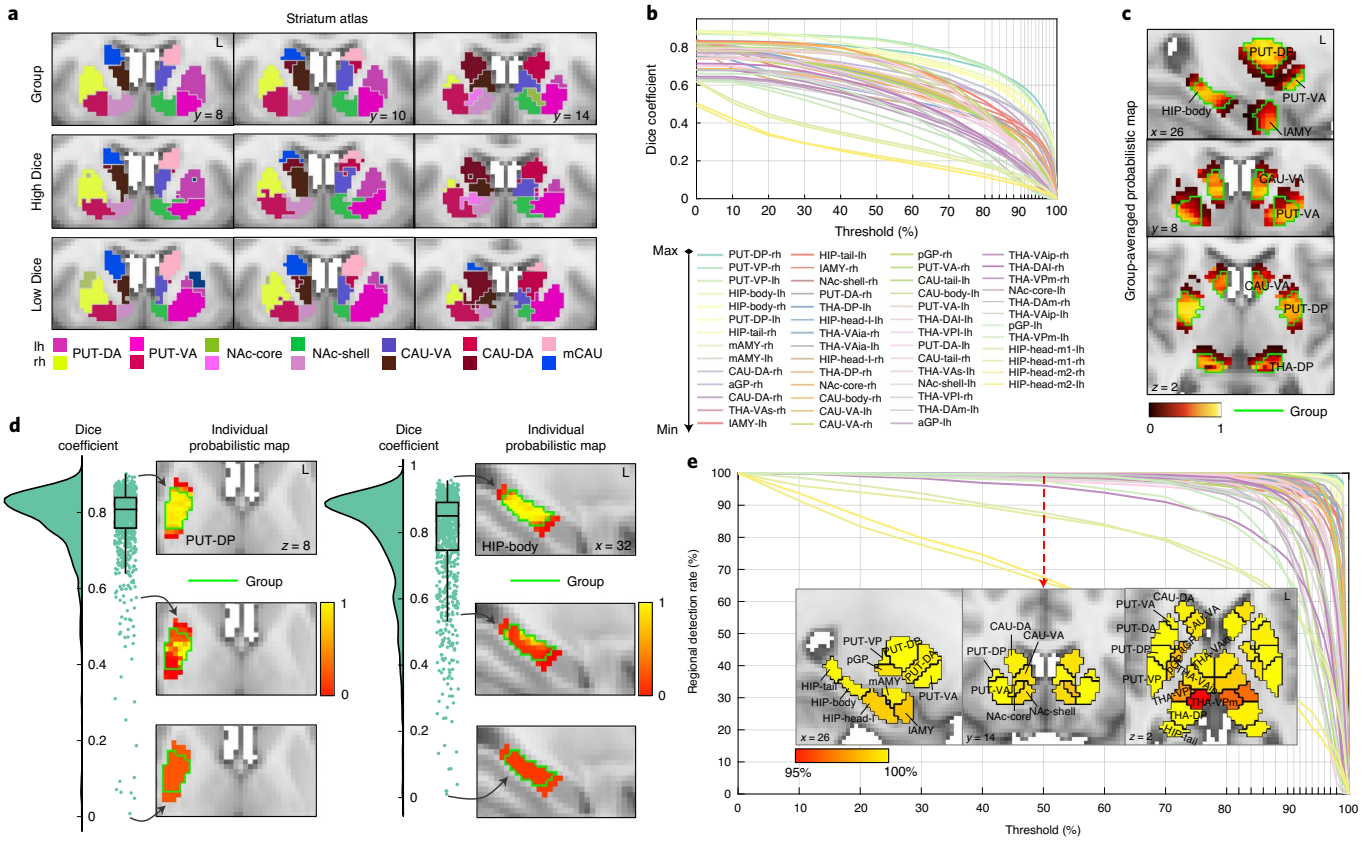


Fig. 7 | Personalization of the scale IV atlas. a, Group-consensus atlas for striatal regions (top row) and personalized atlases for representative individuals with relatively high (middle row, Dice = 0.81) and low (bottom row, Dice = 0.15) similarity with the group-consensus atlas. **b**, Curves showing group-averaged Dice coefficients as a function of the classification probability threshold (0–100%). A separate curve is shown for each of the 54 regions constituting the scale IV atlas. The classification probability is the probability that a subcortical voxel is classified as belonging to a specific region in a given individual. Parcellations were realized for each classification probability threshold and compared to the group-consensus atlas using the Dice coefficient. The area under the curve was computed for each region, and the legend is shown in descending order from top to bottom and left to right. **c**, Group-averaged classification probability maps exemplified in seven regions. The voxel color is scaled by the classification probability of the voxel belonging to the given region. The group-consensus boundary is shown in green. **d**, Box plots showing the distribution of individual variation in Dice coefficients of the dorsoposterior putamen (PUT-DP, left) and the hippocampal body (HIP-body, right). Each data point represents the Dice coefficient of one of the 921 individuals used to evaluate classification performance. The bottom and top edges of the boxes indicate the 25th and 75th percentiles of the distribution, respectively. The central mark indicates the median. The whiskers extend to the most extreme data points that are not considered outliers (1.5-times the interquartile range). Classification probability maps are shown in anatomical space for representative individuals with relatively high (top), moderate (middle) and low (bottom) Dice coefficients. The group-consensus boundary is shown in green. **e**, Curves showing the regional detection rates as a function of the classification probability threshold. The inset shows anatomical renderings of regional detection rates for a nominal classification probability threshold of 50%. The two hippocampal regions (bilateral HIP-head-m1 and HIP-head-m2) with the lowest regional detection rates are obscured in the slices shown. The dashed red arrow indicates the threshold (50%) used for the images shown in the inset. All slice coordinates are indicated relative to MNI space (mm). A reference structural MRI image is used as the background in anatomical visualizations.

Fig. 19d). Task-evoked reconfiguration of functional organization was not due to differences in the number of fMRI volumes acquired between task and rest conditions (Methods).

Links between subcortical topography and cortical networks. Next, we investigated functional connectivity between canonical cortical networks and subcortical regions (scale IV). Similarities in patterns of functional connectivity with the subcortex were quantified between pairs of 12 established cortical networks[8] (Supplementary Fig. 20a). Based on the similarity in the subcortical areas to which they most strongly connected, the 12 cortical networks could be parsed into three distinct groups and positioned on a task-positive to task-negative[17] organizational axis (Supplementary Fig. 20b). One extreme of the axis comprised cortical networks that typically showed increased activity during attention-demanding cognitive tasks (that is, task-positive), including the salience, cingulo–parietal, cingulo–opercular, frontoparietal and dorsal attention network. In contrast, the default mode network, which is often characterized by task-related deactivation (that is, task-negative) occupied the other extreme. Between them, sensorimotor-related networks (visual, auditory, dorsal and ventral somatomotor) and ventral attention and retrosplenial–temporal networks formed a third group, in which the latter two also linked to the default mode network. This result suggests that there is a transition from sensorimotor functions toward task-negative functions.

Using the new atlas to relate human behavior to subcortical connectivity. Finally, we used the new atlas to unveil new relationships between subcortical functional connectivity and individual variation in human behaviors. Five behavioral dimensions characterizing (1) cognition, (2) illicit substance use, (3) tobacco use, (4) personality and emotional traits and (5) mental health were

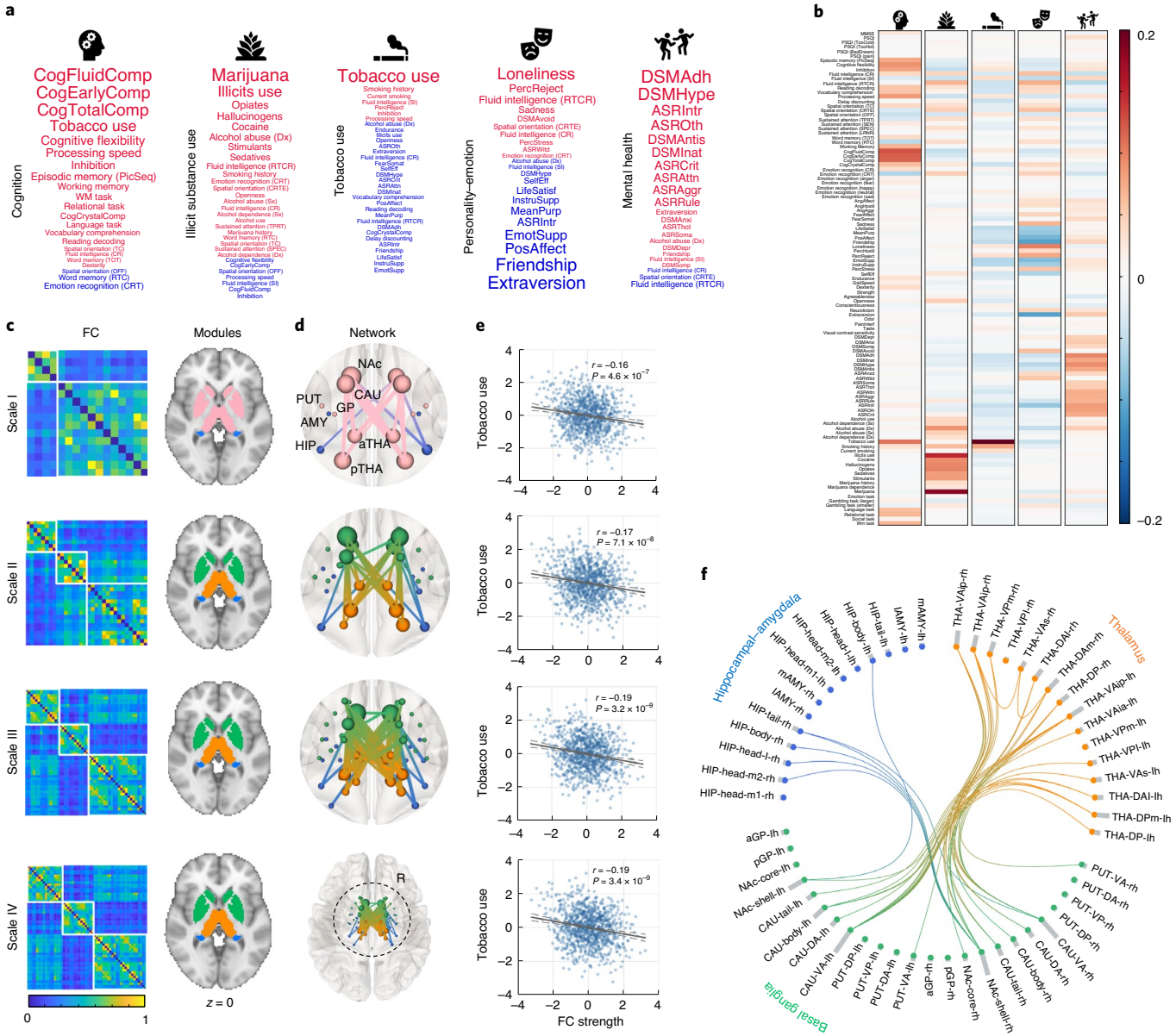


Fig. 8 | Associations between individual variation in behavioral dimensions and subcortical functional connectivity. a, Word clouds characterizing five behavioral dimensions derived from 109 behavioral items using ICA. Only the most highly weighted behavioral items are shown. The font size is scaled according to the absolute weight of the item in the ICA de-mixing matrix. The font color indicates weight polarity (red, positive; blue, negative). **b**, A consensus de-mixing matrix estimated using ICA. Rows correspond to behavioral items. Columns correspond to the five latent dimensions. Cell color is modulated by de-mixing weight. **c**, Left: group-averaged functional connectivity (FC) matrices for scale I–IV atlases. Rows and columns are reordered to accentuate the modular structure (white blocks). Right: modules are also rendered in anatomical space, where regions constituting the same module are identically colored. Scale I comprises two modules (blue, the hippocampus and the amygdala; pink, the basal ganglia and the thalamus). The latter module was divided into two submodules that separated the basal ganglia (green) and the thalamus (orange) at scales II–IV. **d**, The subcortical network for which functional connectivity significantly associated with individual variation in the behavioral dimension characterizing tobacco use ($n = 958$). The linear association was significant for all atlas scales (scales I–IV, $P < 0.0001$, permutation test, $n = 10{,}000$, one-sided, as implemented in NBS). Nodes and edges are colored according to module allegiance. Thicker edges are associated with stronger effects. Each row shows results for a distinct atlas scale. **e**, Scatter plots and lines of best fit for the linear association between subcortical functional connectivity and individual variation in the dimension characterizing tobacco use. Each data point represents one of the 958 individuals. Lines of best fit are indicated with solid gray lines and dashed gray lines show 95% CI. *R* values are the Pearson correlation coefficients and *P* values assess the null hypothesis of zero correlation. Each row shows results for a distinct atlas scale. **f**, The subcortical network associated with tobacco use shown as a circular network for the scale IV atlas, highlighting the role of thalamus–striatum–hippocampal circuits. Nodes and connections are colored according to module allegiance. The histogram (gray bar) shown for each node indicates the nodal degree.

considered (Fig. 8a,b and Supplementary Fig. 21). These dimensions were derived from 109 behavioral items (Supplementary Table 4) using independent component analysis (Methods). Using the network-based statistic (NBS)[28], higher tobacco use was significantly associated with lower functional connectivity in the thalamus–caudate, the thalamus–NAc and the hippocampus–NAc

circuits (Fig. 8c–f). This is consistent with the involvement of the cortical–basal-ganglia–thalamus–cortical circuit and mesolimbic dopamine pathways in reward and goal-directed behaviors[29] such as smoking (Discussion). Although connectivity explained 4% of the individual variation in the behavioral dimension characterizing tobacco use, the relationship was highly consistent across all four parcellation scales (scale I: $r=-0.16$, $P=4.6\times10^{-7}$; scale II: $r=-0.17$, $P=7.1\times10^{-8}$; scale III: $r=-0.19$, $P=3.2\times10^{-9}$; scale IV: $r=-0.19$, $P=3.4\times10^{-9}$; Fig. 8e) and reproducible across fMRI sessions (Supplementary Fig. 22). The remaining four dimensions did not significantly relate to subcortical connectivity after correction for multiple testing.

Discussion

The preponderance of the research field toward the cerebral cortex, coupled with technical challenges inherent to subcortical imaging, has led to the subcortex remaining a terra incognita[30]. Through the provision of high-quality, ultrahigh field strength MRI data, collaborative initiatives such as the HCP[18] herald new opportunities to overcome some of the challenges associated with reliably imaging this deep and anatomically complex brain structure.

To address the incomplete representation of subcortical regions in many leading MRI atlases, we used multi-session MRI data of brain function acquired in more than 1,000 healthy adults participating in the HCP to provide fundamental new insight into the organizational architecture and connectivity of the human subcortex. Putative functional boundaries were recursively delineated at locations of sharp spatial change in subcortical-to-whole-brain functional connectivity fingerprints, which led to the semiautomated delineation of a new multiscale parcellation atlas. The new atlas is openly available as a standalone parcellation and has been integrated into established cortex-only[2,8] and cerebellar[14] atlases. Crucially, the new subcortical atlas was replicated using ultrahigh field strength MRI, and the delineated regions were functionally homogeneous and identifiable within individual participants, thus enabling the delineation of personalized atlases that accounted for individual variation in connectivity. We used the new atlas to link cortical networks with the subcortex and to uncover a robust and reproducible relationship between individual variation in behavioral dimensions and subcortical functional connectivity.

Reconciling parcellations and gradients. Topographic representations of variation in brain structure, function and connectivity usually follows one of two paradigms: (1) a mosaic of discrete parcels separated by hard boundaries[2,3,8,14] and, more recently, (2) gradients of continuous topographic variation[11–13,15,23,31]. We introduced a principled way forward to reconcile these two seemingly incompatible paradigms that resulted in a hybrid representation that parsimoniously accommodated both discrete boundaries and continuous gradients. Boundaries were only delineated at locations where gradient magnitudes were significantly larger than what would be expected under an appropriate null hypothesis. This was formalized with a model selection process and an accompanying null model to test the null hypothesis of an absence of discrete spatial boundaries at candidate locations. Without model selection, boundaries would be delineated for all gradient magnitude peaks, which could potentially result in spurious boundaries that represent geometric constrictions rather than sharp changes in connectional topography. The bow-tie constriction shown in Supplementary Fig. 5b provides an example of spurious boundary delineation, whereby a gradient peak appears at the bow knot, despite uniform spatial variation in connectivity. While the sheet-like geometry of the cerebral cortex is less likely to be affected by this phenomenon, complex subcortical geometry is more vulnerable to false-positive boundaries and over-parcellation.

Gradientography was developed to enable gradient visualization and accurate localization of candidate boundaries. Gradientography is a fMRI analog of diffusion MRI tractography and can be considered a form of fMRI tractography. Whereas tractography is conventionally used to map white matter fiber trajectories, gradientography, as introduced here, was used to map trajectories of maximum change in connectopic gradients. Future applications of gradientography are not limited to the subcortex, and the method could provide a bridge between cortical gradients and parcellations.

A new multiscale subcortical atlas. The new subcortical atlas comprises four scales, labeled scale I to scale IV, each providing a self-contained parcellation atlas. Additional scales were not warranted because the model selection procedure decided against boundary delineation for all regions constituting scale IV. Researchers seeking to use the new atlas should select the atlas scale that provides adequate resolution to address the research question at hand and approximately matches the scale of any cortical atlas that is used in terms of the total number of regions. While the new atlas is unimodal, rfMRI connectivity is argued to be one the most useful modalities in predicting areal boundaries[2].

Hierarchy is a hallmark of brain organization[32], and hierarchical organization is not necessarily a fait accompli of the recursive application of the model selection procedure used in this study (see "Further methodological considerations" in the Methods). Scale I of the atlas recapitulated subcortical regions delineated in existing MRI atlases, such as those available as part of Lead-DBS, Freesurfer and FSL. The position of gradient peaks enabled automated boundary demarcation among the amygdala, the hippocampus, the thalamus, the caudate, the putamen, the NAc and the GP. Discrete partition of the basal ganglia into the latter four regions and separation between the amygdala and the hippocampus were clearly supported by model selection. Contrastingly, the few existing connectivity-based subcortical atlases[6,33] generally do not preserve established anatomical boundaries[34], which suggests that there is structure–function divergence or methodological variation. Given that these broad subcortical regions are anatomically distinguishable, rudimentary alignment with functional architecture might be expected[1]. Indeed, this assumption motivates the parcellation of regions in isolation, such as the hippocampus[31,35], the striatum[23,36] and the thalamus[37], without first establishing functional boundaries between them. Despite correspondence between the principal connectional topography (gradient I) and anatomy at scale I, fine variation within specific structures was captured by the secondary connectional gradients. As shown in Supplementary Fig. 10b, the dominant striatal gradient separates the putamen, the NAc and the caudate, whereas the second and third gradients are organized along a dorsal-to-ventral axis, thus reflecting connectional variation between the dorsal (putamen and caudate) and ventral (NAc) striatum[38]. Similarly, the dominant thalamic gradient follows an anteroposterior trajectory, whereas the second and third gradients capture connectional variation between the mediodorsal and ventrolateral thalamus (Supplementary Fig. 10c), which may relate to organizational differences between subgroups of thalamic nuclei[39].

Scale II delineates functional divisions within each of the scale I regions. The NAc was partitioned into regions potentially representing its shell and core, and anterior (head) and posterior (body and tail) caudate subdivisions were identified, and the amygdala was divided into lateral and medial subregions. A striking divergence between anatomy and function was evident for the GP. The GP is anatomically divided along a mediolateral axis into the internal and external GP[34], whereas functional connectivity gradients indicated an anteroposterior partition. Scales III and IV differed only in the parcellation of the thalamus and the hippocampus.

Parcellation validation. While histological validation is the gold standard, functional parcellations do not necessarily converge toward anatomical or cytoarchitectural divisions to be deemed

useful[1]. To establish confidence in the new atlas, we first demonstrated that all atlas scales, except scale I, were significantly more homogenous[8] than expected due to chance. While scale I regions converged with subcortical anatomy, they encompassed multiple functional systems, thereby rendering scale I too coarse to achieve homogeneity. Homogeneity of functional signals within delineated subregions is a fundamental principle of functional parcellation[1]. Interestingly, existing structural connectivity and histological parcellations of the thalamus[37] and the hippocampus[22], respectively, were not functionally homogenous (Supplementary Fig. 12), which indicates that there is a need for modality-specific atlases.

Second, we reproduced the majority of regions using 7T fMRI. The improved contrast-to-noise ratio and spatial resolution of 7T compared with 3T MRI is particularly important for subcortical imaging[24]. Despite remarkable consistency between the 3T and 7T atlases, 7T fMRI enabled the delineation of finer structures. For example, a bipartite partition of the amygdala (medial and lateral) was delineated at 3T, whereas 7T fMRI aided further division of the medial amygdala into central and superior components, which broadly recapitulated the three cytoarchitectural zones of the amygdala[22]. Conversely, the NAc was consistently parcellated into two subdivisions at 3T and 7T, thus possibly representing the immunohistochemically distinct shell and core subdivision that is common to primates[40]. Therefore, while subcortical cartography is viable with functional connectivity inferred from high-quality 3T fMRI data, the level of detail that can be resolved at 7T is superior for several regions.

The subcortex atlas was personalized to account for individual connectivity differences. We showed that while the group-consensus atlas was sufficient to represent the majority of individuals, personalized subcortex atlases were warranted for a small proportion of others. Deviations from the group-consensus atlas were specific to particular individuals rather than specific regions (Supplementary Fig. 18), which suggests that deviations may capture inherent inter-individual differences in functional architecture. Further work is needed to understand whether individual variation in subcortical connectional topography relates to anatomy, task-evoked activation and behavior. Individual-specific atlases of the subcortex can potentially facilitate personalization of targeted therapies in psychiatry[41] and to improve prediction of behavior[26].

Dynamic and intrinsic subcortical topography. Using tfMRI, we identified subtle reconfigurations in the functional topography of the subcortex in response to changing cognitive demands. While a previous study[27] examined variation in parcel size in response to task stimuli, diversity curves enabled the characterization of changes in functional boundaries. During task conditions, the anterior putamen integrated more extensively with higher-order association networks, whereas the hippocampus segregated along its long axis, yielding a more integrated anterior hippocampal–amygdala system that may have served cognitive–emotional processing, and a more integrated posterior hippocampal–thalamus that potentially benefited learning and spatial memory[21]. These task-induced dynamic reconfigurations may reflect a process of neuronal recruitment into specific functional processing systems to cope with cognitive demands. The flexible reconfiguration of neural networks may largely depend on the intrinsic functional organization within local cortical circuits given that a task-positive to task-negative organizational axis was evident in the subcortex (Supplementary Fig. 20). However, context-dependent recruitment across intrinsic parcels, leading to the adjustment of functional boundaries, may additionally assist adaptive task responses. Further work is needed to understand task-evoked reconfigurations of functional boundaries, not only in the subcortex but also across the brain.

Tobacco and subcortical connectivity. We performed a hypothesis-free decomposition of HCP cognitive and behavioral measures into five latent dimensions to facilitate an investigation of relationships between brain connectivity and behavior. Previous HCP investigations typically investigate hundreds of individual measures, which leads to a formidable multiple testing problem, or preselect a limited number of specific behavioral domains or measures. The five latent dimensions identified here condense information from more than 100 individual measures.

The new atlas unveiled a novel relationship between individual variation in functional connectivity and the behavioral dimension characterizing tobacco use. Higher tobacco use was associated with lower thalamus–caudate, thalamus–NAc and hippocampus–NAc functional connectivity. The shell of the NAc and the adjacent ventroanterior caudate (CAU–VA) were most implicated (Fig. 8f). This accords with the primary role of the shell of the NAc and the anterior caudate in reward anticipation, incentive motivation and action[42,43]. The NAc integrates glutamatergic (excitatory) inputs from the hippocampus and the thalamus[44,45], which enables the regulation of dopamine neuron activity in the ventral tegmental area[45]. While nicotine, the main neuroactive compound of tobacco, stimulates dopamine release and transmission in the NAc, especially the medial shell[46], chronic nicotine administration yields neuronal damage in the hippocampus and the striatum[47,48], which potentially manifests in lower functional connectivity in the thalamus–striatum–hippocampus system. Therefore, the putative downregulation of the mesolimbic circuit by nicotine may provide insight into the increased prevalence of tobacco smoking in individuals with schizophrenia[49]. In particular, this downregulation effect of nicotine on the hyperdopaminergic state in the mesolimbic system may correspond with the upregulation effect of nicotine in the prefrontal cortex[50], which alleviates symptoms in the disorder.

Conclusions

We unveiled the complex topographic organization of the human subcortex and parsed this complexity into four scales constituting a new atlas for the brain's remaining terra incognita. The new atlas is scalable, personalizable, reproducible at ultrahigh field strengths and openly available. Future work will focus on the addition of structures such as subthalamic regions, the red nucleus and the hypothalamus. The new atlas can be incorporated with existing cortex-only atlases to aid the investigation of cortico–subcortical interactions and the mapping of holistic connectomes using MRI.

Online content

Any methods, additional references, Nature Research reporting summaries, source data, extended data, supplementary information, acknowledgements, peer review information; details of author contributions and competing interests; and statements of data and code availability are available at https://doi.org/10.1038/s41593-020-00711-6.

Received: 29 November 2019; Accepted: 21 August 2020;
Published online: 28 September 2020

References

1. Eickhoff, S. B., Yeo, B. T. T. & Genon, S. Imaging-based parcellations of the human brain. *Nat. Rev. Neurosci.* **19**, 672–686 (2018).
2. Glasser, M. F. et al. A multi-modal parcellation of human cerebral cortex. *Nature* **536**, 171–178 (2016).
3. Yeo, B. T. et al. The organization of the human cerebral cortex estimated by intrinsic functional connectivity. *J. Neurophysiol.* **106**, 1125–1165 (2011).
4. Shepherd, G. M. Corticostriatal connectivity and its role in disease. *Nat. Rev. Neurosci.* **14**, 278–291 (2013).
5. Choi, E. Y., Yeo, B. T. & Buckner, R. L. The organization of the human striatum estimated by intrinsic functional connectivity. *J. Neurophysiol.* **108**, 2242–2263 (2012).
6. Ji, J. L. et al. Mapping the human brain's cortical–subcortical functional network organization. *NeuroImage* **185**, 35–57 (2019).
7. Cohen, A. L. et al. Defining functional areas in individual human brains using resting functional connectivity MRI. *NeuroImage* **41**, 45–57 (2008).

8. Gordon, E. M. et al. Generation and evaluation of a cortical area parcellation from resting-state correlations. *Cereb. Cortex* **26**, 288–303 (2016).
9. Schaefer, A. et al. Local–global parcellation of the human cerebral cortex from intrinsic functional connectivity MRI. *Cereb. Cortex* **28**, 3095–3114 (2018).
10. Huntenburg, J. M., Bazin, P. L. & Margulies, D. S. Large-scale gradients in human cortical organization. *Trends Cogn. Sci.* **22**, 21–31 (2018).
11. Haak, K. V., Marquand, A. F. & Beckmann, C. F. Connectopic mapping with resting-state fMRI. *NeuroImage* **170**, 83–94 (2018).
12. Margulies, D. S. et al. Situating the default-mode network along a principal gradient of macroscale cortical organization. *Proc. Natl Acad. Sci. USA* **113**, 12574–12579 (2016).
13. Guell, X., Schmahmann, J. D., Gabrieli, J. & Ghosh, S. S. Functional gradients of the cerebellum. *eLife* **7**, e36652 (2018).
14. King, M., Hernandez-Castillo, C. R., Poldrack, R. A., Ivry, R. B. & Diedrichsen, J. Functional boundaries in the human cerebellum revealed by a multi-domain task battery. *Nat. Neurosci.* **22**, 1371–1378 (2019).
15. Tian, Y. & Zalesky, A. Characterizing the functional connectivity diversity of the insula cortex: subregions, diversity curves and behavior. *NeuroImage* **183**, 716–733 (2018).
16. Coalson, T. S., Van Essen, D. C. & Glasser, M. F. The impact of traditional neuroimaging methods on the spatial localization of cortical areas. *Proc. Natl Acad. Sci. USA* **115**, E6356–E6365 (2018).
17. Fox, M. D. et al. The human brain is intrinsically organized into dynamic, anticorrelated functional networks. *Proc. Natl Acad. Sci. USA* **102**, 9673–9678 (2005).
18. Van Essen, D. C. et al. The WU–Minn Human Connectome Project: an overview. *NeuroImage* **80**, 62–79 (2013).
19. Finn, E. S. et al. Functional connectome fingerprinting: identifying individuals using patterns of brain connectivity. *Nat. Neurosci.* **18**, 1664 (2015).
20. Müller, E. et al. Core and matrix thalamic sub-populations relate to spatio-temporal cortical connectivity gradients. *NeuroImage* **222**, 117224 (2020).
21. Poppenk, J., Evensmoen, H. R., Moscovitch, M. & Nadel, L. Long-axis specialization of the human hippocampus. *Trends Cogn. Sci.* **17**, 230–240 (2013).
22. Amunts, K. et al. Cytoarchitectonic mapping of the human amygdala, hippocampal region and entorhinal cortex: intersubject variability and probability maps. *Anat. Embryol.* **210**, 343–352 (2005).
23. Marquand, A. F., Haak, K. V. & Beckmann, C. F. Functional corticostriatal connection topographies predict goal directed behaviour in humans. *Nat. Hum. Behav.* **1**, 0146 (2017).
24. Vu, A. et al. Tradeoffs in pushing the spatial resolution of fMRI for the 7T Human Connectome Project. *NeuroImage* **154**, 23–32 (2017).
25. Gordon, E. M. et al. Precision functional mapping of individual human brains. *Neuron* **95**, 791–807.e7 (2017).
26. Kong, R. et al. Spatial topography of individual-specific cortical networks predicts human cognition, personality, and emotion. *Cereb. Cortex* **29**, 2533–2551 (2019).
27. Salehi, M. et al. There is no single functional atlas even for a single individual: functional parcel definitions change with task. *NeuroImage* **208**, 116366 (2020).
28. Zalesky, A., Fornito, A. & Bullmore, E. T. Network-based statistic: identifying differences in brain networks. *NeuroImage* **53**, 1197–1207 (2010).
29. Maia, T. V. & Frank, M. J. From reinforcement learning models to psychiatric and neurological disorders. *Nat. Neurosci.* **14**, 154–162 (2011).
30. Forstmann, B. U., de Hollander, G., van Maanen, L., Alkemade, A. & Keuken, M. C. Towards a mechanistic understanding of the human subcortex. *Nat. Rev. Neurosci.* **18**, 57–65 (2016).
31. Vos de Wael, R. et al. Anatomical and microstructural determinants of hippocampal subfield functional connectome embedding. *Proc. Natl Acad. Sci. USA* **115**, 10154–10159 (2018).
32. Churchland, P. S. & Sejnowski, T. J. Perspectives on cognitive neuroscience. *Science* **242**, 741–745 (1988).
33. Fan, L. et al. The Human Brainnetome Atlas: a new brain atlas based on connectional architecture. *Cereb. Cortex* **26**, 3508–3526 (2016).
34. Pauli, W. M., Nili, A. N. & Tyszka, J. M. A high-resolution probabilistic in vivo atlas of human subcortical brain nuclei. *Sci. Data* **5**, 180063 (2018).
35. Plachti, A. et al. Multimodal parcellations and extensive behavioral profiling tackling the hippocampus gradient. *Cereb. Cortex* **29**, 4595–4612 (2019).
36. Janssen, R. J., Jylänki, P., Kessels, R. P. C. & van Gerven, M. A. J. Probabilistic model-based functional parcellation reveals a robust, fine-grained subdivision of the striatum. *NeuroImage* **119**, 398–405 (2015).
37. Behrens, T. E. et al. Non-invasive mapping of connections between human thalamus and cortex using diffusion imaging. *Nat. Neurosci.* **6**, 750–757 (2003).
38. Haber, S. N. & Knutson, B. The reward circuit: linking primate anatomy and human imaging. *Neuropsychopharmacology* **35**, 4–26 (2010).
39. Morel, A., Magnin, M. & Jeanmonod, D. Multiarchitectonic and stereotactic atlas of the human thalamus. *J. Comp. Neurol.* **387**, 588–630 (1997).
40. Meredith, G. E., Pattiselanno, A., Groenewegen, H. J. & Haber, S. N. Shell and core in monkey and human nucleus accumbens identified with antibodies to calbindin-D28k. *J. Comp. Neurol.* **365**, 628–639 (1996).
41. Cocchi, L. & Zalesky, A. Personalized transcranial magnetic stimulation in psychiatry. *Biol. Psychiatry Cogn. Neurosci. Neuroimaging* **3**, 731–741 (2018).
42. Castro, D. C. & Bruchas, M. R. A motivational and neuropeptidergic hub: anatomical and functional diversity within the nucleus accumbens shell. *Neuron* **102**, 529–552 (2019).
43. Pauli, W. M., O'Reilly, R. C., Yarkoni, T. & Wager, T. D. Regional specialization within the human striatum for diverse psychological functions. *Proc. Natl Acad. Sci. USA* **113**, 1907–1912 (2016).
44. MacAskill, A. F., Little, J. P., Cassel, J. M. & Carter, A. G. Subcellular connectivity underlies pathway-specific signaling in the nucleus accumbens. *Nat. Neurosci.* **15**, 1624–1626 (2012).
45. Perez, S. M. & Lodge, D. J. Convergent inputs from the hippocampus and thalamus to the nucleus accumbens regulate dopamine neuron activity. *J. Neurosci.* **38**, 10607–10618 (2018).
46. Pontieri, F. E., Tanda, G., Orzi, F. & Di Chiara, G. Effects of nicotine on the nucleus accumbens and similarity to those of addictive drugs. *Nature* **382**, 255–257 (1996).
47. Gallinat, J. et al. Abnormal hippocampal neurochemistry in smokers: evidence from proton magnetic resonance spectroscopy at 3T. *J. Clin. Psychopharmacol.* **27**, 80–84 (2007).
48. Xu, Z., Seidler, F. J., Ali, S. F., Slikker, W. Jr. & Slotkin, T. A. Fetal and adolescent nicotine administration: effects on CNS serotonergic systems. *Brain Res.* **914**, 166–178 (2001).
49. de Leon, J. & Diaz, F. J. A meta-analysis of worldwide studies demonstrates an association between schizophrenia and tobacco smoking behaviors. *Schizophrenia Res.* **76**, 135–157 (2005).
50. Koukouli, F. et al. Nicotine reverses hypofrontality in animal models of addiction and schizophrenia. *Nat. Med.* **23**, 347–354 (2017).

Publisher's note Springer Nature remains neutral with regard to jurisdictional claims in published maps and institutional affiliations.

© The Author(s), under exclusive licence to Springer Nature America, Inc. 2020

Methods

Data and preprocessing. *HCP dataset.* Human neuroimaging data acquired as part of the HCP S1200 release[18] were analyzed here. Participants were healthy young adults ranging between 22 and 37 years old. Some participants were genetically related. These relationships were controlled in statistical analyses by constraining permutations[51,52]. HCP datasets used in this study include three main imaging sessions. (1) Two sessions (REST1 and REST2) of rfMRI) acquired using multiband echo planar imaging (EPI) on a customized Siemens 3T MR scanner (Skyra system), where each session comprised two runs (left-to-right and right-to-left phase encoding) of 14 min and 33 s each (repetition time (TR) = 720 ms, echo time (TE) = 33.1 ms, voxel dimension: 2-mm isotropic). The two runs were temporally concatenated for each session, yielding 29 min and 6 s of data in each session. Concatenation of the two different phase-encoded data ensured that any potential effect of phase encoding on gradient direction was counterbalanced by the opposing phase encoding. (2) tfMRI data acquired using the identical multiband EPI sequence as the rfMRI session; however, the run duration ranged between 2 and 5 min depending on the specific task (7 tasks). (3) rfMRI acquired on a Siemens Magnetom 7T MR scanner using a multiband acquisition (TR = 1,000 ms, TE = 22.2 ms, voxel dimension: 1.6-mm isotropic), where participants completed 4 runs of approximately 16 min each. The first two runs (posterior-to-anterior and anterior-to-posterior phase encoding) were used in this study. We refer to this dataset as 7T-rfMRI. Details pertaining to the acquisition of rfMRI[24,53] and tfMRI[54] are described elsewhere. The seven tfMRI tasks were chosen to tap a broad range of cognitive and affective processes and activated a wide range of neural systems[54]. Participants that had completed at least two runs in each dataset were included. As a consequence, 33 of the original 1,113 individuals were excluded from the primary dataset (REST1) and 92 individuals were excluded from the replication dataset (REST2). Supplementary Table 1 shows the sample size and basic participant demographics for each dataset.

The second 3T-rfMRI session (REST2) was used for replication. Minimally preprocessed volumetric rfMRI and tfMRI data were sourced from the online HCP repository. Details of the minimal preprocessing pipeline can be found elsewhere[55]. The pipeline includes correction of head motion and spatially structured physiological noise with ICA+FIX[56,57]. ICA-based denoising methods outperform, or equal, the performance of alternative approaches on most benchmarks[58]. After eliminating spatial artifacts and distortions, the functional images were spatially aligned to the Montreal Neurological Institute (MNI) standard space using the FNIRT nonlinear registration algorithm. MNI standard space herein always refers to the MNI ICBM 152 nonlinear sixth generation stereotaxic registration model. Additional nuisance regression and temporal filtering were not performed as part of the pipeline. However, head motion registration parameters estimated as part of spatial alignment were curated, reduced to a single summary measure known as framewise displacement[59] and included as a confound in statistical analyses to control for individual variation in head motion[60,61].

The subcortical SNR and sensitivity of the blood-oxygenation-level-dependent (BOLD) signal was lower compared with the cortex because T2* signal decay times are shorter in subcortical regions compared with cortical regions due to iron enrichment of subcortical tissue[62]. Therefore, to enhance subcortical SNR and BOLD sensitivity, the minimally preprocessed data were subjected to two additional operations (Supplementary Fig. 8a). First, spatial smoothing was performed with a Gaussian smoothing kernel of 6-mm full width at half maximum (FWHM) for 3T images and 4-mm FWHM for 7T images. This choice of kernel width was guided by evaluations of gradient magnitude images derived from a range of smoothing kernels (4, 6 and 8 mm) and filtering options (that is, the Wishart filter, see below). Second, to further improve subcortical SNR and to suppress the effects of unstructured and autocorrelated noise that share similar temporal and spatial properties, the fMRI time series were reconstructed from a principal component analysis (PCA), whereby the components were filtered according to an empirically fitted Wishart distribution to dampen the effects of noise[2,63,64]. This PCA-based data reconstruction (that is, the Wishart filter) has been previously used in a multimodal cortical parcellation study[2] and comprehensively documented by Glasser and colleagues[63,64]. The Wishart filter was performed over all gray matter voxels for each individual separately in all datasets. In addition, task block regressors were created for each task condition based on the time of onset, the duration and the relative magnitude of each stimulus, and then convolved with hemodynamic response functions (spm_hrf.m function from SPM12, https://www.fil.ion.ucl.ac.uk/spm). The relevant regressors corresponding to each task were then regressed from the tfMRI data to ensure that functional connectivity was disambiguated from the potential confound of task co-activation effects[65]. The residuals remaining from this regression were used for all subsequent analyses.

Independent validation dataset. An independent fMRI dataset was acquired in Australia to test the reproducibility of the parcellation homogeneity results. Ten healthy adults were recruited and confirmed not to have any current or history of any neurological or psychiatric disorders at the time of MRI scanning (mean age 26 ± 2.1 years, 6 males). Imaging was performed in all participants using a Siemens Prisma 3T MRI scanner. Structural images of brain anatomy were acquired using an optimized magnetization-prepared rapid acquisition gradient echo (MPRAGE) T1-weighted sequence with 176 sagittal slices of 1-mm thickness, field of view of 240 × 256 mm^2, flip angle of 9°, TR of 1,900 ms, TE of 2.98 ms and voxel size of 1.0 × 1.0 × 1.0 mm^3. rfMRI was acquired using a T2*-weighted multiband gradient-echo EPI sequence of approximately 12 min, resulting in 880 volumes (TR = 810 ms, TE = 30 ms, voxel size = 2.0 × 2.0 × 2.0 mm^3).

rfMRI data were preprocessed using the fMRIPrep-1.5.9 pipeline[66]. In brief, each T1-weighted volume was corrected for intensity non-uniformity and skull-stripped. The extracted brain was spatially normalized to MNI standard space through nonlinear registration using ANTs. Cortical surfaces were reconstructed using FreeSurfer. Functional data were motion-corrected using mcflirt (FSL) followed by co-registration to the corresponding T1-weighted image using boundary-based registration with six degrees of freedom. Motion-correcting transformations, BOLD-to-T1w transformation and T1w-to-MNI warp were concatenated and applied in a single step using antsApplyTransforms (ANTs).

Confounds including the 24 head-motion parameters (6 basic motion parameters + 6 temporal derivatives + 12 quadratic terms and their 6 temporal derivatives), mean white matter and cerebrospinal fluid signals were computed and regressed from the preprocessed fMRI data for each individual. The residuals of this regression were then subjected to spatial smoothing with a Gaussian-smoothing kernel of 6-mm FWHM and Wishart filtering[63,64].

For all datasets, statistical methods were not used to predetermine sample sizes. All relevant and appropriate data provisioned by the HCP were included to maximize samples. Our use of HCP datasets and our recruitment of the independent dataset complied with the Australian NHMRC national framework for the conduct of human research. Informed consent was obtained from all the participants. Data collection and analyses were not performed blind to the conditions of the experiments.

Mask delineation. A binary subcortex mask comprising the left and right basal ganglia, the thalamus, the hippocampus and the amygdala was delineated using three steps. First, the probabilistic Harvard–Oxford Subcortical Structural Atlas (https://fsl.fmrib.ox.ac.uk/fsl/fslwiki/Atlases) was used to delineate a binary mask for each of the following subcortical regions: the thalamus, the caudate, the putamen, the NAc, the GP, the hippocampus and the amygdala. Voxels with a probability of 50% or more of belonging to one of these regions were included in the relevant mask, except for the GP. A higher threshold (60%) was applied to the GP to minimize potential white matter contamination of the fMRI signal due to the numerous myelinated axons of the striato–pallido–nigral bundle abutting the periphery of this region[67]. Second, the masks for each individual subcortical region were merged to yield a binary mask for the entire subcortex. Finally, the subcortex mask was left–right symmetrized. Left–right symmetrization accords with previous subcortical atlas literature[34,68] and enabled symmetrization of subsequent computations to improve the SNR. Symmetrization is not an unprecedented step given that intra-hemispheric asymmetries in the volume of subcortical nuclei are less evident in healthy young adults compared with cortical asymmetries[69]. Mask symmetrization was achieved by reflecting the left hemisphere of the mask around the mid-sagittal plane and computing the intersection between the right hemisphere of the mask and this reflection. Voxels constituting the intersection yielded a left subcortex mask, which was merged with its reflection to yield the final left–right symmetric subcortex mask. The final mask comprised a total of $N = 7{,}984$ voxels (63.87 cm^3). The subthalamic nuclei, the substantia nigra and comparably small subcortical nuclei were not included because the spatial resolution of the fMRI data was deemed insufficient to accurately resolve putative substructures within these nuclei (for example, the pars reticulata and compacta). Submillimeter fMRI and multi-echo EPI would benefit the investigation of the functional architecture of these exceedingly small nuclei[70]. A binary gray matter mask was delineated using the MNI152 probabilistic gray matter atlas. Voxels belonging to cortical gray matter were included in the gray matter mask as well as any voxels constituting the final subcortex mask. fMRI data were consistently absent for a majority of individuals in a small proportion of voxels constituting the gray matter mask. After eliminating these voxels, the final gray matter mask comprised $M = 164{,}360$ voxels (1,314.9 cm^3), which included the midbrain, the pons and the cerebellum. The subcortex and gray matter masks were delineated in 2-mm isotropic space and were used for the 3T fMRI data. To suit the 7T-rfMRI data, which was in 1.6-mm isotropic space, the masks were resliced to this resolution and median filtered to smooth the mask edges.

Functional connectivity and eigenmaps. Whole-brain functional connectivity was mapped for each subcortex voxel. Spatial gradients in the resulting maps were then computed to yield a continuous representation of functional connectivity variation across the subcortex. Connectopic mapping[11] was used to map spatial gradients for each individual, which involved computing a sequence of eigendecompositions to yield a Laplacian eigenmap[71]. Specifically, following the procedure described by Haak and colleagues[11], the temporally concatenated fMRI signals were represented for each individual in a matrix of dimension $T \times M$, where T denotes the number of time frames and M denotes the number of gray matter voxels. PCA was used to reduce the dimensionality of this matrix to $T \times (T-1)$. The fMRI signal at each subcortical voxel was then correlated (Pearson correlation) with each column of the PCA-transformed matrix, resulting in a connectivity matrix of dimension $N \times (T-1)$, where N denotes the number of subcortex voxels. Correlation

coefficients were r-to-z transformed using the Fisher transformation. Each row of this matrix provided a connectional fingerprint[19] for a particular subcortical voxel in the PCA-transformed space. Similarity in the connectional fingerprints between each pair of subcortical voxels was then quantified with the η^2 coefficient, which results in a symmetric matrix of dimension $N \times N$ for every individual. The similarity matrix was transformed into a sparse graph using the weighted adjacency matrix, whereby the weights of all connections with a Euclidean distance less than ε were set to zero. The connection density was determined by the smallest value of ε that ensured a connected graph[11,72,73]. This threshold varied between individuals, yielding graphs with a connection density of 0.4% on average. The Laplacian matrix, L, was then computed according to $L = D - W$, where D denotes the diagonal matrix of node strengths and W denotes the sparse adjacency matrix. In particular, $D_{ij} = \sum W_{ij}$ if $i = j$, otherwise $D_{ij} = 0$. Finally, the eigenvectors and eigenvalues of the Laplacian matrix were computed. The smallest eigenvalue was necessarily zero, while all other eigenvalues were positive due to the connectedness of the graph. The eigenvector with a zero eigenvalue was a constant and discarded. The eigenvectors with the second, third and fourth smallest eigenvalues were referred to as gradients I, II and III respectively. These steps are shown in Fig. 1a. Each of the three gradients, or eigenmaps, characterized a continuous mode of spatial variation in functional connectivity across the spatial extent of the subcortex. We use the terms eigenmap and gradient interchangeably. Eigenvectors corresponding to the next largest eigenvalues typically explained substantially less variance in the Laplacian matrix than the first four eigenvectors (Supplementary Fig. 2) and were thus given no further consideration here. The N values defining each gradient were projected onto the three-dimensional (3D) anatomy of the subcortex in MNI standard space for visualization and further analyses. Unless otherwise specified, the same process described above was used to estimate gradients for each individual and for each imaging modality, including 3T-rfMRI, 7T-rfMRI and tfMRI.

Gradientography. Tractography is an established 3D modeling technique to visually represent axonal fiber bundles using diffusion MRI[74]. We developed an analogous technique for fMRI called gradientography to characterize spatial gradients in functional connectivity. Gradientography was performed at the group level using a group-consensus representation of each eigenmap. In particular, similarity matrices were averaged across all individuals, and eigenmaps were computed for the group-averaged similarity matrix using the same process described above. The resulting group-consensus eigenmaps were projected onto the 3D anatomy of the subcortex in MNI standard space (Fig. 1b, column I and Supplementary Fig. 1, column I). Using the Sobel gradient operator, directional gradients were computed for each subcortical voxel constituting the 3D image representing each eigenmap. Each subcortical voxel was therefore endowed with a gradient directed along each of the three canonical axes as well as a gradient magnitude (Fig. 1b, column II and Supplementary Fig. 1, column II). We denote the gradient direction and magnitude at a given voxel with $g = \left[g_x, g_y, g_z\right]^T$ and $|g|$, respectively. The gradient magnitude indicated how rapidly the functional connectivity of a local area of subcortex changed per unit length. Before application of the Sobel operator, the peripheral boundary of the subcortex in each eigenmap image was dilated by approximately one voxel to diminish spurious gradients from appearing along the direction that is perpendicular to the boundary. Erosion was performed after application of the Sobel operator to reverse this dilation and restore the original volume of the subcortex. The gradient directions and magnitudes were approximately mirror symmetric in the sagittal plane (Supplementary Fig. 3a). Therefore, to enhance the SNR, the gradient directions were left–right symmetrized (to be consistent with the symmetrization of the subcortex mask). In particular, gradient directions in the left hemisphere were reflected into the right hemisphere around the mid-sagittal plane and averaged with the corresponding directions in the right hemisphere. These averaged gradient directions were then reflected back into the left hemisphere, and gradient magnitudes were recomputed (Supplementary Fig. 3b). This was performed separately for each of the three eigenmaps, and the difference in the gradient direction before and after symmetrization was quantified (gradient I: $\theta = 5.42 \pm 4.98°$; gradient II: $\theta = 5.04 \pm 5.0°$; gradient III: $\theta = 4.95 \pm 5.36°$).

We developed the new gradientography procedure to provide a principled framework to visualize and analyze spatial gradients in functional connectivity. First, 3D tensors were fitted to each subcortical voxel using the constrained tensor model[75,76], which is synonymous with diffusion tensor imaging. The constrained tensor model is given by

$$D = \beta g g^T + \alpha I$$

where D denotes a 3×3 symmetric tensor, g is a column vector denoting the normalized gradient direction computed with the Sobel operator, I is the identity matrix, and β and α are parameters that quantify the strength of anisotropic and isotropic diffusion, respectively. Here, we set $\beta = Kc|g|$ and $\alpha = K(1 - c)$, where $c = 0.995$ is a weighting factor that determines the extent of tensor anisotropy and K is a scale factor that governs the tensor size for visualization purposes. In this way, cigar-shaped tensors indicated rapid change in subcortical functional connectivity along the orientation of the longest axis of the tensor. In contrast, spherical tensors indicated functional connectivity that was constant along all spatial directions. It is important to note that tractography was only dependent on the gradient direction, g. The choice of β, α and c only influenced visualization of the tensor field (Fig. 1b, column III and Supplementary Fig. 1, column III). While tensors were separately fitted for each of the three eigenmaps, an alternative methodology would have been to fit a bi-tensor or multi-tensor model to each voxel[77], enabling representation of multiple eigenmaps within a single tensor field. This is conceptually analogous to modeling crossing fibers in diffusion MRI tractography[78]. However, the potential utility of modeling interactions between crossing gradients in this way remains unclear; thus, each eigenmap was independently analyzed. We relegate multidirectional gradientography to future work. Streamline propagation was performed using the interpolated streamline method with a step length of 1 mm, angle threshold of 30° and seeding 20 streamlines from randomly chosen coordinates within each subcortical voxel, yielding a total of approximately 15,000 streamlines. Streamline propagation was terminated when reaching the subcortex mask boundary. Gradientography was performed using Diffusion Toolkit software and visualized with TrackVis[79]. Streamlines were virtually unchanged when left–right symmetrization of the gradient directions was not performed. All streamlines were permitted to follow curvilinear trajectories of arbitrary complexity. The gradient magnitude image was projected onto the streamlines to parameterize the magnitude of change in functional connectivity and to visualize transitions in the gradient field with respect to the curvature of streamlines. In particular, each spatial coordinate constituting a streamline was assigned a gradient magnitude based on trilinear interpolation of the gradient magnitude image (Fig. 1b, right most). Gradientography was also performed for gradients II and III using the same procedure (Supplementary Fig. 1). While streamline trajectories varied among gradients I, II and III, the locations of local maxima in the gradient magnitude images of the three gradients were consistent (Supplementary Figs. 1 and 3). The gradient magnitude images for gradients II and III were spatially correlated (Spearman correlation) to gradient I (gradient I/II: $r = 0.44$, gradient I/III: $r = 0.73$); thus, only gradient I was used to delineate functional boundaries.

We also observed that head motion (framewise displacement (FD)) showed minimal effect on the group-consensus connectivity gradients. Specifically, individuals were ranked according to head motion, and individuals in the top 20% (mean FD: 0.26 ± 0.06 mm) and bottom 20% (mean FD: 0.10 ± 0.01 mm) defined two distinct subgroups. Group-consensus gradient magnitude images were computed for each of two subgroups and compared with the group-consensus gradient magnitude image generated within all individuals. We found that the group-consensus gradient magnitude images were strongly correlated between each pair of the three groups (Spearman correlation, $r > 0.9$).

To preclude streamlines from traversing the slender anatomical gap between the tail of the caudate nucleus and the most anterior extent of the thalamus, the subcortex mask was separated at this precise location, giving rise to three spatially contiguous subcortical components: (1) the left basal ganglia, which comprised the striatum and the GP; (2) the right basal ganglia; and (3) the left and right thalamus, the hippocampus and the amygdala. Because these three components were spatially discontiguous, tractography was performed separately for each component. A boundary between the caudate and the thalamus was therefore imposed a priori, consistent with established anatomical knowledge. Due to left–right symmetrization of gradient directions, streamlines for the left and right basal ganglia were mirror symmetric; thus, it was sufficient to analyze only one of the hemispheres of the basal ganglia. We refer to the streamlines traversing the basal ganglia as the dorsal streamlines and the dorsal connectional topography (Fig. 2a), while collectively referring to the streamlines traversing the left and right thalamus, the hippocampus and the amygdala as the ventral streamlines and ventral connectional topography (Fig. 2b). Permitting streamlines to traverse the caudate–thalamus gap did not alter the location of local maxima in gradient magnitudes, although they were less prominent in this case (Fig. 1b).

Diversity curves. The dorsal and ventral group of streamlines each comprised hundreds of distinct streamlines that characterized the connectional topographies associated with these regions. Streamlines shorter than 60 mm and 160 mm were discarded from the dorsal and ventral group, respectively. The remaining streamlines within each group traversed trajectories that shared similar profiles; thus, it was feasible to determine a single representative streamline for each group. To determine a representative streamline, the mean closest point distance[80] was computed between all pairs of streamlines constituting a group. In particular, the distance from one streamline to another was determined by first computing the distance between each point on the first streamline to all points on the second streamline. The minimum distance was then determined for each point on the first streamline. The distance from the first to second streamline was defined as the mean of these minimum distances. This was repeated for all pairs of streamline to generate a $J \times J$ distance matrix, where J denotes the number of streamlines. The distance matrix was symmetrized in a way that the mean of the two distances between a pair of streamlines was used[80]. The representative streamline was chosen as the streamline with the shortest distance, on average, to all other streamlines. Having defined a representative streamline for the dorsal and ventral group of streamlines, it was then possible to compute a diversity curve with respect to each of the representative streamlines. This yielded a curvilinear parameterization of

the group-consensus eigenmaps and their gradient magnitudes, thereby enabling statistical inference. The diversity curve concept is described in detail elsewhere[15].

Diversity curves were mapped in three steps: (1) projection of the gradient magnitude image onto each streamline; (2) spatial alignment of streamlines to the representative streamline using dynamic time warping[81]; and (3) averaging across the aligned streamlines to yield a group-representative diversity curve to provide a basis for statistical inference. Specifically, each spatial coordinate constituting a streamline was assigned a gradient magnitude based on trilinear interpolation of the gradient magnitude image. While each streamline comprised the same number of equidistant coordinates, the exact lengths of streamlines varied, resulting in some degree of misalignment between streamlines in terms of coordinate-to-anatomy correspondence. For example, the tenth coordinate on a given streamline was not necessarily closest to the tenth coordinate on a neighboring streamline. Thus, averaging across a set of streamlines could not be performed based on correspondence in the index of coordinates. Dynamic time warping was used to spatially align individual streamlines to the representative streamline and to facilitate averaging of any measure parameterized along the length of each individual streamline.

Dynamic time warping is typically used to align signals in time, whereas the method was used here to achieve spatial alignment. A warping path was computed for each individual streamline such that the sum of the Euclidean distance was minimal between the warped and representative streamline. This involved either stretching or compressing coordinates along the trajectory of each individual streamline to achieve alignment with the representative streamline. Alignment quality was visually assessed, and streamlines with a warp distance exceeding the averaged warping distance over all streamlines (dorsal: 1.72 mm, ventral: 0.54 mm) were omitted. This yielded a total of 4,693 and 3,862 aligned streamlines for the dorsal and ventral group, respectively. The gradient (eigenmap) and gradient magnitude images projected onto each of these streamlines were then averaged for each point along the streamline trajectory, yielding a single gradient and gradient magnitude diversity curve for the dorsal (Fig. 2c) and ventral group (Fig. 2d). Gradient magnitude peaks in the diversity curves indicated putative functional boundaries between regions. Consistent with the gradient magnitude image across the entire subcortex, the gradient magnitude images for gradients II and III were also spatially correlated (Spearman correlation) to gradient I for both dorsal (gradient I/II: $r=0.79$, gradient I/III: $r=0.79$) and ventral (gradient I/II: $r=0.80$, gradient I/III: $r=0.54$) components. Statistical inference was therefore confined to the dominant gradient (gradient I).

Focusing on the dominant gradient is not without precedent, and this gradient shows good correspondence with underlying neuroanatomy[23], although non-dominant gradients can reveal complementary connectivity topographies[11,23]. Three local maxima were evident in the dorsal streamline group, corresponding to established neuroanatomical boundaries among the GP–putamen, the putamen–NAc and the NAc–caudate (Fig. 2c). For the ventral streamline group, nine local maxima were evident in the diversity curve representing the gradient magnitude, which suggests that there are putative functional boundaries among the amygdala–anterior hippocampus, the anterior–posterior hippocampus, the posterior hippocampus–posterior thalamus, the anterior–posterior thalamus and the left–right thalamus (Fig. 2d).

Null model. Although local maxima in the gradient magnitude images or the diversity curves representing these images indicated putative functional boundaries, these maxima could have also potentially arisen as a matter of random fluctuations reflecting inter-individual variation and finite sample effects or due to the geometry of the subcortex (Supplementary Fig. 5). Therefore, null data were generated to statistically determine whether local maxima in the gradient images were larger than expected due to these random (sample) effects and/or confounds. The null hypothesis was of a spatially homogeneous gradient magnitude such that the rate at which whole-brain connectivity changed per unit length was constant at all points in the subcortex. Under this null hypothesis, any spatial heterogeneity was assumed to be due to sample effects or geometry. Functional boundaries were deemed to present at local maxima in the empirical gradient magnitude images when this null hypothesis could be locally rejected. Null data were generated by rewiring edges in the graph defined by the sparse adjacency matrix W. As detailed above (see "Functional connectivity and eigenmaps"), W defines a graph in which each node corresponds to a subcortical voxel, and the edge weights quantify similarity in functional connectivity profiles. A rewiring algorithm was developed to randomly reposition each edge, subject to the constraint that edges were more likely to be placed between pairs of voxels in close spatial proximity. This constraint was imposed to preserve the effect of smoothing in the null data. The following methodology was used to determine where edges should be repositioned to respect fMRI smoothing and subcortex geometry.

First, the fMRI data for each subcortical voxel was replaced with independent and randomly sampled Gaussian data that were matched in length and amplitude distribution. Second, the Gaussian data were smoothed using the same FWHM as the fMRI data. Third, the Pearson correlation coefficient was computed using the smoothed Gaussian data between all pairs of subcortical voxels. Finally, all voxel pairs were ranked from highest to lowest on the basis of the correlation coefficient. At each iteration of the rewiring algorithm, the edge being rewired was repositioned to the highest-ranking pair of voxels that had not yet received a rewired edge. To ensure that the rewired graphs were not fragmented, the first $N-1$ edges were repositioned according to a minimum spanning tree (MST), where the MST was computed for a lattice graph in which each node corresponded to a subcortical voxel. Edges in the rewired graphs inherited their edge weights from W. An ensemble of 100 rewired graphs and corresponding sparse adjacency matrices $\bar{W}_1, \bar{W}_2, \ldots, \bar{W}_{100}$ were generated by repeatedly initializing this rewiring procedure with randomly sampled Gaussian data. We found that repositioning edges to randomly chosen pairs of spatially neighboring voxels yielded virtually identical null data.

Supplementary Fig. 5a shows the graph corresponding to W and $\bar{W}_1$ for an axial slice that exemplifies the functional boundary between the GP and the putamen. Very few edges in the graph for W intersect this boundary, whereas the graph for $\bar{W}_1$ comprises numerous rewired edges that interconnect the GP and the putamen. Consistent with anatomy, this suggests that the strong gradient in functional connectivity that yields the boundary between these two regions is most likely not due to chance or the effect of smoothing and/or subcortex geometry. Supplementary Fig. 5b shows an example that demonstrates the importance of preserving geometry in the null data. In the bow-tie-shaped region constituting this example, binary edges are randomly positioned between neighboring pixels constituting the bow tie. This positioning of edges is consistent with the null hypothesis of a spatially homogenous gradient magnitude. However, the bow knot is the location of a geometric constriction, and if this geometry is not preserved in the null data, a specious boundary between the left and right sides of the bow is suggested.

Laplacian eigenmaps and gradient magnitude images were computed for each of $\bar{W}_1, \bar{W}_2, \ldots, \bar{W}_{100}$ by following the same procedure described above for W (see "Functional connectivity and eigenmaps"). An ensemble of 100 diversity curves were then computed by projecting each of these gradient magnitude images onto the original streamlines that were computed with respect to W. These diversity curves were consistent with the null hypothesis and we refer to them as null diversity curves (Fig. 2c,d).

Boundary delineation. Statistical inference was performed to determine whether each local maximum in the gradient magnitude images was sufficiently large to warrant delineation of a discrete functional boundary. If the null hypothesis could not be rejected and thus delineation was not warranted, connectional topography was deemed to be most parsimoniously represented as a continuum. The decision to delineate a boundary or not was informed by statistical testing of the null hypothesis performed on both the gradient magnitude images and the diversity curves onto which these images were projected. All local maxima in the gradient magnitude images were considered as candidate boundaries, but candidate boundaries were delineated only if the null hypothesis was rejected; that is, the gradient magnitude was larger than expected due to chance and the effects of smoothing and subcortex geometry. In particular, a P value for each local maximum on a diversity curve was estimated as the proportion of null diversity curves with local maxima that (1) exceeded or equaled the observed maximum and (2) were located within the same vicinity as the observed maximum. The FDR was controlled at a threshold of 5% across the set of all maxima. The decision to delineate a boundary was supported for maxima with P values that survived FDR correction. Figure 2c,d shows examples of diversity curve maxima for which the null hypothesis was rejected (denoted by blue asterisks).

The null hypothesis could also be tested with respect to the gradient magnitude images. In this case, the Kolmogorov–Smirnov (KS) test was used to assess the null hypothesis of equality in the distribution across voxels between the observed gradient magnitudes and the null gradient magnitudes. The null hypothesis was rejected if the tail of the distribution of gradient magnitudes was longer in the observed data compared with the null data. The main reasons for reverting to the KS test at finer scales were that (1) generally, only one candidate boundary was evident within each region constituting scales II–IV (Supplementary Fig. 23) and (2) we found that mapping diversity curves for relatively small regions did not provide substantial additional insight. Diversity curves and gradientography yield most insight when applied across a relatively large expanse that comprises multiple candidate boundaries (that is, scale I). Supplementary Fig. 23 shows examples of using the KS test to determine whether or not to delineate a candidate boundary in two specific subcortical regions. A strong gradient is evident in the anterior putamen (Supplementary Fig. 23a, yellow strip), and the KS test indicates that the gradient magnitude distribution across the voxels of this region (green curve) is significantly longer tailed than the null data (gray curves, $P<0.01$). Therefore, a boundary was delineated that resulted in the parcellation of the anterior putamen into one dorsal and one ventral component. In contrast, the null hypothesis could not be rejected with the KS test for the NAc-shell (Supplementary Fig. 23b, $P=0.22$); thus, subdivision of this region was not warranted despite the presence of a candidate boundary (yellow strip).

The final decision to delineate a boundary was not exclusively determined by whether the null hypothesis could be rejected or not. Other criteria that informed this decision were as follows:

1. Size criterion: a candidate boundary was not delineated if at least one of the regions resulting from boundary delineation would have comprised fewer than 100 voxels, irrespective of whether the null hypothesis was rejected.

2. Prior knowledge: a candidate boundary that corresponded with established subcortex anatomy or cytoarchitecture was delineated, irrespective of whether the null hypothesis was rejected.
3. Inter-hemispheric homolog: a candidate boundary was not delineated if the null hypothesis could not be rejected for the corresponding contralateral boundary. Edges in the rewired graphs (null data) inherited their edge weights from *W*, which was not necessarily symmetric. Therefore, the null data were not symmetrized; thus, discrepancies in statistical inference were possible between contralateral boundaries.

These criteria were only ever used for three boundaries of the more than 50 decisions pertaining to boundary delineation (Supplementary Fig. 6). In particular, the size criterion prevented further segmentation of a region of the caudate (CAU-DA), the prior knowledge criterion was used to delineate the thalamus–hippocampus boundary at scale I, despite failure to reject the null hypothesis, and the homolog criterion was used for the medial amygdala (mAMY) at scale II. These criteria were not used for any other cases, and all other boundary delineations were supported by the model selection procedure.

Hierarchical parcellation. The subcortex was parcellated into distinct functional regions in a hierarchical manner. Each successive scale of the hierarchy involved delineation of additional boundaries that conveyed finer details in connectional topography. Foremost, boundaries were delineated on the basis of maxima in the dorsal and ventral diversity curves for which the null hypothesis was rejected. This resulted in a subcortex parcellation comprising eight bilateral regions that recapitulated well-known subcortical regions and established anatomical boundaries (Fig. 3a). These eight bilateral regions defined scale I of the hierarchical parcellation (16 regions in total). Scale I is not intended to provide a novel parcellation, but rather establishes the validity of the model selection procedure and represents a necessary first step to delineate the novel scale II–IV atlases at finer scales. The next scale of the hierarchy (scale II) was delineated by separately computing Laplacian eigenmaps and gradient magnitudes for each of the 16 regions using the same procedure that was initially applied to the entire subcortex. This process was repeated in a recursive manner until the null hypothesis could not be rejected for any candidate boundaries, a condition that was satisfied at scale IV of the hierarchy (Figs. 3b and 4). A given region in scale k appeared as either two or more subregions in scale $k+1$, if the null hypothesis was rejected, otherwise it appeared unaltered. For each scale, the FDR was controlled at 5% across the family of null hypothesis tests performed for all candidate boundaries. Unlike alternative multiple testing corrections, the FDR is scalable and adaptive[82], meaning that the greater number of candidate boundaries tested at scale IV, compared with scale I, did not make FDR correction at scale IV inherently more stringent. Note that the FDR test was performed independently for each scale. Successive scales of the parcellation hierarchy conveyed finer boundaries and more regions (scale I: 16 regions; scale II: 32 regions; scale III: 50 regions; scale IV: 54 regions). The diameter of all regions constituting scale IV substantially exceeded the FWHM of the smoothing kernel width (minimum: 10.2 mm, maximum: 24.4 mm, median: 17.2 mm). While exceedance of the FWHM is a heuristic criterion, this suggests that the extent of smoothing was sufficiently constrained to enable delineation of the smallest region.

For scale I, the null hypothesis was tested by performing inference on maxima in the dorsal and ventral diversity curves. In particular, inference was performed to determine whether each maximum in the gradient magnitude was significantly larger than expected due to chance, geometry and smoothing (see "Boundary delineation"). For scale II and beyond, as described above, the KS statistic was used to test the null hypothesis due to challenges in mapping diversity curves for the relatively small regions constituting these scales. Delineation of small regions was also more susceptible to the effects of noise, especially signal contamination from surrounding white matter and cerebrospinal fluid. To reduce these effects, for scale II and beyond, the adjacency matrix (W) used to compute Laplacian eigenmaps was thresholded using the disparity filter[83]. The significance level for the disparity filter was set to the minimum value required to yield a graph that was not fragmented.

Watershed algorithm. The watershed transform algorithm[84] was used to cluster voxels and thereby identify spatially contiguous regions that resulted from delineation of a boundary, as applied elsewhere to parcellate the cortex[8]. The watershed transform was applied to the 3D gradient magnitude images. To initiate the watershed, seed voxels were first chosen such that exactly one seed voxel resided on each side of a boundary. Seed voxels were approximately positioned to reside within a regional minimum of the gradient magnitude image. A regional minimum that was distant from the boundary was preferred, although the parcellation was robust against the precise seed voxel location. Clusters were then iteratively grown for each seed region until locations were reached where voxels could no longer be unequivocally assigned to one of the clusters. Clusters were therefore analogous to water catchment basins (that is, minima in the gradient magnitude images), while boundaries represented watershed ridge lines (that is, maxima in these images). Before applying the watershed transform, the gradient magnitude images were (1) normalized to ensure that all values resided on the unit interval and (2) morphologically reconstructed to ensure that regional minima were only present at the location of the chosen seed voxels. The latter step aimed to enhance the contrast between voxels within the expected cluster and boundary voxels. The output of the watershed transform was a cluster of voxels for each seed voxel. Voxels that resided at boundary locations where not necessarily assigned to any cluster, yielding empty space between parcellated subregions. To fill the empty space, for each unallocated voxel, the shortest path was computed to each seed voxel. Shortest paths were computed with respect to the sparse adjacency matrix (W) following a strength-to-distance remapping of the edge weights. Unallocated voxels were then assigned to subregions with the minimum shortest path distance.

Parcellation validation and replication. *Homogeneity estimation.* A valid functional parcellation should comprise regions that are internally homogenous with respect to the functional connectivity profile of each constituent voxel. The regional homogeneity of scale I–IV parcellations was compared with the extent of homogeneity achieved with alternative subcortex parcellations as well as the homogeneity that could be expected due to chance.

The fMRI data for a region was represented as a matrix of dimension $N \times T$, where N and T denote the number of voxels constituting the region and the number of time frames, respectively. Regional homogeneity was defined as the variance explained by the first principal component of this matrix, which was estimated using PCA. Homogeneity therefore quantified the extent of synchrony in fMRI activity across voxels constituting a region. While homogeneity can be computed with respect to functional connectivity[8], we performed estimation directly on the fMRI time series acquired in the second session (REST2). This ensured that validation was performed using independent data and an independent quantity. Homogeneity was separately computed for each region and each individual. For each individual, homogeneity was then averaged across all regions to yield an overall estimate of homogeneity for the parcellation as a whole, referred to as parcellation homogeneity (Supplementary Fig. 11a).

Parcellation homogeneity increased from scale I to scale IV (Fig. 5a, red dotted line). This was because small regions were inherently more homogeneous than large regions[8]. To determine whether the observed homogeneity values were larger than expected due to chance, the subcortex was randomly parcellated such that the total number of regions and the distribution of region size were matched between the random and observed parcellations (Supplementary Fig. 11b). Parcellation homogeneity was then estimated for 100 such random parcellations to yield a null distribution for homogeneity under the null hypothesis of randomly delineated regions. A P value for this null hypothesis was estimated as the proportion of random parcellations with homogeneity exceeding or equaling the observed homogeneity. Parcellations were deemed homogeneous if the null hypothesis was rejected ($P < 0.05$). Random parcellations were generated by (1) randomly placing seed voxels throughout the subcortex mask in such a way that the Euclidean distance between all pairs of seed voxels was approximately maximized and (2) assigning all non-seed voxels to their closest seed voxel in terms of the Euclidean distance. This assignment process defined a set of randomly delineated regions. The number of seed voxels was set to the number of desired regions. Parcellations were discarded if they contained any regions that were not spatially contiguous or not matched with respect to the distribution of region sizes. Discarded parcellations were replaced until 100 valid random parcellations were generated.

Parcellation homogeneity was also computed for existing subcortex parcellation atlases (Supplementary Table 3). The scale (I–IV) that comprised the same or fewer parcels than the existing parcellation was chosen for comparison. Choosing a scale with fewer parcels provided an advantage to the existing parcellations. We specifically evaluated the homogeneity of two existing parcellation atlases for the entire subcortex[6,33] as well as parcellation atlases for the hippocampus[22,35,85], the thalamus[37] and the striatum[36]. Cerebellar and brainstem regions were omitted from the parcellation delineated by Ji et al.[6] and Fan et al.[33] to ensure homogeneity estimates were specific to the subcortex and therefore comparable to the other parcellations. To facilitate a fair comparison across parcellations containing a disparate number of regions, observed parcellation homogeneity values were normalized with respect to the mean homogeneity across the set of random parcellations. Ratios exceeding one indicated that parcellations were more homogeneous than expected due to chance.

7T replication. High-resolution fMRI acquired at ultrahigh magnetic field strength (7T) can enhance functional contrast-to-noise ratios, improve spatial localization and alleviate partial volume effects[24]. We sought to test the extent to which parcellations delineated using 3T-rfMRI could be replicated using 7T-rfMRI. To this end, the subcortex was hierarchically parcellated by applying the same procedures described above to the 7T-rfMRI data. This involved mapping Laplacian eigenmaps and gradient magnitudes, null hypothesis testing for each maximum comprising the gradient magnitude images and application of the watershed transform to delineate subregions. This yielded a 7T parcellation atlas of the subcortex that also comprised four scales (scale I: 16 regions; scale II: 34 regions; scale III: 54 regions; scale IV: 62 regions).

To enable comparisons between 3T and 7T parcellations, the 3T parcellations were up-sampled to the same spatial resolution as 7T (1.6-mm isotropic), and the spatial similarity between each scale of 3T and 7T parcellations was estimated using normalized mutual information (NMI)[86]. NMI is an information

theoretic measure that quantifies the extent to which knowledge of a parcellation reduces the uncertainty in the location of regions in a second parcellation. NMI ranges between zero and one, with higher NMI values indicating greater spatial correspondence between parcellations.

Personalized parcellation. Following Glasser and colleagues[2], a machine-learning approach was used to personalize the group-consensus parcellations and to distinguish individual differences in functional organization, thereby yielding a unique parcellation for each individual. This enabled quantification of the extent of variation among individuals for each region. The subcortex mask remained fixed for all individuals; thus, only variation in functional boundaries within the subcortex was permitted, without variation in the overall subcortical volume. The periphery of each region comprising the scale IV parcellation was first dilated by approximately 4–6 mm to define a zone of uncertainty around each region. The uncertainty zone enabled flexibility in the location of boundaries for individuals who exceeded the group-consensus boundary. The extent of dilation was such that each region in the group-consensus atlas comprised approximately the same number of voxels as its uncertainty zone, meaning that a voxel was equally likely to be randomly classified as belonging to the region compared to its uncertainty zone. Enlarging the uncertainty zone would have permitted individual boundary locations to deviate to a greater extent from the group-consensus boundaries, although major deviations were not expected in young and healthy adults, which is consistent with previous work on the cortex[2]. A binary support vector machine (SVM) classifier was trained to classify whether a voxel resided in the region or its uncertainty zone. We use M to denote the combined number of voxels constituting the region and its uncertainty zone.

Combining REST1 and REST2 would potentially yield more accurate estimates of functional connectivity compared with any of the individual sessions. However, given that parcellation was performed using data from the first 3T-rfMRI session (REST1), to assess inter-session reproducibility and to minimize circularity, the SVM was trained and evaluated using data from the second session (REST2). One hundred individuals were randomly selected to train the SVM, and the trained SVM was then applied to delineate a personalized parcellation for the remaining 921 individuals. It is important to remark that each individual contributed M training samples because classification was undertaken on a per-voxel basis. The SVM feature space was defined over the symmetric $N \times N$ similarity matrix, whereby each cell in this matrix stored the similarity in functional connectivity fingerprints between a pair of subcortex voxels (see "Functional connectivity and eigenmaps"). The feature vector for a particular voxel was selected as the relevant row in this matrix. The feature space was separately mapped for each individual and required computation of individual similarity matrices. A radial basis function kernel was used, and the feature space was standardized.

For each of the 921 individuals in the test set, the SVM was used to predict the likelihood (posterior probability) of each voxel belonging to the region under consideration, as opposed to belonging to the uncertainty zone of the region. See Supplementary Fig. 17 for a schematic of this binary classification problem. The threshold for the posterior probability of a voxel belonging to the region was varied between 0 and 100%, whereby a threshold of 0% led to all voxels, including those in the uncertainty zone, being classified as belonging to the region. Increasing the threshold eventually resulted in loss of spatial contiguity. The extent to which the threshold could be increased while preserving these properties provided insight into parcellation robustness. This process was repeated separately for each region comprising the scale IV parcellation, requiring an SVM to be independently trained for each region. It was possible for voxels to be included in the uncertainty zones of multiple regions. A voxel could therefore be assigned a probability of belonging to each of many regions. To delineate a personalized parcellation for each individual, a winner-takes-all rule was used to break ties, such that voxels were allocated to regions with the highest probability. Crucially, if the highest probability region did not exceed the posterior probability threshold, the voxel remained unassigned. This introduced the possibility of certain regions in the group-consensus parcellation being absent from the personalized parcellation of an individual. The regional detection rate was the proportion of individuals for which a given region was allocated at least one voxel. The detection rate of each region was evaluated as a function of the posterior probability threshold. The group-consensus parcellation was assumed to provide a valid representation of individuals for regions with high detection rates.

The spatial correspondence between the group-consensus and personalized parcellations was also evaluated with the Dice coefficient. In particular, the Dice coefficient was separately computed for each individual and each region as a function of the posterior probability threshold. If X and Y denote the indices of the voxels constituting the personalized region of an individual and the group-consensus region, respectively, the Dice coefficient was computed as $2|X \cap Y|/(|X| + |Y|)$. An average Dice coefficient was then computed for each individual by averaging the regional Dice coefficients.

Task-evoked connectional gradients. We aimed to investigate whether the connectional topography of the subcortex would exhibit significant variation between task conditions and rest[27,87–89]. The tasks considered were emotion processing, gambling, language processing, motor execution, relational matching, social inference and working memory. Details pertaining to each task condition are described elsewhere[54].

Following the same procedure described above (see "Functional connectivity and eigenmaps"), group-consensus eigenmaps and gradient magnitude images were computed for each of the seven tasks. For each task, the gradient magnitude image for gradient I was projected onto the dorsal and ventral streamlines. This yielded diversity curves for each task (Supplementary Fig. 19a). Tractography of the task-derived gradients was not performed, and streamlines previously determined at rest (see "Diversity curves") were used as references. To facilitate comparisons of diversity curves between different tasks, only the 725 individuals (360 males) that completed all nine conditions (two rest and seven tasks) were included. The mean diversity curve across the nine conditions was first computed and regressed from the diversity curves for each of the nine conditions. This eliminated the common variance across the conditions. The Pearson correlation coefficient was computed between the resulting residuals to generate a correlation matrix of dimension 9×9, whereby each element corresponded to a pair of task conditions. Permutation testing was used to determine a P value for each correlation coefficient. Specifically, for each pair of comparisons, the points on one of the diversity curves were randomly permutated and the correlation was recomputed on the permuted diversity curves. This was repeated for 10,000 permutations, yielding a null distribution for the correlation coefficient. The P value was given by the proportion of permutations with the correlation coefficient that exceeded or equalled the correlation coefficient in the unpermuted data. Bonferroni correction was controlled at $0.05/36 = 0.0014$ across the set of all unique pairs of conditions. The pairs of conditions that survived correction are shown in Supplementary Fig. 19b and visualized as a graph to show similarities in task conditions (Supplementary Fig. 19c). Furthermore, a matrix of dimension $H \times 9$ was then constructed, where H denotes the number of points along the diversity curve and each column corresponds to one of the nine conditions. Each cell in the matrix stored the residual value of each diversity curve point. Rows and columns were reordered according to average-linkage clustering based on the Pearson correlation coefficient (Supplementary Fig. 19d).

Given that substantially fewer fMRI volumes were acquired during task compared to rest (see "Data and pre-processing"), supplementary analyses were undertaken to test whether task-related changes in connectional gradients could be attributed to the acquisition of fewer volumes. Specifically, the group-consensus eigenmaps and the gradient magnitude images were recomputed using only the first quarter of time frames ($T = 278$) from each run of the rfMRI data (278×2 in total), thereby matching the average number of time frames across the seven tasks. We found that the gradient magnitude images computed using the shortened and full-length rfMRI acquisitions were highly correlated (Spearman correlation: $r > 0.98$ for both REST1 and REST2). This suggests that differences in the number of volumes between the tfMRI and rfMRI acquisitions do not explain the task-evoked reconfiguration of connectional gradients and diversity curves.

Relating subcortical functional network to behaviors. Individual variation in functional connectivity associates with human behaviors that relate to cognition, emotion and psychopathology in both health and mental illness[19,90–92]. While cortico–cortical connections have been well studied and predict individual variation in human behavior, less is known about the predictive utility of functional connectivity within the subcortex. Our multiscale subcortex parcellation facilitated investigations of associations between intrasubcortical functional connectivity and behavioral phenotypes for each atlas scale.

Functional connectivity and modular structure. Subcortical functional connectivity matrices were mapped for each individual and each scale of the parcellation. To this end, representative fMRI time series were determined for each region by averaging across all relevant voxels. Pearson correlation coefficients in regional time series were computed for all pairs of regions and represented in the form of a symmetric functional connectivity matrix. The connectivity matrices were then r-to-z transformed (Fisher transformation). The rows and columns of the connectivity matrices were reordered to accentuate modular structure, whereby the modular structure was determined using the Louvain community detection algorithm[93]. Separate connectivity matrices were mapped for the first (REST1) and second (REST2) 3T-rfMRI sessions to provide a discovery and within-sample replication set.

Behavioral phenotypes. Behavioral measurements and procedures for the HCP are described in detail elsewhere[54]. Items that tapped alertness, cognition, emotion, sensory–motor function, personality, psychiatric symptoms, substance use and life function were selected for further analyses, subject to the following conditions:

1. Only total or subtotal scores were selected for psychological assessments.
2. Only raw scores were selected for items with both raw and age-adjusted scores.
3. Items based on strictly binary responses were excluded.
4. Items with missing responses in more than 10% of individuals were excluded.

Items relating to task performance in emotional processing, language processing, social recognition, motor execution, working memory, relational

matching and reward/decision-making processing were also included. This resulted in a total of 109 behavioral measures for each individual (Supplementary Table 4). Participants with missing responses for any of these 109 items were then excluded, resulting in a final sample comprising 958 individuals (453 males, mean age of 28.7 ± 3.7 years). Two 3T-rfMRI sessions were acquired in all these individuals.

Independent component analysis (ICA) was used to reduce the set of behavioral measures to a set of latent dimensions with the aim of performing inference on the dimensions rather than the full set of behaviors. Before performing ICA, behavioral items with continuously distributed scores (87 out of 109) were normalized with a rank-based inverse Gaussian transformation[94]. Age and sex were then regressed from all items and ICA was performed on the residuals that resulted from this regression. Other confounding factors such as blood pressure, hemoglobin, height and weight were not included due to missing responses for several individuals. ICA was performed using the Icasso package[95] for Matlab, which provides an implementation of the FastICA algorithm[96]. Under ICA, the matrix of residuals (behaviors × individuals), denoted with Y, was factorized into the product $Y = A^{-1}S$, where A^{-1} denotes the mixing matrix (behaviors × components) and S denotes the estimated independent sources (components × individuals). The inverse of A^{-1} is denoted A (components × behaviors) and referred to as the de-mixing matrix.

To estimate the de-mixing matrix, FastICA was performed using default parameter settings, including a cubic nonlinearity and deflationary orthogonalization. Bootstrapping was used to sample individuals with replacement, and ICA was performed independently on each bootstrapped sample using randomly chosen initial conditions. A total of 500 bootstrapped samples were generated. Independent components that represented a consensus across the 500 samples were then derived using a clustering procedure. In particular, agglomerative clustering with average linkage was used to partition the de-mixing matrix into putative clusters. The number of dimensions in the feature space was the number of behaviors, and each cluster comprised groups of components (that is, rows from A). Clearly separated clusters indicated that independent components were consistently and reliably estimated despite randomization of initial conditions and bootstrapping. A cluster quality index was used to quantify cluster separation and provided a metric to select the number of independent components (see below). Cluster separation was quantified by the difference in average intra-cluster similarity and average inter-similarity, denoted by Iq. A higher Iq suggests compact clusters, whereas a lower Iq suggests that clusters are not well separated. These operations were performed internally in the Icasso package, and further details are available in the documentation of the package.

In addition to these internal procedures, we performed a sampling and matching process to ensure stability and reliability of the estimated independent components. Specifically, the ICA as described above was repeated for ten trials, yielding an ensemble of de-mixing matrices, $A_1, A_2, \ldots, A_{10}$ and corresponding independent components, $S_1, S_2, \ldots, S_{10}$. Variability in A_u and S_u across trials was due to randomization of initial conditions and random sampling inherent to bootstrapping. Each row of A corresponded to an independent component, and each column quantified the weighting of a behavioral item in the given component. We sought to evaluate the similarity of the resulting estimates across trials to investigate whether the Icasso procedure yielded reproducible independent components across the ten trials. For each pair of trials u and v, a correlation matrix of dimension $I \times I$ was computed, where I denotes the number of independent components. Element (i,j) of this correlation matrix stored the Pearson correlation coefficient between row i of A_u and row j of A_v. We denote the correlation matrix between trial u and v with C_{uv}, $u,v = 1,2\ldots,10$. Given that independent components are resolved up to an arbitrary sign flip, the absolute value of all correlation coefficients was considered. The nth component in trial u did not necessarily correspond to the nth component in trial v; thus, a one-to-one matching of components was required for each pair of trials. The Hungarian algorithm[97] was applied to C_{uv} to determine a one-to-one matching that maximized the correlation coefficients between the matched pairs of components. If ICA estimates were reproducible between trials u and v, each column of C_{uv} should comprise a correlation coefficient that is substantially larger than all others in the column, indicating an obvious matching. The trial that was best matched to all other trials was chosen as the reference trial, whereby matching quality was quantified as the average correlation coefficient computed over all matched pairs of components in C_{uv}.

Once the reference trial was determined, the components in each of the other trials were reordered to match the reference, as dictated by the optimal one-to-one matching computed using the Hungarian algorithm. The polarity of the component was potentially flipped to ensure consistency with the reference trial. The reordered de-mixing matrices $A_1, A_2, \ldots A_{10}$ were then averaged across trials to yield a single de-mixing matrix that represented a consensus across the ten trials. The independent components $S_1, S_2, \ldots, S_{10}$ were reordered and then averaged in the same way.

Due to the effects of bootstrapping and randomization, the de-mixing matrix was not necessarily perfectly orthogonal, and some components were minimally correlated. The Pearson correlation coefficient was computed between all pairs of components in the de-mixing matrix. The reciprocal of the largest correlation coefficient was used to quantify the extent of interdependence between components such that higher values of the reciprocal were desired. This was performed for each of the reordered de-mixing matrices $A_1, A_2, \ldots, A_{10}$, and the average across trials resulted in a consensus index of the independence.

Three criteria were therefore used to evaluate ICA performance and to assist in determining the best number of components to estimate:

1. Cluster separation: the extent of separation between clusters among independent components found across bootstrapped samples. This was estimated internally as part of the Icasso package and provides an estimate of reliability and stability of independent components.
2. Trial matching quality: the quality of the one-to-one matching of independent components across ICA trials. This quantified the reproducibility of independent components and was measured as the average distance between matching independent components of each trial and the reference trial.
3. Independence index: the independence of components in the de-mixing matrix. This was quantified as the reciprocal of the largest correlation coefficient between all pairs of components.

The ICA procedure described above, including bootstrap resampling and trial matching, was separately repeated for candidate models ranging from 3 to 30 independent components. The optimal model (that is, the number of components) was informed by plotting the above measures of cluster separation, trial matching quality and independence index as a function of the number of components and identifying abrupt changes based on the elbow criterion (Supplementary Fig. 24). While both cluster separation (Supplementary Fig. 24a) and trial matching quality (Supplementary Fig. 24b) showed abrupt reductions when moving from six to seven components, which suggests that six components was optimal, the independence index (Supplementary Fig. 24c) suggested that five components was most suitable. We could therefore narrow down model selection from 28 candidates to only 2 candidate models: 5 or 6 independent components. To break the tie between these two models, the independent components constituting both models were visualized as word clouds, with the font size of each behavior scaled according to its de-mixing weight. Although, the five-component and six-component models were highly comparable, we selected the five-component model because it was the simpler model and enabled clear labeling of each independent component. The five independent components characterized cognitive performance, illicit substance use, tobacco use, personality and emotional traits, as well as mental health. Hence, the 109 behavioral items initially selected were decomposed into five independent components, which we refer to as behavioral dimensions (Fig. 8a,b and Supplementary Fig. 21).

NBS analysis. The NBS[28] was used to test whether functional connectivity mapped within each parcellation scale (scales I–IV) significantly associated with any of the five behavioral dimensions. The NBS was applied independently to each dimension and parcellation scale. For each pair of regions, a general linear model was formulated in which functional connectivity was the dependent variable and the independent variables included an intercept term, the behavioral dimension (that is, the relevant column from the estimated independent sources) and confounds including head motion parameters summarized by the framewise displacement[59] and total subcortical volume estimated by FreeSurfer (https://surfer.nmr.mgh.harvard.edu/), as provided by the HCP. Given that age and sex were initially regressed from all behavioral scores before performing ICA, these potential confounds were not included in the statistical model. Each connection was endowed a t-statistic and a corresponding uncorrected P value for the null hypothesis that the association between functional connectivity and the behavioral dimension was not significantly different from zero. The premise of the NBS is to reject the null hypothesis for connected graph components[28] rather than for individual connections, thereby relinquishing some precision in effect localization for a gain in statistical power. To this end, connected components were identified among the set of connections with a t-statistic exceeding 4. This t-statistic threshold was chosen to ensure that the smallest effect size of interest that could be detected was approximately a Cohen's d of 0.1. The number of suprathreshold connections constituting each component defined the size of the component. Permutation testing was used to generate an empirical null distribution for component size. For each of the 10,000 permutations, an established method[98] was used to refit the general linear model to data in which the correspondence between individuals and behaviors was permuted. Permutation sequences were obtained using multilevel block permutation[51,52] to ensure that the data were shuffled in a way that respected known familial relationships among individuals. In particular, each family could only be shuffled as a whole, and family members could only be permuted within their family. Dizygotic twins and non-twin siblings were assumed to share the same kinship and they could therefore be permuted. The size of the largest connected component was stored for each permutation to ensure control of the family-wise error rate across all components identified. The family-wise-error-corrected P value for an observed component was given by the proportion of permutations for which the largest component identified was larger than or equal in size to the observed component. The NBS was repeated independently for each of the five behavioral dimensions and for the two alternative hypotheses of positive and negative correlation. This resulted in a total

of ten multiple comparisons. The FDR was controlled at 5% across these multiple comparisons.

The NBS was performed on functional connectivity mapped using 3T-rfMRI data from the second acquisition (REST2) given that the new atlas was delineated using the first acquisition (REST1). The reproducibility of any significant associations identified with the NBS in REST2 were evaluated using functional connectivity mapped using 3T-rfMRI data from REST1. To enable comparisons, functional connectivity mapped with an alternative subcortex atlas (Subcortex-II)[33] was also tested for associations with behavioral dimensions following the same procedure described above.

Statistical analysis. Null hypothesis tests were used to perform statistical analyses. Statistical significance was determined using permutation tests and resampling. Specifically, for atlas delineation, the null hypothesis was that peaks in the gradient magnitude images were consistent with the geometry of the subcortex and/or fMRI confounds. The alternative hypothesis was that the peaks were larger than attributable to subcortical geometry and confounds. Each rejection of this null hypothesis provided evidence of a discrete boundary in subcortical topography. A dedicated geometry-preserving null model was developed to perform inference on the local maxima of the gradient magnitude images (see "Null model"). This facilitated the generation of an empirical null distribution for peak magnitudes by repeatedly drawing random samples from the null model. The *P* value for each peak was estimated as the proportion of samples constituting the null distribution with peaks that equalled or exceeded the magnitude of the actual peak (see "Boundary delineation"). The FDR was controlled at 5% across the set of all peaks identified at each scale using the Benjamini–Hochberg procedure. For the behavioral analyses, the null hypothesis was that the five behavioral dimensions did not explain significant individual variation in subcortical functional connectivity. This null hypothesis was tested using linear regression analysis and the NBS[28]. All null hypothesis tests were nonparametric and did not mandate strong assumptions about data normality.

Further methodological considerations. *Connectivity gradients and subcortical geometry.* A clear peak in the diversity curve separates the hippocampus and the thalamus (Fig. 2d). However, the transition between the hippocampus and the thalamus is narrow and represents a local constriction in the geometry of the subcortex. Because our resampling preserves the geometry of the empirical data, a relatively abrupt transition is also present between the thalamus and the hippocampus in the null data. In other words, the functional separation between the hippocampus and the thalamus can be largely explained by the intrinsic geometry of the subcortex. This does not imply that the hippocampus and the thalamus are not functionally separated, but simply suggests that the functional separation is consistent with the underlying geometry of the two structures and does not require an additional disruption in the functional connectivity gradients. Conversely, there are occasional peaks in the null diversity curves that are not present in the real data (for example, the broad peak within the caudate shown in Fig. 2c). This presumably arises when the local functional connectivity gradient is smoother (more homogenous) in the real data across a geometric feature than predicted by the null data.

Multiscale organization and model selection. Multiscale (hierarchical) organization is not necessarily a fait accompli of the recursive application of model selection. Indeed, we explicitly tested for the possibility of an absence of multiscale structure for each region comprising scale I, but found that the null hypothesis could be rejected for all regions, which is suggestive of a multiscale organizational structure. If we were unable to reject the null hypothesis, this would have instead suggested an absence of any multiscale structure. Furthermore, the number of scales substantially differed between subcortical nuclei. For example, the thalamus, the hippocampus and the caudate each comprised four levels, which suggests a deeper and more complex multiscale structure relative to the amygdala and the GP, which only comprised two levels. This is consistent with the greater organizational complexity of the thalamic nuclei, from molecular[99] and cellular[39] to connectivity[20,37] and function[100,101]. In contrast, the GP is primarily involved in the regulation of movement control[102] and the amygdala plays an essential role in emotional processes[103].

Reporting Summary. Further information on research design is available in the Nature Research Reporting Summary linked to this article.

Data availability

Neuroimaging data analyses were undertaken using publicly available human neuroimaging datasets acquired and maintained by the HCP[18]. These datasets are available for download to anyone agreeing to the Open Access Data Use Terms (https://db.humanconnectome.org/). Access to family structure data and several behavioral measures requires acceptance of the HCP Restricted Data Use Terms (https://www.humanconnectome.org/study/hcp-young-adult/document/restricted-data-usage). The independent validation dataset used to assess the reproducibility of the parcellation homogeneity results is currently not publicly available. The new atlas is openly available in the form of NIFTI (Neuroimaging Informatics Technology Initiative) and CIFTI (Connectivity Informatics Technology Initiative) files. To facilitate mapping of whole-brain connectomes, we have also integrated the new atlas into several well-known cortex-only parcellation atlases and the combined cortex–subcortex atlases are made openly available. Supplementary Table 5 provides details about the atlas formats that can be downloaded from the GitHub repository (https://github.com/yetianmed/subcortex).

Code availability

The Matlab (R2018b) codes to compute Laplacian eigenmaps, gradient magnitudes, diversity curves and other computational analyses undertaken as part of this study are openly available at https://github.com/yetianmed/subcortex. The following additional software packages used for this study are freely and openly available: Diffusion Toolkit (v.0.6.4.1) and TrackVis (v.0.6.1): http://trackvis.org/; NBS (v.1.2): https://www.nitrc.org/projects/nbs/; Icasso (v.1.21): https://research.ics.aalto.fi/ica/icasso/; NeuroMArVL: https://immersive.erc.monash.edu/neuromarvl/; PALM (v.alpha116): https://fsl.fmrib.ox.ac.uk/fsl/fslwiki/PALM/ExchangeabilityBlocks; and fMRIPrep (v.1.5.9): https://fmriprep.org/en/stable/index.html.

References

51. Winkler, A. M., Ridgway, G. R., Webster, M. A., Smith, S. M. & Nichols, T. E. Permutation inference for the general linear model. *NeuroImage* **92**, 381–397 (2014).
52. Winkler, A. M., Webster, M. A., Vidaurre, D., Nichols, T. E. & Smith, S. M. Multi-level block permutation. *NeuroImage* **123**, 253–268 (2015).
53. Smith, S. M. et al. Resting-state fMRI in the Human Connectome Project. *NeuroImage* **80**, 144–168 (2013).
54. Barch, D. M. et al. Function in the human connectome: task-fMRI and individual differences in behavior. *NeuroImage* **80**, 169–189 (2013).
55. Glasser, M. F. et al. The minimal preprocessing pipelines for the Human Connectome Project. *NeuroImage* **80**, 105–124 (2013).
56. Salimi-Khorshidi, G. et al. Automatic denoising of functional MRI data: combining independent component analysis and hierarchical fusion of classifiers. *NeuroImage* **90**, 449–468 (2014).
57. Griffanti, L. et al. ICA-based artefact removal and accelerated fMRI acquisition for improved resting state network imaging. *NeuroImage* **95**, 232–247 (2014).
58. Parkes, L., Fulcher, B., Yucel, M. & Fornito, A. An evaluation of the efficacy, reliability, and sensitivity of motion correction strategies for resting-state functional MRI. *NeuroImage* **171**, 415–436 (2018).
59. Power, J. D., Barnes, K. A., Snyder, A. Z., Schlaggar, B. L. & Petersen, S. E. Spurious but systematic correlations in functional connectivity MRI networks arise from subject motion. *NeuroImage* **59**, 2142–2154 (2012).
60. Satterthwaite, T. D. et al. An improved framework for confound regression and filtering for control of motion artifact in the preprocessing of resting-state functional connectivity data. *NeuroImage* **64**, 240–256 (2013).
61. Van Dijk, K. R., Sabuncu, M. R. & Buckner, R. L. The influence of head motion on intrinsic functional connectivity MRI. *NeuroImage* **59**, 431–438 (2012).
62. Puckett, A. M. et al. Using multi-echo simultaneous multi-slice (SMS) EPI to improve functional MRI of the subcortical nuclei of the basal ganglia at ultra-high field (7T). *NeuroImage* **172**, 886–895 (2018).
63. Glasser, M. F. et al. The Human Connectome Project's neuroimaging approach. *Nat. Neurosci.* **19**, 1175–1187 (2016).
64. Glasser, M. F. et al. Using temporal ICA to selectively remove global noise while preserving global signal in functional MRI data. *NeuroImage* **181**, 692–717 (2018).
65. Cole, M. W. et al. Multi-task connectivity reveals flexible hubs for adaptive task control. *Nat. Neurosci.* **16**, 1348–1355 (2013).
66. Esteban, O. et al. fMRIPrep: a robust preprocessing pipeline for functional MRI. *Nat. Methods* **16**, 111–116 (2019).
67. Percheron, G., Yelnik, J. & Francois, C. A Golgi analysis of the primate globus pallidus. III. Spatial organization of the striato–pallidal complex. *J. Comp. Neurol.* **227**, 214–227 (1984).
68. Yushkevich, P. A. et al. Quantitative comparison of 21 protocols for labeling hippocampal subfields and parahippocampal subregions in in vivo MRI: towards a harmonized segmentation protocol. *NeuroImage* **111**, 526–541 (2015).
69. Guadalupe, T. et al. Human subcortical brain asymmetries in 15,847 people worldwide reveal effects of age and sex. *Brain Imaging Behav.* **11**, 1497–1514 (2017).
70. de Hollander, G., Keuken, M. C., van der Zwaag, W., Forstmann, B. U. & Trampel, R. Comparing functional MRI protocols for small, iron-rich basal ganglia nuclei such as the subthalamic nucleus at 7 T and 3 T. *Hum. Brain Mapp.* **38**, 3226–3248 (2017).
71. Belkin, M. & Niyogi, P. Laplacian eigenmaps for dimensionality reduction and data representation. *Neural Comput.* **15**, 1373–1396 (2003).

72. Fornito, A., Zalesky, A. & Breakspear, M. Graph analysis of the human connectome: promise, progress, and pitfalls. *NeuroImage* **80**, 426–444 (2013).
73. Cerliani, L. et al. Probabilistic tractography recovers a rostrocaudal trajectory of connectivity variability in the human insular cortex. *Hum. Brain Mapp.* **33**, 2005–2034 (2012).
74. Jeurissen, B., Descoteaux, M., Mori, S. & Leemans, A. Diffusion MRI fiber tractography of the brain. *NMR Biomed.* **32**, e3785 (2019).
75. Alexander, D. C. in *Visualization and Processing of Tensor Fields* (eds Weickert J. & Hagen, H.) Ch. 5 (Springer, 2006).
76. Friman, O., Farneback, G. & Westin, C. F. A Bayesian approach for stochastic white matter tractography. *IEEE Trans. Med. Imaging* **25**, 965–978 (2006).
77. Peled, S., Friman, O., Jolesz, F. & Westin, C. F. Geometrically constrained two-tensor model for crossing tracts in DWI. *Magn. Reson. Imaging* **24**, 1263–1270 (2006).
78. Behrens, T. E., Berg, H. J., Jbabdi, S., Rushworth, M. F. & Woolrich, M. W. Probabilistic diffusion tractography with multiple fibre orientations: what can we gain? *NeuroImage* **34**, 144–155 (2007).
79. Wang, R., Benner, T., Sorensen, A. & Wedeen, V. Diffusion Toolkit: a software package for diffusion imaging data processing and tractography. *Proc. Int. Soc. Magn. Reson. Med.* **15**, 3720 (2007).
80. O'Donnell, L. J. & Westin, C. F. Automatic tractography segmentation using a high-dimensional white matter atlas. *IEEE Trans. Med. Imaging* **26**, 1562–1575 (2007).
81. Müller, M. in *Information Retrieval for Music and Motion* 69–84 (Springer, 2007).
82. Benjamini, Y. Discovering the false discovery rate. *J. R. Stat. Soc. Ser. B* **72**, 405–416 (2010).
83. Serrano, M. Á., Boguñá, M. & Vespignani, A. Extracting the multiscale backbone of complex weighted networks. *Proc. Natl Acad. Sci. USA* **106**, 6483–6488 (2009).
84. Meyer, F. Topographic distance and watershed lines. *Signal Process.* **38**, 113–125 (1994).
85. Eickhoff, S. B. et al. A new SPM toolbox for combining probabilistic cytoarchitectonic maps and functional imaging data. *NeuroImage* **25**, 1325–1335 (2005).
86. Lancichinetti, A., Fortunato, S. & Kertész, J. Detecting the overlapping and hierarchical community structure in complex networks. *N. J. Phys.* **11**, 033015 (2009).
87. Greene, A. S., Gao, S., Scheinost, D. & Constable, R. T. Task-induced brain state manipulation improves prediction of individual traits. *Nat. Commun.* **9**, 2807 (2018).
88. Cole, M. W., Bassett, D. S., Power, J. D., Braver, T. S. & Petersen, S. E. Intrinsic and task-evoked network architectures of the human brain. *Neuron* **83**, 238–251 (2014).
89. Medaglia, J. D., Lynall, M. E. & Bassett, D. S. Cognitive network neuroscience. *J. Cogn. Neurosci.* **27**, 1471–1491 (2015).
90. Smith, S. M. et al. A positive-negative mode of population covariation links brain connectivity, demographics and behavior. *Nat. Neurosci.* **18**, 1565–1567 (2015).
91. Fornito, A., Zalesky, A., Pantelis, C. & Bullmore, E. T. Schizophrenia, neuroimaging and connectomics. *NeuroImage* **62**, 2296–2314 (2012).
92. Xia, C. H. et al. Linked dimensions of psychopathology and connectivity in functional brain networks. *Nat. Commun.* **9**, 3003 (2018).
93. Blondel, V. D., Guillaume, J.-L., Lambiotte, R. & Lefebvre, E. Fast unfolding of communities in large networks. *J. Stat. Mech. Theory Exp.* **2008**, P10008 (2008).
94. Van der Waerden, B. Oder tests for two-sample problem and their power. *Proc. K. Nederlandse Akademie van Wetenschappen. Ser. A* **55**, 453–458 (1952).
95. Himberg, J., Hyvarinen, A. & Esposito, F. Validating the independent components of neuroimaging time series via clustering and visualization. *NeuroImage* **22**, 1214–1222 (2004).
96. Hyvarinen, A. Fast and robust fixed-point algorithms for independent component analysis. *IEEE Trans. Neural Netw.* **10**, 626–634 (1999).
97. Kuhn, H. W. The Hungarian method for the assignment problem. *Nav. Res. Logist. Q* **2**, 83–97 (1955).
98. Freedman, D. & Lane, D. A nonstochastic interpretation of reported significance levels. *J. Bus. Economic Stat.* **1**, 292–298 (1983).
99. Phillips, J. W. et al. A repeated molecular architecture across thalamic pathways. *Nat. Neurosci.* **22**, 1925–1935 (2019).
100. Hwang, K., Bertolero, M. A., Liu, W. B. & D'Esposito, M. The human thalamus is an integrative hub for functional brain networks. *J. Neurosci.* **37**, 5594–5607 (2017).
101. Shine, J. M. et al. The low-dimensional neural architecture of cognitive complexity is related to activity in medial thalamic nuclei. *Neuron* **104**, 849–855.e3 (2019).
102. Mink, J. W. The basal ganglia: focused selection and inhibition of competing motor programs. *Prog. Neurobiol.* **50**, 381–425 (1996).
103. Janak, P. H. & Tye, K. M. From circuits to behaviour in the amygdala. *Nature* **517**, 284–292 (2015).

Acknowledgements

We thank M. Glasser (Washington University) for provision of the Wishart filter code. We thank L. Cocchi (QIMR Berghofer Medical Research Institute) for provision of the additional validation dataset. All other data were provided by the HCP, the WU–Minn Consortium (1U54MH091657; Principal Investigators: D. Van Essen and K. Ugurbil) funded by the 16 National Institutes of Health (NIH) institutes and centers that support the NIH Blueprint for Neuroscience Research, and by the McDonnell Center for Systems Neuroscience at Washington University. Y.T. was supported by a NHMRC Project Grant awarded to A.Z. (APP1142801). M.B. and A.Z. were each supported by research fellowships from the NHMRC (APP1136649 and APP1118153, respectively).

Author contributions

Y.T. and A.Z. conceived the idea and designed the study. Y.T. compiled the data, performed the analyses and prepared the visualizations. Y.T. and A.Z. drafted the manuscript. D.S.M. and M.B. provided critical conceptual input. All authors provided critical feedback and editing of the final manuscript. A.Z. supervised the research.

Competing interests

The authors declare no competing interests.

Additional information

Supplementary information is available for this paper at https://doi.org/10.1038/s41593-020-00711-6.

Correspondence and requests for materials should be addressed to Y.T. or A.Z.

Peer review information *Nature Neuroscience* thanks Janine Bijsterbosch, Rodrigo Braga and Evan Gordon for their contribution to the peer review of this work.

Reprints and permissions information is available at www.nature.com/reprints.

nature research

Corresponding author(s): Ye Tian, Andrew Zalesky

Last updated by author(s): Jul 28, 2020

Reporting Summary

Nature Research wishes to improve the reproducibility of the work that we publish. This form provides structure for consistency and transparency in reporting. For further information on Nature Research policies, see Authors & Referees and the Editorial Policy Checklist.

Statistics

For all statistical analyses, confirm that the following items are present in the figure legend, table legend, main text, or Methods section.

n/a	Confirmed	
☐	☒	The exact sample size (*n*) for each experimental group/condition, given as a discrete number and unit of measurement
☐	☒	A statement on whether measurements were taken from distinct samples or whether the same sample was measured repeatedly
☐	☒	The statistical test(s) used AND whether they are one- or two-sided *Only common tests should be described solely by name; describe more complex techniques in the Methods section.*
☐	☒	A description of all covariates tested
☐	☒	A description of any assumptions or corrections, such as tests of normality and adjustment for multiple comparisons
☐	☒	A full description of the statistical parameters including central tendency (e.g. means) or other basic estimates (e.g. regression coefficient) AND variation (e.g. standard deviation) or associated estimates of uncertainty (e.g. confidence intervals)
☐	☒	For null hypothesis testing, the test statistic (e.g. *F*, *t*, *r*) with confidence intervals, effect sizes, degrees of freedom and *P* value noted *Give P values as exact values whenever suitable.*
☒	☐	For Bayesian analysis, information on the choice of priors and Markov chain Monte Carlo settings
☒	☐	For hierarchical and complex designs, identification of the appropriate level for tests and full reporting of outcomes
☐	☒	Estimates of effect sizes (e.g. Cohen's *d*, Pearson's *r*), indicating how they were calculated

Our web collection on statistics for biologists contains articles on many of the points above.

Software and code

Policy information about availability of computer code

Data collection	Analyses were undertaken on publicly available human neuroimaging datasets acquired and maintained by the Human Connectome Project (HCP). Specifically, 3T functional MRI data was acquired using multiband echo planar imaging (EPI) on a customized Siemens 3T MR scanner (Skyra system); 7T functional MRI data was acquired on a Siemens Magnetom 7T MR scanner. See Van Essen et al (2013) for further details. Van Essen et al (2013) The WU-Minn Human Connectome Project: An Overview. NeuroImage. 80:62-79 The independent validation dataset for assessing the reproducibility of the parcellation homogeneity results was acquired using a Siemens Prisma 3T MRI scanner.
Data analysis	Computer codes (MATLAB; R2018b) to compute Laplacian eigenmaps, gradient magnitudes, diversity curves and other computational analyses undertaken as part of this study are openly available in a community repository (https://github.com/yetianmed/subcortex). All additional software packages used for this study are freely and openly available: - Diffusion Toolkit (v.0.6.4.1) and TrackVis (v.0.6.1; gradientography visualization): http://trackvis.org/ - NBS (v.1.2; connectome inference): https://www.nitrc.org/projects/nbs/ - Icasso (v.1.21; mapping of behavioral dimensions): https://research.ics.aalto.fi/ica/icasso/ - NeuroMArVL (connectome visualization): https://immersive.erc.monash.edu/neuromarvl/ - PALM (v.alpha116; permutation sequences constrained by family structure): https://fsl.fmrib.ox.ac.uk/fsl/fslwiki/PALM/ExchangeabilityBlocks -fMRIPrep (v.1.5.9; fMRI data preprocessing for the independent validation dataset): https://fmriprep.org/en/stable/index.html

For manuscripts utilizing custom algorithms or software that are central to the research but not yet described in published literature, software must be made available to editors/reviewers. We strongly encourage code deposition in a community repository (e.g. GitHub). See the Nature Research guidelines for submitting code & software for further information.

Data

Policy information about availability of data

All manuscripts must include a data availability statement. This statement should provide the following information, where applicable:

- Accession codes, unique identifiers, or web links for publicly available datasets
- A list of figures that have associated raw data
- A description of any restrictions on data availability

All primary analyses were undertaken on publicly available human neuroimaging, demographic and behavioral datasets acquired and maintained by the Human Connectome Project (HCP). These datasets are available for download to anyone agreeing to the open access data use terms (https://db.humanconnectome.org/). All datasets were acquired by the Washington University and University of Minnesota Consortium of the HCP. In the current work, minimally preprocessed resting-state and task-evoked functional MRI datasets were used from the S1200 data release of the HCP. Access to family structure data for permutation testing and several behavioral measures required acceptance of the HCP Restricted Data Use Terms (https://www.humanconnectome.org/study/hcp-young-adult/document/restricted-data-usage).
The independent resting-state functional MRI dataset comprising ten healthy adults was acquired in Australia to test the reproducibility of the parcellation homogeneity results. This dataset is currently not publicly available.
The new atlas developed in this study is openly available (https://github.com/yetianmed/subcortex) in the form of NIFTI (Neuroimaging Informatics Technology Initiative) and CIFTI (Connectivity Informatics Technology Initiative) files. Further details are provided on the GitHub repository.

Field-specific reporting

Please select the one below that is the best fit for your research. If you are not sure, read the appropriate sections before making your selection.

☒ Life sciences ☐ Behavioural & social sciences ☐ Ecological, evolutionary & environmental sciences

For a reference copy of the document with all sections, see nature.com/documents/nr-reporting-summary-flat.pdf

Life sciences study design

All studies must disclose on these points even when the disclosure is negative.

Sample size	Human neuroimaging data acquired as part of the Human Connectome Project S1200 release (n=1113, Van Essen et al 2013) were analyzed in this study. The primary dataset comprised 1080 individuals (585 females) who had completed all two runs in the first 3T resting-sate functional MRI session (REST1). The second 3T resting-state functional MRI session (REST2, n=1021, 550 females) was used for replication. Participants ranged between 22 and 37 years of age. In addition to the primary datasets, 7 Tesla resting-state functional MRI (n=183, 111 females) and 3 Tesla task-evoked functional MRI (n=725, 365 females) images were analyzed to address the study aims. No statistical methods were used to pre-determine sample sizes. All relevant and appropriate data provisioned by the Human Connectome Project were included to maximize sample sizes. An independent resting-state functional MRI dataset comprising 10 healthy adults (mean age 26±2.1yrs, 6 males) was used to test the reproducibility of the parcellation homogeneity results. The independent validation dataset was used to provide an additional validation for the parcellation homogeneity results and was sufficient to replicate these results.
Data exclusions	Each resting-sate functional MRI session (REST1 and REST2) comprising two runs. Participants that had completed at least two runs in each dataset were included. As a consequence, a total of 33 of the original 1113 participants (2.9%) were excluded from REST1, and 92 (8.2%) individuals were excluded from REST2 due to absence of one of the two resting-state functional MRI runs in each session, respectively. For behavioral analyses, an additional 155 participants (13.9%) with missing behavioral responses for any one of the 109 behavioral items were excluded. This yielded a final sample size comprising 958 individuals (505 females) for the analyses relating subcortical functional networks to behavioral dimensions. All exclusions were performed before undertaking any analyses and inference.
Replication	Reproducibility of the current work was established by analyzing: i) two fMRI data sessions; ii) two different magnetic field strengths (3T and 7T); iii) two image modalities (task and rest); and, iv) an independent validation dataset (parcellation homogeneity). Specifically, the 1113 individuals comprising the primary dataset participated in two separate resting-state functional MRI sessions (REST1 and REST2). The relation between subcortical connectivity and behavior was identified in REST2 and subsequently reproduced in REST1. This established reproducibility in the context of MRI inter-session variability. The relation between subcortical connectivity and behavior was reproduced for each of the four atlas scales (Scale I-IV). The new atlas was delineated using 3 Tesla and 7 Tesla resting-state functional MRI. While 7 Tesla unveiled finer subdivisions of hippocampus and amygdala, compared to 3 Tesla, the atlas showed significant spatial concordance between the two field strengths (normalized mutual information > 0.8). The parcellation homogeneity was estimated using the second 3T MRI session (REST2), whereas the first session (REST1) was used for atlas delineation. Moreover, the parcellation homogeneity results were replicated in an independent validation dataset comprising ten healthy adults.
Randomization	Participants were not allocated to experimental groups. Randomization was therefore not applicable. Further details pertaining to experimental design are described by Van Essen et al (2013). For permutation testing, permutation sequences were constrained to control for family structure. For behavioral analyses, covariates that were controlled as part of the general linear model included head motion parameters and subcortical volumes. Age and sex were regressed from all behavioral items before performing ICA.
Blinding	Participants were not allocated to experimental groups during recruitment, data processsing and/or statistical analyses. Blinding was therefore not applicable.

Reporting for specific materials, systems and methods

We require information from authors about some types of materials, experimental systems and methods used in many studies. Here, indicate whether each material, system or method listed is relevant to your study. If you are not sure if a list item applies to your research, read the appropriate section before selecting a response.

Materials & experimental systems

n/a	Involved in the study
☒	☐ Antibodies
☒	☐ Eukaryotic cell lines
☒	☐ Palaeontology
☒	☐ Animals and other organisms
☐	☒ Human research participants
☒	☐ Clinical data

Methods

n/a	Involved in the study
☒	☐ ChIP-seq
☒	☐ Flow cytometry
☐	☒ MRI-based neuroimaging

Human research participants

Policy information about studies involving human research participants

Population characteristics	The primary dataset comprised 1080 healthy young adults ranging between 22 and 37 years of age (585 females). The Human Connectome Project aimed to recruit a cohort that was generally representative of the population at large, thereby capturing a wide range of variability in healthy individuals with respect to behavioral, ethnic, and socioeconomic diversity (Van Essen et al 2013). See Van Essen et al (2013) for further details. Van Essen et al (2013) The WU-Minn Human Connectome Project: An Overview. NeuroImage. 80:62-79 The independent validation dataset was acquired in Australia and comprised 10 healthy adults (mean age 26±2.1yrs, 6 males).
Recruitment	The Human Connectome Project made efforts to recruit participants broadly reflecting the ethnic and racial composition of the U.S. population as represented in the 2000 decennial census (Van Essen et al 2013). Exclusion criteria included severe neurodevelopmental disorders, documented neuropsychiatric disorders or neurologic disorders. Individuals with illnesses such as diabetes or high blood pressure were also excluded during recruitment. See Van Essen et al (2013) for further details. Detailed exclusion criteria: 1. Significant history of psychiatric disorder, substance abuse, neurological, or cardiovascular disease a) Participant report of diagnosis by a treating physician; or b) Hospitalization for the condition for two days or longer; or c) Pharmacologic or behavioral treatment by a cardiologist, psychiatrist, neurologist, or endocrinologist for a period of 12 months or longer, other than treatment for childhood-only ADHD. 2. Participant report of diagnosis by a treating physician; or 3. Hospitalization for the condition for two days or longer; or 4. Participant report of diagnosis by a treating physician; or 5. Hospitalization for the condition for two days or longer; or 6. Pharmacologic or behavioral treatment by a cardiologist, psychiatrist, neurologist, or endocrinologist for a period of 12 months or longer, other than treatment for childhood-only ADHD. 7. Two or more seizures after age 5 or a diagnosis of epilepsy 8. Any genetic disorder, such as cystic fibrosis or sickle cell disease 9. Multiple sclerosis, cerebral palsy, brain tumor or stroke 10. Any of the following head injuries a) Loss of consciousness for > 30 minutes; or b) Amnesia for > 24 hours; or c) Change in mental status for > 24 hours; or d) CT findings consistent with traumatic brain injury; or e) Three or more concussive (mild) incidences of head injury 11. Premature birth (for twins, before 34 weeks; for non-twin siblings, before 37 weeks. If weeks unknown, less than 5 lbs. at birth for non-twins) 12. Currently on chemotherapy or immunomodulatory agents, or history of radiation or chemotherapy that could affect the brain. 13. Thyroid hormone treatment in the past month 14. Treatment for diabetes in the past month (other than gestational or diet-controlled diabetes) 15. Use of daily prescription medications for migraines in the past month 16. A score of 25 or below on the Folstein Mini Mental State Exam on visit Day 1 17. Moderate or severe claustrophobia 18. Pregnancy 19. Unsafe metal in the body The independent validation dataset was recruited from the general community. Individuals aged between 18 and 65 years were eligible. Exclusion criteria included neurodevelopmental disorders, neurologic disorders and/or neuropsychiatric disorders.
Ethics oversight	The HCP datasets were acquired by the WU-Minn HCP consortium with local human research ethics approval and shared with

Ethics oversight	the authors in accordance with the WU-Minn HCP Consortium Open Access and Restrict Data Use Terms. Our use of HCP datasets and our recruitment of the independent dataset complied with the Australian NHMRC national framework for the conduct of human research. Informed consent was obtained from all the participants.

Note that full information on the approval of the study protocol must also be provided in the manuscript.

Magnetic resonance imaging

Experimental design

Design type	Resting-state and task block/event design function MRI. Resting state: 3 and 7 Tesla. Task: 3 Tesla.
Design specifications	The resting-state functional MRI design is described in Glasser et al (2013), while the task-evoked functional MRI design is described in Barch et al (2014). Seven distinct tasks were chosen to tap a broad range of cognitive and affective processes and activated a wide range of neural systems. The tasks considered were emotion processing, gambling, language processing, motor execution, relational matching, social inference and working memory. The number of blocks/events varied according to the specific task. Glasser et al (2013) The minimal preprocessing pipelines for the Human Connectome Project. NeuroImage. 80:105-24 Barch et al (2014) Function in the human connectome: task-fMRI and individual differences in behavior. NeuroImage. 80:169-89
Behavioral performance measures	An extensive set of task performance measures were acquired by the Human Connectome Project. Behavioral items relating to task performance in emotional processing, language processing, social recognition, motor execution, working memory, relational matching and reward/decision making processing were included in the mapping of behavioral dimensions. Further details pertaining to task-evoked functional MRI are provided in Barch et al (2014).

Acquisition

Imaging type(s)	Functional magnetic resonance imaging
Field strength	3 Tesla and 7 Tesla
Sequence & imaging parameters	HCP datasets: 3T functional MRI sequence: Gradient-echo EPI; Imaging parameters: TR=720ms, TE=33.1ms, flip angle=52 degrees, FOV=208x180mm, Matrix=104x90, Slice thickness=2.0mm, 72 slices and 2.0 mm isotropic voxels, alternated LR and RL phase encoding. 7T functional MRI sequence: Gradient-echo EPI; Imaging parameters: TR=1000ms, TE=22.2ms, flip angle=45 degrees, FOV=208x208mm, Matrix=130x130, Slice thickness=1.6mm, 85 slices and 1.6 mm isotropic voxels, alternated AP and PA phase encoding. Independent validation dataset: 3T functional MRI sequence: Gradient-echo EPI; Imaging parameters: TR=810ms, TE=30ms. flip angel=53 degrees, FOV=240x256mm, Matrix=106x106, Slice thickness=2.0mm, 72 slices and 2.0 mm isotropic voxels, PA phase encoding.
Area of acquisition	Whole brain scan

Diffusion MRI ☐ Used ☒ Not used

Preprocessing

Preprocessing software	HCP datasets: Minimally preprocessed resting-state and task fMRI data were sourced from the Human Connectome Project. Details of the minimal preprocessing pipeline can be found elsewhere (Glasser et al., 2013). The minimally preprocessed data were subjected to two additional operations. First, spatial smoothing was performed with a Gaussian smoothing kernel of 6mm FWHM (full width at half maximum) for 3T and 4mm FWHM for 7T images. Second, to further improve subcortical SNR and suppress the effects of unstructured and autocorrelated noise that share similar temporal and spatial properties, the fMRI time series were reconstructed from a principal component analysis (PCA), where the components were filtered according to an empirically-fitted Wishart distribution to dampen the effects of noise (Glasser et al., 2016). Custom code to perform these two steps are available in a community repository (https://github.com/yetianmed/subcortex). Independent validation dataset: Resting-state fMRI data were preprocessed using fMRIPrep-1.5.9 (Estenban et al., 2019). Esteban O, Markiewicz CJ, Blair RW, Moodie CA, Isik AI, Erramuzpe A, Kent JD, Goncalves M, DuPre E, Snyder M, Oya H, Ghosh SS, Wright J, Durnez J, Poldrack RA, Gorgolewski KJ. 2019. fMRIPrep: a robust preprocessing pipeline for functional MRI. Nature methods. 16:111-116.
Normalization	The functional images were spatially aligned to the MNI (Montreal Neurological Institute) standard space using the FNIRT nonlinear registration algorithm as part of the minimal preprocessing pipeline (Glasser et al., 2013).

Normalization template	MNI ICBM 152 nonlinear 6th generation
Noise and artifact removal	HCP datasets: The correction of head motion and spatially structured physiological noise were performed with ICA+FIX (Salimi-Khorshidi et al.,2014; Griffanti et al., 2014) as part of the minimal preprocessing pipeline (Glasser et al., 2013). A summary measure of head motion was included as a covariate when testing for associations between behavioral associations and connectivity. Independent validation dataset: Confounds including the 24 head motion parameters (six basic motion parameters + six temporal derivatives + 12 quadratic terms and their six temporal derivatives), mean white matter and CSF signals were computed and regressed from the preprocessed fMRI data for each individual. The residuals of this regression were then subjected to spatial smoothing with a Gaussian smoothing kernel of 6mm FWHM and Wishart filtering.
Volume censoring	Volume censoring was not performed on this data.

Statistical modeling & inference

Model type and settings	Univariate (linear regression), multivariate (principle component analysis and independent component analysis) and predictive (support vector machine learning)
Effect(s) tested	For atlas delineation, the null hypothesis was that peaks in the gradient magnitude images could be explained by geometry and/or other confounds. A dedicated geometry-preserving null model was developed to perform inference on the local maxima of the gradient magnitude images. For the behavioral analyses, the null hypothesis was that the five behavioral dimensions did not explain significant individual variation in subcortical functional connectivity. This null hypothesis was tested using linear regression analysis and the network-based statistic.

Specify type of analysis: ☐ Whole brain ☐ ROI-based ☒ Both

Anatomical location(s)	The probabilistic Harvard-Oxford Subcortical Structural Atlas (https://fsl.fmrib.ox.ac.uk/fsl/fslwiki/Atlases) was used to delineate a binary mask for each of the following subcortical regions: thalamus, caudate, putamen, nucleus accumbens, globus pallidus, hippocampus and amygdala.
Statistic type for inference (See Eklund et al. 2016)	Non-parametric permutation testing, network-based statistic (Zalesky et al., 2010)
Correction	Non-parametric permutation testing, FDR correction and Bonferroni correction.

Models & analysis

n/a	Involved in the study
☐	☒ Functional and/or effective connectivity
☐	☒ Graph analysis
☐	☒ Multivariate modeling or predictive analysis

Functional and/or effective connectivity	Pearson correlation and Fisher transformation.
Graph analysis	The Louvain community detection algorithm (Blondel et al., 2008) was used to determine the modular structure in the subcortical functional connectivity matrix.
Multivariate modeling and predictive analysis	In the analysis of mapping functional connectivity and eigenmaps, whole-brain functional connectivity was mapped for each subcortex voxel. Spatial gradients in the resulting maps were then computed to yield a continuous representation of functional connectivity variation across the subcortex. Connectopic mapping (Haak et al., 2017) was used to map spatial gradients for each individual, which involved computing a sequence of eigendecompositions to yield a Laplacian eigenmap (Belkin et al.,2003). In the analysis of personalized parcellation, a machine learning approach was used to personalize the group-consensus parcellations and distinguish individual differences in functional organization, yielding a unique parcellation for each individual. A binary support vector machine (SVM) classifier was trained to classify whether a voxel resided in the region or its uncertainty zone. One hundred individuals were randomly selected to train the SVM and the trained SVM was then applied to delineate a personalized parcellation for the remaining 921 individuals. The SVM feature space was defined over the symmetric similarity matrix, where each cell in this matrix stored the similarity in functional connectivity fingerprints between a pair of subcortex voxels. The feature vector for a particular voxel was selected as the relevant row in this matrix. The feature space was mapped separately for each individual and required computation of individual similarity matrices. A radial basis function kernel was used and the feature space was standardized. For each of the 921 individuals in the test set, the SVM was used to predict the likelihood (posterior probability) of each voxel belonging to the region under consideration, as opposed to belonging to the region's uncertainty zone.

In the analysis of relating subcortical functional network to behaviors, independent component analysis (ICA) was used to reduce the set of behavioral measures to a set of latent dimensions, with the aim of performing inference on the dimensions rather than the full set of behaviors. Before performing ICA, behavioral items with continuously distributed scores (87 of 109) were normalized with a rank-based inverse Gaussian transformation. Age and sex were then regressed from all items and ICA was performed on the residuals that resulted from this regression.

nature research

https://doi.org/10.1038/s41593-020-00711-6

Supplementary information

Topographic organization of the human subcortex unveiled with functional connectivity gradients

In the format provided by the authors and unedited

Topographic organization of the human subcortex unveiled with functional connectivity gradients

Ye Tian[1*], Daniel S. Margulies[2], Michael Breakspear[3], Andrew Zalesky[1,4*]

1. Melbourne Neuropsychiatry Centre, Department of Psychiatry, The University of Melbourne, Parkville, VIC, Australia
2. Centre National de la Recherche Scientifique (CNRS) UMR 8002, Integrative Neuroscience & Cognition Center, Université de Paris, France
3. Discipline of Psychiatry, Faculty of Health and Medicine, and School of Psychology, Faculty of Science, University of Newcastle, NSW, Australia
4. Department of Biomedical Engineering, Melbourne School of Engineering, The University of Melbourne, Parkville, VIC, Australia

[*]Correspondence: Dr Ye Tian ye.tian2@unimelb.edu.au

Dr Andrew Zalesky azalesky@unimelb.edu.au

Supplementary Information

Table of Contents

Supplementary Figures

Figure 1. Mapping of Gradient II and III.

Figure 2. Variance explained by successive gradients.

Figure 3. Impact of left-right symmetrization on gradient magnitude images.

Figure 4. Spatial variation in primary MRI signal properties in the subcortex.

Figure 5. Testing whether gradient magnitude peaks are large enough to warrant boundary delineation.

Figure 6. Criteria used to justify boundary delineation.

Figure 7. Organization of connectivity gradients in the human subcortex.

Figure 8. Schematic of fMRI data preprocessing and boundary delineation.

Figure 9. Spatial correspondence between the new atlas and histological parcellations of thalamus and hippocampus.

Figure 10. Projection of gradients within specific subcortical nuclei onto the cortical surface.

Figure 11. Schematic of parcellation homogeneity estimation.

Figure 12. Parcellation homogeneity of the new and existing subcortical parcellation atlases.

Figure 13. Parcellation homogeneity estimated in an independent validation dataset.

Figure 14. Quantifying the extent to which task-evoked activity is circumscribed to regions comprising the atlas for Scale I-IV.

Figure 15. 3 Tesla and 7 Tesla subcortex parcellation at Scale IV.

Figure 16. Quantitative comparison between 3 Tesla and 7 Tesla atlas across parcellation scales.

Figure 17. Schematic of methodology for parcellation personalization.

Figure 18. Within-subject variation in Dice coefficient across subcortical regions.

Figure 19. Variation in subcortical connectivity gradients between rest and task-evoked conditions.

Figure 20. Linking canonical cortical networks based on their functional connectivity with subcortical regions.

Figure 21. Behavioral dimensions.

Figure 22. Association between subcortical functional connectivity and the behavioral dimension characterizing tobacco use reproduced using functional MRI from a second session.

Figure 23. Model selection with Kolmogorov-Smirnov (KS) test.

Figure 24. Determining the optimal number of independent components.

Supplementary Tables

Table 1. Basic demographic characteristics and acquisition details.

Table 2. Nomenclature for 3T parcellation hierarchy.

Table 3. Comparison parcellation atlases of the human subcortex and specific subcortical nuclei.

Table 4. List of 109 selected behavioral items.

Table 5. NIFTI and CIFTI file names for 3T and 7T atlas.

Supplementary References

Supplementary Figures

All anatomical images and renderings are shown in Montreal Neurological Institute (MNI, 6th generation) anatomical reference space. Slice location of images is indicated in MNI coordinates (millimeters). Background images are derived from the MNI152 standard-space T1-weighted average reference image. For visualization of the 7T atlas, the reference image was resliced to the resolution of the 7T functional MRI data.

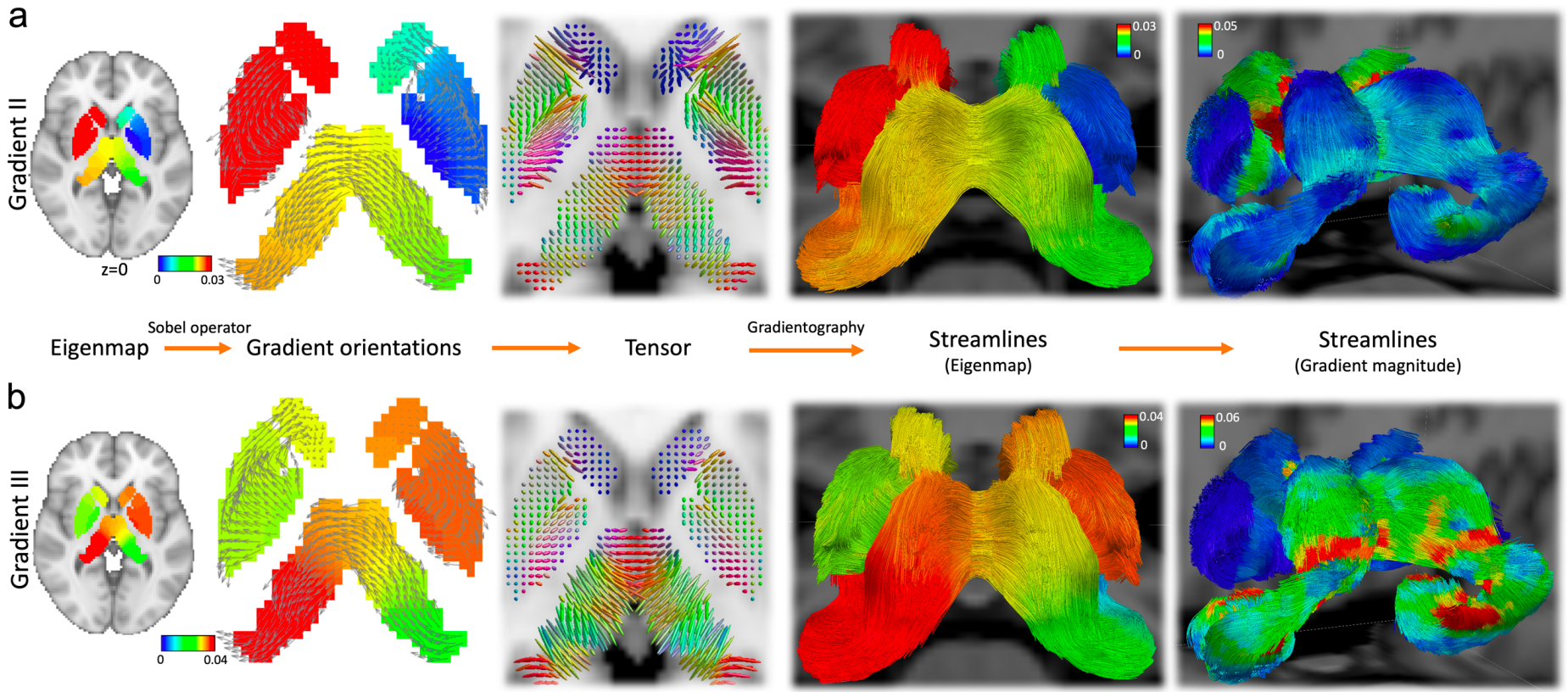


Figure 1. Mapping of Gradient II and III. Group-consensus eigenmaps, tensors and gradientography for Gradient II (**a**) and Gradient III (**b**). Gradients were mapped to subcortical voxels to enable anatomical visualization. Eigenmaps for each gradient are shown as axial slices, with a reference structural MRI image used as the background. The Sobel operator was used to estimate the local gradient direction and magnitude for each subcortical voxel. The arrows shown point in the direction of the estimated gradients. Arrow lengths are commensurate with gradient magnitude. Tensors were fitted to the gradient field. Tensors are colored according to gradient direction (blue: superior-inferior, red: left-right, green: posterior-anterior). Long cigar-shaped tensors indicate large gradient magnitudes. Streamlines were propagated through the tensor field using tools for diffusion MRI tractography. Streamlines are colored according to eigenmaps (second from right) and gradient magnitude (rightmost). Local maxima in the gradient magnitude are evident within circumscribed bands along streamlines, indicating putative functional boundaries. While Gradient I characterized an ipsilateral

organizational axis with extremes located at amygdala and globus pallidus (see Figure 1b), Gradient II and III maximally differentiated contralateral regions in dorsal (bilateral globus pallidus) and ventral (bilateral amygdala), respectively. Of note, the anterior-posterior or rostrocaudal axis explains much of the spatial variation in cortical microstructure, which is evident in a broad range of the mammalian species, including rodents, marsupials and primates[1-4]. This rostrocaudal organization also aligns with the spatial gradients in neurodevelopment[5, 6].

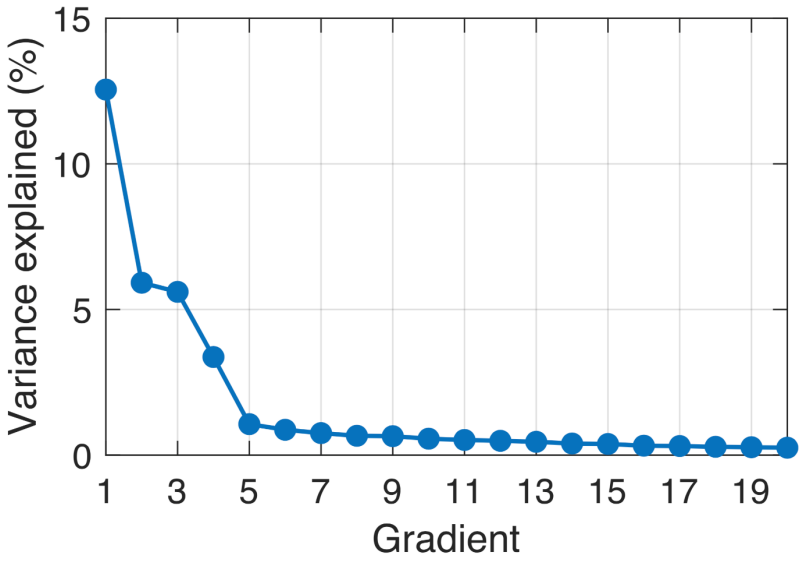


Figure 2. Variance explained by successive gradients. Variance explained in subcortical functional connectivity by successive gradients (Laplacian eigenvectors) shown as a function of gradient index, ordered from smallest to largest eigenvalue. The eigenvector associated with the second smallest eigenvalue is labelled Gradient I, while the eigenvector with the third smallest eigenvalue is labelled Gradient II, and so on. The variance explained by the first 20 eigenvectors is shown. The variance explained by Gradient IV and beyond falls below 5%, and thus only Gradients I-III are analyzed in this study.

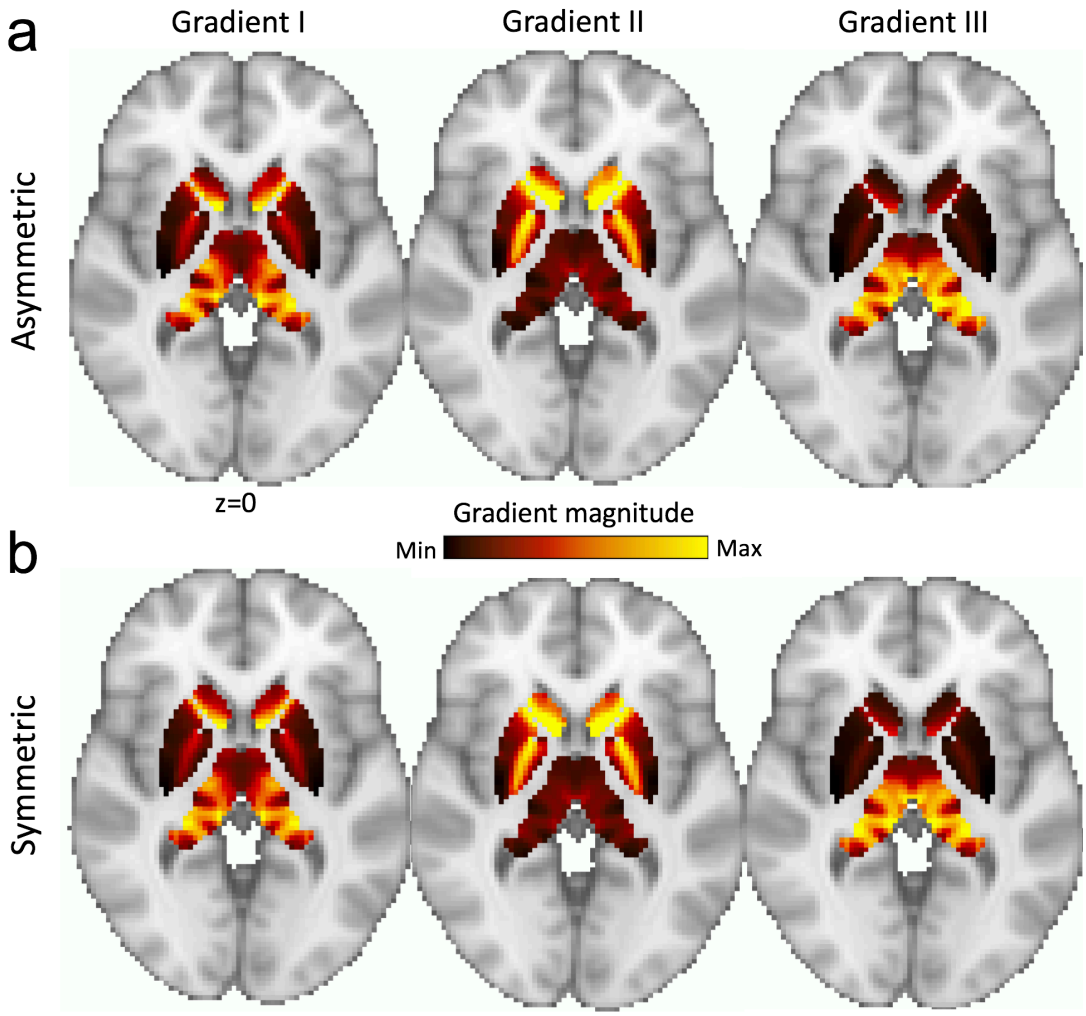


Figure 3. Impact of left-right symmetrization on gradient magnitude images. Left-right symmetrization was performed to enhance the signal-to-noise ratio. **a,** Gradient magnitude images for Gradient I-III without left-right symmetrization. Images show a large degree of left-right symmetry, even without explicit symmetrization. **b,** Left-to-right symmetrized gradient magnitude images. Images are shown as axial slices, with a reference structural MRI image used as the background. The same axial slice is used for all images.

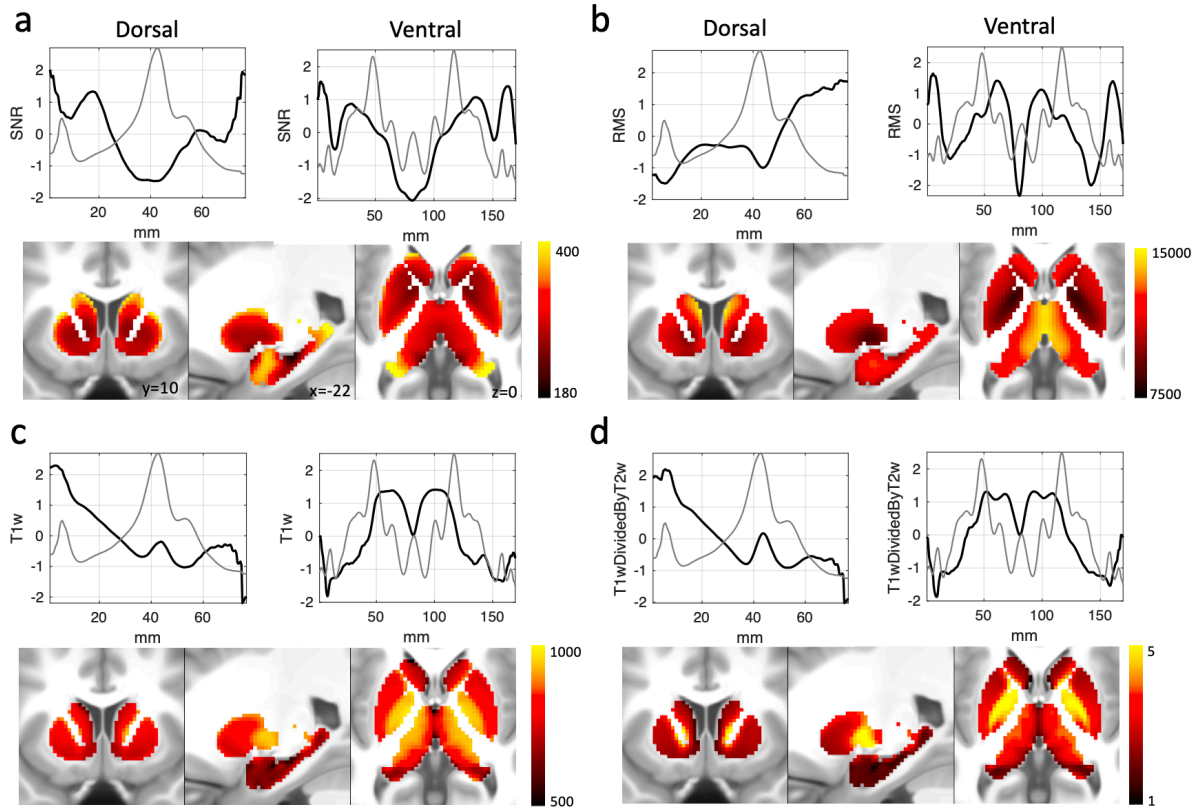


Figure 4. Spatial variation in primary MRI signal properties in the subcortex. a, Signal-to-noise ratio (SNR) was computed for each subcortical voxel by averaging the signal intensity across all time frames in each run of the preprocessed fMRI data and normalizing by the standard deviation over time[7]. SNR was averaged across runs for each individual and then averaged across individuals (REST1, n=1080) to yield a group-consensus subcortical SNR map. **b,** Blood-oxygenation level dependent (BOLD) signal magnitude was computed for each subcortical voxel by calculating the root mean squared (RMS) of the signal intensity over time. RMS was then averaged across individuals, yielding a group-consensus subcortical BOLD signal magnitude map. **c,** Group-averaged (S1200) T1-weighted contrast in the subcortex resliced to 2mm isotropic voxel resolution. **d,** Group-averaged (S1200) T1/T2-weighted contrast resliced to 2mm isotropic voxel resolution. The spatial correlation between each of the four group-consensus signal maps and the connectivity gradient magnitude map (Figure 6a) was quantified by the Spearman correlation coefficient (SNR: r=-0.21; RMS: r=0.42; T1-weighted: r=0.02; T1/T2-weighted: r=0.02).The four group-consensus signal maps were then projected onto the previously mapped streamlines (Figure 2), yielding dorsal and ventral diversity curves (black) for each of the four signal maps. The diversity curves for each of these four measures do not recapitulate peaks in the gradient magnitude images (light gray), suggesting that spatial variation in structural factors and SNR does not appear to confound the computation of functional connectivity gradients.

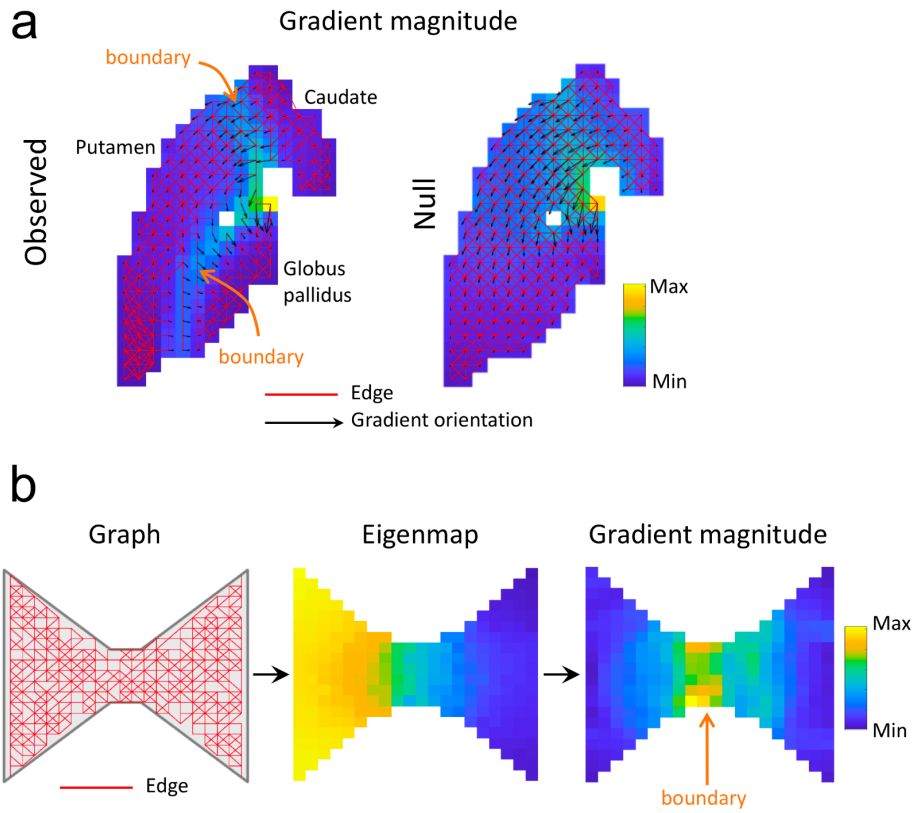


Figure 5. Testing whether gradient magnitude peaks are large enough to warrant boundary delineation. Null data was generated to test the null hypothesis that a gradient magnitude peak was due to chance, the geometry of the subcortex and/or other confounds. The alternative hypothesis was that the peak demarcated a discrete boundary in functional connectivity topography. **a,** Graph defined by the sparse adjacency matrix W computed from empirical fMRI data (observed data) is compared to one rewired graph generated from the null data ($\overline{W}_1$). Nodes in the graph correspond to subcortical voxels. Edges (solid red lines) are drawn between voxels that share similar functional connectivity profiles. Axial slices from the gradient magnitude images are shown in the background of each graph. It should be noted that very few edges in the graph for W (observed data) traverse the functional boundary between globus pallidus and putamen (indicated by orange arrows), whereas the graph for $\overline{W}_1$ (null data) comprises a number of rewired edges that cross this boundary. Therefore, unlike the observed data, a peak in the gradient magnitude image between the globus pallidus and putamen is absent in the null data, suggesting that the null hypothesis can be rejected for this particular boundary. Indeed, this was confirmed by generating 100 rewired graphs ($\overline{W}_1$, $\overline{W}_2$,…, $\overline{W}_{100}$) and showing that the proportion of rewired graphs with peaks at this location that exceeded the peak in W did not exceed 5%. **b,** Hypothetical example demonstrating how the effect of geometry alone can intrinsically lead to delineation of spurious boundaries. Edges (solid red lines) were randomly placed between pairs of neighboring pixels residing within a hypothetical bow-tie shaped object (left). Random placement of edges between neighboring pixels is consistent with the null hypothesis of a uniform spatial gradient (i.e. rate of change in gradient is homogenous across the extent of the bow tie). The Laplacian eigenmap (center) and the eigenmap's gradient magnitude (right) is shown for the graph (left). Note the peak in the gradient magnitude image that is located at the knot of the bow tie (indicated by the orange arrow), providing evidence for a putative boundary, despite the null hypothesis being true by design. The

gradient magnitude peak is exclusively due to the geometric constriction owing to the knot. Edges are more likely to be placed within the ends of the bow tie, rather than within the knot, because the ends occupy a comparably larger area. This hypothetical example demonstrates the importance of accounting for geometry when generating null data to test whether gradient magnitude peaks are sufficiently large to warrant boundary delineation. Without accounting for the effect of geometry, specious boundaries could potentially be delineated due to the convoluted geometry of the subcortex.

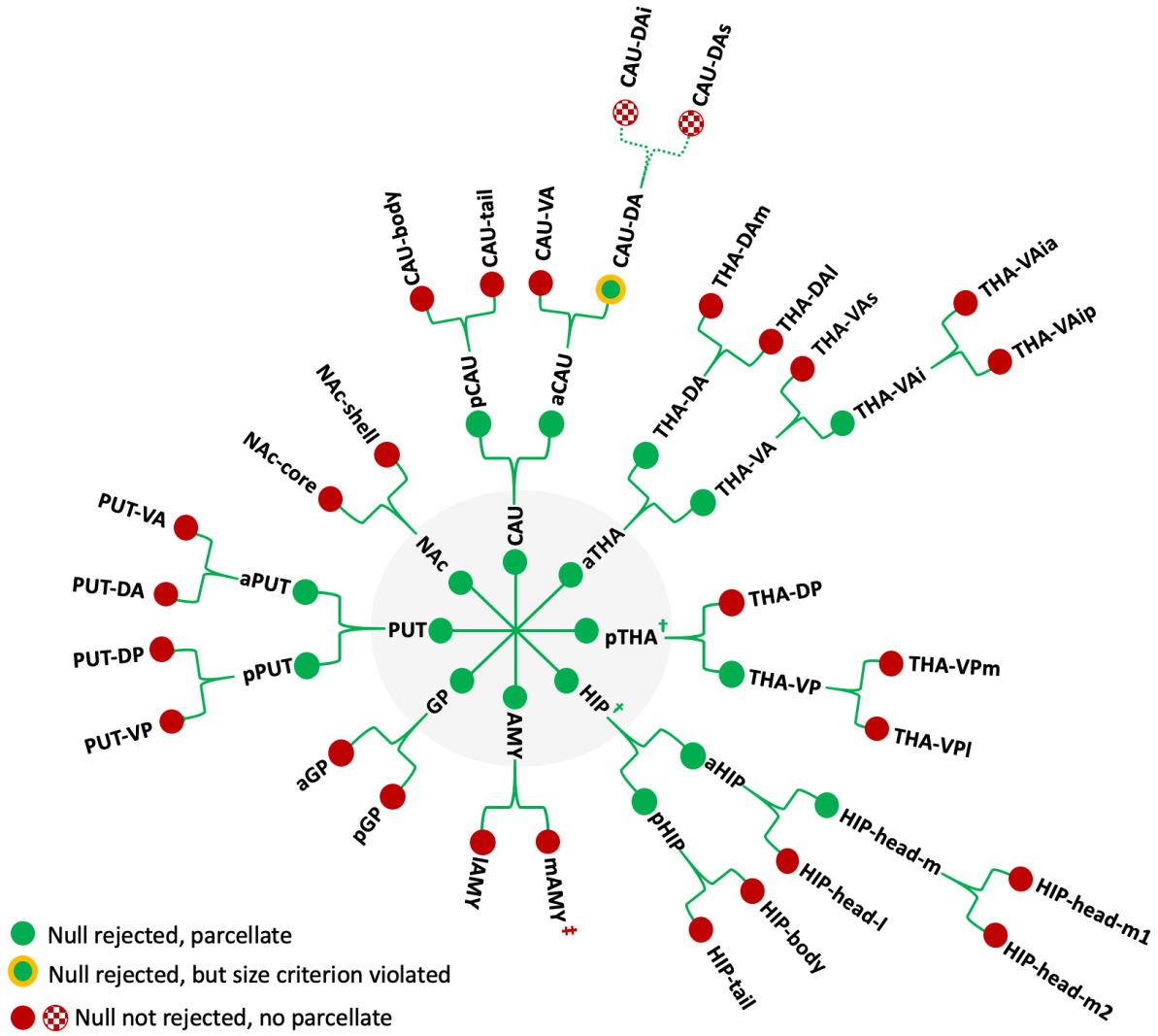


Figure 6. Criteria used to justify boundary delineation. Model selection and null hypothesis testing was used to determine whether gradient magnitude peaks were sufficiently large to warrant boundary delineation. This process was repeated recursively for each new region delineated, unveiling a multiscale parcellation architecture. The parcellation hierarchy is visualized in the form of a circular tree. The central node represents the entire subcortex and other nodes represent distinct regions. Regions are arranged within four concentric circles, where the innermost circle (gray) is the first level (Scale I). Nodes are colored according to criterion used to justify further boundary delineation within the region or to terminate the branch of the hierarchy. For the vast majority of regions, null hypothesis testing determined whether or not a boundary was delineated. However, additional criteria were used for three regions (see Methods). Green: null rejected, parcellate; green with yellow circle: null rejected, but size criterion violated and resulting parcels considered too small to delineate (size criterion); red: null not rejected, no parcellate. †: prior knowledge criterion; ‡: inter-hemispheric homologue criterion. If the size criterion were to be relaxed, the dorsoanterior caudate (CAU-DA) would be subdivided into inferior and superior component.

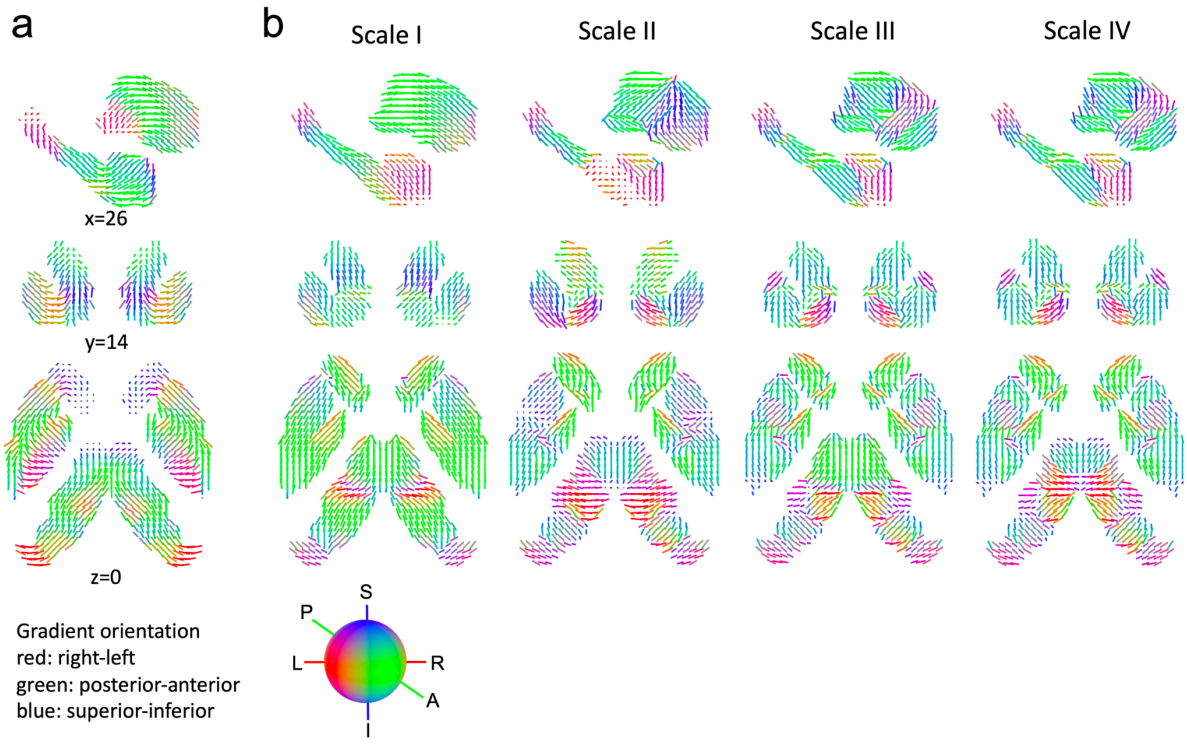


Figure 7. Organization of connectivity gradients in the human subcortex. a, The quiver lines represent gradient directions for each voxel. Each quiver is colored according to gradient direction (red: left-right, green: posterior-anterior, blue: superior-inferior) and scaled to unit length. **b,** Gradients are hierarchically organized along the parcellation hierarchy. Local gradient direction in each subcortical voxel was estimated within each region at each atlas scale (Scale I–IV).

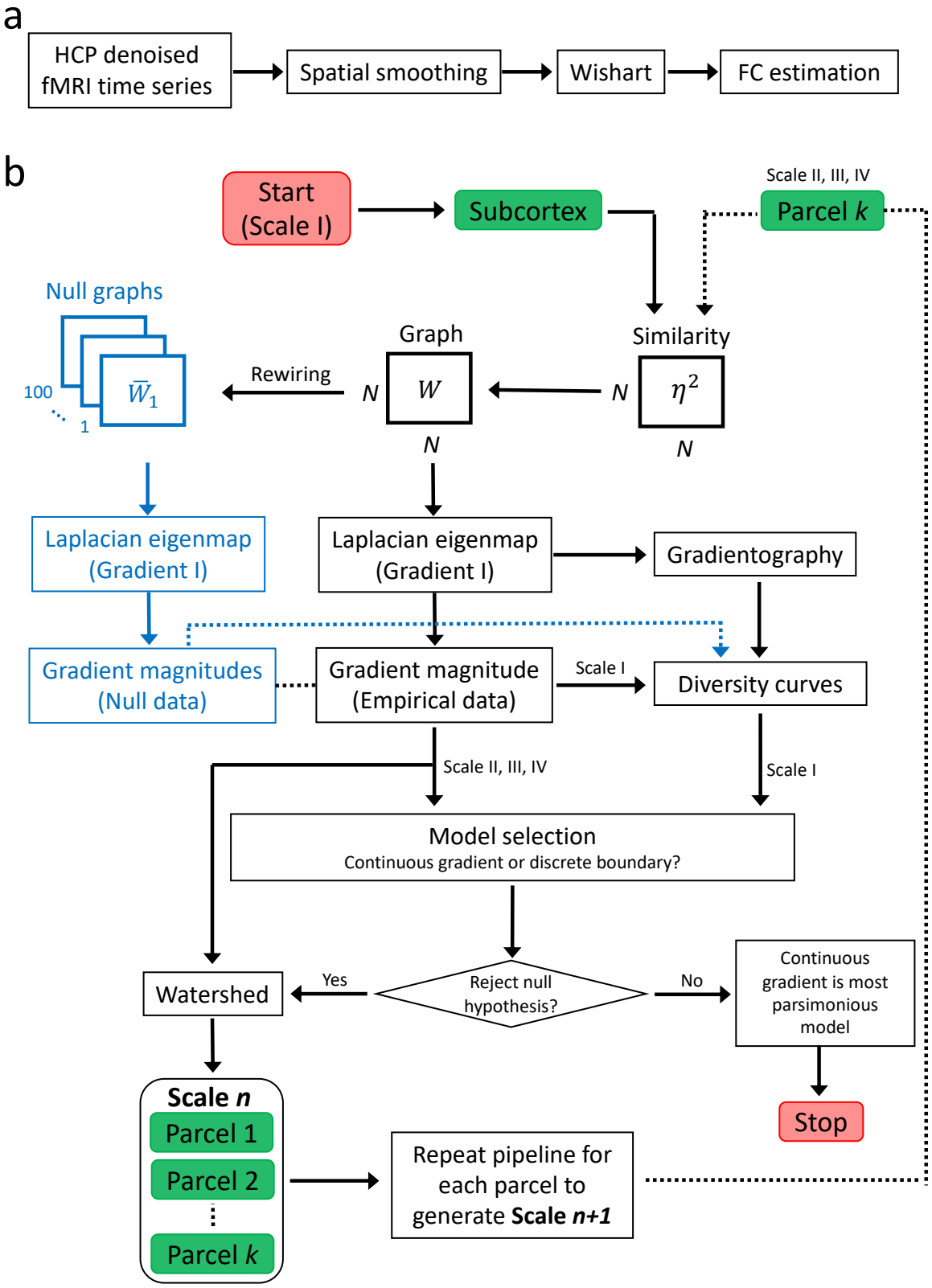


Figure 8. Schematic of fMRI data preprocessing and boundary delineation. a, The minimally preprocessed and denoised (ICA+FIX) fMRI data were sourced from the HCP. The preprocessed data were spatially smoothed and then adjusted using a recently developed Wishart filter[8, 9] to further improve the signal-to-noise ratio. The 3T images were smoothed with a Gaussian smoothing kernel of 6mm FWHM (full width at half maximum), whereas

4mm FWHM was used for the 7T images. Using the preprocessed fMRI data, functional connectivity (FC) was then measured between each subcortical voxel and all other cortical and subcortical voxels, as shown in Figure 1a. A similarity matrix was computed for each individual to quantify the extent of similarity in the functional connectivity profiles of all pairs of subcortical voxels. **b,** Boundary delineation pipeline. The subcortex was recursively parcellated into increasingly fine functional subdivisions, until the null hypothesis of a single, continuous region with no discrete boundaries could no longer be rejected, yielding a multiscale characterization of subcortical architecture. Rejection of the null hypothesis indicated that further subdivision of a region was warranted, leading to delineation of a finer scale. Model selection refers to the decision of whether to delineate a discrete boundary or represent spatial variation in functional connectivity as a gradual continuum. The arrow connecting the end of the pipeline to the beginning indicates the recursive nature of the pipeline, where each new recursion designates a finer parcellation scale. The flowchart shows that the entire pipeline (i.e. gradient mapping, null data and model selection) is performed separately for each newly delineated region, until the null hypothesis cannot be rejected. Model selection was performed differently for Scale I compared to the finer scales. For Scale I, where multiple candidate boundaries were observed, local peaks in the gradient magnitude in the diversity curves generated from the empirical data were benchmarked against the diversity curves generated with the null model (blue blocks). Model selection was performed to test whether the peak magnitude was sufficiently large (i.e. exceeded the null distribution) to warrant boundary demarcation. Next, the watershed transform algorithm was used to segment subcortical voxels into contiguous parcels. For finer scales (Scale >1), where regions were small and usually comprised a single candidate boundary, the Kolmogorov-Smirnov (KS) test was used to assess the null hypothesis of equality in the distribution across voxels between the observed gradient magnitudes and the null gradient magnitudes. The null hypothesis was rejected if the tail of the distribution of the gradient magnitude was longer in the empirical data. Other criteria that informed the decision of boundary delineation include: i) minimum size criterion to avoid excessively small regions; ii) prior anatomical knowledge; and, iii) presence of inter-hemispheric homologues. Similarly, the watershed transform algorithm was used to generate subcortical parcels. See Figure 1 for detailed gradient mapping and gradientography pipelines.

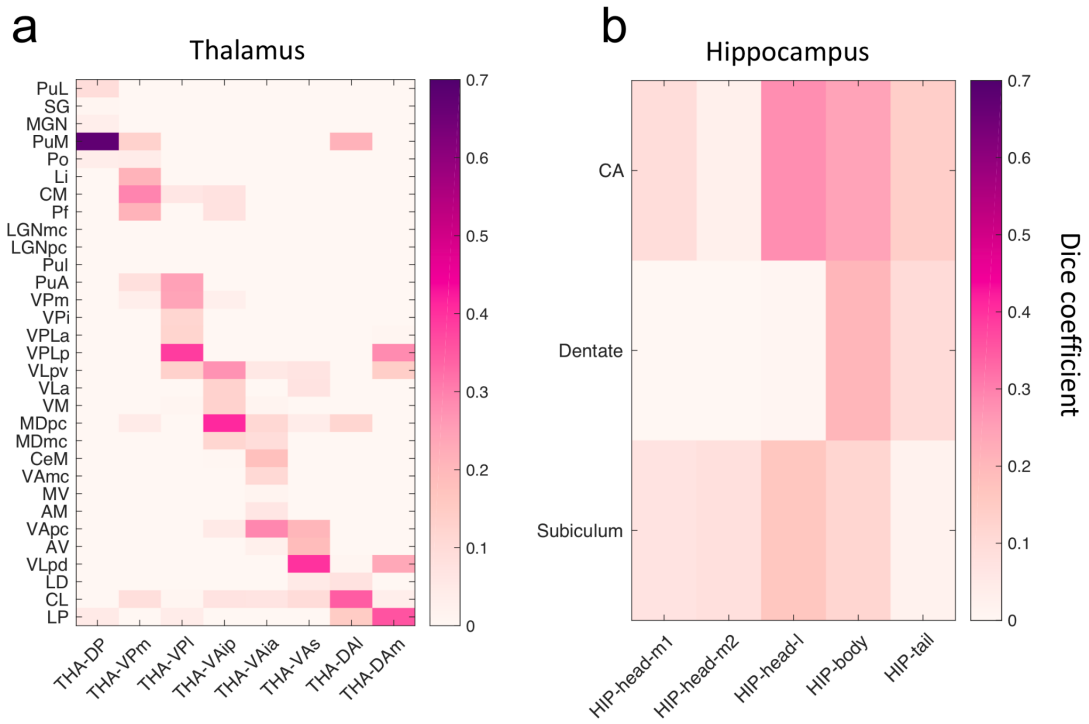


Figure 9. Spatial correspondence between the new atlas and histological parcellations of thalamus and hippocampus. a, Dice coefficient is shown between each thalamic anatomical nucleus comprising an existing histological atlas[10] (vertical axis) and each functional thalamic region delineated at Scale IV (horizontal axis). Despite the mismatch in parcellation resolution, several thalamic regions comprising the new atlas can be uniquely mapped to one, or a cluster, of histologically delineated nuclei. For example, THA-DP uniquely maps to PuM, whereas THA-VPm maps to Pf, CM and Li. The spatial correspondence is moderate to good (Dice coefficient: 0.3-0.7), although several histological nuclei cannot be uniquely assigned to a region in the new atlas (e.g. SG). Abbreviations of anatomical nuclei: PuL, inferior pulvinar; SG, suprageniculate nucleus; MGN, medial geniculate nucleus; PuM, medial pulvinar; Po, posterior pulvinar; Li, limitans nucleus; CM, centre median nucleus; Pf, parafascicular nucleus; LGNmc, lateral geniculate nucleus (manocellular part); LGNpc, lateral geniculate nucleus (parvocellular part); PuL, lateral pulvinar; PuA, anterior pulvinar; VPm, ventral posterior medial nucleus; VPi, ventral posterior inferior nucleus; VPLa, ventral posterior lateral nucleus (anterior part); VPLp, ventral posterior lateral nucleus (anterior part); VLpv, ventral lateral posterior nucleus (ventral part); VLa, ventral lateral anterior nucleus; VM, ventral medial nucleus; MDpc, mediodorsal nucleus (parvocellular part); MDmc, mediodorsal nucleus (manocellular part); CeM, central medial nucleus; VAmc, ventral anterior nucleus (magnocellular part); MV, medioventral nucleus; AM, anterior medial nucleus; VApc, ventral anterior nucleus (parvocellular part); AV, anterior ventral nucleus; VLpd, ventral lateral posterior nucleus (anterior part); LD, lateral dorsal nucleus; CL, central lateral nucleus; LP, lateral posterior nucleus. **b,** Dice coefficient is shown between each hippocampal subfield[11, 12] (vertical axis) and each functional hippocampal region delineated at Scale IV (horizontal axis). Unlike the thalamus, spatial correspondence between the histologically defined hippocampal subfields and the new atlas is relatively poor. This is because the subfields are delineated approximately parallel to the longitudinal hippocampal axis, whereas hippocampus is parcellated perpendicular to this axis in the new atlas. CA, cornu ammonis subfield. Dentate, dentate gyrus.

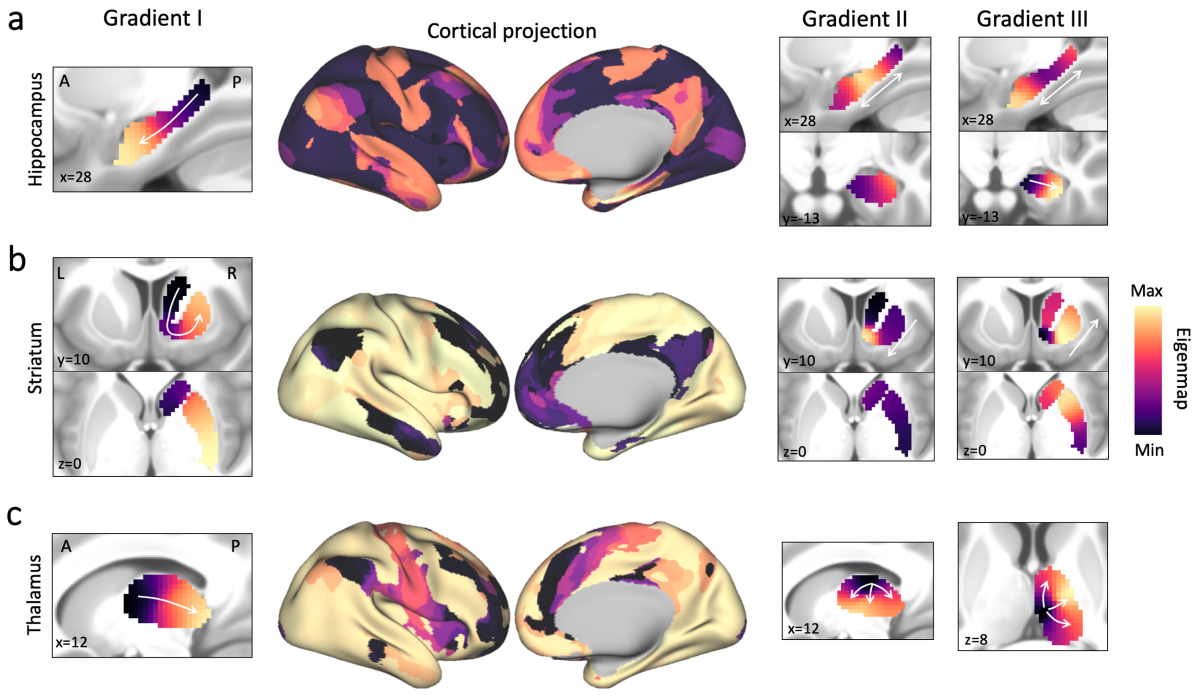


Figure 10. Projection of gradients within specific subcortical nuclei onto the cortical surface. Connectivity gradients within hippocampus (**a**) striatum (**b**), and thalamus (**c**) are shown as projections on the cortical surface for Gradient I. Eigenmaps for Gradients II and III are shown in anatomical space. **a,** Cortical surface projections show that progressively more anterior areas of hippocampus project to progressively more ventromedial parts of the frontal and cingulate cortices. **b,** The dominant striatal gradient separates putamen, NAc and caudate, with NAc and caudate differentially projecting to association networks (i.e. default mode[13] and frontoparietal network[14]) along a ventromedial-to-dorsolateral gradient, and putamen widely projects to other parts of the brain. In contrast, the second and third striatal gradients, are organized along a dorsal-to-ventral axis[15-17]. **c,** The anterior thalamus is primarily connected to dorsoanterior cingulate, dorsolateral prefrontal, medial superior frontal and anterior insular cortices, which together form the cingulo-opercular network[18, 19]. In contrast, the middle-to-posterior thalamus is widely connected to unimodal and multimodal areas, including somatosensory, motor, premotor, visual and auditory cortices, as well as orbital frontal cortex. Gradient I (eigenmap) was projected onto the cortical surface by coloring cortical vertices according to the subcortical voxel with which they were most strongly connected. White arrows indicate principal gradient directions. Functional connectivity between each subcortical voxel and cortical vertex was computed using the preprocessed dense connectome matrix (S1200 release) from the HCP, where the functional connectivity between all pairs of grayordinates (subcortical voxels and cortical vertices) was averaged across 812 individuals and across four runs.

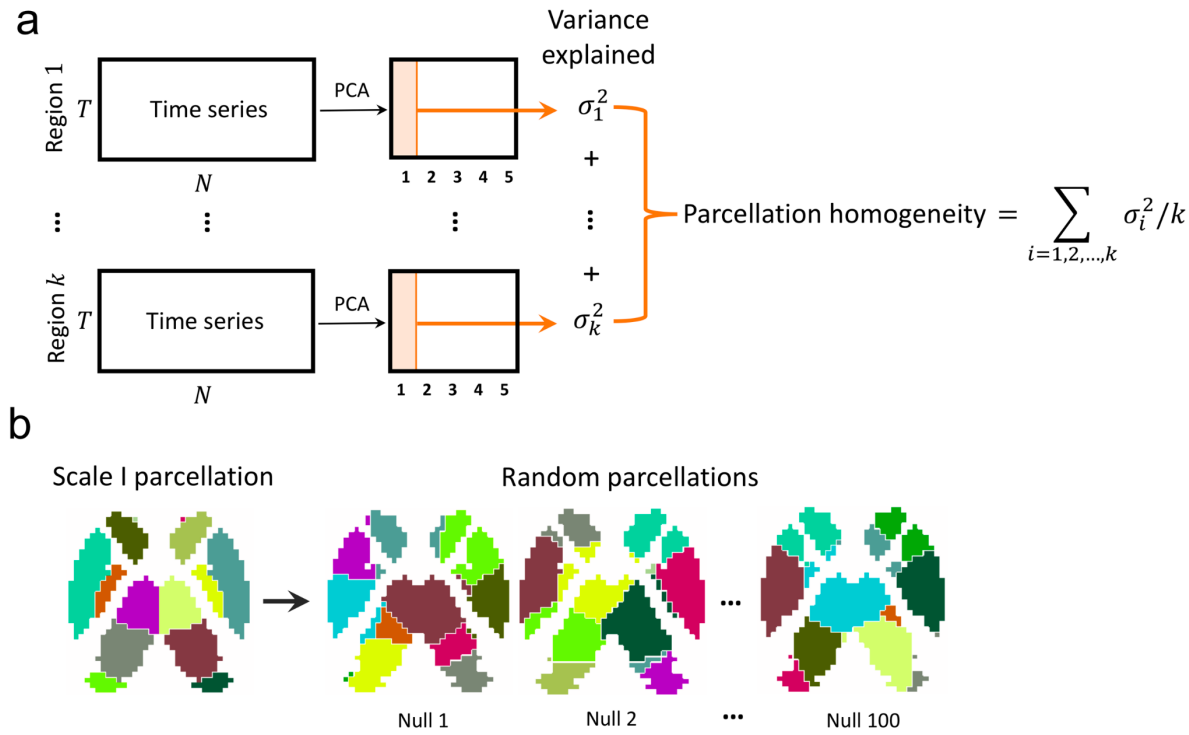


Figure 11. Schematic of parcellation homogeneity estimation. a, Schematic and formula representing the computation of parcellation homogeneity. Functional MRI time series for each voxel in a given region were concatenated, yielding a matrix of dimension $N \times T$, where N and T denote the number of voxels comprising the region and the number of time frames, respectively. Following previous work[20], principal component analysis (PCA) was applied to this matrix and the variance explained by the first principal component was estimated and referred to as regional homogeneity. The regional homogeneity was computed for each region and for each individual separately. For each individual, regional homogeneity was then averaged across all regions, yielding an overall estimate of parcellation homogeneity. **b,** Images show anatomical visualizations of the Scale I atlas (leftmost) and three instantiations of randomized versions of the atlas (right images). The random parcellations comprise an identical number of regions and comparable distribution of region sizes.

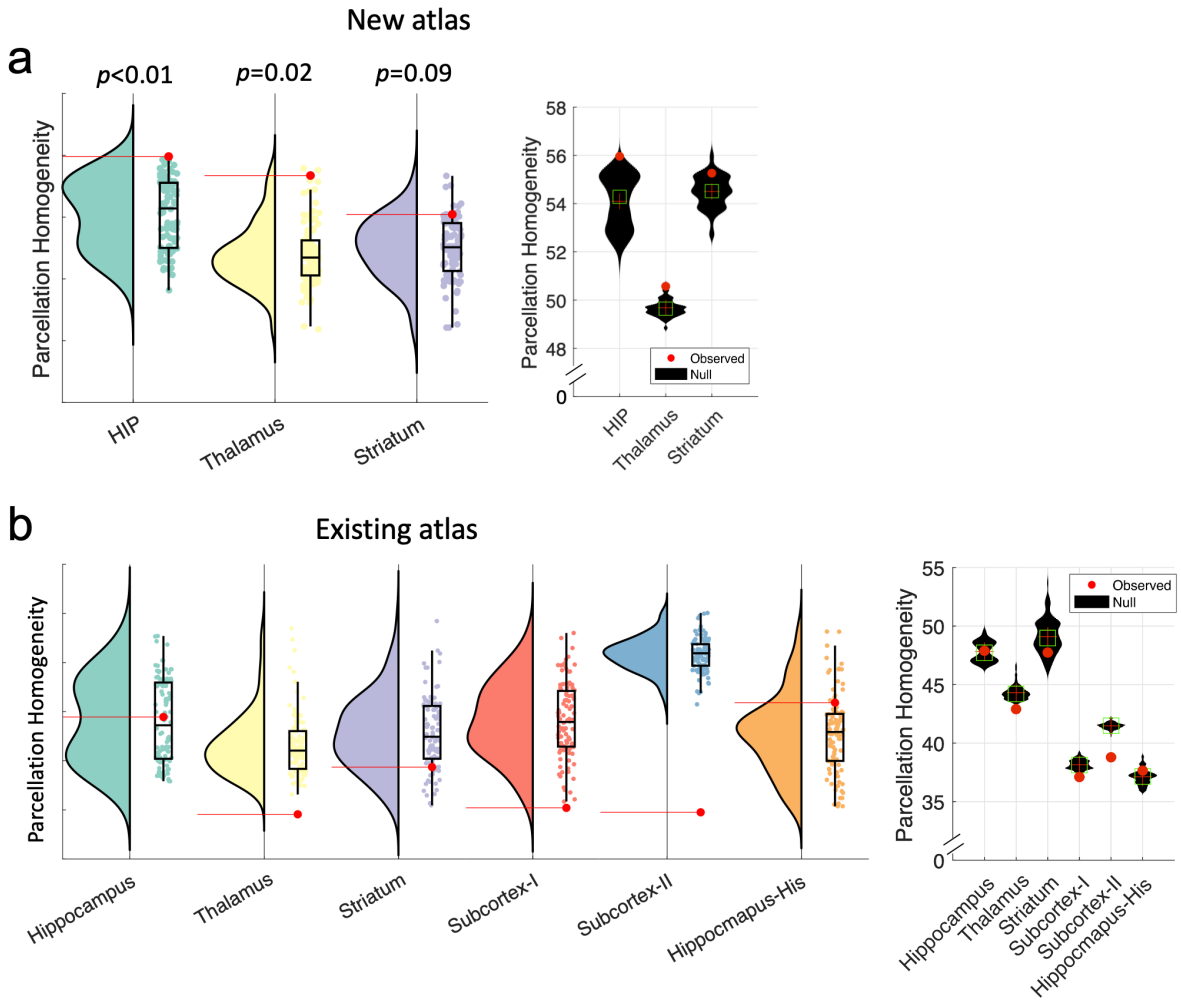


Figure 12. Parcellation homogeneity of the new and existing subcortical parcellation atlases. a, Parcellation homogeneity of the new atlas within the hippocampus (HIP), thalamus and striatum were benchmarked to random parcellations comprising an identical number of regions and a comparable distribution of region sizes. The p-value shown for each atlas is the proportion of random parcellations (n=100) comprising the ensemble with equal or greater homogeneity than the observed parcellation (one-sided). **b,** Parcellation homogeneity of five existing atlases was benchmarked to random parcellations comprising an identical number of regions and a comparable distribution of region sizes. Violin plots show the distribution of parcellation homogeneity measured within ensembles of 100 such random parcellations. Red dots and horizontal red lines indicate the observed parcellation homogeneity values. Bottom and top edges of the boxes indicate 25th and 75th percentiles of the distribution, respectively. The central mark indicates the median. The whiskers extend to the most extreme data points that are not considered outliers (1.5 × interquartile range). The vertical axis is omitted to aid visualization. See Supplementary Table 3 for details pertaining to each atlas.

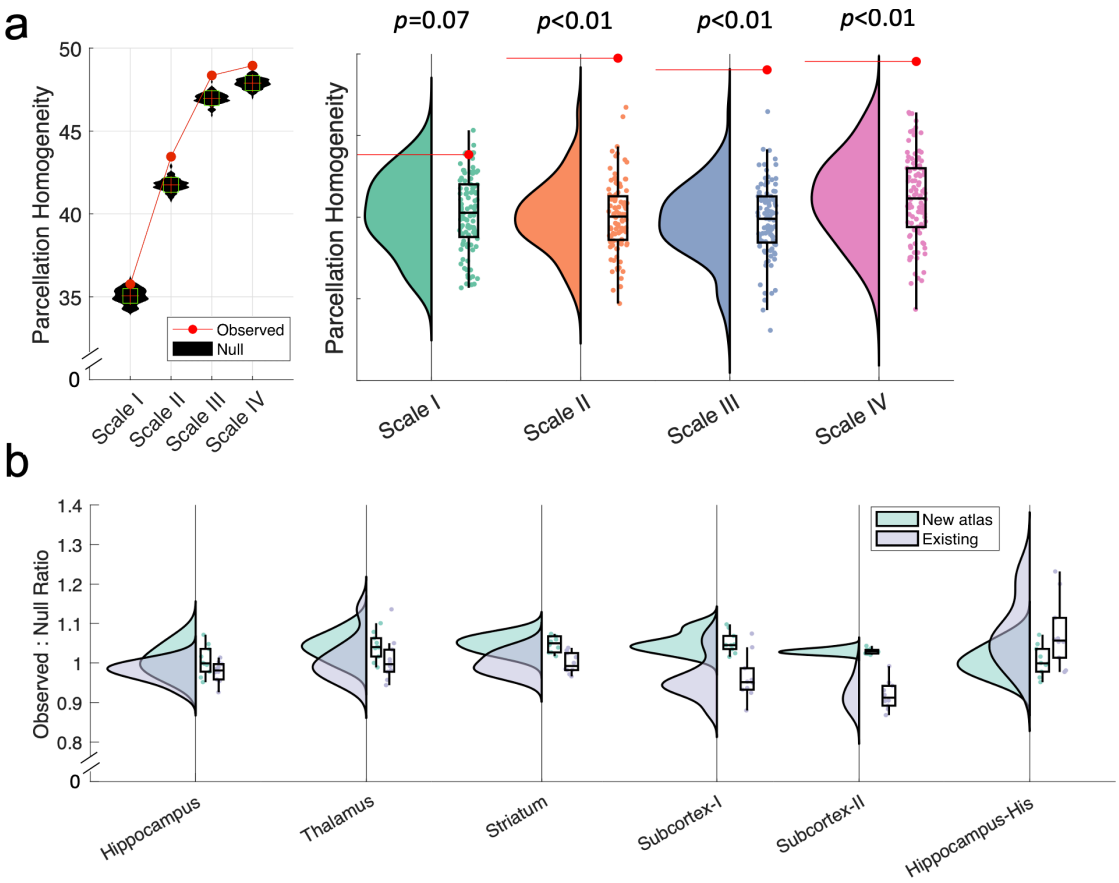


Figure 13. Parcellation homogeneity estimated in an independent validation dataset. Parcellation homogeneity was investigated in an independent dataset comprising 10 healthy individuals (Supplementary Table 1) to exclude potential circularity confounds. **a,** Parcellation homogeneity of the new subcortex atlas was estimated and benchmarked to random parcellations of the subcortex comprising an identical number of regions and a comparable distribution of region size. The same computations performed on the primary dataset were repeated on the validation dataset (see Methods and Figure 5). Violin plots show the distribution of parcellation homogeneity measured within ensemble of 100 random parcellations. One-sided p-value shown for each scale is the proportion of random parcellations comprising the ensemble that were more homogenous than the observe parcellation. Horizontal red lines indicate the observed parcellation homogeneity values. Bottom and top edges of the boxes indicate 25th and 75th percentiles of the distribution, respectively. The central mark indicates the median. Whiskers extend to the maximum and minimal data points that are not considered outliers. The vertical axis is omitted to aid visualization. The null hypothesis of parcellation homogeneity that is no better than chance could be rejected for all scales, except Scale I. **b,** Parcellation homogeneity comparison between the new atlas and existing parcellation atlases of the entire subcortex and specific subcortical nuclei (Supplementary Table 3). Parcellation homogeneity was computed separately for each individual (n=10) and normalized by the random parcellation homogeneity, yielding and observed-to-null ratio. The box plots show the distribution of this ratio across individuals for the new (turquoise) and existing (violet) parcellation atlases. Homogenous parcellations have a ratio that exceeds one. Bottom and top edges of the boxes indicate 25th and 75th percentiles of the distribution, respectively. The central mark indicates the median. The whiskers extend to the most extreme data points that are not considered outliers (1.5 × interquartile range).

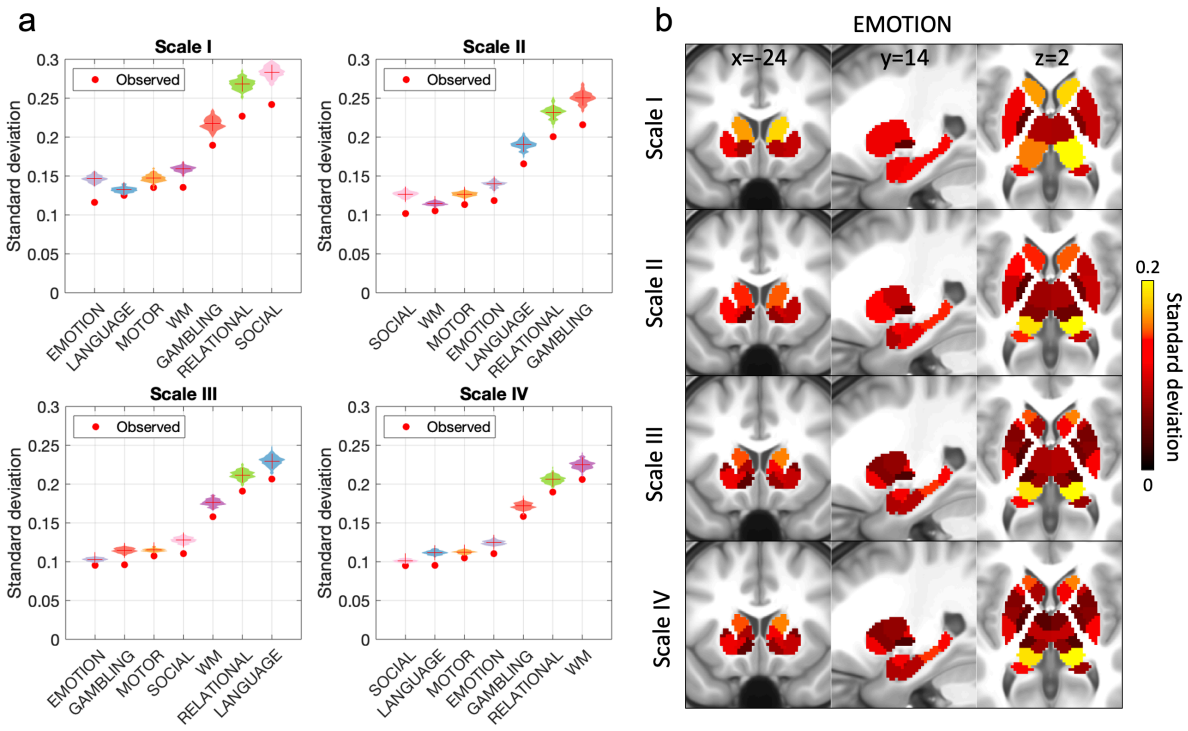


Figure 14. Quantifying the extent to which task-evoked activity is circumscribed to regions comprising the atlas for Scale I-IV. Task-evoked activity for seven distinct task conditions was computed by averaging over all blocked contrasts[21] and across 997 individuals (https://balsa.wustl.edu/), yielding a group- and contrast-averaged effect size map (Cohen's d) for each task condition. **a,** The standard deviation in task-evoked activity (i.e. effect size maps) was computed across voxels comprising each region and then averaged over all regions. This was repeated for Scale I-IV. The lower the standard deviation, the more circumscribed task-evoked activity was to particular atlas regions. The standard deviation was computed in the same way for ensembles of random subcortical parcellations (n=100). This enabled testing of the null hypothesis that the extent to which task-evoked activity was circumscribed to specific atlas regions was no greater than expected for a random parcellation. Violin plots show the distribution of standard deviation computed within ensembles of 100 random parcellations and red dots indicate the observed standard deviation values. **b,** Examples of activation homogeneity in each region at Scale I-IV in the emotional processing task.

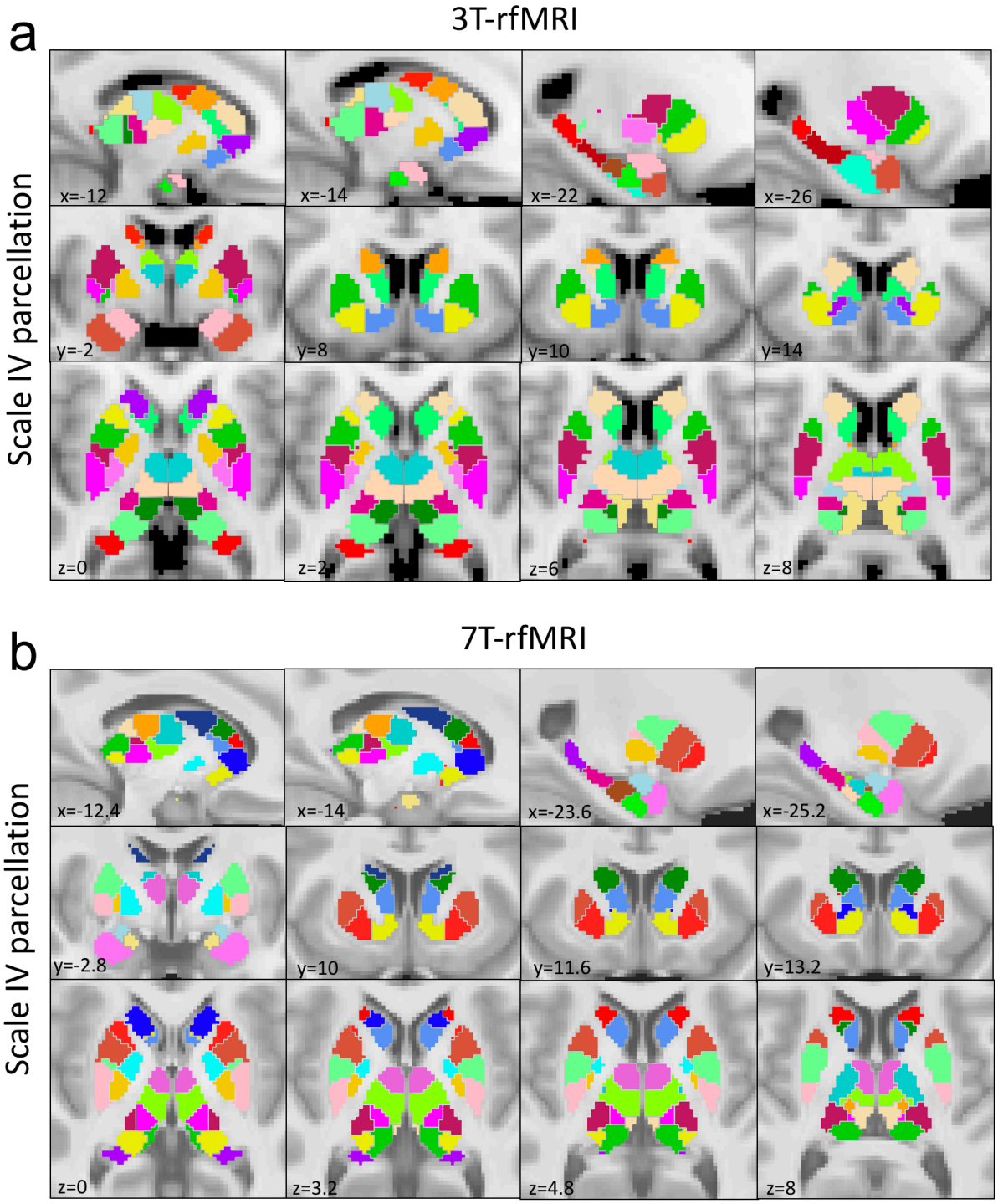


Figure 15. 3 Tesla and 7 Tesla subcortex parcellation at Scale IV. A total of four hierarchical scales were delineated using both 3T and 7T resting-state functional MRI (rfMRI) to parcellate the subcortex. Images show sagittal (x), coronal (y) and axial (z) slices from the group-consensus atlas at Scale IV delineated using 3T (**a**) and 7T (**b**) functional MRI. Scale IV at 3T comprises 27 bilateral regions, whereas Scale IV comprises 31 bilateral regions at 7T. The additional regions delineated at 7T include central and superior subregions of the medial amygdala, lateral and medial subregions of the hippocampal body, superior and inferior subregions of the lateral hippocampal head, and one more subregion in thalamus. All slice coordinates are indicated relative to MNI space (mm). A reference structural MRI image is used as the background. Homologous regions are colored identically.

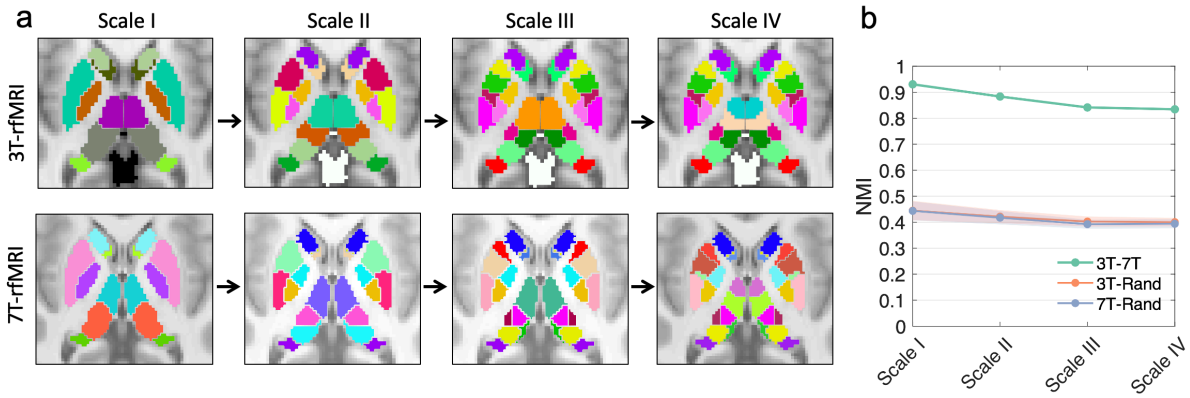


Figure 16. Quantitative comparison between 3 Tesla and 7 Tesla atlas across parcellation scales. a, Images show axial slices from the 3T and 7T group-consensus atlases across the four hierarchical parcellation scales (Scale I-IV, left to right). **b,** Spatial correspondence between the 3T and 7T atlas was estimated at each parcellation scale using normalized mutual information (NMI). NMI between 3T and 7T atlas (NMI, Scale I: 0.93; II: 0.88, III: 0.84, IV: 0.83, green) was benchmarked against ensembles of 100 random parcellations (3T-Rand, orange; 7T-Rand, blue) at each parcellation scale. Shading indicates 95% confidence intervals. NMI ranges from zero to one with higher value indicating greater spatial correspondence. The 3T atlas (2mm isotropic) was up-sampled to the same resolution as 7T (1.6mm isotropic) before computing NMI.

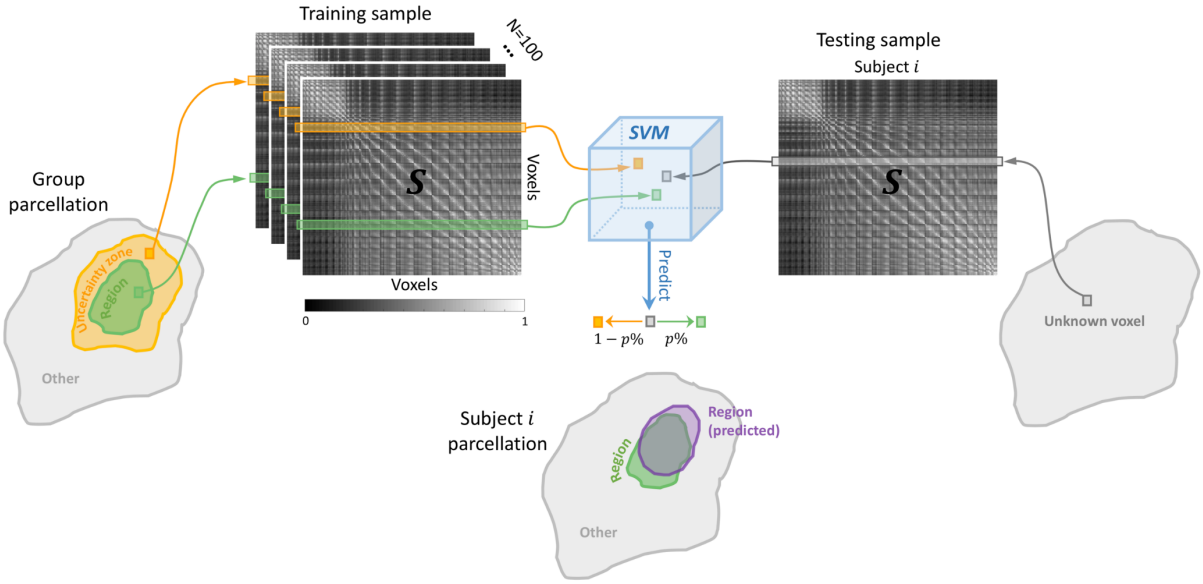


Figure 17. Schematic of methodology for parcellation personalization. A binary support vector machine (SVM) classifier (blue box) was trained to classify whether a voxel resided in the region proper (green) or its uncertainty zone (orange). The SVM feature space was defined over the similarity matrix (S), where each cell stored the similarity in functional connectivity between a pair of subcortical voxels. The feature for a particular voxel was selected as the relevant row in this matrix, highlighted by green and orange colored strips. One hundred randomly selected individuals were used to train a separate SVM classifier for each region. The uncertainty zone for each region was delineated by dilating the region's mask (see Methods). For a new individual (Subject i), the trained classifier was used to predict the posterior probability ($p\%$) of an unknown voxel (gray) belonging to the region as opposed to belonging to the region's uncertainty zone ($1 - p\%$). This was repeated for each region comprising the Scale IV atlas. The uncertainty zones of two distinct regions could potentially overlap, meaning that voxels could be assigned a probability of belonging to multiple regions. Such voxels were assigned to the region associated with the highest posterior probability, yielding a personalized parcellation atlas for Subject i (purple).

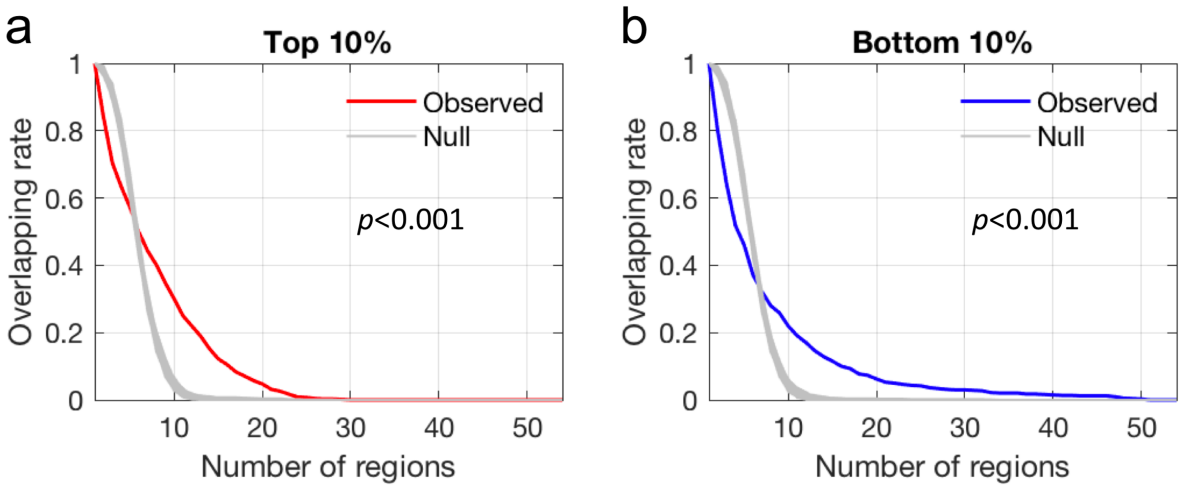


Figure 18. Within-subject variation in Dice coefficient across subcortical regions. The Dice coefficient for each Scale IV subcortical region in each individual was encoded in a Dice-matrix of dimension 921 × 54, where 921 is the total number individuals and 54 is the number of subcortical regions. Rows in this matrix were then re-ordered from the highest to lowest Dice coefficient. This re-ordering was performed separately for each column. Individuals ranked among the top 10% (high Dice) or bottom 10% (low Dice) for at least one column (region) were selected, yielding 696 and 739 unique individuals in each group, respectively. Some individuals only presented once, whereas some individuals repeatedly presented in more than one region. The proportions of individuals (overlapping rate) that repeatedly presented in at least one or more subcortical regions were computed. The curves show the overlapping rate as a functional of the number of regions in the high Dice (**a,** red curve) and low Dice (**b,** blue curve) group separately. The area under the curve of the overlapping rate was computed. Permutation testing (n=1000) was used to test whether the overlapping rate was larger than expected due to chance. Note that each row in the Dice-matrix was shuffled as a whole in each permutation to control the relationship across regions. The overlapping rate was recomputed for each permuted sample and plotted as a functional of number of regions (Null, gray curves). The one-sided p-values shown are given by the proportion of null curves that had larger area under the curve than the observed curve.

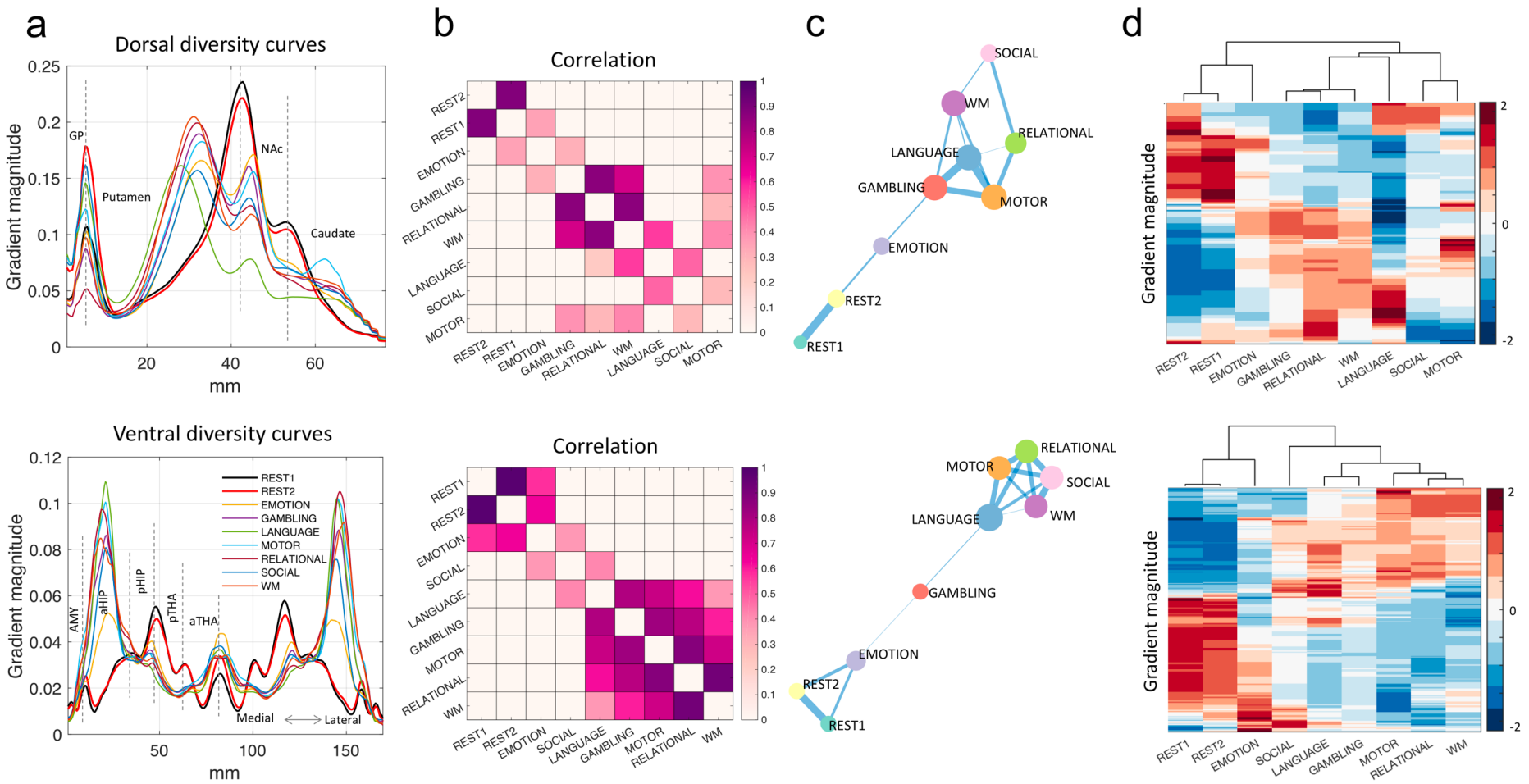


Figure 19. Variation in subcortical connectivity gradients between rest and task-evoked conditions. a, Dorsal and ventral diversity curves are shown for each rest and task condition separately. **b,** Similarity in the diversity curves between each pair of conditions was estimated using the Pearson correlation coefficient. Permutation testing (n=10,000) was used to determine the significance (p-value) of each correlation coefficient using a corrected significance threshold of $p < 0.05/36=0.0014$ (Bonferroni correction). Correlation coefficients surviving Bonferroni correction are colored in the matrix shown and also visualized as a graph. **c,** In the graph, each node represents one

of the nine conditions and the edges between them indicate correlations. Node size is scaled by nodal degree, whereas edge thickness varies according to the correlation coefficient magnitude. **d,** Matrix representation of diversity curves for rest and task conditions. Matrix rows correspond to specific points along the diversity curves. Matrix columns correspond to rest and task conditions. Rows and columns are reordered to accentuate similarity between diversity curves. Average-linkage clustering was used to determine the reordering and the cluster tree shown.

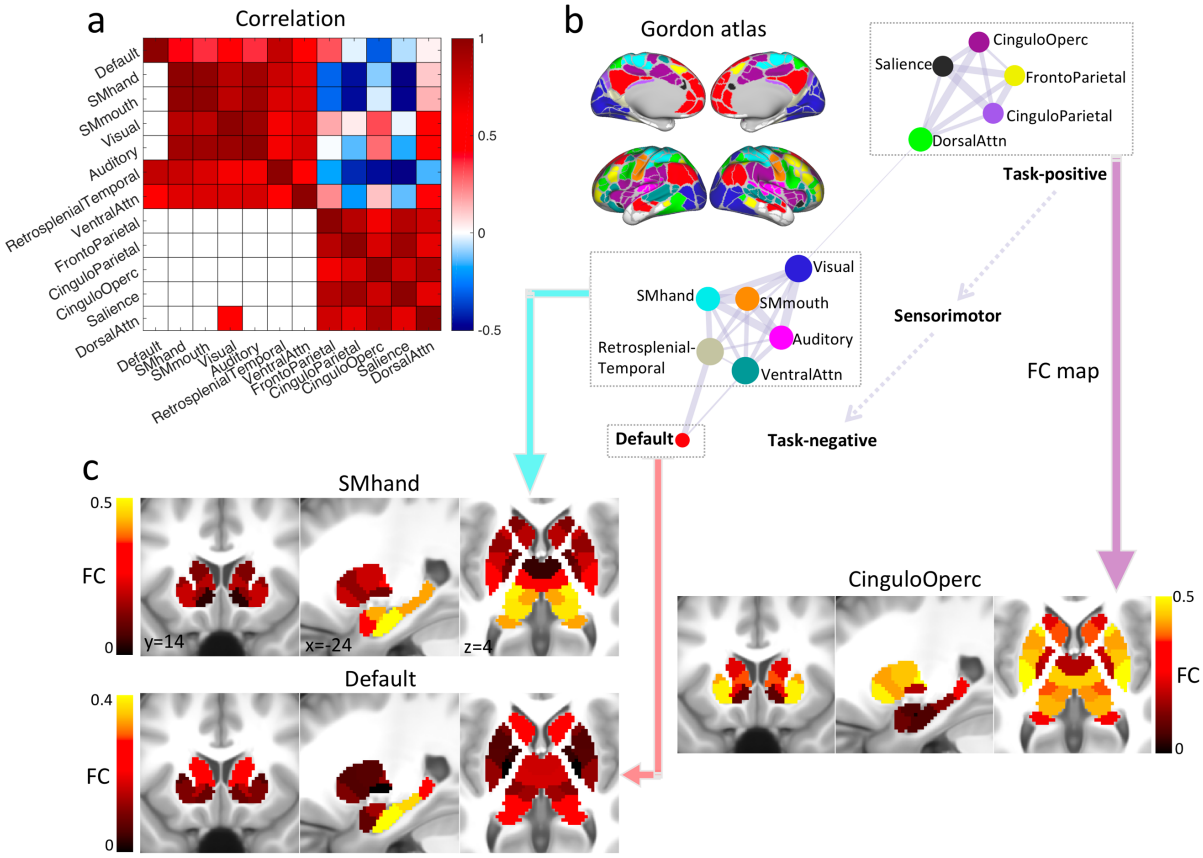


Figure 20. Linking canonical cortical networks based on their functional connectivity with subcortical regions. Functional connectivity (FC) was computed between each Scale IV subcortical region and each cortical parcel delineated in an existing cortical atlas[20], yielding a connectivity matrix of dimension 54 x 333 for each individual. The connectivity matrices were then averaged across all individuals (REST1, n=1080) to enable a group-consensus representation of cortical-subcortical connectivity. Each column in this matrix thus represents a subcortical connectivity map for a given cortical parcel. Subcortical connectivity maps were averaged across cortical parcels that belong to the same canonical network[20], yielding 12 FC maps that represent how each cortical network connects to the subcortex. The 12 networks are as follows: visual, dorsal somatomotor (SMmouth), ventral somatomotor (SMhand), auditory, default, frontoparietal, dorsal attention, ventral attention, cingulo-opercular (cinguloOperc), salience, cingulo-parietal and retrosplenial-temporal network. **a,** Similarity in subcortical FC maps between each pair of cortical networks was estimated using the Pearson correlation coefficient, yielding a 12×12 correlation matrix. The rows and columns of this matrix were reordered to accentuate modular structure, which was determined by the Louvain community detection algorithm[22]. The 12 × 12 correlation matrix was thresholded using a statistical approach based on null hypothesis testing. A p-value was computed for each correlation coefficient as follows. Permutation testing (n=1000) was used to determine the significance (p-value) of each correlation coefficient using a corrected significance threshold of $p<0.05/66=0.008$ (Bonferroni correction). Correlation coefficients that survived correction are shown in the lower triangle of the correlation matrix and visualized as a graph. **b,** In this graph, each node represents a canonical cortical network. Edges are drawn between pairs of networks that share common patterns of functional connectivity with subcortical regions. Node size is scaled by nodal degree, whereas edge thickness

varies according to the correlation coefficient. Nodes were parsed into three groups (gray blocks) and positioned on a task-positive to task-negative organizational axis. **c,** Representative subcortical FC maps for each group of canonical networks. It can be seen that the cingulo-opercular network (task-positive) is preferentially connected to thalamus and striatum, especially the dorsal striatum. In contrast, sensorimotor networks are predominantly connected to the hippocampus, amygdala and posterior thalamus. The default mode network (task-negative) is preferentially connected to the hippocampus but also show moderate connectivity with posterior thalamus and caudate.

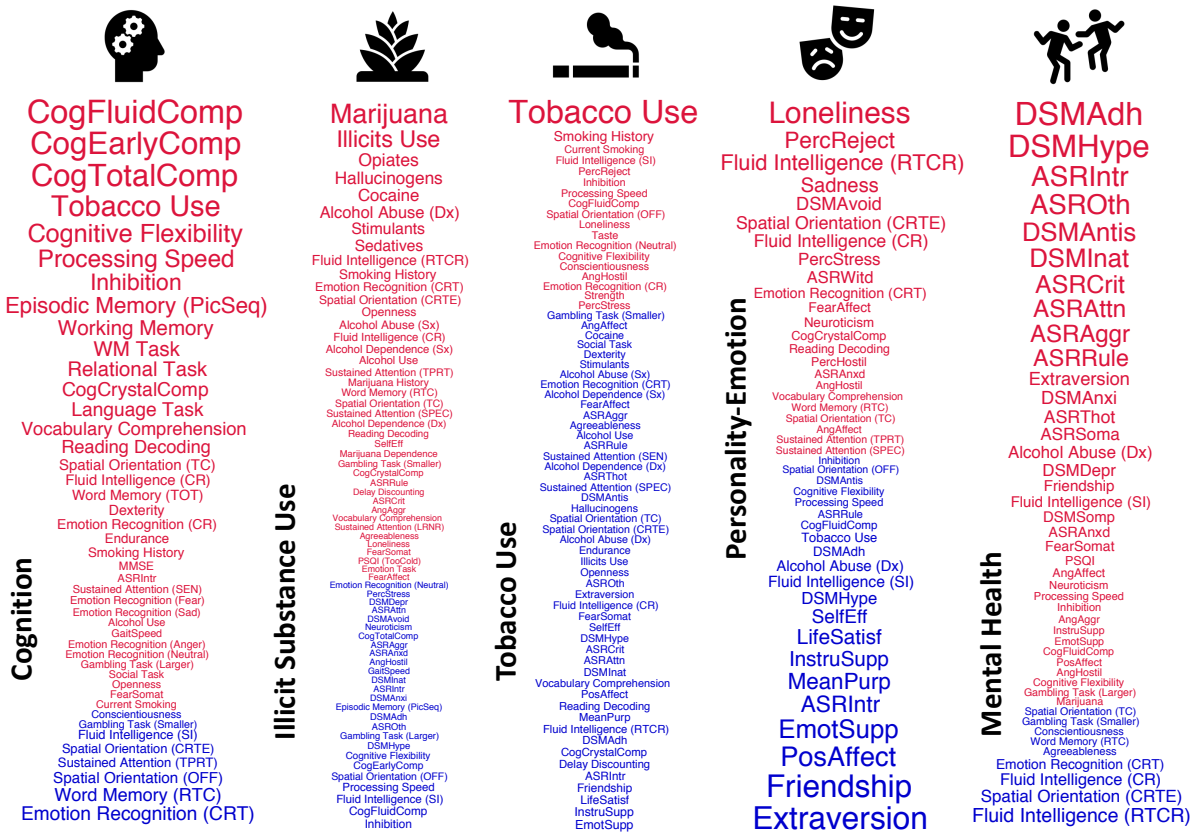


Figure 21. Behavioral dimensions. Five orthogonal behavioral dimensions characterizing: i) cognition, ii) illicit substance use, iii) tobacco use, iv) personality and emotion traits, as well as v) mental health were derived from a total of 109 behavioral items using independent component analysis (see Methods). The top weighted (30-40%) behavioral items in each dimension are visualized as word clouds. The font size of each item is scaled according to its absolute weight in the ICA de-mixing matrix, and the font color denotes weight polarity (red-positive, blue-negative).

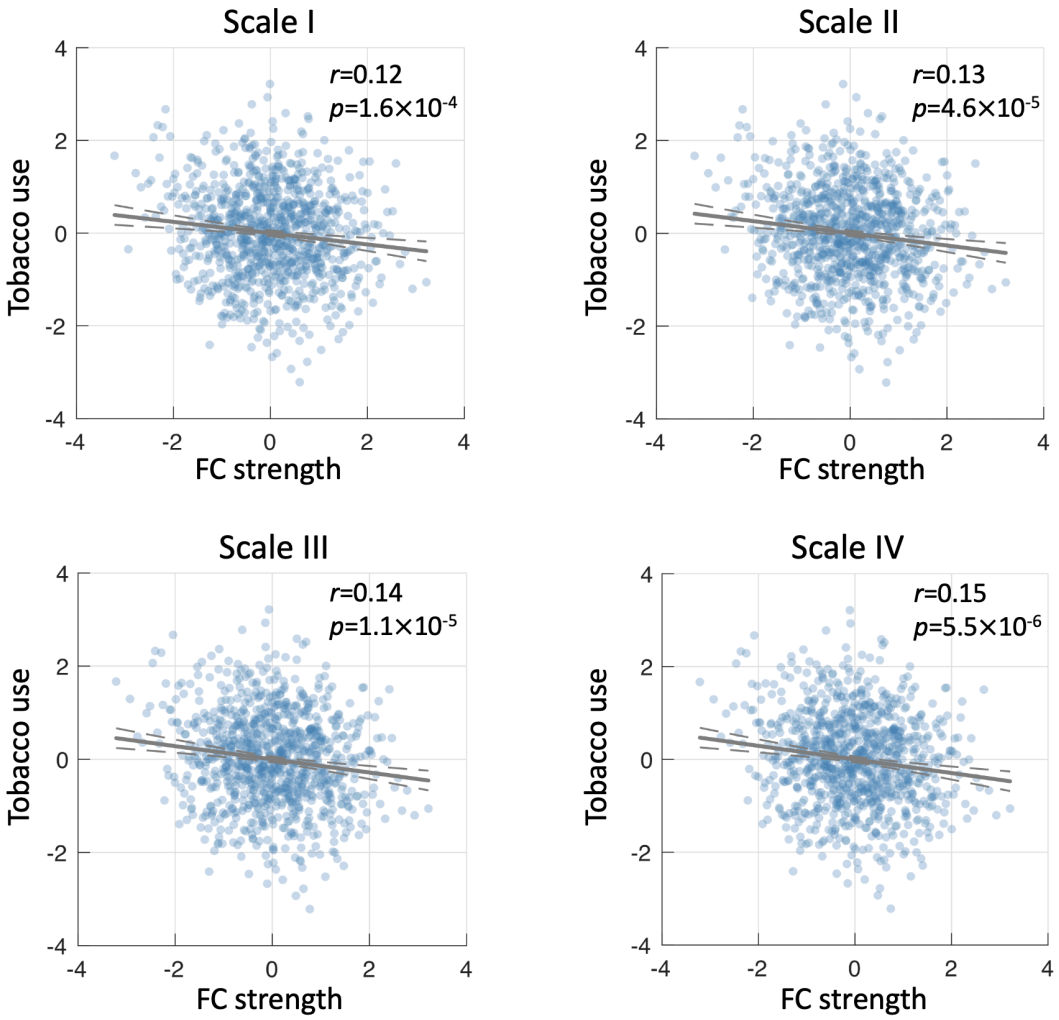


Figure 22. Association between subcortical functional connectivity and the behavioral dimension characterizing tobacco use reproduced using functional MRI from a second session. Scatter plots and lines of best fit show the association between individual variation in tobacco use dimension and functional connectivity (FC) strength within the thalamo-striato-hippocampal network measured using functional MRI acquired in the REST1 session. The significant association was discovered using functional MRI acquired in REST2 (see Figure 8). Each blue dot in the scatter plot represents one individual (n=958). Solid gray lines indicate lines of best fit. Dashed lines indicate 95% confidence intervals. R-values are the Pearson correlation coefficients and p-values assess the null hypothesis of zero correlation. The association between subcortical functional connectivity and tobacco use was reproducible across independent functional MRI sessions (REST1 and REST2) and across parcellation scales (Scale I-IV).

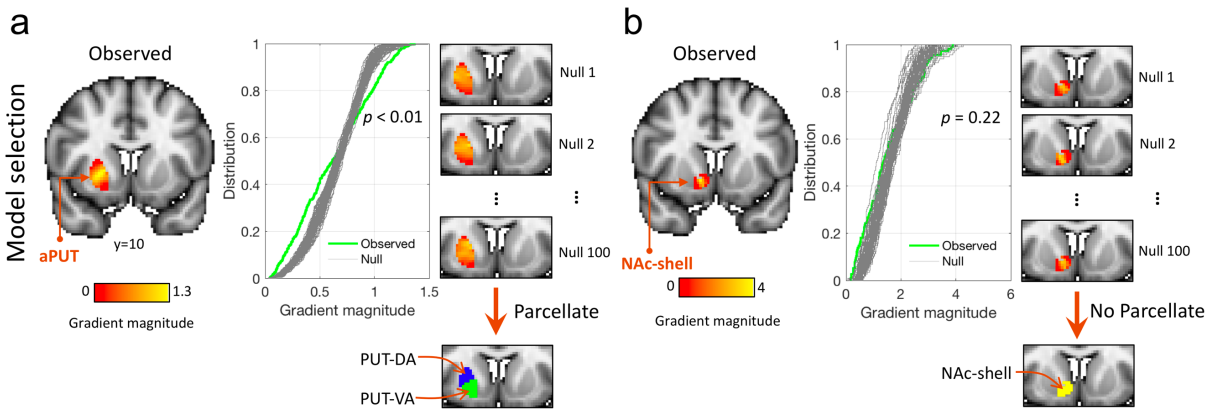


Figure 23. Model selection with Kolmogorov-Smirnov (KS) test. **a,** Gradient magnitude image for anterior putamen (aPUT) is shown as a coronal slice (left). The yellow colored strip within the aPUT indicates a gradient magnitude peak, suggesting the location of a putative boundary. The KS test suggests that the gradient magnitude distribution across the voxels in this region (green curve) is significantly longer tailed than the null data (gray curves, n=100, p<0.01, one-sided). Therefore, a boundary was delineated that resulted in parcellation of the anterior putamen into one dorsal (PUT-DA, blue) and one ventral (PUT-VA, green) component. **b,** KS test for the shell of the nucleus accumbens (NAc-shell). Although a strong gradient is evident, the null hypothesis could not be rejected with the KS test (p=0.22, one-sided), and thus subdivision of NAc-shell was not warranted.

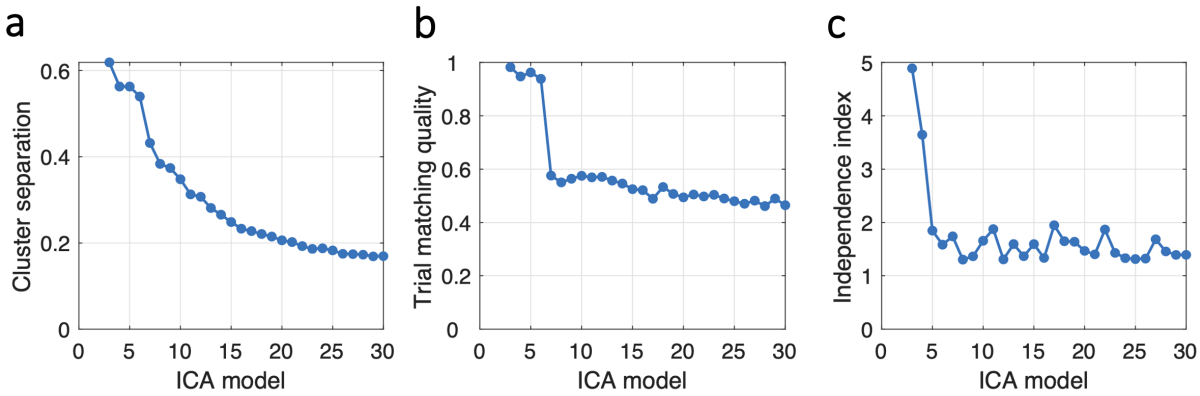


Figure 24. Determining the optimal number of independent components. Independent component analysis (ICA) was used to decompose a total of 109 behavioral measures into a set of latent behavioral dimensions. ICA performance for candidate ICA models (i.e. total number of components) ranging from 3 to 30 was evaluated based on cluster separation (**a**), trial matching quality (**b**) and independence index (**c**). Each measure was computed as a function of the total number of components and selection of the optimal model was guided by identifying abrupt changes in these measures as a function of the ICA model.

Supplementary Tables

Table 1. Basic demographic characteristics and acquisition details

Dataset	Modality	Magnetic field	Sample size	Age (mean ± std yrs)	Sex (M/F)
3T-rfMRI (REST1)	Resting-state	3 Tesla	1080	28.8 ± 3.7	495/585
3T-rfMRI (REST2)	Resting-state	3 Tesla	1021	28.7 ± 3.7	471/550
7T-rfMRI	Resting-state	7 Tesla	183	29.4 ± 3.3	72/111
tfMRI	Task-evoked	3 Tesla	725	28.7 ± 3.7	360/365
Independent validation dataset	Resting-state	3 Tesla	10	26.0 ± 2.1	6/4

Table 2. Nomenclature for 3T parcellation hierarchy

Name	Abbreviation	Name	Abbreviation
Hippocampus	HIP	**Amygdala**	AMY
Anterior hippocampus	aHIP	Lateral amygdala	lAMY
Hippocampus head, medial division	HIP-head-m	Medial amygdala	mAMY
Subdivision1	HIP-head-m1	**Caudate nucleus**	CAU
Subdivision2	HIP-head-m2	Anterior caudate	aCAU
Hippocampus head, lateral division	HIP-head-l	Dorsoanterior caudate	CAU-DA
Posterior hippocampus	pHIP	Ventroanterior caudate	CAU-VA
Hippocampus body	HIP-body	Posterior caudate	pCAU
Hippocampus tail	HIP-tail	Caudate tail	CAU-tail
Thalamus	THA	Caudate body	CAU-body
Anterior thalamus	aTHA	**Nucleus accumbens***	NAc
Dorsoanterior thalamus	THA-DA	Nucleus accumbens, shell	NAc-shell
Lateral dorsoanterior thalamus	THA-DAl	Nucleus accumbens, core	NAc-core
Medial dorsoanterior thalamus	THA-DAm	**Putamen**	PUT
Ventroanterior thalamus	THA-VA	Anterior putamen	aPUT
Superior ventroanterior thalamus	THA-Vas	Dorsoanterior putamen	PUT-DA
Inferior ventroanterior thalamus	THA-VAi	Ventroanterior putamen	PUT-VA
Anterior division	THA-VAia	Posterior putamen	pPUT
Posterior division	THA-VAip	Dorsoposterior putamen	PUT-DP
Posterior thalamus	pTHA	Ventroposterior putamen	PUT-VP
Dorsoposterior thalamus	THA-DP	**Globus pallidus**	GP
Ventroposterior thalamus	THA-VP	Anterior globus pallidus	aGP
Medial ventroposterior thalamus	THA-VPm	Posterior globus pallidus	pGP
Lateral ventroposterior thalamus	THA-VPl		

*The nucleus accumbens subdivisions bear moderate resemblance to the anatomical shell and core of the NAc and have thus been named as such. However, this correspondence was not formally tested.

Table 3. Comparison parcellation atlases of the human subcortex and specific subcortical nuclei

Atlas	Study	Modality	Metric	Number of regions
Hippocampus	Plachti et al. 2019[23]	Resting-state fMRI	Functional connectivity	5
Thalamus	Behrens et al. 2003[24]	Diffusion MRI	Tractography	7
Striatum	Janssen et al. 2015[25]	Resting-state fMRI	Functional connectivity	6
Subcortex-I	Ji et al. 2019[26]	Resting-state fMRI	Functional connectivity	12
Subcortex-II	Fan et al. 2016[27]	Diffusion MRI	Tractography	36
Hippocampus - His	Amunts et al 2005[11]; Eickhoff et al 2005[12]	Histology	Cytoarchitecture	3

Table 4. List of 109 selected behavioral items

Category	Formal Name	Intuitive Name	Psychological Test
	MMSE_Score	MMSE	Mini Mental Status Exam
	PSQI_Score	PSQI	Pittsburgh Sleep Questionnaire
	PSQI_TooCold	PSQI (TooCold)	Pittsburgh Sleep Questionnaire
Alertness	PSQI_TooHot	PSQI (TooHot)	Pittsburgh Sleep Questionnaire
	PSQI_BadDream	PSQI (BadDream)	Pittsburgh Sleep Questionnaire
	PSQI_Pain	PSQI (Pain)	Pittsburgh Sleep Questionnaire
	PicSeq_Unadj	Episodic Memory (PicSeq)	NIH Toolbox Picture Sequence Memory Test
	CardSort_Unadj	Cognitive Flexibility	NIH Toolbox Dimensional Change Card Sort
	Flanker_Unadj	Inhibition	NIH Toolbox Flanker Inhibitory Control and Attention
	PMAT24_A_CR	Fluid Intelligence (CR)	Penn Progressive Matrices
	PMAT24_A_SI	Fluid Intelligence (SI)	Penn Progressive Matrices
	PMAT24_A_RTCR	Fluid Intelligence (RTCR)	Penn Progressive Matrices
	ReadEng_Unadj	Reading Decoding	NIH Toolbox Oral Recognition Test
	PicVocab_Unadj	Vocabulary Comprehension	NIH Toolbox Picture Vocabulary Test
	ProcSpeed_Unadj	Processing Speed	NIH Toolbox Pattern Comparison Processing Speed Test
	DDisc_AUC_200	Delay Discounting	Delay Discounting
	VSPLOT_TC	Spatial Orientation (TC)	Variable Short Penn Line Orientation
	VSPLOT_CRTE	Spatial Orientation (CRTE)	Variable Short Penn Line Orientation
	VSPLOT_OFF	Spatial Orientation (OFF)	Variable Short Penn Line Orientation
	SCPT_TPRT	Sustained Attention (TPRT)	Short Penn Continuous Performance Test
	SCPT_SEN	Sustained Attention (SEN)	Short Penn Continuous Performance Test
Cognition	SCPT_SPEC	Sustained Attention (SPEC)	Short Penn Continuous Performance Test
	SCPT_LRNR	Sustained Attention (LRNR)	Short Penn Continuous Performance Test
	IWRD_TOT	Word Memory (TOT)	Penn Word Memory Test
	IWRD_RTC	Word Memory (RTC)	Penn Word Memory Test
	ListSort_Unadj	Working Memory	NIH Toolbox List Sorting Working Memory Test
	CogFluidComp_Unadj	CogFluidComp	NIH Toolbox Cognition Fluid Composite
	CogEarlyComp_Unadj	CogEarlyComp	NIH Toolbox Cognition Early Childhood Composite
	CogTotalComp_Unadj	CogTotalComp	NIH Toolbox Cognition Total Composite Score
	CogCrystalComp_Unadj	CogCrystalComp	NIH Toolbox Cognition Crystallized Composite
	ER40_CR	Emotion Recognition (CR)	Penn Emotion Recognition Test
	ER40_CRT	Emotion Recognition (CRT)	Penn Emotion Recognition Test
	ER40ANG	Emotion Recognition (Anger)	Penn Emotion Recognition Test
	ER40FEAR	Emotion Recognition (Fear)	Penn Emotion Recognition Test
	ER40HAP	Emotion Recognition (Happy)	Penn Emotion Recognition Test
	ER40NOE	Emotion Recognition (Neutral)	Penn Emotion Recognition Test
	ER40SAD	Emotion Recognition (Sad)	Penn Emotion Recognition Test
	AngAffect_Unadj	AngAffect	NIH Toolbox Anger-Affect Survey
	AngHostil_Unadj	AngHostil	NIH Toolbox Anger-Hostility Survey

Emotion	AngAggr_Unadj	AngAggr	NIH Toolbox Anger-Physical Aggression Survey
	FearAffect_Unadj	FearAffect	NIH Toolbox Fear-Affect Survey
	FearSomat_Unadj	FearSomat	NIH Toolbox Fear-Somatic Arousal Survey
	Sadness_Unadj	Sadness	NIH Toolbox Sadness Survey
	LifeSatisf_Unadj	LifeSatisf	NIH Toolbox General Life Satisfaction Survey
	MeanPurp_Unadj	MeanPurp	NIH Toolbox Meaning and Purpose Survey
	PosAffect_Unadj	PosAffect	NIH Toolbox Positive Affect Survey
	Friendship_Unadj	Friendship	NIH Toolbox Friendship Survey
	Loneliness_Unadj	Loneliness	NIH Toolbox Loneliness Survey
	PercHostil_Unadj	PercHostil	NIH Toolbox Perceived Hostility Survey
	PercReject_Unadj	PercReject	NIH Toolbox Perceived Rejection Survey
	EmotSupp_Unadj	EmotSupp	NIH Toolbox Emotional Support Survey
	InstruSupp_Unadj	InstruSupp	NIH Toolbox Instrumental Support Survey
	PercStress_Unadj	PercStress	NIH Toolbox Perceived Stress Survey
	SelfEff_Unadj	SelfEff	NIH Toolbox Self-Efficacy Survey
Motor	Endurance_Unadj	Endurance	NIH Toolbox 2-minute Walk Endurance Test
	GaitSpeed_Comp	GaitSpeed	NIH Toolbox 4-Meter Walk Gait Speed Test
	Dexterity_Unadj	Dexterity	NIH Toolbox 9-hole Pegboard Dexterity Test
	Strength_Unadj	Strength	NIH Toolbox Grip Strength Test
Personality	NEOFAC_A	Agreeableness	NEO-FFI
	NEOFAC_O	Openness	NEO-FFI
	NEOFAC_C	Conscientiousness	NEO-FFI
	NEOFAC_N	Neuroticism	NEO-FFI
	NEOFAC_E	Extraversion	NEO-FFI
Sensory	Odor_Unadj	Odor	NIH Toolbox Odor Identification Scale
	PainInterf_Tscore	PainInterf	NIH Toolbox Pain Interference Survey
	Taste_Unadj	Taste	NIH Toolbox Regional Taste Intensity
	Mars_Final	Visual Contrast Sensitivity	Mars Contrast Sensitivity Score
Psychiatric and Life Function	DSM_Depr_Raw	DSMDepr	ASR-DSM
	DSM_Anxi_Raw	DSMAnxi	ASR-DSM
	DSM_Somp_Raw	DSMSomp	ASR-DSM
	DSM_Avoid_Raw	DSMAvoid	ASR-DSM
	DSM_Adh_Raw	DSMAdh	ASR-DSM
	DSM_Inat_Raw	DSMInat	ASR-DSM
	DSM_Hype_Raw	DSMHype	ASR-DSM
	DSM_Antis_Raw	DSMAntis	ASR-DSM
	ASR_Anxd_Raw	ASRAnxd	ASR-DSM
	ASR_Witd_Raw	ASRWitd	ASR-DSM
	ASR_Soma_Raw	ASRSoma	ASR-DSM
	ASR_Thot_Raw	ASRThot	ASR-DSM
	ASR_Attn_Raw	ASRAttn	ASR-DSM
	ASR_Aggr_Raw	ASRAggr	ASR-DSM

	ASR_Rule_Raw	ASRRule	ASR-DSM
	ASR_Intr_Raw	ASRIntr	ASR-DSM
	ASR_Oth_Raw	ASROth	ASR-DSM
	ASR_Crit_Raw	ASRCrit	ASR-DSM
Substance Use	Num_Days_Drank_7days	Alcohol Use	Alcohol Use 7-Day Retrospective
	SSAGA_Alc_D4_Dp_Sx	Alcohol Dependence (Sx)	Alcohol Use and Dependence
	SSAGA_Alc_D4_Ab_Dx	Alcohol Abuse (Dx)	Alcohol Use and Dependence
	SSAGA_Alc_D4_Ab_Sx	Alcohol Abuse (Sx)	Alcohol Use and Dependence
	SSAGA_Alc_D4_Dp_Dx	Alcohol Dependence (Dx)	Alcohol Use and Dependence
	Num_Days_Used_Any_Tobacco_7days	Tobacco Use	Tobacco Use 7-Day Retrospective
	SSAGA_TB_Smoking_History	Smoking History	Tobacco Use and Dependence
	SSAGA_TB_Still_Smoking	Current Smoking	Tobacco Use and Dependence
	SSAGA_Times_Used_Illicits	Illicits Use	Illicit Drug Use
	SSAGA_Times_Used_Cocaine	Cocaine	Illicit Drug Use
	SSAGA_Times_Used_Hallucinogens	Hallucinogens	Illicit Drug Use
	SSAGA_Times_Used_Opiates	Opiates	Illicit Drug Use
	SSAGA_Times_Used_Sedatives	Sedatives	Illicit Drug Use
	SSAGA_Times_Used_Stimulants	Stimulants	Illicit Drug Use
	SSAGA_Mj_Use	Marijuana History	Marijuana Use and Dependence
	SSAGA_Mj_Ab_Dep	Marijuana Dependence	Marijuana Use and Dependence
	SSAGA_Mj_Times_Used	Marijuana	Marijuana Use and Dependence
In-Scanner Task	Emotion_Task_Acc	Emotion Task	In-Scanner Task Performance
	Gambling_Task_Perc_Larger	Gambling Task (Larger)	In-Scanner Task Performance
	Gambling_Task_Perc_Smaller	Gambling Task (Smaller)	In-Scanner Task Performance
	Language_Task_Acc	Language Task	In-Scanner Task Performance
	Relational_Task_Acc	Relational Task	In-Scanner Task Performance
	Social_Task_Perc_TOM	Social Task	In-Scanner Task Performance
	WM_Task_Acc	WM Task	In-Scanner Task Performance

Table 5. NIFTI and CIFTI file names for 3T and 7T atlas

Magnetic strength	Scale	Number of regions	Spatial resolution (mm)[a]	File name[b]
3 Tesla	I	16	2×2×2	Tian_Subcortex_S1_3T.nii Tian_Subcortex_S1_3T_dscalar.nii
	II	32		Tian_Subcortex_S2_3T.nii Tian_Subcortex_S2_3T_dscalar.nii
	III	50		Tian_Subcortex_S3_3T.nii Tian_Subcortex_S3_3T_dscalar.nii
	IV	54		Tian_Subcortex_S4_3T.nii Tian_Subcortex_S4_3T_dscalar.nii
7 Tesla	I	16	1.6×1.6×1.6	Tian_Subcortex_S1_7T.nii Tian_Subcortex_S1_7T_dscalar.nii
	II	34		Tian_Subcortex_S2_7T.nii Tian_Subcortex_S2_7T_dscalar.nii
	III	54		Tian_Subcortex_S3_7T.nii Tian_Subcortex_S3_7T_dscalar.nii
	IV	62		Tian_Subcortex_S4_7T.nii Tian_Subcortex_S4_7T_dscalar.nii

a, Atlas is in MNI standard space (MNI ICBM 152 nonlinear 6th generation)
b, NIFTI: *.nii; CIFTI: *dscalar.nii. Atlas is openly available at: https://github.com/yetianmed/subcortex

Supplementary References

1. Collins, C.E., Airey, D.C., Young, N.A., Leitch, D.B. & Kaas, J.H. Neuron densities vary across and within cortical areas in primates. *Proceedings of the National Academy of Sciences* **107**, 15927-15932 (2010).
2. Cahalane, D.J., Charvet, C.J. & Finlay, B.L. Systematic, balancing gradients in neuron density and number across the primate isocortex. *Front Neuroanat* **6**, 28 (2012).
3. Charvet, C.J., Cahalane, D.J. & Finlay, B.L. Systematic, Cross-Cortex Variation in Neuron Numbers in Rodents and Primates. *Cerebral Cortex* **25**, 147-160 (2013).
4. Charvet, C.J., Stimpson, C.D., Kim, Y.D., Raghanti, M.A., Lewandowski, A.H., Hof, P.R., Gómez-Robles, A., Krienen, F.M. & Sherwood, C.C. Gradients in cytoarchitectural landscapes of the isocortex: Diprotodont marsupials in comparison to eutherian mammals. *Journal of Comparative Neurology* **525**, 1811-1826 (2017).
5. Cahalane, D.J., Charvet, C.J. & Finlay, B.L. Modeling local and cross-species neuron number variations in the cerebral cortex as arising from a common mechanism. *Proceedings of the National Academy of Sciences* **111**, 17642-17647 (2014).
6. Charvet, C.J. & Finlay, B.L. Evo-Devo and the Primate Isocortex: The Central Organizing Role of Intrinsic Gradients of Neurogenesis. *Brain, Behavior and Evolution* **84**, 81-92 (2014).
7. Choi, E.Y., Yeo, B.T. & Buckner, R.L. The organization of the human striatum estimated by intrinsic functional connectivity. *Journal of neurophysiology* **108**, 2242-2263 (2012).
8. Glasser, M.F., Coalson, T.S., Bijsterbosch, J.D., Harrison, S.J., Harms, M.P., Anticevic, A., Van Essen, D.C. & Smith, S.M. Using temporal ICA to selectively remove global noise while preserving global signal in functional MRI data. *NeuroImage* **181**, 692-717 (2018).
9. Glasser, M.F., Smith, S.M., Marcus, D.S., Andersson, J.L., Auerbach, E.J., Behrens, T.E., Coalson, T.S., Harms, M.P., Jenkinson, M., Moeller, S., Robinson, E.C., Sotiropoulos, S.N., Xu, J., Yacoub, E., Ugurbil, K. & Van Essen, D.C. The Human Connectome Project's neuroimaging approach. *Nature neuroscience* **19**, 1175-1187 (2016).
10. Morel, A., Magnin, M. & Jeanmonod, D. Multiarchitectonic and stereotactic atlas of the human thalamus. *The Journal of comparative neurology* **387**, 588-630 (1997).
11. Amunts, K., Kedo, O., Kindler, M., Pieperhoff, P., Mohlberg, H., Shah, N.J., Habel, U., Schneider, F. & Zilles, K. Cytoarchitectonic mapping of the human amygdala, hippocampal region and entorhinal cortex: intersubject variability and probability maps. *Anatomy and embryology* **210**, 343-352 (2005).
12. Eickhoff, S.B., Stephan, K.E., Mohlberg, H., Grefkes, C., Fink, G.R., Amunts, K. & Zilles, K. A new SPM toolbox for combining probabilistic cytoarchitectonic maps and functional imaging data. *Neuroimage* **25**, 1325-1335 (2005).
13. Greicius, M.D., Krasnow, B., Reiss, A.L. & Menon, V. Functional connectivity in the resting brain: A network analysis of the default mode hypothesis. *Proceedings of the National Academy of Sciences* **100**, 253-258 (2003).
14. Vincent, J.L., Kahn, I., Snyder, A.Z., Raichle, M.E. & Buckner, R.L. Evidence for a frontoparietal control system revealed by intrinsic functional connectivity. *Journal of neurophysiology* **100**, 3328-3342 (2008).

15. Marquand, A.F., Haak, K.V. & Beckmann, C.F. Functional corticostriatal connection topographies predict goal directed behaviour in humans. *Nature human behaviour* **1**, 0146 (2017).
16. Haber, S.N., Fudge, J.L. & McFarland, N.R. Striatonigrostriatal pathways in primates form an ascending spiral from the shell to the dorsolateral striatum. *The Journal of neuroscience : the official journal of the Society for Neuroscience* **20**, 2369-2382 (2000).
17. Haber, S.N. & Knutson, B. The reward circuit: linking primate anatomy and human imaging. *Neuropsychopharmacology* **35**, 4-26 (2010).
18. Dosenbach, N.U., Fair, D.A., Miezin, F.M., Cohen, A.L., Wenger, K.K., Dosenbach, R.A., Fox, M.D., Snyder, A.Z., Vincent, J.L., Raichle, M.E., Schlaggar, B.L. & Petersen, S.E. Distinct brain networks for adaptive and stable task control in humans. *Proceedings of the National Academy of Sciences of the United States of America* **104**, 11073-11078 (2007).
19. Dosenbach, N.U.F., Visscher, K.M., Palmer, E.D., Miezin, F.M., Wenger, K.K., Kang, H.C., Burgund, E.D., Grimes, A.L., Schlaggar, B.L. & Petersen, S.E. A Core System for the Implementation of Task Sets. *Neuron* **50**, 799-812 (2006).
20. Gordon, E.M., Laumann, T.O., Adeyemo, B., Huckins, J.F., Kelley, W.M. & Petersen, S.E. Generation and Evaluation of a Cortical Area Parcellation from Resting-State Correlations. *Cerebral cortex (New York, N.Y. : 1991)* **26**, 288-303 (2016).
21. Barch, D.M., Burgess, G.C., Harms, M.P., Petersen, S.E., Schlaggar, B.L., Corbetta, M., Glasser, M.F., Curtiss, S., Dixit, S., Feldt, C., Nolan, D., Bryant, E., Hartley, T., Footer, O., Bjork, J.M., Poldrack, R., Smith, S., Johansen-Berg, H., Snyder, A.Z. & Van Essen, D.C. Function in the human connectome: task-fMRI and individual differences in behavior. *Neuroimage* **80**, 169-189 (2013).
22. Blondel, V.D., Guillaume, J.-L., Lambiotte, R. & Lefebvre, E. Fast unfolding of communities in large networks. *Journal of Statistical Mechanics: Theory and Experiment* **2008**, P10008 (2008).
23. Plachti, A., Eickhoff, S.B., Hoffstaedter, F., Patil, K.R., Laird, A.R., Fox, P.T., Amunts, K. & Genon, S. Multimodal Parcellations and Extensive Behavioral Profiling Tackling the Hippocampus Gradient. *Cerebral cortex (New York, N.Y. : 1991)* (2019).
24. Behrens, T.E., Johansen-Berg, H., Woolrich, M.W., Smith, S.M., Wheeler-Kingshott, C.A., Boulby, P.A., Barker, G.J., Sillery, E.L., Sheehan, K., Ciccarelli, O., Thompson, A.J., Brady, J.M. & Matthews, P.M. Non-invasive mapping of connections between human thalamus and cortex using diffusion imaging. *Nature neuroscience* **6**, 750-757 (2003).
25. Janssen, R.J., Jylänki, P., Kessels, R.P.C. & van Gerven, M.A.J. Probabilistic model-based functional parcellation reveals a robust, fine-grained subdivision of the striatum. *NeuroImage* **119**, 398-405 (2015).
26. Ji, J.L., Spronk, M., Kulkarni, K., Repovs, G., Anticevic, A. & Cole, M.W. Mapping the human brain's cortical-subcortical functional network organization. *Neuroimage* **185**, 35-57 (2019).
27. Fan, L., Li, H., Zhuo, J., Zhang, Y., Wang, J., Chen, L., Yang, Z., Chu, C., Xie, S., Laird, A.R., Fox, P.T., Eickhoff, S.B., Yu, C. & Jiang, T. The Human Brainnetome Atlas: A New Brain Atlas Based on Connectional Architecture. *Cerebral cortex (New York, N.Y. : 1991)* **26**, 3508-3526 (2016).

CHAPTER 6

GENERAL DISCUSSION

Summary

In this thesis, I investigated the topographic organization of the human insular cortex and the subcortex in health and neuropsychiatric illness. In particular, I developed a new methodology to reconcile classical models of topographic organization based on discrete regions and contemporary representations involving continuous gradients. I addressed several knowledge gaps by evaluating three primary questions:

i. How is the functional topography of the human insular cortex organized? Is the insula's topography most parsimoniously represented with discrete subregions or continuous gradients? Does the insula's topography relate to inter-individual variation in functions associated with the insula (Chapter 3)?

ii. Is the functional connectivity architecture of the insular cortex affected in individuals with severe neuropsychiatric illness (schizophrenia)? Do alterations in insula's functional organization relate to clinical symptoms of the disorder (Chapter 4)?

iii. How is the functional connectivity of the human subcortex topographically organized? Does the topography of the subcortex link to the functional organization of cortical networks and reconfigure dynamically in response to changing cognitive demands? To what extent does the connectivity architecture of the subcortex vary across individuals and does this variability associate with behavior (Chapter 5)?

In Chapter 3, I proposed a new data-driven approach to characterize the topographic organization of the human brain, particularly with respect to the insular cortex and the subcortex, using functional MRI. I first showed evidence to support the notion that the insular cortex is a functionally heterogeneous cortical lobe. To parse this heterogeneity, I showed that the insula's topography is best modeled as a continuum of gradual change along an anterior-posterior axis. This contrasts with previous studies that have sought to parse the insula's heterogeneity by subdividing it into distinct subregions. I contended that using subregions to represent the insula's topographic heterogeneity is suboptimal and has significantly contributed to the discrepant findings among previous studies in terms of the number of putative subregions. Under my proposal, the insula's topography is modeled as a continuum, without the need to delineate any discrete boundaries. This was supported by a formal model selection process and null hypothesis testing, which revealed that there are no peaks in the insula's gradient magnitude that are large enough to suggest a discrete boundary.

Moreover, inter-individual variation in this connectional diversity was found to relate to variation in human behaviors associated with cognitive, affective and sensorimotor functions.

Having characterized the topography of the insular cortex in healthy individuals, I next turned to investigate whether this topography is altered in individuals with neuropsychiatric illness. In Chapter 4, I found that the normal pattern of connectional diversity in the insular cortex was altered in individuals with schizophrenia and connectional deficits in the insular cortex explained a moderate amount of variance in cognitive impairment, negative symptoms, poor psychosocial functioning and longer duration of illness in the disorder. In particular, individual variation in functional connectivity between the insular cortex and cortical regions involved in the salience network, language and auditory processes contributed the most to this association, suggesting that disturbances of the salience network in integrating sensory perception are involved in the pathophysiology of schizophrenia.

Finally, in Chapter 5, I applied the principles and model selection procedure developed for the insula to the entire subcortex, with the goal of developing a new MRI atlas of the subcortex and investigating the extent to which the subcortex is topographically organized. Four hierarchical scales of subcortical organization were identified, recapitulating well-known anatomical nuclei at the coarsest scale and delineating 27 bilateral subregions at the finest. The new atlas provides fundamental insight into the functional organization of the human subcortex and has enabled holistic connectome mapping and characterization of cortico-subcortical circuits. The atlas is currently being used to guide the targeting of brain stimulation therapies and numerous researchers have used the atlas to map connectomes. In Chapter 5, I also investigated the relationship between subcortical functional connectivity and a broad set of behavioral dimensions, unveiling a novel association between tobacco use and subcortical functional connectivity, confirming the role of the subcortex in the reward system and goal-directed behaviors, such as the tobacco smoking. The new subcortex atlas was personalized to account for connectivity differences across individuals and can be used to improve personalized intervention and targeted therapies in psychiatry (Cocchi and Zalesky 2018).

Insular connectional topography is best modeled as a continuum of gradual changes rather than distinct subregions

The insular cortex is a functionally and connectionally heterogenous cortical lobe, in which function and connectivity vary along a putative anterior-posterior axis (see Chapter 1 and Chapter 3). Using functional MRI, many studies have sought to resolve the connectional heterogeneity using clustering approaches. However, this has yielded a discordant number of insular subregions (clusters) across studies (Chapter 3, Table 1). I first comprehensively examined traditional clustering methodologies by parsing the heterogeneous connectional architecture of the insular cortex into a range of distinct subregions. Consistent with the discrepant findings across previous studies, I found that the optimal number of insular subregions (clusters) varied markedly across individuals and was substantially influenced by the extent to which the fMRI data was spatially smoothed. Moreover, insular subregions delineated by clustering methodologies were not functionally homogeneous for the majority of individuals studied when benchmarked to null data in which the insula was repeatedly repositioned to random gray matter locations. These results led me to question whether subdividing the insula into distinct subregions is a desirable approach to represent its heterogeneity. In particular, I contended that the question of how many subregions comprise the insula (Cauda and Vercelli 2013) is ambiguous, which may explain the marked inconsistency across previous insula parcellation studies. At this point, I sought to investigate alternative representations and models of brain topography that could be applied to the insula.

As previously suggested by Cerliani and colleagues (2012), perhaps models of insular connectivity topography that do not mandate the delineation of distinct subregional boundaries can provide a more profitable characterization than classical models. One such model is based on the concept of cortical gradients (Huntenburg et al. 2018). I therefore proposed such an alternative model based on the concept of diversity curves (Chapter 3), which provides an intuitive way to continuously parameterize and perform model selection on the spatial gradient of insular functional connectivity. I performed model selection with respect to three benchmark diversity curves for: i) an absence of any connectional variation (i.e. homogeneous); ii) two discrete subregions; and, iii) a continuum of gradual change. I

found that the variation in functional connectivity across the topography of the insular cortex was most accurately modeled by the benchmark characterizing a continuum of gradual change, avoiding the disputed task of determining an optimal number of insular subregions. I referred to this topographic variation as connectional diversity. A region with greater connectional diversity shows greater variation across its topography with respect to cortical and subcortical regions to which it connects. I found that this topographic variation in insula functional connectivity is largely consistent across left and right hemispheres.

While not explicitly tested in Chapter 3, it is possible that the spatial variation in functional connectivity across the topography of the insular cortex is associated with the insula's underlying anatomy, such as patterns of cortical folding and myeloarchitecture or confounded by the spatial variation in SNR of fMRI signals. Interestingly, most previous anatomical evidence that supports the notion of a continuum of gradual change across the insula's topography is from histological investigations in postmortem brains and axonal tracing studies of the macaque insular cortex (Mufson et al. 1981; Mesulam and Mufson 1982; Mufson and Mesulam 1982; Mesulam and Mufson 1985). Recently, the anterior-posterior topographic gradient in insula's microstructure was recapitulated using *in vivo* myelin sensitive MRI contrast (Royer et al. 2019), suggesting structure-function convergence in the insula's topography.

More importantly, I found that inter-individual variation in the continuum of insular connectional diversity was significantly associated with variation in human behaviors related to cognitive-affective and sensorimotor functions, which recapitulated a pattern of functional specialization along an anterior-posterior axis. Specifically, individuals who scored high on measures of cognitive-emotional, viscerosensory function and motor dexterity, showed greater connectional diversity in the anterior aspect of the insula. In contrast, for individuals who scored high on measures of somatosensory function, the posterior insula was more diverse with respect to variation in the cortical areas to which it connects. The behavioral response along the anterior-posterior division of the insular cortex is consistent with previous studies. In particular, previous studies reported that the anterior insula is associated with subjective emotion (Uddin et al. 2014), viscerosensory function (Small et al. 2003) and high-order cognition (Uddin 2015) including attentional control for motor dexterity (Craig 2002;

Rinne et al. 2017). Contrastingly, the posterior insula primarily responds to somesthetic stimuli (Craig et al. 2000; Ostrowsky et al. 2000; Stephani et al. 2011). This suggests that the anterior-posterior division of insula's function is facilitated, at least in part, by the connectional diversity across the topography of the insular cortex. In addition, previous studies suggest a ventral-to-dorsal functional differentiation within the anterior insula, in which the ventral component is predominantly involved in affective processing, whereas the dorsal extreme plays a more important role in higher order cognitive function (Chang et al. 2013; Uddin 2015). While this ventral-to-dorsal functional gradient was not reflected by the most dominant functional connectivity gradient within the insula, finer variation could be captured in successive connectivity gradients, which would be worthy of further investigation in future work.

The topographic organization of the insular cortex is reorganized in schizophrenia and relates to clinical symptoms

The insular cortex is widely connected to cortical and subcortical networks and the functional dysconnectivity of the insular cortex is consistently observed in psychosis spectrum disorders across different illness stages (Kasparek et al. 2013; Moran et al. 2013; Palaniyappan et al. 2013; Dandash et al. 2014; Wotruba et al. 2014; Wang et al. 2016; Pang et al. 2017; Mallikarjun et al. 2018). Having characterized the functional connectivity architecture of the insular cortex in a healthy population (Chapter 3), I next investigated whether the normal pattern of insular connectional topography is altered in individuals with schizophrenia.

In Chapter 4, I comprehensively characterized the connectional pathology across the topography of the insular cortex in individuals with established schizophrenia. Specifically, I assessed the two topographic representations of insular functional connectivity architecture in schizophrenia and a healthy comparison group. Consistent with our previous findings in Chapter 3, insular functional connectivity varied gradually along an anterior-posterior axis in both groups. I found no evidence of discrete boundaries between putative insular subregions, despite variation in image quality, image acquisition parameters and voxel resolutions. As hypothesized, I found that schizophrenia was associated with reduced insular connectional diversity, meaning that the variation across insular topography with respect to the cortical

and subcortical regions to which it connects was reduced in schizophrenia compared to healthy individuals. To further investigate the affected cortical and subregions regions, I mapped the connectivity profiles of the anterior and posterior extremes of the insular cortex and compared them between the schizophrenia and healthy control group. Consistent with previous work (Kasparek et al. 2013; Moran et al. 2013; Palaniyappan et al. 2013; Dandash et al. 2014; Wotruba et al. 2014; Wang et al. 2016; Pang et al. 2017; Mallikarjun et al. 2018), insular functional connectivity was overall reduced in individuals with schizophrenia. In particular, I found reduced differentiation between the connectional profiles of putative insular subregions in the schizophrenia group. Moreover, connectivity profiles of putative insular subregions were altered, as evidenced by a significant interaction between diagnosis and insular subregions. Specifically, anterior insula showed increased connectivity in schizophrenia to regions that normally connected with posterior insula (i.e. somatosensory, somatomotor, occipital and parietal cortices as well as motor regions of cerebellum). In contrast, the posterior insula in schizophrenia connected with increased strength to regions that preferentially connected with anterior insula in healthy individuals (i.e. thalamus, prefrontal cortex and cerebellar nonmotor regions). This interaction effect suggested that connectivity profiles between putative insular subregions were less well differentiated in schizophrenia, consistent with the lack of insular connectional diversity in the disorder. In particular, the reduced connectional diversity manifested most strongly in the anterior aspect of the insular cortex, suggesting that the anterior insula may be abnormally homogeneous in individuals with schizophrenia.

Importantly, while we showed that schizophrenia does not preferentially affect the left or right insula, the extent of impairment (reduction) in connectivity between insular subregions (right hemisphere)and key regions of the salience network (anterior cingulate cortex and supplementary motor area) and auditory cortex was associated with inter-individual variation in poor clinical outcomes, including cognitive impairment and general, social and occupational functioning, as well as the severity of psychosis symptoms, particularly negative symptoms. These findings further support the critical role of the insular cortex, particularly the right insula in the pathophysiology of schizophrenia. Of note, I found that the reduced functional connectivity was also associated with longer illness duration, potentially suggesting progressive deterioration of insular connectivity over the course of illness, although a

longitudinal study design would be required to address this hypothesis. Moreover, given the absence of an untreated drug-naïve schizophrenia group, medication cannot be excluded as a potential confound (Radua et al. 2012; Abbott et al. 2013), although antipsychotic dose was not correlated to any of the functional connectivity estimates reported in this study.

Investigating the topographic organization of the human subcortex

Having established that the insular cortex is most parsimoniously represented as a continuous gradient of gradual change over discrete subregions (Chapter 3), I then asked, is this continuous representation of connectional topography also appropriate for other brain regions? Compared to the cortex, the subcortex is the part of the brain that has been less well characterized (Alkemade et al. 2013), partially due to technical challenges inherent to subcortical imaging (Evans et al. 2012; Forstmann et al. 2016; Puckett et al. 2018). Using the methods and model selection principles I developed in Chapter 3, I characterized the connectivity architecture of the human subcortex using functional MRI in more than 1000 healthy adults, yielding a hybrid map that parsimoniously accommodated both discrete regions/boundaries and continuous gradients in the human subcortex (Chapter 5).

As I have demonstrated in Chapter 3, variation in functional connectivity across the expanse of the insular cortex is evident (i.e. not homogeneous), but too gradual over the spatial extent to warrant discrete boundary delineation, and thus a continuum is deemed to provide the most parsimonious representation. Likewise, to what extent the variation in functional connectivity across the topography of the subcortex is sufficiently large to warrant boundary delineation? This question was referred to as model selection in this thesis. Interestingly, the idea of model selection in mapping brain topography is not an entirely new concept, both from a qualitative and quantitative perspective (see Chapter 2). Qualitatively, von Economo and Koskinas (1925) described transitional zones of cortical cytoarchitecture where abrupt local changes could not be clearly observed. Quantitatively, the Mahalanobis distance was used to quantify the degree of spatial variation in the gray level index, an index that measures the volume fraction of neuronal bodies along the cortical ribbons (Amunts et al. 2000; Schleicher et al. 2005). Visual inspections by von Economo and Koskinas (1925) might be considered biological valid but also subjective and observer dependent. While the

Mahalanobis distance provides an objective estimation, the extent to which the Mahalanobis distance in the gray level index between two spatially adjacent regions is larger than expected due to chance was not established. Any locations with increased Mahalanobis distance can be potentially considered as boundaries. Contrastingly, the model selection framework with null hypothesis testing developed in this thesis takes into account the extent of variation in the spatial gradient of connectivity that is attributable to noise and other confounds, such as the effect of spatial smoothing in fMRI data and subcortex geometry as well as random effects. Of note, the intrinsic geometry of the subcortex is preserved in the null data, given that recent work emphasizes the importance of the spatial embedding of brain networks (Roberts et al. 2016; Tadić et al. 2019) and that an abrupt change in connectivity gradient could emerge solely as a consequence of geometric constriction (Chapter 5, Supplementary Fig S5). To this end, I developed *gradientography*, an fMRI analogue of diffusion MRI tractography, which enables quantification of connectivity gradients along the complex geometry of the subcortex and a statistically principled formalism to guide boundary delineation in the subcortex.

While this thesis only assessed functional connectivity architecture of the insular cortex (Chapter 3) and the subcortex (Chapter 5), the framework of model selection and null hypothesis testing are applicable to different neurobiological modalities and at different spatial scales, from gene expression, cyto- and myeloarchitecutre, cortical architecture to structural connectivity, electrophysiology and function. Future applications of gradientography are not limited to the subcortex and the method could provide a bridge between cortical gradients and parcellations in humans as well as other species. One methodological challenge in mapping cortical gradients using gradientography is the necessity of considering the morphology of cortical folding, which means that the principal directions of streamlines propagation should be constrained to follow gyral crests and sulcal fundi. I intend to explore this further in future work.

Multiscale subcortex atlas

The model selection process enabled the disambiguation of continuous gradients from discrete boundaries. By performing the model selection and gradient mapping recursively, I showed that connectivity topography of the subcortex is hierarchically organized, yielding a

multiscale subcortex functional atlas. Scale I of the atlas hierarchy comprises regions that recapitulate well-known anatomical nuclei, whereas more functional subregions were delineated in Scale II-IV. The atlas hierarchy for the amygdala and globus pallidus ends at Scale II, whereas subdivisions of thalamus and hippocampus extend to Scale IV. This is consistent with the greater functional and organizational complexity within the thalamus (Hwang et al. 2017; Shine et al. 2019) and hippocampus (Poppenk et al. 2013; Strange et al. 2014) compared to the more specific functional role of amygdala and globus pallidus in emotional process (Janak and Tye 2015) and motor control (Mink 1996), respectively. Importantly, while the subcortex atlas was largely replicated in a subset of individuals using ultra-high magnetic field strength (7T) fMRI, the improved spatial resolution and contrast-to-noise ratio of 7T compared to 3T extends the organizational scales, resulting in finer functional subdivisions for several regions, including the amygdala and hippocampus. By performing a machine learning based personalization approach, I found that the group-consensus subcortex atlas was sufficient to represent the connectivity topography for the majority of individuals studied, whereas personalized atlases were warranted for some individuals, due to large difference in patterns of connectivity for these individuals. Further investigation is required to understand potential idiosyncrasies that may relate to individual variation in the functional connectivity architecture. Such idiosyncrasies may associate with brain anatomy, patterns of brain activity as well as unique cognitive, emotional and personality traits.

Intrinsic and dynamic functional topography

Throughout this thesis, I have mainly focused on understanding functional connectivity topography when the brain is at rest (i.e. resting-state fMRI), without explicit task stimuli. Of note, the spatial pattern of resting-state functional network architecture is largely present during task performance (Cole et al. 2014). Similarly, there is extensive evidence suggesting that the spatial pattern of task-related activation is intrinsically represented in the brain at rest (Fox et al. 2005; Smith et al. 2009; Tavor et al. 2016). Cortical networks are intrinsically organized into a task-related dichotomy, in which one extreme comprises networks that typically show increased activity during cognitive task performance, whereas regions on the other extreme often associate with task-related deactivation (Fox et al. 2005). One theory is that functional networks are continuously interacting with each other at rest in the absence

of explicit task stimuli, being prepared to be utilized by the brain in action (Smith et al. 2009; Tavor et al. 2016). While studies have primarily examined the cerebral cortex, I observed task-rest correspondence in subcortical connectivity architecture in two phenomena (Chapter 5). First, task-evoked activation within the parcels delineated in the new subcortex atlas is significantly more homogeneous than expected due to chance, suggesting a recapitulation of task activation level changes in the atlas, although the atlas was delineated based on brain connectivity at rest. Second, canonical cortical networks could be arranged along an intrinsic organizational axis from task-positive to task-negative based on similarity in patterns of connectivity with subcortical regions, suggesting a recapitulation of the task-related dichotomy (Fox et al. 2005) in the subcortex.

While similar, changes in the functional connectome over time under specific cognitive processes are nonnegligible (Cole et al. 2013; Cole et al. 2014) and behaviorally significant (Bijsterbosch et al. 2018; Greene et al. 2018). However, most studies defined nodes of the connectome with the use of a uniform brain parcellation, without considering possible topographic variation in nodes across different cognitive states. A recent study instead characterized the spatial reconfiguration of brain parcellation, particularly the variation in parcel size across a variety of task-evoked states (Salehi et al. 2019). Consistent with the finding from Salehi and colleagues (2019), I identified variation in the functional topography of the subcortex in response to changing cognitive demands under seven task domains (task-evoked fMRI, see Chapter 5) compared to the rest. Rather than measuring the parcel size (Salehi et al. 2019), which is relatively coarse, I accurately characterized changes in functional boundaries using the concept of diversity curves that I introduced in Chapter 3. In particular, changes in both location and magnitude of functional boundaries were characterized. While the extent of reconfiguration was relatively subtle, the pattern was presented in a way toward forming specific functional subsystems, so as to facilitate complex cognitive processing. For example, the hippocampus was more strongly segregated along its longitudinal axis during task conditions, whereas the separation between amygdala and hippocampus was weaker, resulting in a more integrated amygdala-anterior hippocampal system that potentially facilitated emotional processes (Poppenk et al. 2013; Strange et al. 2014). The separation between hippocampus and thalamus was also weaker during the task compared to the rest, suggesting a more integrated posterior hippocampus-thalamus functional system that may

have given rise to cognitive processes relating to learning and spatial memory (Poppenk et al. 2013) (see Discussion in Chapter 5).

Relationship between tobacco use and subcortical functional connectivity

Finally, I investigated the extent to which functional connectivity strength between subcortical regions relate to a broad set of human behaviors (Chapter 5). Importantly, I first performed a hypothesis-free decomposition of a large number of cognitive and behavioral measures into five latent dimensions, characterizing behaviors in cognitive performance, illicit substance use, tobacco use, personality and emotional traits as well as mental health. Previous studies utilizing the HCP dataset typically investigate hundreds of individuals measures (Smith et al. 2015), so does the study I present in Chapter 3. This leads to an enormous problem of multiple comparisons across a large number of independent tests. Alternatively, studies preselect a limited number of psychometric measures that tap specific behavioral or cognitive domains, such as the fluid intelligence (Finn et al. 2015). Here, I performed statistical inference on each of the five dimensions rather than the full set of behaviors.

Using the new atlas, I found a novel relationship between individual variation in subcortical functional connectivity and the behavioral dimension characterizing tobacco use. I found that Individuals with higher tobacco use are associated with lower functional connectivity in thalamo-nucleus accumbens, thalamo-caudate and hippocampo-nucleus accumbens neural circuits. Of note, although the functional connectivity explained approximately 4% of individual variation in tobacco use, this relationship is highly robust, in that it is consistent across subcortex parcellation scales and reproducible across fMRI data sessions. The importance of reproducibility in neuroimaging research has been particularly highlighted in a recent review (Poldrack et al. 2017). Further, this finding of behavioral association is consistent with the engagement of the cortico-basal ganglia-thalamo-cortical circuit and mesolimbic dopamine pathways in reward and goal-directed behaviors (Maia and Frank 2011), such as the behavior of tobacco use studied here. The low functional connectivity in the thalamo-striato-hippocampus in individuals with high tobacco use may suggest a down-regulation effect of nicotine in the system. Given the well-studied epidemiology of increased

prevalence of tobacco smoking in individuals with schizophrenia (de Leon and Diaz 2005), I speculated that the putative down-regulation effect of nicotine on the hyper-dopaminergic state in the mesolimbic system (Howes et al. 2012) may correspond with the up-regulation effect of nicotine in the prefrontal cortex (Koukouli et al. 2017), facilitating symptom alleviation in the disorder (see Discussion in Chapter 5). It is important to note that I have only assessed the contribution of subcortical-to-subcortical functional connectivity in relation to tobacco use. Futures studies incorporating cortical regions, especially the prefrontal cortex, would provide more insight into the potential effect of nicotine on the reward circuits in individuals with schizophrenia.

It is also noteworthy that I did not find significant associations between intra-subcortical functional connectivity and the other four behavioral dimensions. In particular, although the subcortex is engaged in a number of cognitive processes (Maia and Frank 2011; Shepherd 2013), my finding suggests that the subcortex alone may not be sufficient to cope with complex higher-order cognitive tasks. This conclusion is perhaps not of surprise given that in contrast to the highly expanded association cortices (Van Essen and Dierker 2007; Ardesch et al. 2019), the subcortex in humans is evolutionarily conserved (Stephenson-Jones et al. 2011; Satizabal et al. 2019), and nuclei in the subcortex typically act through networks and circuits modulating input and output information to and from the cerebral cortex (Alexander et al. 1986; Jahanshahi et al. 2015). This highlights an important direction for future work of holistic connectome mapping and characterization of cortico-subcortical functional connectivity, to further elucidate neural correlates of the behavioral traits that relate to complex and abstract higher-order cognition.

Limitations and future work

Limitations of each study described in this thesis are described in detail within the respective chapters (Chapter 3-5). In this section, I will highlight several general limitations that may have impacted all three studies. In some cases, I will also attempt to propose potential solutions to overcome these limitations in future work.

First, and as discussed in Chapter 3, functional MRI data is inherently discrete (voxelized) and thus the extent to which spatial variation in functional connectivity can be modeled as a continuum or sharp transition is limited by the voxel resolution. In other words, the topographic representation of brain connectivity is limited by the spatial scale of the imaging modality studied. The inability to unequivocally parcellate a brain region (e.g. insular cortex) with a certain modality (e.g. resting-state fMRI) should not be interpreted as no subdivisions in that region. The absence of subregions may potentially be a consequence of inherent limitations in the imaging modality. Distinct differentiation may be evident at different spatial scales such as molecular and cellular and may be evident with alternative imaging modalities. Given the intrinsic laminar cytoarchitecture of cortical regions, differentiation may also be evident at specific cortical layers. However, the spatial resolution of standard neuroimaging techniques is insufficient to distinguish fMRI signals at the level of cortical layers, although several recent breakthroughs are worth noting (Finn et al. 2019). This highlights the importance of multi-scale and multi-modal investigations of brain topography in future work.

Second, ambiguity in the number of functional subregions across studies may be due to limitations in fMRI acquisition and data quality. The high-quality HCP data I used in Chapter 3 and Chapter 5 are characterized by higher spatial (2mm isotropic voxel size) and temporal (TR=720ms) resolution compared to most previous parcellation studies as well as the study I performed in Chapter 4 (voxel dimension: $3.3\times3.3\times3.5$ mm^3; TR=2000ms). While additional procedures were implemented in Chapter 4 to assist in alleviating the effects of noise, the accuracy and robustness of insular connectivity gradients might still be affected by the poorer data quality, precluding precise characterization of differences in insular connectional diversity between the schizophrenia and healthy control group.

Third, some degree of spatial smoothing is unavoidable with fMRI, which may have led to the blurring of functional boundaries between putative cortical and subcortical regions. It might be argued that the connectivity topography should be characterized using unsmoothed fMRI data, although the data is intrinsically smoothed due to the point spread function associated with the MRI acquisition. Voxel-wise and individual-level analyses without any additional smoothing can be very challenging due to the effect of temporal artifacts. Functional connectivity estimated between spatially distant voxels may thus arise from unstructured and

autocorrelated noise rather than the actual BOLD-related fluctuations. Indeed, spatial smoothing is one the most common strategies to reduce the unstructured noise and to increase the signal-to-noise ratio (SNR). Rather than using traditional Gaussian smoothing kernels, Glasser and colleagues (2016) proposed to selectively smooth unstructured noise more than BOLD signals, and thus preserve spatial fidelity while enhancing the SNR. Specifically, BOLD signals were reconstructed from a principal component analysis, where the components were filtered according to an empirically-fitted Wishart distribution to dampen the effects of noise (Glasser et al. 2016a; Glasser et al. 2016b; Glasser et al. 2018). They showed that this method substantially improved cortical SNR with minimal spatial blurring. Of note, I also found that the method of Wishart filtering is very useful in increasing the SNR of fMRI signals in the subcortex, whereas the pipeline coupled with a smoothing kernel of 6mm full width at half maximum (FWHM) yielded the most lucid gradient maps (Figure 6.1).

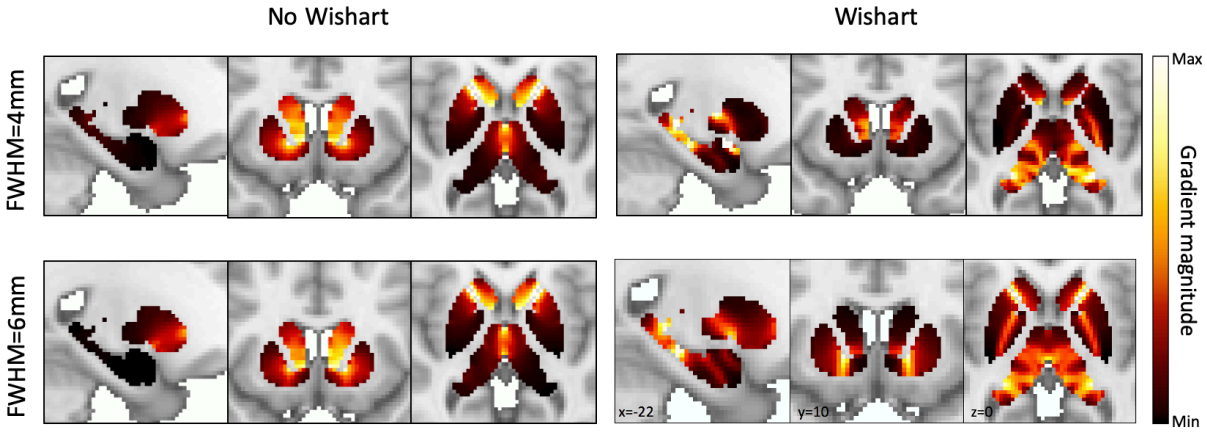


Figure 6.1. Effects of Gaussian smoothing kernel and Wishart filter on connectivity gradient mapping.

Indeed, imaging the subcortex is particularly challenging due to iron enrichment in subcortical nuclei and the relatively large distance from the MRI head coil (Puckett et al. 2018). The T2* signal decay times are shorter in subcortical regions compared to the cortex, whereas most echo-planar based imaging (EPI) protocols, including the HCP, are optimized for the cerebral cortex. This yields overall lower SNR and lower BOLD signal sensitivity in the subcortex compared to the cortex. Small subcortical nuclei such as subthalamic and substantia nigra are more susceptible and were not included (Chapter 5) due to this matter as well as the limited spatial resolution. For example, the subthalamic nuclei has a volume of approximately 100 mm^3 (de Hollander et al. 2015; Zwirner et al. 2017; Pauli et al. 2018), meaning that the entire subthalamic nuclei spans no more than approximately ~10 voxels at 3T fMRI (2mm isotropic

resolution) or ~20 voxels at 7T fMRI (1.6mm isotropic resolution). Investigating the functional architecture and subregions of these small nuclei would require greater spatial resolution, particularly given that putative subregions of the subthalamic nuclei would not compromise more than a few voxels at most. The BOLD signals obtained from so few voxels would most likely be unreliable and sensitive to the impact of residual misalignment errors remaining after spatial normalization. Even at 7T, with overall improved SNR, the echo time (TE=22.2ms) is still relatively long to acquire a reliable BOLD contrast in the subthalamic nuclei, of which the T2* relaxation value is about 15ms. By the time of echo, the signal in the cortex is still strong, whereas the subthalamic signal has decayed to a large extent (Figure 6.2). Future work with the use of optimized 7T acquisition protocols, including multi-echo planar and sub-millimetre spatial resolution would be more suited to resolve the functional architecture of these small nuclei (de Hollander et al. 2017). Additional spatial smoothing may not be required in the future.

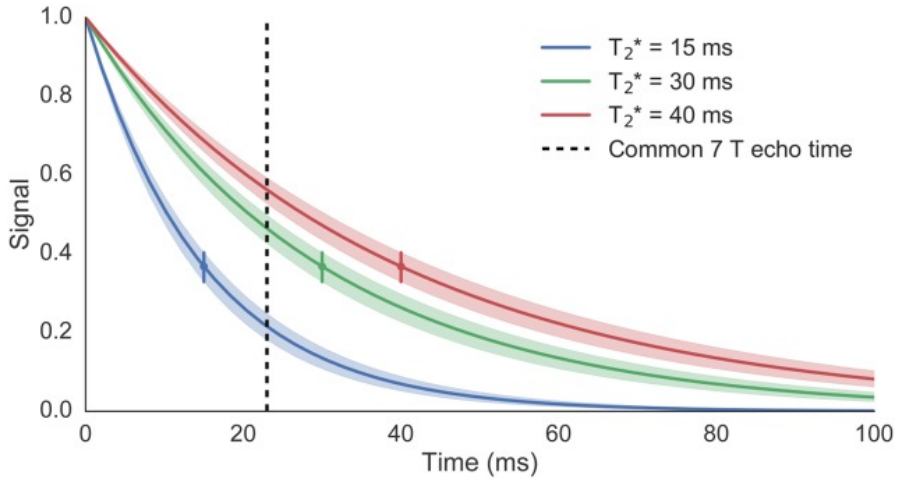


Figure 6.2. BOLD signal decays as a function of time for different T2* relaxation value at 7T. The T2* relaxation value for the subthalamic nuclei is about 15ms, whereas the relaxation time in the cerebral cortex is about 30-40ms. The black dotted line indicates a common echo time at 7T of 22ms. Colored dots indicate the signal of the T2* curve at its respective T2* relaxation value (reproduced from de Hollander et al. 2017).

Another general limitation is that I have only investigated one neuroimaging modality. In particular, I have examined the connectivity architecture using functional MRI. Although functional MRI is argued to be one of the most useful modalities in predicting cortical areal borders (Glasser et al. 2016a), an interesting avenue for future investigation is to characterize the topographic organization of the brain by integrating data from multiple imaging modalities. While most anatomical and functional evidence supports the continuum model of

insula's topography, the topographic organization of other brain regions may be divergent across modalities. One such example is the hippocampus. The complexity of hippocampal topography is evident in different modalities as well as different organizational axes, see a review by Strange et al. (2014). Specifically, the hippocampus comprises three main anatomical subfields (i.e. subiculum, cornu ammonis and dentate gyrus) that are organized along a medio-lateral axis (Amunts et al. 2005), whereas patterns of hippocampal function and connectivity vary along a longitudinal axis from anterior to posterior (Strange et al. 2014). Gene expression profiles suggest multiple functional domains in the hippocampus along the longitudinal axis, while often presented as abrupt changes, some genes show continuous gradients of expression (Thompson et al. 2008; Vogel et al. 2020). In contrast, hippocampal connectivity, findings from electrophysiological recording and behavioral lesions in rodents typically suggest a continuous topographic gradient. However, exceptions of distinct differentiation were also overserved (Strange et al. 2014). This accentuates the complexity of brain organization and motives the use of multi-modal imaging to provide a comprehensive picture of the topographic organization of the human brain.

The availability of multi-modal imaging provides a unique opportunity to untangle the relationship in the topographic organization between different neurobiological properties, from molecules and cells to brain structure, connectivity and function, and eventually toward the path to understand how neural information is integrated to give rise to human behaviors and cognition. Indeed, none of these neurobiological properties exist and operate in isolation. It has been established that the anatomy of cortical and subcortical structure is heritable (Satizabal et al. 2019; Grasby et al. 2020). Studies suggest that regions with similar gene expression profiles are more likely to co-vary in structure (e.g. structural covariance) and are more strongly connected (Fornito et al. 2019; Vogel et al. 2020). Similarly, connectivity strength is stronger between regions that share similar cyto- and myeloarchitecture (van den Heuvel et al. 2015; Goulas et al. 2016; Huntenburg et al. 2017). Another research avenue is the investigation of the extent to which one property can be predicted by another. There is evidence that anatomical connectivity measured by diffusion MRI tractography can predict resting-state functional connectivity (Honey et al. 2009) and brain activation (Saygin et al. 2011; Osher et al. 2016), whereas individual variation in brain activation during task

performance is also predictable from inter-regional functional connectivity during task engagement (Cole et al. 2013; Salehi et al. 2019) or at rest (Cole et al. 2016; Tavor et al. 2016).

Many studies have sought to investigate whether individual variation in brain structure and function associates with behavioral variability in health (Dickerson et al. 2008; Gabrieli et al. 2015; Smith et al. 2015; Sabuncu et al. 2016; Kong et al. 2019) and symptom variability in neuropsychiatric illness (Dwyer et al. 2018; Xia et al. 2018). Studies often investigate each neural feature separately, among which functional connectivity has been most commonly employed and often outperforms others in the amount of behavioral variance explained, or the accuracy in behavioral prediction (Greene et al. 2018; Liégeois et al. 2019; Seguin et al. 2020). Consistent with previous studies, I found that patterns of functional connectivity of the insular cortex significantly associate with individual variation in behaviors that relate to cognitive-affective and somatosensory functions in health and explains some variance in the severity of clinical symptoms in schizophrenia. Likewise, subcortical functional connectivity was found to associate with individual variation in behaviors relating to cognitive processes in reward and decision making. Nevertheless, functional connectivity is the only imaging measure examined in this thesis, which is an important limitation. While most neural features and imaging modalities are related to a certain extent, a single feature usually cannot explain all or the vast majority of the behavioral variance. Therefore, it is important to investigate how these neural features cooperate and give rise to individual differences in the various domains of behaviors in health as well as symptom heterogeneity in neuropsychiatric disorders. Moreover, within-sample correlational analyses were often used throughout this thesis to investigate brain-behavior associations. Cross-validation and out-of-sample prediction strategies are likely to yield more reproducible and generalizable brain-behavior relationship, although these methodologies demand large sample sizes. Given that many neuropsychiatric disorders emerge during childhood and adolescence, when changes in brain structure, function and connectivity are remarkable (Paus et al. 2008), future work integrating multi-dimensional neural features should also consider the critical window of neurodevelopment.

To answer these questions, large datasets of participants across a wide age range, from childhood and adolescence to adulthood, as well as cross-sectional and longitudinal cohorts

would be required. Opportunities to address these questions are emerging through the provision of high-quality publicly available, multi-modal imaging data, which include rich cognitive and psychopathological testing as well as genetic data from collaborative initiatives such as the Human Connectome Project in Development (Somerville et al. 2018), the Adolescent Brain and Cognitive Development (Casey et al. 2018), the Philadelphia Neurodevelopmental Cohort (Satterthwaite et al. 2016) and the UK Biobank (Miller et al. 2016).

Conclusions

I comprehensively characterized the macroscale functional connectivity architecture of the human insular cortex and the subcortex using non-invasive *in vivo* functional magnetic resonance imaging in health and schizophrenia. New methodologies were proposed to address longstanding challenges in brain cartography associated with demarcating discrete boundaries and representing spatial variation as continuous gradients of gradual change. Using these new maps, I unveiled fundamental new insight into the functional organization of the human brain. Novel relationships were uncovered that link the brain's functional topography to human behavioral traits and cognition in health as well as severity of clinical symptoms in schizophrenia.

References

Abbott CC, Jaramillo A, Wilcox CE, Hamilton DA. 2013. Antipsychotic drug effects in schizophrenia: a review of longitudinal FMRI investigations and neural interpretations. Curr Med Chem 20:428-437.

Alexander GE, DeLong MR, Strick PL. 1986. Parallel organization of functionally segregated circuits linking basal ganglia and cortex. Annu Rev Neurosci 9:357-381.

Alkemade A, Keuken M, Forstmann B. 2013. A perspective on terra incognita: uncovering the neuroanatomy of the human subcortex. Frontiers in Neuroanatomy 7.

Amunts K, Kedo O, Kindler M, Pieperhoff P, Mohlberg H, Shah NJ, Habel U, Schneider F, Zilles K. 2005. Cytoarchitectonic mapping of the human amygdala, hippocampal region and entorhinal cortex: intersubject variability and probability maps. Anat Embryol (Berl) 210:343-352.

Amunts K, Malikovic A, Mohlberg H, Schormann T, Zilles K. 2000. Brodmann's areas 17 and 18 brought into stereotaxic space-where and how variable? Neuroimage 11:66-84.

Ardesch DJ, Scholtens LH, Li L, Preuss TM, Rilling JK, van den Heuvel MP. 2019. Evolutionary expansion of connectivity between multimodal association areas in the human brain compared with chimpanzees. Proceedings of the National Academy of Sciences 116:7101-7106.

Bijsterbosch JD, Woolrich MW, Glasser MF, Robinson EC, Beckmann CF, Van Essen DC, Harrison SJ, Smith SM. 2018. The relationship between spatial configuration and functional connectivity of brain regions. eLife 7:e32992.

Casey BJ, Cannonier T, Conley MI, Cohen AO, Barch DM, Heitzeg MM, Soules ME, Teslovich T, Dellarco DV, Garavan H et al. 2018. The Adolescent Brain Cognitive Development (ABCD) study: Imaging acquisition across 21 sites. Dev Cogn Neurosci 32:43-54.

Cauda F, Vercelli A. 2013. How many clusters in the insular cortex? Cereb Cortex 23:2779-2780.

Chang LJ, Yarkoni T, Khaw MW, Sanfey AG. 2013. Decoding the role of the insula in human cognition: functional parcellation and large-scale reverse inference. Cereb Cortex 23:739-749.

Cocchi L, Zalesky A. 2018. Personalized Transcranial Magnetic Stimulation in Psychiatry. Biol Psychiatry Cogn Neurosci Neuroimaging 3:731-741.

Cole MW, Bassett DS, Power JD, Braver TS, Petersen SE. 2014. Intrinsic and task-evoked network architectures of the human brain. Neuron 83:238-251.

Cole MW, Ito T, Bassett DS, Schultz DH. 2016. Activity flow over resting-state networks shapes cognitive task activations. Nat Neurosci 19:1718-1726.

Cole MW, Reynolds JR, Power JD, Repovs G, Anticevic A, Braver TS. 2013. Multi-task connectivity reveals flexible hubs for adaptive task control. Nat Neurosci 16:1348-1355.

Craig AD. 2002. How do you feel? Interoception: the sense of the physiological condition of the body. Nat Rev Neurosci 3:655-666.

Craig AD, Chen K, Bandy D, Reiman EM. 2000. Thermosensory activation of insular cortex. Nat Neurosci 3:184-190.

Dandash O, Fornito A, Lee J, Keefe RS, Chee MW, Adcock RA, Pantelis C, Wood SJ, Harrison BJ. 2014. Altered striatal functional connectivity in subjects with an at-risk mental state for psychosis. Schizophr Bull 40:904-913.

de Hollander G, Keuken MC, Forstmann BU. 2015. The Subcortical Cocktail Problem; Mixed Signals from the Subthalamic Nucleus and Substantia Nigra. PLOS ONE 10:e0120572.

de Hollander G, Keuken MC, van der Zwaag W, Forstmann BU, Trampel R. 2017. Comparing functional MRI protocols for small, iron-rich basal ganglia nuclei such as the subthalamic nucleus at 7 T and 3 T. Human Brain Mapping 38:3226-3248.

de Leon J, Diaz FJ. 2005. A meta-analysis of worldwide studies demonstrates an association between schizophrenia and tobacco smoking behaviors. Schizophr Res 76:135-157.

Dickerson BC, Fenstermacher E, Salat DH, Wolk DA, Maguire RP, Desikan R, Pacheco J, Quinn BT, Van der Kouwe A, Greve DN et al. 2008. Detection of cortical thickness correlates of cognitive performance: Reliability across MRI scan sessions, scanners, and field strengths. Neuroimage 39:10-18.

Dwyer DB, Cabral C, Kambeitz-Ilankovic L, Sanfelici R, Kambeitz J, Calhoun V, Falkai P, Pantelis C, Meisenzahl E, Koutsouleris N. 2018. Brain Subtyping Enhances The Neuroanatomical Discrimination of Schizophrenia. Schizophrenia Bulletin 44:1060-1069.

Evans AC, Janke AL, Collins DL, Baillet S. 2012. Brain templates and atlases. Neuroimage 62:911-922.

Finn ES, Huber L, Jangraw DC, Molfese PJ, Bandettini PA. 2019. Layer-dependent activity in human prefrontal cortex during working memory. Nature Neuroscience 22:1687-1695.

Finn ES, Shen X, Scheinost D, Rosenberg MD, Huang J, Chun MM, Papademetris X, Constable RT. 2015. Functional connectome fingerprinting: identifying individuals using patterns of brain connectivity. Nature Neuroscience 18:1664.

Fornito A, Arnatkevičiūtė A, Fulcher BD. 2019. Bridging the Gap between Connectome and Transcriptome. Trends in Cognitive Sciences 23:34-50.

Forstmann BU, de Hollander G, van Maanen L, Alkemade A, Keuken MC. 2016. Towards a mechanistic understanding of the human subcortex. Nature Reviews Neuroscience 18:57.

Fox MD, Snyder AZ, Vincent JL, Corbetta M, Van Essen DC, Raichle ME. 2005. The human brain is intrinsically organized into dynamic, anticorrelated functional networks. Proc Natl Acad Sci U S A 102:9673-9678.

Gabrieli JDE, Ghosh SS, Whitfield-Gabrieli S. 2015. Prediction as a humanitarian and pragmatic contribution from human cognitive neuroscience. Neuron 85:11-26.

Glasser MF, Coalson TS, Bijsterbosch JD, Harrison SJ, Harms MP, Anticevic A, Van Essen DC, Smith SM. 2018. Using temporal ICA to selectively remove global noise while preserving global signal in functional MRI data. NeuroImage 181:692-717.

Glasser MF, Coalson TS, Robinson EC, Hacker CD, Harwell J, Yacoub E, Ugurbil K, Andersson J, Beckmann CF, Jenkinson M et al. 2016a. A multi-modal parcellation of human cerebral cortex. Nature 536:171-178.

Glasser MF, Smith SM, Marcus DS, Andersson JL, Auerbach EJ, Behrens TE, Coalson TS, Harms MP, Jenkinson M, Moeller S et al. 2016b. The Human Connectome Project's neuroimaging approach. Nat Neurosci 19:1175-1187.

Goulas A, Werner R, Beul S, Säring D, Heuvel Mvd, Triarhou L, Hilgetag C. 2016. Cytoarchitectonic similarity is a wiring principle of the human connectome. In: bioRxiv.

Grasby KL, Jahanshad N, Painter JN, Colodro-Conde L, Bralten J, Hibar DP, Lind PA, Pizzagalli F, Ching CRK, McMahon MAB et al. 2020. The genetic architecture of the human cerebral cortex. Science 367:eaay6690.

Greene AS, Gao S, Scheinost D, Constable RT. 2018. Task-induced brain state manipulation improves prediction of individual traits. Nature Communications 9:2807.

Honey CJ, Sporns O, Cammoun L, Gigandet X, Thiran JP, Meuli R, Hagmann P. 2009. Predicting human resting-state functional connectivity from structural connectivity. Proceedings of the National Academy of Sciences 106:2035-2040.

Howes OD, Kambeitz J, Kim E, Stahl D, Slifstein M, Abi-Dargham A, Kapur S. 2012. The Nature of Dopamine Dysfunction in Schizophrenia and What This Means for Treatment: Meta-analysis of Imaging Studies. JAMA Psychiatry 69:776-786.

Huntenburg JM, Bazin PL, Goulas A, Tardif CL, Villringer A, Margulies DS. 2017. A Systematic Relationship Between Functional Connectivity and Intracortical Myelin in the Human Cerebral Cortex. Cereb Cortex 27:981-997.

Huntenburg JM, Bazin PL, Margulies DS. 2018. Large-Scale Gradients in Human Cortical Organization. Trends Cogn Sci 22:21-31.

Hwang K, Bertolero MA, Liu WB, D'Esposito M. 2017. The Human Thalamus Is an Integrative Hub for Functional Brain Networks. J Neurosci 37:5594-5607.

Jahanshahi M, Obeso I, Rothwell JC, Obeso JA. 2015. A fronto-striato-subthalamic-pallidal network for goal-directed and habitual inhibition. Nat Rev Neurosci 16:719-732.

Janak PH, Tye KM. 2015. From circuits to behaviour in the amygdala. Nature 517:284-292.

Kasparek T, Prikryl R, Rehulova J, Marecek R, Mikl M, Prikrylova H, Vanicek J, Ceskova E. 2013. Brain functional connectivity of male patients in remission after the first episode of schizophrenia. Hum Brain Mapp 34:726-737.

Kong R, Li J, Orban C, Sabuncu MR, Liu H, Schaefer A, Sun N, Zuo XN, Holmes AJ, Eickhoff SB et al. 2019. Spatial Topography of Individual-Specific Cortical Networks Predicts Human Cognition, Personality, and Emotion. Cereb Cortex 29:2533-2551.

Koukouli F, Rooy M, Tziotis D, Sailor KA, O'Neill HC, Levenga J, Witte M, Nilges M, Changeux J-P, Hoeffer CA et al. 2017. Nicotine reverses hypofrontality in animal models of addiction and schizophrenia. Nature Medicine 23:347.

Liégeois R, Li J, Kong R, Orban C, Van De Ville D, Ge T, Sabuncu MR, Yeo BTT. 2019. Resting brain dynamics at different timescales capture distinct aspects of human behavior. Nature Communications 10:2317.

Maia TV, Frank MJ. 2011. From reinforcement learning models to psychiatric and neurological disorders. Nature Neuroscience 14:154.

Mallikarjun PK, Lalousis PA, Dunne TF, Heinze K, Reniers RL, Broome MR, Farmah B, Oyebode F, Wood SJ, Upthegrove R. 2018. Aberrant salience network functional connectivity in auditory verbal hallucinations: a first episode psychosis sample. Transl Psychiatry 8:69.

Mesulam MM, Mufson EJ. 1982. Insula of the old world monkey. I. Architectonics in the insulo-orbito-temporal component of the paralimbic brain. J Comp Neurol 212:1-22.

Mesulam MM, Mufson EJ. 1985. The Insula of Reil in Man and Monkey. In: Peters A, Jones EG, editors. Association and Auditory Cortices Boston, MA: Springer US p 179-226.

Miller KL, Alfaro-Almagro F, Bangerter NK, Thomas DL, Yacoub E, Xu J, Bartsch AJ, Jbabdi S, Sotiropoulos SN, Andersson JL et al. 2016. Multimodal population brain imaging in the UK Biobank prospective epidemiological study. Nat Neurosci 19:1523-1536.

Mink JW. 1996. THE BASAL GANGLIA: FOCUSED SELECTION AND INHIBITION OF COMPETING MOTOR PROGRAMS. Progress in Neurobiology 50:381-425.

Moran LV, Tagamets MA, Sampath H, O'Donnell A, Stein EA, Kochunov P, Hong LE. 2013. Disruption of anterior insula modulation of large-scale brain networks in schizophrenia. Biological Psychiatry 74:467-474.

Mufson EJ, Mesulam MM. 1982. Insula of the old world monkey. II: Afferent cortical input and comments on the claustrum. J Comp Neurol 212:23-37.

Mufson EJ, Mesulam MM, Pandya DN. 1981. Insular interconnections with the amygdala in the rhesus monkey. Neuroscience 6:1231-1248.

Osher DE, Saxe RR, Koldewyn K, Gabrieli JD, Kanwisher N, Saygin ZM. 2016. Structural Connectivity Fingerprints Predict Cortical Selectivity for Multiple Visual Categories across Cortex. Cereb Cortex 26:1668-1683.

Ostrowsky K, Isnard J, Ryvlin P, Guenot M, Fischer C, Mauguiere F. 2000. Functional mapping of the insular cortex: clinical implication in temporal lobe epilepsy. Epilepsia 41:681-686.

Palaniyappan L, Simmonite M, White TP, Liddle EB, Liddle PF. 2013. Neural primacy of the salience processing system in schizophrenia. Neuron 79:814-828.

Pang L, Kennedy D, Wei Q, Lv L, Gao J, Li H, Quan M, Li X, Yang Y, Fan X et al. 2017. Decreased Functional Connectivity of Insular Cortex in Drug Naïve First Episode Schizophrenia: In Relation to Symptom Severity. PLoS One 12.

Pauli WM, Nili AN, Tyszka JM. 2018. A high-resolution probabilistic in vivo atlas of human subcortical brain nuclei. Sci Data 5:180063.

Paus T, Keshavan M, Giedd JN. 2008. Why do many psychiatric disorders emerge during adolescence? Nat Rev Neurosci 9:947-957.

Poldrack RA, Baker CI, Durnez J, Gorgolewski KJ, Matthews PM, Munafò MR, Nichols TE, Poline JB, Vul E, Yarkoni T. 2017. Scanning the horizon: towards transparent and reproducible neuroimaging research. Nat Rev Neurosci 18:115-126.

Poppenk J, Evensmoen HR, Moscovitch M, Nadel L. 2013. Long-axis specialization of the human hippocampus. Trends Cogn Sci 17:230-240.

Puckett AM, Bollmann S, Poser BA, Palmer J, Barth M, Cunnington R. 2018. Using multi-echo simultaneous multi-slice (SMS) EPI to improve functional MRI of the subcortical nuclei of the basal ganglia at ultra-high field (7T). Neuroimage 172:886-895.

Radua J, Borgwardt S, Crescini A, Mataix-Cols D, Meyer-Lindenberg A, McGuire PK, Fusar-Poli P. 2012. Multimodal meta-analysis of structural and functional brain changes in first episode psychosis and the effects of antipsychotic medication. Neuroscience & Biobehavioral Reviews 36:2325-2333.

Rinne P, Hassan M, Fernandes C, Han E, Hennessy E, Waldman A, Sharma P, Soto D, Leech R, Malhotra PA et al. 2017. Motor dexterity and strength depend upon integrity of the attention-control system. Proc Natl Acad Sci U S A.

Roberts JA, Perry A, Lord AR, Roberts G, Mitchell PB, Smith RE, Calamante F, Breakspear M. 2016. The contribution of geometry to the human connectome. Neuroimage 124:379-393.

Royer J, Paquola C, Larivière S, de Wael RV, Tavakol S, Lowe AJ, Benkarim O, Evans AC, Bzdok D, Smallwood J et al. 2019. Myeloarchitecture gradients in the human insula serve as blueprints for its diverse connectivity and function. bioRxiv:839837.

Sabuncu MR, Ge T, Holmes AJ, Smoller JW, Buckner RL, Fischl B. 2016. Morphometricity as a measure of the neuroanatomical signature of a trait. Proc Natl Acad Sci U S A 113:E5749-5756.

Salehi M, Greene AS, Karbasi A, Shen X, Scheinost D, Constable RT. 2019. There is no single functional atlas even for a single individual: Functional parcel definitions change with task. NeuroImage:116366.

Satizabal CL, Adams HHH, Hibar DP, White CC, Knol MJ, Stein JL, Scholz M, Sargurupremraj M, Jahanshad N, Roshchupkin GV et al. 2019. Genetic architecture of subcortical brain structures in 38,851 individuals. Nature Genetics 51:1624-1636.

Satterthwaite TD, Connolly JJ, Ruparel K, Calkins ME, Jackson C, Elliott MA, Roalf DR, Ryan Hopsona KP, Behr M, Qiu H et al. 2016. The Philadelphia Neurodevelopmental Cohort: A publicly available resource for the study of normal and abnormal brain development in youth. Neuroimage 124:1115-1119.

Saygin ZM, Osher DE, Koldewyn K, Reynolds G, Gabrieli JD, Saxe RR. 2011. Anatomical connectivity patterns predict face selectivity in the fusiform gyrus. Nat Neurosci 15:321-327.

Schleicher A, Palomero-Gallagher N, Morosan P, Eickhoff SB, Kowalski T, de Vos K, Amunts K, Zilles K. 2005. Quantitative architectural analysis: a new approach to cortical mapping. Anat Embryol (Berl) 210:373-386.

Seguin C, Tian Y, Zalesky A. 2020. Network communication models improve the behavioral and functional predictive utility of the human structural connectome. bioRxiv:2020.2004.2021.053702.

Shepherd GM. 2013. Corticostriatal connectivity and its role in disease. Nat Rev Neurosci 14:278-291.

Shine JM, Hearne LJ, Breakspear M, Hwang K, Müller EJ, Sporns O, Poldrack RA, Mattingley JB, Cocchi L. 2019. The Low-Dimensional Neural Architecture of Cognitive Complexity Is Related to Activity in Medial Thalamic Nuclei. Neuron 104:849-855.e843.

Small DM, Gregory MD, Mak YE, Gitelman D, Mesulam MM, Parrish T. 2003. Dissociation of neural representation of intensity and affective valuation in human gustation. Neuron 39:701-711.

Smith SM, Fox PT, Miller KL, Glahn DC, Fox PM, Mackay CE, Filippini N, Watkins KE, Toro R, Laird AR et al. 2009. Correspondence of the brain's functional architecture during activation and rest. Proceedings of the National Academy of Sciences 106:13040-13045.

Smith SM, Nichols TE, Vidaurre D, Winkler AM, Behrens T, Glasser M, Ugurbil K, Barch D, Van Essen D, Miller KL. 2015. A positive-negative mode of population covariation links brain connectivity, demographics and behavior. Nature Neuroscience 18:1565-1567.

Somerville LH, Bookheimer SY, Buckner RL, Burgess GC, Curtiss SW, Dapretto M, Elam JS, Gaffrey MS, Harms MP, Hodge C et al. 2018. The Lifespan Human Connectome Project in Development: A large-scale study of brain connectivity development in 5-21 year olds. Neuroimage 183:456-468.

Stephani C, Fernandez-Baca Vaca G, Maciunas R, Koubeissi M, Luders HO. 2011. Functional neuroanatomy of the insular lobe. Brain Struct Funct 216:137-149.

Stephenson-Jones M, Samuelsson E, Ericsson J, Robertson B, Grillner S. 2011. Evolutionary Conservation of the Basal Ganglia as a Common Vertebrate Mechanism for Action Selection. Current Biology 21:1081-1091.

Strange BA, Witter MP, Lein ES, Moser EI. 2014. Functional organization of the hippocampal longitudinal axis. Nature Reviews Neuroscience 15:655-669.

Tadić B, Andjelković M, Melnik R. 2019. Functional Geometry of Human Connectomes. Scientific Reports 9:12060.

Tavor I, Jones OP, Mars RB, Smith SM, Behrens TE, Jbabdi S. 2016. Task-free MRI predicts individual differences in brain activity during task performance. Science 352:216-220.

Thompson CL, Pathak SD, Jeromin A, Ng LL, MacPherson CR, Mortrud MT, Cusick A, Riley ZL, Sunkin SM, Bernard A et al. 2008. Genomic anatomy of the hippocampus. Neuron 60:1010-1021.

Uddin LQ. 2015. Salience processing and insular cortical function and dysfunction. Nat Rev Neurosci 16:55-61.

Uddin LQ, Kinnison J, Pessoa L, Anderson ML. 2014. Beyond the tripartite cognition-emotion-interoception model of the human insular cortex. J Cogn Neurosci 26:16-27.

van den Heuvel MP, Scholtens LH, Feldman Barrett L, Hilgetag CC, de Reus MA. 2015. Bridging Cytoarchitectonics and Connectomics in Human Cerebral Cortex. The Journal of Neuroscience 35:13943-13948.

Van Essen DC, Dierker DL. 2007. Surface-Based and Probabilistic Atlases of Primate Cerebral Cortex. Neuron 56:209-225.

Vogel JW, La Joie R, Grothe MJ, Diaz-Papkovich A, Doyle A, Vachon-Presseau E, Lepage C, Vos de Wael R, Thomas RA, Iturria-Medina Y et al. 2020. A molecular gradient along the longitudinal axis of the human hippocampus informs large-scale behavioral systems. Nat Commun 11:960.

Wang C, Ji F, Hong Z, Poh JS, Krishnan R, Lee J, Rekhi G, Keefe RSE, Adcock RA, Wood SJ et al. 2016. Disrupted salience network functional connectivity and white-matter microstructure in persons at risk for psychosis: findings from the LYRIKS study. Psychological Medicine 46:2771-2783.

Wotruba D, Michels L, Buechler R, Metzler S, Theodoridou A, Gerstenberg M, Walitza S, Kollias S, Rossler W, Heekeren K. 2014. Aberrant coupling within and across the default mode, task-positive, and salience network in subjects at risk for psychosis. Schizophr Bull 40:1095-1104.

Xia CH, Ma Z, Ciric R, Gu S, Betzel RF, Kaczkurkin AN, Calkins ME, Cook PA, García de la Garza A, Vandekar SN et al. 2018. Linked dimensions of psychopathology and connectivity in functional brain networks. Nature Communications 9:3003.

Zwirner J, Möbius D, Bechmann I, Arendt T, Hoffmann K-T, Jäger C, Lobsien D, Möbius R, Planitzer U, Winkler D et al. 2017. Subthalamic nucleus volumes are highly consistent but decrease age-dependently—a combined magnetic resonance imaging and stereology approach in humans. Human Brain Mapping 38:909-922.